Crystallography Reports, Vol. 46, No. 3, 2001, pp. 341–348. Translated from Kristallografiya, Vol. 46, No. 3, 2001, pp. 391–398.
Original Russian Text Copyright © 2001 by Lider, Baronova, Stepanenko.

DIFFRACTION AND SCATTERING OF X-RAY AND SYNCHROTRON RADIATION

Experimental Characterization of Bent Focusing Crystals

V. V. Lider*, E. O. Baronova, and M. M. Stepanenko****

** Shubnikov Institute of Crystallography, Russian Academy of Sciences,*
Leninskiĭ pr. 59, Moscow, 117333 Russia
*** Russian Research Centre Kurchatov Institute, pl. Kurchatova 1, Moscow, 123182 Russia*

Received November 4, 1999

Abstract—It has been established with the aid of a double-crystal X-ray diffractometer that the nonuniform curvature of cylindrically, spherically, or thoroidally bent silicon and quartz crystals is of a periodic character. It is shown that this periodicity influences the spectral (energy) resolution of a focusing crystal, which becomes noticeable at the Bragg angle θ obeying the condition $\tan^2\theta \gg 1$. *© 2001 MAIK "Nauka/Interperiodica".*

INTRODUCTION

Bent crystals are widely used as focusing optical elements in X-ray spectroscopy [1–3] and microdiffraction [4, 5].

The main parameters characterizing a bent crystal as an element of X-ray optics are the integrated intensity, the energy (spectral) resolution, and the dimension of the formed focus. The first parameter can be determined theoretically [4, 6]. As is shown in the next section, the second and the third parameters are essentially dependent on the width of the intrinsic rocking curve and the adjustment conditions, i.e., the deviation of the local curvature from the set value.

The present study is aimed at the experimental determination of the curvature nonuniformity of the crystal subjected to forced bending (a crystal rigidly fixed on the substrate and thus acquiring the substrate shape).

OPTICS OF A BENT CRYSTAL

The conditions for a crystal bending to the curvature ρ is given by the expression

$$2\rho = \gamma_0/p + \gamma_h/q, \tag{1}$$

where p is the distance between the source of the polychromatic X-ray radiation and the crystal (segment SO in Fig. 1); q is the crystal–focus distance (OF); and γ_0 and γ_h are the directional cosines of the incident and the diffracted X-ray beams, respectively.

For the spectral band $\Delta\lambda/\lambda$ of such a crystal, the following formula is valid [4]:

$$\Delta\lambda/\lambda = (L/2)(\gamma_0/p - \gamma_h/q)\cot\theta, \tag{2}$$

where L is the illuminated region of the focusing crystal, λ is the radiation wavelength, and θ is the Bragg angle. In this case, the angular sweep of the spectral transmission band is used for recording emission [1] and absorption (EXAFS) [2, 3] spectra.

If a point radiation source and a bent crystal are located on the Rowland circle of radius $R = 1/2\rho$, the focus should also lie on the Rowland circle, so that the following conditions are fulfilled:

$$p_0 = \gamma_0/\rho, \quad q_0 = \gamma_h/\rho. \tag{3}$$

Then, as follows from formulas (2) and (3), we obtain achromatic focusing. Then, for an extended radiation source S, it is necessary to place the recording device M_1M_2 (a photographic film, one-dimensional positional detector, etc.) also onto the Rowland circle, where $p_0 = N_1O$ and $q_0 = OM_1$ (Fig. 1).

The spectral resolution $\delta\lambda/\lambda$ of the focusing crystal is limited by several parameters such as the halfwidth of its rocking curve, ω, the transverse size w of the radi-

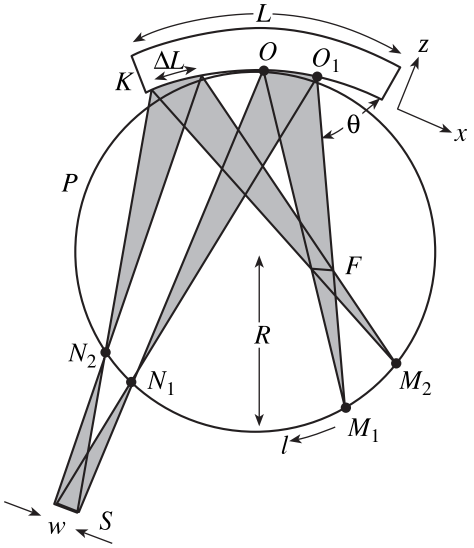

Fig. 1. Johann focusing scheme; K is a bent crystal, S is a source of X-ray radiation, P is a Rowland circle, and θ is the Bragg angle.

ation source, and also the inaccurate fulfillment of the following conditions for achromatic focusing [5, 6]:

$$\delta\lambda/\lambda = \delta\theta\cot\theta, \qquad (4a)$$

$$\delta\theta = ((w/p)^2 + \omega^2 + \beta^2)^{1/2}, \qquad (4b)$$

where β is the divergence of the diffracted X-rays caused by the violation of conditions (3) because of the change in the source–crystal distance p_0 (the point N_1 in Fig. 1 is an imaginary point source) and the change in the curvature along the surface of a bent crystal. It should also be noted that, in fact, the "aberration size" of the focus depends on the same parameters as its spectral resolution [4, 5] and is defined as $q\delta\theta$.

The conditions for achromatic focusing for the Johann optical scheme (Fig. 1) [4, 5] are rigorously fulfilled only for point O of the crystal surface, which lies on the Rowland circle. Since the radius of the Rowland circle is twice as small as the curvature radius, the relationship (3) becomes invalid for the peripheral regions of the crystal. In turn, this results in the appearance of the so-called defocusing parameter β_1, whose value for the symmetric diffraction (where $\gamma_0 = \gamma_h = \sin\theta$) is determined by the following formula [6]:

$$\beta_1 = (\rho L/m)|6m^2 - 8m + 1|(\cos\theta)/8, \qquad (5)$$

where $m = p/p_0$ and $1/2 < m < \infty$.

There are two efficient methods for reducing defocusing: (1) the use of the Johannson defocusing scheme [4, 5] for which the working surface of the crystal is preliminarily given the shape of a circular cylinder, so that upon its bending, the whole surface would be located on the Rowland circle and (2) the use of the focusing crystal in the shape of an elliptical cylinder [3].

The other difficulty that can be encountered is the local deviation of the curvature from the set value. Such deviations can be caused by shortcomings inherent in the device used for bending of a crystal or preparation (in the case of a focusing crystal of a varying curvature), the poor contact of the crystal with the substrate, and the insufficient quality of the surface (in "forced" bending). It follows from Fig. 1 and formulas (1) and (2) that for the symmetric diffraction, the following condition should be fulfilled:

$$\beta_2 = \Delta\rho w/|m - 1|, \qquad (6a)$$

where $\Delta\rho$ is the deviation of the crystal curvature from its set value.

For the achromatic focusing ($m = 1$), we have

$$\beta_2 = \Delta\rho L. \qquad (6b)$$

A special attention should be given to the halfwidth of the intrinsic rocking curve of a bent crystal. It is well known [4, 7] that the rocking-curve shape and, therefore, also the FWHM depend on the "force" B [see (7)] changing the trajectory of an X-ray beam propagating in a crystal with a deformation gradient. For a constant deformation gradient (it should be remembered that such a deformation is caused by elastic bending) and the symmetric Bragg diffraction, we have

$$B = (\Lambda/2\pi)^2|\mathbf{H}|(\rho_x\cot^2\theta - K(\rho_x + \rho_y)), \qquad (7)$$

where Λ is the extinction length of an ideal crystal [4], $\mathbf{H}$ is the diffraction vector, ρ_x is the bending curvature in the meridian (diffraction) plane, and ρ_y is the curvature of the sagittal bending [4, 8]. (The orthogonal reference system is chosen in such a way that the z-axis is normal to the crystal surface and the x-axis lies in the diffraction plane, Fig. 1.) The sagittal bending is used to focus an X-ray beam along the y-axis. To focus an X-ray beam into a point, it is necessary that the condition $\rho_x = \rho_y\sin^2\theta$ should be met [8]. It was shown [1] that toroidal and spherical bending provide a sufficiently good focusing at moderate ($\theta > 45°$) and large ($\theta > 85°$) Bragg angles, respectively.

It has also been established [7] that at forced bending, the coefficient K in Eq. (7), dependent on the elastic constants of the crystal, has a low anisotropy for the (10.0)-oriented quartz. For the (10.1)-oriented quartz, the maximum K-value (0.289) is observed along the [1–2.0] direction, whereas the minimum value (0.072), along the normal direction. In the isotropic approximation, we have $K = \nu/(1 - \nu)$, where ν is Poisson's ratio.

The above stated allows us to assume that the following relationship is valid:

$$\omega \approx \omega_0 + \Delta\omega(B), \qquad (8)$$

where ω_0 is the halfwidth of the intrinsic rocking curve from an undeformed crystal and $\Delta\omega(B)$ is an increase in the FWHM due to elastic bending. Usually, $\Delta\omega(B) \gg \omega_0$ at $B > 1$. However, as follows from Eq. (7), the gradient parameter B at large Bragg angles can have such a low value that $\Delta\omega(B) \approx 0$.

It should be noted that with an increase of the parameter B, the integrated intensity of the focused beam also increases although at a lower rate than the halfwidth of the rocking curve [4, 9].

SPECIMENS STUDIED

The specimens studied were plane-parallel crystalline silicon wafers and quartz plates of various thicknesses and orientations, which were either rigidly glued to the substrate surface or were brought in the optical contact with it in such a way that the working surface of the wafer or plate would inherite the substrate shape.

Single crystal silicon wafers 100 mm in diameter and ~150 μm in thickness had the (110)-oriented surfaces and were glued onto aluminum substrates with a specially made polished spherical deepening with a radius of 85 cm. Prior to experiments, both wafer sur-

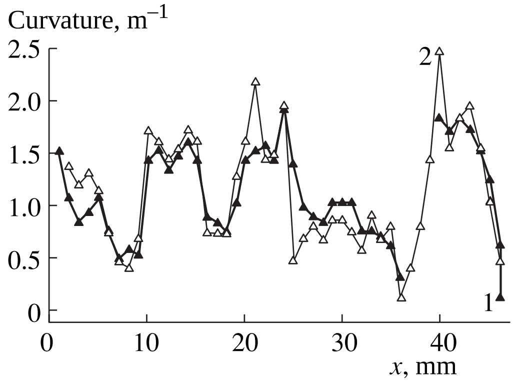

Fig. 2. Variation in the curvature of a spherically bent silicon wafer (specimen no. 1) along its radius determined by (–▲–) method 1, and (–△–) method 2.

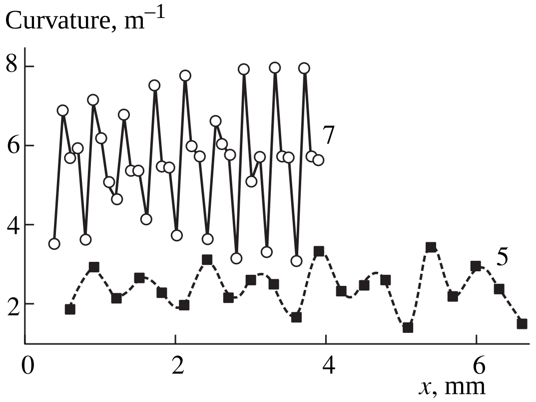

Fig. 3. The variation in the curvature along the diameter of spherically bent quartz specimens nos. 5 and 7.

faces were thoroughly ground. The damaged layer thus formed was removed away from the working surface by chemical–mechanical polishing.

The quartz specimens were 80- to 100-μm-thick crystalline plates in the optical contact [10] with the spherical, toroidal, or cylindrical fused-quartz substrates. The accuracy of substrate preparation along the radius was 0.1 mm. The optical contact is a junction of two surfaces without any intermediate layer of a varying thickness (glue) which provides a high quality of the surface thus obtained. In our case, the quality of the substrates and the crystal surfaces in contact with these substrates were checked by optical methods. The results obtained showed that the substrate surfaces and the surfaces of bent crystals participating in the an optical contact matched with a high accuracy.

The initial quartz crystals were plane parallel within 10″, the deviation of the reflecting planes from the mechanically treated crystal surface did not exceed 1.5 min. In order to improve the reflectivity characteristics, the crystals were also chemically polished.

The crystals thus prepared are widely used in X-ray spectrometry. They are also used for focusing an X-ray beam in two mutually perpendicular planes, including the case of the successive diffraction from two bent crystals [11].

EXPERIMENTAL METHODS

The curvature of nonuniform bending of crystals was studied on a double-crystal diffractometer by two methods.

Method 1 is based on recording the spectral K_α doublet in the nonparallel diffraction scheme (n, $-m$) [5]. The bending curvature was determined from the measured angular spacing between the doublets, $\Delta\theta_{obs}$:

$$\rho = \Delta\theta/\Delta x, \tag{9a}$$

$$\Delta\theta = \Delta\theta_0 - \Delta\theta_{obs}, \tag{9b}$$

$$\Delta\theta_0 = (\Delta\lambda/\lambda)|\tan\theta_0 - \tan\theta_M|, \tag{9c}$$

$$\Delta x = (\Delta\lambda/\lambda)p\tan\theta_M/\sin\theta_0, \tag{9d}$$

where $\Delta\theta_0$ are the angular distances between the doublets at $\rho = 0$ and $\Delta\lambda/\lambda = 2(\lambda_2 - \lambda_1)/(\lambda_2 + \lambda_1)$, λ_1, λ_2 corresponding to the wavelengths of the spectral lines α_1, α_2; θ_0 and θ_M are the Bragg angles of the specimen and the monochromator; and Δx is the spacing between the points of beam intersections corresponding to the spectral lines of the doublet with the crystal surface.

However, this method has several drawbacks. First, the dispersive diffraction geometry makes the method sensitivity to small changes in the halfwidth of the rocking curves very low. Second, the method locality, set by the parameter Δx [formula (9d)], is limited by the geometry of the experiment.

Method 2 is based on recording a number of rocking curves from a continuously and automatically rotated bent crystal and simultaneously displaced, for discrete steps Δx. Thus, we have

$$\rho = \Delta\psi/\Delta x, \tag{10a}$$

$$\Delta x > \omega/\rho, \tag{10b}$$

where $\Delta\psi$ is the angular spacing between two neighboring rocking curves. The use of the quasiparallel diffraction geometry (n, $-n$), Eq. (5), provides a higher accuracy of the determination of $\Delta\psi$ and the curve similar to the intrinsic rocking curve, i.e., improves the locality characteristics of the method.

In order to obtain the correct experimental data by method (2), the diffractometer should meet the following requirements:

(i) the mechanism of the linear translation of the specimen should not introduce any noticeable error into the measured $\Delta\psi$ values;

(ii) in order to exclude the systematic error in the determined Δx values, the diffractometer should be preliminarily adjusted in such a way that an incident X-ray

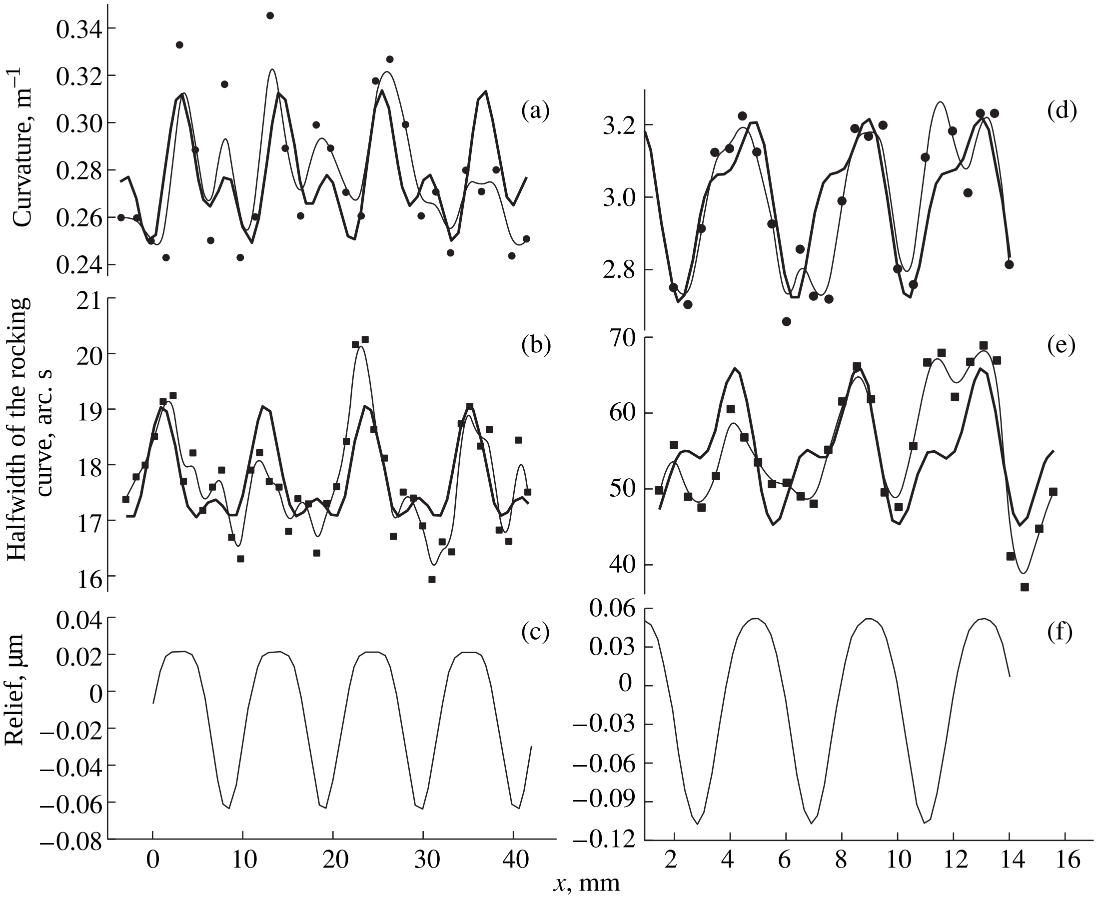

Fig. 4. (a, d) Variations in the curvature, (b, e) the rocking-curve halfwidth and (c, f) the surface-relief profile calculated by Eq. (14) at (c) $k = -0.51$ and (f) $k = -0.35$ for spherically and toroidally bent (a, b, c) quartz specimen no. 4 and (d, e, f) quartz specimen no. 6. Thin lines (a, b, d, e) correspond to the approximation by a spline, solid lines correspond to the calculation by Eqs. (13) and (14) with the use of the experimental data and the least squares method.

beam and the specimen surface should lie on the diffractometer axis, normal to the diffraction plane.

RESULTS AND DISCUSSION

Figure 2 shows the curvature of silicon specimen no. 1 on the coordinate of its surface (the coordinate $x = 0$ corresponds to the specimen center) obtained by the above two methods. It is seen that both methods yield practically the same results. Because of the reasons considered in the previous section, we use method 2 in what follows.

The curves similar to those shown in Fig. 2 were also obtained for all the other six specimens. The relative measurement error did not exceed 3%. For all the specimens, the dependence $\rho(x)$ is of a periodic character (Figs. 3, 4a, and 4d). The dependence $\omega(x)$ is also periodic (the average measurement error is 0.5″ and usually correlates with $\rho(x)$ (Figs. 4b, 4e), which confirms the validity of Eq. (8). The characteristic feature here is the formation of a period not by one but by two maxima (minima). This can be explained either by the presence of the second mode or the existence of a certain mathematical law governing this periodicity.

Assuming the existence of such a mathematical law and taking into account the analogy with the crystals with the epitaxial film of a variable composition subjected to forced bending [12], we can state that the lattices of the bent crystal and the heterolayer should accommodate themselves to the substrate lattice. As a result, the "latent" bending moments arise [7]. Using this analogy, the angular spacing between the neighboring rocking curves obtained in symmetric diffraction can be written in the form [13]

$$\Delta\psi = \Delta\psi_0 + \partial u_z/\partial x - (\partial u_z/\partial z)\tan\theta + \delta\psi, \qquad (11)$$

where u_z is the displacement along the z-axis, $\Delta\psi_0$ is the angular spacing determining the average curvature ρ_0, and $\delta\psi$ is the correction for the angular displacement of the rocking curve caused by the deformation gradient [12]. The estimation of this correction is given in Appendix.

Using the experimental results obtained, we can represent the displacement u_z as a product of the peri-

Experimental conditions and characterization of bent crystals

Specimen	Material, surface shape	Thickness, μm	Reflection, radiation	Monochromator	θ_0, θ_M, deg	ρ_0, m^{-1}	$\Delta\rho$, m^{-1}	T, mm	h, μm	$\Omega_x \times 10^4$	$\Omega_z \times 10^4$	$\Omega_y \times 10^4$ ($m = 2$)
1	Si, sphere	150	(440) $Cu_{K\alpha}$	(440) Si (100)	53.3 53.3	1.11	0.42	9.8	1.0	4.1	0.7	10.1
2	Si, sphere	150	(440) $Cu_{K\alpha}$	(440) Si (100)	53.3 53.3	1.21	0.11	9.3	0.25	1.1	0.7	2.16
3	Quartz, cylinder	100	(10.1) $Cu_{K\alpha}$	(111) Si (111)	13.3 14.2	2.1	0.07	0.80	1.2×10^{-3}	0.06	0.11	0
4	Quartz, sphere	100	(24.0) $Co_{K\alpha}$	(331) Si (111)	46.7 45.9	0.29	1.7×10^{-2}	10.4	4.3×10^{-2}	0.17	0.10	0.42
5	Quartz, sphere	100	(10.1) $Cu_{K\alpha}$	(111) Si (111)	13.3 14.2	2.4	0.26	1.51	1.5×10^{-2}	0.39	1.22	0.98
6	Quartz, toroid	80	(10.1) $Co_{K\alpha}$	(111) Si (111)	15.5 16.9	3.0	0.17	4.0	0.07	0.69	2.77	1.72
7	Quartz, sphere	100	(20.0) $Cu_{K\alpha}$	(111) Si (111)	21.2 14.2	5.56	1.27	0.40	5.2×10^{-3}	0.52	0.64	1.78

odic function $F(x)$ and the function $f(z)$ monotonically decreasing with the argument, so that $f(0) = 1$. Then, it follows from Eq. (11) that

$$\begin{aligned}\Delta\psi \approx \Delta\psi_0 + f(z)(\partial F(x)/\partial x) \\ -(\partial f(z)/\partial z)F(x)\tan\theta.\end{aligned} \tag{12}$$

Since $\rho = \partial(\Delta\psi)/\partial x$, we obtain

$$\rho \approx \rho_0 + \Delta\rho(x) - f'(t)(\partial F(x)/\partial x)\tan\theta, \tag{13a}$$

$$\Delta\rho(x) = f(t)(\partial^2 F(x)/\partial x^2). \tag{13b}$$

Here, $f(t)$ and $f'(t)$ are the function $f(z)$ and its first derivative with respect to z averaged over the depth t of X-ray penetration into the crystal. Since the penetration depth of the radiation into a bent crystal is limited by the linear absorption coefficient μ [4, 7], we have $t = \sin\theta/2\mu$.

Let us choose as a periodic function in the form

$$\begin{aligned}F(x) = h\sin(2\pi x/T)(1 + k\sin(2\pi x/T)), \\ (-1 \le k \le 1),\end{aligned} \tag{14}$$

where T is the period and h is the amplitude. This choice is justified by the fact that the first and the second derivatives of this function in formulas (13) include the trigonometric function of a doubled argument. This can explain the experimentally observed frequency of the periodic dependence $\rho(x)$.

Choosing the function $f(z)$ as the exponential dependence $\exp(-z/\tau)$; taking into account that under the specified experimental conditions (see table) $\sin\theta/2\mu\tau \ll 1$; and using the experimental data, formulas (13) and (14), and the least squares procedure, one can determine the parameters h, T, and $\Delta\rho = f(t)$, $F''(T)$ (where $F''(T)$ is the second derivative of the function $F(x)$ averaged over the half-period calculated for each

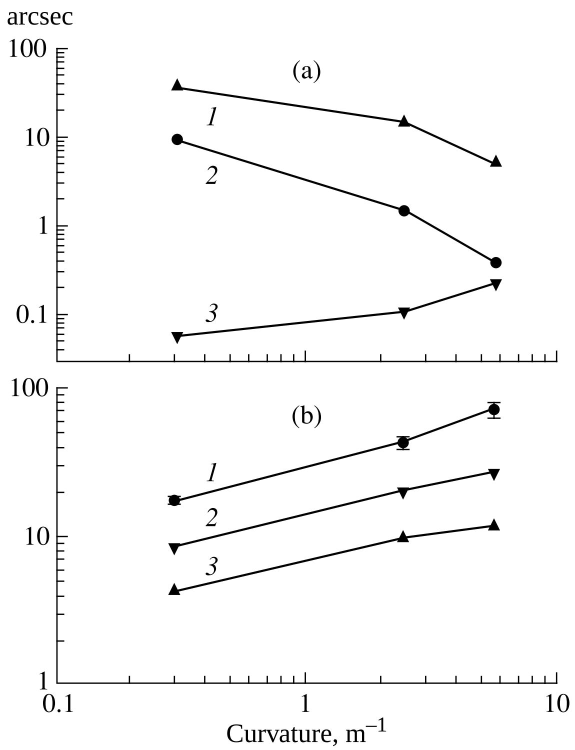

Fig. 5. (a) Periodic structural parameters (*1*) amplitude *h* (nm), (*2*) period *T* (mm), (*3*) averaged relative change in curvature $\Delta\rho/\rho_0$ as functions of crystal curvature and (b) dependence of parameters determining the spectral resolution of a focusing crystal (*1*) $\omega \pm \delta\omega$ (*B*) halfwidth of the rocking curve and its mean-square deviation $\delta\omega$ over the specimen, (*2*) mosaicity Ω, and (*3*) mosaicity $(\Omega_y)_{av}$ on crystal curvature.

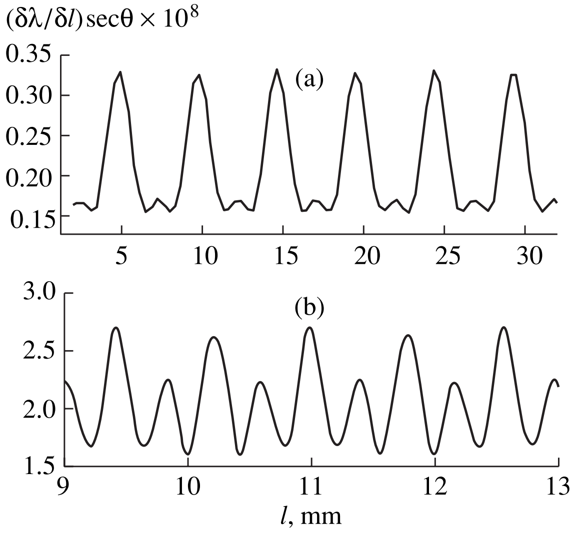

Fig. 6. Periodicity in dispersion variation $\partial\lambda/\partial l$ (where *l* is the detector coordinate) for specimens (a) no. 1 and (b) no. 5 calculated by Eqs. (17) and (13) at (a) $k = -0.24$, $2d = 1.92$ Å and (b) $k = -0.95$, $2d = 6.68$ Å and other parameters listed in table.

specimen). The results obtained are tabulated. We made an attempt to establish the laws governing the variation of these parameters depending on the function of the curvature for spherically bent quartz specimens of equal thicknesses (nos. 4, 5, and 7) (Fig. 5a).

We also determined the values of the parameter *k* in Eq. (14), but it produces an effect at the surface profile alone (Figs. 4c, 4f), which is reflected in the function $F(x)$ under the assumption that the surface has the zero roughness (is smooth). The minimum value of the parameter τ characterizing the "superlattice thickness" is ~55 μm, which is consistent with the above approximation $t/\tau \ll 1$.

If the condition

$$T \le \Delta L \tag{15}$$

is fulfilled, where $\Delta L = w/|m-1|$ is the bent-crystal region focusing the X-ray beam achromatically into a point on the Rowland circle without chromatic aberration (the points M_1 and M_2 in Fig. 1), then an observer would "see" such a periodic variation in the bending curvature as certain mosaicity Ω. Using formula (12), one can assume that

$$\Omega^2 = \Omega_x^2 + \Omega_z^2\tan^2\theta, \tag{16a}$$

$$\Omega_x = f(t)F'(T), \tag{16b}$$

$$\Omega_z = f'(t)F(T), \tag{16c}$$

where $F(T)$ and $F'(T)$ are the function $F(x)$ and its first derivative averaged over the half-period $T/2$, respectively. The values of Ω_x and Ω_z calculated by Eqs. (16b) to (16c) are given in the table.

One can obtain the formulas relating the spatial dispersion $\partial\lambda/\partial l$ and the bending curvature of the crystal by considering Fig. 1 and using formula (2):

$$\partial\lambda/\partial l = 2\rho(x)d\cos\theta, \tag{17}$$

where $\rho(x) = \rho_0 + \Delta\rho(x)$ [see formulas (13)], *l* is the coordinate along the detector (recording device, Fig. 1), and *d* is the interplanar spacing. If the "transfer function" $\rho(x)$ is periodic, the detector records the spectral distribution $\delta\lambda(l)$ with a certain distortion characterized by the function $\partial F^2(x)/\partial x^2$ [see formulas (13a) and (13b)]. Figure 6 shows the dispersion $(\partial\lambda/\partial l)\sec\theta$ as a function of the coordinate *l* for specimens nos. 1 and 5.

In the case of sagittal X-ray focusing onto the Rowland circle used to increase the sensitivity of the spectral analysis [8], the detector records X-rays reflected from the regions of the crystal lying on both sides of the meridian line formed by intersecting diffraction plane and the crystal surface. The period of the curvature variation in these regions does not necessarily coincide with the analogous period along the meridian line; therefore, the detector can record the regions where the dependences $(\delta\lambda/l)(l)$ corresponding to the meridian and sagittal focusing are in antiphase. This results in a new source of deterioration of the spectral resolution—

$(\Delta\lambda/\lambda)_y$. It follows from Eq. (17) and the relationship $\partial L/\partial l = m/|m-1|$ obtained from the optical-scheme geometry (Fig. 1) that

$$(\delta\lambda/\lambda)_y = \Omega_y \cot\theta, \tag{18a}$$

$$\Omega_y = (|m-1|/m)(T/2)\Delta\rho, \quad 0 < |m-1|/m < 1. \tag{18b}$$

The values $(\Omega_y)_{\text{av}}$ calculated for the averaged value $(|m-1|/m)_{\text{av}} = 0.5$ are also indicated in the table.

With due regard for formulas (3) and (6a), formulas (4a) and (4b) acquire the form

$$\delta\lambda/\lambda = ((w/p)^2(1+(\beta^*)^2) + \beta_1^2 + \omega^2 + \Omega^2 + \Omega_y^2)^{1/2}\cot\theta, \tag{19}$$

where $\beta^* = \beta_2 p/w = (\Delta\rho/\rho_0)m\sin\theta/|m-1|$ is the correction to the contribution of the transverse dimension of the radiation source, which is associated with the nonuniformity of the bending curvature, to the spectral resolution of the crystal. It is seen from Fig. 5a and the tabulated data that the $\Delta\rho/\rho_0$ value has the tendency to increase with an increase of the bending curvature and can attain a value of several dozen percent. However, the use of the optimum experimental conditions allows one to attain the situation where $(\beta^*) \ll 1$.

It seems that, in the first approximation, the mosaicity Ω and Ω_y can also be considered as the corrections to the contribution of the halfwidth of the rocking curve to the spectral resolution of the focusing crystal, which is confirmed, e.g., by the plot in Fig. 5b for a spherically bent quartz crystals of the same thickness (see table). The only exception is the case of large Bragg angles, i.e., $\tan^2\theta \gg 1$. As follows from Eqs. (7), (8), and (16a), the spectral resolution is determined here not by the halfwidth of the rocking curve but by its mosaicity Ω.

The periodicity of the dependence of crystal curvature on the surface coordinate is beyond the scope of the present study. Nevertheless, in view of the analogy between the forced crystal bending and the heteroepitaxial film, it is worth mentioning the data obtained in [14]. It was shown that the sinusoidal change in the displacements u_z and u_x along the surface for some epitaxial films reduces the elastic energy of the heterostructure.

The question whether the periodic displacement u_z along the surface normal is the key factor of the giving rise to the periodicity in crystal curvature or whether it is simply deformation relaxation caused by the displacement u_x along the surface cannot be answered using the experimental data obtained on the symmetric reflections alone [13].

CONCLUSIONS

It has been shown that a bent crystal can be characterized as an element of X-ray optics using the data of the double-crystal X-ray diffractometry.

It has been proved experimentally that the change of the crystal curvature irrespectively of the method of the crystal fixation on the substrate (glue or optical contact) and the bending shape (a cylinder, a sphere, a toroid) is of a periodic character.

The variation in the rocking-curve halfwidth along the bent crystal is also of a periodic character and usually correlates with the variation in the crystal curvature. This confirms the dependence of the rocking-curve halfwidth on the deformation gradient.

The periodicity observed seems to be explained by relaxation of elastic stresses caused by the specific features of crystal bending. It manifests itself in the periodic displacement along the surface normal, which is satisfactorily described by the function represented as a sum of sines and squared sines. It is shown that the displacement amplitudes and the periods, with the other conditions (crystal thickness, shape of its bending) being the same, decrease with an increase of the crystal curvature, whereas the values of the parameters determining the optical characteristics of the focusing crystal increase.

The effect of the periodicity of the crystal curvature on its spectral (energy) resolution becomes noticeable at $\tan^2\theta \gg 1$.

APPENDIX

It was shown [12] that the displacement of the maximum of the rocking-curve of the crystal caused by a constant deformation gradient can be estimated by analytical expressions. Using Eq. (7) and Eqs. (9) and (10) from [12], we find that the displacement of the rocking-curve maximum $\delta\psi$ caused by the curvature variation $\delta\rho$ is

$$\delta\psi \approx 0.61\delta\rho(d/\rho_0)^{1/2}((1-\nu)/\nu - 2\tan^2\theta)^{1/2}. \tag{A.1}$$

The relative error in the determination of the local bending curvature can be evaluated from the expression $2(\delta\psi)_{\max}/\Delta\theta(T)$, where $(\delta\psi)_{\max}$ is determined from formula (A.1) at $\delta\rho = 2\Delta\rho$, and $\Delta\theta(T)$ is the angle of crystal rotation necessary for providing X-ray diffraction upon the beam displacement by the period T: $\Delta\theta(T) \approx \rho_0 T$. Thus, the relative error for specimen no. 7 evaluated from the parameters indicated in the table and in [7] amounts to 2.6%. For other specimens studied, the relative error is even less.

It should also be noted that the relative error is systematic. The allowance for this error only slightly changes the parameters ρ_0, $\Delta\rho$ listed in the table.

ACKNOWLEDGMENTS

The authors are grateful to M.V. Kovalchuk for his interest in their study, N.V. Zhavoronkov for preparing silicon specimens, and A.A. Dyshekov for the useful discussion of the results.

REFERENCES

1. E. Forster, K. Gable, and I. Uschmann, Laser Part. Beams **9**, 135 (1991).
2. T. Matsushita and R. P. Phizackerley, Jpn. J. Appl. Phys. **20** (11), 2223 (1981).
3. H. Tolentino, F. Baudelet, E. Dartyge, *et al.*, Nucl. Instrum. Methods Phys. Res. A **289**, 307 (1990).
4. R. Caciuffo, S. Melone, F. Rustichelli, and A. Boeuf, Phys. Rep. **152** (1), 1 (1987).
5. T. Matsushita and H.-O. Hashizume, in *Handbook on Synchrotron Radiation*, Ed. by E. E. Koch (North-Holland, Amsterdam, 1983), Vol. 1A, pp. 261–314.
6. M. Lemonnier, R. Fourme, F. Rousseaux, and R. Kahn, Nucl. Instrum. Methods **152**, 173 (1978).
7. F. N. Chukhovskii, G. Holzer, O. Wohrhan, and E. Forster, J. Appl. Crystallogr. **29**, 438 (1996).
8. E. Forster, E. E. Fill, K. Gabel, *et al.*, J. Quant. Spectrosc. Radiat. Transf. **51** (1/2), 101 (1994).
9. A. Boeuf, S. Lagomarsino, S. Mazkedian, *et al.*, J. Appl. Crystallogr. **11**, 442 (1978).
10. A. B. Gil’varg, Dokl. Akad. Nauk SSSR **72** (3), 489 (1950).
11. P. Kirkpatrick and A. V. Baez, J. Opt. Soc. Am. **39**, 766 (1948).
12. V. V. Lider, F. N. Chukhovskiĭ, Yu. P. Khapachev, and M. N. Barashev, Fiz. Tverd. Tela (Leningrad) **31** (4), 74 (1989) [Sov. Phys. Solid State **31**, 587 (1989)].
13. F. N. Chukhovskiĭ and V. V. Lider, Kristallografiya **38** (4), 259 (1993) [Crystallogr. Rep. **38**, 567 (1993)].
14. F. Glas, J. Appl. Phys. **62** (8), 3201 (1987).

Translated by L. Man

Crystallography Reports, Vol. 46, No. 3, 2001, pp. 349–354. Translated from Kristallografiya, Vol. 46, No. 3, 2001, pp. 399–404.
Original Russian Text Copyright © 2001 by Nosik.

Suppression of Anomalous X-ray Transmission under the Effect of Periodic Nonresonance Deformations

V. L. Nosik
Shubnikov Institute of Crystallography, Russian Academy of Sciences, Leninskiĭ pr. 59, Moscow, 117333 Russia
e-mail:koval@ns.crys.ras.ru

Received July 27, 2000

Abstract—An analytical theory for interpreting the suppression of the Borrmann effect in the Laue diffraction from thick crystals with the deformation superlattice with the period exceeding the extinction length has been developed. The theory has been used to describe the diffraction from hematite crystals in which the domain structure is rearranged in an applied magnetic field. *© 2001 MAIK “Nauka/Interperiodica”.*

INTRODUCTION

Dynamical diffraction of X-rays and neutrons from perfect crystals with superlattices have repeatedly been studied both theoretically and experimentally [1–7]. The constant interest in such studies is associated with the effective control over the X-ray and synchrotron-radiation beams provided by time-periodic distortion of the reflecting planes in crystals. Depending on the ratio of the extinction length Λ to the ultrasonic wavelength λ_s, one distinguishes the high-frequency ultrasound with $\Lambda \gg \lambda_s$, [2, 8], X-ray acoustic resonance with $\Lambda \simeq \lambda_s$ [3, 4], and low-frequency ultrasound with $\Lambda \ll \lambda_s$ [5]. In the first case (high-frequency ultrasound), the rocking curves are characterized by the presence of the so-called satellites (independent reflections corresponding to diffraction with the participation of one or several coherent phonons). In the X-ray acoustic resonance, the position of the first satellite coincides with or is close to the position of the main reflection, which results in the rearrangement of the structure of Bloch waves [9]. One of the most obvious manifestations of the X-ray acoustic resonance is the suppression of anomalous transmission of X-rays in thick crystals in Laue diffraction ($\mu t \geq 10$, where μ is the linear absorption coefficient and t is the crystal thickness) [10, 11].

As is well known, anomalous X-ray transmission (the so-called Borrmann effect) is associated with the formation of two Bloch waves in the dynamical diffraction—one with the antinodes lying in the crystallographic planes (a strongly absorbed wave) and the other with antinodes lying between these planes (a weakly absorbed wave). The ultrasonic vibrations efficiently mix these Bloch states.

According to the existing concepts [5, 12], the low-frequency ultrasound should not influence the diffraction intensities, because the X-ray wave field has enough time to “accommodate” to the changed positions of the reflecting planes.

Recently, new results on the suppression of anomalous X-ray transmission have been obtained in diffraction from hematite (α-Fe_2O_3) crystals possessing a regular domain structure in the absence of an external magnetic field [13]. The strong magnetoelastic interactions in the (111) plane of hematite result in the formation of 180°-domains separated by Neél-type domain walls [14] accompanied by the magnetic moment rotating in the (111) plane. The domains are grouped into rather large systems forming layers parallel to the (111) plane and separated by Bloch walls. According to the X-ray topography data, the characteristic domain size is about 40 μm and the size of the Bloch- and the Neél-type domain walls, on the order of 100 μm [15]. Hematite crystals in a weak ferromagnetic state are characterized by magnetostriction deformations caused by the rotation of a magnetic moment (and the antiferromagnetic vector normal to it) and displacement of domain boundaries. The bands observed on the corresponding X-ray topographs lead to the conclusion that deformations observed between individual domains do not change the X-ray image since they are averaged over a large crystal volume. Therefore, one has to take into account only the deformations between the layers. In this case, the interlayer deformations resemble a periodic stress wave analogous to the wave arising in the excitation of ultrasonic vibrations with a period of 180–200 μm considerably exceeding the extinction length for the given reflection ($\Lambda \approx 22$ μm).

An increase of the intensity of an applied constant magnetic field up to the saturation value $H > H_m$ resulted in the transition of the crystal to the single-domain state and complete disappearance of magnetoelastic deformations.

Figure 1 shows the experimental diffraction intensity I_g [13] as a function of the magnetic-field intensity H for the MoK_α radiation diffracted by a 1-cm^2-large and 1.36-mm-thick hematite plate cut out in such a way that its surface coincides with the crystallographic

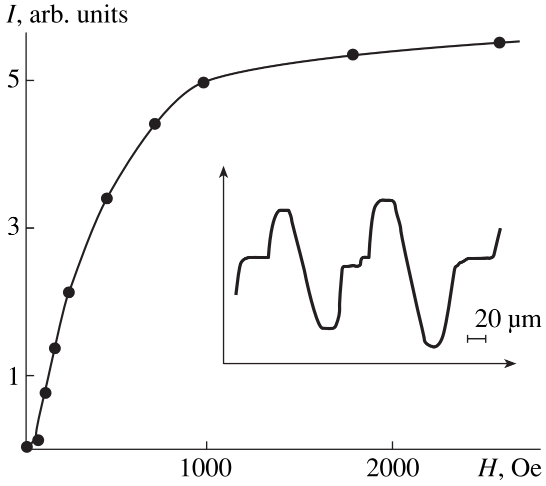

Fig. 1. Experimental diffraction intensity I_g [13] as a function of the magnetic-field strength H; MoK_α radiation, the $1\bar{1}0$ reflection. In the inset: a microphotograph obtained from the topograph of a hematite crystal [15] used for determining the deformation period.

(111) plane, the $1\bar{1}0$ reflection. The periodic deformation of the crystal varies along the surface normal. For the comparative analysis of deformation, the inset in Fig. 1 shows the microphotograph made from the X-ray topograph of a hematite plate [15] cut out in such a way that its [111]-direction lies in the plane of the plate surface. It is seen that the saturation field intensity attains a value of 1 kOe, whereas magnetic domains (or, more exactly, magnetostriction deformations) provide almost complete suppression of the Borrmann effect. Below, we shall try to interpret the phenomenon theoretically.

DYNAMICAL WAVE FIELDS IN HEMATITE CRYSTAL

In order to describe the propagation of a wave field in crystals with the large-scale distortions, one has to invoke the Takagi–Taupin equations (see, e.g., [12]).

Let the *z*-axis be directed along the surface normal of a crystalline plate of thickness *T*. Consider scattering of the radiation transmitted by a monochromator, which can be approximated by a plane wave deviating by the angle $\delta\theta$ from the exact Bragg angle. We assume that the incident-wave amplitude at the entrance surface of the crystal ($z = 0$) equals $E_0(0)$. In the dynamical diffraction, the total wave field in a the crystal with the given polarization can be represented by the sum

$$E(\mathbf{r}) = E_0(\mathbf{r})\exp(i\mathbf{k}_0\mathbf{r}) + E_g(\mathbf{r})\exp(i\mathbf{k}_g\mathbf{r}), \tag{1}$$

where $E_{0\,g}$ is the amplitude of the transmitted wave with the wave vector $\mathbf{k}_0$ and the diffracted wave with the wave vector $\mathbf{k}_g = \mathbf{k}_0 + \mathbf{g}$ (where $\mathbf{g}$ is the diffraction vector). If deformations in the crystal vary only along the surface normal *z*, the propagation of the transmitted and diffracted waves is described by the following system of equations:

$$\begin{aligned} \frac{dE_0}{dz} &= i\sigma_{00}E_0 + i\sigma_{01}E_g\exp(-igu_x), \\ \frac{dE_g}{dz} &= i(\sigma_{11} + \eta_0)E_0 + i\sigma_{10}E_g\exp(igu_x), \end{aligned} \tag{2}$$

where

$$\sigma_{00,\,11} = \frac{\pi\chi_0}{\lambda\gamma_{0,\,g}}, \quad \sigma_{01} = \frac{\pi C\chi_g}{\lambda\gamma_0},$$

$$\sigma_{10} = \frac{\pi C\chi_{-g}}{\lambda\gamma_g}, \quad \eta_0 = \frac{2\pi\sin(2\theta_0)(\theta - \theta_0)}{\lambda\gamma_g}, \tag{3}$$

$$u_x = w\cos(K_s z). \tag{4}$$

Here, $\chi_{0\,g}$ are the Fourier-components of polarizability; $\gamma_{0\,g}$ are the cosines of the angles formed by the internal surface normal e_z and the beams; *C* is the polarization factor equal to unity; and $\cos 2\theta$ for the σ- and π-polarizations, respectively. For the Laue diffraction, $\gamma_g > 0$, λ is the wavelength of the incident radiation; u_x are the displacements of the crystallographic planes caused by deformations, *w* is the amplitude, and $K_s = 2\pi/\lambda_s$, where λ_s are the deformation periods.

As is well known, the general equations for the polarizability component have the form

$$\chi_g = -r_0\frac{\lambda^2}{\pi}F(\mathbf{g}),$$

where the structure factor for the unit-cell with a volume of $V_c = 100.5$ Å^3 is expressed in terms of the atomic structure factors f_i

$$F(\mathbf{g}) = \frac{1}{V_c}\sum_i f_i\exp(i\mathbf{g}\mathbf{r}_i).$$

For the $1\bar{1}0$ reflection of a hematite crystal ($u = 0.355$), we obtain

$$F(0) = \frac{1}{V_c}(4f_{\mathrm{Fe}} + 6f_{\mathrm{O}}) \approx 153.3 + i4.83,$$

$$F(g) = \frac{1}{V_c}(4f_{\mathrm{Fe}} - 2f_{\mathrm{O}}(1 + 2\sin(2\pi u))) \approx 72 + i3.2,$$

then

$$\chi_0 = (6.85, 0.21)\times 10^{-6}, \quad \chi_g = (3.1, 0.14)\times 10^{-6}.$$

For the given reflection, a crystal with a set thickness can be considered as a "thick" one ($\mu T \approx 26$). The ratio of the ultrasound wavelength to the extinction length is $\frac{\lambda_s}{\Lambda} \approx 9.1$.

In the Laue diffraction, the substitution

$$E_{0\,g} = e_{0\,g}\exp[i(\sigma_{00} \mp \eta/2)z \pm g u_x/2] \quad (5)$$

results in the following form of the system of Takagi–Taupin equations:

$$\begin{aligned}\left(\frac{d}{dz} - i\eta/2\right)e_0 &= i\sigma_{01}e_g,\\ \left(\frac{d}{dz} + i\eta/2\right)e_g &= i\sigma_{10}e_0,\end{aligned} \quad (6)$$

where

$$\eta = \eta_0 + g\frac{du_x}{dz}. \quad (7)$$

We failed to obtain an analytical solution to system (6) in the general case; therefore, we constructed the solution based on the quasiclassical approximation, which provided the adequate description of the propagation of the X-ray wave field at low values of the deformation gradient [16].

In our case, the constant deformation gradient

$$B = g\frac{d^2u_x}{dz^2} = gwK_s^2\cos(K_s z)$$

is limited by its maximum value

$$B_m = gwK_s^2. \quad (8)$$

As is well known [16], the applicability range of the quasiclassical solution in crystals with constant deformation gradient is determined by the condition

$$|Y^2 + 4\nu| \gg 1, \quad (9)$$

where the variable Y depends on the distance between the entrance surface and the "turning point" z^*, where the deviation η equals zero

$$Y = \sqrt{iB}(z - z^*),$$

whereas ν takes the form

$$\nu_{\min} = i\frac{\pi^2}{2B_m\Lambda^2} = i\frac{\lambda_s^2}{\Lambda^2}\frac{1}{2gw}. \quad (10)$$

In our case, estimate (9) allows the use of the quasiclassical approximation up to very high values of the deformation amplitude,

$$gw < 2\frac{\lambda_s^2}{\Lambda^2} \approx 165.$$

In the quasiclassical approximation [17], the solution to system of equations (6) should be sought for in the form

$$e_{0\,g}(z) = \sum_{j=1}^{2}\exp(iS_j)F^j_{0\,g}, \quad (11)$$

where the eikonal coefficients S_j are determined, upon the substitution of Eq. (11) into Eq. (6), by the Hamilton–Jacobi-type equations

$$\frac{dS_j}{dz} = (-1)^{j+1}Q(z), \quad Q(z) = \sqrt{\eta^2/4 + \sigma_{10}\sigma_{01}}, \quad (12)$$

whence the eikonal functions are obtained in the form

$$S_j(z) = (-1)^{j+1}S(z), \quad S(z) = \int_0^z Q(z')dz'. \quad (13)$$

In the first approximation, the orthonormalized amplitudes $F_j^{0\,g}$ are determined as the solutions of the homogeneous transfer equation [17] in the form

$$\begin{aligned}&F_j^0(z) = \Psi_j N_j(z), \quad F_j^g(z) = \Psi_j N_j(z) b_j(z),\\ &N_j(z) = \frac{1}{\sqrt{1+b_j^2}}, \quad b_j(z) = \frac{1}{\sigma_{01}}((-1)^{j+1}Q - \eta/2),\end{aligned} \quad (14)$$

where the initial excitation amplitudes of each of the Bloch waves Ψ_j are determined from the boundary conditions.

It follows from system of equations (6) that the parameter describing the deviation of the incident plane wave is a periodic function of the coordinate z,

$$\eta = \eta_0 - gK_s w\sin(K_s z). \quad (15)$$

In terms of physics, this signifies that a plane wave penetrated into the crystal is scattered by spatially modulated crystallographic planes.

Since the deformation is periodic, the crystal can be divided into a number of thin plates and diffraction is considered only from one of these plates. Taking into account the crystal thickness and the average layer thickness $\lambda_s = 200$ μm, the total number of such layers ranges from six to seven. Let a plate be limited by the planes $z = n\lambda_s$ and $z = (n+1)\lambda_s$. Then the transformation of the system of the wave fields

$$\hat{e}^{(n+1)} = (e_0^{(n+1)}, e_g^{(n+1)}) \quad (16)$$

upon the passage of the wave for one period can be described with the aid of the matrix $\hat{a}$,

$$\hat{e}^{(n+1)} = \hat{a}\hat{e}^{(n)}. \quad (17)$$

At the interface, the deviation of each plane wave coincides with the initial deviation $\eta = \eta_0$. Then the incident wave field and the field inside the plate are related by the equations

$$e_0^{(n)} = F_0^1 + F_0^2, \quad e_g^{(n)} = F_1^0 b_1 + F_2^0 b_2.$$

The field at the exit from the layer has the form

$$\begin{aligned}e_0^{(n+1)} &= F_1^0\exp(iS_0) + F_2^0\exp(-iS_0),\\ e_g^{(n+1)} &= F_1^0 b_1\exp(iS_0) + F_2^0 b_2\exp(-iS_0),\end{aligned}$$

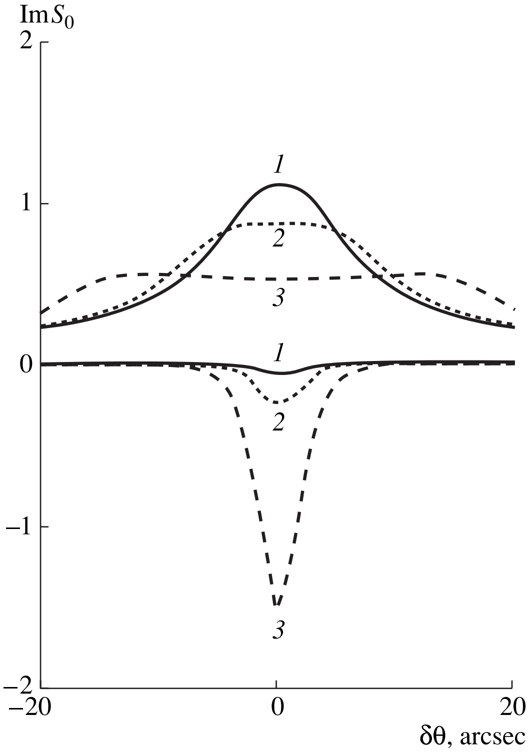

Fig. 2. Calculated imaginary part of the phase S_0 of the wave which has passed one period as a function of the deviation angle $\delta\theta$. The upper curves represent the rigorous calculation; the lower curves represent ΔS, 10^3; gw = (*1*) 4, (*2*) 8, and (*3*) 20.

where

$$S_0 = S(\lambda_s).$$

Then the elements of the matrix $\hat{a}$ in Eq. (17) have the form

$$\begin{aligned} a_{11,22} &= (b_2\exp(\pm iS_0) - b_1\exp(\mp iS_0))\frac{1}{b_2 - b_1}, \\ a_{21,12} &= \frac{\mp 1}{b_2 - b_1}(\exp(iS_0) - \exp(-iS_0)), \end{aligned} \quad (18)$$

whereas the determinant of this matrix equals unity (which can readily be verified). Using the well-known Abeles theorem (see also [18, 19]), we can write the transformation matrix for a wave passed N layers $\hat{a}^N$ in terms of the second-order Chebyshev polynomials U_N

$$\begin{aligned} a^N_{11,22} &= a_{11,22}U_{N-1}(x) - U_{N-2}(x), \\ a^N_{12,21} &= a_{12,21}U_{N-1}(x), \end{aligned} \quad (19)$$

where

$$x = \frac{1}{2}(a_{11} + a_{22}) = \cos(S_0),$$

$$U_{N-1}(x) = \frac{\sin(N\arccos(x))}{\sqrt{1-x^2}} = \frac{\sin(NS_0)}{\sin(S_0)}.$$

In the Laue diffraction, the boundary conditions have the form

$$\hat{e}^{(0)} = E_0(0)(1, 0) \quad (20)$$

and the amplitude of the diffracted wave at the exit from the crystal is determined by the equation

$$\begin{aligned} e_g &= a_{21}U_{N-1}(x) \\ &= \frac{b_1b_2}{b_2 - b_1}(\exp(iNS_0) - \exp(-iNS_0)). \end{aligned} \quad (21)$$

An analogous formula is also obtained within the accuracy up to the substitution $NS_0 \longrightarrow Q_0t$ for diffraction from an undeformed crystal.

Thus, the possible effect of ultrasound is associated with the difference of S_0 from $Q_0\lambda_s$ (upper curves in Fig. 2). Obviously, with an increase of the ultrasound (or deformation) amplitude, the maximum absorption coefficient decreases and the range of dynamical diffraction increases.

In this case, the maximum change in the deviation ($\sim\Delta\eta = gwK_s$) is small in comparison with the rocking-curve width ($\sim 2\sigma_{10} = \pi/\Lambda$), i.e.,

$$\frac{gwK_s}{2\sigma_{10}} = gw\frac{\Lambda}{\lambda_s} \ll 1.$$

Therefore, the analytical calculation of the quantity S_0 can be performed by expanding it in degrees of gwK_s,

$$\begin{aligned} S_0 &\approx \int_0^{\lambda_s} dz\left(Q_0 + \frac{Q_0''}{2}(\Delta\eta\sin(K_sz))^2 + \ldots\right) \\ &= \lambda_sQ_0 + \Delta S + \ldots, \end{aligned} \quad (22)$$

$$\Delta S = \lambda_s(gwK_s)^2\frac{\sigma_{10}\sigma_{01}}{4Q_0^3}.$$

It is seen from the lower curves in Fig. 2 that, similar to the case of the X-ray acoustic resonance, the correction to the phase due to ultrasound rapidly decreases with an increase of the deviation. However, the calculation by the simplified formula results in the considerable overestimation of the ultrasound effect on the suppression of the Borrmann effect; moreover, they also fail to describe the rocking-curve broadening.

The periodic variation in the deviation parameter η denotes that all the waves deviating from the exact Bragg condition within the range

$$\eta_0 \in [-gwK_s, gwK_s] \quad (23)$$

propagate in the crystal depth, periodically leaving the region of strong diffraction scattering (an increase of the distance from the turning point). At first glance, it

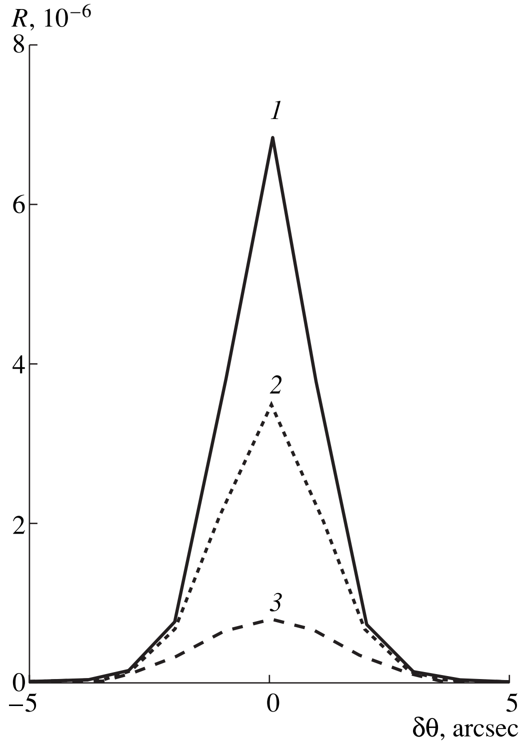

Fig. 3. Diffracted-wave intensity as a function of the deviation from the exact Bragg condition, $\delta\theta$; gw = (*1*) 0, (*2*) 2, and (*3*) 4.

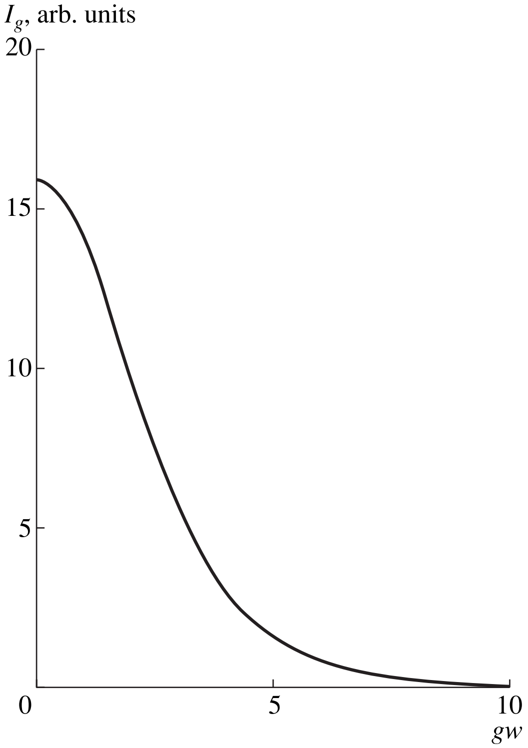

Fig. 4. Integrated diffraction intensity as a function of the ultrasound amplitude.

seems that the intensity of the diffracted wave should increase proportionally to deformation ε [13] as

$$\frac{\Delta I_g}{I_g^0} \sim \frac{g\varepsilon}{S_0}, \quad \varepsilon = wK_s, \tag{24}$$

where S_0 is the area under the diffraction peak having no ultrasonic deformation. Indeed, this is really the case in the Bragg diffraction (a relatively small depth of X-ray penetration into the crystal). However, in the transmission diffraction, the change in the phases for waves with slight deviation from the Bragg condition is more important than the change of the rocking-curve width.

In a thick crystal ($\mu T \approx 26$), the amplitude of the second Bloch wave is rather small because its antinodes are at the sites of the crystallographic planes and, therefore, its contribution can be ignored. The intensity of the diffracted wave at the exit from the crystal (Fig. 3) can be represented as

$$I_g \approx \frac{\sigma_{10}^2}{4Q_0^2}\exp(2NImS_0 - \mu t).$$

When interpreting the experimental results (Figs. 1, 4), the emphasis is made on the dependence of the magnetostriction deformation w on the magnetic-field intensity H. The complicated character of this dependence is indicated by a smoother attainment of the saturation by the diffraction intensity with an increase of the magnetic-field strength. Moreover, unlike the case of diffraction from an "ultrasonic superlattice," the spatial structure of magnetic domains changes—they become larger and the number of the superlattice layers can decrease at almost constant deformation (magnetic moment). The analysis of the behavior of magnetic domains is of great interest but it is beyond the scope of the present article and, therefore, is not considered.

CONCLUSION

Thus, we suggested the theoretical interpretation of the suppression of the Borrmann effect (anomalous X-ray transmission) under the effect of periodic (ultrasonic or magnetostriction) deformations with a period considerably exceeding the extinction length. The nature of this effect is associated with the periodic deviations of the reflecting planes from their exact Bragg positions, which results in the destruction of the dynamical structure of Bloch X-ray waves. In this case, the antinodes of a weakly absorbed Bloch wave are displaced toward the atomic planes, thus increasing absorption and suppressing the effect of anomalous X-ray transmission.

In practice, this effect can be used in designing high-speed X-ray choppers whose functioning, in fact, is determined by the rate of magnetization reversal of domains. It would be possible to use the experimental

X-ray data to determine the specific features of magnetoelastic deformations induced by the effect of an applied magnetic field. The use of the synchrotron radiation with a clearly pronounced temporal structure opens new vistas for studying temporal evolution of magnetic subsystems.

In the case of diffraction from vibrating crystals, the suppression of the Borrmann effect by long-wavelength ultrasonic vibrations also creates the conditions for controlling the angular width and the intensity of the diffracted beam. Unlike the case of X-ray acoustic resonance, the ultrasonic wavelength does not exactly coincide with the extinction length here. Moreover, the waves with a large period are absorbed to a lesser degree and, therefore, can be excited by simpler methods.

ACKNOWLEDGMENTS

The author is grateful to V.A. Somenkov and V.V. Kvardakov for their interest in his study and for providing the possibility of using their experimental data. The study was supported by the Ministry of Industry, Science, and Technologies of the Russian Federation within the project “Development of New Methods for Studying Condensed Media with the Use of X-ray Radiation” (no. N04.004).

REFERENCES

1. E. M. Iolin and I. R. Éntin, Zh. Éksp. Teor. Fiz. **85**, 1692 (1983) [Sov. Phys. JETP **58**, 985 (1983)].
2. R. Köhler, W. Möhling, and H. Peibst, Phys. Status Solidi B **61**, 173 (1974).
3. I. R. Entin, Phys. Status Solidi B **90**, 575 (1978).
4. I. R. Entin and K. P. Assur, Acta Crystallogr., Sect. A: Cryst. Phys., Diffr., Theor. Gen. Crystallogr. **A37**, 575 (1981).
5. V. I. Zasimchuk and E. F. Tikhonova, Fiz. Tverd. Tela (Leningrad) **26**, 1306 (1984) [Sov. Phys. Solid State **26**, 795 (1984)].
6. R. Michalek, L. Sedlakova, B. Chalupa, *et al.*, Acta Crystallogr., Sect. A: Cryst. Phys., Diffr., Theor. Gen. Crystallogr. **A27**, 410 (1971).
7. R. Michalek, B. Chalupa, L. Sedlakova, *et al.*, J. Appl. Crystallogr. **7**, 588 (1974).
8. V. L. Nosik, Kristallografiya **36** (5), 1091 (1991) [Sov. Phys. Crystallogr. **36**, 615 (1991)].
9. V. L. Nosik, Kristallografiya **38** (2), 44 (1993) [Crystallogr. Rep. **38**, 158 (1993)].
10. G. Borrmann, Z. Phys. **42**, 157 (1941).
11. M. Laue, Acta Crystallogr. **2**, 106 (1949).
12. Z. G. Pinsker, *X-ray Crystal Optics* (Nauka, Moscow, 1982).
13. V. V. Kvardakov and V. A. Somenkov, Kristallografiya **41** (1), 183 (1996) [Crystallogr. Rep. **41**, 171 (1996)].
14. J. A. Eaton and A. H. Morrish, J. Appl. Phys. **40**, 3180 (1969).
15. V. G. Labushkin, A. A. Lomov, N. N. Faleev, and V. A. Figin, Fiz. Tverd. Tela (Leningrad) **22**, 1725 (1980) [Sov. Phys. Solid State **22**, 1006 (1980)].
16. F. Balibar, F. N. Chukhovskii, and C. Malgrange, Acta Crystallogr., Sect. A: Found. Crystallogr. **A34**, 387 (1983).
17. F. N. Chukhovskiĭ and A. A. Shtol’berg, Zh. Éksp. Teor. Fiz. **64**, 1033 (1973) [Sov. Phys. JETP **37**, 525 (1973)].
18. V. L. Nosik, Kristallografiya **38** (1), 4 (1993) [Crystallogr. Rep. **38**, 1 (1993)].
19. V. L. Nosik, Kristallografiya **38** (3), 13 (1993) [Crystallogr. Rep. **38**, 9 (1993)].

Translated by L. Man

Crystallography Reports, Vol. 46, No. 3, 2001, pp. 355–360. Translated from Kristallografiya, Vol. 46, No. 3, 2001, pp. 405–410.

The Factors Affecting the Polarization Transformations of X-rays in Laue Diffraction from Crystals with Dislocations

N. M. Olekhnovich and A. V. Pushkarev

*Institute of Solid-State and Semiconductor Physics, Belarussian Academy of Sciences,
ul. Brovki 17, Minsk, 220072 Belarus*

Received September 21, 2000

Abstract—The transformations of X-ray polarization with coherent σ- and π-components have been studied for the Laue diffraction from LiF crystals with a high dislocation density (10^4–10^5 mm^{-2}). The dependence of the parameter characterizing the diffraction-induced birefringence and the degree of coherence of the transmitted beam on the squared reciprocal-lattice vector ($H^2 = 4\sin^2\theta/\lambda^2$) is determined. It is shown that the parameter characterizing the diffraction-induced birefringence in crystals with dislocations is determined by the static Debye–Waller factor ($\exp(-L)$) and the effective thickness Δ of the crystal. The exponent L increases and the parameter Δ decreases with the dislocation density. *© 2001 MAIK "Nauka/Interperiodica".*

INTRODUCTION

The diffraction-induced transformations of X-ray polarization (hereafter referred to as diffraction polarization) are among the important phenomena in X-ray diffraction optics. These phenomena underlay the development of X-ray polarimetry, the diffraction–polarization analysis of real crystals, and other research fields [1–10].

In X-ray diffraction with coherent σ- and π-components of the electric vector of the incident wave (the σ-component is normal and the π-components is parallel to the scattering plane), a perfect crystal demonstrates the phenomenon of birefringence. If a linearly polarized radiation with the electric-field vector inclined to the scattering plane is incident onto a crystal, the transmitted and diffracted beams, in the general case, are elliptically polarized because the advanced phase difference arising between the above components. The diffraction-induced polarization transformations are associated with the dynamical scattering and, thus, are not observed in the case of kinematical scattering. The parameters characterizing such polarization transformations in perfect crystals can be calculated from the experimental data in the dynamical approximation [1–6].

In two- and multibeam Laue diffraction in real crystals, the birefringence and depolarization phenomena were revealed in [11–13]. Their characteristic parameters of these phenomena depend on the dislocation density and the deviation of the scattering angle from the exact Bragg angle. The phenomenon of X-ray birefringence in crystals with dislocations with due regard for its manifestation provided the construction of a quarter-wave plate and perform the exhaustive polarization analysis of X-ray beams with the angular divergence characteristic of conventional diffraction experiments [14].

The studies of diffraction polarization in real crystals are important for getting a deeper insight into the scattering mechanisms of the short-wave radiation in crystals. The parameter κ characterizing the diffraction-induced birefringence (or simply diffraction birefrigence) is determined by the phase difference δ arising between the σ- and π-components of the electric-field vector related to the optical path length t, namely, $\kappa = \delta/t$.

It was found [6, 12] that in contrast to perfect crystals, parameter κ in crystals with a high dislocation density gradually decreases with an increase of the deviation of the crystal orientation from the exact Bragg position, with the absolute value of this parameter being many times lower than that in a perfect crystal. Such a behavior of the diffraction-birefringence parameter in crystals with dislocations can be related to the static Debye–Waller and other factors determining the diffraction conditions in such crystals. The role of these factors can be estimated by studying the diffraction-induced polarization transformations for reflections of different order. Bearing this in mind, we undertook this study with the aim to establish the characteristic features of the diffraction transformations of the transmitted-beam polarization under the conditions of the Laue diffraction (the 002, 022, and 004 reflection) from LiF crystals with dislocations.

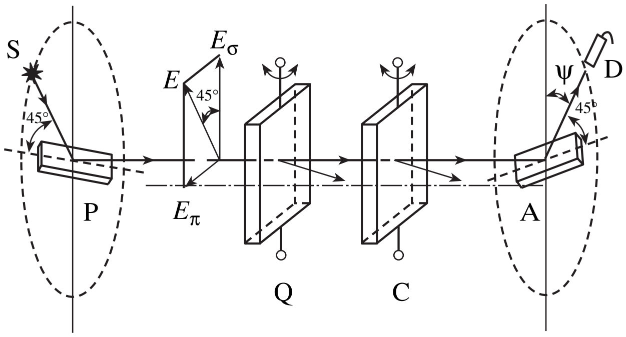

Fig. 1. Schematic of a polarimeter [12]: S is a source of X-ray radiation; P is a crystal–polarizer; Q is a quarter-wave plate; C is the crystal–specimen; A is a crystal–analyzer; and D is an X-ray detector.

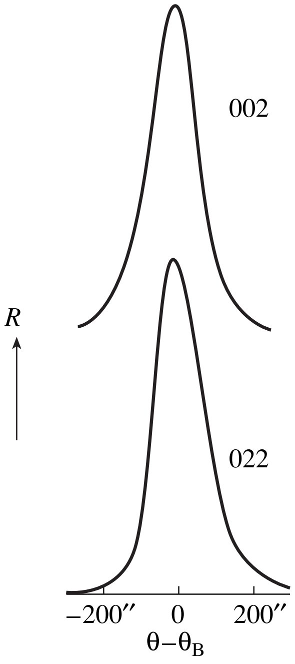

Fig. 2. Scattering curves for the 020 and 022 reflection in a LiF crystal with $N_d = 3 \times 10^5$ mm^{-2}.

EXPERIMENTAL. THE METHOD OF DETERMINING THE POLARIZATION PARAMETERS

The polarization characteristics of the X-ray beam analyzed were studied with the use of an X-ray polarimeter (CuK_α radiation) (Fig. 1). Both the polarizer–monochromator and the analyzer were germanium single crystals (333 Bragg reflection). The unit consisting of an X-ray tube and a crystal–analyzer was installed in such a way that the electric vector of the linearly polarized beam would form an angle of 45° with the σ-direction in the crystal-specimen and a quarter-wave plate. The angular divergence of the incident linearly polarized beam in the scattering plane of the crystal-specimen was lower than the half-width of the obtained curve. The quarter-wave plate was prepared from a LiF single crystal with the dislocation density ~10^3 mm^{-2}. Its angular aperture corresponded to the divergence of the incident linearly polarized beam in the scattering plane. The the working beam of the quarter-wave plate was the transmitted beam under the conditions of symmetric Laue diffraction (the 002 reflection).

The specimens had the shape of plane-parallel plates prepared from LiF single crystals with the entrance and exit surfaces being parallel to the (100) plane. The dislocation density (N_d) was about 10^4–10^5 mm^{-2} for specimens prepared from crystals with the most homogeneous dislocation distribution. These specimens were characterized by Gaussian-like curves of Bragg scattering for all the reflections studies (Fig. 2). The dislocation density was determined from the pits obtained upon selective etching. The dislocation distributions in the crystals with a high dislocation density were slightly inhomogeneous. The polarization analysis of the transmitted beam in the symmetric Laue diffraction was made for the same region of the crystal plate for all the reflections (002, 022, and 004). The crystal was mounted in positions providing the maximum intensity of the diffracted beam.

To determine the polarization characteristics, we measured the integral intensities $I(\psi)$ of scattering from the crystal–analyzer at different angles ψ of its rotation about the axis of the analyzed beam. The angle ψ varied from 0° to 180°. The dependence $I(\psi)$ was measured in two schemes—with and without the quarter-wave plate. In the scheme without the quarter-wave plate, the angular dependence $I(\psi)$ can be written in the form [15]

$$I(\psi) = \frac{1}{2} I_{\sigma\sigma}(\cos^2\psi + x\sin^2\psi + P_\text{к}\sqrt{x}\cos\delta\sin 2\psi), \quad (1)$$

where δ is the phase difference between the σ- and the π components; $x = I_{\pi\pi}/I_{\sigma\sigma}$ is the dichroism parameter; $P_\text{c} = |I_{\sigma\pi}|/\sqrt{I_{\sigma\sigma}I_{\pi\pi}}$ is the degree of coherence of the σ- and the π-components of the analyzed beam, which is related to the degree of polarization (P) as

$$P = \sqrt{1 - \frac{4x}{(1+x)^2}(1 - P_\text{c}^2)},$$

where $I_{\sigma\sigma}$, $I_{\pi\pi}$, and $I_{\sigma\pi}$ are the coherence matrix components [12]. In the scheme with the quarter-wave plate, the scattering intensity from the crystal–analyzer $I'(\psi)$ is determined by the relationship

$$I'(\psi) = \frac{1}{2} I'_{\sigma\sigma}(\cos^2\psi + xx_0\sin^2\psi - P_\text{c}P_{0\,\text{c}}\sqrt{xx_0}\sin\delta\sin 2\psi), \quad (2)$$

where $P_{0\,c}$ and x_0 are the parameters polarization characteristics of the quarter-wave plate [14]. It follows from Eqs. (1) and (2) that

$$x = \frac{I_{90}}{I_0}, \quad xx_0 = \frac{I'_{90}}{I'_0}, \tag{3}$$

$$P_c\cos\delta\frac{2\sqrt{x}}{1+x} = \frac{I_{45}-I_{135}}{I_{45}+I_{135}}, \tag{4}$$

$$P_cP_{0\,c}\sin\delta\frac{2\sqrt{xx_0}}{1+xx_0} = -\frac{I'_{45}-I'_{135}}{I'_{45}+I'_{135}}. \tag{5}$$

Using Eqs. (3)–(5) and the experimentally obtained dependences $I'(\psi)$ at $\psi = 0°, 45°, 90°$, and 135°, one can determine the polarization characteristics δ, P_c, and x of the analyzed beam.

RESULTS AND DISCUSSION

According to Eqs. (4) and (5), we used the following reduced intensity in the analysis of the experimental data:

$$J(\psi) = \frac{I(\psi)}{I_{45°}+I_{135°}}.$$

The angular dependence of the reduced intensities of the beam transmitted through a LiF crystal with the thickness $t_0 = 0.388$ mm and the dislocation density 3.1×10^4 mm^{-2} for the 002, 022, and 004 reflections are presented in Fig. 3. For comparison, Figure 3 also shows the angular dependence of the reduced intensity for the linearly polarized incident beam. It is seen that the transmitted and the incident beam have different polarizations for all the reflections studied. The quantitative analysis of the observed $J(\psi)$ and $J'(\psi)$ curves based on Eqs. (3)–(5) provided the determination of the phase difference δ and the degree of coherence P_c. Using the δ values determined, we calculated the birefringence parameter $\kappa = \delta/t$ ($t = t_0/\cos\theta_B$, where t_0 is the thickness of the crystal–specimen) (table). These parameters and the measured half-widths W of the scattering curve with due regard for the of incident-beam divergence are indicated in the table. It is seen that, with an increase of the reflection order (the squared reciprocal-lattice vector H^2), the birefringence parameter considerably decreases, whereas the coherence degree increases.

Now, compare the measured birefringence parameter κ with its values calculated for a perfect crystal. The calculation was performed for a spherical incident wave with the limited wavefront corresponding to the experimental conditions.

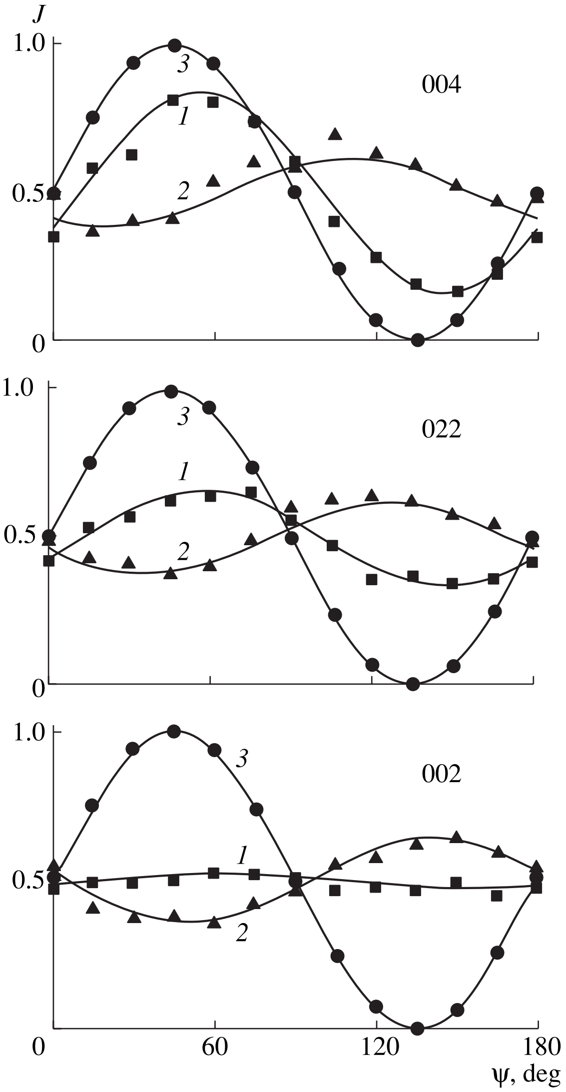

Fig. 3. Angular dependence of the normalized intensity of the transmitted beam scattered by the crystal–analyzer. The curves are plotted for the 002, 022, and 004 reflections: (*1*) with a quarter-wave plate; (*2*) without a quarter-wave plate; (*3*) for the incident beam.

The phase difference δ for the σ- and the π-components of the transmitted beam in Laue diffraction of a spherical wave with the limited wavefront is given by the following equation [6]:

$$\delta = \arctan\frac{\mathrm{Im}J_{\sigma\pi}^{\mathrm{int}}}{\mathrm{Re}J_{\sigma\pi}^{\mathrm{int}}}. \tag{6}$$

Here, $\mathrm{Im}J_{\sigma\pi}^{\mathrm{int}}$ and $\mathrm{Re}J_{\sigma\pi}^{\mathrm{int}}$ are the imaginary and the real parts of the matrix element (integrated over the angle) for the coherence matrix of the plane wave

$$J_{\sigma\pi}^{\mathrm{int}} = \frac{2\pi}{k'}\int_{-y_1}^{y_1} D_\sigma^0 D_\pi^0 dy, \tag{7}$$

where D_σ^0 and D_π^0 are the σ- and the π-components of the amplitude D^0 of the transmitted plane wave at the diffraction angle $y = (\theta_B - \theta)\sin 2\theta_B/\sqrt{\chi_h \chi_{\bar{h}}}$, $\theta_B - \theta$ is the deviation from the Bragg angle, χ_h and $\chi_{\bar{h}}$ are the Fourier components of polarizability, and $k' = \frac{2\pi}{\lambda}\frac{\gamma_0}{\gamma_h}\cot 2\theta_B \sqrt{\chi_h \chi_{\bar{h}}}$. The amplitude D^0 for the transmitted wave is given by the equation

$$\begin{aligned} D^0 = {} & B_1^\sigma \exp[-iA(y + \sqrt{y^2+1})] \\ & + B_2^\sigma \exp[-iA(y - \sqrt{y^2+1})] \\ & + B_1^\pi \exp[-iA(y + \sqrt{y^2+C^2})] \\ & + B_2^\pi \exp[-iA(y - \sqrt{y^2+C^2})], \end{aligned}$$

where the σ- and the π-components of the amplitude of the transmitted plane wave are

$$B_j^{\sigma,\pi} = \frac{E_0^{\sigma,\pi}(\sqrt{y^2 + C_{\sigma,\pi}^2} \mp y)\exp[-gA(1 \pm (\varepsilon_0 C_{\sigma,\pi}^2/\sqrt{y^2 + C_{\sigma,\pi}^2}))]}{2\sqrt{y^2 + C_{\sigma,\pi}^2}}.$$

Here, $E_0^{\sigma,\pi}$ are the σ- and the π-components of the incident-wave amplitude; j is equal either to 1 or 2; $C_\sigma = 1$ and $C_\pi = |\cos 2\theta_B|$; $A = \pi\chi_h t_0/(\lambda\sqrt{\gamma_0\gamma_h})$; t_0 is the crystal thickness; $g = \mu/(2\pi k_0 \chi_h)$; μ is the linear coefficient of photoelectric absorption; $\varepsilon_0 = |\chi_{hi}/\chi_{0i}|$; and γ_0 and γ_h are the directional cosines of the incident and the diffracted wave, respectively. The integration limits in Eq. (7) are determined by the incident-beam divergence with respect to the half-width of the scattering curve.

For a thick crystal ($\mu t \gg 1$), the value of δ varies linearly with the crystal thickness and is proportional to the Fourier component of polarizability. Using the phase difference calculated by Eq. (6) for the thickness of the specimens studied, we determined the birefringence parameter κ_p for a perfect crystal (table). It is seen from the table that the birefringence parameter for a crystal with dislocations is many times lower than that for a perfect crystal, with the difference between κ and κ_p increasing with H^2.

Birefringence parameter κ, degree of coherence P_c for the transmitted beam, and the half-width of the scattering curve for the 002, 022, and 004 reflections for a crystal with dislocations (W) and a perfect crystal (W_p)

hkl	κ, rad/mm	P_c	W, arc s	κ_p, rad/mm	W_p, arcsec	N_d, mm^{-2}
002	3.49	0.39	58	38.82	4.70	3.1×10^4
022	2.79	0.44	61	80.35	2.22	
004	0.51	0.69	64	40.70	1.25	
002	1.95	0.48	117	54.26	4.70	3×10^5
022	0.61	0.58	119	82.35	2.22	
004	0.17	0.75	129	68.20	1.25	

One of the factors providing a decrease in the birefringence parameter for real crystals is the Debye–Waller factor $\exp(-L) = \exp(-BH^2)$, because the Fourier component of polarizability for a crystal with defects is reduced just by this factor. Now, analyze the dependence of $\ln(\kappa/\kappa_p)$ on H^2 (Fig. 4). The dependence observed can be approximated by the following equation:

$$\ln(\kappa/\kappa_p) = a - bH^2, \tag{8}$$

where a and b are the approximation parameters. The scatter of the experimental points around the straight line seems to be associated with the inhomogeneity of the dislocation distribution. This assumption is confirmed by the observed difference in the half-width of the scattering curves for the 002 and 020 or 022 and $0\bar{2}0$ reflections. This difference was the most pronounced (about 15%) for the specimens with $N_d = 3 \times 10^5$ mm^{-2}.

The straight line in Fig. 4 has the negative slope, which agrees with the effect produced by the static Debye–Waller factor. However, if a decrease in κ in comparison with a decrease in κ_p was determined only by the static Debye–Waller factor, then the straight line would have crossed the origin of the coordinate system (i.e., parameter a would have had the zero value), but, in fact, this parameter has a certain negative value dependent on the dislocation density. Hence, in crystals with dislocations, the birefringence parameter is determined not only by the static Debye–Waller factor but also by other factors characterizing the specific features of dynamical scattering in the crystals, which is associated with the fact that the effect of diffraction birefringence is observed within almost the entire angular range of Bragg scattering [12] broadening with an increase of the dislocation density. Thus, the angular range of coherent scattering broadens with the introduction of dislocations into crystals. This fact leads to the assumption that at the given diffraction angle, some crystal regions, in which the dislocations distort the crystal lattice, do not participate in coherent scattering determining the birefringence effect and, thus, cannot make considerable contributions to the phase difference between the σ- and the π-components of the radiation. This fact can be taken into account with the aid of the effective thickness t_{eff} of the crystal. Obviously, the less the effective thickness, the greater the half-width of the scattering curve. Now, assume that

$$t_{\text{eff}} = t(W/W_{\text{p}}\exp(-L))^{\beta}, \tag{9}$$

where W_{p} is the half-width of the scattering curve for a perfect crystal and β is a certain parameter dependent on the degree of coherence between individual scattering regions and on the interband scattering from the displacement fields of dislocations, which provides mixing of the Bloch states of the upper and the lower branches of the dispersion surface. With an increase of the coherence between the individual scattering regions β should decrease, whereas with an increase of the interband scattering (resulting in a decrease of the phase difference), β should increase. Taking into consideration the effective thickness Eq. (9) of the crystal and the static Debye–Waller factor, the birefringence parameter for a crystal with dislocations can be evaluated by the following equation:

$$\kappa_d = \kappa_{\text{p}}\exp(-BH^2)\left(\frac{W_{\text{p}}\exp(-BH^2)}{W}\right)^{\beta}. \tag{10}$$

Thus, the diffraction-birefringence parameter for a crystal with dislocations is determined by both static Debye–Waller factor and factor associated with the effective crystal thickness, $\Delta = W_{\text{p}}\exp(-BH^2)/W$. Equation (10) provides the description of the dependence of κ on H^2. Obviously, Eq. (10) corresponds to approximation (8) and, as follows from the analysis of the data in the table, $\ln(W_{\text{p}}/W)$ increases with a decrease in H^2 approximately as

$$\ln(W_{\text{p}}/W) = d - qH^2, \tag{11}$$

where the approximation parameters d and q depend on the dislocation density. Thus, Eq. (10) can be rewritten as

$$\ln(\kappa/\kappa_{\text{p}}) = \beta d - (\beta q + (1+\beta)B)H^2,$$

which corresponds to Eq. (8). The values of B and β were determined using the parameters a, b, and q determined in fitting of Eqs. (8) and (11) to the experimental data. It was found that $B = 0.54$ Å^2 and $\beta = 0.86$ for $N_d = 3.1 \times 10^4$ mm^{-2} and $B = 0.84$ Å^2 and $\beta = 0.96$ for $N_d = 3 \times 10^5$ mm^{-2}.

The B-values obtain correspond to the data determined in the analysis of the integrated scattering intensities [16]. It should be indicated that similar to the half-width of the scattering curve, the birefringence parameter κ is sensitive to the inhomogeneity in the dislocation distribution in crystals.

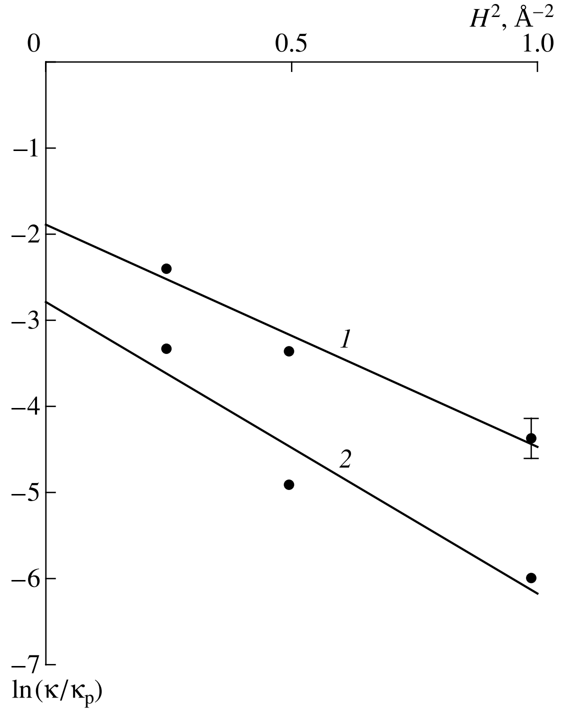

Fig. 4. $\ln(\kappa/\kappa_{\text{p}})$ versus H^2 for the crystals with dislocation densities equal to (*1*) 3×10^4 and (*2*) 3×10^5 mm^{-2}. The straight lines are constructed with the use of the parameters determined and Eq. (8).

The effective-thickness factor for a crystal with dislocations decreases for higher dislocation densities and the reflection orders. In turn, this results in a decrease in the depolarization of the transmitted beam, i.e., to an increase of its coherence degree (see table).

Thus, our studies demonstrate that the birefringence parameter κ for crystals with dislocations is determined by both the static Debye–Waller and Δ factors characterizing the effective thickness of the crystal, which is also dependent on the half-width of the scattering curve.

REFERENCES

1. P. Skalicky and C. Malgrange, Acta Crystallogr., Sect. A: Cryst. Phys., Diffr., Theor. Gen. Crystallogr. **A28**, 501 (1972).
2. M. Hart, Philos. Mag. B **38**, 41 (1978).
3. S. Annaka, J. Phys. Soc. Jpn. **51**, 1927 (1982).
4. O. Brümmer, Ch. Eisenschmidt, and H.-R. Höche, Z. Naturforsch. A **37**, 524 (1982).
5. V. A. Belyakov and V. E. Dmitrienko, Usp. Fiz. Nauk **158**, 679 (1989) [Sov. Phys. Usp. **32**, 697 (1989)].
6. N. M. Olekhnovich, A. I. Olekhnovich, and A. V. Pushkarev, Metallofizika **13**, 77 (1991).

7. K. Okitsu, J. Phys. Soc. Jpn. **62**, 911 (1993).
8. N. M. Olekhnovich and A. V. Pushkarev, Poverkhnost', No. 7, 52 (1996).
9. W. Leitenberger, C. Eisenschmidt, and H.-R. Höche, Acta Crystallogr., Sect. A: Found. Crystallogr. **A52**, 621 (1996).
10. Y. Hasegawa, Y. Ueji, K. Okitsu, *et al.*, Acta Crystallogr., Sect. A: Found. Crystallogr. **A55**, 955 (1999).
11. N. M. Olekhnovich and A. V. Pushkarev, Kristallografiya **34**, 558 (1989) [Sov. Phys. Crystallogr. **34**, 332 (1989)].
12. N. M. Olekhnovich and A. V. Pushkarev, Phys. Status Solidi A **119**, 27 (1990).
13. N. M. Olekhnovich and A. V. Pushkarev, Dokl. Akad. Nauk Belarusi **40**, 56 (1996).
14. N. M. Olekhnovich and A. V. Pushkarev, Pis'ma Zh. Tekh. Fiz. **15**, 4 (1989) [Sov. Tech. Phys. Lett. **15**, 288 (1989)].
15. M. Born and É. Wolf, *Principles of Optics* (Pergamon, Oxford, 1969; Nauka, Moscow, 1973).
16. N. M. Olekhnovich, Metallofizika **8**, 48 (1986).

Translated by K. Kugel

Crystallography Reports, Vol. 46, No. 3, 2001, pp. 361–364. Translated from Kristallografiya, Vol. 46, No. 3, 2001, pp. 411–414.
Original Russian Text Copyright © 2001 by Yatsenko.

Optimization of the Calculation of a Local Electric Field in Crystals by the Transient-Region Method

A. V. Yatsenko

Tavrian State University, ul. Yaltinskaya 4, Simferopol, 333036 Ukraine

Received June 27, 2000

Abstract—The specific features of using the method of transient-region for calculating local electric fields and the corresponding potentials are considered on examples of the calculations for NaF, CsCl, and $LiNbO_3$ crystals. It is shown that for crystals with a primitive cubic lattice, this method can provide any given accuracy of the calculated Madelung constant; for displacive-type ferroelectrics ($LiNbO_3$), the method allows the calculation of the local electric field with a very high accuracy. It is emphasized that for each specific object, one has to carefully select the parameters of the convergence function. *© 2001 MAIK “Nauka/Interperiodica”.*

INTRODUCTION

Recently, computer simulations have been widely used in the studies of the structural order in various crystalline and amorphous materials, as well as complex multiatomic macromolecules. Computer simulation is based on the calculation of Coulomb interactions in the object either in the approximation of the point dipoles [1] or on the first principles with due regard for the spatial electron-density distribution of ions in the object [2]. The expressions for the local electric-field and its potential created by the ions in the crystal lattice involve slowly convergent lattice sums, whose convergence is usually improved by two main methods—the Ewald method and the fast multipole method [3]. The latter method is based on the expansion of the potential into series in spherical harmonics. The classical Ewald method requires analytical integration over the lattice, but its modern computer-oriented modifications are based on the algorithm of the fast Fourier transformation with the replacement of the continuous volume-charge distribution by a discrete net [4, 5].

Both the Ewald and fast multipole methods are designed for calculations of the potential at the points of a periodic crystal lattice, which hinders their use for calculating potential reliefs, the analysis of objects with random spatial distributions of charged defects, and the analysis of ferroelectrics because of the difficulties encountered in the calculation of the polarization contribution to the local electric field.

At the same time, there is a fundamentally different method for improving the convergence of the lattice sums free of the above limitations [6]. It is based on the consideration of the region which is transient between the Lorentz sphere with discretely localized point charges and the uniformly polarized medium and can be called transient-region (TR) method. Below, we analyze the specific features of the optimum use of this method with the emphasis on the accuracy and convergence of the results obtained.

OPTIMIZATION OF THE TRANSIENT FUNCTION

The detailed substantiation of the TR method for calculating the potential φ_{loc} and the local electric field E_{loc} was given elsewhere [6]. It was shown that, introducing into consideration the region transient from the zone of localized point charges and point multipoles (a sphere of the radius R_1) to the zone of a uniformly polarized medium (the outer radius of the transient region is $R_2 > R_1$), we can represent E_{loc} in the center of an isotropic crystal of the spherical shape in the following form:

$$E_{\mathrm{loc}} = E_i' + E_{\mathrm{m}} + E_{\mathrm{dep}}, \tag{1}$$

where E_{m} is the contribution of the multipole electrical moments of ions located within a sphere of radius R_2 and E_{dep} is the depolarization field. The contribution of point charges of lattice ions E_i' has the form

$$E_i' = \frac{1}{4\pi\varepsilon_0}\sum_{k=1}^{N}\sum_{j=1}^{l_k}\frac{q_k Q(R_{0\,jk})}{R_{0\,jk}^3}R_{0\,jk}, \tag{2}$$

where N is the number of different types of ions in the object; the subscripts k and j indicate the ion type sequential and number of ions the given type, respectively; l_k is the number of ions of the kth type within the sphere of radius R_2; $R_{0\,jk}$ is the radius-vector between the point at which E_{loc} is calculated and the jth ion of the kth type; q_k is the effective charge of ions of the kth

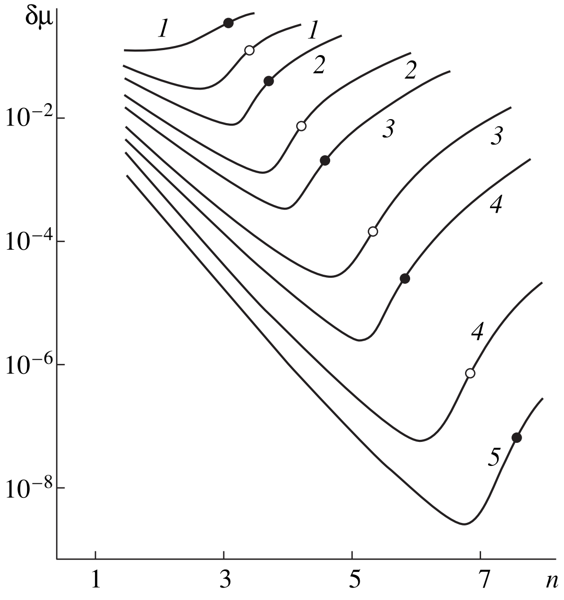

Fig. 1. Relative root-mean-square error δμ versus parameter *n* for NaF (○) and CsCl (●) structures at several σ values: (*1*) 0.25; (*2*) 0.5; (*3*) 1.0; (*4*) 2; and (*5*) 4 nm.

type; and $Q(R_{0\,jk})$ is the transient function responsible for the convergence such that

$$Q(R_{0\,jk}) = 1 \quad \text{at} \quad R_{0\,jk} \le R_1,$$

$$0 \le Q(R_{0\,jk}) \le 1 \quad \text{at} \quad R_1 < R_{0\,jk} \le R_2,$$

$$Q(R_{0\,jk}) = 0 \quad \text{at} \quad R_{0\,jk} > R_2.$$

In the similar way, we can determine the contribution φ_i of point charges to the potential of the local electric field

$$\varphi_i = \frac{1}{4\pi\varepsilon_0}\sum_{k=1}^{N}\sum_{j=1}^{l_k}\frac{q_k Q(R_{0\,jk})}{R_{0\,jk}}. \tag{3}$$

It can readily be seen that this approach is valid not only for an polarized isotropic spherical specimen but also for an electrically anisotropic crystal of an arbitrary shape. In the latter case, one has to introduce an additional term, which describes the contribution to E_{loc} from the specimen regions lying outside the sphere of maximum radius inscribed into the specimen volume.

Two specific forms of the transient function were considered in [6]; however, no function optimization made. The variants of $Q(R_{0\,jk})$ considered in [6] are the particular cases of the following function:

$$Q(R_{0\,jk}) = \exp\left[-\frac{(R_{0\,jk} - R_1)^n}{2\sigma^n}\right], \tag{4}$$

where σ and *n* are positive numbers. The classical object for checking the efficiency of any method used for calculating the potential of the local electric field is a primitive cubic structure of the NaF [2] or CsCl type. Figure 1 shows the dependence of the relative root-mean-square error δμ of the Madelung constant μ in the NaF and CsCl structures calculated by the transient-region method on the parameter *n* at several values of σ. The δμ value was determined from series *M* ($M = 10$) of computations of μ at fixed *n* and σ and $(R_2 - R_1) =$ 10 nm and $R_1 = (2.0 + 0.05k)$ nm. Thus, we have

$$\delta\mu = \frac{1}{\bar{\mu}}\left[\frac{1}{M}\sum_{k=1}^{M}(\mu_k - \bar{\mu})^2\right]^{1/2}, \tag{5}$$

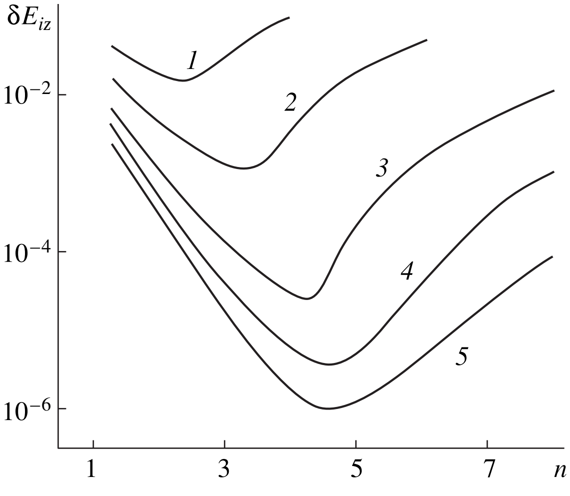

Fig. 2. $\delta E_i'$ versus parameter *n* for the position of a Li^+-ion in an ideal $LiNbO_3$ structure at the following σ values: (*1*) 0.25; (*2*) 0.5; (*3*) 1.0; (*4*) 1.5; and (*5*) 2.0 nm.

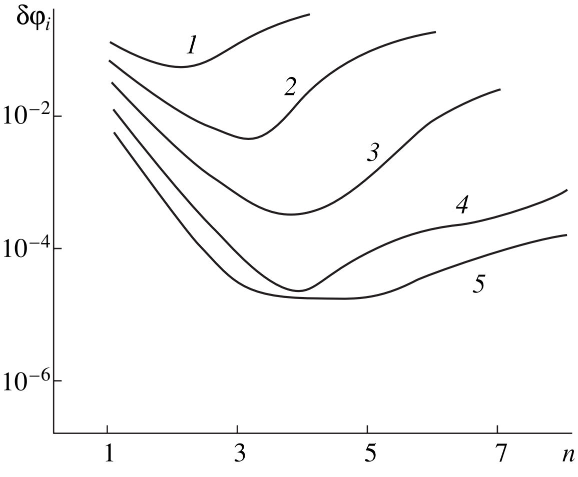

Fig. 3. $\delta\varphi_i$ versus parameter *n* for the position of a Li^+-ion in $LiNbO_3$ at several σ values: (*1*) 0.25; (*2*) 0.5; (*3*) 1.0; (*4*) 2.0; and (*5*) 3.0 nm.

where $\bar{\mu}$ is the arithmetical mean within the series M. It is seen from Fig. 1 that, at the appropriate choice of the parameters characterizing the transient function and the dimensions of the summation region, the transient-region method provides any specified accuracy in the calculations of μ in the structures of the NaF and CsCl types. Note that the μ-value for the NaF structure accurate up to ninth decimal digit can be determined by the transient-region method with the summation over 6×10^3 unit cells of the crystal ($R_1 = 0$, $R_2 = 5.2$ nm, $\sigma = 3$ nm, $n = 7.125$), whereas the modified Ewald method uses the summation over 10^3 unit cells [2].

APPLICATION OF THE TRANSIENT-REGION METHOD TO POLAR STRUCTURES

The main purpose of transient-region method is the calculation of E_{loc} in structures with defects having and in structures with the symmetry lower than cubic. Following [6], we studied a stoichiometric rhombohedral ferroelectric $LiNbO_3$ crystal (point group $3m$, sp. gr. $R3c$) as a model object. In the hexagonal setting, the lattice constants are $c_H = 1.3865$ nm and $a_H = 0.5151$ nm [7], the unit cell contains six formula units. The convergence function was optimized separately for the calculation of the ionic contributions to the local field E_i' and the potential φ_i. The values of the effective ionic charges in the lattice were close to those used in [6]. The root-mean-square errors $\delta E_i'$ and $\delta\varphi_i$ were determined in a way similar to that used for $\delta\mu$, but at the different series parameter M: $R_1 = (6.0 + 0.1k)$ nm, $(R_2 - R_1) = 10$ nm, and $M = 13$, i.e., for R_1 changing by a value close to the maximum lattice constant. The plots of E_i' and φ_i versus n for the Li^+-position in the $LiNbO_3$ structure at different σ values are presented in Figs. 2 and 3, respectively. Comparing Figs. 2 and 3, we see that at low σ values the optimum values of n used for calculating E_i' and φ_i are practically the same, but with an increase of σ there appears an obvious tendency to the reduction of the ultimate accuracy of φ_i determination.

To find out the causes of such a difference, we analyzed the effect of internal radius R_1 of the transient region on φ_i and $\delta\varphi_i$. It was found that no such effect is observed for the NaF and CsCl structures; the corresponding dependence for the potential in the Li^+ position in $LiNbO_3$ is shown in Fig. 4. The qualitatively similar behavior of the difference $\Delta\varphi_i = [\varphi_i(0) - \varphi_i(R_1)]$ (where $\varphi_i(0)$ is the value of φ_i at $R_1 = 0$) was also found for the Nb^{5+}-position. The dependence of φ_i on R_1 results from the fact that lithium niobate belongs to the displacive-type ferroelectrics, and the Li^+ and Nb^{5+} positions cannot be identified with the center of an ideal uniformly-polarized sphere. Thus, the existence of the dependence $\varphi_i(R_1)$ leads to the systematic error in the determined $\delta\varphi_i$ value, and the true relative accuracy of the potential calculation is higher at high σ values than is shown in Fig. 2. The calculations of φ_i in the nonpolar materials should not result in the $\varphi_i(R_1)$ dependence.

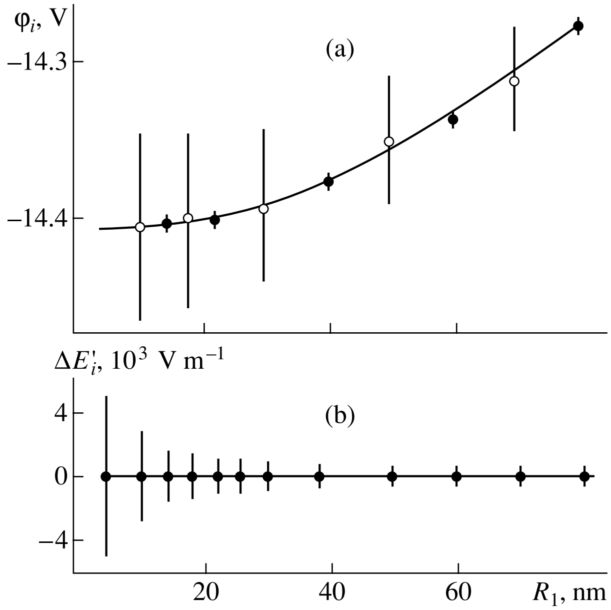

Fig. 4. (a) φ_i versus R_1 for Li^+-ion position in $LiNbO_3$ at $\sigma = 0.5$ (○), 1.0 (●), and 2.0 nm (solid line); (b) difference $\Delta E_i' = [E_i'(R_1) - E_i'(R_0)]$ versus R_1 for Li^+-ion position at $R_0 = 4.0$ nm and $E_i'(R_0) = -2.51298 \times 10^9$ V m^{-1}.

Figure 4 also shows the calculated z-component of the field E_i at Li^+-ions (E_{iz}) in $LiNbO_3$ as a function of R_1 at $\sigma = 2.0$ nm and $n = 4.5$. The calculations of E_{iz} at Nb^{5+} and O^{2-} ions confirmed the absence of divergence and an improved accuracy for higher R_1 values. Note also that the limiting R_1 values used in the calculations are rather high and exceed the mean linear dimension of real microscopic $LiNbO_3$ particles [8].

CONCLUSION

It has been shown that the transient-region method can successively be used for calculating the absolute value of the ionic contribution to E_{loc} for a wide class of objects and, within an accuracy of a constant, also for the calculation of the potential relief of the internal electric field in crystals. There are grounds to believe that, in the calculations of the ionic contribution to the potential in nonpolar materials, the absolute accuracy of the transient-region method is also rather high at the sufficiently fast divergence. The main advantage of the transient-region method in comparison with the Ewald and the fast multipole methods is its simplicity and applicability to any crystal structure.

It should be emphasized that, for minimizing the time of the calculation of the ion contribution to the potential and the electric-field intensity by the transient-region method, it is reasonable to use the minimum possible σ value, which would provide the necessary relative and absolute accuracy of the calculations, because, in this case, both necessary value of the difference $R_2 - R_1$ and the total number of ions participating in the calculation considerably decrease.

REFERENCES

1. J. H. Calderwood, Philos. Trans. R. Soc. London, Ser. A **355**, 1 (1997).
2. G. Su and P. Coppens, Acta Crystallogr., Sect. A: Found. Crystallogr. **A51**, 27 (1995).
3. L. Greengard and V. Rokhlin, J. Comput. Phys. **73**, 325 (1987).
4. D. Fincham, Mol. Simul. **13**, 1 (1994).
5. B. Luty, I. Tironi, and W. Gunsteren, J. Chem. Phys. **103**, 3014 (1995).
6. A. V. Yatsenko, Kristallografiya **45** (1), 139 (2000) [Crystallogr. Rep. **45**, 133 (2000)].
7. S. C. Abrahams and P. Marcsh, Acta Crystallogr., Sect. B: Struct. Sci. **B42**, 61 (1986).
8. D. Bork and P. Heitjans, J. Phys. Chem. B **102**, 7303 (1998).

Translated by K. Kugel

Crystallography Reports, Vol. 46, No. 3, 2001, pp. 365–367. Translated from Kristallografiya, Vol. 46, No. 3, 2001, pp. 415–417.
Original Russian Text Copyright © 2001 by Rastsvetaeva, Pekov, Nekrasov.

Crystal Structure and Microtwinning of a Calcium-Rich Analogue of Labuntsovite

R. K. Rastsvetaeva[1]*, I. V. Pekov, and Yu. V. Nekrasov***

**Shubnikov Institute of Crystallography, Russian Academy of Sciences, Leninskiĭ pr. 59, Moscow, 117333 Russia*
[1]e-mail: rast@ns.crys.ras.ru
***Faculty of Geology, Moscow State University, Vorob'evy gory, Moscow, 119899 Russia*

Received June 26, 2000

Abstract—The structure of a new representative of the labuntsovite family, which was found in the Khibiny alkaline massif (the Kola Peninsula), was established by the method of X-ray diffraction analysis. The unit-cell parameters are a = 14.365(7) Å, b = 13.887(7) Å, c = 7.814(2) Å, β = 117.36(5)°, sp. gr. Cm, R_{aniso} = 0.058, 1385 $F > 4\sigma(F)$. The mineral differs from other members of the family by the absence of Na-atoms and the high Ca-content. The Ca-polyhedron is reduced to a seven-vertex polyhedron (the average Ca–O distance is 2.48 Å) compared to the eight-vertex Na-polyhedron (the average Na–O distance is 2.57 Å). The structure channels are orderly occupied, thus lowering the symmetry to Cm. *© 2001 MAIK "Nauka/Interperiodica".*

The minerals of the labuntsovite family are characterized by a considerable heterovalent isomorphism, which should be taken into account while predicting ion-exchange properties of micro- and mesoporous materials based on this structure type. Sodium-rich orthorhombic representatives (nenadkevichite and korobitsynite) contain up to nine Na atoms per eight Si atoms. In the monoclinic minerals, the Na content can be reduced by more than 50% because of the incorporation of larger K, Ba, H_3O, or Sr cations. In kuzmenkoite [1], sodium atoms are virtually absent (0.35 atoms). A new sodium-depleted representative of the family, which was found in the cavities of a pegmatite khibinite counterlode from the Malyi Mannepakhk mountain of the Khibiny alkaline massif (the Kola Peninsula), differs from kuzmenkoite and other members of the labuntsovite family by high Ca content.

The new mineral exists as prismatic pale pink crystals up to 0.5 mm in length. Its chemical composition was studied by the electron probe analysis at seven points (no water-content determination was made). The empirical formula (calculated for 16 Si-atoms) reflects the intraphase inhomogeneity of the sample: $Na_{0.05-0.8}Ca_{0.67-2.71}K_{1.91-3.76}Sr_{0-0.05}Ba_{0.05-0.21}Mg_{0.05-0.11} \cdot Mn_{1.65-1.81}Fe_{0.08-0.28}Zn_{0-0.12}Zr_{0-0.04}Ti_{6.57-7.78}Nb_{0.44-1.51} \cdot Al_{0-0.16}Si_{15.84-16}$, with the inverse correlation for the Ca/K ratio.

The parameters of the orthorhombic unit cell with a fourfold period c = 27.76 (7 × 4) Å indicate crystal twinning analogous to that observed in vuoriyarvite [2] and oxonium labuntsovite [3] with the following matrix of the transformation from the experimental orthorhombic unit cell to the true monoclinic one: [–1 0 0/0 –1 0/0.25 0 0.25] + [1 0 0/0 1 0/–0.25 0 0.25]. The

Table 1. Crystallographic data and details of X-ray diffraction experiment

Characteristic	Data and conditions
Parameters of the orthorhombic unit cell, Å	a = 14.365(7)
	b = 13.887(7)
	c = 27.76(2)
Parameters of the monoclinic unit cell, Å, deg	a = 14.365(7)
	b = 13.887(7)
	c = 7.814(2)
	β = 117.36(5)
Volume of the monoclinic unit cell, Å^3	1384.4
Sp. gr., Z	Cm; 1
Radiation, λ, Å	CuK_α; 1.5418
Ratio of the twin components	0.6/0.4
Density, g/cm^3	2.5
Crystal dimensions, mm	0.1 × 0.06 × 0.08
Diffractometer	SYNTEX $P2_1$
Range of indices for measured reflections	$-16 < h < 16$; $0 < k < 14$; $0 < l < 32$
$\sin\theta/\lambda$	<0.59
Total number of reflections	1551 $I > 2\sigma(I)$
Number of independent reflections	1385 $F > 4\sigma(F)$
R factor for anisotropic refinement	0.058
Program used for calculations	AREN [5]
Program used for absorption correction	DIFABS [6]

Table 2. Atomic coordinates, equivalent thermal parameters, multiplicities (Q), and occupancies (q) of the positions

Atom	x/a	y/b	z/c	Q q	B_{eq}, Å^2
Ti(1)	–0.0002(1)	0.2316(1)	0.5002(1)	4 1	1.69(5)
Ti(2)*	0.2522(3)	0.2510(2)	0.4968(8)	4 1	1.79(4)
Si(1)	0.2112(2)	0.1081(2)	0.8019(4)	4 1	1.76(7)
Si(2)	0.7972(2)	0.1114(2)	0.1972(4)	4 1	1.16(7)
Si(3)	0.3225(2)	0.1108(2)	0.2435(4)	4 1	1.41(8)
Si(4)	0.6903(2)	0.1115(2)	0.7518(4)	4 1	1.46(7)
Mn	0.0031(4)	0	0.496(1)	2 0.89(1)	1.99(5)
Ca	0.919(1)	0.2325(8)	0.017(2)	4 0.30(1)	3.9(3)
K(1)	0.425(2)	0	0.709(3)	2 0.26(1)	4.6(3)
K(2)	0.5844(7)	0	0.294(1)	2 0.53(1)	3.7(2)
K(3)	0.5744(7)	0.0547(4)	0.275(1)	4 0.33(1)	2.3(2)
O(1)	0.2396(7)	0.1291(7)	0.026(1)	4 1	2.9(2)
O(2)	0.7750(6)	0.1304(6)	0.981(1)	4 1	2.1(2)
O(3)	0.2748(6)	0.1799(5)	0.734(1)	4 1	1.7(2)
O(4)	0.7323(6)	0.1824(6)	0.268(1)	4 1	2.3(2)
O(5)	0.1031(6)	0.2302(5)	0.387(1)	4 1	1.4(2)
O(6)	0.9064(7)	0.2275(6)	0.601(1)	4 1	2.0(2)
O(7)	0.2506(8)	0	0.794(2)	2 1	1.4(3)
O(8)	0.762(1)	0	0.212(2)	2 1	2.6(3)
O(9)	0.4253(6)	0.1778(6)	0.309(1)	4 1	2.2(2)
O(10)	0.5861(6)	0.1817(6)	0.696(1)	4 1	2.0(2)
O(11)	0.2702(6)	0.1273(6)	0.388(1)	4 1	2.0(2)
O(12)	0.7455(7)	0.1292(5)	0.619(1)	4 1	2.2(2)
O(13)	0.3675(9)	0	0.267(2)	2 1	1.7(3)
O(14)	0.652(1)	0	0.737(2)	2 1	2.2(3)
O(15)	0.0874(6)	0.1174(6)	0.677(1)	4 1	2.1(2)
O(16)	0.9232(5)	0.1189(5)	0.333(1)	4 1	1.5(2)
H_2O(1)*	0.106(1)	0	0.343(1)	2 1	5.9(1)
H_2O(2)*	0.907(1)	0	0.655(2)	2 1	4.3(3)
H_2O(3)	0.516(2)	0.128(1)	0.049(2)	4 0.67(2)	6.0(3)
H_2O(4)	0.011(2)	0.150(1)	0.000(3)	4 0.88(2)	6.3(3)

* The compositions of the positions: Ti(2) = 0.95Ti + 0.05Nb; H_2O(1) = 0.9H_2O + 0.1Ba; H_2O(2) = 0.9H_2O + 0.1K.

refined weighting coefficients of the twin components are 0.6 and 0.4.

The structure was studied within the centrosymmetric sp. gr. $C2/m$ typical of labuntsovites with the use of the coordinates of the framework atoms reported previously in [4]. The lowering of the symmetry (sp. gr. Cm) made it possible to reveal a number of additional partly occupied positions and to refine these positions with the use of the mixed atomic scattering curves.

The main characteristics of the crystal and the details of X-ray diffraction study are indicated in Table 1. The coordinates of the basis atoms are listed in Table 2.

The crystallochemical formula of the mineral ($Z = 1$) can be written as $K_{3.2}Ca_{1.2}Ba_{0.2}[Mn_{1.7}Fe_{0.1}(H_2O)_{3.6}]$ $[Ti_4(Ti_{3.8}Nb_{0.2})(O,OH)_8][Si_4O_{12}]_4 \cdot 6.1H_2O$.

The structure of the sample studied (figure) is characterized by a mixed framework typical of labuntsovites. This framework consists of chains of vertex-sharing (Ti,Nb) octahedra linked through four-membered rings of Si tetrahedra. The channels parallel to the coordinate axes are occupied by K, Ba, Ca, and Mn atoms

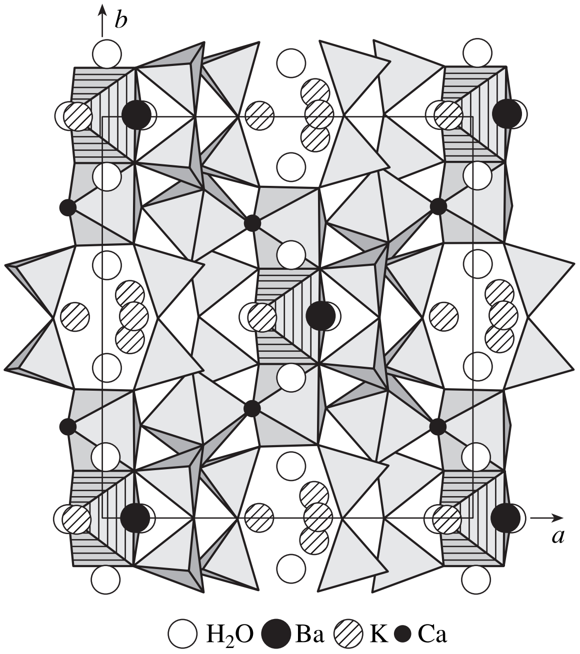

Structure of the calcium-rich analogue of labuntsovite projected onto the (001) plane. The Mn octahedra are hatched. Circles of different types represent large cations and water molecules.

and water molecules. The Ca atoms occupy one of two Na positions related by a pseudocenter of symmetry. The Ca polyhedron is reduced to a seven-vertex polyhedron (with the average Ca–O distance 2.48 Å) compared to the eight-vertex Na polyhedron (with the average Na–O distance 2.57 Å) [4]. Because of the considerable mobility of a $H_2O(4)$ molecule, the distance from this molecule to the Ca position, similar to that in the Na polyhedron, is somewhat shortened. The mineral is also characterized by almost full occupancy of the Mn position and by the ordered distribution of small amounts (0.2 atoms) of potassium and barium over the vertices of Mn octahedra statistically occupied mainly by $H_2O(1, 2)$ molecules.

ACKNOWLEDGMENTS

This study was supported by the Russian Foundation for Basic Research, project no. 99-05-65035.

REFERENCES

1. N. I. Golovina, G. V. Shilov, N. V. Chukanov, and I. V. Pekov, Dokl. Akad. Nauk **362** (3), 350 (1998).
2. R. K. Rastsvetaeva, R. A. Tamazyan, D. Yu. Pushcharovskiĭ, *et al.*, Kristallografiya **39** (6), 994 (1994) [Crystallogr. Rep. **39**, 908 (1994)].
3. R. K. Rastsvetaeva, N. I. Organova, I. V. Rozhdestvenskaya, *et al.*, Dokl. Akad. Nauk **371** (3), 336 (2000).
4. R. K. Rastsvetaeva, N. V. Chukanov, and I. V. Pekov, Dokl. Akad. Nauk **357** (1), 64 (1997).
5. V. I. Andrianov, Kristallografiya **32** (1), 228 (1987) [Sov. Phys. Crystallogr. **32**, 130 (1987)].
6. N. Walker and D. Stuart, Acta Crystallogr., Sect. A: Found. Crystallogr. **A39** (2), 158 (1983).

Translated by T. Safonova

Crystallography Reports, Vol. 46, No. 3, 2001, pp. 368–372. Translated from Kristallografiya, Vol. 46, No. 3, 2001, pp. 418–422.
Original Russian Text Copyright © 2001 by Evstigneeva, Kabalov.

STRUCTURE OF INORGANIC COMPOUNDS

Crystal Structure of the Cubic Modification of Cu_2FeSnS_4

T. L. Evstigneeva* and Yu. K. Kabalov**

**Institute of Geology of Ore Deposits, Petrography, Mineralogy, and Geochemistry (IGEM),*
Russian Academy of Sciences, Staromonetnyĭ per. 35, Moscow, 109017 Russia

***Faculty of Geology, Moscow State University, Vorob'evy gory, Moscow, 119899 Russia*

Received November 11, 1999; in final form, March 14, 2000

Abstract—The structure of $Cu_{2-x}Fe_{1-x}SnS_4$, the last member of the isomorphous series Cu_3FeS_4–Cu_2FeSnS_4, was synthesized for the first time and solved by the Rietveld method (the WYRIET 3.3 version). The compound occurs as a cubic phase (a_0 = 5.4179(5) Å) crystallizing in the sp. gr. $P\bar{4}3m$. One-half of the tetrahedral cavities in the close packing of sulfur atoms [4e (*xxx*), x = 0.2583(5)] are statistically filled with metal atoms (Sn + Fe) and (Cu + Fe + Sn) [1*a* (0 0 0) and 3*c* (0 1/2 1/2), respectively]. The results of X-ray study (R_p = 2.33, R_{wp} = 3.00, s = 1.20, D = 1.53, R_B = 2.52, and R_F = 2.00) confirm the existence of the stannite "prototype" with a "small" cubic unit cell. © *2001 MAIK "Nauka/Interperiodica".*

INTRODUCTION

The Cu_2FeSnS_4 compound, which is the basic phase of the Cu–Fe–Sn–S system, is an analogue of widely occurring mineral stannite. The Cu_2FeSnS_4 compound has the sphalerite-type structure. However, the unit-cell symmetry is lowered to tetragonal (sp. gr. $I\bar{4}2m$, a = 5.45 Å, c = 10.76 Å) [1] because of the ordered arrangement of the metal atoms in the cubic cell. In spite of the fact that compounds of this type often have high-temperature cubic polymorphous modifications with disordered sphalerite-like structures, no reliable indications to the existence of this Cu_2FeSnS_4 modification are known. The mineral isostannite, Cu_2FeSnS_4, has been studied insufficiently [2–4] and was considered as the cubic modification of stannite ($a \approx 5.42$ Å) based on the X-ray diffraction data. However, upon the refinement of the compositions of several isostannite samples and the discovery of the mineral kesterite $Cu_2(Zn,Fe)SnS_4$ (sp. gr. $I\bar{4}$, a = 5.40 Å, c = 10.80 Å, c/a = 2) [1, 5], isostannite was discredited by the Commission on New Minerals and Mineral Names of the International Mineralogical Association (CNMMN IMA). Many attempts were made to reveal the number of polymorphous modifications of Cu_2FeSnS_4 and to study the high-temperature modification [6–12]. However, the available data are contradictory, the structures of the phases and the phase ratios in the composition range close to Cu_2FeSnS_4 remain unclear, and the question about the existence of the cubic modification of stannite remains open.

The majority of researchers believed that the following three phases exist in the temperature range of 420–820°C:

(a) $Cu_2FeSnS_{3.95}$ (sp. gr. $I\bar{4}3m$, a = 10.837–10.85 Å), which is stable at T = 420–500°C; the composition ranges from $Cu_5Fe_{2.5}Sn_{2.5}S_{10}$ (=Cu_2FeSnS_4) to $Cu_{5.3}Fe_{2.3}Sn_{2.4}S_{9.8}$ (=$Cu_{2.16}Fe_{0.94}Sn_{0.98}S_4$) at 500°C [6, 8, 10];

(b) chalcopyrite-like tetragonal stannite with the composition $Cu_2(Fe,Sn)_2S_{3.9}$ (a = 5.42 Å, c = 10.70 Å, c/a = 1.97), which was prepared at 600°C [6, 11]; and

(c) the intermediate phase of the composition $Cu_{5.2}Fe_{2.3}Sn_{2.5}S_{10}$–$Cu_{5.6}Fe_2Sn_{2.4}S_{9.7}$ with an unknown symmetry, which was obtained by the slow reversible (without the DTA effects) transformation of the cubic phase in the temperature range of 580–600°C [10]. It should also be noted that only two polymorphous modifications of Cu_2FeSnS_4, which undergo the phase transition at the temperature of 565°C, were revealed in [7], namely, cubic "low" stannite (a_0 = 10.838 Å) and tetragonal "high" stannite (a_0 = 5.454 Å, c_0 = 10.735 Å).

Below, we report the results of the structure determination of the cubic $Cu_{2-x}FeSnS_4$ phase synthesized in the course of our investigation of the isomorphous series Cu_3SnS_4–Cu_2FeSnS_4.

EXPERIMENTAL

When studying the phase formation in the pseudobinary Cu_3SnS_4–Cu_2FeSnS_4 system, a number of phases with the variable Cu : Fe ratio were synthesized. The synthesis was performed in quartz tubes. Weighed samples of crushed and thoroughly mixed chemical elements (the total weight was 1 g) were placed into quartz tubes, evacuated to 10^{-6} torr, and sealed. Then, the tubes were first heated to 900°C (at a step of 200°C and storage for 0.5 h at each step), kept at this temperature

Table 1. Compositions of the phases in the B11 sample

No. of test	Content									Formula
	Fe		Cu		Sn		S		total	
	wt %	at. %	wt %	at. %	wt %	at. %	wt %	at. %	wt %	
1	12.5	12.1	30.2	25.6	26.0	11.8	30.1	50.6	98.8	$Cu_{2.02}Fe_{0.96}Sn_{0.93}S_4$
2	11.8	11.5	29.8	25.5	26.5	12.2	29.9	50.8	98.1	$Cu_{2.01}Fe_{0.91}Sn_{0.96}S_4$
3	12.15	11.8	30.0	25.55	26.25	12.0	30.0	50.7	98.45	$Cu_{2.01}Fe_{0.94}Sn_{0.94}S_4$
4	28.6	24.7	28.7	21.8	6.6	2.7	33.8	50.9	97.7	$Cu_{0.86}Fe_{0.97}Sn_{0.11}S_2$

Note: CAMEBAX (accelerating voltage 25 kV; probe current 10 nA; counting time 5 s; metallic iron, $CuFeS_2$, and SnO_2 standards; analytical lines: FeK_α, CuK_α, SK_α, and SnL_α; $3\sigma < 0.71\%$); row 3 represents the data obtained by averaging the data of rows 1 and 2; in 4, small (<50 μm) single chalcopyrite grains form less than 0.5% of the sample volume.

for 6 h, and finally cooled to 400°C and annealed at this temperature for 10 days. Upon annealing, the tubes with the samples were cooled in the furnace to ~80°C, taken away from the furnace, and opened. The products obtained were ground, and the synthesis procedure was repeated with a week-long annealing at 400°C.

The X-ray spectrum of the compounds thus obtained was measured on an ADP-2 diffractometer (CuK_α radiation; Ni filter; the scanning range $13.5° < 2\Theta < 155.0°$; the scan step (2Θ) was 0.02°; the exposure time per step was 5 s). Calculations were performed by of the WYRIET program (version 3.3) [13]. The peak profiles were approximated by the pseudo-Voigt function (PV) with 6FWHM (the peak regions was limited by six values of the full width at the maximum half-height). We used the asymmetry that was refined at $2\Theta < 60°$. We used the scattering curves for neutral atoms [14].

RESULTS AND DISCUSSION

We studied the B11 sample, which was the terminal member of the Cu_3SnS_4–Cu_2FeSnS_4 series and had the composition close to that of stannite ($Cu_{2-x}FeSnS_4$) (Table 1). The X-ray diffraction pattern of this sample (Table 2) was comparable with the X-ray diffraction patterns of the stannite-type high-temperature phases described earlier and those of the mineral isostannite. Attempts to index the X-ray pattern of B11 with the use of the "large" cubic unit cell ($a \approx 10.83$ Å) suggested in some studies have failed. Indexing of the X-ray pattern from B11 with the use of the TREOR program [15] led to a tetragonal unit cell ($a = 3.8293(5)$ Å, $c = 5.4204(5)$ Å, $M(20) = 64$, $F(20) = 23$ (0.015, 59)).[1] Satisfactory results were also obtained in indexing within the cubic unit cell ($a_0 = 5.4787(3)$ Å, $M(20) = 65$, $F(20) = 22$ (0.016, 59)). These two unit cells represent, in fact, the same lattice [$a_{\text{cub}} = a_{\text{tetr}} \times \sqrt{2}$] described (according to the *hkl* set) by one of the following space groups: $P\bar{4}3m$, $F\bar{4}3m$, $P23$, or $P432$.

We considered 12 sphalerite-based structural models of sphalerite taking into account the symmetry (tetragonal or cubic), the unit-cell dimensions, different modes of centering, and the distribution of metal atoms over the tetrahedral positions. As regards the number of reflections, which agree with the experimental data, and the spectrum form, the best results were achieved for the model whose structural parameters are given in Table 3 (sp. gr. $P\bar{4}3m$, $a_0 = 5.4179(3)$ Å).

The "isostannite" structure is characterized by statistical filling of the tetrahedral positions with the metal atoms. The sulfur atoms ($4e$ (xxx), $x = 0.2583(5)$) form the cubic close packing. The tin and iron atoms statistically occupy the tetrahedral positions in the vertices of the cubic unit cell [$1a$ (0 0 0)]. The tetrahedral positions of the second type located in the centers of the cube faces [$3c$ – (0 1/2 1/2)] are mixed (Cu + Fe + Sn). It was most reasonable to assume that the copper and (iron +

Table 2. Calculation of the X-ray diffraction pattern of B11 ("isostannite"), CuK_{α_1}

NN	I/I_{max}	*hkl*	$2\theta_{exp}$	NN	I/I_{max}	*hkl*	$2\theta_{exp}$
1	3	001	16.34	11	1	222	59.04
2	4	011	23.17	12	1	123	64.34
3	100	111	28.52	13	4	004	69.34
4	11	002	33.04	14	7	133	76.60
5	4	012	37.08	15	1	024	78.94
6	2	112	40.76	16	5	224	88.29
7	45	022	47.45	17	2	115, 333	95.24
8	1	003, 122	50.48	18	1	044	107.05
9	1	013	53.48	19	4	135	114.46
10	23	113	56.30	20	2	026	128.04
				21	1	335	137.50

---

[1] $M(n)$ and $F(n)$, where n is the number of reflections used in indexing, are the criteria of the indexing reliability [16, 17].

Table 3. Atomic coordinates, interatomic distances, and bond angles in the structures of B11 (isostannite) and stannite

B11 (“isostannite”) ($Cu_{1.86}Fe_{0.80}Sn_{0.99}S_{4.0}$; $P\bar{4}3m$; a = 5.4179(5) Å)

Atom	Position, coordinates	Multiplicity	Me–S distances, Å	S–Me–S angles, deg	B, Å^2
Sn	1*a* (000)	0.64(1)	2.424(4)	109.5(1)	0.8(1)
Fe	1*a* (000)	0.36(1)	2.424(4)	109.5(1)	0.8(1)
Cu	3*c* (0 1/2 1/2)	1.86(2)	2.321(4)	111.3(1) 105.8(1)	2.3(1)
Fe	3*c* (0 1/2 1/2)	0.44(2)	2.321(4)	111.3(1) 105.8(1)	2.3(1)
Sn	3*c* (0 1/2 1/2)	0.33(2)	2.321(4)	111.3(1) 105.8(1)	2.3(1)
S	4*e* (0.2583 0.2583 0.2583) (5)	4.00			1.7(2)
Stannite [1] ($Cu_{1.99}(Fe_{0.81}Zn_{0.18}Cd_{0.02})Sn_{1.0}S_{4.0}$; $I\bar{4}2m$; a = 5.449, c = 10.757(4) Å)					
(Fe + Zn)	2*a* – 000	2	2.348(2)	107.0(1)	0.93
Sn	2*b* – 1/2 1/2 0	2	2.411(2)	109.2(1) 109.6(2)	0.78
Cu	4*d* – 0 1/2 1/4	4	2.320(2)	108.1(1) 112.3(1)	1.55
S	8*i* – *xxz* (*x* = 0.7551 *z* = 0.8702)	8			0.93

tin) atoms are distributed in an ordered fashion over their positions: the centers of the lateral faces of the cube with the coordinates (1/2 0 1/2) and (0 1/2 1/2), by Cu atoms and the centers of the cube bases with the coordinates of (1/2 1/2 0), by (Fe + Sn) atoms. However, the structure solution did not confirm this assumption. Thus, the R factor and the position occupancies were worse than the corresponding data obtained for disordered distribution. In the latter case, the calculated X-ray spectrum agreed with the experimental data. The refinement yielded $R_p = 2.33$, $R_{wp} = 3.00$, $s = 1.20$, D–$WD = 1.53$, $R_B = 2.52$, $R_F = 2.00$. According to the X-ray data, the composition of the phase under study is characterized by partial occupancy of the position 3*c* resulting in the compound “nonstoichiometry” $(Cu_{1.86}Fe_{0.44}Sn_{0.33})_{2.63}(Sn_{0.64}Fe_{0.36})_{1.00}S_{4.00}$.

The interatomic distances in the structure of B11 are in good agreement with the corresponding distances in the structures of analogous compounds [14]. The structures of B11 (“isostannite”) and stannite have close characteristics of the coordination polyhedra of metal atoms (Table 3). In B11, the coordination polyhedron about (Sn + Fe) is a regular tetrahedron with the edge (the Me–S distance, where Me is metal) of 2.424(4) Å and the S–Me–S bond angle of 109.5(1)°.[2] In stannite [1], the coordination tetrahedron of the Sn atom formed by sulfur atoms is almost regular (Sn–S is 2.411(2) Å and the S–Sn–S bond angles are 109.4(1)° and 109.5(1)°). A similar situation is also observed in kesterite [1] (Sn–S = 2.408(1) Å and the S–Sn–S bond angles are 109.4(1)° and 109.5(1)°). The Cu–S distances (in stannite) and (Cu + Fe + Sn)–S distances (in “isostannite”)[3] are almost identical (2.320(2) and 2.321(4) Å, respectively). However, the bond angles in the polyhedra of “copper” atoms are somewhat different: Cu–S–Cu in stannite are 108.1(1)° and 112.3(1)°, and S–Me–S in “isostannite” are 105.8(1)° and 111.3(1)°.

The thermal parameters –B(Å^2) are 2.3(1) (Cu + Fe + Sn in the position 3*c*), 0.8(1) (Sn + Fe in the position 1*a*), and 1.7(2) (S in the position 4*e*). These values are comparable with those in the analogous structures [1, 14, 18].

The composition of the minerals of the stannite group can be represented by the general formula $M1_2M2M3S_4$ ($M1$ = Cu, Ag, or In; $M2$ = Fe, Cu, Zn, Cd, Mn, or Hg; and $M3$ = Sn or Ge). The structures of all the minerals of the stannite group and the related compounds are based on the cubic sphalerite structure (ZnS_{cub}). Three types of metal atoms ($M1$, $M2$, and $M3$) occupy equally oriented tetrahedral positions in the cubic close packing of sulfur atoms. Different order of filled tetrahedra provides the formation of similar but not identical structures, namely, stannite, kesterite, and

---

[2] The position 1*a* (0 0 0) is occupied predominantly by Sn; Sn : Fe = 0.64 : 0.36.

[3] The position 3*c* (0 1/2 1/2) is mixed; Cu : Fe : Sn = 1.86 : 0.44 : 0.33.

velikite. The layers of tetrahedra perpendicular to the threefold axis consist either of atoms of one kind (for example, Cu in stannite and velikite) or atoms of two kinds (Zn–Sn and Cu–Sn in kesterite and Fe–Sn in stannite). The composite of the layers of tetrahedra in the B11 structure is intermediate between the compositions of such layers in stannite and kesterite. The tetrahedra located at $z = 1/2$ are occupied predominantly by copper atoms, whereas the positions at $z = 0$ are mixed (Sn + Fe and Cu + Fe + Sn).[4] Thus, there is partial disorder: the Fe and Sn atoms are distributed over the vertices of the cube in the ratio Sn : Fe ≈ 2 : 1, whereas the positions in the centers of the faces are occupied by the atoms of all the three metals in the ratios Cu : Fe : Sn ≈ 1.86 : 0.44 : 0.33 (Table 3). Therefore, the positions at the vertices and in the centers of the faces of the elementary cube are not identical—the former are occupied by the Sn and Fe atoms, and the latter are mixed (Cu + Fe + Sn). As was mentioned above, an attempt to distribute the copper and (Sn + Fe) atoms over the tetragonal positions orderly [to place Cu and (Sn + Fe) to the positions (0 1/2 1/2) and (1/2 1/2 0), respectively] reduced the reliability factor. Thus, the distribution of metal atoms confirms the cubic and not the tetragonal unit cell.

The results of structure solution obtained differ from those known for stannite [12] annealed at 640°C. The latter was characterized by the sp. gr. $I\bar{4}$ (or $I\bar{4}2m$) and had the following parameters of the tetragonal unit cell: $a = 5.4194(5)$ Å, $c = 10.851(2)$ Å, $c/a = 1.988$. In the latter study, the absence of the statistical (disordered) distribution of the cations (metal atoms) over the tetrahedral positions was stated on the basis of ^{57}Fe and ^{118}Sn Mössbauer spectroscopy data [10]. Today, similar conclusions based only on the Mössbauer spectra and X-ray diffraction patterns (without the determination of the composition and structure) do not seem to be sufficiently justified. Moreover, it is quite obvious that the objects studied were, in fact, different phases because the annealing temperatures were different (400 and 640°C for the B11 phase and the phase prepared by Pietzsch and Frietzsch [12], respectively) and the phases had different compositions, namely, $Cu_2FeSnS_{3.949}$ with the ratio Me : S > 1 [12] and $Cu_{1.86}Fe_{0.80}Sn_{0.99}S_{4.00}$ with Me : S < 1 (the present study).

The question about the valences of the Fe, Cu, and Sn atoms and their distribution over the positions in stannite-like phases is rather intricate. To answer this question, the compounds of the isomorphous series Cu_3SnS_4–Cu_2FeSnS_4 were studied by different methods, including the Mössbauer spectroscopy. According to the preliminary results (V.S. Rusakov, the Faculty of Physics of the Moscow State University, the private communication), iron atoms in the compound under study are in the divalent state. The available data with due regard for the "size factor" (the ionic radii) and the well-known concepts, lead to the following general crystallochemical formula of the compound $Cu^{+1}_{1.28}Cu^{+2}_{0.58}Fe^{+2}_{0.80}Sn^{+2}_{0.80}S_4$.

The high-temperature sphalerite-type cubic modification of Cu_3GeS_4 ($a = 5.247(3)$ Å) [19] is structurally similar to the phase considered in the article. As regards "isostannite" [2] and other "stannite-like" compounds, for example, a "cubic phase with a large unit cell" [6–8, 10–12], they all drastically differ from $Cu_{1.86}Fe_{0.80}Sn_{0.99}S_{4.00}$ because of the metal-to-sulfur ratio. For all the phases described earlier, this ratio exceeds unity, whereas this ratio for B11 is less than unity, which undoubtedly should be reflected in the electron-density distributions.

CONCLUSIONS

The cubic modification of stannite with a "small" unit cell of the composition $Cu_{1.86}Fe_{0.80}Sn_{0.99}S_{4.00}$ has been synthesized for the first time.

Full-profile analysis demonstrated that the $Cu_{2-x}FeSnS_4$ structure (sp. gr. $P\bar{4}3m$, $a_0 = 5.4179(5)$ Å) is characterized by the statistical distribution of the Cu, Fe, and Sn atoms over the tetrahedral positions of the cubic close packing of sulfur atoms. As a result, the layers of tetrahedra filled with the Sn and Fe atoms alternate with the layers of "mixed" tetrahedra (Cu + Fe + Sn).

Taking into account the atomic distributions and the Mössbauer-spectroscopy data, the crystallochemical formula $Cu_{2-x}FeSnS_4$ can be written as $Cu^{+1}_{1.28}Cu^{+2}_{0.58}Fe^{+2}_{0.80}Sn^{+4}_{0.99}S_4$.

The existence of the "prototype" structure for the stannite group at room temperature has been established. This "prototype" structure is characterized by a "small" unit cell and the disordered distribution of the metal atoms.

ACKNOWLEDGMENTS

This study was supported by the Russian Foundation for Basic Research, project no. 96-05-64296.

REFERENCES

1. S. R. Hall, J. T. Szymanski, and J. M. Stewart, Can. Mineral. **16**, 131 (1978).
2. G. F. Claringbull and M. H. Hey, Mineral. Abstr. **13**, 31 (1956).
3. P. Ramdohr, *Die Erzmineralien und ihre Verwachsungen* (Akademie-Verlag, Berlin, 1960; Inostrannaya Literatura, Moscow, 1962).
4. P. Ramdohr, *Ore Minerals and Their Intergrowths* (Springer-Verlag, New York, 1975).

---

[4] The height $z = 1/2$ corresponds to $z = 1/4$ in the tetragonal unit cell of the stannite–kesterite type ($c \approx 2a$).

5. T. N. Chvileva, M. S. Bezsmertnaya, É. M. Spiridonov, *et al.*, *Handbook for Identification of Ore Minerals in Reflected Light* (Nedra, Moscow, 1988).
6. E. D. Franz, Neues Jahrb. Mineral., Monatsh. **5**, 218 (1971).
7. T. Ohtsuki, A. Kitakaze, and A. Sugaki, Sci. Rep. Tohoku Imp. Univ., Ser. S **14** (3), 269 (1980).
8. T. A. Kalinina and S. N. Nenasheva, Dokl. Akad. Nauk SSSR **305** (2), 421 (1989).
9. G. Springer, Can. Mineral. **11**, 535 (1972).
10. N. Wang, Neues Jahrb. Mineral., Abh. **144** (3), 319 (1982).
11. N. Wang, in *Ore Genesis—the State of the Art*, Ed. by G. C. Amstutz, A. El. Goresy, G. Frenzel, C. Kluth, and G. Moh (Springer-Verlag, Berlin, 1982), p. 726.
12. E.-D. Pietzsch and E. Frietzsch, Chem. Erde **43** (2), 117 (1984).
13. J. Schneider, *Profile Refinement on IBM-PS's*, Petten, IU Cryst., 1989.
14. J. T. Szymanski, Can. Mineral. **16**, 147 (1978).
15. P. E. Werner, L. Ewriksson, and M. Westdahl, J. Appl. Crystallogr. **18**, 367 (1985).
16. P. M. De Wolff, J. Appl. Crystallogr. **1**, 108 (1968).
17. G. S. Smith and R. L. Snider, J. Appl. Crystallogr. **10**, 12 (1979).
18. Yu. K. Kabalov, T. L. Evstigneeva, and É. M. Spiridonov, Kristallografiya **43** (1), 21 (1998) [Crystallogr. Rep. **43**, 16 (1998)].
19. N. Wang, Neues Jahrb. Mineral., Abh. **159** (2), 137 (1988).

Translated by T. Safonova

Crystallography Reports, Vol. 46, No. 3, 2001, pp. 373–376. Translated from Kristallografiya, Vol. 46, No. 3, 2001, pp. 423–426.
Original Russian Text Copyright © 2001 by Grippa, D'yachenko, Abakumov, Antipov.

STRUCTURE OF INORGANIC COMPOUNDS

Crystal Structure of $BaNb_{0.9}S_3$

A. Yu. Grippa, O. G. D'yachenko, A. M. Abakumov, and E. V. Antipov
Chemistry Department, Moscow State University, Vorob'evy gory, Moscow, 119899 Russia
e-mail: grippa@icr.chem.msu.ru

Received March 2, 2000

Abstract—Single crystals of the composition $BaNb_{0.9}S_3$ have been synthesized from the BaS, Nb, and S mixture and the $BaCl_2$ flux at 900°C. The $BaNb_{0.9}S_3$ structure was refined by X-ray single-crystal and electron diffraction data. The compound is crystallized in the sp. gr. $P6_3/mmc$ ($z = 2$) with the unit-cell parameters $a = 6.839(1)$ Å and $c = 5.745(1)$ Å. It was established that the cationic vacancies in the niobium positions are statistically distributed over the structure. *© 2001 MAIK "Nauka/Interperiodica".*

INTRODUCTION

Transition metals of group V of the Periodic Table form sulfides of the composition $BaMS_3$. All these compounds possess the hexagonal structure of the $BaNiO_3$ type, sp. gr. $P6_3/mmc$ (Fig. 1). The structure is formed by the hexagonal close packing of BaS_3 layers, with one-fourth of the octahedral voids between these layers being occupied by transition-metal atoms. Such a packing provides the formation of the chains of MS_6-octahedra sharing the faces along the c-axis [1, 2].

Despite the simple structure, the data on the stoichiometry of $BaNbS_3$ are inconsistent. Thus, it is stated that single-phase specimens are formed only at the Ba/Nb ratio equal to 1 : 0.8 [3], which indicates that the compound is nonstoichiometric ($BaNbS_3$). However, it was also shown [4] that such a Ba/Nb ratio provides the formation of the $BaNbS_3$ and BaS mixture, whereas the single-phase $BaNbS_3$ specimen can be formed only at the cationic ratio equal to 1 : 1. The data obtained in [5] showed that both stoichiometric compound $BaNbS_3$ and the compound with vacancies in the Nb and S sublattices, $BaNb_{0.83}S_{2.8}$, can be formed. In the latter case, the composition was calculated from the X-ray powder diffraction data (the refinement of the $BaNb_{1-x}S_{3-\delta}$ structure by the Rietveld method with the invocation of the gravimetric data). Recent studies of these compounds indicate the narrower range of anionic nonstoichiometry for the compound $BaNbS_{3-\delta}$, where $-0.07 < \delta < 0.06$ [6]. However, no synthesis of $BaNbS_3$ crystals appropriate for the X-ray diffraction analysis was reported in the above studies. The elemental composition of the synthesized compounds has not been determined either.

In the present study, we synthesized $BaNbS_3$ single crystals and determined their crystal structure. We also established cationic vacancies in the niobium positions.

EXPERIMENTAL

The starting materials for the synthesis of $BaNbS_3$ crystals were barium sulfide, extrapure-grade metallic niobium, and extrapure-grade sulfur. Barium sulfide BaS was obtained by annealing of analytic-grade $BaSO_4$ in a hydrogen flow at 900°C for 48 h. The content of the $BaCl_2$ flux did not exceed 10% of the initial mass of the mixture. The BaS, Nb, S, and $BaCl_2$ mixture was placed into a quartz ampule, which was then evacuated and sealed. The synthesis was performed for 72 h at 900°C. The cooling rate was 1°C/min.

The X-ray phase analysis of polycrystal specimens was performed in an FR-552 Guinier-type focusing camera with the effective diameter 228 mm ($CuK_{\alpha1}$-radiation). The inner standard (germanium) was added to the specimens.

The experiment was performed on a four-circle single-crystal diffractometer CAD-4F (Enraf-Nonius). The experimental conditions are indicated in Table 1.

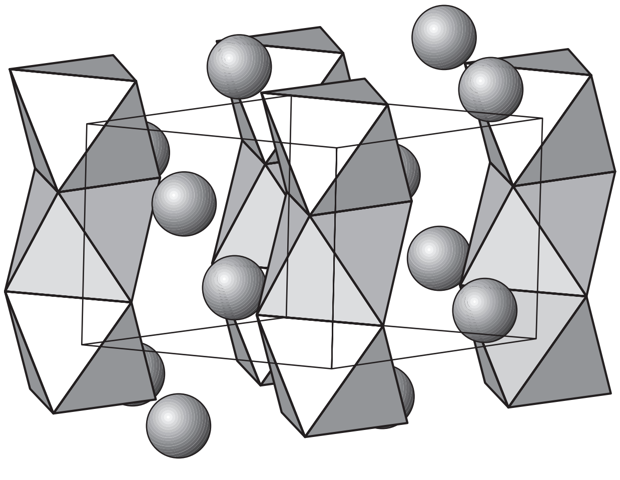

Fig. 1. Structure of complex $BaNbS_3$ sulfide.

Table 1. Crystallographic data and the parameters of the diffraction experiment for $BaNb_{0.9}S_3$

Sp. gr.	$P6_3/mmc$
a, Å	6.839(1)
c, Å	5.745(1)
V, Å^3	232.7(1)
Z	2
Calculated density, g/cm^3	4.658(2)
Absorption coefficient, cm^{-1}	121.03
Absorption correction	Proceeding from the real shape of crystals
Scanning type	$\omega/1.33\theta$
Radiation	MoK_α
Wavelength, Å	0.71069
Crystal dimensions, mm	0.06 × 0.07 × 0.19
Diffractometer	Enraf-Nonius CAD-4F
Maximum, $\sin\theta/\lambda$	0.742
Weighting scheme	$1/\sigma(F)^2$
Total number of measured reflections	947
Number of independent refections	181
Number of reflections used in refinement	143
Significance criterion	$F \geq 6\sigma(F)$
Number of refined parameters	10
R_F; R_w	0.0240; 0.0238

The structure was solved with the use of the CSD complex of programs [7].

The crystal composition was determined by the energy-dispersive X-ray microanalysis in a JEOL JSM-820 scanning transmission electron microscope with the LINK AN10 000 system for microanalysis at the accelerating voltage 20 kV. Prior to the analysis, the specimens were placed onto the conductive carbon film glued to an aluminum holder. The element content was averaged over five to six measurements with the use of the K_α-line of sulfur and the L_α-lines of barium and niobium. The standards were the corresponding metals and sulfur.

Electron diffraction patterns from the $BaNbS_3$ specimens were obtained in a JEOL 2000 FX II transmission-electron microscope operating at an accelerating voltage of 200 kV. Prior to the electron-microscopy study, specimens were crushed in butanol in an agate mortar and the drops of the obtained suspension were applied to a copper grid with an amyl acetate glue.

RESULTS AND DISCUSSION

In the course of growth experiment, we synthesized $BaNbS_3$ crystals from the $BaCl_2$ flux. The X-ray phase analysis showed, in addition to the complex sulfide and the flux, the presence of some amounts of $BaNb_2S_5$ and NbS_2. The synthesized black single crystals had the shape of rectangular parallelepipeds.

The X-ray diffraction analysis was performed on a 0.06 × 0.07 × 0.19-mm-large single crystal. The parameters of the diffraction experiment are listed in Table 1.

The analysis of reflections with $F \geq 6\sigma(F)$ revealed the $hh2\bar{h}l$ ($l = 2n$) extinctions characteristic of the sp. gr. $P6_3/mmc$. The unit-cell parameters were refined over 24 reflections from the range 16° < θ < 18°.

We used as the initial model for the refinement of $BaNbS_3$ the structure of $BaVS_3$ crystals. The least squares refinement in the isotropic approximation of atomic displacement parameters (ADP) was performed under the assumption that all the positions are fully (100%) occupied up to the value of the reliability factor $R_F = 0.0775$. The structure refinement with the anisotropic ADP reduced this value to $R_F = 0.0326$.

The problem of the $BaNbS_3$ stoichiometry was still open. At 100% occupancy of the niobium positions, the

Table 2. Positional and atomic-displacement parameters in the $BaNb_{0.9}S_3$ structure

Atom	Position	x	y	z	B_{eq}, Å^2	Occupancy
Ba	2d	1/3	2/3	3/4	1.63(3)	1
Nb	2a	0	0	0	1.52(4)	0.892(8)
S	6h	0.1702(2)	2x	1/4	1.49(4)	1

Table 3. Anisotropic atomic-displacement parameters in the $BaNb_{0.9}S_3$ structure ($B_{13} = B_{23} = 0$)

	B_{11}	B_{22}	B_{33}	B_{12}
Ba	1.49(3)	1.49(3)	1.91(5)	1/2 B_{11}
Nb	1.03(5)	1.03(5)	2.52(9)	1/2 B_{11}
S	1.48(8)	0.79(9)	1.99(10)	1/2 B_{12}

Table 4. Selected interactomic distances (Å) and valence angles (deg) in the $BaNb_{0.9}S_3$ structure

Ba–S 3.420(3) × 6	Nb–S 2.476(2) × 6	S–Nb–S 89.72(5) × 2
Ba–S 3.462(1) × 6	Nb–Nb 2.873(1) × 2	S–Nb–S 90.28(5) × 2
		S–Nb–S 180.00(6) × 2

isotropic ADP equals 1.99(6) Å^2. In the analogous $BaVS_3$ structure, the ADP of vanadium atoms equals 0.5 Å^2. The refinement of the niobium-position occupancy resulted in the value $g = 0.892(8)$ with the simultaneous decrease of the ADP down to 1.52(4) Å^2 and the reliability factor to 0.0240. In both cases, the refinement of the occupancies of the barium and the sulfur positions yielded $g = 1$. Tables 2, 3, and 4 list the atomic positions, ADP, and selected Table 4 interactomic distances.

The $BaNbS_3$ compound crystallizes in the $BaNiO_3$ structure-type (Fig. 1). The structure of this complex sulfide is built by sharing-faces NbS_6-octahedra forming infinite linear chains along the c-axis of the unit cell, whereas the barium atoms are located between these chains. Barium atoms in this structure are characterized by the coordination number 12 (the coordination polyhedron is an hexagonal analogue of a cuboctahedron).

The analysis of the interatomic distances and the valence angles in the $BaNb_{0.9}S_3$ structure shows that they agree with the corresponding data for $BaVS_3$ [1] and $BaTaS_3$ [2]. The NbS_6-octahedra are practically undistorted. The Nb–S distances are equal to 2.476 Å and are slightly longer than the analogous distances in the stoichiometric $BaNbS_3$ (2.455 Å) but are shorter than in $BaNb_{0.8}S_3$ (2.529 Å) [5]. The existence of cationic vacancies in the niobium positions explains an increase of the ADP B_{eq} of cations in comparison with the ADP in the analogous $BaVS_3$ and $BaTaS_3$ structures. At the same time, the analysis of the ADP of Nb atoms indicate the anisotropy of thermal vibrations. Thus, the parameter B_{33} corresponding to thermal vibrations along the c-axis of the unit cell (i.e., along the chain of Nb–Nb atoms) exceeds $B_{11} = B_{22}$ by a factor of almost 2.4. The similar situation also takes place in the $BaTaS_3$ structure ($B_{33} > B_{11}$ by a factor of 2.7) [2] and in the structure-prototype of this row of compounds, namely, $BaNiO_3$ ($B_{33} > B_{11}$ by a factor of 2.5) [8].

The conclusion about the cationic vacancies in the niobium positions was made from the X-ray single crystal data and was confirmed by the energy-dispersive X-ray microanalysis, according to which the Ba : Nb : S ratio equals 19.6(1) : 17.7(3) : 62.7(2) (for the stoichiometric $BaNbS_3$, Ba : Nb : S = 20 : 20 : 60, which corresponds to the formula $Ba_{0.94(1)}Nb_{0.85(1)}S_3$). Thus, the elemental analysis with due regard for its accuracy confirms the Ba : Nb ratio obtained from the occupancy refinement of cationic positions by the data of the single-crystal diffraction experiment.

Figure 2 shows the electron diffraction patterns from $BaNb_{0.9}S_3$ taken along the [0001], [11$\bar{2}$0], and [10$\bar{1}$0] directions.

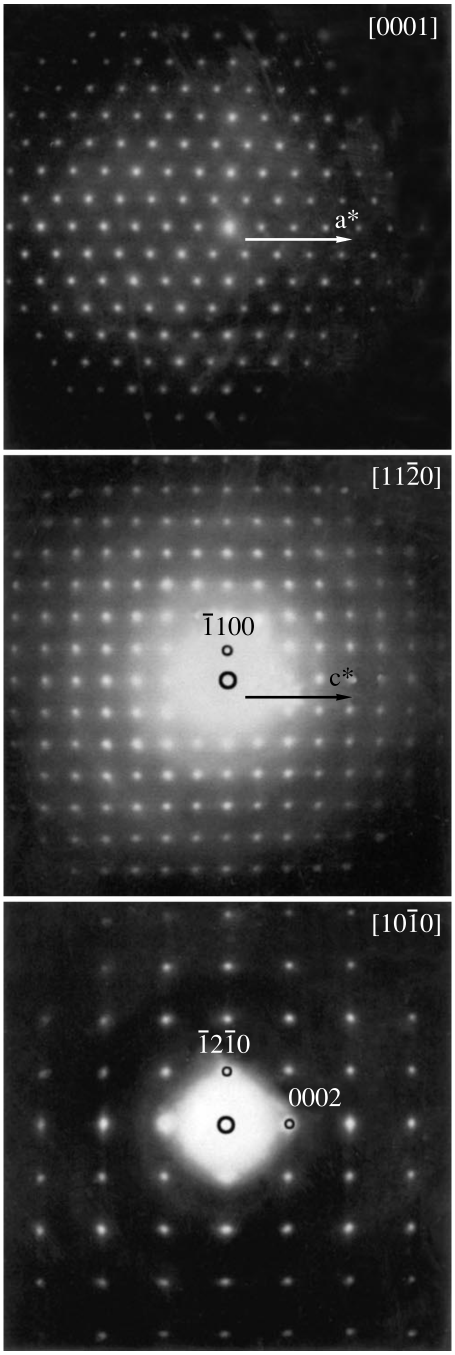

Fig. 2. Electron diffraction patterns from $BaN_{0.9}S_3$ compound taken along the [0001], [11$\bar{2}$0], and [10$\bar{1}$0] directions.

In the [0001] zone, the location of reflections corresponds to the hexagonal symmetry. In the electron diffraction pattern from the [10$\bar{1}$0] zone, the $hh\bar{2}hl$ reflections with odd l are systematically absent, which indicates the most symmetric sp. gr. $P6_3/mmc$. The $000l$-type reflections with $l = 2n + 1$ in the [11$\bar{2}$0] zone are formed as a result of double diffraction. This is also confirmed by the fact that no such reflections were observed in the $[10\bar{1}0]$ zone.

The electron-diffraction study of $BaNb_{0.9}S_3$ showed that the formation of cationic vacancies did not give rise to the formation of any superstructure, which indicates the statistical character of the vacancy distribution.

CONCLUSIONS

Single crystals of complex sulfide of the composition $BaNb_{0.9}S_3$ have been synthesized and studied for the first time. The structure of this sulfide was determined by the X-ray diffraction method. The X-ray diffraction data and the local X-ray diffraction analysis showed the existence of cationic vacancies in the niobium positions. The electron diffraction study of $BaNb_{0.9}S_3$ crystallites showed the absence of any superstructure, which indicated the statistical distribution of these vacancies over the structure.

ACKNOWLEDGMENTS

The study was supported by the Russian Foundation for Basic Research, project no. 00-03-32558. We are also grateful to Dr. Gunnar Svensson from the Arrhenius Laboratory of the University of Stockholm for his help in the elemental analysis of complex $BaNb_{0.9}S_3$ sulfide.

REFERENCES

1. R. A. Gardner, M. Vlasse, and A. Wold, Acta Crystallogr., Sect. B: Struct. Crystallogr. Cryst. Chem. **B25**, 781 (1969).
2. R. A. Gardner, M. Vlasse, and A. Wold, Inorg. Chem. **8**, 2784 (1969).
3. P. C. Donohue and J. F. Weiher, J. Solid State Chem. **10**, 142 (1974).
4. J. Yan, K. V. Ramanujachary, and M. Greenblatt, Mater. Res. Bull. **30**, 463 (1995).
5. S.-J. Kim, H.-S. Bae, K.-A. Yee, *et al.*, J. Solid State Chem. **115**, 427 (1995).
6. N. Kiijima, K. Morie, S. Chikazawa, *et al.*, J. Solid State Chem. **142**, 57 (1999).
7. L. G. Akselrud, Yu. N. Gryn, P. Yu. Zavalij, *et al.*, *CSD. Thes. Report on 12th ESM, Moscow, 1989*, Vol. 3, p. 155.
8. Y. Takeda, F. Kanamaru, M. Shimada, and M. Koizumi, Acta Crystallogr., Sect. B: Struct. Crystallogr. Cryst. Chem. **B32**, 2464 (1976).

Translated by L. Man

Crystallography Reports, Vol. 46, No. 3, 2001, pp. 377–382. Translated from Kristallografiya, Vol. 46, No. 3, 2001, pp. 427–432.

STRUCTURE OF COORDINATION COMPOUNDS

Crystal Structure of Strontium Aqua(ethylenediaminetetraacetato)cobaltate(II) Tetrahydrate $Sr[Co\mathit{Edta}(H_2O)] \cdot 4H_2O$

L. A. Zasurskaya*, I. N. Polyakova, A. L. Poznyak***,**
T. N. Polynova*, and V. S. Sergienko**

** Moscow State University, Vorob'evy gory, Moscow, 119899 Russia*
*** Kurnakov Institute of General and Inorganic Chemistry, Russian Academy of Sciences, Leninskiĭ pr. 31, Moscow, 117907 Russia*
**** Institute of Molecular and Atomic Physics, Belarussian Academy of Sciences, pr. F. Skoriny 70, Minsk, 220100 Belarus*

Received December 16, 1999

Abstract—The complex $Sr[Co^{II}\mathit{Edta}] \cdot 5H_2O$ (**I**) (where Edta^{4-} is the ethylenediaminetetraacetate ion) has been synthesized. The crystal structure of this compound is determined by X-ray diffraction. Crystals are monoclinic, $a = 7.906(2)$ Å, $b = 12.768(2)$ Å, $c = 18.254(3)$ Å, $\beta = 95.30(3)°$, $V = 1834.8$ Å^3, space group $P2_1/n$, $Z = 4$, and $R = 0.036$. The structure is built up of the binuclear complex fragments $\{Sr(H_2O)_3[Co\mathit{Edta}(H_2O)]\}$, which consist of the anionic $[Co\mathit{Edta}(H_2O)]^{2-}$ and cationic $[Sr(H_2O)_3]^{2+}$ units linked by the Sr–O bonds into a three-dimensional framework. The coordination polyhedra of the Co and Sr atoms are mono- and bicapped trigonal prisms. The coordination sphere of the Co atom (the coordination number is equal to 6 + 1) involves six donor atoms (2N and 4O) of the Edta^{4-} ligand and the O_w atom of water molecule. One of the Co–O distances (2.718 Å) is considerably longer than the other Co–O_{lig} distances (2.092–2.190 Å) and the Co–$O_w(1)$ distance (2.079 Å). The Sr coordination polyhedron (the coordination number is eight) contains three water molecules, three carbonyl O atoms of the three different anionic complexes, and two O atoms of one acetate group of the fourth anionic complex. The Sr–O distances fall in the range 2.535–2.674 Å. The structural formula of the compound is $\{Sr(H_2O)_3[Co\mathit{Edta}(H_2O)]\}_{3\infty} \cdot H_2O$. *© 2001 MAIK "Nauka/Interperiodica".*

INTRODUCTION

Unlike cobalt(III) ethylenediaminetetraacetates, which are characterized by the formation of octahedral anionic complexes, the structure of cobalt(II) complexes can differ in various crystal structures. This reflects the kinetic lability of complexes with a $3d^7$ high-spin configuration of complexing metal atom. For example, in the chain structure of $Mg[Co^{II}\mathit{Edta}] \cdot 6H_2O$ (where Edta^{4-} is the ethylenediaminetetraacetate ion), the anionic chain fragments $[Co^{II}\mathit{Edta}]^{2-}$ exhibit an octahedral structure [1]. The same structure was observed for the $[Co^{III}\mathit{Edta}]^-$ anions in island crystal structures of $Mg[Co^{III}\mathit{Edta}]_2 \cdot 10H_2O$ and $Ca[Co^{III}\mathit{Edta}]_2 \cdot 7H_2O$ in our earlier work [2]. At the same time, in the $Ca[Co^{II}\mathit{Edta}] \cdot 5H_2O$ complex with a framework structure [3], the Co(II) coordination polyhedron is completed by water molecule, which leads to the formation of the $[Co^{II}\mathit{Edta}(H_2O)]^{2-}$ anionic fragments with the Co polyhedron in the form of a strongly distorted monocapped trigonal prism. It was of interest to determine in more details the structure of complexes with a similar composition involving other alkaline-earth cations and to elucidate the role of these cations in the formation of crystal structure. However, we succeeded in preparing crystals of only a strontium analogue. The present paper reports the results of their X-ray structure analysis.

EXPERIMENTAL

Crystals were prepared as follows. Equimolar amounts of $CoSO_4 \cdot 7H_2O$ and $H_4\mathit{Edta}$ were dissolved in a minimum volume of hot water. Then, strontium or barium carbonate was added portionwise to the mixture until the liberation of carbon dioxide ceased. After the filtration, the solution was left to evaporate at room temperature. In the first case, pink crystals of composition $Sr[Co\mathit{Edta}] \cdot 5H_2O$ (**I**) were formed within a few days. In the second case, the evaporation of the solution led to the formation of a powder precipitate. Attempts at its recrystallization through the evaporation of an aqueous solution at room temperature or slow cooling of a hot saturated solution resulted in the formation of a similar precipitate without crystals suitable for X-ray diffraction analysis.

Crystals **I** are monoclinic, $a = 7.906(2)$ Å, $b = 12.768(2)$ Å, $c = 18.254(3)$ Å, $\beta = 95.30(3)°$, $V = 1834.8$ Å^3, $Z = 4$ (formula unit $C_{10}H_{22}N_2O_{13}CoSr$), space group $P2_1/n$, and $d_{calcd} = 1.900$ g/cm^3. The X-ray

Table 1. Atomic coordinates and thermal parameters in structure **I**

Atom	*x*	*y*	*z*	U_{eq}/U_{iso}, Å^2
Co(1)	0.57680(7)	0.15431(4)	0.76076(3)	0.0207(2)
Sr(1)	0.24295(5)	0.33464(3)	0.94305(2)	0.0220(1)
O(1)	0.6952(4)	0.2629(3)	0.8320(2)	0.027(1)
O(2)	0.9402(5)	0.3204(3)	0.8847(2)	0.043(1)
O(3)	0.6806(4)	0.1849(3)	0.6557(2)	0.029(1)
O(4)	0.8280(5)	0.1036(3)	0.5747(2)	0.035(1)
O(5)	0.4354(5)	0.0424(3)	0.6948(2)	0.035(1)
O(6)	0.2662(4)	–0.0967(3)	0.6946(2)	0.035(1)
O(7)	0.3617(5)	0.1813(3)	0.8671(2)	0.035(1)
O(8)	0.4346(5)	0.1735(3)	0.9874(2)	0.033(1)
$O_w(1)$	0.4001(5)	0.2657(3)	0.7206(2)	0.036(1)
$O_w(2)$	0.5507(5)	0.3940(3)	0.9373(2)	0.034(1)
$O_w(3)$	0.1356(6)	0.5246(3)	0.9533(2)	0.047(1)
$O_w(4)$	0.0522(7)	0.2215(4)	1.0273(3)	0.051(2)
$O_w(5)$	0.1990(8)	0.2360(5)	0.5822(3)	0.079(2)
N(1)	0.8438(5)	0.0954(3)	0.7722(2)	0.023(1)
N(2)	0.5589(5)	0.0187(3)	0.8345(2)	0.023(1)
C(1)	0.8570(5)	0.2624(4)	0.8421(2)	0.024(1)
C(2)	0.9487(5)	0.1887(4)	0.7931(3)	0.029(1)
C(3)	0.7892(6)	0.1202(4)	0.6384(2)	0.024(1)
C(4)	0.8803(6)	0.0551(4)	0.6995(3)	0.029(1)
C(5)	0.8654(6)	0.0133(4)	0.8287(3)	0.030(1)
C(6)	0.7048(6)	–0.0509(4)	0.8271(3)	0.029(1)
C(7)	0.3659(6)	–0.0314(3)	0.7264(3)	0.025(1)
C(8)	0.4017(6)	–0.0370(4)	0.8093(3)	0.029(1)
C(9)	0.4415(6)	0.1418(3)	0.9229(2)	0.024(1)
C(10)	0.5565(6)	0.0500(4)	0.9121(2)	0.028(1)
H(2*A*)	0.9501(5)	0.2191(4)	0.7465(3)	0.05
H(2*B*)	1.0640(5)	0.1765(4)	0.8124(3)	0.05
H(4*A*)	1.0044(6)	0.0501(4)	0.6928(3)	0.05
H(4*B*)	0.8011(6)	–0.0205(4)	0.6954(3)	0.05
H(5*A*)	0.9158(6)	0.0480(4)	0.8741(3)	0.05
H(5*B*)	0.9505(6)	–0.0343(4)	0.8243(3)	0.05
H(6*A*)	0.7208(6)	–0.0994(4)	0.8713(3)	0.05
H(6*B*)	0.6819(6)	–0.0830(4)	0.7792(3)	0.05
H(8*A*)	0.3170(6)	0.0041(4)	0.8211(3)	0.05
H(8*B*)	0.3976(6)	–0.1012(4)	0.8221(3)	0.05
H(10*A*)	0.6484(6)	0.0767(4)	0.9386(2)	0.05
H(10*B*)	0.5261(6)	–0.0002(4)	0.9384(2)	0.05
$H(1)_{w1}$	0.343(8)	0.297(5)	0.748(4)	0.05(2)
$H(2)_{w1}$	0.316(8)	0.256(5)	0.677(4)	0.06(2)
$H(1)_{w2}$	0.61(1)	0.356(6)	0.914(4)	0.08(3)
$H(2)_{w2}$	0.597(8)	0.447(5)	0.943(3)	0.05(2)
$H(1)_{w3}$	0.100(8)	0.542(5)	0.908(3)	0.05(2)
$H(2)_{w3}$	0.115	0.568	0.979	0.05
$H(1)_{w4}$	0.09(1)	0.242(7)	1.072(5)	0.09(3)
$H(2)_{w4}$	–0.046(9)	0.233(6)	1.016(4)	0.06(2)
$H(1)_{w5}$	0.123(8)	0.256(5)	0.564(3)	0.04(2)
$H(2)_{w5}$	0.245	0.172	0.553	0.05

diffraction data were collected on an Enraf–Nonius CAD4 diffractometer (MoK_α radiation, graphite monochromator, ω scan mode, $\theta_{max} = 27°$). The structure was solved by the direct method. The calculations were performed according to the SHELX76 [4] and SHELXS86 [5] software packages. The coordinates of hydrogen atoms were determined from difference Fourier syntheses. The positional and thermal parameters were refined by the least-squares procedure using 3232 reflections with $I > 3\sigma(I)$ to $R = 0.036$ ($wR = 0.040$, *Goof* = 1.9115) in the anisotropic approximation for all non-hydrogen atoms and in the isotropic approximation for the hydrogen atoms in water molecules [except for the $H(2)_{w3}$ and $H(2)_{w5}$ atoms, for which the positions and thermal parameters were fixed]. The hydrogen atoms in methylene groups were refined according to the riding-atom model with the fixed value $U_{iso} = 0.05$ Å^2. Table 1 lists the atomic coordinates and thermal parameters U_{eq} (U_{iso}).

RESULTS AND DISCUSSION

The framework structure of Sr[Co*Edta*] · $5H_2O$ (**I**) is built up of the binuclear complex fragments $\{Sr(H_2O)_3[Co\mathit{Edta}(H_2O)]\}$, which consist of the anionic $[Co\mathit{Edta}(H_2O)]^{2-}$ and cationic $[Sr(H_2O)_3]^{2+}$ units linked by the Sr–O bonds (Fig. 1).

The nearest environment of the Co(II) atom in the anionic units involves six donor atoms (2N and 4O) of the Edta^{4-} ligand and the $O_w(1)$ atom of water molecule. The coordination polyhedron can be represented as a distorted monocapped trigonal prism. The prism bases are formed by the O(1), O(3), N(1) and O(5), O(7), N(2) donor atoms of the ligand. The $O_w(1)$ atom (“cap”) is located above the O(1)O(3)O(5)O(7) face. The distortions of the monocapped trigonal prism predominantly manifest themselves in the fact that its edges are nonparallel: the N(1)–N(2) line forms an angle of 11.6° with the O(1)–O(7) line and an angle of 20.7° with the O(3)–O(5) line.

Upon incorporation of an additional water molecule into the coordination sphere of a metal, two situations become possible. In the first case, one acetate group is displaced from the coordination sphere of the metal, which brings about a decrease in the dentate capacity of the ligand. For example, in the framework structure of $Co_2\mathit{Edta} \cdot 2H_2O$ [6], the coordination number of one of three symmetrically independent Co(II) atoms in the $[Co\mathit{Edta}(H_2O)]^{2-}$ anionic complex remains equal to six. In the other case, the introduction of a water molecule does not affect the dentate capacity of the ligand and an increase in the coordination number to seven leads to a uniform elongation of the metal–ligand distances. Specifically, in the structure of $Co_5(\mathit{Edta})_2(ClO_4)_2 \cdot 20H_2O$ [7], the coordination number of one of three symmetrically independent Co(II) atoms in the $[Co\mathit{Edta}(H_2O)]^{2-}$ anionic fragment is equal to seven and the coordination polyhedron is a monocapped trigonal prism. A certain intermediate variant is realized in the structures of compound **I**, an analogous calcium complex of composition Ca[Co*Edta*] · $5H_2O$ [3], and Zn[Co*Cdta*] · $9H_2O$ (where $Cdta^{4-}$ is the cyclohexanediaminetetraacetate ion) [8]. The incorporation of a water molecule into the coordination sphere of the Co(II) atom results only in an elongation of one $Co–O_{lig}$ bond (the coordination number of cobalt is equal to 6 + 1) rather than in the complete displacement of one acetate group. As a consequence, a partly opened quasi-ring G_q is formed in the equatorial plane in these complexes in addition to the normal *E*, two *R*, and one *G* metallocycles.

The specific structural feature of compound **I** and the calcium complex is the concurrent participation of both oxygen atoms [O(7) and O(8)] of one quasi-free acetate group in the coordination of the Sr^{2+} and Ca^{2+} cations, which brings about the formation of the four-membered ring $–C\overset{O}{\underset{O}{\langle\,\rangle}}M'$. Moreover, the anionic and cationic fragments are linked together by the elongated bond Co–O(7). In this respect, the $\{Sr(H_2O)_3[CoEdta(H_2O)]\}$ binuclear fragment can be formally treated as a structural unit of crystal **I**.

The mutual arrangement of metallocycles in structure **I**, as in other complexes with a polyhedron in the form of a monocapped trigonal prism, can be designated as *E*, *R*/*G* [9]. All glycinate rings adopt a distorted envelope conformation, and the *E* ring has an asymmetric *gauche* conformation. The deviations of the C(5) and C(6) atoms from the N(1)CoN(2) plane are equal to 0.203 and –0.477 Å, respectively.

The five-membered rings in the complex are considerably distorted, as evidenced by the sums of endocyclic angles. As could be expected, the differences between these sums and the ideal value (538.4°) are the largest in the $G_q(2)$ quasi-ring (512.5°) and the *G*(1) ring (523.9°). The differences are smaller in the *R*(1) and *R*(2) rings (529.0° and 528.9°) and also in the *E* ring (516.4°) for which the ideal value is equal to 527.9°. The endocyclic angles at the Co atom varies from 65.4(1)° in the $G_q(2)$ ring to 78.3(1)° in the *R*(1) ring. Similar bond angles are observed in the Ca^{2+} complex [3], for which the minimum endocyclic angle in the partly opened ring is also equal to 65.4(2)° and the maximum endocyclic angle is 79.2(2)° (*E* ring).

The bond lengths in the Co(II) complexes with the Sr^{2+} and Ca^{2+} cations are also close to each other (Table 2). As mentioned above, the structure of the anionic complexes is rather unusual. One Co–O(7) distance [2.718(3) and 2.743(5) Å in the Sr and Ca complexes, respectively] in the $G_q(2)$ ring is substantially longer than the other $Co–O_{lig}$ distances. The remaining metal–ligand bonds have normal lengths. The $Co–O_R$ distances [with mean values of 2.092(3) and 2.107(5) Å in the Sr and Ca complexes, respectively] are less than the $Co–O_{G(1)}$ [2.190(3) and 2.195(5) Å] and Co–N [2.220(4) and 2.207(4) Å] distances. The $Co–O_w(1)$ distances in two complexes [2.079(4) and 2.059(5) Å] are close to the $Co–O_R$ distances.

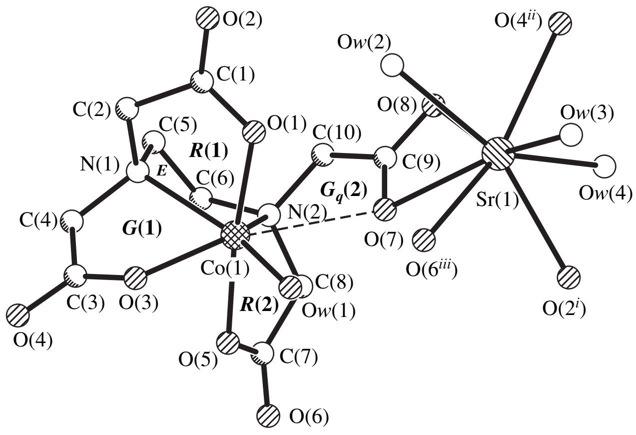

Fig. 1. Binuclear fragment $\{Sr(H_2O)_3[CoEdta(H_2O)]\}$ in structure **I**.

Similar characteristics of the Co(II) polyhedron in the form of a monocapped trigonal prism were obtained earlier for the $[CoH_2Edta(H_2O)]$ complex with the protonated ligands [3]. However, in this case, the nonequality of two $Co–O_G$ bonds [their difference Δ is equal to 0.199(3) Å] is less pronounced compared to that in the complexes with the Sr^{2+} and Ca^{2+} cations

Table 2. Bond lengths in the Co and *M*' polyhedra in structures of *M*'[Co*Edta*(H_2O)] · $4H_2O$

Bond	*d*, Å	
	M' = Sr^{2+}(**I**)	*M*' = Ca^{2+}[3]
Co(1)–O(1)	2.065(3)	2.078(5)
Co(1)–O(3)	2.190(3)	2.195(5)
Co(1)–O(5)	2.119(3)	2.136(5)
Co(1)–O(7)	2.718(3)	2.743(5)
Co(1)–O_w(1)	2.079(4)	2.059(5)
Co(1)–N(1)	2.233(4)	2.215(4)
Co(1)–N(2)	2.292(4)	2.199(4)
M'(1)–O(2^i)	2.535(4)	2.382(6)
M'(1)–O(4^{ii})	2.559(3)	2.416(6)
M'(1)–O(6^{iii})	2.655(3)	2.538(6)
M'(1)–O(7)	2.622(3)	2.474(6)
M'(1)–O(8)	2.638(3)	2.536(6)
M'(1)–O_w(2)	2.560(4)	2.414(7)
M'(1)–O_w(3)	2.582(4)	2.427(7)
M'(1)–O_w(4)	2.674(5)	2.628(7)

Note: Symmetry codes: (*i*) *x* – 1, *y*, *z*; (*ii*) *x* – 0.5, –*y* + 0.5, *z* + 0.5; and (*iii*) –*x* – 0.5, *y* + 0.5, –*z* + 1.5.

Table 3. Characteristics of hydrogen bonds in structure **I**

D–H ⋯*A* bond	Distance, Å			*DHA* angle, deg	Symmetry codes for *A* atom
	D–H	H⋯*A*	*D*⋯*A*		
$O_w(1)–H(1)_{w1}\cdots O(6)$	0.80(6)	1.97(6)	2.755(5)	166(6)	$-x + 1/2, y + 1/2, -z + 3/2$
$O_w(1)–H(2)_{w1}\cdots O_w(5)$	0.99(7)	1.91(7)	2.884(7)	167(6)	x, y, z
$O_w(2)–H(1)_{w2}\cdots O(1)$	0.81(8)	2.08(8)	2.865(5)	165(8)	x, y, z
$O_w(2)–H(2)_{w2}\cdots O(4)$	0.78(7)	2.11(7)	2.859(6)	161(7)	$-x + 3/2, y + 1/2, -z + 3/2$
$O_w(3)–H(1)_{w3}\cdots O(5)$	0.87(6)	1.88(6)	2.720(5)	162(6)	$-x + 1/2, y + 1/2, -z + 3/2$
$O_w(4)–H(1)_{w4}\cdots O(3)$	0.88(9)	1.88(9)	2.741(6)	166(8)	$x - 1/2, -y + 1/2, z + 1/2$
$O_w(5)–H(1)_{w5}\cdots O(8)$	0.70(6)	2.15(6)	2.833(7)	165(7)	$x - 1/2, -y + 1/2, z - 1/2$
$O_w(5)–H(2)_{w5}\cdots O_w(3)$	1.06	2.11	3.094(7)	153	$-x + 1/2, y - 1/2, -z + 3/2$

[Δ = 0.527(3) and 0.548(5) Å] and stems from the protonation of the acetate group in the $G_q(2)$ ring. The specific feature of this complex resides in the fact that the protonated acetate group is not displaced from the coordination of the Co(II) atom, as is the case in sixfold-coordinated complexes of transition metals [9]. Actually, in the structure of the Co[CoH*Edta*]$_2 \cdot 10H_2O$ complex [10], the octahedral anionic complexes $[Co(H_2O)_6]^{2+}$ are formed in addition to the aqua cations [CoH*Edta*(H_2O)]$^{2-}$.

In structure **I**, the C–C and C–N bond lengths are close to normal values and, on average, are equal to 1.516(6) and 1.474(6) Å [1.503(8) and 1.479(8) Å in the Ca complex].

The C–O distances in two complexes vary in a similar way: the difference $\Delta_{C–O}$ between the C–O_c and C–O_u bond lengths (where O_c and O_u are the oxygen atoms coordinated and uncoordinated by the Co atom, respectively) in the Sr complex is maximum in the *R*(1) ring [$\Delta_{C–O}$ = 0.055(6) Å] and is identical and close to zero in the *R*(2), *G*(1), and $G_q(2)$ rings [0.005(6) Å]; in the Ca complex, the difference $\Delta_{C–O}$ is somewhat larger in the *R*(1), *R*(2), and *G*(1) rings [0.071(8), 0.016(8), and 0.011(8) Å, respectively] and has a negative value in the $G_q(2)$ ring [–0.012(8) Å]. Note that the maximum values of $\Delta_{C–O}$ are observed in the *R*(1) rings for the groups in which the carbonyl $O_u(2)$ atoms form the shortest bonds with the Sr^{2+} and Ca^{2+} cations. The equalization of the C–O bonds in the other carboxylate groups can be explained by the fact that these bonds are involved in hydrogen bonding (Table 3) in addition to the formation of bonds with the Co atom and the alkaline-earth cations (Table 2).

The Sr^{2+} cation is coordinated by the O(7) and O(8) atoms of one quasi-free acetate group of the binuclear complex; three water molecules *W*2, *W*3, and *W*4; and the carbonyl $O_u(2^i)$, $O_u(4^{ii})$, and $O_u(6^{iii})$ atoms of three different anionic fragments. The coordination polyhedron of the Sr atom (the coordination number is equal to eight) is a distorted bicapped trigonal prism in which the $O_u(2^i)$ and $O_u(8)$ atoms occupy the cap positions (Fig. 1). The Sr–O_w and Sr–O_u distances in the polyhedron fall in different ranges: from 2.560(4) to 2.674(5) Å and from 2.535(4) to 2.655(3) Å, respectively. However, their mean values [2.605(5) and 2.602(4) Å] are identical to within the error of determination in contrast to the similar distances Ca–O_w and Ca–O_u [2.490(7) and 2.469(8) Å]. As can be seen from the data presented in Table 2, all the Ca–O distances are less than the similar Sr–O distances, and the Co–O_{lig} distances in the Sr^{2+} complex under investigation are shorter than the corresponding distances in the Ca^{2+} complex. This is likely due to the fact that Ca^{2+} cations whose ionic radius is smaller than that of Sr^{2+} cations possess a higher polarizing ability and, hence, affect the Co(II) polyhedron to a greater extent.

As noted above, structure **I** is built up of the binuclear complex fragments {Sr(H_2O)$_3$[Co*Edta*(H_2O)]}. In these fragments, all carbonyl oxygen atoms are involved in the formation of the Sr–O_u bonds, which brings about the formation of a framework structure (Fig. 2). The structural formula of the complex is {Sr(H_2O)$_3$[Co*Edta*(H_2O)]}$_{3\infty} \cdot H_2O$.

It can be seen from Fig. 2 that the anionic and cationic units in structure **I** are irregularly arranged in the crystal and lie in the layers parallel to the *xy* plane. Therefore, in structure **I**, we can conventionally separate the layers composed of anionic complex fragments (at z = 1/4 and 3/4) and cationic units (at z = 0 and 1/2). The layers that consist of the anionic fragments related by the $2_1(y)$ axes alternate with the layers of cationic units related by inversion centers. A similar “irregular” arrangement of the anionic and cationic fragments in the crystal is also observed in other complexes of the given class.

The hydrogen bonds further strengthen the framework structure **I** (Table 3). The anionic fragments are

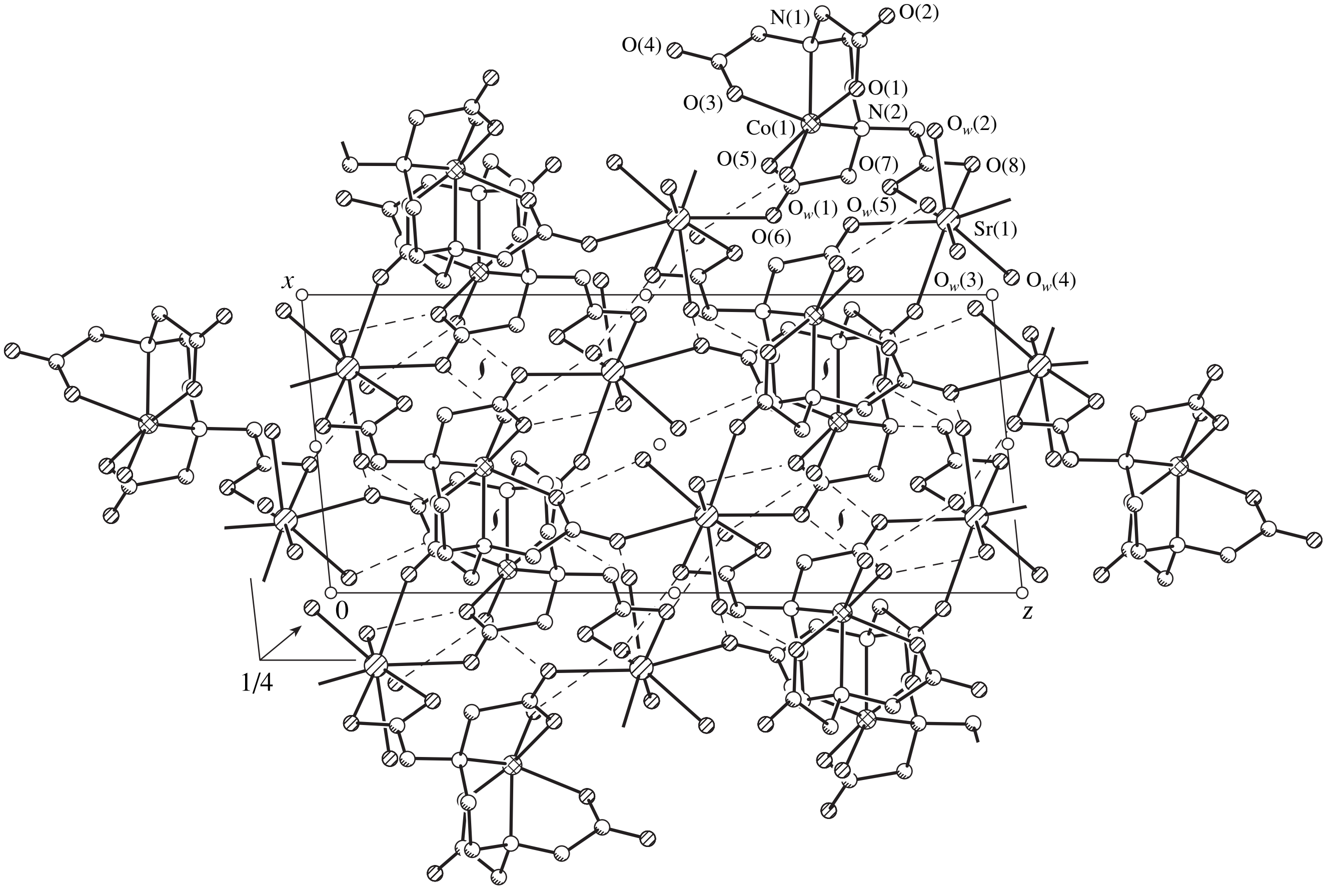

Fig. 2. Projection of structure **I** along the *y*-axis.

linked to each other and to the Sr^{2+} cations through the bonds formed by the *W*1 water molecule, which is involved in the Co coordination, and the $O_u(6)$ atom of the other complex related to the initial complex by the $2_1(y)$ axis. The *W*1 molecule also forms the hydrogen bond with the sole molecule of crystallization water *W*5, which, in turn, is bonded to the $O_u(8)$ atom. The *W*2, *W*3, and *W*4 water molecules in the Sr environment participate in the formation of hydrogen bonds with the carboxyl $O_c(1)$, $O_u(4)$, and $O_c(5)$ atoms, respectively, which are involved in the Co coordination of different anionic fragments. Furthermore, the cationic units are joined by the $W2\cdots O_u(4)$ bonds.

Let us now consider the role of different metals in the structure formation by comparing the structures of Co(II) complexes of similar compositions containing different alkaline-earth cations with one another and also with other related structures. In all the structures with alkaline-earth cations, the latter are outer-sphere cations; i.e., they do not coordinate the nitrogen atoms of the ligand. For example, the isostructural crystals of $M'[Co^{II}Edta] \cdot 6H_2O$ (where M' = Mg [1], Mn [11], and Co [12]) are built up of the polymeric zigzag chains $\{M'(H_2O)_4[CoEdta]\}_{1\infty}$ in which the alternating anionic and tetrahydrate cationic units are linked through the interaction between the M' atoms and carbonyl O_u atoms of two anionic complex fragments adjacent in the chain. In the aforementioned bimetallic complex $Zn[Co^{II}Cdta] \cdot 9H_2O$ [8], oligomers—the tetranuclear complexes $\{Zn(H_2O)_4[CoCdta(H_2O)]\}_2$ in which the atoms are related in pairs by an inversion center—are formed through similar bridging bonds of the Zn atoms.

The diversity of structural functions of the three symmetrically independent Co(II) atoms with different coordinations are observed in the island structure of the $Co_5(Edta)_2(ClO_4)_2 \cdot 20H_2O$ complex [7]. One Co(II) atom that is located at the inversion center fulfills a bridging function between two symmetrically related anionic fragments $[CoEdta(H_2O)]^{2-}$, which leads to the formation of the $\{Co(H_2O)_4[CoEdta(H_2O)]_2\}$ trinuclear complex. Like the M' cation in the chain structure, the bridging Co atom coordinates two carbonyl O_u atoms of two complexes and completes its own coordination number to six by four water molecules. Finally, the third Co atom forms the $[Co(H_2O)_6]^{2+}$ aqua cations and, hence, plays the role of an actual outer-sphere cation. A different situation is observed in the studied structure **I** with the Sr^{2+} (or Ca^{2+}) cation in which all the carbonyl O_u atoms of the ligand and the O atoms of the acetate group in the quasi-opened cycle form the bonds with the alkaline-earth cations. An active interaction of the Sr^{2+} and Ca^{2+} cations with the O atoms of the ligand allows us to treat each of these cations as the second complexing metal.

Complex **I** is identical in composition to the complex with the Ca^{2+} cation whose structure was solved earlier in the space group $P2_1/b$. The crystal data reported in [3] were recalculated for the space group $P2_1/n$. The parameters obtained are as follows: a = 7.825 Å, b = 12.627 Å, c = 17.993 Å, β = 95.59°, and V = 1768.4 $Å^3$. These values are close to those for structure **I**. Furthermore, all the inferences drawn for structure **I** are also true for the structure of calcium complex. The natural difference between these compounds primarily lies in the shorter Ca–O distances, which is responsible for the smaller volume of the unit cell (V = 1768.4 $Å^3$). Thus, the crystals of the $Edta^{4-}$ complexes of Co(II) with the Sr^{2+} and Ca^{2+} cations are isostructural.

ACKNOWLEDGMENTS

This work was supported in part by the Belarussian Republican Foundation for Basic Research, project no. F98-243.

REFERENCES

1. A. I. Pozhidaev, N. N. Neronova, T. N. Polynova, *et al.*, Zh. Strukt. Khim. **13** (4), 738 (1972).
2. L. A. Zasurskaya, A. L. Poznyak, T. N. Polynova, *et al.*, Zh. Neorg. Khim. **41** (10), 1647 (1996).
3. Ya. M. Nesterova and M. A. Poraĭ-Koshits, Koord. Khim. **8** (7), 994 (1982).
4. G. M. Sheldrick, *SHELX76: Program for Crystal Structure Determination* (Cambridge Univ., Cambridge, 1976).
5. G. M. Sheldrick, Acta Crystallogr., Sect. A: Found. Crystallogr. **A46** (6), 467 (1990).
6. P. Gómez-Romero, G. B. Jameson, N. Casan-Pastor, *et al.*, Inorg. Chem. **25** (18), 3171 (1986).
7. I. M. Bezrukavnikova, Author's Abstract of Candidate's Dissertation in Chemistry (Inst. Obshcheĭ i Neorganicheskoĭ Khimii Akad. Nauk SSSR, Moscow, 1990).
8. A. Fuertes, C. Miravitlles, E. Escriva, *et al.*, J. Chem. Soc., Dalton Trans., No. 5, 863 (1989).
9. M. A. Poraĭ-Koshits and T. N. Polynova, Koord. Khim. **10** (6), 725 (1984).
10. X. Solans, M. Font-Bardia, M. Aguilo, *et al.*, Acta Crystallogr., Sect. C: Cryst. Struct. Commun. **C43** (4), 648 (1987).
11. X. Solans, M. Font-Altaba, J. Oliva, and J. Herrera, Acta Crystallogr., Sect. C: Cryst. Struct. Commun. **C39**, 435 (1983).
12. E. F. K. McCandlish, T. K. Michael, J. A. Neal, *et al.*, Inorg. Chem. **17** (6), 1383 (1978).

Translated by O. Borovik-Romanova

Crystallography Reports, Vol. 46, No. 3, 2001, pp. 383–384. Translated from Kristallografiya, Vol. 46, No. 3, 2001, pp. 433–434.
Original Russian Text Copyright © 2001 by Andreev, Antipin, Fedoseev, Budantseva.

STRUCTURE OF COORDINATION COMPOUNDS

Synthesis and Crystal Structure of Bis(carbamide)chromatoneptunyl $NpO_2CrO_4 \cdot 2[OC(NH_2)_2]$

G. B. Andreev*, M. Yu. Antipin, A. M. Fedoseev*, and N. A. Budantseva***

** Institute of Physical Chemistry, Russian Academy of Sciences, Leninskiĭ pr. 31, Moscow, 117915 Russia*
*** Nesmeyanov Institute of Organoelement Compounds, Russian Academy of Sciences,*
ul. Vavilova 28, Moscow, 117813 Russia

Received August 1, 2000

Abstract—The crystal structure of the hexavalent neptunium complex $NpO_2CrO_4 \cdot 2[OC(NH_2)_2]$ is determined. The crystal data are $a = 7.192(2)$ Å, $b = 12.902(4)$ Å, $c = 11.226(3)$ Å, $\beta = 92.19(2)°$, $V = 1040.9(4)$ Å^3, space group $P2_1/n$, $Z = 4$, $d_{calcd} = 3.223$ g/cm^3, $R = 0.045$, and $R_w = 0.130$. The coordination polyhedron of the Np atom is the pentagonal bipyramid whose equatorial plane is formed by the oxygen atoms of the chromate ions and carbamide molecules. © *2001 MAIK “Nauka/Interperiodica”.*

The studies on chromate compounds of hexavalent actinides are few in number and deal only with uranyl complexes [1–3]. (No data on chromates of transuranic elements in the +6 oxidation state are available in the literature.) In this work, we report the results of our X-ray diffraction study of a complex between neptunyl chromate and carbamide.

Compound $NpO_2CrO_4 \cdot 2[OC(NH_2)_2]$ (**I**) was prepared by isothermal evaporation at 20°C of a NpO_2CrO_4 solution (~0.05 mol/l) in the presence of carbamide in equimolar amounts.

Table 1. Selected crystal data and parameters of structure refinement

Crystal system	Monoclinic
a, Å	7.192(2)
b, Å	12.902(4)
c, Å	11.226(3)
β, deg	92.19(2)
Space group	$P2_1/n$
Z	4
V, Å^3	1040.9(4)
ρ_{calcd}, g/cm^3	3.223
Radiation (λ, Å)	MoK_α(0.71073)
Scan mode	$\theta/2\theta$
$2\theta_{max}$, deg	56
Number of reflections	2841
Number of unique reflections	2529
F(000)	2780
Number of parameters refined	145
R, R_w	0.045, 0.130
GooF	1.084

Table 2. Atomic coordinates and equivalent thermal parameters

Atom	x	y	z	U_{eq}, Å^2
Np	0.23879(5)	0.07395(3)	0.29862(3)	0.0129(2)
Cr	–0.2580(2)	0.0110(1)	0.3706(1)	0.0162(3)
C(1)	0.019(2)	0.1614(9)	0.056(1)	0.032(3)
C(2)	0.487(2)	0.1562(8)	0.063(1)	0.027(2)
O(1)	0.237(1)	–0.0621(5)	0.2845(7)	0.025(2)
O(2)	0.2417(9)	0.2117(6)	0.3099(6)	0.020(2)
O(3)	–0.267(1)	–0.0680(7)	0.2624(8)	0.037(2)
O(4)	0.248(1)	0.0601(6)	0.5039(7)	0.029(2)
O(5)	0.554(1)	0.0869(7)	0.3646(9)	0.034(2)
O(6)	–0.066(1)	0.0838(6)	0.3667(8)	0.029(2)
O(7)	0.423(1)	0.0866(6)	0.1286(7)	0.029(2)
O(8)	0.036(1)	0.0876(6)	0.1289(7)	0.030(2)
N(1)	0.054(2)	0.149(1)	–0.057(1)	0.053(4)
N(2)	–0.027(2)	0.257(1)	0.093(2)	0.068(5)
N(3)	0.477(2)	0.2574(8)	0.089(1)	0.051(4)
N(4)	0.572(2)	0.1306(8)	–0.037(1)	0.049(4)
H(1)	0.090(2)	0.090(1)	–0.083(1)	0.064
H(2)	0.041(2)	0.201(1)	–0.106(1)	0.064
H(3)	–0.044(2)	0.268(1)	0.166(2)	0.081
H(4)	–0.038(2)	0.306(1)	0.042(2)	0.081
H(5)	0.424(2)	0.2771(8)	0.153(1)	0.062
H(6)	0.523(2)	0.3026(8)	0.042(1)	0.062
H(7)	0.583(2)	0.0667(8)	–0.057(1)	0.059
H(8)	0.616(2)	0.1784(8)	–0.082(1)	0.059

1063-7745/01/4603-0383$21.00 © 2001 MAIK “Nauka/Interperiodica”

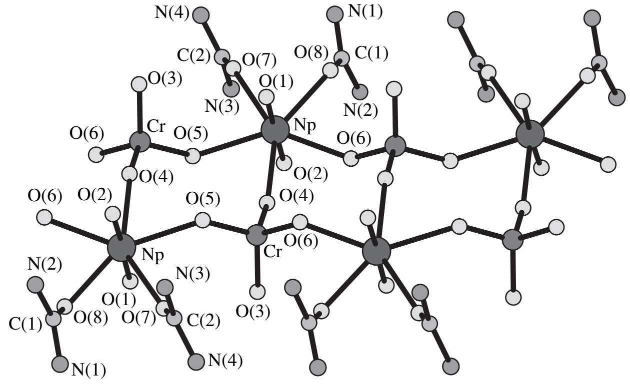

A fragment of the $NpO_2CrO_4 \cdot 2[OC(NH_2)_2]$ crystal structure.

The experimental data were collected on a Siemens P3/PC diffractometer. The structure was solved by the direct method and refined by the full-matrix least-squares procedure in the anisotropic approximation for all non-hydrogen atoms according to the SHELXTL PLUS program. The data were not corrected for absorption. Selected crystal data and parameters of structure refinement are summarized in Table 1. Atomic coordinates and equivalent thermal parameters are listed in Table 2.

Crystal structure **I** is built of infinite $[NpO_2CrO_4 \cdot 2OC(NH_2)_2]_\infty$ ribbons running along the [100] direction (figure).

The coordination polyhedron of the Np atom is the pentagonal bipyramid. The NpO_2 group is nearly linear and symmetric [the Np–O distances are 1.762(7) and 1.782(8) Å and the O(1)–Np–O(2) angle is 178.9(3)°]. It is inclined to the mean equatorial plane at an angle of 90.9°. The equatorial sites are occupied by two oxygen atoms of two carbamide groups and three oxygen atoms of three different chromate ions CrO_4^{2-}. The Np–O distances are 2.310(8)–2.366(8) Å. The deviations of atoms from the mean equatorial plane do not exceed 0.125 Å.

The CrO_4^{2-} groups act as tridentate bridging ligands and link the neighboring coordination polyhedra of neptunium atoms. The shortest Np…Np distance is 6.075 Å. The coordination polyhedron of the Cr atom is the tetrahedron. Three of the four oxygen atoms at its vertices are the bridging oxygen atoms and the remaining atom is terminal. The Cr–O distances are equal to 1.667(9)–1.680(8) Å for the bridging atoms, and the length of the terminal Cr–O bond is 1.586(9) Å. The O–Cr–O angles vary from 106.9(5)° to 111.4(5)°.

The geometry of the carbamide molecules in **I** shows no significant linear or angular differences from that of the free molecule [4]. Although the carbamide oxygen atoms coordinate neptunium, the C–O bond lengths in **I** and in the free molecule are almost equal [1.26(2) and 1.261 Å, respectively].

A similar ribbon structure was found, for example, in the $[UO_2CrO_4 \cdot 2OC(CH_3)(NH_2)]$ complex of uranyl chromate with acetamide [3]. The structure of $UO_2CrO_4 \cdot 5.5H_2O$ is also built of infinite ribbons $(UO_2CrO_4 \cdot 2H_2O)_\infty$, which consist of the CrO_4 tetrahedra and the $UO_2O_3(H_2O)_2$ bipyramids. The remaining water molecules intervene between the ribbons [2].

ACKNOWLEDGMENTS

This work was supported by the Russian Foundation for Basic Research, project nos. 00-15-97359 and 99-07-90133.

REFERENCES

1. Yu. N. Mikhaĭlov, Yu. E. Gorbunova, E. A. Demchenko, *et al.*, Zh. Neorg. Khim. **43** (11), 1831 (1988).
2. V. N. Serezhkin and V. K. Trunov, Kristallografiya **26** (2), 301 (1981) [Sov. Phys. Crystallogr. **26**, 169 (1981)].
3. V. N. Serezhkin, M. A. Soldatkina, V. A. Efremov, and V. K. Trunov, Koord. Khim. **7**, 629 (1981).
4. S. Swaminathan, B. M. Craven, and R. K. McMullan, Acta Crystallogr., Sect. B: Struct. Sci. **B40**, 300 (1984).

Translated by I. Polyakova

Crystallography Reports, Vol. 46, No. 3, 2001, pp. 385–388. Translated from Kristallografiya, Vol. 46, No. 3, 2001, pp. 435–438.
Original Russian Text Copyright © 2001 by Rybakov, Zhukov, Babaev, Sonneveld.

X-ray Mapping in Heterocyclic Design: IV. Crystal Structure Determination of 3-(*p*-Nitrobenzoyl)-2-Oxooxazolo[3,2-*a*]pyridine from Powder Diffraction Data

V. B. Rybakov*, S. G. Zhukov*, E. V. Babaev*, and E. J. Sonneveld**

** Faculty of Chemistry, Moscow State University, Vorob'evy gory, Moscow, 119899 Russia*
e-mail: rybakov@biocryst.phys.msu.su
*** Laboratory of Crystallography, Faculty of Chemistry, University of Amsterdam,*
Nieuwe Achtergracht 166, 1018 WV Amsterdam, Netherlands

Received May 15, 2000

Abstract—The structure of 3-(*p*-nitrobenzoyl)-2-oxooxazolo[3,2-*a*]pyridine is determined by the powder diffraction technique. The crystals are monoclinic, $a = 13.642(2)$ Å, $b = 22.278(3)$ Å, $c = 3.917(1)$ Å, $\beta = 90.63(2)°$, $Z = 4$, and space group $P2_1/n$. The structure is solved by a modified Monte Carlo method and refined by the Reitveld method. The six-membered heterocycle is characterized by the alternation of partially single and partially double bonds. The system of two conjugated heterocycles is planar and forms a dihedral angle of 46.1(1)° with the plane of the phenyl ring. The nitro group is virtually coplanar with the phenyl fragment. An extensive system of intramolecular and intermolecular contacts involving hydrogen, oxygen, and nitrogen atoms is observed in the crystal. © *2001 MAIK "Nauka/Interperiodica".*

INTRODUCTION

This paper continues a series of structural investigations of the heterocyclic compounds that are able to enter readily into reactions of ring transformations and various chemical rearrangements. Our previous studies in this field were reported in [1–7]. The crystal structure of the mesoionic compound 3-benzoyl-2-oxooxazolo[3,2-*a*]pyridine was determined by X-ray diffraction in [8]. In the present work, we concentrated on the structural study of its analogue, namely, 3-(*p*-nitrobenzoyl)-2-oxooxazolo[3,2-*a*]pyridine. There are no data on its structure in the Cambridge Structural Database [9]. The compound was prepared according to the procedure described earlier in [10].

Our interest in the structure and properties of this subclass of mesoionic heterocycles is due to, first, the unusual (ilide) structural type of these heterocycles [8] and, second, the possibility of readily opening the oxazolone ring and its transforming into the oxazolium ring [11] according to the following scheme:

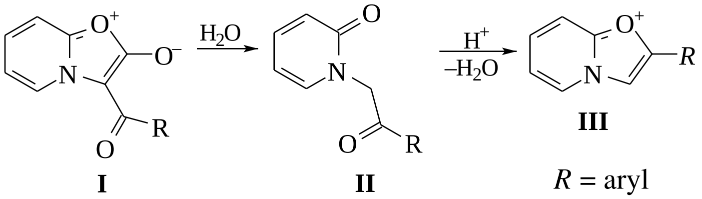

Earlier [2, 3], we performed the X-ray structure analysis of compounds **II** and **III** ($R = C_6H_5$), that is, both products of hydrolysis of the mesoionic system **I** [2]. Thus, the crystal structure determination of compound **I** with $R = p\text{-}NO_2\text{-}C_6H_4$ (**Ia**) as a precursor of compounds **II** and **III** provides one more example of the principle of the X-ray mapping of reactions [5–7].

EXPERIMENTAL

The diffraction experiment was performed using an evacuated Enraf–Nonius Guinier–Johansson FR552 camera ($\lambda CuK_{\alpha 1}$, quartz monochromator). The intensities of the X-ray spectrum were measured with an LS18 densitometer in 0.01° steps in the 2θ range 4°–86° and the *hkl* range $0 \le h \le 12$; $0 \le k \le 19$, $-3 \le l \le 3$. The unit

Table 1. Atomic coordinates ($\times 10^4$) and isotropic thermal parameters U_{iso} ($\text{Å}^2 \times 10^3$)

Atom	*x*	*y*	*z*	U_{iso}
C(1)	4146(10)	3112(6)	5472(15)	49(6)
C(2)	4264(10)	3699(6)	4050(15)	49(6)
C(3)	5684(10)	4169(6)	999(17)	49(6)
C(4)	6651(10)	4060(6)	–29(15)	51(7)
C(5)	7074(10)	3476(6)	731(15)	51(7)
C(6)	6639(10)	3018(6)	2317(15)	49(7)
C(7)	5644(10)	3155(6)	3446(15)	49(7)
C(8)	3666(10)	4217(6)	3267(15)	49(7)
C(9)	2604(10)	4109(6)	4369(15)	49(7)
C(10)	2131(10)	4565(6)	6060(15)	49(7)
C(11)	1106(10)	4525(6)	6786(15)	49(7)
C(12)	648(10)	4004(6)	5890(15)	49(7)
C(13)	1065(10)	3515(6)	4150(15)	49(7)
N(1)	5251(8)	3692(6)	2745(12)	49(7)
O(1)	5084(10)	2759(6)	5105(15)	49(7)
O(2)	3575(10)	2802(6)	6992(15)	49(7)
C(14)	2093(10)	3577(6)	3478(15)	49(7)
N(12)	–476(10)	3949(6)	6708(15)	49(7)
O(3)	3904(6)	4705(6)	2475(11)	49(7)
O(12A)	–767(6)	4373(6)	8055(11)	109(11)
O(12B)	–782(6)	3474(5)	5695(15)	67(11)
H(3)	5338	4585	525	51*
H(4)	7048	4405	–1328	51*
H(5)	7855	3421	–169	51*
H(6)	6908	2571	2980	51*
H(10)	2526	4971	6841	51*
H(11)	740	4897	8106	51*
H(13)	685	3107	3517	51*
H(14)	2457	3210	2242	51*

* The thermal parameter was fixed and not refined.

cell parameters were determined by the ITO indexing program [13], and the space group was determined from the systematic absences of reflections. Crystals **Ia** ($C_{14}H_8N_2O_5$) are monoclinic, a = 13.642(2) Å, b = 22.278(3) Å, c = 3.917(1) Å, β = 90.63(2)°, V = 1190.4(4) Å^3, d_{calcd} = 1.653 g/cm^3, μ(Cu) = 10.8 cm^{-1}, Z = 4, and space group $P2_1/n$.

The structure was solved by the modified Monte Carlo method [14, 15] with the use of the known molecular fragments. The full-profile refinement of the structure was performed by the Rietveld method with the MRIA program [16]. The reflection profiles were described by the function proposed in [17], and the background was approximated by the Chebyshev polynomials of the fifth order. The texture parameters were refined within the March–Dollase model [18] in the [001] direction. The procedure of the structural investigation of **Ia** is described in more detail in [19]. The final *R* factors of the full-matrix refinement were R_p = 0.053, R_b = 0.155, and R_e = 0.024, where $R_p = \sum|I_{\text{obs}} - I_{\text{calcd}}|/\sum I_0$, $R_b = \sum|I_{\text{obs}} - I_{\text{calcd}}|/\sum|I_{\text{obs}} - Bckgr|$, $R_e = \sum\sigma I_{\text{obs}}/\sum I_{\text{obs}}$, I_{obs} is the observed intensity, and I_{calcd} is the calculated intensity; the χ^2 criterion was equal to 6.9.

The atomic coordinates are listed in Table 1 (the positions of the H atoms were calculated from geometric considerations; in the course of the refinement, the H atoms were rigidly bound to the corresponding carbon atoms). The schematic drawing of the molecule (see figure) was obtained with the PLUTON96 program [20]. The atomic numbering in **Ia** is the same as that in [8] for convenient comparison of the geometric parameters of the molecules.

RESULTS AND DISCUSSION

The binuclear fragment of molecule **Ia** is planar, and its structure is essentially the same as that of its analogue **Ib** (R = C_6H_5) [8]; specifically, the bond lengths in the C(3)–C(4)–C(5)–C(6) fragment of the six-membered heterocycle alternate, the lengths of the C(1)–O(1) endocyclic bonds in the two structures completely coincide, and the O(1)–C(7) bond in **Ia** is only 0.05 Å longer than that in **Ib**. This structure suggests that the six-membered fragment of the mesoionic bicyclic molecule can be represented by the pyridine-like (butadiene) structure to a greater extent than by the delocalized pyridine ring. From structural considerations, it follows that the positive charge is distributed over the N(1)–C(7)–O(1) bonds and the pyridine fragment of the molecule is not involved in delocalization.

According to the above scheme, the C(1)–C(2) bond should be of the double type, but it is actually substantially longer [1.43(2) Å]. On the other hand, the length of the C(1)–O(2) exocyclic bond [1.20(2) Å] corresponds to the double bond. Therefore, the geometry of the O(2)–C(1)–C(2)–C(8)–O(3) fragment corresponds to a combination of two carbonyl groups connected through the C(2) atom without significant delocalization. Possibly, this indicates that the negative charge is localized at the C(2) atom.

The molecular structures under comparison considerably differ in the arrangement of the phenyl rings with respect to the heterocyclic nucleus. The angles

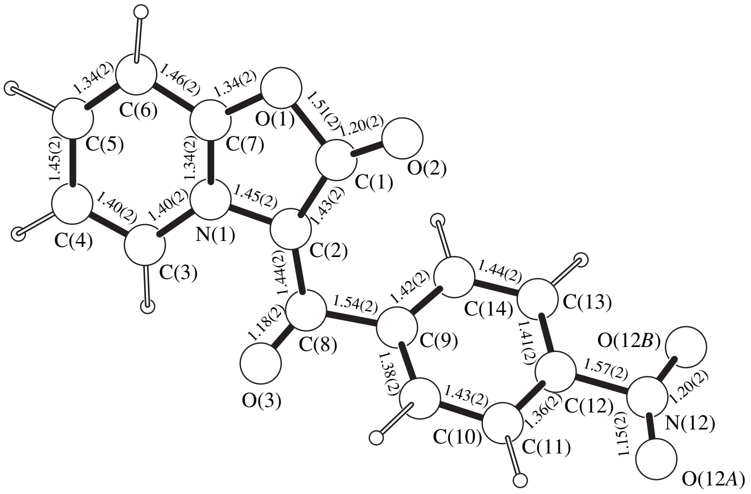

Structure of the molecule studied and the atomic numbering.

between the planes of the phenyl ring and the oxazolo[3,2-*a*]pyridine bicyclic fragment are 66.8(2)° and 46.1(2)° in molecules **Ib** [8] and **Ia**, respectively. The pronounced decrease in the angle of ring rotation in the molecule studied is most likely due to the packing effects caused by the nitro group in the *para* position of the phenyl fragment. The nitro group itself is virtually coplanar with the phenyl ring: the rotation angle is 1(1)°.

A system of intramolecular and intermolecular C–H···O and C–H···N contacts is formed in the crystal (Table 2). These contacts were calculated with the PARST95 program [21].

Table 2. Parameters of the interatomic contacts* [19]

D–H	*d*(*D*–H)	*d*(*D*··*A*)	*d*(H··*A*)	ω*DHA*	*A* (symmetry operation)
C(3)–H(3)	1.06(9)	2.77(2)	2.13(8)	117(6)	O(3) (*x*; *y*; *z*)
C(13)–H(13)	1.07(9)	2.60(2)	2.33(8)	92(5)	O(12B) (*x*; *y*; *z*)
C(11)–H(11)	1.10(8)	2.63(2)	2.36(8)	91(5)	O(12A) (*x*; *y*; *z*)
C(10)–H(10)	1.10(9)	2.83(1)	2.62(7)	89(4)	O(3) (*x*; *y*; *z*)
C(14)–H(14)	1.08(8)	2.98(2)	2.56(7)	103(5)	O(2) (*x*; *y*; *z*)
C(3)–H(3)	1.06(9)	2.91(2)	2.23(8)	120(5)	O(3) (1 – *x*;1 – *y*; –*z*)
C(4)–H(4)	1.07(8)	3.01(2)	2.41(9)	114(5)	O(3) (1 – *x*;1 – *y*; –*z*)
C(11)–H(11)	1.10(8)	3.13(2)	2.91(7)	91(4)	O(12A) (–*x*;1 – *y*; 1 – *z*)
C(11)–H(11)	1.10(8)	3.22(2)	2.22(7)	150(5)	O(12A) (–*x*;1 – *y*; 2 – *z*)
C(10)–H(10)	1.10(9)	3.48(1)	2.94(7)	111(4)	O(3) (*x*; *y*; 1 + *z*)
C(14)–H(14)	1.08(8)	3.69(2)	2.73(7)	149(4)	O(2) (*x*; *y*; *z* – 1)
C(4)–H(4)	1.07(8)	3.68(2)	2.99(8)	122(5)	O(12A) (1 + *x*; *y*; *z* – 1)
C(5)–H(5)	1.13(8)	3.86(2)	2.85(8)	148(5)	N(12) (1 + *x*; *y*; *z* – 1)
C(5)–H(5)	1.13(8)	3.72(2)	2.92(9)	127(5)	O(12A) (1 + *x*; *y*; *z* – 1)
C(5)–H(5)	1.13(8)	3.55(1)	2.48(7)	156(5)	O(12B) (1 + *x*; *y*; *z* – 1)
C(5)–H(5)	1.13(8)	3.49(1)	2.94(6)	110(4)	O(12B) (1 + *x*; *y*; *z*)

* *D* is a donor, *A* is an acceptor, and H is a hydrogen atom (the *d* distances and ω angles are given in Å and degrees, respectively).

ACKNOWLEDGMENTS

This study was supported by the Netherlands Society of Basic Research (NWO). The synthetic part of this work was supported by the Russian Foundation for Basic Research, project no. 99-03-33076. We also acknowledge the support of the RFBR in the payment of the license for using the Cambridge Structural Database, project no. 99-07-90133.

REFERENCES

1. E. V. Babaev, A. V. Efimov, S. G. Zhukov, and V. B. Rybakov, Khim. Geterotsikl. Soedin., No. 7, 983 (1998).
2. E. V. Babaev, S. V. Bozhenko, D. A. Maiboroda, *et al.*, Bull. Soc. Chim. Belg. **106** (11), 631 (1997).
3. S. G. Zhukov, V. B. Rybakov, E. V. Babaev, *et al.*, Acta Crystallogr., Sect. C: Cryst. Struct. Commun. **C53**, 1909 (1997).
4. E. V. Babaev, S. V. Bozhenko, S. G. Zhukov, and V. B. Rybakov, Khim. Geterotsikl. Soedin., No. 8, 1105 (1997).
5. V. B. Rybakov, S. G. Zhukov, E. V. Babaev, *et al.*, Kristallografiya **44** (6), 1067 (1999) [Crystallogr. Rep. **44**, 997 (1999)].
6. V. B. Rybakov, S. G. Zhukov, E. V. Babaev, *et al.*, Kristallografiya **45** (1), 108 (2000) [Crystallogr. Rep. **45**, 103 (2000)].
7. V. B. Rybakov, S. G. Zhukov, E. V. Babaev, *et al.*, Kristallografiya **45** (2), 292 (2000) [Crystallogr. Rep. **45**, 261 (2000)].
8. S. G. Zhukov, E. V. Babaev, V. V. Chernyshev, *et al.*, Z. Kristallogr. **215**, 306 (2000).
9. F. H. Allen and O. Kennard, Chem. Des. Autom. News **8** (1), 31 (1993).
10. G. V. Boyd and P. H. Wright, J. Chem. Soc. C, No. 10, 1486 (1970).
11. E. V. Babaev and I. A. Orlova, Khim. Geterotsikl. Soedin., No. 4, 569 (1997).
12. E. V. Babaev, V. B. Rybakov, S. G. Zhukov, and I. A. Orlova, Khim. Geterotsikl. Soedin., No. 4, 542 (1999).
13. J. W. Visser, J. Appl. Crystallogr. **2**, 89 (1969).
14. K. D. M. Harris, M. Tremayne, P. Lightfoot, and P. G. Bruce, J. Am. Chem. Soc. **116**, 3543 (1994).
15. Yu. G. Andreev, P. Lightfoot, and P. G. Bruce, J. Appl. Crystallogr. **30**, 294 (1997).
16. V. B. Zlokazov and V. V. Chernyshev, J. Appl. Crystallogr. **25**, 447 (1992).
17. H. Toraya, J. Appl. Crystallogr. **19**, 440 (1986).
18. W. A. Dollase, J. Appl. Crystallogr. **19**, 267 (1986).
19. S. G. Zhukov, V. V. Chernyshev, E. V. Babaev, *et al.*, Z. Kristallogr. **216** (1), 5 (2001).
20. A. L. Spek, *PLUTON96: Molecular Graphics Program* (Univ. of Utrecht, Netherlands, 1996).
21. M. Nardelli, J. Appl. Crystallogr. **28**, 659 (1995).

Translated by I. Polyakova

Crystallography Reports, Vol. 46, No. 3, 2001, pp. 389–393. Translated from Kristallografiya, Vol. 46, No. 3, 2001, pp. 439–443.
Original Russian Text Copyright © 2001 by Prezhdo, Bykova, Glowiak, Daszkiewicz, Koll, Kyziol, Zhukhlistova.

STRUCTURE OF ORGANIC COMPOUNDS

Molecular and Crystal Structures of *N*-Methyl-*N*-Nitro-2-Chloroaniline

V. V. Prezhdo[1,2], A. S. Bykova[2], T. Glowiak[3], Z. Daszkiewicz[4],
A. Koll[3], J. Kyziol[4], and N. E. Zhukhlistova[5]
[1] Institute of Chemistry, Pedagogical University, ul. Checinska 5, Kielce, 25-020 Poland
e-mail: victor@pu.kielce.pl
[2] Kharkov State Polytechnical University, ul. Frunze 21, Kharkov, 61002 Ukraine
e-mail: leopold@kpi.kharkov.ua
[3] Department of Chemistry, University of Wroclaw, ul. Joliot-Curie 14, Wroclaw, 50-383 Poland
[4] Institute of Chemistry, University of Opole, ul. Oleska 48, Opole, 45-052 Poland
[5] Shubnikov Institute of Crystallography, Russian Academy of Sciences, Leninskiĭ pr. 59, Moscow, 117333 Russia

Received May 17, 2000; in final form, October 11, 2000

Abstract—The crystal structure of *N*-methyl-*N*-nitro-2-chloroaniline is determined by X-ray diffraction [a = 9.218(2) Å, b = 12.593(3) Å, c = 14.510(2) Å, space group *Pbca*, and $Z = 8$]. The structure is solved by the direct method and refined in the anisotropic approximation to $R = 0.0377$. All hydrogen atoms are localized. The structural parameters obtained agree with the data of the *ab initio* quantum-chemical B3LYP/6-31G** calculations. The data obtained are compared with those for *N*-methyl-*N*-nitro-4-chloroaniline. Conclusions on the interaction of the functional groups in the molecule are drawn. © *2001 MAIK "Nauka/Interperiodica".*

INTRODUCTION

Due to the use of *N*-nitro compounds as explosives and components of rocket fuels [1], their properties and molecular structure currently receive much attention. The properties of the N–N bond impart the molecules of these compounds high photochemical reactivity [2]. The crystal and molecular structures of *N*,*N*-dimethylnitramine and some cyclic and aliphatic nitramines were studied earlier in [3, 4]. Only two members of the series of aromatic *N*-nitramines were characterized, namely, 2,4,6-trinitro-*N*-methyl-*N*-nitroaniline (tetryl) [5] and *N*-methyl-*N*-nitro-4-nitroaniline [6]. The compounds of this series have attracted particular interest, because the nitro group in *N*-methyl-*N*-nitroaniline and its derivatives can undergo a rearrangement at elevated temperatures, under acid conditions, or on photolysis [7]. The products of rearrangement of *N*-methyl-*N*-nitroaniline were identified only recently [8]. However, its mechanism is still not completely understood. In the present work, we performed X-ray diffraction analysis and quantum-chemical calculations of the structure of *N*-methyl-*N*-nitro-2-chloroaniline

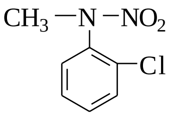

I

The molecular and crystal structures of *N*-methyl-*N*-nitro-4-chloroaniline (**II**) were determined in the recent work [9]. In was of interest to reveal how the structural parameters of molecules depend on the position of the chlorine atom in the molecule. In addition, investigation into the molecular structure of secondary arylnitramines aids in the elucidation of the mechanism of the nitramine rearrangement.

EXPERIMENTAL

Compound **I** was obtained by a reaction of *n*-butyl nitrate with the Grignard reagent that was prepared *in situ* from *N*-methyl-2-chloroaniline and ethylmagnesium bromide according to the procedure described in [10]. The product obtained was recrystallized from *n*-hexane. Single crystals were grown by slow cooling a solution of **I** in methylene chloride. A single crystal used for the X-ray data collection had a parallelepiped-like shape and was 0.20 × 0.25 × 0.25 mm in size. The parameters of the monoclinic unit cell were determined on a Kuma KM-4 diffractometer; a = 9.218(2) Å, b = 12.593(3) Å, c = 14.510(2) Å, space group *Pbca*, M = 186.60, V = 1684.4(6) Å^3, and $Z = 8$. The asymmetric unit contains one molecule **I**, that is, twelve non-hydrogen and seven hydrogen atoms.

A three-dimensional set of 1828 unique reflections ($\theta = 2.4°–36°$) was collected at 293(2) K on a Kuma KM-4 diffractometer by the $\theta/2\theta$ technique. The collection and processing of the experimental data were performed with the Kuma KM-4 program [11]. The structure was solved with the SHELXTLPlus software package [12]. The E synthesis revealed all non-hydro-

1063-7745/01/4603-0389$21.00 © 2001 MAIK "Nauka/Interperiodica"

Table 1. Atomic coordinates and equivalent isotropic displacement parameters (U_{eq}, Å^2) in structure **I**

Atom	*x*	*y*	*z*	U_{eq}
Cl	0.1671(1)	0.36881(4)	0.14192(4)	0.0654(2)
O(1)	–0.2018(2)	0.3543(1)	0.1320(1)	0.0630(4)
O(2)	–0.1855(2)	0.4335(1)	–0.0003(1)	0.0782(5)
N(1)	–0.0682(2)	0.2830(1)	0.0213(1)	0.0482(4)
N(2)	–0.1552(2)	0.3624(1)	0.0532(2)	0.0503(4)
C(1)	–0.0117(3)	0.2112(1)	0.0882(1)	0.0406(4)
C(2)	0.0984(2)	0.2415(1)	0.1482(1)	0.0442(4)
C(3)	0.1528(2)	0.1706(2)	0.2124(1)	0.0528(5)
C(4)	0.0970(3)	0.0690(2)	0.2155(2)	0.0583(6)
C(5)	–0.0104(2)	0.0383(2)	0.1560(2)	0.0617(6)
C(6)	–0.0654(2)	0.1085(3)	0.0921(2)	0.0527(5)
C(7)	0.0018(3)	0.2988(2)	–0.0675(2)	0.0648(6)
H(3)	0.226	0.191	0.253	0.063
H(4)	0.133	0.021	0.258	0.070
H(5)	–0.047	–0.031	0.159	0.074
H(6)	–0.138	0.087	0.052	0.063
H(7*a*)	0.053	0.245	–0.085	0.097
H(7*b*)	0.069	0.357	–0.063	0.097
H(7*c*)	–0.070	0.315	–0.113	0.097

gen atoms. Their positional and thermal parameters were refined (SHELXL93 [13]) first in the isotropic approximation and then in the anisotropic approximation to $R = 0.0624$. At this stage, the positions of the hydrogen atoms were calculated. The hydrogen atoms were refined within the riding-atom model [13]. Their thermal parameters were taken equal to 1.2 B_{eq} of the non-hydrogen atoms to which they were attached. The final R factor was 0.0377 for 1280 reflections with $I \geq 2\sigma(I)$. The atomic coordinates and equivalent isotropic displacement parameters are listed in Table 1. The quantum-chemical *ab initio* calculations were performed at the B3LYP/6-31G** level with a complete geometry optimization using the Gaussian 94 program package [14].

RESULTS AND DISCUSSION

The molecular structure of **I** is shown in Fig. 1. The nitramine group is planar. The bond lengths and angles in the nitramine group agree with the corresponding values in *N*,*N*-dimethylnitramine [4] and *N*-methyl-*N*-nitro-4-chloroaniline [9]. The differences do not exceed 0.03 Å and 2°, respectively. The aromatic nucleus is planar; the atomic deviations are within 0.006(2) Å (Table 2). The N(1) nitrogen atom virtually lies in the plane of the benzene ring [its deviation is only 0.009(3) Å]. This geometry differs from that, for example, in **II**, in which the corresponding atomic deviation is 0.065(6) Å [9]. The N(1) atom is involved in a strong interaction with the nitro group, which is evident from the planarity of the nitramino group in **I** [the N(2) atom deviates from this plane most of all, by 0.015(2) Å]. The bond lengths and angles in **I** agree with the corresponding values in **II** [9]; the differences in bond lengths are no larger than 0.02 Å. The largest angular disagreement is observed for the C(1)–N(1)–C(7) angle (1.4°), which is probably due to different positions of the chlorine atom, namely, the 2-position in **I** and the 4-position in **II**. The N–N bond in *N*-nitramines (1.341 Å in $(CH_3)_2NNO_2$ [4], 1.350 Å in **II** [9], and 1.362(2) Å

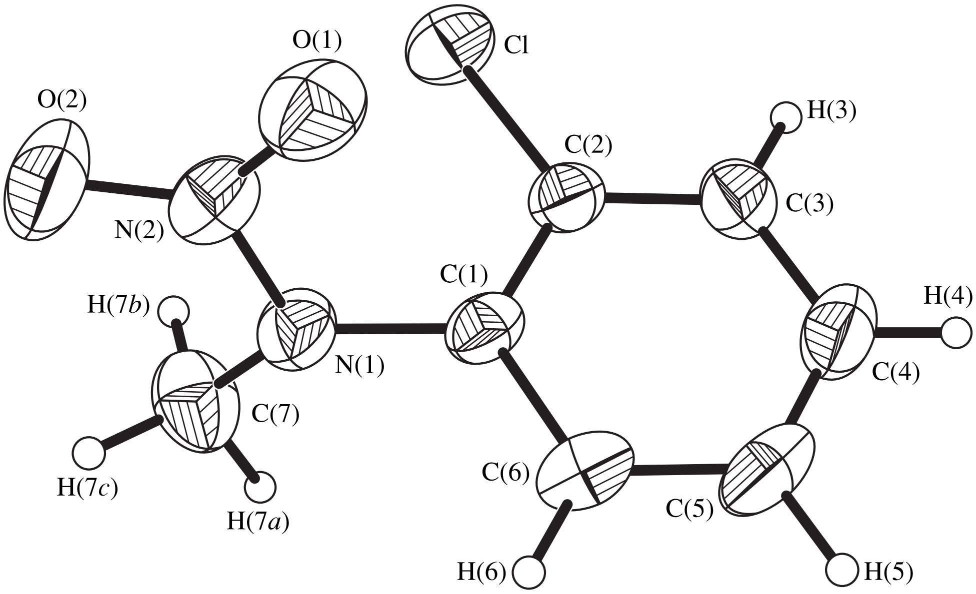

Fig. 1. Structure of molecule **I**. The atoms are shown by the thermal-vibration ellipsoids at the 50% probability level.

in **I**) is significantly longer than that in the hyponitrous acid esters or azo compounds (1.25 Å [15]) but shorter than the single N–N bond (1.48 Å [16]). This indicates that one pair out of the six π electrons that occupy a set of four-center π orbitals migrates to the antibonding orbital [9].

In molecule **II**, as well as in the molecules of other 4-substituted *N*-methyl-*N*-nitroanilines, no steric hindrances occur between the nitramine group and the substituent in the aromatic nucleus. However, the value of the N(2)–N(1)–C(1)–C(2) dihedral angle (66.5° [9]) indicates that, as in *N*-methyl-*N*-nitro-4-nitroaniline (72.3°) [6], the conjugation between the two π-electron systems is absent. This value corresponds to the first of the two minima in the dependence of the potential energy on the angle of rotation of the nitro group about the N(1)–N(2) bond relative to the plane of the benzene ring (Fig. 2a). The dipole moment of compound **II**, which was calculated for this minimum (3.545 D), agrees with the measured value (3.58 D [17]). In arylnitramines that contain two nitro groups in the *ortho* positions, the NNO_2 group is perpendicular to the plane of the aromatic ring [9]. In molecule **I**, the steric effect of the chlorine atom in the *ortho* position also forces the nitramino group to be almost perpendicular to the plane of the aromatic ring (73.5°). The calculated value of the N(2)–N(1)–C(1)–C(2) dihedral angle (80.8°) agrees closely with the rotation angle φ that corresponds to the first minimum in the curve (Fig. 2b). The calculated dipole moment (4.900 D) is consistent with the measured value (4.73 D). The relative position of the molecular fragments in **I**, **II**, and other 4-substituted *N*-methyl-*N*-nitroanilines explains why their spectral and electrooptical characteristics are not affected by the substituent in the aromatic ring [17]. The nitramine group is polar. Quantum-chemical calculations demonstrate that in molecules **I** and **II**, the N(2) atoms bear large positive charges (0.6570 and 0.6419, respectively) and all the neighboring atoms are negatively charged (Table 3). Interaction between the N–O dipoles could affect the crystal structure; however, the shortest intermolecular N···O distance (3.10 Å) exceeds the sum of the van der Waals atomic radii.

Table 2. Atomic deviations (Å) from the rms plane of the ring

Atom	Deviation	Atom	Deviation
C(1)*	0.006(1)	N(1)	0.009(3)
C(2)*	−0.005(1)	Cl	0.024(3)
C(3)*	0.000(1)	C(7)	1.287(5)
C(4)*	0.003(1)	N(2)	−1.012(4)
C(5)*	−0.002(1)	O(1)	−2.044(4)
C(6)*	0.003(1)	O(2)	−0.893(5)

* Atoms included in the plane definition.

The dihedral and bond angle are listed in Table 4. The bond lengths are presented in Table 5. The close agreement between the experimental and calculated values indicates that the molecule is only slightly dis-

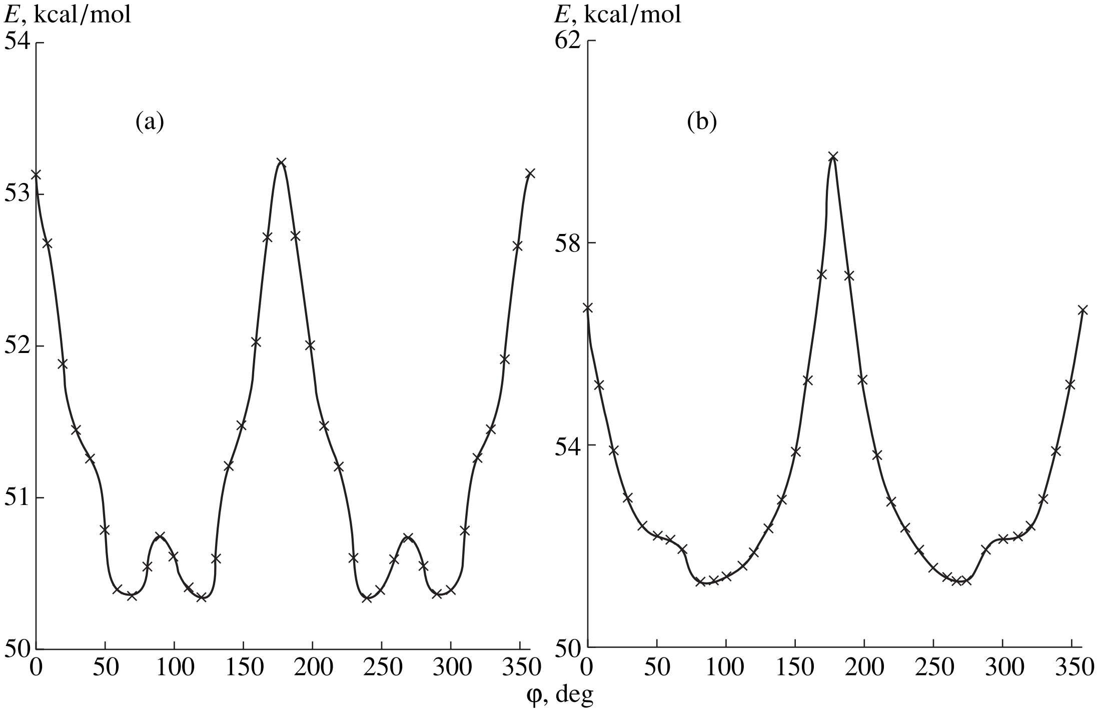

Fig. 2. Dependences of the potential energy (*E*, kcal/mol) on the angle of rotation of the NO_2 group about the N(1)–N(2) bond relative to the plane of the benzene ring (φ, deg) in molecules (a) **II** and (b) **I**.

Table 3. The Mulliken charges at the atoms of molecules **I** and **II**

Atom	Charge		Atom	Charge	
	I	**II**		**I**	**II**
C(3)	–0.0881	–0.0837	O(1)	–0.4224	–0.4179
C(2)	–0.0871	–0.0856	O(2)	–0.4264	–0.4206
C(1)	0.2624	0.2647	H(2)	–	0.1186
C(6)	–0.0545	–0.0461	H(3)	0.1037	0.1208
C(5)	–0.1001	–0.0865	H(4)	0.1063	–
C(4)	–0.0664	–0.0873	H(5)	0.1195	0.1208
N(1)	–0.3888	–0.3960	H(6)	0.1046	0.1057
C(7)	–0.1680	–0.1687	H(7*a*)	0.1335	0.1374
N(2)	0.6570	0.6419	H(7*b*)	0.1327	0.1333
			H(7*c*)	0.1600	0.1594

torted in the crystal field. The dihedral angles involving the N(1), N(2), C(1), C(2), and C(7) atoms show the largest differences (up to 7°) between the experimental and calculated values (Table 4). In molecule **II**, the closeness of the C(7)–N(1)–N(2)–O(1) and C(1)–N(1)–N(2)–O(2) dihedral angles to 180° and the C(1)–N(1)–N(2)–O(1) and C(7)–N(1)–N(2)–O(2) angles to 0° (the largest deviation of 6.7(6)° is observed for the C(1)–N(1)–N(2)–O(1) angle [9]) indicates that the molecular fragments involving these atoms are almost planar, as is the case in other 4-substituted *N*-methyl-*N*-nitroanilines [6]. In **I**, the substituent in the *ortho* position distorts the structure of the aforementioned molecular fragments (Table 4): the torsion angles become 14.2° (instead of 0°) and 168.7° (instead of 180°).

Further comparison between the structural parameters of molecules **I** and **II**, which differ only in the position of the substituent in the aromatic ring, shows that the N(1)–N(2) bond in **I** (1.362 Å) is slightly longer than that in **II** (1.350 Å), whereas the C(1)–N(1) bond lengths are virtually identical [1.424(4) ≈ 1.425(2) Å]. It is remarkable that the N(2)–N(1)–C(1), N(2)–N(1)–C(7), and C(1)–N(1)–C(7) bond angles in **I** decrease compared to those in **II** [116.7(2)° < 118.4(2)°, 117.5° < 118.8(3)°, and 121.9(2)° < 123.3(3)°, respectively]. This is also attributed to the effect of the *ortho* substituent, because the replacement of the substituent in the *para* position (for example, of the NO_2 group [6] by Cl [9]) does not affect the angles [N(2)–N(1)–C(1), 118.8(2)° ≈ 118.4(3)°; N(2)–N(1)–C(7), 119.1(4)° ≈ 118.8(3)°; and C(1)–N(1)–C(7), 121.9(2)° ≈ 122.0(2)°]. Analysis of the charge distribution over the N(1), N(2), O(1), O(2), C(1), and C(7) atoms of molecules **I** and **II** in comparison with that in *N*,*N*-dimethylnitramine reveals that the aromatic ring produces some effect on the NNO_2 group: when going from *N*,*N*-dimethylnitramine to *N*-methyl-*N*-nitroaniline, **I**, and **II**, the charges at the N(1), N(2), and O atoms increase (–0.182 → –0.362, –0.389, –0.396; 0.452 → 0.640, 0.657, 0.642; and –0.226 → –0.426, –0.426, –0.421, respectively) and the charge at the C(7) atom (–0.426 → –0.2615, –0.168, –0.169) decreases in magnitude. Replacement of the CH_3 group in the $(CH_3)_2NNO_2$ molecule by the aromatic ring leads to a change in the charge at the aromatic carbon atom that is bound immediately with N(1) (–0.426 → +0.2615). This charge at the C(1) atom remains virtually unchanged upon introduction of a substituent into the aromatic ring (0.2615 ≈ 0.2624 ≈ 0.2647). The above data indicate that the *n* electrons of

Table 4. Selected bond and torsion angles (α, deg) in molecule **I**

Angle	α_{exp}	α_{calcd}	Angle	α_{exp}	α_{calcd}
N(2)–N(1)–C(1)	116.7(1)	117.56	C(4)–C(3)–C(2)	119.0(2)	119.25
N(2)–N(1)–C(7)	117.5(2)	116.60	C(3)–C(4)–C(5)	120.7(2)	120.38
C(1)–N(1)–C(7)	121.9(2)	122.56	C(6)–C(5)–C(4)	120.6(2)	119.66
O(1)–N(2)–O(2)	125.1(2)	126.73	C(1)–C(6)–C(5)	119.7(2)	120.71
O(1)–N(2)–N(1)	117.5(2)	116.12	C(1)–N(1)–N(2)–O(2)	168.7(2)	168.77
O(2)–N(2)–N(1)	117.3(2)	117.13	C(7)–N(1)–N(2)–O(2)	10.5(3)	10.06
C(6)–C(1)–C(2)	119.4(2)	119.04	C(1)–N(1)–N(2)–O(1)	–14.2(2)	–13.05
C(6)–C(1)–N(1)	119.3(2)	120.05	C(7)–N(1)–N(2)–O(1)	–172.4(2)	–171.76
C(2)–C(1)–N(1)	121.2(2)	120.34	N(2)–N(1)–C(1)–C(6)	108.0(2)	101.36
C(1)–C(2)–C(3)	120.6(2)	120.47	C(7)–N(1)–C(1)–C(6)	–94.9(2)	–101.32
C(3)–C(2)–Cl	120.1(2)	120.28	N(2)–N(1)–C(1)–C(2)	–73.5(2)	–80.80
C(1)–C(2)–Cl	119.3(1)	120.49	C(7)–N(1)–C(1)–C(2)	83.6(2)	76.52

Table 5. Selected bond lengths (L, Å) in molecule **I**

Bond	L_{exp}	L_{calcd}	Bond	L_{exp}	L_{calcd}
Cl–C(2)	1.727(2)	1.7477	C(1)–C(6)	1.386(2)	1.3986
O(1)–N(2)	1.226(2)	1.2302	C(1)–C(2)	1.390(3)	1.4034
O(2)–N(2)	1.217(2)	1.2270	C(2)–C(3)	1.384(3)	1.3942
N(1)–N(2)	1.362(2)	1.3893	C(3)–C(4)	1.380(3)	1.3944
N(1)–C(1)	1.425(2)	1.4259	C(4)–C(5)	1.370(3)	1.3927
N(1)–C(7)	1.455(3)	1.4592	C(5)–C(6)	1.377(3)	1.3952

the imide nitrogen are involved in conjugation with the π electrons of the nitro group to a larger extent than with those of the aromatic ring. As a consequence, the NNO_2 functional group exhibits a low sensitivity to various effects (including substitution of C_6H_5 for CH_3 and introduction of various substituents into the aromatic nucleus).

REFERENCES

1. D. H. L. Williams, in *The Chemistry of Amino, Nitroso, and Nitro Compounds and Their Derivatives* (Wiley, Chichester, 1982).
2. J. C. Mialocq and J. C. Stephenson, Chem. Phys. **106**, 281 (1986).
3. R. Stolevik and P. Rodemacher, Acta Chem. Scand. **23**, 672 (1969).
4. A. Filhol, Acta Crystallogr., Sect. B: Struct. Crystallogr. Cryst. Chem. **B36**, 575 (1980).
5. H. H. Cady, Acta Crystallogr. **23**, 601 (1967).
6. R. Anulewicz, T. M. Krygowski, R. Gawinecki, *et al.*, J. Phys. Org. Chem. **6**, 257 (1993).
7. B. G. Growenlock, J. Pfab, and V. M. Young, J. Chem. Soc., Perkin Trans. 2, 915 (1997).
8. Z. Daszkiewicz, M. Nowakowska, and J. B. Kyziol, Tetrahedron **54**, 5991 (1998).
9. K. Ejsmont, J. Kyziol, Z. Daszkiewicz, *et al.*, Acta Crystallogr., Sect. C: Cryst. Struct. Commun. **C54**, 672 (1998).
10. Z. Daszkiewtcz, A. Domanski, and J. B. Kyziol, Org. Prep. Proced. Int. **26**, 337 (1994).
11. Kuma, *Kuma KM-4 User Guide. Version KM-4b8. Kuma Diffraction* (Wroclaw, 1997).
12. G. M. Sheldrick, *SHELXTL Plus Manual* (Simens Analytical X-ray Instrument Inc., Madison, 1990).
13. G. M. Sheldrick, *SHELXL93: Programs for the Refinement of Crystal Structures* (Univ. of Göttingen, Göttingen, 1993).
14. M. J. Frish, *Gaussian 94* (Gaussian Inc., Pittsburgh, 1994).
15. C. A. Ogle, K. A. van der Kooi, G. D. Mendenhall, *et al.*, J. Am. Chem. Soc. **105**, 5114 (1982).
16. A. F. Cameron, N. J. Hair, and D. G. Morris, J. Chem. Soc., Perkin Trans. 2, 1071 (1972).
17. Z. Daszkiewicz, E. Nowadowska, V. V. Prezhdo, *et al.*, Pol. J. Chem. **26**, 1437 (1995).

Translated by I. Polyakova

Crystallography Reports, Vol. 46, No. 3, 2001, pp. 394–397. Translated from Kristallografiya, Vol. 46, No. 3, 2001, pp. 444–447.
Original Russian Text Copyright © 2001 by Chuev, Nikonova, Atovmyan, Utenyshev, Aldoshin.

STRUCTURE OF ORGANIC COMPOUNDS

Molecular and Crystal Structures of the Products of Crystallization of (*N*'-Furfurylidene)isonicotinoylhydrazide from Aqueous Solutions of Hydrochloric and Acetic Acids

I. I. Chuev, L. A. Nikonova, E. G. Atovmyan, A. N. Utenyshev, and S. M. Aldoshin

Institute of Chemical Physics, Russian Academy of Sciences, Chernogolovka, Moscow oblast, 142432 Russia

e-mail: sma@icp.ac.ru

Received March 3, 1998; in final form, October 5, 1999

Abstract—Crystals of (*N*'-furfurylidene)isonicotinoylhydrazide (**I**), which have been isolated from a water–methanol solution of hydrochloric acid (**Ia**) and an aqueous solution (~50%) of acetic acid (**Ib**), are studied by X-ray diffraction. In **Ia**, the nitrogen atom of the pyridine ring is protonated. In the crystal, the intermolecular $C{=}O\cdots HN(Py)$ hydrogen bonds link the $\mathbf{I}\cdot H^+$ cations into chains which are bound through centrosymmetric $NH\cdots W\cdots Cl^-\cdots W'\cdots HN'$ bridges. In molecule **Ib**, no protonation occurs; however, its pyridine N atom is blocked by the hydroxyl H atom of a solvate molecule of acetic acid. Crystals **Ib** have a layered structure. The crystallization water molecule is involved in the formation of three intermolecular hydrogen bonds, namely, those with the H atom of the amide group and the carbonyl O atoms of molecule **I** and an acetic acid molecule of the neighboring layer. *© 2001 MAIK “Nauka/Interperiodica”.*

Earlier [1, 2], we studied the effect of the nature and composition of the solvent on the intermolecular hydrogen bonds formed in crystals of [*N*'-(5-nitrofurfurylidene)]isonicotinoylhydrazide. In the present work, we carried out the X-ray diffraction study of the crystals of the related compound (*N*'-furfurylidene)isonicotinoylhydrazide (**I**) which were obtained from aqueous solutions of strong (HCl) and weak (CH_3COOH) acids.

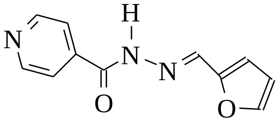

I

Compound **I** precipitates from a water–methanol solution of HCl as bright yellow monoclinic needle crystals **Ia** [3]. The crystals are characterized by the following crystallographic parameters: $C_{11}H_9N_3O_2\cdot HCl\cdot H_2O$, $a = 7.307(1)$ Å, $b = 17.976(4)$ Å, $c = 9.687(2)$ Å, $\beta = 106.15(3)°$, $M = 269.69$, $V = 1222.2(2)$ Å^3, $Z = 4$, $d_{calcd} = 1.465(2)$ g/cm^3, and space group $P2_1/c$. The set of experimental data was collected from a crystal $0.6\times 0.03\times 0.05$ mm in size on a DAR-UM three-circle diffractometer (CuK_α radiation). The number of reflections with $I > 2\sigma(I)$ was 979.

Crystals **Ib** were isolated from an aqueous solution of acetic acid (~50%) as yellowish triclinic prisms. The crystals are characterized by the following crystallographic parameters: $C_{11}H_9N_3O_2\cdot CH_3COOH\cdot H_2O$, $a = 13.327(3)$ Å, $b = 8.565(2)$ Å, $c = 6.646(1)$ Å, $\alpha = 75.21(3)°$, $\beta = 91.88(3)°$, $\gamma = 95.86(3)°$, $M = 293.28$, $V = 729.6(2)$ Å^3, $Z = 2$, $d_{calcd} = 1.335(2)$ g/cm^3, and space group $P\bar{1}$. The set of experimental data was obtained on an KM-4 four-circle diffractometer (MoK_α radiation) from a crystal $0.2\times 0.05\times 0.5$ mm in size. The number of reflections with $I > 2\sigma(I)$ was 2155. The structures were solved by the direct method with the SHELXS86 program package [4] and refined in the anisotropic approximation by the full-matrix least-squares procedures with the SHELXL93 program package [5]. The hydrogen atoms were revealed from the difference Fourier synthesis and included in the refinement in the isotropic approximation. The H atoms of the crystallization water molecule in **Ia** were not located. However, according to the data of IR spectroscopy, these atoms are involved in rather strong intermolecular hydrogen bonds of approximately equal energy. The final *R* factors are 0.058 and 0.056 for **Ia** and **Ib**, respectively. The atomic coordinates are listed in Table 1.

Compound **Ia** is the $\mathbf{I}\text{-}H^+Cl^-\cdot H_2O$ salt (Fig. 1), whereas compound **Ib** is the acetic acid–water solvate $\mathbf{I}\cdot CH_3COOH\cdot H_2O$ (Fig. 2). In both compounds, the central part of molecule **I** is essentially planar and has the *syn* orientation of the O(1), N(2), and O(2) heteroatoms. The deviation of the molecules from planarity is due to the rotation of the pyridine fragment about the C(1)–C(7) bond by 21.9° and 4.7° in **Ia** and **Ib**, respectively. In **Ib**, the furan fragment is rotated about the C(2)–C(3) bond by 2.8°, whereas in **Ia** it is coplanar with the ketohydrazone fragment.

Table 1. Atomic coordinates ($\times 10^4$ for non-hydrogen atoms and $\times 10^3$ for H atoms) and equivalent or isotropic thermal parameters U_{eq}/U_{iso} ($\times 10^3$) in structures **Ib** (the upper row) and **Ia** (the lower row)

Atom	x	y	z	U_{eq}/U_{iso}, Å^2	Atom	x	y	z	U_{eq}/U_{iso}, Å^2
Cl	4122(2)	5822(1)	1641(3)	62(1)	C(12)	8462(2)	−474(4)	572(6)	94(1)
O(1)	6351(1)	6922(2)	1138(2)	72(1)	C(13)	7770(2)	532(3)	1271(4)	68(1)
	4399(3)	2636(2)	4465(3)	43(1)	O(3)	7437(2)	1686(3)	126(3)	111(1)
O(2)	9401(1)	3964(2)	2178(3)	84(1)	O(4)	7536(1)	20(2)	3238(3)	76(1)
	10239(2)	3920(2)	4603(3)	46(1)	O_w	7133(2)	4991(3)	8774(2)	80(1)
N(1)	6954(1)	5759(2)	4331(3)	50(1)		3051(2)	4287(2)	206(2)	50(2)
	4608(3)	3379(1)	2626(2)	42(2)	HN(1)	689(2)	554(2)	569(4)	57(5)
N(2)	7723(1)	5176(2)	3471(2)	51(1)		426(2)	357(1)	151(2)	2(11)
	6487(3)	3558(2)	3390(2)	42(2)	HN(3)	−310(2)	209(2)	54(1)	62(36)
N(3)	3889(1)	8471(2)	5551(3)	68(1)	H(2)	808(2)	395(3)	613(4)	78(7)
	−1915(3)	2293(2)	1076(2)	32(2)		675(1)	428(1)	196(2)	20(14)
C(1)	6303(1)	6635(2)	3034(3)	51(1)	H(4)	969(2)	226(4)	653(5)	97(6)
	12053(2)	4228(1)	4919(3)	43(2)		966(2)	504(1)	193(2)	46(18)
C(2)	8249(1)	4236(2)	4778(3)	52(1)	H5	1099(2)	162(3)	438(5)	92(6)
	580(3)	3121(2)	1360(3)	44(2)		315(1)	504(2)	383(2)	74(23)
C(3)	9094(1)	3552(2)	4149(3)	53(1)	H6	1052(2)	337(4)	069(5)	99(6)
	−1252(2)	2902(2)	672(3)	34(2)		1295(1)	399(2)	595(2)	13(12)
C(4)	9711(2)	2553(3)	5317(4)	72(1)	H8	501(2)	850(3)	135(5)	86(5)
	12091(3)	4722(1)	3913(3)	51(2)		165(1)	170(1)	365(2)	25(14)
C(5)	10437(2)	2276(3)	3984(4)	78(1)	H9	365(2)	946(3)	272(4)	89(5)
	1005(3)	2064(1)	2777(2)	51(2)		−126(1)	154(1)	232(1)	48(22)
C(6)	10239(2)	3144(4)	2153(5)	87(1)	H10	434(2)	727(3)	829(5)	87(6)
	9182(2)	4265(1)	3403(2)	43(2)		−208(2)	324(1)	−000(2)	12(12)
C(7)	5475(1)	7244(2)	4032(3)	51(1)	H(11)	567(2)	619(3)	710(4)	85(6)
	1715(3)	2699(2)	2411(2)	43(2)		99(2)	350(1)	93(1)	17(13)
C(8)	4843(2)	8224(3)	2720(4)	71(1)	$H_w(1)$	704(2)	548(4)	958(5)	95(7)
	7225(3)	4041(2)	2785(2)	51(2)	$H_w(2)$	729(2)	412(4)	935(5)	89(7)
C(9)	4071(2)	8815(3)	3557(5)	77(1)	$H_0(4)$	706(3)	052(4)	339(5)	101(5)
	3732(2)	2899(2)	3285(2)	43(2)	H(121)	850(2)	−155(4)	147(5)	102(7)
C(10)	4490(2)	7506(3)	6819(4)	70(1)	H(122)	852(3)	−002(4)	−084(6)	106(7)
	−842(2)	1875(2)	2091(2)	41(2)	H(123)	905(3)	−004(4)	090(6)	112(7)
C(11)	5296(2)	6881(3)	6130(3)	60(1)					
	10270(3)	4751(2)	2944(2)	54(2)					

Table 2. Selected geometric parameters of molecule **I** in structures **Ia** and **Ib** in comparison with the corresponding values for [*N*'-(5-nitrofurfurylidene)]isonicotinoylhydrazide [1]

Structure	C(1)–O(1), Å	C(1)–N(1), Å	N(1)–N(2), Å	C(1)–C(7), Å	N(2)–C(2), Å	CN(1)N(2), deg	N(1)N(2)C, deg	CN(3)C, deg
Ia	1.205(7)	1.340(7)	1.405(8)	1.525(8)	1.253(7)	114.9(2)	113.1(2)	120.4(2)
Ib	1.223(2)	1.346(2)	1.384(2)	1.508(2)	1.270(2)	118.2(2)	114.7(2)	117.4(2)
[1]	1.244(8)	1.338(9)	1.364(8)	1.504(8)	1.300(8)	117.8(6)	116.5(4)	118.2(7)

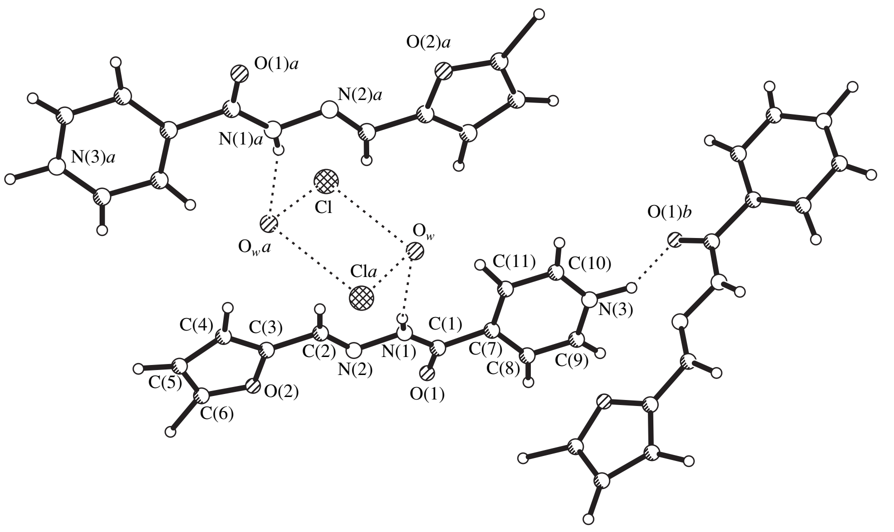

Fig. 1. The two-dimensional network of intermolecular hydrogen bonds in crystal **Ia**.

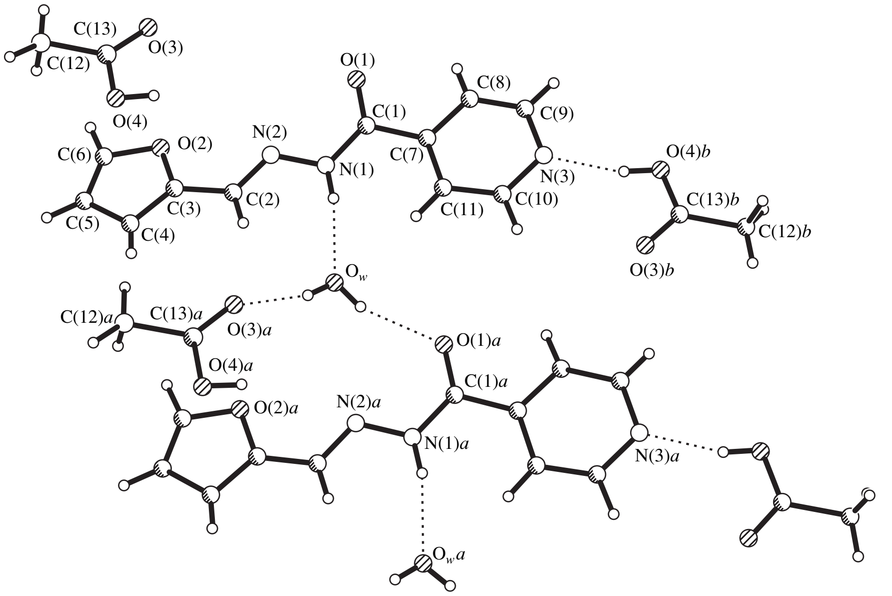

Fig. 2. A fragment of crystal structure **Ib**.

The protonation of the pyridine fragment in **Ia** is accompanied by the increase in the bond angle at the N(3) atom to 120.4(2)° relative to the standard value for pyridine (118°) [6]. The geometric parameters of the pyridine fragment in **Ib** coincide within the experimental error with the standard values. The bond lengths in the central ketohydrazone fragment of molecule **I** coincide within the experimental error with the corresponding values in the [*N*'-(5-nitrofurfurylidene)]isonicotinoylhydrazide complex studied earlier in [1] (Table 2). There is a tendency for change in the bond lengths in **Ia** with respect to those in **Ib**: the C(1)–C(7) and N(1)–N(2) bonds lengthen, and the C(1)–O(1) and C(2)–N(2) bonds shorten. This is probably due to the weakening of the conjugation in **Ia** upon protonation of the pyridine ring. However, we cannot be sure in this conclusion because of the large errors in the determination of bond lengths. Note a significant decrease in the C(1)N(1)N(2) bond angle in **Ia** (114.9°) in comparison with its values (117°–121°) observed in **Ib** and all the *N*'-substituted isonicotinoylhydrazide compounds studied earlier [1, 2].

Protonation of molecule **I** in **Ia** results in the formation of the additional HN_{Py} proton-donating center. As a consequence, two types of intermolecular hydrogen bonds are formed in the crystal: the $\mathrm{N}_{Py}\mathrm{H}^+\cdots\mathrm{O{=}C}$ bonds [O(1)···N(3), 2.714(3) Å; $\mathrm{H}^+\cdots$O(1), 1.90(1) Å;

$N(3)H^+O(1)$, 143°; and $C(1)O(1)H^+$, 119.5°] link molecules **I** into zigzag chains, and the centrosymmetric $N(1)H\cdots W\cdots Cl\cdots W'\cdots HN(1)'$ bridges {$H[N(1)]\cdots O_W$, 1.84(1) Å; $N(1)\cdots O_W$, 2.824(3) Å; $N(1)H[N(1)]O_W$, 146.8°; $O_W\cdots Cl^-$, 3.09 Å; and $O_W Cl^- O_{W'}$, 79°} connect molecules **I** of adjacent chains. Note also a short intermolecular $N(2)\cdots N(3)'$ contact (2.960 Å), which arises from the formation of the intermolecular $N_{Py}H^+\cdots O{=}C$ bond. A combination of intermolecular hydrogen bonds in the crystal gives rise to a two-dimensional network (Fig. 1). Molecules **I**, which are related by the *c* translation, are packed into stacks. The channels between the stacks accommodate water molecules and chlorine anions.

In crystal structure **Ib**, molecules of **I**, CH_3COOH, and H_2O form layers. The molecule of crystallization water is involved in the formation of three intermolecular hydrogen bonds (Fig. 2), namely, the hydrogen bonds with the amide hydrogen atom [$O_W\cdots N(1)$, 2.864 Å; $O_W\cdots H$, 2.01 Å; and $O_W HN(1)$, 165.1°], the carbonyl oxygen atom of molecule **I** [$O_W\cdots O(1)a$, 2.842 Å; $H_W(1)\cdots O(1)a$, 2.09 Å; $O_W H_W(1)O(1)a$, 160.4°; and $H_W(1)O(1)aC(1)a$, 123.5°], and the carbonyl group of the acetic acid molecule from the adjacent layer [$O_W\cdots O(3)a$, 2.810 Å; $H_W(2)\cdots O(3)a$, 2.04 Å; $O_W H_W(2)O(3)a$, 164.6°; and $H_W(2)O(3)aC(13)a$, 149.4°]. The angle between the plane of the water molecule and the mean plane of molecule **I** is 37.0°. The N(3) nitrogen atom of the pyridine fragment forms the intermolecular hydroxyl hydrogen bond with the hydrogen atom of the acetic acid molecule from the same layer [$H(Ac)\cdots N(3)$, 1.86 Å; $O(4)a\cdots N(3)$, 2.657 Å; and $O(4)(Ac)N(3)$, 164.6°] (Fig. 2).

REFERENCES

1. S. M. Aldoshin, L. A. Nikonova, E. G. Atovmyan, *et al.*, Izv. Akad. Nauk, Ser. Khim., No. 9, 2263 (1996).
2. S. M. Aldoshin, E. G. Atovmyan, L. A. Nikonova, *et al.*, Izv. Akad. Nauk, Ser. Khim., No. 10, 2501 (1996).
3. H. Fujiwara, J. Pharm. Soc. Jpn. **78**, 817 (1958).
4. G. M. Sheldrick, Acta Crystallogr., Sect. A: Found. Crystallogr. **A46**, 467 (1990).
5. G. M. Sheldrick, *SHELXL93: Program for the Refinement of Crystal Structures* (Univ. of Göttingen, Göttingen, 1993).
6. F. H. Allen, O. Kennard, D. G. Watson, *et al.*, J. Chem. Soc., Perkin Trans. 2, S1 (1987).

Translated by I. Polyakova

Crystallography Reports, Vol. 46, No. 3, 2001, pp. 398–401. Translated from Kristallografiya, Vol. 46, No. 3, 2001, pp. 448–451.
Original Russian Text Copyright © 2001 by Vishnyakov, A. Polishchuk, I. Polishchuk, Grineva.

STRUCTURE OF ORGANIC COMPOUNDS

Electron Effects of the Substituents on the Structure of 4,4'-Dipyridylium Dications

A. Yu. Vishnyakov, A. P. Polishchuk, I. Yu. Polishchuk, and L. G. Grineva

Institute of Physics, National Academy of Sciences of Ukraine, pr. Nauki 46, Kiev-39, 03650 Ukraine

Received June 9, 2000; in final form, October 30, 2000

Abstract—The crystal structure of *N*,*N*'-di(2-hydroxyethyl)-4,4'-dipyridylium diperchlorate $C_{14}H_{18}Cl_2N_2O_{10}$ is determined by X-ray diffraction at 293 K. The crystals are monoclinic, $a = 6.446(1)$ Å, $b = 14.479(3)$ Å, $c = 9.912(1)$ Å, $\beta = 99.24(2)°$, space group $P2_1/c$, and $Z = 2$; 1562 reflections measured; and $wR2 = 0.086$ and $R1 = 0.033$ for 1209 reflections with $F > 4\sigma(F)$. It is found that, in the absence of charge transfer from the counterion to the dication, the planarity of the dipyridylium skeleton of the molecule is primarily due to the conjugation between the lone electron pairs of the hydroxyl groups and the π system of the dication. This inference is supported by the intramolecular O···N contact (2.847 Å).© *2001 MAIK “Nauka/Interperiodica”.*

INTRODUCTION

Currently, a search for new materials exhibiting combinations of useful properties is a principal trend. In this respect, investigation into the structure and properties of photochromic and electrochromic compounds based on the organic salts of the dipyridylium series (viologens) is a topical problem. Complexes based on viologens can serve as reduction–oxidation indicators, electron phototransfer catalysts, and photosensitive systems. Particular interest in viologens is also due to their increasing applications in electrochromic displays, variable-density light filters [1–9], and detecting media for optical data recording [10].

Earlier [11–13], we studied the influence of the structural properties on the photoinitiated electron transfer from the counterion to the dication which results in the formation of stable radical cations in the crystal state. We also examined the dependence of the molecular structure on electron-donating properties of anions. In particular, it was shown that, in the crystal state, the intramolecular charge-transfer complex contributes to the stabilization of the planar structure of the central dipyridylium fragment of the molecules and is a necessary condition for photochromism. In the ground (nonexcited) state, the planar structure arises from the shift of the electron density from the anion to the dication followed by its redistribution throughout the dipyridylium fragment. The absence of the charge-transfer interaction predetermines the twisted conformation of the dipyridylium skeleton in these molecules, as is the case in *N*,*N*'-dimethyl-4,4'-dipyridylium tetrachloropalladate ($MD^{2+}PdCl_4^{2-}$) [14] and *N*,*N*'-diheptyl-4,4'-dipyridylium perchlorate ($HD^{2+}2ClO_4^-$) [11]. This is explained by the minor electron effect of the ClO_4^-

Table 1. Crystallographic parameters and experimental data for structure **I**

Parameter	**I**
Empirical formula	$C_{14}H_{18}Cl_2N_2O_{10}$
M_r	445.20
Crystal system	Monoclinic
Space group	$P2_1/c$
Z	2
a, Å	6.446(1)
b, Å	14.479(1)
c, Å	9.912(2)
β, deg	99.24(2)
V, Å^3	913.1(3)
D_{calcd}, g/cm^3	1.619
μ, mm^{-1}	0.415
$F(000)$	460
Diffractometer	Enraf-Nonius CAD-4
λ, Å	0.71073
T, K	293
θ_{max}, deg	24
Number of reflections measured	1562
Number of reflections with $F > 4\sigma(F)$	1209
Refinement on	F^2
$R1$	0.033
$wR2$	0.086
S	0.928

Table 2. Coordinates ($\times 10^4$) and thermal parameters ($Å^2 \times 10^3$) of non-hydrogen atoms in structure **I**

Atom	*x*	*y*	*z*	U_{eq}
Cl	2721(1)	3468(1)	2275(1)	58(1)
N	1299(3)	6383(1)	2362(2)	45(1)
O	4657(3)	5779(2)	1031(2)	72(1)
O(1)	762(18)	3328(7)	2783(14)	96(5)
O(2)	1880(3)	4201(9)	1562(16)	83(4)
O(3)	3126(36)	2778(18)	1482(30)	83(4)
O(4)	4252(30)	3733(11)	3174(16)	161(6)
O(1A)	2076(25)	3361(7)	3456(12)	110(4)
O(2A)	1939(25)	4172(11)	1140(15)	86(4)
O(3A)	2632(42)	2595(14)	1468(33)	96(5)
O(4A)	4927(13)	3799(12)	2511(10)	78(2)
O(1B)	3227(38)	3117(17)	3823(21)	115(8)
O(2B)	733(37)	3663(27)	2088(39)	203(17)
O(3B)	3587(57)	2684(26)	1892(40)	154(19)
O(4B)	3915(38)	4253(10)	2447(22)	114(6)
C(1)	261(3)	5302(1)	4447(2)	42(1)
C(2)	2191(4)	5745(2)	4555(2)	54(1)
C(3)	2665(4)	6272(2)	3517(2)	54(1)
C(4)	–592(4)	5987(2)	2240(3)	55(1)
C(5)	–1124(4)	5453(2)	3258(2)	54(1)
C(6)	1928(4)	6886(2)	1194(3)	56(1)
C(7)	2901(4)	6241(2)	296(3)	61(1)

anions because of their weakest electron-donating ability in the anion series $I^- > Br^- > Cl^- > ClO_4^-$. However, among the structurally characterized viologens, only two aforementioned molecules adopt the twisted conformation of the dipyridylium nucleus. These molecules have only alkyl substituents ($R = CH_3$ for $MD^{2+}PdCl_4^{2-}$ and $R = C_7H_{15}$ for $HD^{2+}2ClO_4^-$) without any functional groups containing atoms with lone electron pairs. In this connection, it is important to investigate the electron effects of the substituents containing lone electron pairs on the structure of the dipyridylium skeleton of viologens in the absence of charge transfer. For this purpose, we performed the X-ray structure analysis of *N*,*N*'-di(2-hydroxyethyl)-4,4'-dipyridylium diperchlorate (**I**) [$R = (CH_2)_2OH$ and $A = ClO_4^-$], which is characterized by the absence of the charge-transfer interactions and contains the electron-donating OH hydroxyl group.

EXPERIMENTAL

Compound **I** was synthesized according to the procedure described in [12]. Single-crystal samples were grown by slow evaporation of an isopropyl solution. In the course of crystallization, transparent single crystals were obtained in the form of plates. The X-ray experiment was carried out on an Enraf–Nonius CAD4 four-circle diffractometer (graphite monochromator, $\omega/2\theta$ scan mode).

The structure was solved by the direct method, and the non-hydrogen atoms were refined in the anisotropic approximation by the full-matrix least-squares procedure. The refinement of the structure revealed the disordering of all four oxygen atoms of the ClO_4^- anion over three positions (each with the occupancy $G = 0.33$). All hydrogen atoms in the structure studied were located from the difference Fourier synthesis and included in the refinement in the isotropic approximation. The calculations were performed on an IBM AT personal computer with the SHELXS86 [15] and SHELXL93 [16] software packages. The main crystallographic parameters and experimental data at room temperature are listed in Table 1. The atomic coordinates, bond lengths, and bond angles are given in Tables 2–4, respectively.

RESULTS AND DISCUSSION

In crystal **I**, the position of the dication at the center of symmetry determines the exactly planar structure of the dipyridylium skeleton. The dication as a whole has

Table 3. Bond lengths (Å) in structure **I**

Bond	*d*	Bond	*d*
Cl–O(1)	1.447(8)	Cl–O(4B)	1.368(13)
Cl–O(2)	1.341(11)	N–C(3)	1.337(3)
Cl–O(3)	1.32(2)	N–C(4)	1.335(3)
Cl–O(4)	1.278(9)	N–C(6)	1.479(3)
Cl–O(1A)	1.312(8)	O–C(7)	1.412(3)
Cl–O(2A)	1.542(14)	C(1)–C(1)*	1.483(4)
Cl–O(3A)	1.49(2)	C(1)–C(2)	1.388(3)
Cl–O(4A)	1.484(8)	C(1)–C(5)	1.377(3)
Cl–O(1B)	1.60(2)	C(2)–C(3)	1.355(3)
Cl–O(2B)	1.30(2)	C(5)–C(4)	1.358(3)
Cl–O(3B)	1.35(3)	C(6)–C(7)	1.497(4)

Note: In Tables 3 and 4, the C(1)* atom is related to the reference atom by the symmetry operation $-x$, $-y + 1$, $-z + 1$.

Table 4. Bond angles (deg) in structure **I***

Angle	ω	Angle	ω
O(2)–Cl–O(1)	89.6(8)	O(3B)–Cl–O(1B)	89(2)
O(3)–Cl–O(1)	111.6(9)	O(3B)–Cl–O(4B)	119(2)
O(3)–Cl–O(2)	113(2)	O(4B)–Cl–O(1B)	96.9(13)
O(4)–Cl–O(1)	114.8(11)	C(3)–N–C(6)	120.3(2)
O(4)–Cl–O(2)	109.3(10)	C(4)–N–C(3)	119.5(2)
O(4)–Cl–O(3)	116(2)	C(4)–N–C(6)	120.1(2)
O(1A)–Cl–O(2A)	127.9(8)	C(2)–C(1)–C(1)*	121.5(2)
O(1A)–Cl–O(3A)	112.8(11)	C(5)–C(1)–C(1)*	122.2(2)
O(1A)–Cl–O(4A)	109.3(8)	C(5)–C(1)–C(2)	116.3(2)
O(3A)–Cl–O(2A)	101(2)	C(3)–C(2)–C(1)	120.7(2)
O(4A)–Cl–O(2A)	95.4(9)	N–C(3)–C(2)	121.4(2)
O(4A)–Cl–O(3A)	108.2(11)	N–C(4)–C(5)	120.9(2)
O(2B)–Cl–O(1B)	105(2)	C(4)–C(5)–C(1)	121.3(2)
O(2B)–Cl–O(3B)	126(2)	N–C(6)–C(7)	110.6(2)
O(2B)–Cl–O(4B)	111(2)	O–C(7)–C(6)	111.5(2)

* See note to Table 3.

an *S*-like shape (figure), as judged from the C(3)–N–C(6)–C(7), C(4)–N–C(6)–C(7), and N–C(6)–C(7)–O torsion angles (88.3°, –87.5°, and –57.4°, respectively). The hydroxyl groups are located over the pyridine rings and participate in the formation of the O···H–O hydrogen bonds with the oxygen atoms of the $\mathrm{ClO_4^-}$ anions, whose disordering is responsible for different lengths of these bonds [O···O(4B), 2.69 Å; O···O(2A), 2.92 Å; and O···O(2), 3.00 Å].

The specific *S*-like shape of dication **I** results in the intramolecular O···N contact (2.847 Å), whose length is close to the sum of van der Waals radii of the N (1.50 Å [17]) and O (1.29 Å [18]) atoms. A similar *S*-like shape of the dication and a close value of the O···N contact (2.966 Å) were found in the earlier studied *N*,*N*'-di(2-hydroxyethyl)-4,4'-dipyridylium dichloride (HO*Et*$D^{2+}2Cl^-$) [12], which differs from **I** only in the type of the counterion (Cl^- instead of $\mathrm{ClO_4^-}$) and, as a consequence, is characterized by the charge-transfer interaction.

The absence of charge transfer in **I** predetermines the minimal electron effect of the $\mathrm{ClO_4^-}$ anions on the stabilization of the planar structure of the dipyridylium nucleus of the molecule. Note that, in addition to the packing effects, whose role was discussed in [11], the electron effects of the hydroxyl groups can also contribute to the flattening of the central dipyridylium fragment in **I**. This contribution is due to the ability of the lone electron pairs of the oxygen atoms of the OH groups to participate in the conjugation with the electron-deficient π system of the pyridine rings, as evidenced by the O···N contact (2.847 Å). As a result, the electron density shifts from the electron-donating OH groups to the electron-seeking dication and then is redistributed throughout the π system. As in the case of charge-transfer complexes, this conjugation stabilizes the planar structure of the dipyridylium nucleus.

Therefore, in the absence of charge transfer in **I**, the electron effects of the hydroxyl groups contribute to the flattening of the dipyridylium skeleton. At the same time, in *N*,*N*'-diheptyl-4,4'-dipyridylium diiodide ($HD^{2+}2I^-$) [19, 20], which contains alkyl substituents ($R = C_7H_{15}$) producing a minor effect on the dication, the flattening is associated with the charge transfer from the counterions ($2I^-$) to the dication (D^{2+}). In the charge-transfer complex (HO*Et*$D^{2+}2Cl^-$) [12], which contains the same electron-donating substituents as in **I** [$R = (CH_2)_2OH$], both the charge transfer and the electron effects of the hydroxyl groups contribute to the stabilization of the planar dipyridylium skeleton.

In [13], we investigated the physicochemical properties of the dipyridylium compounds which contain the carboxyl groups ($R = CH_2COOH$) and differ only in the counterions. These were *N*,*N*'-di(carboxymethyl)-4,4'-dipyridylium dichloride ($COMD^{2+}2Cl^-$), dibromide ($COMD^{2+}2Br^-$), and diiodide ($COMD^{2+}2I^-$). It was emphasized that the planar structure of the dipyridylium nucleus results from the charge transfer [13]. However, from the aforesaid, it is reasonable to assume that the electron effects of the carboxyl COOH groups containing lone electron pairs additionally contribute to the flattening in these structures. It is notable that the dications in the $COMD^{2+}2$*Hlg* compounds (*Hlg* = Cl^-, Br^-, or I^-) also have an *S*-like shape and contain the intramolecular O···N contacts (2.739, 2.743, and 2.711 Å, respectively).

Thus, the X-ray diffraction study of **I** and analysis of the structure and properties of viologens that contain

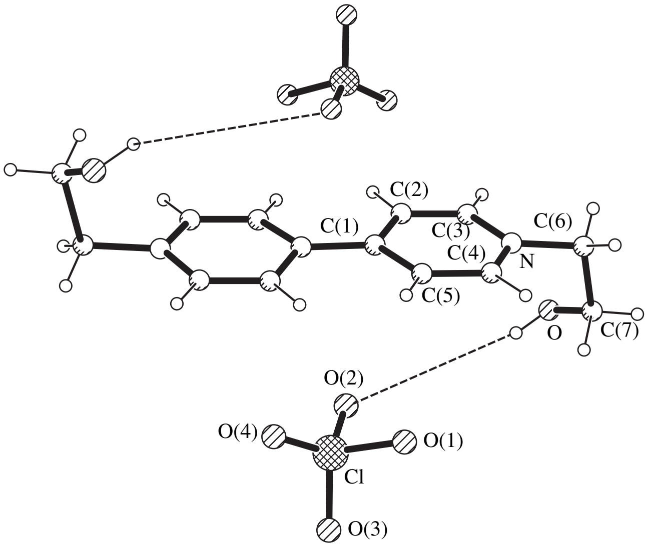

Structure of molecule **I** and atomic numbering. Dashed lines indicate hydrogen bonds.

the hydroxyl and carboxyl groups allow us to conclude that the O···N contacts, whose length lies in the range 2.711–2.966 Å, can bring about the conjugation of the lone electron pairs of the oxygen atoms with the π system of the dication. This conjugation can contribute to the stabilization of the planar structure of the central dipyridylium fragment of the molecule, as it takes place in **I**, or serve as an additional factor enhancing the stabilization in charge-transfer viologens.

REFERENCES

1. P. M. S. Monk, R. D. Farwweafher, M. D. Ingram, and J. A. Duffy, J. Electroanal. Chem. **359** (1–2), 301 (1993).
2. H. Byker, US Patent No. 5 336 448 (1994).
3. M. Hiroshi, Jpn. Patent No. 93 224 242 (1993).
4. U. Tooru and Y. Akio, Jpn. Patent No. 94 301 065 (1993).
5. K. Keiichi, O. Natsuko, D. Yuzo, O. Sanae, and S. Satoshi, Jpn. Patent No. 9 415 245 (1992).
6. K. Koseki, N. Shimizu, and Y. Demizu, Patent Np. EP0 682 284 (1995).
7. M. H. Miles, R. A. Henry, and D. A. Fine, US Patent No. 5 516 462 (1996).
8. K. Masaaki and N. Yoshinori, Patent No. EP0 897 127 (1999).
9. M. Kobayashi, Y. Nishikitani, and I. Sugiura, Patent No. WO9 932 926 (1999).
10. A. G. Iljin, G. V. Klimusheva, L. P. Yatsenko, *et al.*, Proc. SPIE **3488**, 16 (1998).
11. I. Yu. Polishchuk, L. G. Grineva, A. P. Polishchuk, and A. N. Chernega, Zh. Obshch. Khim. **66** (9), 1530 (1996).
12. I. Yu. Polishchuk, L. G. Grineva, A. P. Polishchuk, and A. N. Chernega, Zh. Obshch. Khim. **67** (11), 1893 (1997).
13. I. Yu. Polishchuk, L. G. Grineva, A. P. Polishchuk, and A. N. Chernega, Zh. Obshch. Khim. **68** (4), 647 (1998).
14. C. K. Prout and P. Murrau-Rust, J. Chem. Soc. A, No. 10, 1520 (1969).
15. G. M. Sheldrick, *SHELXS86: Program for the Solution of Crystal Structures* (Univ. of Göttingen, Göttingen, 1986).
16. G. M. Sheldrick, *SHELXL93: Program for the Refinement of Crystal Structures* (Univ. of Göttingen, Göttingen, 1993).
17. L. Pauling, *The Nature of the Chemical Bond and the Structure of Molecules and Crystals* (Cornell Univ. Press, London, 1960, 3rd ed.).
18. Yu. V. Zefirov and P. M. Zorky, Zh. Strukt. Khim. **15** (1), 118 (1974).
19. I. Yu. Grineva, I. P. Kraĭnov, A. P. Polishchuk, *et al.*, Kristallografiya **37** (6), 1485 (1992) [Sov. Phys. Crystallogr. **37**, 805 (1992)].
20. I. Grineva, I. Krainov, A. Polishchuk, and A. Tolmachev, Mol. Cryst. Liq. Cryst. **211** (5), 397 (1992).

Translated by I. Polyakova

Crystallography Reports, Vol. 46, No. 3, 2001, pp. 402–410. Translated from Kristallografiya, Vol. 46, No. 3, 2001, pp. 452–460.
Original Russian Text Copyright © 2001 by Nesterov, Kuleshova, Antipin.

Formation of Crystal Structure of Cyanovinylbenzene Derivatives: X-ray Structure Investigation of Ethyl Esters of 3,4-Dimethoxy-, 3,4,5-Trimethoxy-, and 4-Fluorobenzylidenecyanoacetic Acids

V. N. Nesterov, L. N. Kuleshova, and M. Yu. Antipin

Nesmeyanov Institute of Organoelement Compounds, Russian Academy of Sciences,
ul. Vavilova 28, Moscow, 117813 Russia

Received June 26, 2000

Abstract—Ethyl esters of 3,4-dimethoxy-, 3,4,5-trimethoxy-, and 4-fluorobenzylidenecyanoacetic acids are investigated by X-ray diffraction analysis with the aim of elucidating the factors responsible for the formation of crystal structures of cyanovinylbenzene derivatives. The crystal data for other known derivatives of this series are analyzed. It is revealed that, in the absence of strong hydrogen bonding, the main structure-forming function in crystals is fulfilled by intermolecular contacts of two types, namely, staking contacts of parallel and antiparallel molecules. The staking contacts of antiparallel molecules are most frequently realized. It is assumed that their presence in the structure determines the prevailing formation of centrosymmetric packings in the compounds under consideration. *© 2001 MAIK "Nauka/Interperiodica".*

INTRODUCTION

Organic compounds with a relatively long conjugated π electron system and donor–acceptor substituents (on opposite sides of a conjugated chain) are promising materials for nonlinear optics [1, 2]. Organic molecules readily undergo chemical modification and can achieve maximum values of the molecular optical nonlinear susceptibilities β and γ, which is one of the most important advantages of organic compounds over inorganic substances. Nowadays, the design of chromophores with high values of β (including the synthesis of promising derivatives and the evaluation of their molecular nonlinear susceptibilities) has become a sufficiently well developed procedure [3]. At the same time, the formation of a noncentrosymmetric crystal structure, which is necessary for further practical applications of these compounds, presents considerable difficulties. In this respect, the investigation into the crystal structure of large series of related chromophore compounds with nonlinear optical properties is of particular importance. Analysis of their packings can be helpful in the determination of the factors responsible for the formation of crystal structures. The aim of the present work was to perform the X-ray structure investigation and detailed examination of the packing in three cyanovinylbenzene derivatives: ethyl esters of 3,4-dimethoxy-, 3,4,5-trimethoxy-, and 4-fluorobenzylidenecyanoacetic acids (**I**, **II**, and **III**, respectively).

EXPERIMENTAL

Synthesis. Compounds **I**–**III** were prepared according to the Knoevenagel reaction by the condensation of aromatic aldehydes with ethyl cyanoacetic ester in alcohol in the presence of an organic base (morpholine) in catalytic amounts. The yield of the reaction products was 78–85%.

Colorless crystals of compounds **I**–**III** were obtained by slow isothermal evaporation of ethanol solutions for three days.

X-ray structure analysis. Crystals **I** are monoclinic; at 25°C, the unit cell parameters are as follows: $a = 13.099(3)$ Å, $b = 8.025(2)$ Å, $c = 13.855(3)$ Å, $\beta = 114.24(2)°$, $V = 1328.0(6)$ Å^3, $d_{calcd} = 1.307$ g/cm^3, $Z = 4$, and space group $P2_1/n$. Crystals **II** are monoclinic; at 25°C, the unit cell parameters are $a = 12.549(5)$ Å, $b = 16.082(6)$ Å, $c = 7.330(2)$ Å, $\beta = 90.43(3)°$, $V = 1479.2(9)$ Å^3, $d_{calcd} = 1.308$ g/cm^3, $Z = 4$, and space group $P2_1/c$. Crystals **III** are triclinic; at 25°C, the unit cell parameters are $a = 7.322(2)$ Å, $b = 7.511(3)$ Å, $c = 10.858(3)$ Å, $\alpha = 90.22(3)°$, $\beta = 97.30(3)°$, $\gamma = 109.22(2)°$, $V = 558.6(3)$ Å^3, $d_{calcd} = 1.303$ g/cm^3, $Z = 2$, and space group $P\bar{1}$.

The unit cell parameters and the intensities of 2414, 2988, and 2092 reflections (for structures **I**, **II**, and **III**, respectively) were measured on a Siemens P3/PC four-circle automated diffractometer (λMoK_α, graphite monochromator, $\theta/2\theta$ scan mode, $\theta_{max} = 26°$). The structures were solved by the direct method for all the non-hydrogen atoms. The refinement was performed

Table 1. Atomic coordinates ($\times 10^4$; for H atoms, $\times 10^3$) and isotropic equivalent (isotropic for H atoms) thermal parameters ($Å^2$, $\times 10^3$) for structure **I**

Atom	x	y	z	U_{eq}/U_{iso}
O(1)	−398(2)	4729(3)	7476(2)	65(1)
O(2)	−2053(2)	5075(3)	6105(1)	51(1)
O(3)	634(2)	374(3)	3002(1)	52(1)
O(4)	2575(2)	−761(3)	4178(2)	55(1)
N(1)	−2142(2)	3583(4)	3858(2)	65(1)
C(1)	921(2)	2115(3)	5573(2)	39(1)
C(2)	445(3)	1739(4)	4476(2)	38(1)
C(3)	1019(2)	795(4)	4043(2)	39(1)
C(4)	2093(2)	189(4)	4683(2)	40(1)
C(5)	2573(3)	577(4)	5748(2)	46(1)
C(6)	1985(3)	1529(4)	6179(2)	47(1)
C(7)	362(3)	3038(4)	6104(2)	42(1)
C(8)	−667(2)	3707(4)	5773(2)	39(1)
C(9)	−1483(3)	3638(4)	4709(2)	43(1)
C(10)	−1004(3)	4543(4)	6554(2)	43(1)
C(11)	−2486(3)	5957(6)	6780(3)	64(1)
C(12)	−3633(4)	6490(7)	6108(4)	72(1)
C(13)	−451(3)	953(6)	2313(3)	60(1)
C(14)	3671(3)	−1419(6)	4790(3)	63(1)
H(2)	−25(3)	216(4)	406(2)	64(10)
H(5)	327(3)	11(4)	618(2)	69(10)
H(6)	231(2)	176(3)	693(2)	34(7)
H(7)	81(2)	318(3)	684(2)	40(7)
H(111)	−242(3)	523(5)	732(3)	89(14)
H(112)	−200(3)	694(5)	710(3)	88(13)
H(121)	−414(3)	548(5)	584(3)	99(14)
H(122)	−370(4)	713(5)	556(3)	114(19)
H(123)	−396(3)	711(5)	654(3)	96(13)
H(131)	−47(3)	214(4)	230(2)	72(13)
H(132)	−58(3)	45(4)	166(3)	77(11)
H(133)	−110(3)	59(4)	253(3)	80(12)
H(141)	366(2)	−221(4)	540(2)	60(9)
H(142)	419(3)	−54(4)	514(3)	72(12)
H(143)	385(3)	−203(4)	432(3)	84(13)

Table 2. Atomic coordinates ($\times 10^4$; for H atoms, $\times 10^3$) and isotropic equivalent (isotropic for H atoms) thermal parameters ($Å^2$, $\times 10^3$) for structure **II**

Atom	x	y	z	U_{eq}/U_{iso}
O(1)	−2549(1)	−277(1)	3334(2)	68(1)
O(2)	−2918(1)	1051(1)	4353(2)	49(1)
O(3)	2740(1)	2041(1)	1993(2)	61(1)
O(4)	3914(1)	655(1)	1435(2)	58(1)
O(5)	3015(1)	−808(1)	1018(2)	61(1)
N(1)	−651(1)	2124(1)	5192(3)	66(1)
C(1)	659(1)	434(1)	2222(2)	39(1)
C(2)	1125(1)	1219(1)	2261(2)	43(1)
C(3)	2208(1)	1303(1)	1959(2)	43(1)
C(4)	2828(1)	606(1)	1594(2)	44(1)
C(5)	2354(1)	−174(1)	1466(2)	43(1)
C(6)	1268(1)	−262(1)	1773(2)	41(1)
C(7)	−455(1)	290(1)	2635(2)	41(1)
C(8)	−1156(1)	769(1)	3536(2)	40(1)
C(9)	−882(1)	1535(1)	4415(3)	46(1)
C(10)	−2274(1)	463(1)	3727(2)	45(1)
C(11)	−4036(1)	801(1)	4562(4)	58(1)
C(12)	−4658(2)	1551(2)	5020(5)	75(1)
C(13)	2137(2)	2785(1)	2071(4)	62(1)
C(14)	4306(2)	1046(2)	−158(4)	67(1)
C(15)	2555(2)	−1612(1)	816(4)	65(1)
H(2)	707(15)	1711(12)	2490(20)	52(5)
H(6)	91(1)	−77(1)	167(2)	42(4)
H(7)	−74(1)	−19(1)	222(2)	42(4)
H(111)	−421(2)	59(1)	336(3)	70(7)
H(112)	−400(2)	38(2)	565(4)	93(8)
H(121)	−535(3)	139(2)	511(4)	102(9)
H(122)	−444(2)	188(2)	602(4)	110(11)
H(123)	−456(2)	197(2)	398(4)	88(8)
H(131)	182(2)	285(2)	324(4)	91(8)
H(132)	155(2)	278(2)	114(4)	95(8)
H(133)	261(2)	321(2)	180(3)	97(8)
H(141)	397(3)	79(2)	−129(5)	128(12)
H(142)	422(2)	168(2)	2(4)	122(10)
H(143)	508(2)	94(2)	−19(3)	95(8)
H(151)	194(2)	−160(1)	−6(4)	93(8)
H(152)	231(2)	−178(1)	198(3)	70(7)
H(153)	312(2)	−197(2)	42(3)	89(8)

according to the full-matrix least-squares procedure in the anisotropic approximation for the non-hydrogen atoms by using 1296, 2043, and 1110 unique reflections. The hydrogen atoms in molecules **I** and **II** were located independently from difference Fourier syntheses and were then refined in the isotropic approximation. In molecule **III**, the positions of hydrogen atoms were calculated geometrically and included in the refinement within the riding-atom model. The final discrepancy factors were as follows: $R_1 = 0.059$ for 1296

Table 3. Coordinates of non-hydrogen atoms ($\times 10^4$) and isotropic equivalent thermal parameters (Å^2, $\times 10^3$) for structure **III**

Atom	x	y	z	U_{eq}
F(1)	7896(4)	6279(4)	–3793(2)	112(1)
O(1)	604(3)	6791(4)	1358(2)	94(1)
O(2)	2886(3)	8305(3)	2921(2)	70(1)
N(1)	7384(4)	9682(4)	2088(3)	79(1)
C(1)	4783(4)	6808(4)	–1002(3)	53(1)
C(2)	6816(5)	7580(4)	–850(3)	65(1)
C(3)	7849(5)	7405(5)	–1794(4)	74(1)
C(4)	6864(5)	6448(5)	–2867(3)	74(1)
C(5)	4879(6)	5632(5)	–3060(3)	79(1)
C(6)	3860(5)	5821(5)	–2123(3)	69(1)
C(7)	3544(4)	6910(4)	–85(3)	55(1)
C(8)	3936(4)	7758(4)	1061(3)	51(1)
C(9)	5862(4)	8825(4)	1646(3)	57(1)
C(10)	2283(4)	7559(5)	1775(3)	60(1)
C(11)	1358(5)	8148(7)	3700(3)	92(1)
C(12)	2246(7)	8937(8)	4922(4)	127(2)

unique reflections with $I > 2\sigma$ and $wR_2 = 0.127$ for 2309 reflections for structure **I**, $R_1 = 0.047$ for 2043 unique reflections with $I > 2\sigma$ and $wR_2 = 0.119$ for 2859 reflections for structure **II**, and $R_1 = 0.069$ for 1110 unique reflections with $I > 2\sigma$ and $wR_2 = 0.195$ for 1930 reflections for structure **III**. All the calculations were performed using the SHELXTL97 software package [4]. The atomic coordinates and isotropic equivalent (isotropic for H atoms) thermal parameters for structures **I**–**III** are presented in Tables 1–3.

RESULTS AND DISCUSSION

The structural data and nonlinear optical activities of a series of dicyanovinylbenzene derivatives have already been published in recent works [5, 6]. Chromophore derivatives of this class have attracted considerable interest, because their molecules contain acceptor dicyanovinyl groups with a long conjugated chain, thus increasing the molecular nonlinear susceptibility. Moreover, dicyano derivatives are characterized by a rather high thermal stability, which is of crucial importance in technological processes. However, noncentrosymmetric crystals of compounds in this series are rare in occurrence (less than 15% of the total number[1]) as compared to those observed, on average, for organic crystals (approximately 25% according to the Cambridge Structural Database (version 1999) [7]). On the other hand, it is known that the number of noncentrosymmetric crystal structures in some classes of nonlinear optical materials (for example, hydrazone derivatives [8]) can be as large as 38%. According to [8], this circumstance can be explained by the presence of hydrogen-bonded acentric fragments in crystal packing, which are characteristic of hydrazone structures and favor the formation of noncentrosymmetric crystals. The role of the symmetry of stable packing fragments (formed by intermolecular hydrogen bonds) in the formation of the resulting crystal structure was discussed in our previous work [9]. In crystal structures of dicyanovinylbenzene derivatives, strong hydrogen bonds are absent and the crystal structure is governed by relatively weak hydrogen bonds (C–H···O and C–H···N) and van der Waals interactions. In this respect, it was of interest to evaluate their role in the formation of crystal packing in compounds of this series.

Earlier [5], we performed the MM3 calculations of the energies of the intermolecular interaction for three main types of molecular packing (Fig. 1) in order to

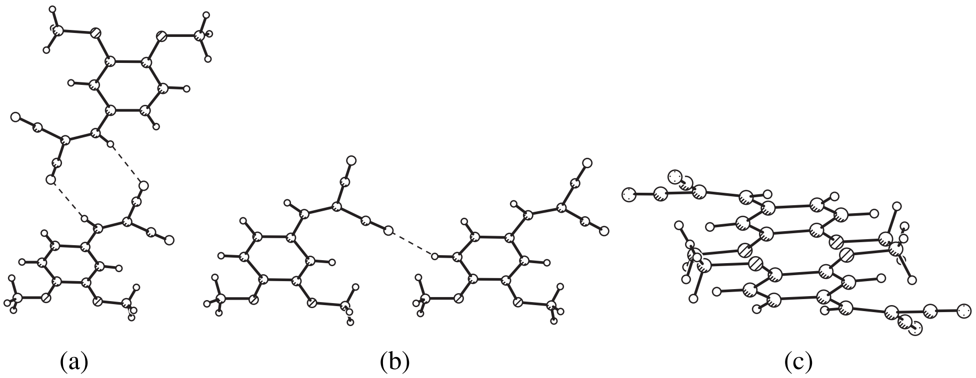

(a) (b) (c)

Fig. 1. Main types of arrangement of a molecular pair in crystals of the dicyanovinylbenzene substituted derivatives: (a) $D\bar{1}$, (b) $D1$, and (c) $D\uparrow\downarrow$.

---

[1] The data for about 30 compounds have been published to date.

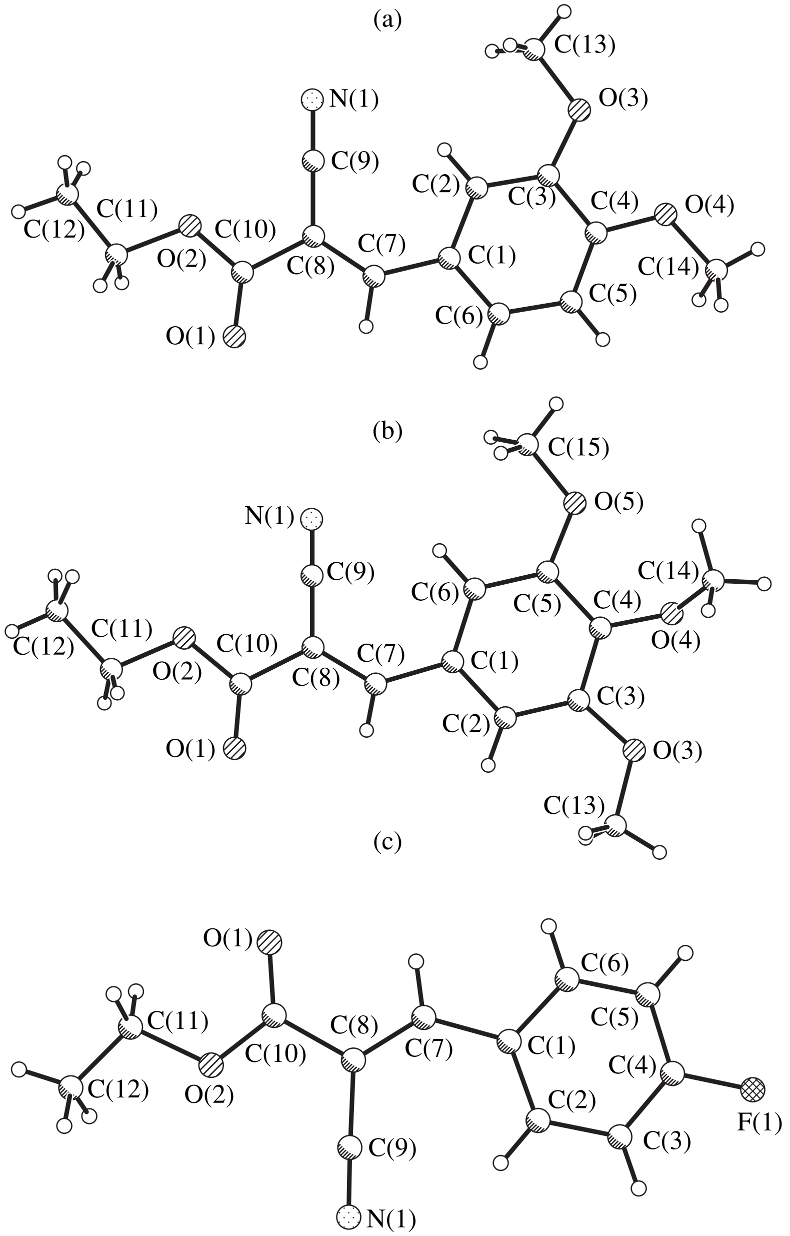

Fig. 2. A general view of molecules (a) **I**, (b) **II**, and (c) **III**.

elucidate the reason why centrosymmetric crystal structures are predominantly formed in dicyanovinylbenzene derivatives. As follows from these calculations, the most energetically favorable molecular packing corresponds to the planar centrosymmetric dimer $D\bar{1}$ (Fig. 1a). At the same time, it is known that this type of interactions does not need to be realized in all centrosymmetric crystals of the given class.

In the present work, we synthesized ethyl esters **I**–**III** (which correspond to the dicyano derivatives studied earlier in [4, 5]) and carried out their X-ray structure investigation in order to exclude the formation of $D\bar{1}$ hydrogen-bonded dimers in the structure.

A general view of the molecules is shown in Fig. 2. The basic parameters characterizing the molecular conformation are listed in Table 4. It is seen from Table 4 that the conjugated systems in molecules of the monocyano derivatives **I** and **III** are virtually planar, whereas molecule **II** is nonplanar. The molecules of the dicyano derivatives **I'**, **II'**, and **III'**, which were studied earlier, have a planar structure: the mean deviations of atoms from the plane passing through the C(1), C(2), C(3), C(4), C(5), C(6), C(7), C(8), and C(10) atoms are equal to 0.029, 0.036, and 0.017 Å, respectively. Compounds **I**–**III** involve the short intramolecular contact H(2)···C(9), whose length is equal to 2.45 Å in **I**, 2.48 Å

Table 4. Basic parameters characterizing the molecular conformation

Parameter	Molecule		
	I	**II**	**III**
Root-mean-square plane of the molecule, δ*, Å	0.032	0.157	0.008
Torsion angle C(2)–C(1)–C(7)–C(8), deg	1.9	–19.0	2.7
Torsion angle C(6)–C(1)–C(7)–C(8), deg	–176.8	160.9	178.6
Torsion angle C(9)–C(8)–C(7)–C(1), deg	–1.0	–4.8	–0.3
Torsion angle O(1)–C(10)–C(8)–C(7), deg	3.0	10.0	–5.1

* Mean atomic deviation from the plane.

Table 5. Selected bond lengths (Å) in the studied compounds

Compound	R_{ph}^{*}	R_{min}–R_{max}^{**}	C(1)–C(7)	C(7)–C(8)	C(8)–C(9)	C(9)–N(1)
I	1.390(4)	1.382–1.418(4)	1.438(4)	1.344(4)	1.423(4)	1.142(3)
II	1.391(2)	1.385–1.396(2)	1.451(2)	1.346(2)	1.431(3)	1.141(2)
III	1.376(5)	1.354–1.370(5)	1.448(4)	1.346(4)	1.435(4)	1.130(4)

* Mean bond length in the benzene ring.
** Range of bond lengths in the benzene ring.

Table 6. Comparison of the structural data for crystals of the cyanoacetic ester derivatives and the dicyano derivatives of vinylbenzene

Compound	Space group	V, Å^3	d, g/cm^3	Packing type	Dimer $D\bar{1}$ $C_{ar}H…N$	Chain $C1$ $C_{ar}H…N$	Stack $C1$, $C\bar{1}$ (“*d*” stacking)	Other interaction type $OCH_3…O$ $OCH_3…N$
I	$P2_1/n$	1328.0	1.307	Layers of ↑↓ stacks		2.49	↑↓ 3.42	
I'	$P\bar{1}$	547.9	1.299	Double layers of ↑↓ stacks	2.58	2.60	↑↓ 3.32	
II	$P2_1/c$	1479.2	1.308	Complex framework of ↑↓ stacks			↑↓ 3.22*	2.62 2.52 2.47 2.49
II'	$P2_1/c$	1242.5	1.306	Layers of ↑↑ stacks			↑↑ 3.49	2.57
III	$P\bar{1}$	558.6	1.303	↑↓ Stacks			↑↓ 3.47	
III'	$P\bar{1}$	424.4	1.347	Layers of ↑↓ stacks		2.52	↑↓ 3.58	

* Distance between the planes of benzene rings in the molecule.

in **III**, and 2.47 Å in molecule **II** with a noticeably nonplanar structure (the sum of the van der Waals radii for hydrogen and carbon atoms is 2.87 Å [10]). It seems likely that the reason for a nonplanar structure of molecule **II** should be looked for in the effect of the crystal environment.

The bond lengths and angles in the molecules under investigation have normal values [11, 12], which are close to the corresponding quantities for the earlier studied structures of dicyano derivatives **I'**–**III'**. The selected bond lengths in structures of molecules **I**–**III** are given in Table 5. These data indicate the conjugation over the *Ph*–C(7)–C(8)–C(9)–N(1) bonds. It should be noted that the alternation of bond lengths is clearly observed in the C(7)–C(8)–C(9)–N(1) chain. The difference in the lengths of the formally single bonds C(1)–C(7) and the formally double bonds C(7)–C(8) is approximately equal to 0.1 Å. The C(1)–C(7) bonds are longer than the C(8)–C(9) bonds. No pronounced alternation of bond lengths occurs in the benzene ring.

Table 6 presents the main crystal data for the structures of cyanoacetic ester derivatives **I**–**III** and the corresponding dicyano derivatives of vinylbenzene **I'**–**III'**,

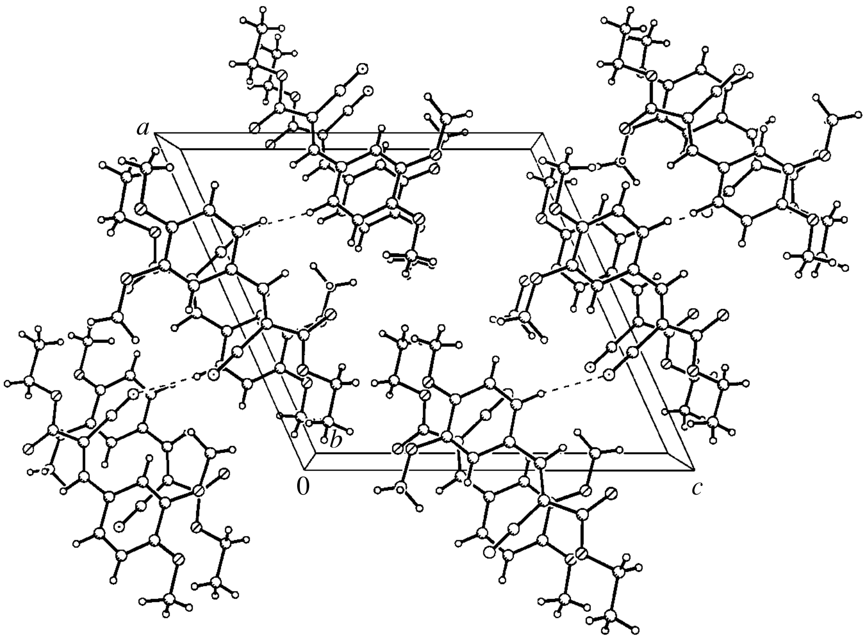

Fig. 3. Molecular packing in crystal **I**.

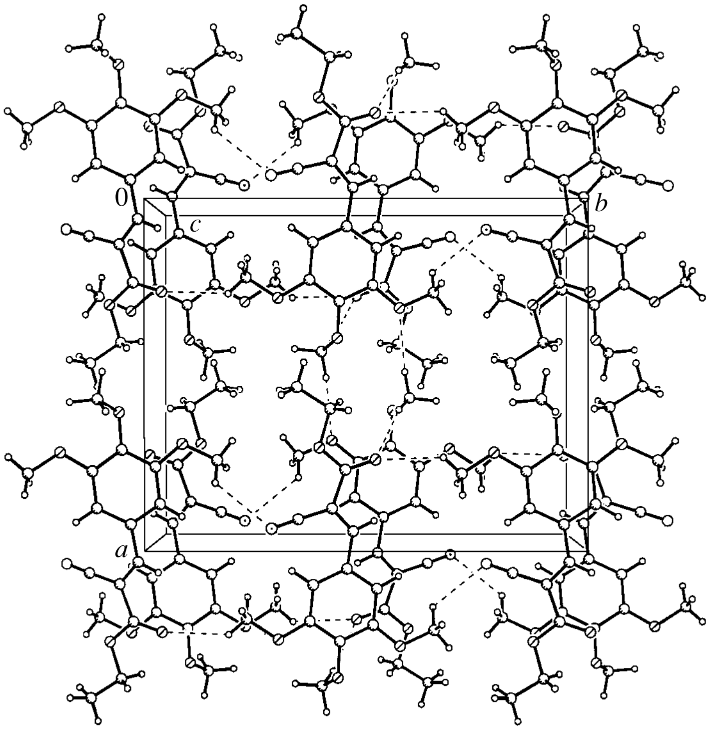

Fig. 4. Molecular packing in crystal **II**.

which were studied earlier in [6]. As was expected, we succeeded in preventing the formation of a planar centrosymmetric dimer of the $D\bar{1}$ type in structure **I**. However, compound **I** crystallizes in the centrosymmetric space group $P2_1/n$. Upon replacement of one cyano group by the ester group in the molecule, the crystal symmetry changes only in compound **I**. The incorporation of the ester group into the molecule leads to an increase in the unit cell volume; however, no decrease in the crystal density occurs.

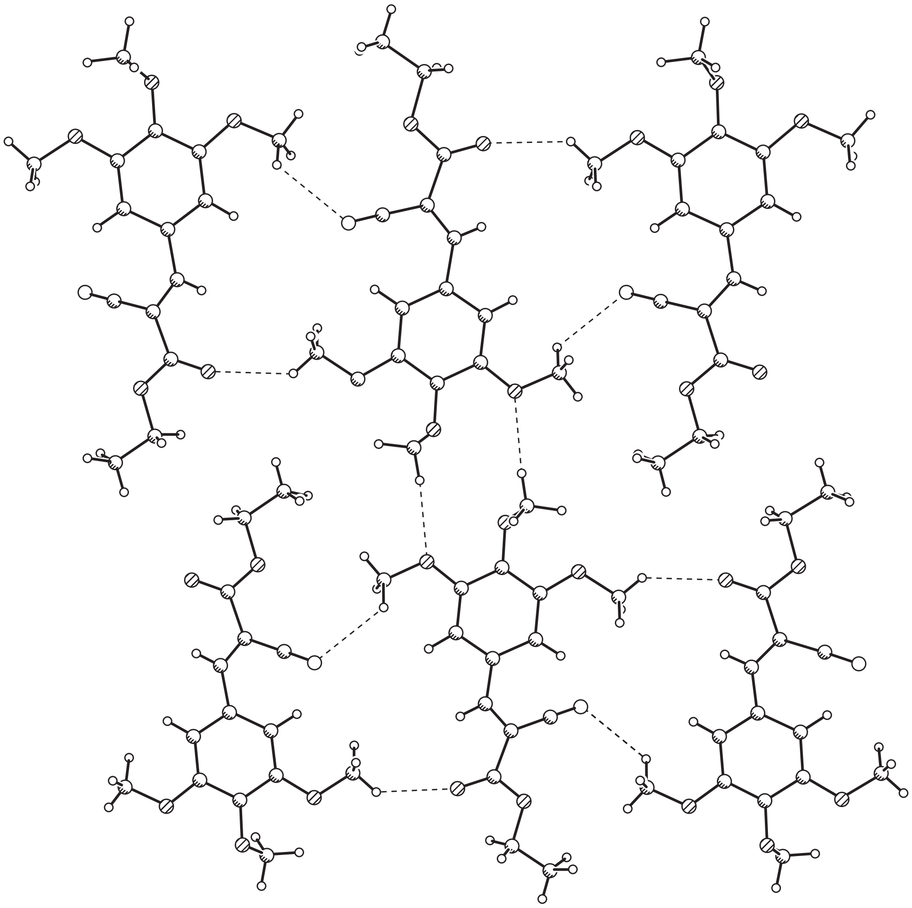

Fig. 5. Molecular layer in crystal structure **II**.

The formation of stacks consisting of antiparallel (↑↓) molecules is a common structural feature of all the crystals studied. The distance *d* between the planes of two adjacent molecules varies over a rather wide range (from 3.58 Å in **III'** to 3.19 Å in **II**). In antiparallel stacks, the donor molecular fragment lies above the acceptor fragment of the adjacent molecule. In this case, the benzene ring planes are shifted with respect to each other in such a way that the formally double bond C(7)–C(8) of one molecule lies above the benzene ring plane of the other molecule. This geometry of contacts indicates the possible $\pi\cdot\cdot\pi$ interaction between adjacent molecules. The stacks that are formed through parallel staking contacts (↑↑) are observed only in structure **II'**.

As follows from analysis of the known crystal structures of this series, it is these contacts that bring about the formation of a noncentrosymmetric structure. Actually, the parallel stacking contacts (↑↑) are observed in the structures of 2-methoxy- ($P2_1$), 2-fluoro- (Pc), and 4-dimethylamino- ($P2_1$) dicyanovinylbenzenes. A distinguishing feature of the crystal structures of these compounds is that they have one small (4–5 Å) crystallographic parameter. The same pattern is observed in [cyano(ethoxycarbonyl)methylene]4,5-dimethyl-2-ylidene-1,3-dithione with a similar structure [13]. It is known that this compound can exist in two polymorphic modifications α ($P\bar{1}$) and β ($P1$) with antiparallel and parallel stacks, respectively. Crystals of the β form (↑↑) possess the nonlinear optical activity. Different packings are formed upon crystallization from different solvents: the α modification is obtained upon slow evaporation of an acetone solution, and the β modification is formed through evaporation of an ethanol solution.

Let us now consider other features in the crystal structures of cyanovinylbenzene derivatives in more detail. It should be noted that the packing fragments will be differentiated only from geometric considerations: the presence or absence of short intermolecular contacts, hydrogen bonds, or other specific interactions between molecules. In the structures under investigation, short contacts (additional to stacking interactions) correspond primarily to the relatively weak hydrogen bonds C_{ar}–H··N. Only in trimethoxy derivatives **II** and **II'** in which the contact with hydrogen atoms of the

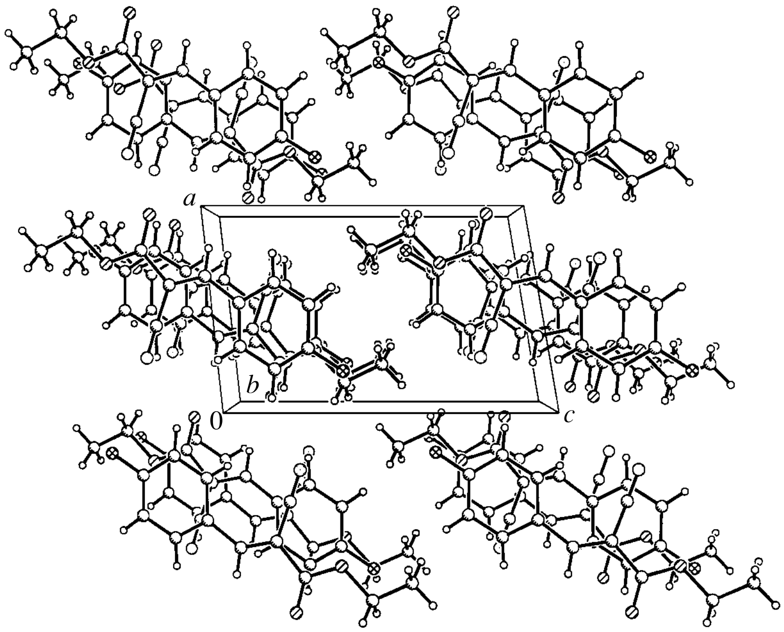

Fig. 6. Molecular packing in crystal **III**.

benzene ring is sterically hindered are the methoxy groups involved in structure-forming interactions (see Table 3).

*Crystal Structure **I***

In crystal structure **I'**, which was determined in [6], the molecules consisting of antiparallel stacks with the $P_c\bar{1}$ symmetry are joined through the C_{ar}–H··N hydrogen bonds (2.58 Å) with one of the cyano groups into layers aligned parallel to the *yz* plane with the $P_l\bar{1}$ symmetry. Another cyano group of the molecule forms the $D\bar{1}$ centrosymmetric contact with a molecule of the adjacent layer. This leads to the formation of double layers with the $P_l\bar{1}$ symmetry and the resulting crystal structure ($P\bar{1}$).

In crystal structure **I**, which is studied in the present work, the molecules built up of antiparallel stacks with the $P_c\bar{1}$ symmetry are linked by the same weak C_{ar}–H··N (2.49 Å) hydrogen contacts as in structure **I'** into layers that, however, have the P_l2_1/n symmetry. The congruent stacking of these layers brings about the formation of the crystal structure with the $P2_1/n$ symmetry (Fig. 3). As was noted above, the $D\bar{1}$ centrosymmetric contacts are absent in structure **I**. In our opinion, it is these antiparallel staking contacts that are responsible for the symmetry of the resulting structure.

*Crystal Structure **II***

In the dicyano derivative **II'** [5], the molecules of parallel stacks with the P_c1 symmetry are joined through the (OCH$_3$)H··O< hydrogen bonds (2.57 Å) into acentric layers with the P_l2_1 symmetry. The antiparallel packing of these layers due to van der Waals interactions brings about the formation of the centrosymmetric structure ($P2_1/c$). Note that, among the structures under consideration, it is the sole structure in which stable acentric packing fragments are formed and the noncentrosymmetric structure can be realized with a change in the crystallization conditions.

Crystal structure **II** is characterized by the formation of antiparallel (↑↓) stacks (Fig. 4). However, these stacks are not uniform due to the nonplanar molecular structure. The distances *d* between the benzene ring plane in the initial molecule and the benzene ring planes in the two molecules adjacent in the stack are different and equal to 3.22 and 3.91 Å, respectively. One more short contact (OCH$_3$)H··O= (2.49 Å) is observed in the staking pair with a short distance *d*. Therefore, the stack in structure **II** is built up of molecular dimers. The molecular network can most clearly be represented by separating out layers with the P_l2_1/c symmetry that are formed by a hydrogen-bond system, including all three methoxy groups of the molecule (Fig. 5): (OCH$_3$)H··N≡ (2.62 Å), (OCH$_3$)H··O= (2.52 Å), and (OCH$_3$)H··O< (2.47 Å). The stacking of centrosymmetric layers due to the aforementioned centrosymmetric stacking interactions and the C–H··O contacts brings about the formation of a structure with the $P2_1/c$ symmetry.

Crystal Structure ***III***

In the dicyano derivative **III'**, the antiparallel stacks formed by stacking contacts ($d = 3.58$ Å) with the $P_c\bar{1}$ symmetry are joined together into chains through the C_{ar}–H··N contacts (2.52 Å). This leads to the formation of layers with the $P_l\bar{1}$ symmetry and the resulting structure $P\bar{1}$. Crystal structure **III** is built up of antiparallel stacks ($d = 3.47$ Å) with the $P_c\bar{1}$ symmetry. This is wholly sufficient for the formation of the centrosymmetric structure (Fig. 6), even though the crystal has no other short contacts.

CONCLUSION

The structural analysis of the series of monocyano and dicyano vinylbenzene derivatives demonstrated that the antiparallel stacking interactions characteristic of this class of compounds are most likely responsible for the prevailing formation of centrosymmetric packings in the studied structures. Among the eight structurally characterized compounds, the stacks of parallel molecules and the stable noncentrosymmetric packing fragments (layers) were revealed only in structure **II'**. Although, as was noted above, the presence of the acentric fragment in the structure does not ensure the formation of a noncentrosymmetric crystal structure, the opportunity to obtain such a structure under other crystallization conditions exists. In this respect, the next step in the investigation of the factors responsible for the formation of crystal packing in cyanovinylbenzene derivatives will be the search for the possible polymorphism in this series.

ACKNOWLEDGMENTS

This work was supported by the Russian Foundation for Basic Research, project no. 00-03-32840a.

REFERENCES

1. *Nonlinear Optical Properties of Organic Molecules and Crystals*, Ed. by D. S. Chemla and J. Zyss (Academic, New York, 1987), Vol. 1, p. 2.
2. *Materials for Nonlinear Optics: Chemical Perspectives*, Ed. by S. R. Marder, J. E. Sohn, and G. D. Stucky (American Chemical Society, Washington, DC, 1991), ACS Symposium Series 455.
3. L. R. Dalton, A. W. Harper, R. Ghosn, *et al.*, Chem. Mater. **7**, 1060 (1995).
4. G. M. Sheldrick, *SHELXTL97: An Integrated System for Solving, Refining, and Displaying Crystal Structures from Diffraction Data, Version 5.10* (Bruker AXS, Madison, 1997).
5. M. Yu. Antipin, R. D. Clark, V. N. Nesterov, *et al.*, Mol. Cryst. Liq. Cryst. **313**, 85 (1998).
6. M. Yu. Antipin, T. V. Timofeeva, R. D. Clark, *et al.*, J. Phys. Chem. A **102**, 7222 (1998).
7. *Cambridge Structural Database* (Univ. of Cambridge, Cambridge, 1999).
8. Ch. Serbutoviez, Ch. Bosshard, G. Knopfle, *et al.*, Chem. Mater. **7**, 1198 (1995).
9. L. N. Kuleshova and V. N. Khrustalev, Kristallografiya **45** (1), 84 (2000) [Crystallogr. Rep. **45**, 78 (2000)].
10. R. S. Rowland and R. Taylor, J. Phys. Chem. **100**, 7384 (1996).
11. F. H. Allen, O. Kennard, D. G. Watson, *et al.*, J. Chem. Soc., Perkin Trans. 2, S1 (1987).
12. A. G. Orpen, L. Brammer, F. H. Allen, *et al.*, J. Chem. Soc., Dalton Trans. 1, S1 (1989).
13. K. Nakatsu, H. Nyoshie, H. Yoshioka, *et al.*, Mol. Cryst. Liq. Cryst. Sci. Technol., Sect. A **182**, 59 (1990).

Translated by O. Borovik-Romanova

Crystallography Reports, Vol. 46, No. 3, 2001, pp. 411–414. Translated from Kristallografiya, Vol. 46, No. 3, 2001, pp. 461–464.
Original Russian Text Copyright © 2001 by Shishkin, Kovalevskiĭ, Shcherbakov, Islyaĭkin, Kudrik, Baranski.

Molecular and Crystal Structures of Dibenzenehemiporphyrazine Complexes with Dimethylformamide

O. V. Shishkin*, A. Yu. Kovalevskiĭ, M. V. Shcherbakov*, M. K. Islyaĭkin***, E. V. Kudrik***, and A. Baranski******

** Institute of Single Crystals, Scientific and Technical Concern, National Academy of Sciences of Ukraine, pr. Lenina 60, Kharkov, 310141 Ukraine*

*** Nesmeyanov Institute of Organoelement Compounds, Russian Academy of Sciences, ul. Vavilova 28, Moscow, 117813 Russia*

**** Ivanovo State University of Chemical Technology, Ivanovo, Russia*

***** Institute of Organic Chemistry and Technology, Krakow Politechnika, Krakow, Poland*

Received March 27, 2000; in final form, July 8, 2000

Abstract—The crystal structures of the 1 : 1 and 1 : 2 complexes between dibenzenehemiporphyrazine (**I**) and dimethylformamide (compounds **II** and **III**, respectively) are determined by X-ray diffraction. In both compounds, the macrocycle has a saddlelike shape. In **III**, the conformation of the macrocycle approximates the C_{2v} symmetry, which agrees closely with the results of quantum-chemical calculations for isolated molecule **I** and complex **II**. The ring conformation in crystal **II** is distorted under the effect of intermolecular interactions, as is evidenced by short intermolecular contacts. The complexes are stabilized by intermolecular N–H···O and C–H···O hydrogen bonds between the hydrogen atoms situated inside the cavity of the macrocycle and the oxygen atoms of the dimethylformamide molecules. *© 2001 MAIK “Nauka/Interperiodica”.*

INTRODUCTION

Nowadays, the chemistry of macroheterocyclic compounds that are structural analogues of phthalocyanine is a rapidly progressing section of organic chemistry. These compounds attract interest due to a number of important and useful properties, such as thermostabilizing and photostabilizing activities [1] as well as catalytic [2], liquid-crystal [3], nonlinear-optical [4], and semiconductor [5] properties, etc.

One of the most interesting representatives of this class of compounds is dibenzenehemiporphyrazine (**I**). It was used as a base for the synthesis of a series of compounds which are of practical importance [1–5]. Spectral studies revealed that compound **I** in solutions can form rather stable complexes with solvents, specifically with demethylformamide (DMF) [6]. However, the structure of these complexes remain unknown. In this work, we performed X-ray structure investigation of the 1 : 1 and 1 : 2 complexes of dibenzenehemiporphyrazine with DMF (compounds **II** and **III**, respectively).

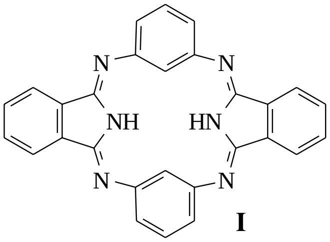

I

EXPERIMENTAL

Compounds **II** and **III** were synthesized according to the procedure described in [6] and purified by a threefold recrystallization from *n*-butanol. Single crystals suitable for X-ray diffraction analysis were obtained by a recrystallization from a DMF–water mixture.

Crystals **II** ($C_{28}H_{18}N_6 \cdot C_3H_7NO$) are monoclinic. At 20°C, $a = 9.900(2)$ Å, $b = 15.852(4)$ Å, $c = 16.418(3)$ Å, $\beta = 92.52(2)°$, $V = 2574(1)$ Å^3, $d_{calcd} = 1.320$ g/cm^3, space group $P2_1/n$, and $Z = 4$. The unit cell parameters and the intensities of 4193 unique reflections ($R_{int} = 0.1$) were measured on a Siemens P3/PC diffractometer (λMoK_α, graphite monochromator, $\theta/2\theta$ scan mode, and $2\theta_{max} = 50°$).

The structure was solved by the direct method using the SHELX97 program package [7]. The positions of the hydrogen atoms were calculated geometrically and refined within the riding-atom model with the fixed values $U_{iso} = nU_{eq}$ of the non-hydrogen atom to which the given hydrogen atom was bonded ($n = 1.5$ for the methyl groups and 1.2 for the remaining hydrogen atoms). The refinement of the non-hydrogen atoms in the anisotropic approximation using the full-matrix least-squares procedure on F^2 led to $wR2 = 0.105$ for 4203 reflections ($R1 = 0.054$ for 1961 reflections with $F > 4\sigma(F)$, $S = 0.908$). The extinction coefficient was

Table 1. Coordinates (×10^4) and equivalent isotropic thermal parameters (×10^3) of non-hydrogen atoms in structure **II**

Atom	*x*	*y*	*z*	U_{eq}, Å^2
N(1)	3230(2)	547(2)	8663(1)	40(1)
N(2)	5151(2)	–282(2)	8257(2)	41(1)
N(3)	3455(3)	645(2)	5539(2)	46(1)
N(4)	1810(2)	1328(2)	6363(2)	43(1)
N(5)	–278(2)	1992(2)	6726(2)	43(1)
N(6)	1318(2)	974(2)	9431(2)	43(1)
C(1)	2092(3)	–628(2)	10415(2)	43(1)
C(2)	2654(3)	–1359(2)	10735(2)	48(1)
C(3)	3803(3)	–1709(2)	10406(2)	50(1)
C(4)	4417(3)	–1339(2)	9761(2)	43(1)
C(5)	3839(3)	–606(2)	9438(2)	38(1)
C(6)	2714(3)	–245(2)	9775(2)	37(1)
C(7)	2324(3)	502(2)	9287(2)	37(1)
C(8)	4186(3)	–106(2)	8726(2)	37(1)
C(9)	5300(3)	153(2)	7515(2)	36(1)
C(10)	4254(3)	224(2)	6923(2)	38(1)
C(11)	4468(3)	601(2)	6179(2)	40(1)
C(12)	5754(3)	892(2)	6019(2)	46(1)
C(13)	6786(3)	837(2)	6609(2)	49(1)
C(14)	6573(3)	457(2)	7342(2)	44(1)
C(15)	2292(3)	958(2)	5668(2)	40(1)
C(16)	1167(3)	1000(2)	5051(2)	41(1)
C(17)	90(3)	1407(2)	5394(2)	40(1)
C(18)	485(3)	1619(2)	6243(2)	38(1)
C(19)	–1105(3)	1550(2)	4936(2)	49(1)
C(20)	–1178(4)	1281(2)	4139(2)	57(1)
C(21)	–108(4)	873(2)	3804(2)	61(1)
C(22)	1102(3)	734(2)	4254(2)	53(1)
C(23)	110(3)	2134(2)	7562(2)	38(1)
C(24)	–154(3)	2918(2)	7900(2)	49(1)
C(25)	101(3)	3051(2)	8719(2)	56(1)
C(26)	605(3)	2407(2)	9215(2)	47(1)
C(27)	897(3)	1627(2)	8895(2)	39(1)
C(28)	620(3)	1491(2)	8066(2)	42(1)
N(1*s*)	5017(3)	2947(2)	6977(2)	54(1)
O(1*s*)	3652(2)	2053(1)	7639(1)	56(1)
C(1*s*)	4769(4)	2344(2)	7492(2)	49(1)
C(2*s*)	6386(4)	3224(3)	6829(3)	97(2)
C(3*s*)	3906(5)	3359(3)	6529(3)	115(2)

Table 2. Coordinates (×10^4) and equivalent isotropic thermal parameters (×10^3) of non-hydrogen atoms in structure **III**

Atom	*x*	*y*	*z*	U_{eq}, Å^2
N(1)	1825(2)	4487(1)	7992(1)	28(1)
N(2)	2173(2)	4548(1)	9651(1)	30(1)
N(3)	–225(2)	375(1)	8606(1)	30(1)
N(4)	–515(2)	938(1)	7090(1)	27(1)
N(5)	–1652(2)	893(1)	5434(1)	31(1)
N(6)	1285(2)	5044(1)	6473(1)	32(1)
C(1)	1108(3)	7156(2)	7631(2)	38(1)
C(2)	976(3)	7944(2)	8299(2)	42(1)
C(3)	1117(3)	7772(2)	9216(2)	41(1)
C(4)	1418(3)	6812(2)	9497(2)	35(1)
C(5)	1581(2)	6034(2)	8828(1)	29(1)
C(6)	1407(2)	6199(2)	7913(1)	30(1)
C(7)	1508(2)	5191(2)	7360(1)	28(1)
C(8)	1887(2)	4943(2)	8898(1)	27(1)
C(9)	2344(2)	3456(2)	9632(1)	27(1)
C(10)	1034(2)	2464(2)	9065(1)	26(1)
C(11)	1146(2)	1384(2)	9114(1)	27(1)
C(12)	2552(3)	1279(2)	9735(1)	33(1)
C(13)	3856(3)	2260(2)	10281(2)	35(1)
C(14)	3754(3)	3340(2)	10238(1)	32(1)
C(15)	–953(2)	258(2)	7729(1)	26(1)
C(16)	–2531(2)	–687(2)	7189(1)	29(1)
C(17)	–2995(2)	–510(2)	6278(1)	29(1)
C(18)	–1675(2)	524(2)	6196(1)	26(1)
C(19)	–4504(3)	–1222(2)	5630(2)	35(1)
C(20)	–5525(3)	–2122(2)	5928(2)	40(1)
C(21)	–5028(3)	–2309(2)	6833(2)	40(1)
C(22)	–3524(3)	–1597(2)	7485(2)	36(1)
C(23)	–362(2)	1926(2)	5440(1)	28(1)
C(24)	562(3)	1910(2)	4807(1)	33(1)
C(25)	1743(3)	2926(2)	4756(2)	37(1)
C(26)	1992(3)	3959(2)	5305(1)	34(1)
C(27)	1089(2)	3977(2)	5951(1)	28(1)
C(28)	–91(2)	2958(2)	6009(1)	29(1)
O(1*s*)	2896(2)	2602(1)	7468(1)	34(1)
O(2*s*)	2110(2)	6813(2)	1986(2)	76(1)
N(1*s*)	4165(2)	1282(1)	7737(1)	35(1)
N(2*s*)	3194(2)	5594(2)	2686(1)	41(1)
C(1*s*)	3919(2)	2249(2)	7968(1)	30(1)
C(2*s*)	3306(3)	560(2)	6811(2)	57(1)
C(3*s*)	5356(3)	921(2)	8381(2)	53(1)
C(4*s*)	2409(3)	5929(2)	1958(2)	50(1)
C(5*s*)	3535(4)	4534(2)	2588(2)	75(1)
C(6*s*)	3819(4)	6301(3)	3608(2)	72(1)

0.005(1). The coordinates of the non-hydrogen atoms are listed in Table 1.

Crystals **III** ($C_{28}H_{18}N_6 \cdot 2C_3H_7NO$) are triclinic. At –120°C, a = 8.712(4) Å, b = 12.460(4) Å, c = 14.977(6) Å, α = 95.82(3)°, β = 104.60(3)°, γ = 108.10(3)°, V = 1467(1) Å^3, $d_{\rm calcd}$ = 1.324 g/cm^3, space group $P\bar{1}$, and Z = 2. The unit cell parameters and the intensities of 5138 unique reflections ($R_{\rm int}$ = 0.07) were

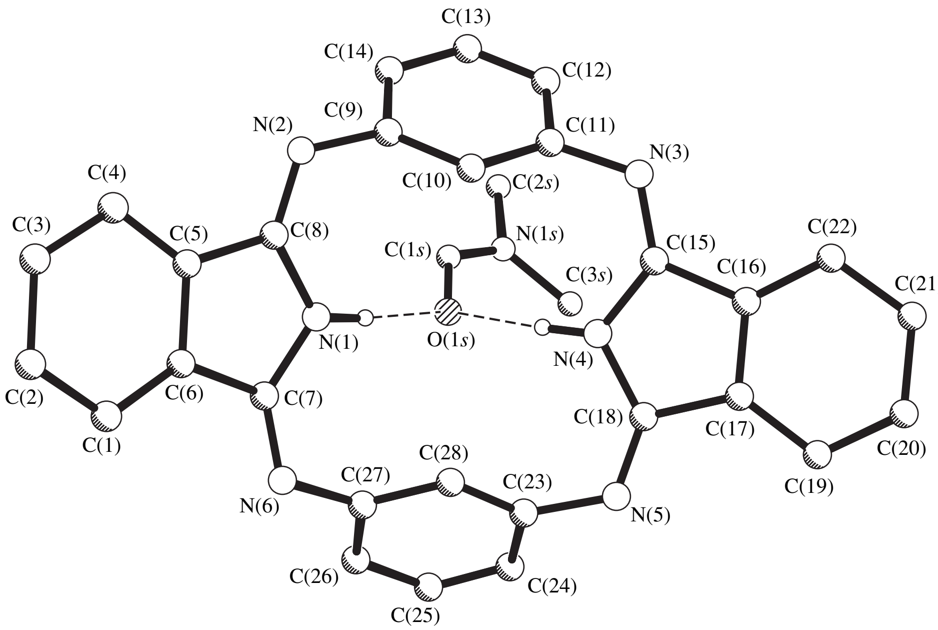

Fig. 1. Structure of complex **II** according to the X-ray diffraction data. (The hydrogen atoms are omitted for clarity.)

measured on a Syntex $P2_1$/PC automated four-circle diffractometer (λMoK_α, graphite monochromator, $\theta/2\theta$ scan mode, and $2\theta_{max} = 50°$).

The structure was solved by the direct method using the SHELXTL PLUS 5.02 program package [8]. The positions of the hydrogen atoms (with the exception of those in the DMF molecules) were found from the difference electron-density synthesis. The positions of the hydrogen atoms of the solvate DMF molecules were calculated geometrically. These atoms were refined as described for **II**. The refinement of the non-hydrogen atoms in the anisotropic approximation and the hydrogen atoms in the isotropic approximation with the use of the full-matrix least-squares procedure on F^2 led to $wR2 = 0.113$ for 5128 reflections [$R1 = 0.043$ for 3312 reflections with $F > 4\sigma(F)$, $S = 0.825$]. The atomic coordinates are listed in Table 2.

The molecular structures of the isolated molecule **I** and complex **II** were calculated within the semiempirical quantum-chemical AM1 approach [9] with complete optimization of the geometry.

RESULTS AND DISCUSSION

The X-ray diffraction analysis of **II** revealed that in the 1 : 1 complex the macrocycle has a saddlelike shape (Fig. 1), which is similar to that in the hydrate studied earlier in [10, 11].

The exocyclic N(2), N(3), N(5), and N(6) nitrogen atoms are coplanar within 0.04 Å. The benzene rings and the isoindole fragments deviate from the mean molecular plane in the opposite directions. However, the angles between the plane defined by the exocyclic nitrogen atoms and the planes of cyclic fragments differ noticeably (Table 3). This conformation of the macrocycle can be determined by the following short intramolecular contacts: H(1N)···C(28), 2.72 Å (the sum of the van der Waals radii is 2.87 Å [12]); H(1N)···C(10), 2.75 Å; H(1N)···C(9), 2.77 Å; H(1N)···C(27), 2.77 Å; H(4N)···C(10), 2.68 Å; H(4N)···C(11), 2.74 Å; H(4N)···C(23), 2.79 Å; and H(4N)···C(28), 2.69 Å.

The macrocycle forms an oval cavity whose size is characterized by the H(10)···H(28) and H(1N)···H(4N) distances (3.33 and 2.64 Å, respectively). The DMF molecule is located over the macrocycle and forms with it the hydrogen bonds N(1)–H(1N)···O(1s) (H···O, (2.14 Å; the N–H···O angle, 160°) and N(4)–H(4N)···O(1s) (2.17 Å; the N–H···O angle, 152°). The same arrangement of the solvate molecule is also observed in the hydrate [10, 11]. However, the DMF molecule is larger than the water molecule; hence, the

Table 3. Dihedral angles (deg) between the plane passing through the N(2), N(3), N(5), and N(6) atoms and the planes of the benzene and isoindole fragments of molecule **I** in structures **I**–**III** according to the X-ray diffraction data and the AM1 calculations

Fragment	**I**	**II**		**III**
	calculated		experimental	
N(1), C(1)···C(8)	21.2	21.3	33.5	34.6
N(4), C(15)···C(22)	21.2	21.3	26.2	33.2
C(9)···C(14)	42.8	40.0	48.7	49.1
C(23)···C(28)	42.8	40.0	49.0	44.5

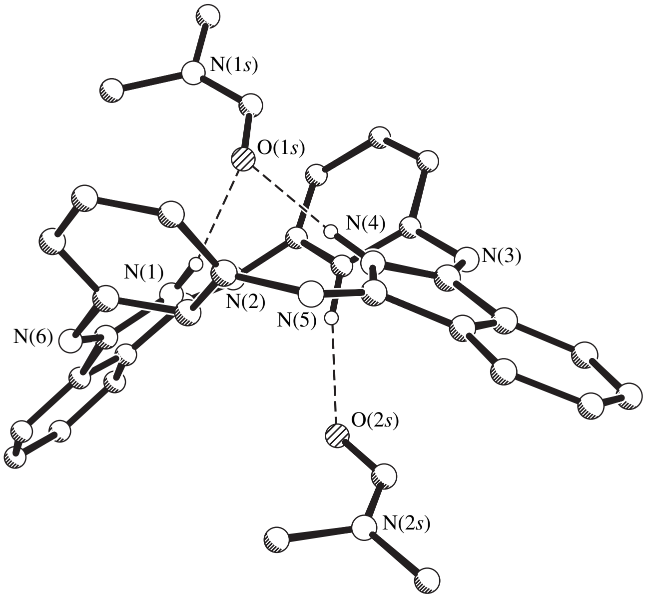

Fig. 2. Structure of complex **III** according to the X-ray diffraction data. (The hydrogen atoms are omitted for clarity.)

repulsion between the methyl groups of DMF and the aromatic rings results in a slight flattening of the macrocycle.

The quantum-chemical calculations of the isolated molecule **I** showed that, in the gaseous phase, the macrocycle has a nonplanar conformation with the C_{2v} symmetry. The formation of a complex with DMF is favorable for energy reasons, because its heat of formation is 6.75 kcal/mol less than the sum of the heats of formation of **I** and DMF. Note that the interaction with DMF results in no fundamental conformational changes in the macrocycle (Table 3). This suggests that the symmetry breaking of the macrocycle conformation in the crystal is caused by intermolecular interactions. For the same reason, apparently, the dibenzenehemiporphyrazine molecule in the crystal hydrate [10, 11] is puckered to a greater extent.

Addition of one more DMF molecule (compound **III**) results in a fundamental conformational change in the macrocycle (Fig. 2 and Table 3). For example, the exocyclic nitrogen atoms in **III** are not coplanar in contrast with those in **II**. The angle between the N(2)···N(6) and N(3)···N(5) segments is 5.8°. The conformation of the macrocycle in **III** becomes on the whole more symmetric. The angles between the mean plane defined by the exocyclic nitrogen atoms and the planes of the cyclic fragments differ by no more than 5° (Table 3). However, the change in the conformation of the macrocycle is not accompanied by the decrease in the steric strain of the molecule, which is evidenced by the following short intramolecular contacts: H(1N)···C(28), 2.80 Å (the sum of the van der Waals radii is 2.87 Å [12]); H(1N)···C(10), 2.78 Å; H(1N)···C(9), 2.75 Å; H(1N)···C(27), 2.78 Å; H(4N)···C(10), 2.59 Å; H(4N)···C(11), 2.80 Å; H(4N)···C(23), 2.70 Å; and H(4N)···C(28), 2.72 Å.

In crystal **III**, one DMF molecule occupies the position similar to that in **II** and forms the hydrogen bonds N(1)–H(1N)···O(1*s*) (H···O, 1.98 Å; the N–H···O angle, 172°) and N(4)–H(4N)···O(1*s*) (2.12 Å; the N–H···O angle, 166°). The changes in the hydrogen-bond parameters in complex **III** in comparison to **II** are probably due to a slight increase in the size of the cavity of the macrocycle: the H(10)···H(28) and H(1N)···H(4N) distances are 3.30 and 2.79 Å, respectively. This favors a more effective interaction between dibenzenehemiporphyrazine and DMF. The second solvent molecule is situated on the opposite side of the macrocycle and is linked with it by a weak C(10)–H(10)···O(2*s*) hydrogen bond (H···O, 2.24 Å; the C–H···O angle, 158°).

REFERENCES

1. R. P. Smirnov, V. M. Kharitonov, and L. N. Smirnov, Tr. Ivanov. Khim.-Tekhnol. Inst. **14**, 111 (1972).
2. V. E. Maĭzlish, M. K. Islyaĭkin, and V. F. Borodkin, Izv. Vyssh. Uchebn. Zaved., Khim. Khim. Tekhnol. **22**, 1441 (1979).
3. M. A. Díaz-García, I. Ledoux, F. Fernández-Lazaro, *et al.*, Nonlinear Opt. **10**, 101 (1995).
4. F. Fernández-Lazaro, T. Torres, B. Hauschel, *et al.*, Chem. Rev. **98**, 563 (1998).
5. F. Fernández-Lazaro, S. Rodríguez-Morgade, and T. Torres, Synth. Met. **62**, 281 (1994).
6. V. F. Borodkin, V. A. Burmistrov, and M. K. Islyaĭkin, Khim. Geterotsikl. Soedin., No. 1, 62 (1981).
7. G. M. Sheldrick, *SHELX97, PC Version: A System of Computer Programs for the Determination of Crystal Structure from X-ray Diffraction Data* (Univ. of Göttingen, Göttingen, 1997).
8. G. M. Sheldrick, *SHELXTL PLUS, PC Version: A System of Computer Programs for the Determination of Crystal Structure from X-ray Diffraction Data* (Siemens Analytical X-ray Instruments Inc., Germany, 1994).
9. M. J. S. Dewar, E. G. Zoebisch, E. F. Healy, *et al.*, J. Am. Chem. Soc. **107**, 3902 (1985).
10. S. M. Peng, Y. Wang, T. F. Ho, *et al.*, J. Chin. Chem. Soc. (Taipei) **33**, 13 (1986).
11. S. M. Peng, H. D. Louh, and G. H. Lee, Bull. Inst. Chem. Acad. Sin. **33**, 35 (1986).
12. Yu. V. Zefirov and P. M. Zorkiĭ, Usp. Khim. **64**, 446 (1995).

Translated by I. Polyakova

Crystallography Reports, Vol. 46, No. 3, 2001, pp. 415–418. From Kristallografiya, Vol. 46, No. 3, 2001, pp. 465–468.
Original English Text Copyright © 2001 by Rajnikant, V. Gupta, Firoz, Shafiullah, R. Gupta.

STRUCTURE OF ORGANIC COMPOUNDS

Structure Analysis of 3β-Chloro-6-Nitrocholest-5-ene[1]

Rajnikant*[2], V. K. Gupta*, J. Firoz, Shafiullah**, and R. Gupta***

** X-ray Crystallography Laboratory, Post-Graduate Department of Physics,*
University of Jammu, Jammu Tawi, 180 006 India
*** Steroid Research Laboratory, Department of Chemistry,*
Aligarh Muslim University, Aligarh, 202 002 India
e-mail: rajni_kant_verma@hotmail.com

Received March 15, 2000; in final form, August 8, 2000

Abstract—The crystal structure of the title compound ($C_{27}H_{44}NO_2Cl$) is determined by X-ray structure analysis. The compound crystallizes in the orthorhombic space group $P2_12_12_1$ with the unit cell parameters a = 7.207(1) Å, b = 11.292(1) Å, and c = 32.373(5) Å. The structure is solved by direct methods and refined to R = 0.060. Rings *A* and *C* exist in the chair conformation. Ring *B* adopts a half-chair conformation, and ring *D* is a 13β envelope. The *A*/*B* ring junction is quasi-*trans*, while the *B*/*C* and *C*/*D* ring systems are *trans* fused about the C(8)–C(9) and C(13)–C(14) bonds, respectively. Molecules are linked together by the C–H···O hydrogen bonds. © *2001 MAIK "Nauka/Interperiodica".*

INTRODUCTION

The X-ray structure analysis of the title compound is a continuation of our crystallographic investigations on steroids [1–6].

EXPERIMENTAL

Synthesis. The compound to be studied was prepared as follows. Sodium nitrite $NaNO_2$ (3.0 g) was gradually (over a period of 3 h) added to a well-stirred mixture of 3β-chloro-cholest-5-ene (12 g), glacial acetic acid (80 ml), and nitric acid (25 ml, $d = 1.52$ g/cm^3) at a temperature below 20°C. After the addition of sodium nitrite, the mixture was further stirred about 1 h. Then, ice cold water (200 ml) was added and the yellowish precipitate thus obtained was filtered off and dried in air. Recrystallization from methanol gave 3β-chloro-6-nitrocholest-5-ene (8.5 g) as needles (mp = 424–425 K). The chemical structure (Fig. 1) was determined on the basis of IR, UV, NMR, and mass spectral data [7].

X-ray diffraction analysis. Three-dimensional intensity data for the steroidal molecule were collected on an Enraf–Nonius CAD4 diffractometer (CuK_α radiation, $\omega/2\theta$ scan mode). Two strong reflections monitored every 100 reflections showed no significant change in the intensity, thus confirming the stability of the crystal toward X-rays. A total of 2247 reflections were measured, of which 1789 ($0 < h < 7$, $0 < k < 13$, $0 < l < 37$) reflections were treated as observed. The data were corrected for Lorentz and polarization effects. No absorption and extinction corrections were applied.

The structure has been solved by direct methods using SHELXS86 software package [8]. The isotropic refinement of the structure was carried out by the least-squares method using SHELXL93 software package [9] followed by the anisotropic refinement of all the non-hydrogen atoms. Among the 44 hydrogen atoms, 29 atoms were located from the difference Fourier map, and their positions and isotropic thermal parameters were refined. The coordinates of the remaining 15 hydrogen atoms were determined geometrically. The final R-factor converged to R = 0.060. Atomic scattering factors were taken from the *International Tables for X-ray Crystallography* (1992, vol. C, Tables 4.2.6.8 and 6.1.1.14). All the calculations were performed on a Pentium computer. The crystallographic data are summarized in Table 1.

RESULTS AND DISCUSSION

The fractional coordinates and equivalent isotropic thermal parameters for non-hydrogen atoms are given in Table 2. Endocyclic torsion angles are listed in Table 3. A general view of the molecule with atomic numbering scheme is shown in Fig. 2 [10].

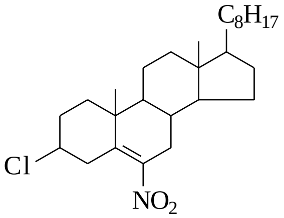

Fig. 1. Chemical structure of 3β-chloro-6-nitrocholest-5-ene.

---

[1] This article was submitted by the authors in English.
[2] Author for correspondence.

Table 1. Crystal data and other experimental details

Crystal habit	Yellowish needles
Chemical formula	$C_{27}H_{44}NO_2Cl$
Molecular weight	450.1
Unit cell parameters, Å	$a = 7.207(1)$ $b = 11.292(1)$ $c = 32.373(5)$
Unit cell volume, Å^3	2634.56
Crystal system	Orthorhombic
Space group	$P2_12_12_1$
Density (calcd.), Mg m^{-3}	1.135
No. of molecules per unit cell (Z)	4
Radiation	CuK_α
Wavelength (λ), Å	1.5418
Absorption coefficient (μ), mm^{-1}	1.44
$F(000)$	984
Crystal size, mm	0.30 × 0.20 × 0.15
Refinement of unit cell:	25 reflections, $8.4° < \theta < 17.3°$
θ range for entire data collection	$2° < \theta < 63°$
No. of measured reflections	2247
No. of unique reflections	2231
No. of observed reflections	1789 $[F_o > 4\sigma(F_o)]$
No. of parameters refined	397
Final R-factor	0.060
wR	0.181
Weighting scheme	$1/[\sigma^2(F_o^2) + (0.1630P)^2 + 2.86P]$, where $P = [F_o^2 + 2F_c^2]/3$
Final residual electron density	$-0.21 < \Delta\rho < 0.23$ eÅ^{-3}
$(\Delta/\sigma)_{max}$ in the final cycle	0.365 (for x H(25))
Flack X parameter	0.04(6)

Table 2. Atomic coordinates and equivalent isotropic thermal parameters (Å^2)

Atom	x	y	z	U_{eq}^*	Atom	x	y	z	U_{eq}^*
Cl(1)	0.7411(4)	0.4673(2)	0.0737(1)	0.138(1)	C(13)	1.5149(9)	0.4366(5)	−0.1230(2)	0.077(2)
C(1)	1.1679(9)	0.4149(4)	−0.0076(2)	0.077(2)	C(14)	1.4294(7)	0.4965(4)	−0.1608(2)	0.064(1)
C(2)	1.0243(11)	0.3895(5)	0.0266(2)	0.092(2)	C(15)	1.3039(9)	0.4094(5)	−0.1836(2)	0.077(2)
C(3)	0.9104(11)	0.4969(5)	0.0341(2)	0.092(2)	C(16)	1.3195(8)	0.6038(4)	−0.1437(2)	0.071(1)
C(4)	0.8104(11)	0.5360(6)	−0.0055(2)	0.092(2)	C(17)	1.2736(11)	0.6769(6)	−0.1821(2)	0.087(2)
C(5)	0.9440(8)	0.5566(4)	−0.0399(2)	0.072(2)	C(18)	1.4342(10)	0.6560(6)	−0.2116(2)	0.083(2)
C(6)	0.9484(9)	0.6535(4)	−0.0615(2)	0.081(2)	C(19)	1.5597(8)	0.5590(4)	−0.1911(2)	0.070(2)
N(1)	0.8249(10)	0.7502(4)	−0.0513(2)	0.103(2)	C(20)	1.6641(8)	0.4844(5)	−0.2237(2)	0.075(2)
O(1)	0.8620(11)	0.8160(5)	−0.0245(3)	0.158(4)	C(21)	1.7702(10)	0.3819(5)	−0.2051(2)	0.099(2)
O(2)	0.6891(13)	0.7646(7)	−0.0703(2)	0.157(4)	C(22)	1.7884(9)	0.5622(5)	−0.2506(2)	0.094(2)
C(7)	1.0716(12)	0.6836(5)	−0.0979(2)	0.087(2)	C(23)	1.8805(12)	0.5005(6)	−0.2867(3)	0.113(3)
C(8)	1.1634(8)	0.5720(4)	−0.1142(2)	0.064(2)	C(24)	2.0217(11)	0.5697(5)	−0.3093(2)	0.100(2)
C(9)	1.2395(8)	0.4994(4)	−0.0777(2)	0.066(2)	C(25)	2.1263(11)	0.5005(6)	−0.3415(2)	0.097(2)
C(10)	1.0837(7)	0.4559(3)	−0.0488(2)	0.066(2)	C(26)	2.2452(12)	0.4065(7)	−0.3239(2)	0.131(3)
C(11)	0.9728(12)	0.3531(5)	−0.0685(3)	0.085(3)	C(27)	2.2407(19)	0.5831(8)	−0.3670(3)	0.163(4)
C(12)	1.3726(9)	0.3999(5)	−0.0912(2)	0.078(2)					

* $U_{eq} = (1/3)\sum_i\sum_j U_{ij} a_i^* a_j^* \mathbf{a}_i \cdot \mathbf{a}_j$.

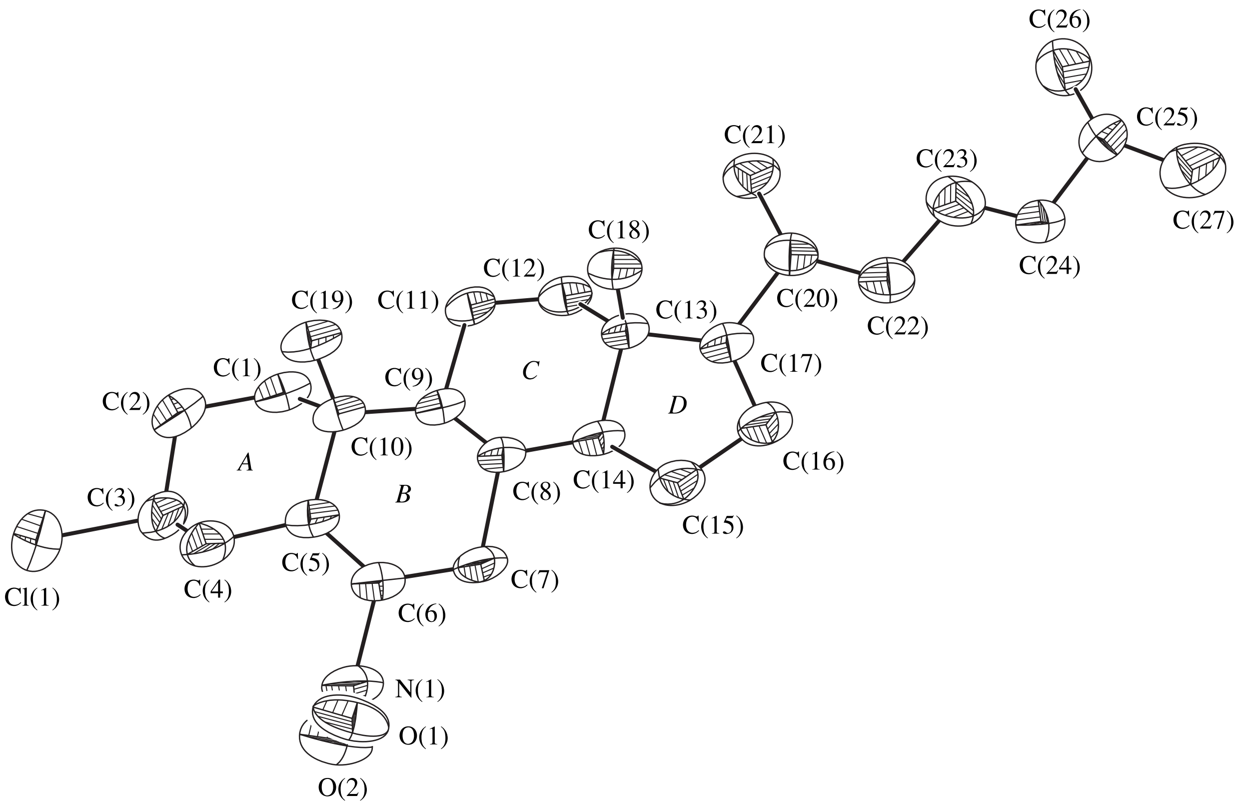

Fig. 2. A general view of the molecule and atomic numbering scheme with thermal ellipsoids at a 50% probability.

The observed bond lengths and angles are in good agreement with the corresponding values obtained in the case of 5-ene steroidal molecules [11]. The mean value of the C(sp^3)–C(sp^3) bonds [1.524(9) Å] agrees with the value given in [12], even though the bond lengths C(2)–C(3) [1.484(9) Å], C(16)–C(17) [1.568(9) Å], C(23)–C(24) [1.477(10) Å], C(25)–C(26) [1.478(11) Å], and C(25)–C(27) [1.494(13) Å] show some significant deviations. The bond angles C(12)–C(13)–C(17) [118.0(5)°], C(14)–C(13)–C(17) [100.5(4)°], C(8)–C(14)–C(15) [118.6(5)°], and C(13)–C(17)–C(20) [119.0(5)°] exhibit significant deviations from the ideal tetrahedral value (109.4°). These deviations are common to steroids as a result of the strain induced by ring junctions, side chains, and bond unsaturations. The bond length C(5)–C(6) is equal to 1.299(7) Å, which indicates a double-bond character.

Ring *A* has a chair conformation with the asymmetry parameters ΔC_s[C(3)–C(10)] = 4.14 and ΔC_2[C(2)–

Table 3. Endocyclic torsion angles (deg) (e.s.d.'s are given in parentheses)

C(2)–C(1)–C(10)–C(5)	49.1(6)	C(14)–C(8)–C(9)–C(11)	−45.7(6)
C(10)–C(1)–C(2)–C(3)	−57.4(7)	C(8)–C(9)–C(10)–C(5)	−44.9(6)
C(1)–C(2)–C(3)–C(4)	58.6(7)	C(8)–C(9)–C(11)–C(12)	45.1(7)
C(2)–C(3)–C(4)–C(5)	−56.3(7)	C(9)–C(11)–C(12)–C(13)	−52.4(7)
C(3)–C(4)–C(5)–C(10)	51.0(7)	C(11)–C(12)–C(13)–C(14)	57.2(6)
C(4)–C(5)–C(10)–C(1)	−46.8(6)	C(12)–C(13)–C(14)–C(8)	−61.3(6)
C(6)–C(5)–C(10)–C(9)	12.1(7)	C(14)–C(13)–C(17)–C(16)	−39.8(5)
C(10)–C(5)–C(6)–C(7)	3.3(9)	C(17)–C(13)–C(14)–C(15)	44.4(5)
C(5)–C(6)–C(7)–C(8)	14.4(9)	C(13)–C(14)–C(15)–C(16)	−31.4(6)
C(6)–C(7)–C(8)–C(9)	−45.7(7)	C(14)–C(15)–C(16)–C(17)	6.2(7)
C(7)–C(8)–C(9)–C(10)	63.6(6)	C(15)–C(16)–C(17)–C(13)	21.5(6)
C(9)–C(8)–C(14)–C(13)	56.7(6)		

C(3)] = 1.55 [13]. Ring *B* adopts a half-chair conformation with the asymmetry parameter ΔC_2[C(5)–C(6)] = 1.7. Ring *C* has a chair conformation with its best rotational axis bisecting the C(9)–C(11) and C(13)–C(14) bonds and the asymmetry parameter ΔC_2[C(9)–C(11)] = 4.75. The best mirror plane passes through the C(9) and C(13) atoms, with ΔC_s[C(9)–C(13)] = 3.44. Ring *D* is a distorted envelope with the phase pseudorotation angle $\Delta = 19.67°$ and the maximum torsion angle $\varphi = 45.06°$ [14]. The asymmetry parameter ΔC_s[C(13)] which gives a distortion from the ideal mirror symmetry bisecting the C(15)–C(16) bond, is equal to 7.72. The C(13) atom is disposed 0.665(5) Å above the plane defined by the other four ring atoms.

One bifurcated intramolecular hydrogen bond is observed for C(4)–H(42)···N(1) [2.839(8)Å] and C(4)–H(42)···O(1) [3.242(9) Å]. There are two intermolecular hydrogen bonds [(i) C(1)–H(11)···O(1*a*), H(11)···O(1), 2.63(4) Å; C(1)···O(1), 3.503(8) Å; CHO, 151(4)°; (ii) C(3)–H(3)···O(2*a*), H(3)···O(2), 2.65(6) Å; C(3)···O(2), 3.558(11) Å; CHO, 175(5)°; symmetry code: (*a*) 1/2 + *x*, 1/2 – *y*, –*z*] which contribute to the stabilization of the crystal structure.

ACKNOWLEDGMENTS

Rajnikant acknowledges the financial support received from the University Grants Commission, Government of India, under the DSA Research Program, project no. F/530/1/DSA/95(SAP-I).

REFERENCES

1. V. K. Gupta, Rajnikant, K. N. Goswami, and K. K. Bhutani, Cryst. Res. Technol. **29**, 77 (1994).
2. V. K. Gupta, K. N. Goswami, K. K. Bhutani, and R. M. Vaid, Mol. Mater. **4**, 303 (1994).
3. V. K. Gupta, Rajnikant, K. N. Goswami, *et al.*, Acta Crystallogr., Sect. C: Cryst. Struct. Commun. **C50**, 798 (1994).
4. A. Singh, V. K. Gupta, Rajnikant, and K. N. Goswami, Cryst. Res. Technol. **29**, 837 (1994).
5. A. Singh, V. K. Gupta, Rajnikant, *et al.*, Mol. Mater. **4**, 295 (1994).
6. A. Singh, V. K. Gupta, K. N. Goswami, *et al.*, Mol. Mater. **6**, 53 (1996).
7. J. Firoz, PhD Thesis (Aligarh Muslim Univ., Aligarh, 1998).
8. G. M. Sheldrick, *SHELXS86: Program for the Solution of Crystal Structures* (Univ. of Göttingen, Göttingen, 1986).
9. G. M. Sheldrick, *SHELXL93: Program for the Refinement of Crystal Structures* (Univ. of Göttingen, Göttingen, 1993).
10. C. K. Johnson, *ORTEP-II: A Fortran Thermal Ellipsoid Plot Program for Crystal Structure Illustrations, Report ORNL-5138* (Oak Ridge National Laboratory, Tennessee, 1976).
11. J. F. Griffin, W. L. Duax, and G. M. Weeks, *Atlas of Steroid Structures* (Plenum, New York, 1984), Vol. 2, p. 21.
12. *Tables of Interatomic Distances and Configurations in Molecules and Ions*, Ed. by L. E. Sutton (The Chemical Society, London, 1965), Chem. Soc. Spec. Publ. No. 18.
13. W. L. Duax, C. M. Weeks, and D. C. Rohrer, *Topics in Stereochemistry,* Ed. by E. L. Eliel and N. Allinger (Wiley, New York, 1976), Vol. 9, p. 271.
14. C. Altona, H. J. Geise, and C. Romers, Tetrahedron **24**, 13 (1998).

Crystallography Reports, Vol. 46, No. 3, 2001, pp. 419–424. Translated from Kristallografiya, Vol. 46, No. 3, 2001, pp. 469–474.

STRUCTURE OF ORGANIC COMPOUNDS

Crystal Structures of *N*-Phenyl-2-(1,4,7,10-Tetraoxa-13-Azacyclopentadecane-13-Carbonyl)benzamide and *N*-(4-Ethoxyphenyl)-2-(1,4,7,10-Tetraoxa-13-Azacyclopentadecane-13-Carbonyl)benzamide

S. T. Malinovskiĭ*, Yu. A. Simonov, and É. V. Ganin*****

** Institute of Chemistry, Academy of Sciences of Moldova, Academiei 3, Chisinau, 20-28 Moldova*

*** Institute of Applied Physics, Academy of Sciences of Moldova, Academiei 5, Chisinau, 20-28 Moldova*

**** Physicochemical Institute for Human and Environmental Protection, Odessa State University, Education Department, National Academy of Sciences of Ukraine, Odessa, Ukraine*

e-mail: simonov.xray@phys.asm.md

Received December 30, 1999; in final form, September 4, 2000

Abstract—The crystal structures of two monoaza-15-crown-5 macrocycles substituted at the nitrogen atom are determined by X-ray diffraction. The structures of these crystals are characterized by the intramolecular and intermolecular N–H···O and C–H···O interactions. The conformation of the 15-membered rings and the specific features of the molecular packing in the crystals are discussed. © *2001 MAIK "Nauka/Interperiodica"*.

INTRODUCTION

A specific feature of crown ethers is their selective ability to form the complexes with metal cations and neutral proton-donating molecules [1–3]. The ring substituents that contain donor groups impart new properties to the ring systems. For crown ethers containing substituents in the side chain, Gokel proposed the term lariate crown ethers [4–6]. Additional donor groups in the substituent can enhance the complexing ability of the new ligand as compared to that of the unsubstituted ligand. This aroused interest in the modification of simple macroheterocycles, specifically in the design of molecules whose physiologically active part (radical) acts as a structural element, that is, a substituent in the macrocycle. These substituents affect the lipophilic [7] and complexing properties [8, 9] of the molecule and enhance its biological activity [10, 11], which is of interest in the modeling of receptors for purposes of bioorganic chemistry and high-selective complexones [9]. The physiological activity of compounds is based on the ability of the macrocycles to increase the membrane permeability, which allows effective delivery of pharmacotropic fragments to the cell.

Earlier [12–16], we studied the lariate crown ethers with sulfamide substituents in the macrocyclic ligand.

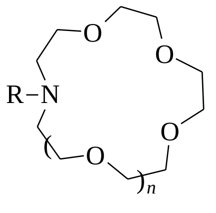

$R = –SO_2PhNH_2$, $n = 1$ [12], $n = 2$ [14],

$R = –CH_2–C(=O)PhSO_2NH_2$, $n = 1$ [15].

As was noted earlier [5], the donor groups in the substituent substantially improve the complexing properties of new ligands. Free lariate macrocycles form crystals with weak intramolecular and intermolecular X–H···O interactions (X = N, O, or C). These interactions result in the formation of molecular (D_0), linear (D_1), layered (D_2), or framework (D_3) structures. The type of the structure is determined by the nature of interactions between the donor groups of the substituent and the acceptor groups of the macrocycle, which can be described in terms of the host–guest complexes [3]. The solvate molecules, in particular, water molecules, can play an important part in crystal structure formation [17].

In the structure of 1,4,7,10,13-pentaoxa-16-(sulfanil)azacyclooctadecane [14], the N–H···O interaction between the radical and the crown ether brings about the formation of the binuclear structure. A similar interaction in *trans*-diaminodibenzo-18-crown-6 with two donor groups in a molecule results in the formation of a layered structure (D_2) [18]. In 4-sulfanilamidobenzo-15-crown-5 [19], the N–H···O interactions also take place, resulting in a linear polymeric structure (D_1). In 1,4,7,10-tetraoxa-13-(4-acetylaminobenzosulfamido) azacyclopentadecane [15], the ether oxygen atoms are not involved in the ring–radical interactions. In this crystal, the chainlike (D_1) structure is formed through the N–H···O interaction between the radicals. The C–H···O contacts that stabilize the mutual arrangement of the ring and the substituent were found, for example, in *N*,*N*'-bis(2-tosylaminoethyl)diaza-18-crown-6 [13].

To continue our studies of the interactions between the ring and the substituent in crystals, we performed the X-ray structure analysis of *N*-phenyl-2-(1,4,7,10-tetraoxa-13-azacyclopentadecane-13-carbonyl)benzamide (**I**) and *N*-(4-ethoxyphenyl)-2-(1,4,7,10-tetraoxa-13-azacyclopentadecane-13-carbonyl)benzamide (**II**)

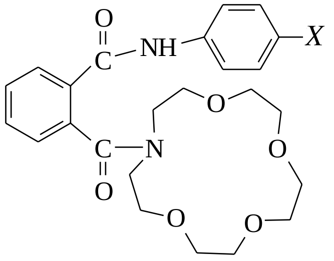

X = H (**I**) or
X = OC_2H_5 (**II**)

Compounds **I** and **II** have different substituents in the 4-position of the terminal aromatic ring: the H atom in **I** is replaced by the ethoxy group in **II**. The purpose of this study was to reveal the specific features of interactions between the macrocyclic part of the molecules and the substituents and to elucudate how the substituents affect the conformational and configurational characteristics of the molecule as a whole.

EXPERIMENTAL

Compounds **I** and **II** were prepared according to the procedure proposed in [20]. A 10% solution of monoaza-15-crown-5 (11 mmol) was added to a 5% solution of phenylisophthalimide or 4-ethoxyphenylisophthalimide (10 mmol), either of which were obtained in benzene at 20°C according to the procedure described in [21]. The mixture was allowed to stand at 20°C for three days. Compounds **I** (mp is 149–150°C) and **II** (mp is 138–139°C) were isolated using column silica gel chromatography (with a 1 : 1 mixture of acetone and hexane as an eluent); the yields were 74% and 40%, respectively. Colorless transparent crystals **I** were obtained by recrystallization from an acetone : hexane (1 : 1) mixture. They were soluble in acetone, methanol, ethanol, and dioxane. IR spectrum (IKS-29, KBr), cm^{-1}: 3315 (N–H), 1650 (C=O), and 1145 (C–O–C). Colorless transparent crystals **II** were recrystallized from an acetone : hexane (1 : 1) mixture and were soluble in methanol, ethanol, acetone, and dioxane. IR spectrum, cm^{-1}: 3310 (N–H), 1650 (C=O), and 1140 (C–O–C).

Chemical analysis data:

For (**I**) $C_{24}H_{30}N_2O_6$ anal. calcd. (%): N, 6.37.

Found (%): N, 6.45.

For (**II**) $C_{26}H_{34}N_2O_7$ anal. calcd. (%): N, 5.76.

Found (%): N, 5.88.

Single crystals **II** suitable for X-ray diffraction analysis were obtained by recrystallization from acetone.

For X-ray structure analysis, we chose prismatic single crystals 0.1 × 0.2 × 0.2 and 0.3 × 0.4 × 0.5 mm in size for **I** and **II**, respectively. Crystals **I** and **II** are triclinic, space group $P\bar{1}$. For **I**, the unit cell parameters are $a = 12.864(3)$ Å, $b = 11.119(2)$ Å, $c = 8.356(5)$ Å, $\alpha = 83.0(2)°$, $\beta = 92.4(3)°$, $\gamma = 80.2(3)°$, $V = 1166.4$ Å^3, $d_{\text{calcd}} = 1.26$ g/cm^3, $Z = 2$, and $\mu = 0.58$ mm^{-1}. For **II**, the unit cell parameters are $a = 14.669(4)$ Å, $b = 11.094(3)$ Å, $c = 8.238(4)$ Å, $\alpha = 97.9(2)°$, $\beta = 103.0(3)°$, $\gamma = 91.2(2)°$, $V = 1292.0$ Å^3, $d_{\text{calcd}} = 1.25$ g/cm^3, $Z = 2$, and $\mu = 0.52$ mm^{-1}. The diffraction data were collected on an RED-4 diffractometer (MoK_α radiation) by ω scans with a constant speed of 8 deg/min. The number of unique reflections with $I \geq 3\sigma(I)$ used for the solution and the refinement of structures **I** and **II** was 1664 and 1321, respectively. The structures were solved by the direct method using the XTL-CM program package [22]. The C, O, and N atoms were refined in the anisotropic approximation. The positions of the H atoms in the CH, CH_2, and CH_3 groups were calculated geometrically. These atoms were assigned the isotropic thermal parameters equal to $1.2U_{\text{iso}}$ of the atoms to which they were attached. The H atoms in the NH groups were located from difference Fourier syntheses. Neither the coordinates nor the thermal parameters of the H atoms were refined. The final R factors were 0.054 and 0.085 for **I** and **II**, respectively. The atomic coordinates are listed in Table 1.

RESULTS AND DISCUSSION

The molecular structures of **I** and **II** are shown in Figs. 1a and 1b, respectively. By convention, each molecule can be divided into three fragments, namely, monoaza-15-crown-5, phthalimide fragment, and a substituent in this fragment (namely, the phenyl group in **I** and the 4-ethoxyphenyl group in **II**).

The conformations of two 15-membered aza-macrocycles are similar. They are described by the following sequences of torsion angles (starting from the O(1)–C(1) bond in the increasing order of atomic numbers): (**I**) 170.4°, 55.6°, –107.0°, 101.6°, 179.4°, –172.7°, –84.1°, 79.9°, 179.1°, 173.0°, –65.9°, 142.6°, –176.5°, 67.3°, and 159.9°; (**II**) –177.1°, –52.2°, 109.0°, –108.4°, –178.5°, 174.5°, 86.7°, –82.0°, –178.9°, –174.3°, 66.9°, –139.1°, 179.3°, –67.0°, and –162.8°.

Analysis of these sequences revealed that the two 15-membered macrocycles have similar conformations, which are characterized by four *gauche* and one *anti* rotamers about the C–C bonds and seven *anti* and one *gauche* rotamers about the C–O bonds. The torsion angles about the C–N bonds have intermediate values close to 100° in magnitude. The above torsion angle sequences result in the formation of the corner fragments [23] at the C(8) atoms. Significant differences between the torsion angles about the C–N bonds and the standard values, together with the corner fragment

Atomic coordinates (Å × 10^4) with estimated standard deviations and equivalent thermal parameters (Å^2 × 10^3) in structures **I** and **II**

Atom	**I**				**II**			
	x/a	y/b	z/c	U_{eq}	x/a	y/b	z/c	U_{eq}
O(1)	2227(6)	9845(7)	–0495(8)	83	2494(7)	5451(9)	–1307(11)	63
C(2)	1617(10)	10951(10)	–0877(14)	78	1892(11)	4433(14)	–1894(19)	70
C(3)	1424(7)	11675(9)	0563(13)	62	1765(9)	3780(12)	–0373(17)	57
N(4)	2392(6)	11834(6)	1463(9)	49	2683(7)	3525(9)	0737(12)	48
C(5)	2702(7)	11090(8)	3036(11)	53	2955(10)	4277(11)	2451(15)	52
C(6)	3569(7)	9998(8)	2946(10)	48	3770(10)	5180(12)	2486(14)	50
O(7)	3762(5)	9379(5)	4588(7)	56	3971(7)	5812(8)	4213(10)	61
C(8)	4637(7)	8410(8)	4812(11)	53	4797(9)	6672(12)	4672(16)	53
C(9)	4412(8)	7211(9)	4422(12)	62	4501(11)	7912(13)	4184(16)	68
O(10)	4390(5)	7241(5)	2685(8)	63	4475(6)	7845(8)	2431(11)	65
C(11)	4162(8)	6142(8)	2152(15)	77	4218(11)	8988(13)	1828(19)	74
C(12)	4032(8)	6357(10)	0383(17)	83	4120(11)	8736(15)	–0091(21)	80
O(13)	3100(5)	7319(6)	–0127(8)	67	3305(7)	7869(9)	–0794(11)	69
C(14)	3241(14)	8161(12)	–1452(16)	128	3462(15)	6965(16)	–2068(22)	96
C(15)	2329(13)	9112(11)	–1776(13)	107	2589(14)	6114(15)	–2687(19)	98
C(16)	2865(7)	12820(8)	1105(11)	47	3096(10)	2472(12)	0506(16)	49
O(17)	3579(5)	13054(6)	1971(8)	67	3762(7)	2143(8)	1554(12)	62
C(18)	2546(6)	13643(7)	–0496(10)	39	2806(9)	1664(12)	–1223(15)	43
C(19)	3036(7)	13317(9)	–1892(12)	54	3223(9)	1995(13)	–2501(16)	59
C(20)	2832(7)	14107(10)	–3339(12)	59	3005(10)	1192(15)	–4081(16)	63
C(21)	2189(7)	15219(9)	–3393(10)	51	2415(10)	0116(13)	–4324(16)	56
C(22)	1698(7)	15573(7)	–2031(10)	44	2032(9)	–0190(12)	–3008(15)	48
C(23)	1894(6)	14782(7)	–0583(10)	37	2230(8)	0576(12)	–1446(14)	41
C(24)	1338(6)	15132(8)	0940(10)	42	1790(8)	0286(13)	–0045(15)	43
O(25)	0949(5)	14377(5)	1775(8)	64	1547(6)	1124(8)	0898(11)	67
C(26)	1309(5)	16318(6)	1188(8)	24	1695(7)	–0922(9)	0032(12)	23
C(27)	0902(6)	16873(7)	2483(11)	42	1316(9)	–1394(11)	1259(15)	43
C(28)	1326(7)	7878(8)	2913(11)	51	1680(10)	–2468(12)	1804(17)	60
C(29)	0943(8)	18461(8)	4204(12)	64	1313(11)	–2996(13)	3026(18)	76
C(30)	0145(8)	18069(9)	5077(12)	56	0622(10)	–2427(13)	3659(16)	57
C(31)	–0281(7)	17087(8)	4683(11)	50	0230(9)	–1369(12)	3137(15)	47
C(32)	0093(6)	16476(8)	3385(11)	49	0608(8)	–0824(12)	1916(16)	49
O(33)					0338(7)	–3013(9)	4872(12)	76
C(34)					–0358(9)	–2448(13)	5674(18)	77
C(35)					–0490(9)	–3311(13)	6956(19)	106

at the C(8) atom, give rise to two transannular C–H···O interactions in both structures. The C(6) and O(10) atoms are linked through the 1,5-interaction which is typical of free crown ethers [24]; the C(6)···O(10) and H···O(10) distances are 3.09 and 2.57 Å in **I** and 3.12 and 2.58 Å in **II**. The same methylene group and the O(1) atom are involved in the 1,6-interaction for which the C···O and H···O distances are 3.32 and 2.59 Å in **I** and 3.32 and 2.60 Å in **II**.

Note that, according to the data of the Cambridge Structural Database [25], the *trans* configuration about one of the C–C bonds is also observed in other substituted monoaza-15-crown-5 compounds, such as 13-(4-

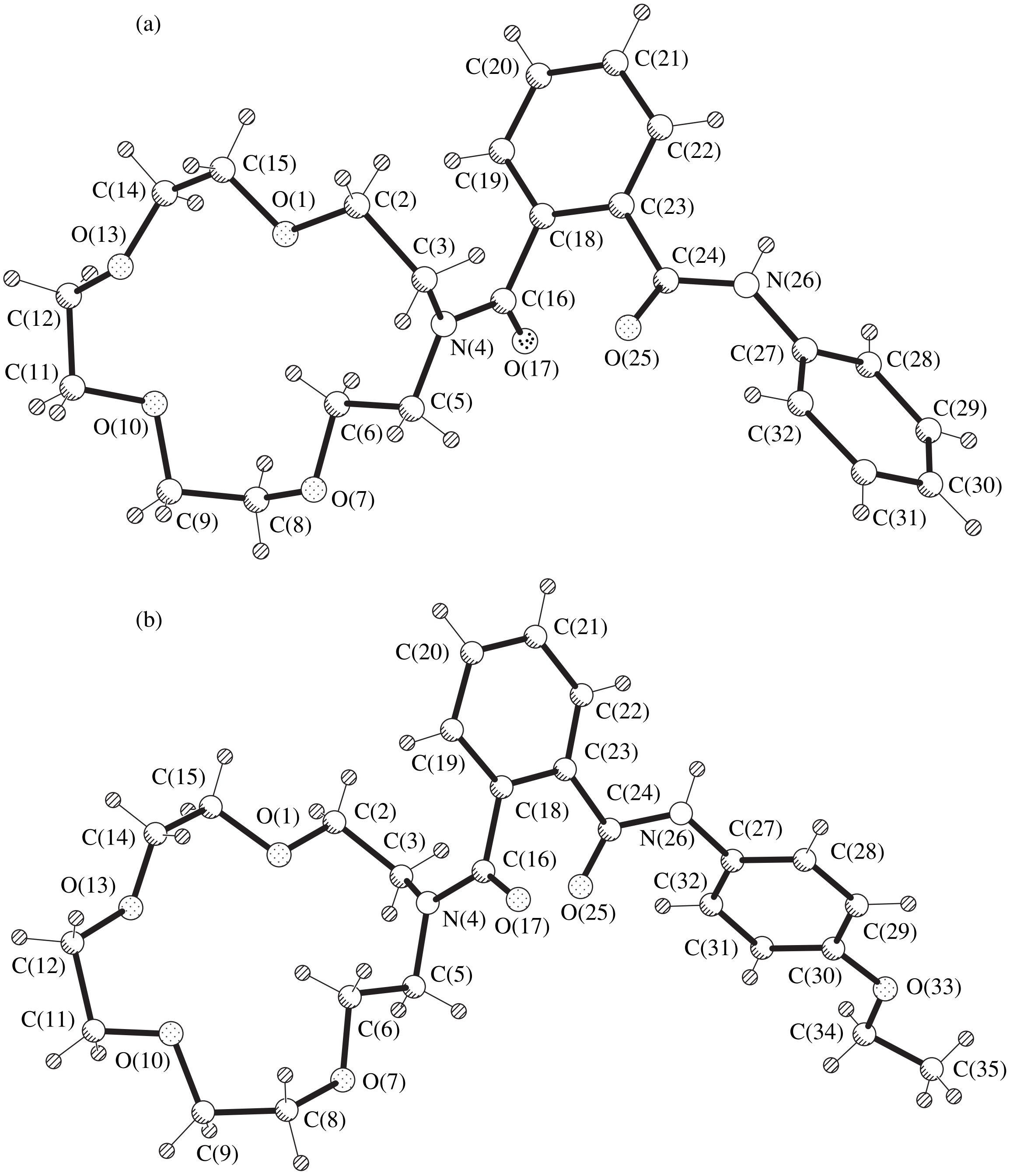

Fig. 1. Molecular structures of (a) **I** and (b) **II**.

acetylaminobenzosulfamido)aza-cyclopentadecane [15], [*N*-(aza-15-crown-5)phenyl](diphenyl)phosphine oxide monohydrate [26], *N*-(cholesteroloxycarbonyl)aza-15-crown-5 [27], and others. However, in all these structures, two corner fragments [23] are formed along the C–C bonds, whereas the rings in **I** and **II** have only one corner fragment. Note once again that the rotamers about the C–N bonds in monoaza-15-crown-5 are intermediate between *gauche* and *trans* rotamers. According to the nomenclature given in [28], they are called *anticlinal*.

The mutual arrangement of the molecular fragments is determined by intramolecular nonbonded interactions between them. These interactions in **I** and **II** are similar, so that the arrangements of planar fragments relative to the monoaza-15-crown-5 skeletons in **I** and **II** are almost identical. The dihedral angles between the plane passing through the heteroatoms and the planes of the aromatic fragments of the phthalic acid residue and of the substituent are equal to 41.5° and 82.2°, respectively, in **I** and 39.2° and 83.5°, respectively, in **II**.

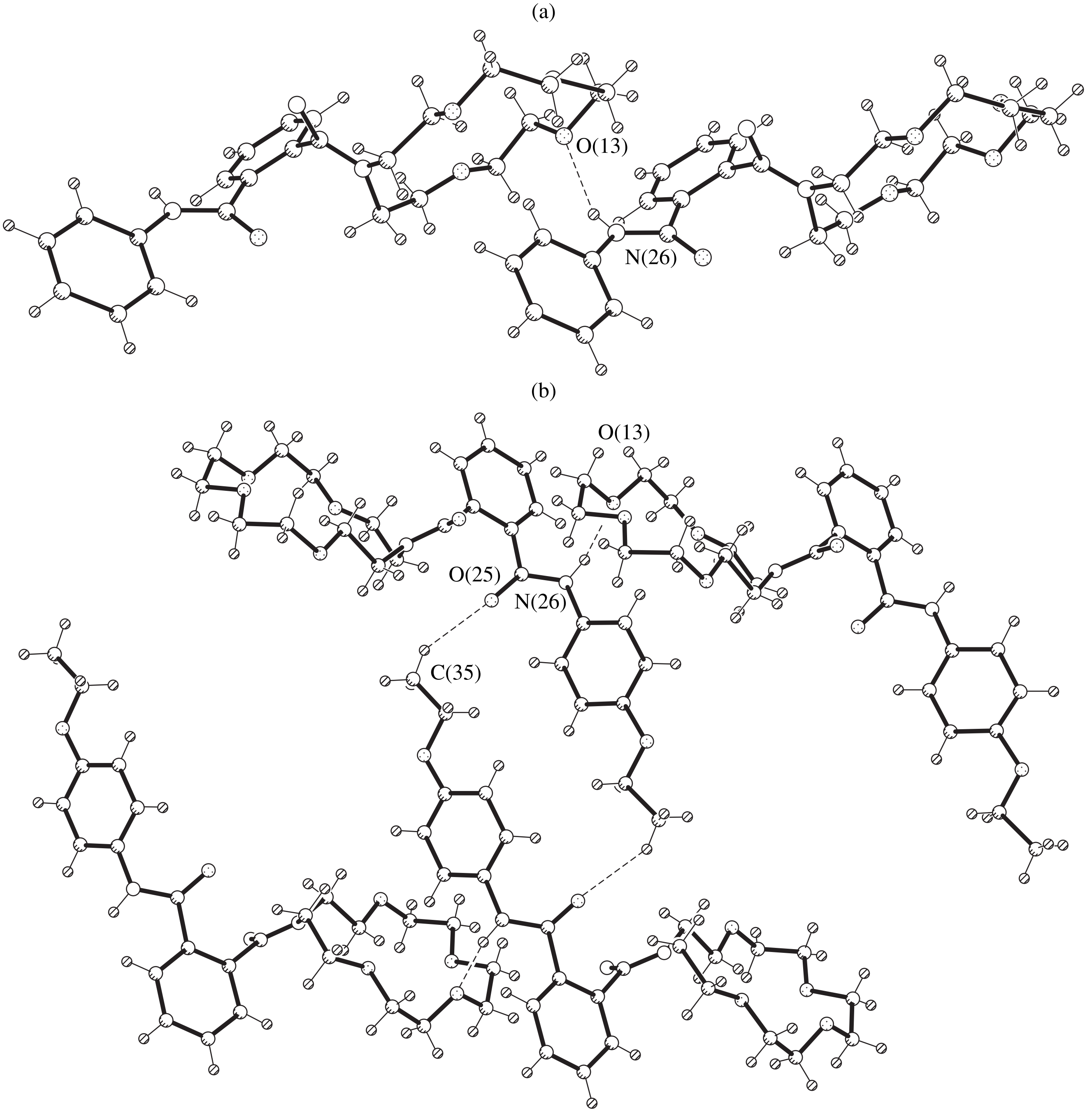

Fig. 2. Fragments of crystal structures (a) **I** and (b) **II**.

We distinguish two main nonbonded interactions between the radicals. The phthalic acid residues are involved in the C=O···C=O dipole–dipole interaction [29], which is characteristic these compounds. The O(25)···C(16) distance is 2.88 Å in**I** and 2.80 Å in **II** (Figs. 1a, 1b). The orientation of the substituents at C(24) is stabilized by the C–H···O 1,5-interaction with the C(32)···O(25) distance of 2.90 (2.86) Å and the H···O(25) distance of 2.39 (2.36) Å.

The mean distances in the 15-membered rings of **I** and **II** are follows: C–C, 1.513(15) Å; C–O, 1.432(12) Å; and C–N, 1.487(11) Å. The angles at the methylene C, N, and O atoms lie in the ranges 102.5°–114.8(1.2)°, 116.6°–118.9(1.1)°, and 111.4°–114.8(1.0)°, respectively. The geometric parameters of **I** and **II** are close to the values observed in other compounds of this class [12, 15, 26, 27]. Certain endocyclic OCC bond angles are increased because of the O···O repulsion.

The main factor that determines the formation of crystal structures is the N(26)–H···O(13) hydrogen bond [in **I**, N(26)···O(13) is 2.970 Å, H···O(13) is 2.17 Å, and the angle at the H atom is 138°; in **II**, the corresponding values are equal to 2.906 Å, 2.24 Å, and 131°, respectively] between the molecules related by the *y* translation (Figs. 2a, 2b). The OC_2H_5 radical produces no fundamental changes in the system of intermolecular interactions in the crystal. For this reason, the molecular packings, the unit cell parameters, and symmetry of crystals **I** and **II** are similar. The presence of the additional ether group in compound **II** leads to the C(35)–H···O(25) interactions between the chains formed by the N–H···O bonds. The C(35)···O(25) and H···O(25) distances (3.480 and 2.56 Å, respectively) are characteristic of the C–H···O hydrogen bonds [30, 31]. The associates in **I** and **II** are linked by van der Waals interactions.

Analysis of the available data and the results of this study allowed us to conclude that the type of the structure observed in the crystal depends on the topology of the donor and acceptor groups in the lariate molecule.

ACKNOWLEDGMENTS

We are grateful to P.N. Bourosh, who helped us prepare the paper for publication.

REFERENCES

1. M. Hiraoka, *Crown Compounds* (Kodansha, Tokyo, 1982; Mir, Moscow, 1986).
2. *Synthesis of Macrocycles: The Design of Selective Complexing Agents*, in *Progress in Macrocyclic Chemistry,* Ed. by R. M. Izatt and J. J. Christensen (Wiley, New York, 1987), Vol. 3, p. 337.
3. *Host Guest Complex Chemistry Macrocycles*, Ed. by F. Vögtle and E. Weber (Springer-Verlag, Berlin, 1985; Mir, Moscow, 1988).
4. U. Elben, H. Fuchs, and K. Frensch, Liebigs Ann. Chem., No. 8, 1102 (1979).
5. W. Weber and G. Gokel, *Phase Transfer Catalysis in Organic Synthesis* (Springer-Verlag, Berlin, 1977; Mir, Moscow, 1986).
6. G. W. Gokel and O. F. Schall, in *Comprehensive Supramolecular Chemistry,* Ed. by G. W. Gokel (Pergamon, New York, 1996), Vol. 1, No. 4, p. 97.
7. P. L. Kio, M. Miki, I. Ikeda, and M. Okahara, J. Am. Oil Chem. Soc. **57**, 227 (1980).
8. R. A. Schultz, D. M. Dishong, and G. M. Golkel, J. Am. Chem. Soc. **104** (2), 625 (1982).
9. E. Sonveaux, Bull. Soc. Chim. Belg. **91** (1), 91 (1982).
10. F. Vogtle and U. Elben, Chem. Ber. **111** (4), 1434 (1978).
11. G. W. Gokel, D. M. Dishong, and C. J. Diamond, J. Chem. Soc. Chem. Commun., 1053 (1980).
12. S. T. Malinovskiĭ, Yu. A. Simonov, É. V. Ganin, *et al.*, Izv. Akad. Nauk Mold. SSR, Ser. Fiz.-Tekh. Mat. Nauk, No. 3, 45 (1989).
13. Yu. A. Simonov, M. S. Fonar’, Yu. A. Popkov, *et al.*, Dokl. Akad. Nauk SSSR **301** (4), 913 (1988).
14. S. T. Malinovskiĭ, Yu. A. Simonov, É. V. Ganin, *et al.*, Zh. Strukt. Khim. **30** (5), 129 (1989).
15. S. T. Malinovskiĭ, Yu. A. Simonov, É. V. Ganin, *et al.*, Zh. Strukt. Khim. **32** (3), 133 (1991).
16. V. I. Kal’chenko, Yu. A. Simonov, A. A. Dvorkin, *et al.*, Zh. Obshch. Khim. **62** (7), 1542 (1992).
17. J. Lipkowski, K. Udachin, Yu. A. Simonov, and D. Soldatov, in *Current Challenges on Large Supramolecular Assemblies*, Ed. by G. Tsoncaris (Kluwer, Dordrecht, 1999), NATO ASI Ser., Ser. C **519**, 157 (1999).
18. Yu. A. Simonov, A. A. Dvorkin, S. I. Lindeman, *et al.*, Kristallografiya **33** (4), 878 (1988) [Sov. Phys. Crystallogr. **33**, 518 (1988)].
19. Yu. A. Simonov, S. T. Malinovskiĭ, D. M. Rudkevich, and V. I. Kal’chenko, Kristallografiya **36** (4), 887 (1991) [Sov. Phys. Crystallogr. **36**, 497 (1991)].
20. É. V. Ganin, V. F. Makarov, N. G. Luk’yanenko, and S. A. Kotlyar, Khim. Geterotsikl. Soedin., No. 1, 536 (1987).
21. É. V. Ganin, V. F. Makarov, and V. I. Nikitin, Ukr. Khim. Zh. (Russ. Ed.) **53** (9), 964 (1987).
22. V. K. Pecharskiĭ, P. O. Zavaliĭ, L. G. Aksel’rud, *et al.*, Vestn. L’vov. Gos. Univ., No. 25, 60 (1984).
23. J. Dale, Acta Chem. Scand., No. 6, 1115 (1973).
24. N. R. Strel’tsova, A. A. Varnek, A. S. Glebov, and V. K. Bel’skiĭ, in *Problems of Crystal Chemistry*, Ed. by M. A. Poraĭ-Koshits (Nauka, Moscow, 1989), p. 47.
25. F. H. Allen and O. Kennard, Chemical Design Automat. News **8** (1), 31 (1993).
26. B. S. Muehl, Shen Bing-Jahn, S. A. Burns, *et al.*, Coord. Chem. **35**, 359 (1995).
27. G. W. Gokel, J. C. Hernández, A. M. Viscariello, *et al.*, J. Org. Chem. **52**, 2963 (1987).
28. W. Klynew and V. Prelog, Experientia **16**, 521 (1960).
29. Yu. G. Ganin, É. V. Ganin, Yu. A. Simonov, *et al.*, Zh. Strukt. Khim. **23** (6), 103 (1982).
30. R. Taylor and O. Kennard, J. Am. Chem. Soc. **104**, 5063 (1982).
31. T. Steiner, Crystallogr. Rev. **6**, 1 (1996).

Translated by I. Polyakova

Crystallography Reports, Vol. 46, No. 3, 2001, pp. 425–434. Translated from Kristallografiya, Vol. 46, No. 3, 2001, pp. 475–484.
Original Russian Text Copyright © 2001 by Serezhkin, Serezhkina, Ulanov, D'yachenko.

CRYSTAL CHEMISTRY

HgX_n Coordination Polyhedra (X= F, Cl, Br, and I) in Crystal Structures

V. N. Serezhkin*, L. B. Serezhkina*, A. S. Ulanov*, and O. A. D'yachenko**

** Samara State University, ul. Akademika Pavlova 1, Samara, 443011 Russia*
*** Institute of Problems in Chemical Physics, Russian Academy of Sciences,*
Chernogolovka, Moscow oblast, 142432 Russia
e-mail: serezhkin@ssu.samara.ru

Received June 9, 2000

Abstract—The crystallochemical analysis of 188 structures containing 252 crystallographic kinds of Hg(II) atoms in HgX_n coordination polyhedra (X = F, Cl, Br, and I) has been performed by the method of intersecting spheres with the use of Voronoi–Dirichlet polyhedra. It was found that halogen atoms surrounded by Hg(II) atoms are characterized by the coordination numbers from 3 to 8. It was demonstrated that, at the unvarying nature of the X atoms, the average Hg–X interatomic distance increases by 0.13–0.57 Å with an increase of the coordination number, whereas the average radius of spheres with the volume equal to that of the Voronoi–Dirichlet polyhedron of a Hg atom is either independent of the coordination number (at X = F) or varies with it only by about 0.02–0.07 Å (at X = Cl, Br, and I). This allows the approximation of mercury atoms in the crystal structures by soft (deformable) spheres of a constant volume. Some results obtained in the analysis of the topology and the geometry of $[\mathrm{Hg}_m X_n]^{z-}$–complexes in crystal structures are also presented. © *2001 MAIK "Nauka/Interperiodica".*

INTRODUCTION

Within the framework of our studies of the effect of the nature and the valence state of metal atoms A on the characteristics of the AX_n coordination polyhedra (X is a nonmetal element) [1–3], we perform the crystallochemical analysis of the structures containing Hg(II) atoms surrounded by halogen atoms. The methods of selection and the analysis of the structural data based on the consideration of Voronoi–Dirichlet polyhedra were described earlier [1–3]. We considered here 7 fluorine-, 105 chlorine-, 34 bromine-, and 42 iodine-containing compounds (the data of all the structure determinations with final reliability factor $R_f \leq 0.1$). These structures contained up to 252 crystallographic types of Hg(II) atoms. The complete list of the considered structures and the characteristics of the mercury atoms in these structures can be obtained from the authors.

It is well known [1–3] that, in the general case, the Voronoi–Dirichlet polyhedron of a certain atom A has the composition AX_nZ_m, where X are atoms chemically bound to the central atom A; Z are the atoms whose Voronoi–Dirichlet polyhedra (as well as those of X atoms) share the faces with the Voronoi–Dirichlet polyhedron of the atom A (but with the $A \cdot\cdot Z$ contacts not being chemical bonds); and n and m are the numbers of atoms X and Z, respectively (with the sum $n + m$ being equal to the total number of faces of the Voronoi–Dirichlet polyhedron of the atom A and n being equal to the coordination number of the atom A). The clear and objective classification of all pairwise interatomic interactions of a certain atom A into the valence (of the A–X type) and the nonvalence (of the $A \cdot\cdot Z$ type) interactions can be made by the method of intersecting spheres [4] in which each atom in the structure is approximated by two spheres with the common center located in the atomic nucleus (Fig. 1). One sphere characterizes conditionally isolated (chemically unbound) atom; its radius for an atom of a certain element in all is a constant assumed to be equal in all the structures to the Slater radius r_S [5] of this atom. The other sphere characterizes a chemically bound atom and its volume equals the volume of the Voronoi–Dirichlet polyhedron of the corresponding atom. For any atom, the radius of this spherical domain (R_{SD}) is uniquely determined by the spatial arrangement of all the neighboring atoms. If the structure of a certain crystal is such that two (I_2), three (I_3), or four (I_4) pairwise intersections of these spheres for neighboring atoms take place (Fig. 1), then these two atoms are considered to be chemically bound. Hereafter, the authors used the abbreviation I to indicate pairwise intersections, which, in some other authors' publications, are abbreviated as O (overlaps). If there are no pairwise intersections (I_0) or only the outer spheres of two atoms overlap (I_1), then the neighboring atoms are considered to be chemically unbound. Then, the contacts are considered as weak (I_0) or specific (I_1) van der Waals interactions and are ignored in the determination of the coordination numbers of these atoms. Thus, according to [4], the strong A–X chemical bonds are taken into account in determination of the

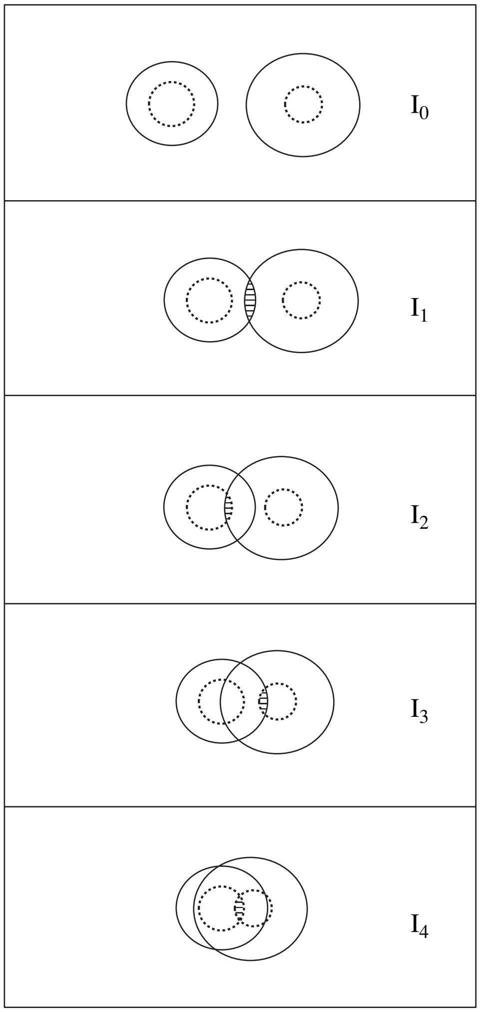

Fig. 1. Possible types of the overlap of “two-sphere” atoms *A* and *X*. Hatched regions are the regions of overlapping of two spheres of neighboring atoms. The existence of these regions is a necessary and a sufficient condition for overlapping of the corresponding type. At fixed radii of atoms *A* and *X*, their approach to one another is accompanied by the changes in the type of overlapping according to the following scheme: $I_0 \longrightarrow I_1 \longrightarrow I_2 \longrightarrow I_3 \longrightarrow I_4$. The role of chemical bonds determining the coordination number of the atom *A* is played by only the pairwise interactions of I_2, I_3, and I_4 types.

coordination number of the atom *A* (interpreted as ionic, covalent, or metallic bonds depending on the nature of these atoms) corresponding to the intersections of the I_2, I_3, or I_4 types. To the van der Waals contacts $A\cdot\cdot Z$ there correspond the intersections of the I_0 and I_1 types. As an example, Table 1 present the coordination numbers calculated by the method of intersecting spheres for Hg atoms in the $(C_5H_5ClN)HgCl_3$ [6] and $(C_{10}D_8S_8)_4(Hg_2Br_6)(HgBr_2)$ [7] structures.

The analysis of all 188 the crystal structures performed by the method reported in [4] demonstrated that the coordination numbers of mercury atoms surrounded by halogen atoms ranges from 3 to 8 (Table 2). In HgX_3 complexes (hereafter, X = F, Cl, Br, or I), the Hg atoms are located in the center of a triangle formed by *X* atoms. At CN = 4, the coordination polyhedron of a mercury atom is a distorted tetrahedron or a bisphenoid. At CN = 5, the polyhedron is a trigonal bipyramid or (relatively rarely) a square pyramid. For CN = 6 and 7, the coordination polyhedron is a tetra-and pentagonal bipyramid, respectively; at CN = 8, it is a cube (the only example here is the fluorite-like HgF_2 structure) or a square antiprism (the $Hg(AuF_4)_2$ structure [8]). Most crystals are characterized by strongly distorted coordination polyhedra of Hg atoms. In particular, trigonal bipyramids are pronouncedly elongated in the direction of the principal symmetry axis, whereas tetragonal and pentagonal bipyramids are compressed along this axis. As a consequence of this distortion (the most pronounced for the chlorine-, bromine-, and iodine-containing complexes), standard deviations for the average r(Hg–X) distances at CN = 5, 6, or 7 (Table 2) are anomalously high (0.35–0.49 Å) since the histograms for the Hg–*X* bond-length distribution are bimodal.

On the whole, the structures discussed here have 45 topological types of $[Hg_mX_n]$ complexes, where the X : Hg ratio ranges from 8 to 2. In these groups, the role of Hg and *X* atoms in the crystal structure is illustrated by Table 3 which yields the crystallochemical formulas written in accordance with [9]. These formulas show that halogen are either the end (M^1) or bridge ligands (M^2, M^3, or M^4, i.e., ligands bonding 2, 3, or four mercury atoms). The interatomic distances corresponding to the valence Hg–*X* contacts in the $[Hg_mX_n]$ complexes fall, depending on the nature of *X* atoms, within the following ranges: 2.16–2.40 Å (*X*-F), 2.24–3.38 Å (*X*-Cl), 2.27–3.43 Å (*X*-Br), and 2.57–3.68 Å (*X*-I); i.e., they change their lengths by about 0.2–1.2 Å (Fig. 2).

According to the data obtained by the method of intersecting spheres [4], of the total number of 3567 faces of the Voronoi–Dirichlet polyhedra for 252 different types of Hg atoms, 1148 faces correspond to the valence Hg–*X* contacts, whereas the remaining ones correspond to the van der Waals $Hg\cdot\cdot Z$ interactions. The *Z* atoms usually correspond to nonmets such as H, C, Cl, N, I, O, Br, S, Se, and F, which form 762, 634, 236, 112, 91, 54, 54, 47, 7, and 6 faces, respectively. The metal atoms, Hg, Cs, Mg, Tl, Cu, Rb, Ag, K, Pd, and Pt, form 164, 162, 24, 20, 16, 14, 8, 3, 3, and 2 faces of the $Hg\cdot\cdot Z$ type.

It is important that despite the significant scatter in the Hg–*X* distances, the volume V_{VDP} of the Voronoi–Dirichlet polyhedra of Hg atoms and the corresponding R_{SD} values are almost independent of the coordination number of Hg atoms (Table 2). The observed constancy of V_{VDP} (or R_{SD}) is, in our opinion, an additional experimental confirmation of the validity of the model of a soft (deformable) sphere of a fixed volume [1–4]. Within the framework of this model, a Voronoi–Dirichlet polyhedron can be considered as a geometri-

Table 1. The coordination of Hg atoms in some structures analyzed by the method of intersecting spheres

Parameters of the Voronoi–Dirichlet polyhedron for Hg atom			Overlap (in Å^3) of two spheres for Hg and *X* atoms (or *Z*), having the following radii				The type and the number of intersections
atoms surrounding *X* or *Z* atoms	interatomic r(Hg–*X*) or r(Hg···*Z*) distance in Å	body angle for the face, Ω(Hg–*X*) or Ω(Hg···*Z*) in percent of 4	$r_S \times r_S$	$r_S \times R_{SD}$	$R_{SD} \times r_S$	$R_{SD} \times R_{SD}$	
1	2	3	4	5	6	7	8
(C_5H_5ClN)$HgCl_3$ [6] Central atom is Hg(1) with CN = 5							
Cl(3)	2.411	23.00	0.015	2.707	0.256	4.684	I_4
Cl(1)	2.432	22.55	0.009	2.557	0.228	4.474	I_4
Cl(2)	2.456	22.24	0.004	2.873	0.198	4.939	I_4
Cl(1)	3.086	14.02	0	0.375	0	1.207	I_2
Cl(5)	3.148	13.86	0	0.280	0	1.028	I_2
Cl(7)	4.146	2.26	0	0	0	0	I_0
#C(4)	4.222	1.17	0	0	0	0	I_0
#Cl(8)	4.609	0.24	0	0	0	0	I_0
#C(8)	4.622	0.49	0	0	0	0	I_0
#C(9)	4.671	0.03	0	0	0	0	I_0
#Cl(7)	4.775	0.10	0	0	0	0	I_0
#C(10)	4.820	0.01	0	0	0	0	I_0
#Cl(4)	5.024	0.01	0	0	0	0	I_0
#Cl(8)	5.107	0.03	0	0	0	0	I_0
#Cl(7)	5.116	<0.01	0	0	0	0	I_0
Central atom is Hg(2) with CN = 5							
Cl(6)	2.331	23.70	0.052	3.324	0.455	5.967	I_4
Cl(4)	2.333	23.40	0.051	3.518	0.451	6.258	I_4
Cl(5)	2.803	16.59	0	1.132	0.001	2.717	I_3
Cl(2)	2.898	16.24	0	1.075	0	2.646	I_2
Cl(5)	3.296	11.87	0	0.086	0	0.731	I_2
Hg(2)	4.143	1.33	0	0	0	0	I_0
Cl(2)	4.640	5.05	0	0	0	0	I_0
#Cl(4)	4.761	0.07	0	0	0	0	I_0
Hg(2)	5.093	1.52	0	0	0	0	I_0
#Cl(6)	5.329	0.20	0	0	0	0	I_0
#Cl(7)	5.451	0.02	0	0	0	0	I_0
#Cl(8)	5.503	<0.01	0	0	0	0	I_0

Table 1. (Contd.)

Parameters of the Voronoi–Dirichlet polyhedron for Hg atom			Overlap (in Å^3) of two spheres for Hg and X atoms (or Z), having the following radii				The type and the number of intersections
atoms surrounding X or Z atoms	interatomic r(Hg–X) or r(Hg$\cdots Z$) distance in Å	body angle for the face, Ω(Hg–X) or Ω(Hg$\cdots Z$) in percent of 4	$r_S \times r_S$	$r_S \times R_{SD}$	$R_{SD} \times r_S$	$R_{SD} \times R_{SD}$	
1	2	3	4	5	6	7	8
$(C_{10}D_8S_8)_4(Hg_2Br_6)(HgBr_2)$ [7] = $(C_{10}D_8S_8)_4[Hg_3Br_8]$ Central atom is Hg(1) with CN = 4							
Br(1)	2.274	25.02	0.274	4.339	1.191	8.241	I_4
Br(2)	2.384	23.75	0.140	4.206	0.893	8.104	I_4
Br(5)	3.408 (×2)	11.36 (×2)	0	0.126	0	1.117	I_2 (×2)
Br(6)	3.779 (×2)	7.29 (×2)	0	0	0	0.085	I_1 (×2)
Hg(3)	3.813	2.45	0	0	0	0	I_0
Hg(2)	3.815	4.44	0	0	0	0	I_0
C(20)	4.513 (×2)	3.41 (×2)	0	0	0	0	I_0 (×2)
#S(9)	4.848 (×2)	0.11 (×2)	0	0	0	0	I_0 (×2)
Central atom is Hg(2) with CN = 4							
Br(6)	2.519 (×2)	22.69 (×2)	0.034	2.575	0.503	5.223	I_4 (×2)
Br(3)	2.729	19.81	0	1.752	0.171	3.973	I_3
Br(4)	2.765	18.67	0	1.846	0.130	4.144	I_3
Hg(3)	3.683	2.94	0	0	0	0.002	I_1
Hg(1)	3.815	4.44	0	0	0	0	I_0
Br(2)	3.954	5.57	0	0	0	0.041	I_1
#S(5)	4.554 (×2)	0.17 (×2)	0	0	0	0	I_0 (×2)
#Br(1)	4.592	1.41	0	0	0	0	I_0
#C(10)	4.787 (×2)	0.11 (×2)	0	0	0	0	I_0 (×2)
#C(10)	5.110 (×2)	0.61 (×2)	0	0	0	0	I_0 (×2)
Central atom is Hg(3) with CN = 4							
Br(5)	2.351 (×2)	24.96 (×2)	0.175	3.859	0.855	7.044	I_4
Br(4)	2.715	20.54	0	2.055	0.175	4.387	I_3
Br(3)	2.908	17.95	0	1.108	0.019	2.864	I_3
Hg(2)	3.683	2.94	0	0	0	0.002	I_1
Hg(1)	3.813	2.45	0	0	0	0	I_0
Br(1)	4.266	3.24	0	0	0	0	I_0
C(11)	4.608 (×2)	0.81 (×2)	0	0	0	0	I_0 (×2)
#C(12)	4.729 (×2)	0.46 (×2)	0	0	0	0	I_0 (×2)
#Br(6)	5.188 (×2)	0.06 (×2)	0	0	0	0	I_0 (×2)
#C(2)	5.440 (×2)	0.06 (×2)	0	0	0	0	I_0 (×2)
#C(1)	5.455 (×2)	0.08 (×2)	0	0	0	0	I_0 (×2)

Note: Symbol # denotes Z atoms for which the segment Hg$\cdots Z$ does not intersect the face of the Voronoi–Dirichlet polyhedron corresponding to it (the so-called minor or indirect neighbors [4]). In the second, third, and last columns, the number in parentheses indicate the numbers of symmetry-equivalent interatomic distances, body angles, and pairwise intersections, respectively.

Table 2. Parameters of the Voronoi–Dirichlet polyhedra for Hg(II) atoms in [HgX_n] complexes (X = F, Cl, Br, and I)

Atom X	CN_{Hg}	The number of Hg atoms	N_f	N_{nb}	V_{VDP}, Å^3	S_{VDP}, Å^2	R_{SD}, Å	D_A, Å	G_3	r(Hg–X), Å	μ	The range of r(Hg–X) values,Å
F	6	5	10(4)	0.7	11.5(3)	30.5(6)	1.40(1)	0	0.0834(1)	2.25(4)	30	2.16–2.32
	8	2	8	0	11.5(6)	29(1)	1.40(2)	0	0.0822(5)	2.38(2)	16	2.36–2.40
	6 and 8	7	10(4)	–	11.5(4)	30(1)	1.40(1)	0	0.0830(6)	2.30(7)	46	2.16–2.40
Cl	3	1	21	6.0	22.6	45.7	1.75	0.03	0.0876	2.38(1)	3	2.37–2.39
	4	80	15(2)	2.7	22(2)	47(4)	1.74(4)	0.10(6)	0.089(3)	2.50(14)	320	2.28–3.10
	5	43	13(2)	1.6	22(1)	47(3)	1.74(4)	0.08(6)	0.088(2)	2.71(35)	215	2.24–3.38
	6	30	12(2)	1.0	22(1)	46(2)	1.73(4)	0.04(5)	0.086(1)	2.82(37)	180	2.26–3.35
	7	2	10(–)	0.4	21.7(3)	45.7(5)	1.73(1)	0.03(1)	0.0847(2)	2.95(43)	14	2.29–3.32
	3–7	156	14(3)	–	22(2)	47(3)	1.74(4)	0.08(6)	0.088(3)	2.64(32)	732	2.24–3.38
Br	4	29	15(2)	2.8	27(2)	55(4)	1.86(4)	0.09(4)	0.091(3)	2.63(18)	116	2.27–3.41
	5	6	13(3)	1.6	26(1)	53(3)	1.83(3)	0.07(3)	0.088(2)	2.83(36)	30	2.43–3.43
	6	4	12(4)	1	25(1)	51(3)	1.82(3)	0.03(4)	0.085(2)	2.97(38)	24	2.41–3.39
	4–6	39	14(3)	–	27(2)	55(4)	1.85(4)	0.08(5)	0.090(3)	2.71(28)	170	2.27–3.43
I	3	3	17(1)	4.7	29(4)	55(7)	1.90(9)	0.07(2)	0.086(3)	2.70(4)	9	2.67–2.77
	4	45	15(3)	2.8	32(2)	61(4)	1.96(4)	0.08(7)	0.089(3)	2.81(17)	180	2.57–3.55
	5	1	15	2.0	32.3	61.6	1.97	0.02	0.088	3.06(49)	5	2.68–3.41
	6	1	14	1.3	29.2	53.9	1.91	0	0.083	3.15(40)	6	2.64–3.41
	3–6	50	16(3)	–	31(2)	60(4)	1.96(4)	0.08(7)	0.089(3)	2.83(20)	200	2.57–3.68

Note: CN_{Hg} is the coordination number of Hg atoms surrounded by halogen atoms; N_f is the average number of faces of the Voronoi–Dirichlet polyhedron; N_{nb} is the average number of nonvalence Hg$\cdots$$Z$ interactions per Hg–X bond; V_{VDP} is the volume of the Voronoi–Dirichlet polyhedron; S_{VDP} is the total area of the faces of the Voronoi–Dirichlet polyhedron; R_{SD} is the radius of the sphere of the volume equal to V_{VDP}; D_A is the displacement of a Hg atom from the geometrical center of gravity of the Voronoi–Dirichlet polyhedron; G_3 is the dimensionless parameter equal to the second moment of inertia of the Voronoi–Dirichlet polyhedron; r(Hg–X) is the average length of the Hg–X bonds in the classical coordination polyhedron at the given coordination number; and μ is the number of such bonds. The root-mean-square deviations are indicated in the parentheses.

cal image of a Hg atom in a certain crystal field, whose influence (caused by mutual deformation of neighboring soft spheres of Hg, X, and Z atoms during their mutual approach in the process of crystal formation) gives rise to the transformation of the sphere with radius R_{SD} corresponding to an isolated Hg atom into a specific Voronoi–Dirichlet polyhedron of the same (within the error of the structural experiment) volume. Therefore, the crystallochemical analysis of crystal structures should necessarily take into account not only the shortest interatomic distances A–X corresponding to strong (valence) chemical interactions. In our opinion, one has to take into account not only the shortest A–X distances corresponding to strong (valence) chemical interactions between the atoms A and X, but also a set of relatively weak (nonvalence) interactions of the A$\cdot\cdot$$Z$ type, which, in the general case, produce a considerable effect on distortion of AX_n coordination polyhedra.

The aforementioned constancy of V_{VDP} for mercury atoms results in the linear dependence of the body angles corresponding to the faces of Voronoi–Dirichlet polyhedra on the interatomic distances corresponding to these faces (Fig. 2). According to the least squares data, these functions for the Hg–X and Hg$\cdot\cdot$$Z$ interactions (in the general case, for Hg ~ X) are described by the following relationships:

$$\Omega(\mathrm{Hg} \sim \mathrm{F}) = 42.2(1) - 11.7(4)r(\mathrm{Hg} \sim \mathrm{F}), \quad (1)$$

$$\Omega(\mathrm{Hg} \sim \mathrm{Cl}) = 41.6(2) - 8.87(8)r(\mathrm{Hg} \sim \mathrm{Cl}), \quad (2)$$

$$\Omega(\mathrm{Hg} \sim \mathrm{Br}) = 44.3(5) - 9.0(2)r(\mathrm{Hg} \sim \mathrm{Br}), \quad (3)$$

$$\Omega(\mathrm{Hg} \sim \mathrm{I}) = 44.1(4) - 8.5(1)r(\mathrm{Hg} \sim \mathrm{I}) \quad (4)$$

with the correlation coefficients ρ ranging from –0.98 to –0.96 for 52, 968, 224, and 291 Hg ~ X contacts for X = F, Cl, Br, and I, respectively. In Eq. (1)–(4) and in the following equations, the Ω values are expressed in the percent of the total body angle (4π steradian). It should be emphasized that Eqs. (1)–(4) describe the Voronoi–Dirichlet polyhedra for all the mercury atoms irrespectively of their coordination numbers and the differentiation of the Hg–X and Hg$\cdot\cdot$$X$ interatomic distances with the change of the crystallochemistry role played by halogen atoms (bridge, end, or outer-sphere-

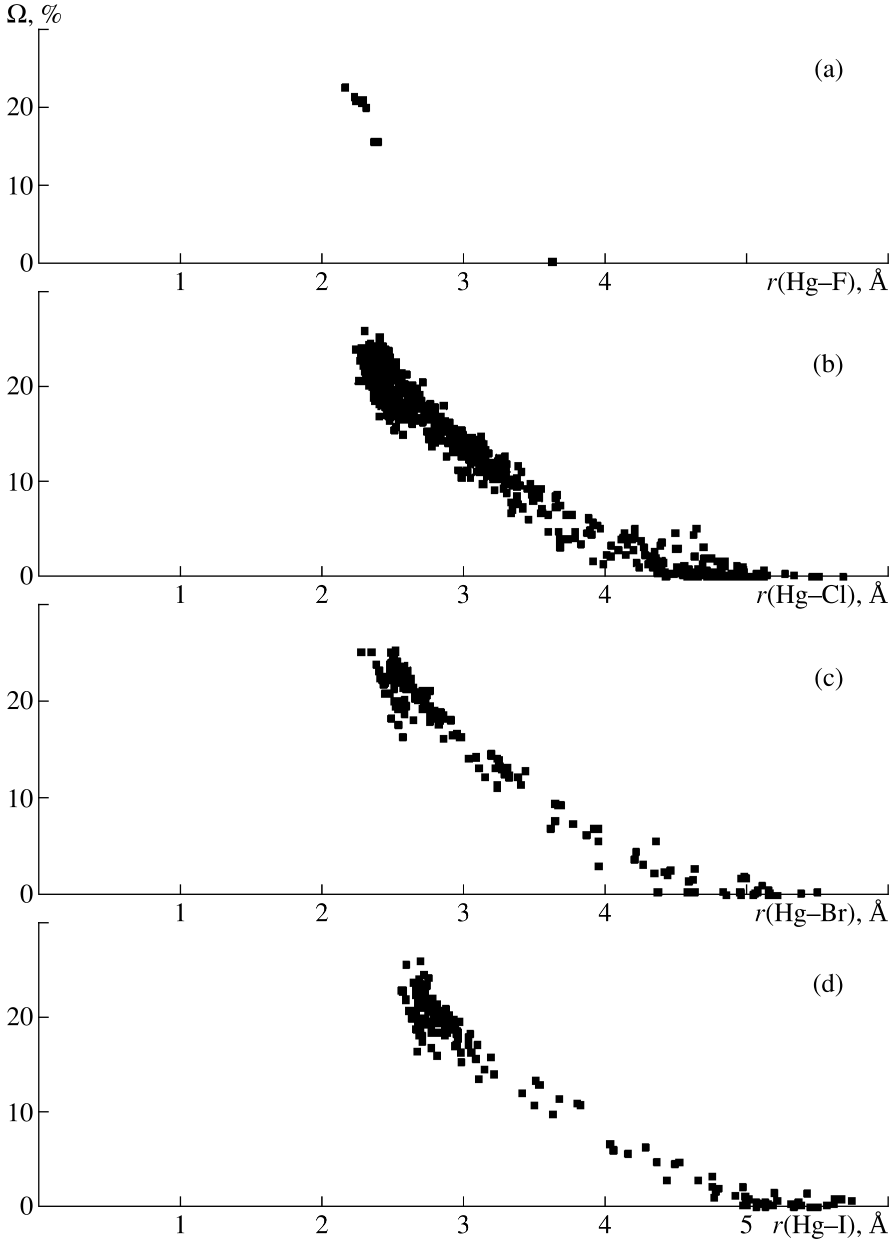

Fig. 2. Body angles Ω (in percent of 4π steradian) corresponding to the shared faces of the Voronoi–Dirichlet polyhedra of Hg(II) and *X* atoms versus interatomic *r*(Hg–*X*) or *r*(Hg··*X*) distances for these faces: (a) HgF_n-complexes; (b) $HgCl_n$-complexes; (c) $HgBr_n$-complexes; (d) HgI_n-complexes.

type atoms). In addition, Figure 2 clearly demonstrates that, in the general case, there is no distinct boundary between the valence (Hg–*X*) and nonvalence (Hg··*X*) interactions in the structure that can be uniquely characterized by a certain interatomic distance or the body angle formed by the faces of the Voronoi–Dirichlet polyhedron. Therefore, it seems that the most efficient method for determining coordinate numbers of Hg atoms is the method of intersecting spheres [4] and not the classical approach based on some systems of crystallochemical atomic radii.

It has already been mentioned [2, 10] that a distortion of the coordination sphere of the complex-forming atoms *A* can be quantitatively characterized by using two parameters of their Voronoi–Dirichlet polyhedra, namely, the displacement D_A of the atom *A* from the center of gravity of its Voronoi–Dirichlet polyhedron and the dimensionless parameter G_3 characterizing the homogeneity of the distribution of the atoms surrounding *A*, whose Voronoi–Dirichlet polyhedra are adjacent to the polyhedron of the atom *A*. In the compounds under discussion, G_3 for Hg atoms varies over a relatively wide range—from 0.082 to 0.099, with the aver-

Table 3. Composition and structure of $[Hg_mX_n]$ complexes in the crystal structures

X : Hg	Complex	X	Crystallochemical formula of the complex [9]	C_T	C_R	Dimensionality	Structure of the complex
8	$[HgX_8]^{6-}$	F	$AM_8^1 = AM_{8/1}$	0	0	0	Square antipism (0, 0, 0)
6	$[HgX_6]^{4-}$	F, Cl, Br, I	$AM_6^1 = AM_{6/1}$	0	0	0	(0, 0, 0) octahedron
5	$[HgX_5]^{3-}$	Cl	$AM^2M_4^1 = AM_{2/2}M_{4/1}$	2	2	1	Chain formed by (2, 0, 0)-octahedra
			$AM_5^1 = AM_{5/1}$	0	0	0	(0, 0, 0) TrB
4	$[HgX_4]^{2-}$	F	$AM_2^2M_2^1 = AM_{4/2}M_{2/1}$	4	4	2	Layer formed by (4, 0, 0)-octahedra
		Cl	$AM_2^2M_2^1 = AM_{4/2}M_{2/1}$	4	2	1	Chain formed by (4, 2, 0)-octahedra
		Cl	$A_2M_3^2M_5^1 = AM_{3/2}M_{3/1} \cdot AM_{3/2}M_{2/1}$	3, 3	3, 3	1	Chain formed by (3, 0, 0)-octahedra and (3, 0, 0)-TrB
		Br	$AM^2M_3^1 = AM_{2/2}M_{3/1}$	2	2	1	Chain formed by (2, 1, 0)-TrB
		Cl, Br	$AM^2M_3^1 = AM_{2/2}M_{3/1}$	2	1	0^2	Dimer formed by (2, 1, 0)-TrB
		Cl, Br, I	$AM_4^1 = AM_{4/1}$	0	0	0	(0, 0, 0) tetrahedron
3.5	$[Hg_2X_7]^{3-}$	Cl	$A_2M_2^2M_5^1 = AM_{2/2}M_{3/1} \cdot AM_{2/2}M_{2/1}$	2, 2	2, 2	1	Chain formed by (2, 0, 0) TrB and (2, 0, 0) tetrahedra
		Cl	$A_2M_2^2M_5^1 = M_{2/2}M_{3/1} \cdot M_{2/2}M_{2/1}$				Dimer formed by (2, 1, 0) TrB and (2, 1, 0) tetrahedron
	$[Hg_4X_{14}]^{6-}$	Cl	$A_2M_2^2M_5^1 = AM_{3/2}M_{2/1} \cdot AM_{1/2}M_{3/1}$	2, 2	1, 1	0^2	Tetramer formed by (3, 1, 0)-TrB and (1, 0, 0)-tetrahedra
3.33	$[Hg_3X_{10}]^{4-}$	Cl	$A_3M_4^2M_6^1 = AM_{4/2}M_{2/1} \cdot 2AM_{2/2}M_{2/1}$	3, 1	2, 1	0^4	Chain formed by (4, 2, 0)-octahedra and (2, 0, 0)-tetrahedra
				4; 2	4; 2	1	Chain formed by (4, 0, 0) and (2, 0, 0)-tetrahedra
3	$[HgX_3]^{-}$	F, Cl	$AM_3^2 = AM_{6/2}$	6	6	3	Frame formed by (6, 0, 0)-octahedra
		Cl	$A_3M_3^3M^2M_5^1 = AM_{2/3}M_{2/2}M_{2/1} \cdot AM_{4/3}M_{2/1} \cdot AM_{3/3}M_{1/1}$	6, 8, 6	4, 5, 5	2	Layers formed by (4, 2, 0)- and (4, 4, 0)-octahedra and (3, 1, 0)-tetrahedra
		Cl	$A_3M_5^2M_4^1 = AM_{3/2}M_{2/1} \cdot AM_{3/2}M_{1/1} \cdot AM_{4/2}M_{1/1}$	3, 3, 4	3, 3, 3	2	Layers formed by (3, 0, 0)-TrB, (3, 0, 0)-tetrahedra, and square pyramids (4, 1, 0)
		Cl, Br	$AM^3M_2^1 = AM_{3/3}M_{2/1}$	6	4	1	Chain formed by (3, 2, 0)-TrB
		Cl, I	$AM_2^2M^1 = AM_{4/2}M_{1/1}$	4	2	1	Chain formed by (4,2,0)-TrB
		Cl	$A_2M^3M_2^2M_3^1 = AM_{1/3}M_{3/2}M_{1/1} \cdot AM_{2/3}M_{1/2}M_{2/1}$	5; 5	3; 3	1	Chain formed by (4, 2, 0)-TrB and (3, 2, 0)
		Cl	$A_2M_3^2M_3^1 = AM_{3/2}M_{2/1} \cdot AM_{3/2}M_{1/1}$	3; 3	2, 2	1	Chain formed by (3, 1, 0)-TrB and (3, 1, 0)-tetrahedra
		Cl	$A_2M_4^2M_2^1 = AM_{4/2}M_{2/1} \cdot AM_{4/2}$	4, 4	2, 2	1	Chain formed by (4, 2, 0)-octahedra and (4, 2, 0)-tetrahedra
		Cl	$AM^3M^2M^1 = AM_{3/3}M_{2/2}M_{1/1}$	8	4	1	Chain formed by (5, 4, 0)-octahedra
		Cl, Br, I	$AM^2M_2^1 = AM_{2/2}M_{2/1}$	2	2	1	Chain formed by (2, 0, 0)-tetrahedra
		Cl, Br	$A_2M_3^2M_3^1 = AM_{4/2}M_{1/1} \cdot AM_{2/2}M_{2/1}$	4, 2	2, 1	0^4	Tetramer formed by (4, 2, 0)-TrB and (1, 1, 0)-tetrahedra
		Cl, Br, I	$AM^2M_2^1 = AM_{2/2}M_{2/1}$	2	1	0^2	Dimer formed by tetrahedra or bisphenoids (2, 1, 0)
		Cl, I	$AM_3^1 = AM_{3/1}$	0	0	0	(0, 0, 0)-triangle

Table 3. (Contd.)

X : Hg	Complex	X	Crystallochemical formula of the complex [9]	C_T	C_R	Dimensionality	Structure of the complex
2.67	$[Hg_3X_8]^{2-}$	Cl	$A_3M_2^3\,M_6^2 = AM_{2/3}M_{4/2} \cdot 2AM_{2/3}M_{4/2}$	8, 8	6, 5	3	Frame formed by (6, 2, 0)- and (6, 3, 0)-octahedra
		Cl	$A_3M_4^3\,M_4^1 = AM_{4/3}M_{2/1} \cdot 2AM_{4/3}M_{1/1}$	8, 8	6, 5	2	Layers formed by (6, 3, 0)-octahedra and (4, 3, 0)-TrB
		I	$A_3M_4^2\,M_4^1 = 2AM_{3/2}M_{1/1} \cdot AM_{2/2}M_{2/1}$	3, 2	3, 2	2	Layer formed by (3, 0, 0)- and (2, 0, 0)-tetrahedra
		I	$A_3M_4^2\,M_4^1 = 2AM_{3/2}M_{1/1} \cdot AM_{2/2}M_{2/1}$	3, 2	2, 2	1	Chain formed by (3, 1, 0)-tetrahedra and (2, 0, 0)-rhombs
		Cl	$A_3M_5^2\,M_3^1 = AM_{4/2}M_{1/1} \cdot 2AM_{4/2} \cdot AM_{2/2}M_{2/1}$	4, 4, 2	3, 3, 2	1	Chain formed by (4, 2, 0)-TrB and (2, 1, 0) and tetrahedra
		Cl, Br	$A_3M_4^2\,M_4^1 = AM_{4/2} \cdot 2AM_{2/2}M_{2/1}$	4, 2	2, 1	0^3	Trimer formed by (4, 2, 0)-tetrahedron and (2, 1, 0) bisphenoids
		I	$A_3M^3M_2^2\,M_5^1 = AM_{1/3}M_{2/2}M_{1/1} \cdot 2AM_{1/3}M_{1/2}M_{2/1}$	4, 3	2, 2	0^3	Trimer formed by (3, 2, 0)-tetrahedron and (2, 1, 0)-tetrahedra
2.5	$[Hg_2X_5]^-$	Cl	$A_2M_2^3\,M_2^2\,M^1 = AM_{4/3}M_{1/2}M_{1/1} \cdot AM_{2/3}M_{3/2}$	9, 7	5, 4	2	Layer formed by (5, 4, 0)-octahedra and (5, 3, 0)-TrB
		Cl	$A_2M^4M^3M_2^2\,M^1 = AM_{2/4}M_{2/3}M_{2/2} \cdot AM_{2/4}M_{1/3}M_{2/2}M_{1/1}$	12, 10	8, 6	2	Layer formed by (6, 4, 0)- and (5, 4, 0)-octahedra
		Cl	$A_2M^4M^2M_3^1 = AM_{2/4}M_{2/1}M_{1/1} \cdot AM_{2/4}M_{2/1}$	8, 6	6, 5	2	Layer formed by (4, 2, 0)-TrB and (2, 1, 0)-bisphenoids
		Cl	$AM_{0.5}^4\,M_2^1 = AM_{2/4}M_{2/1}$	6	5	1	Chain formed by (2, 1, 0)-bisphenoids
		Cl	$A_2M^4M^3M_3^1 = AM_{1/4}M_{2/3}M_{2/1} \cdot AM_{3/4}M_{1/3}M_{1/1}$	7, 11	5, 7	1	Chain formed by (3, 2, 0)-TrB and (4, 4, 0)-TrB
2.2	$[Hg_5X_{11}]^-$	Cl	$A_5M^4M_{10}^3 = AM_{6/3} \cdot 4AM_{1/4}M_{6/3}$	12, 15	8, 9	3	Frame formed by (6, 4, 0)-octahedra and (7, 7, 1) PB
2	$[HgX_2]$	F	$AM_2^4 = AM_{8/4}$	24	12	3	Frame formed by (8, 12, 0)-cubes
		Cl	$AM^3M^2 = AM_{3/3}M_{2/2}$	8	8	2	Layers formed by (5, 0, 0)-TrB
		Br	$AM_2^3 = AM_{6/3}$	12	6	2	Layers formed by (6, 6, 0)-octahedra
		I	$AM_2^2 = AM_{4/2}$	4	4	2	Layers formed by (4, 4, 0)-tetrahedra

Note: In the last column, the numbers in parentheses indicate the numbers of apices, edges, and faces of the corresponding coordination polyhedra collectivized during complex formation. C_T and C_R are the maximum theoretically possible and real numbers of Hg atoms bound by X bridge atoms to the basis metal atom in the structure of the corresponding complex. TrB is the trigonal bipyramid, PB is the pentagonal bipyramid.

age value being 0.088(3). In almost in all the cases, G_3 exceeds the threshold value 0.082 [10] and, hence, we can assume that the Hg–X bonds are mainly of the directional (covalent) nature. If the nature of atoms X remains unchanged, the average G_3 values regularly decrease (Table 2) with an increase of the coordination number of Hg atoms, which indicates an increase of the ionic component of the Hg–X bonds with an increase of their number.

According the data obtained, in fluorides, $D_A = 0$ for mercury atoms, whereas in the other halogenides, the average value of D_A is $D_A = 0.08$ Å (Table 2). Irrespec-

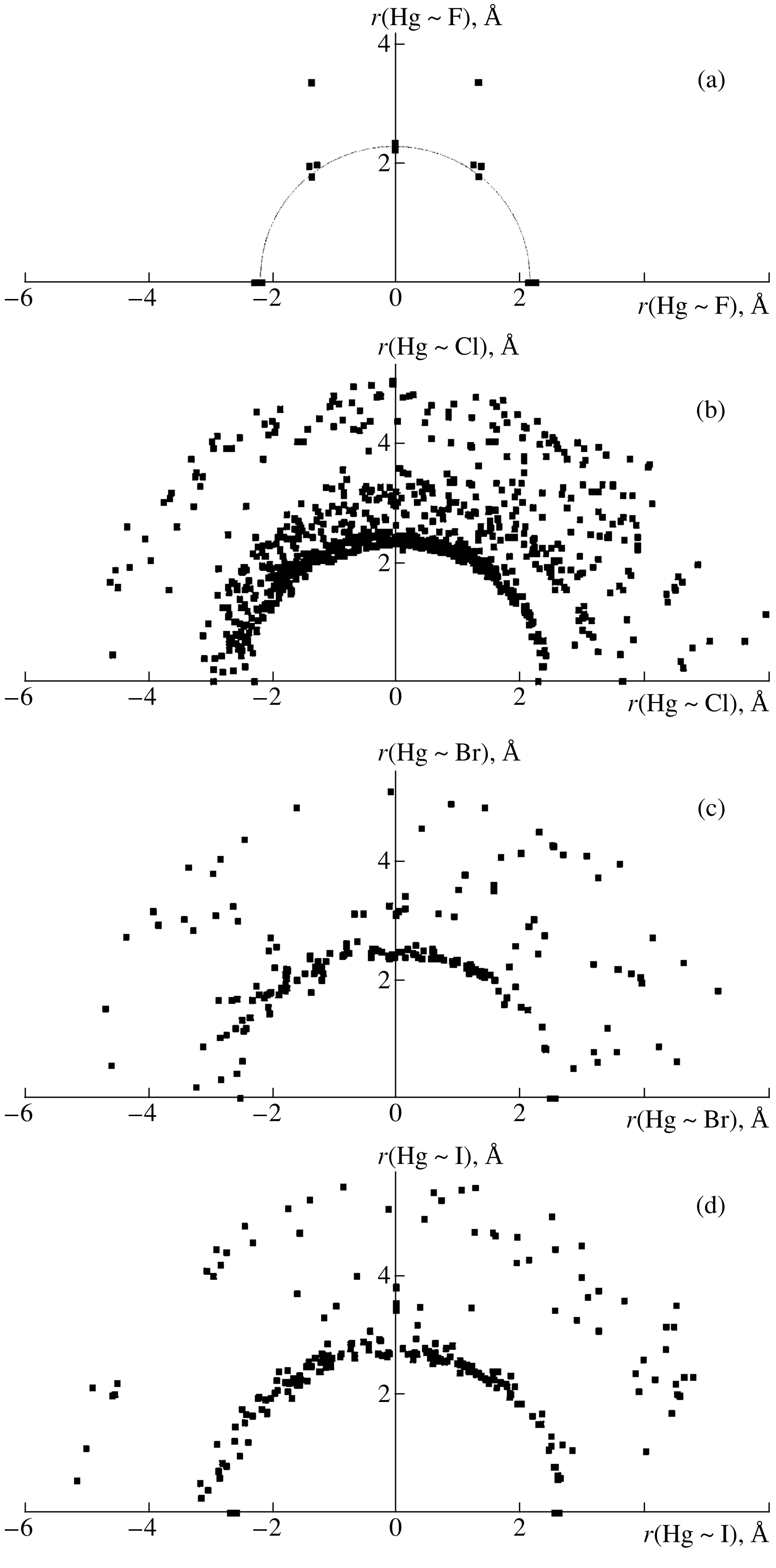

Fig. 3. The (r, φ) distributions for the Voronoi–Dirichlet polyhedra of Hg(II) atoms surrounded by (a) F, (b) Cl, (c) Br, and (d) I atoms. For each polyhedron face, there exists a point whose position is determined by the interatomic distance $r(\mathrm{Hg}–X)$ or $r(\mathrm{Hg}\cdot\cdot X)$ and by the polar angle φ between the direction of the corresponding bond and the D_A vector of the Voronoi–Dirichlet polyhedron of the Hg atom directed from the origin of coordinates to the right-hand side along the horizontal axis. The nucleus of the central Hg atom is located at the origin of polar coordinate system. At $D_A = 0$, the polar axis coincides with the z-axis of the crystallographic coordinates system.

tively of the nature of X atoms, on the (r, φ) distribution [2], a considerable distortion of the contact curves for the faces of the Voronoi–Dirichlet polyhedra of Hg atoms is observed (Fig. 3). These curves correspond to the strong valence Hg–X interactions. Although in all the cases, the contact curves are of the shape close to semicircumference with the center coinciding with the origin of the polar coordinate system, the radii of this semicircumference along the direction coinciding with the horizontal axis ($r_{\parallel}$) and the perpendicular to this axis ($r_{\perp}$) differ by about 0.1 Å. For X = F, Cl, Br, and I, the corresponding values of $r_{\parallel}$ are $r_{\parallel} \approx 2.2$, 2.3, 2.5, and 2.6 Å, whereas $r_{\perp} \approx 2.3$, 2.4, 2.4, and 2.7 Å (Fig. 3). In other words, in the halogenides considered above, the geometrical image of the electron-density distribution $\rho(x, y, z)$ in the vicinity of Hg atoms is an ellipsoid of revolution and not a sphere. For fluoride, chloride, and iodide complexes, this ellipsoid is compressed (since $r_{\parallel} < r_{\perp}$) along the rotation axis coinciding with the vector D_A (or, if $D_A = 0$, along the crystal axis z), whereas for bromide complexes, the situation is reverse (since $r_{\parallel} > r_{\perp}$)—the ellipsoid is not compressed but elongated along this axis.

In the general case, there is no correlation between the parameters D_A and G_3 but, nevertheless, the anomalously large values of both D_A (0.28 and 0.35 Å) and G_3 (0.0987 and 0.0988) in the above crystals correspond to the mercury atoms Hg(1) and Hg(2) in one structure—$(C_{10}H_8S_8)_2HgI_3$ [11]. Since the same mercury atoms have the maximum (in comparison with the other crystals) V_{VDP} (35.3 and 38.0 Å^3) and R_{SD} (2.03 and 2.09 Å) values, we can assume that all the features of the Voronoi–Dirichlet polyhedra considered above are explained by the same reason—the absence of the necessary data on the coordinates of hydrogen atoms in the $(C_{10}H_8D_8)_2HgI_3$ structure.

ACKNOWLEDGMENTS

The study was supported by the Russian Federal Program “Integration,” project no. A0056.

REFERENCES

1. V. N. Serezhkin, V. A. Blatov, and A. P. Shevchenko, Koord. Khim. **21** (3), 163 (1995).
2. V. N. Serezhkin and Yu. A. Buslaev, Zh. Neorg. Khim. **42** (7), 1180 (1997).
3. V. N. Serezhkin and L. B. Serezhkina, Koord. Khim. **25** (3), 182 (1999).
4. V. N. Serezhkin, Yu. N. Mikhaĭlov, and Yu. A. Buslaev, Zh. Neorg. Khim. **42** (12), 2036 (1997).
5. J. C. Slater, J. Chem. Phys. **41** (10), 3199 (1964).
6. A. Linden, B. D. James, J. Liesegang, and N. Gnis, Acta Crystallogr., Sect. B: Struct. Sci. **B55**, 396 (1999).
7. O. A. D’yachenko, V. V. Gritsenko, G. V. Shilov, *et al.*, Synth. Met. **62** (2), 193 (1993).
8. H. Bialowons and B. G. Mueller, Z. Anorg. Allg. Chem. **623**, 1719 (1997).
9. M. A. Poraĭ-Koshits and V. N. Serezhkin, Zh. Neorg. Khim. **39** (12), 1967 (1994).
10. V. A. Blatov, V. A. Pol’kin, and V. N. Serezhkin, Kristallografiya **39** (3), 457 (1994) [Crystallogr. Rep. **39**, 402 (1994)].
11. O. A. D’yachenko, V. V. Gritsenko, G. V. Shilov, *et al.*, Izv. Akad. Nauk, Ser. Khim., No. 7, 1240 (1994).

Translated by K. Kugel

Crystallography Reports, Vol. 46, No. 3, 2001, pp. 435–443. Translated from Kristallografiya, Vol. 46, No. 3, 2001, pp. 485–493.
Original Russian Text Copyright © 2001 by Polyakov.

CRYSTAL CHEMISTRY

Structure of Conduction Channels in Superionic Conductors: Crystallochemical Modeling

V. I. Polyakov

GIPRONIIGAZ, pr. Kirova 54, Saratov, 410600 Russia

Received April 26, 1999; in final form, August 29, 2000

Abstract—The experimental and theoretical studies of the structure of conduction channels of superionic conductors are analyzed. A crystallochemical method of modeling the conduction channels is proposed in which they are treated as sets of polyhedron Voronoi–Dirichlet sections outside of impenetrable spheres of the rigid sublattice. The allowance for both weak flexibility of the spheres and their mean-square displacements relative to the sublattice points yields a channel structure that “wraps” around the Voronoi–Dirichlet polyhedron edges. Modeling the interionic potential for α-AgI with the help of equipotential surfaces suggests that the mobile-ion motion slips along the conduction channel walls. For α-AgI, the set of the equipotential surfaces specifies “the minimum energy trajectory” of transition into a superionic state, while the crystallochemical “wrapping” structure corresponds to a saddle point of a multidimensional potential surface. Symmetry selection rules are used for predicting mechanical trajectories as allowed oscillation modes for the tetrahedral and octahedral fragments of α–CuI. *© 2001 MAIK “Nauka/Interperiodica”.*

INTRODUCTION

The superionic state of a solid electrolyte is interpreted as the existence in a certain temperature range of such a crystalline state in which the mobile ions are not located at fixed crystallographic positions of a rigid sublattice of the atoms of a certain kind or even form a “lattice liquid.” A great number of X-ray [1] and neutron diffraction [2], and theoretical studies of superionic conductors (or simply superionics) resulted in the creation of a large number of structural models: the lattice-gas model [3], continuum stochastic models [4], and a model of retarded rotational diffusion [5]. One of the goals of these studies was the characterization of conduction channels (the determination of their shape as a surface of constant density of the averaged mobile-ion distribution and the determination of the equilibrium positions of mobile ions and the most probable spatial region of motion of mobile ions from one equilibrium position to another). At present, the theoretical crystallochemical analysis of the data on conduction channels of mobile ions in superionics is only at its initial stage.

In this paper, we proposed a method of modeling conduction channels based on the combination of the model of an excluded volume [1] and the model of retarded rotational diffusion. The results obtained are compared with the experimental characteristics of body-centered cubic (bcc) electrolytes. The conductivity path of a mobile ion for a face-centered cubic (fcc) electrolyte is predicted based on the data on Cu^+-ion in α-CuI.

EXPERIMENTAL AND THEORETICAL STUDIES OF CONDUCTION CHANNELS

Consider problems arising in the course of studying conduction channels by example of the α-AgI superionic with the well-studied structure [1, 2]. According to the early X-ray diffraction studies [6], I^--anions form a rigid bcc sublattice α-AgI. Two silver ions of the unit cell continuously migrate over forty-two sites corresponding to three independent crystallographic positions—octahedral 6*b*, tetrahedral 12*d*, and trigonal 24*h* (Fig. 1a). However, the Strock model [6] is inconsistent with the experimental neutron diffraction data obtained by Bührer and Hälg [7], according to which silver ions are displaced by $\Delta x = 0.057$ along the $\langle 100 \rangle$ directions from the tetrahedral positions (the so-called model with displaced equilibrium position). Neutron diffraction studies of an α-AgI [8] single crystal indicate that the maximum density of mobile ions is distributed over the tetrahedral positions. The saddle points with the coordinates of (0.39, 0.39, 0) are located in the vicinity of the (0.375, 0.375, 0) trigonal positions. These conclusions are consistent with the EXAFS data [1].

On the other hand, the above shows that an ion moves between equilibrium tetrahedral sites by a curvilinear rather than linear trajectory along a cuboctahedron edge. However, the curvilinear conduction channels are inconsistent with the simplest structure model, i.e., that of an excluded volume [1].

In the model of an excluded volume, the cation–anion interaction is approximated by the rigid-sphere

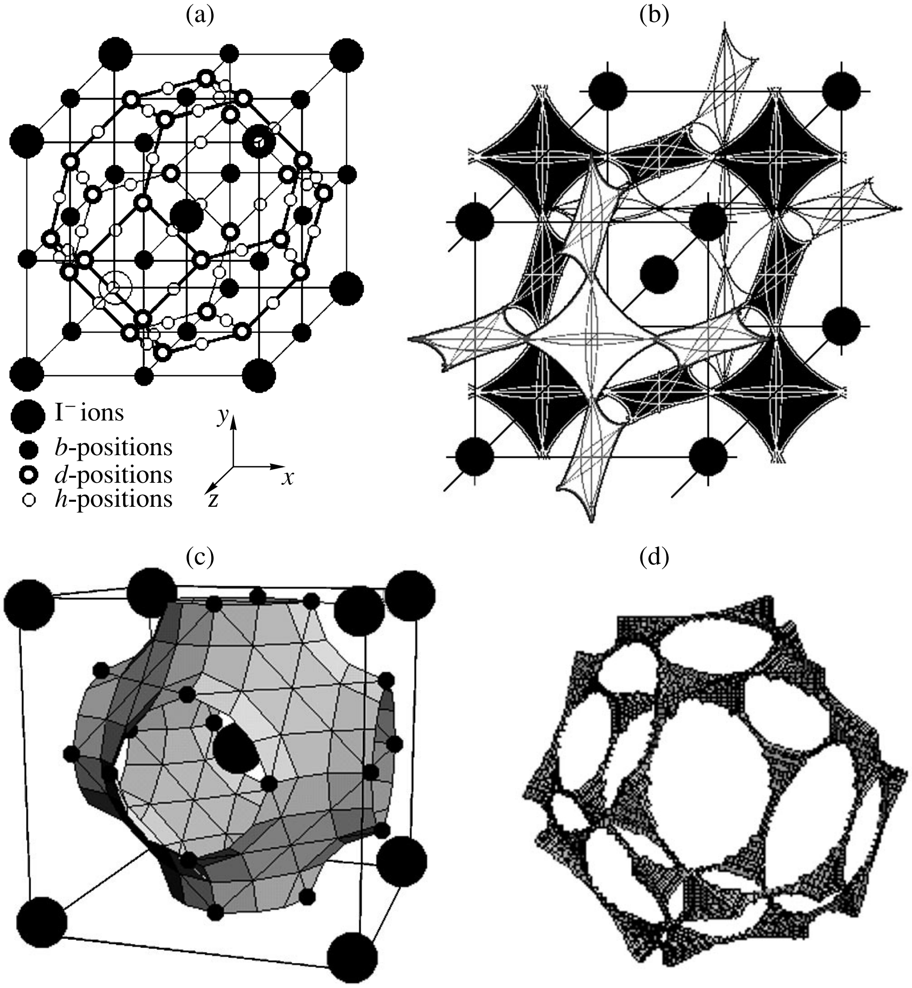

Fig. 1. Distributions of Ag^+ ions in an AgI solid electrolyte. (a) The Strock model. I^--anions form a body-centered cubic lattice; Ag^+-cations are statistically distributed over three crystallographically independent positions *b*, *d*, and *h* corresponding to the centers of tetragonal faces, the vertices, and the middle points of the edges of a Fedorov cuboctahedron. (b) Circular orbits of the model of retarded rotational diffusion. The intersections of the orbits centered at the points of the body-centered cubic unit cell. The motion regions are darkened. (c) A fragment of the periodic zero-potential *P**-surface inscribed into a bcc unit cell, whose points are shown by large "spheres"; the small spheres are located in the tetragonal positions, which can be connected by straight lines, which fully belong to the *P**-surface. (d) The model of an excluded volume. The boundary between the allowed and forbidden volumes is obtained by excluding rigid spheres of the radius r_{exc} located at the points of a bcc lattice. The allowed volume of the conduction-channel net is darkened.

potential

$$V_{ij}(r) = \begin{cases} 0, & \text{if } r > r_i + r_j \\ \infty, & \text{if } r \le r_i + r_j, \end{cases}$$

where r_i and r_j are the effective radii of rigid spheres approximating the *i* and *j* atoms. An important role in this model is played by the parameter $r_{exc} = r_i + r_j$, which, in the case of α-AgI, in a rough approximation, is the sum of the effective ionic radii of silver and iodine. The whole space is divided into an allowed volume, where ions can easily move, and a forbidden volume, where the motion is forbidden (Fig. 1d).

Now compare the approaches in which the analysis of the dynamical processes in α-AgI is based on the assumption that silver ions move along curvilinear trajectories—the models of equidistant zero-potential surfaces [9] and retarded rotational diffusion [5].

The former model states that the tetrahedral equilibrium positions of silver ions are located on the so-called *P**-surface of the zero potential (Fig. 1c). Here, the question about the existence of some preferential positions instead of a uniform ionic density distribution over the *P**-surface can arise.

Construction of the conduction channels in the model of retarded rotational diffusion begins with the comparison of extremum points (minima, maxima, and

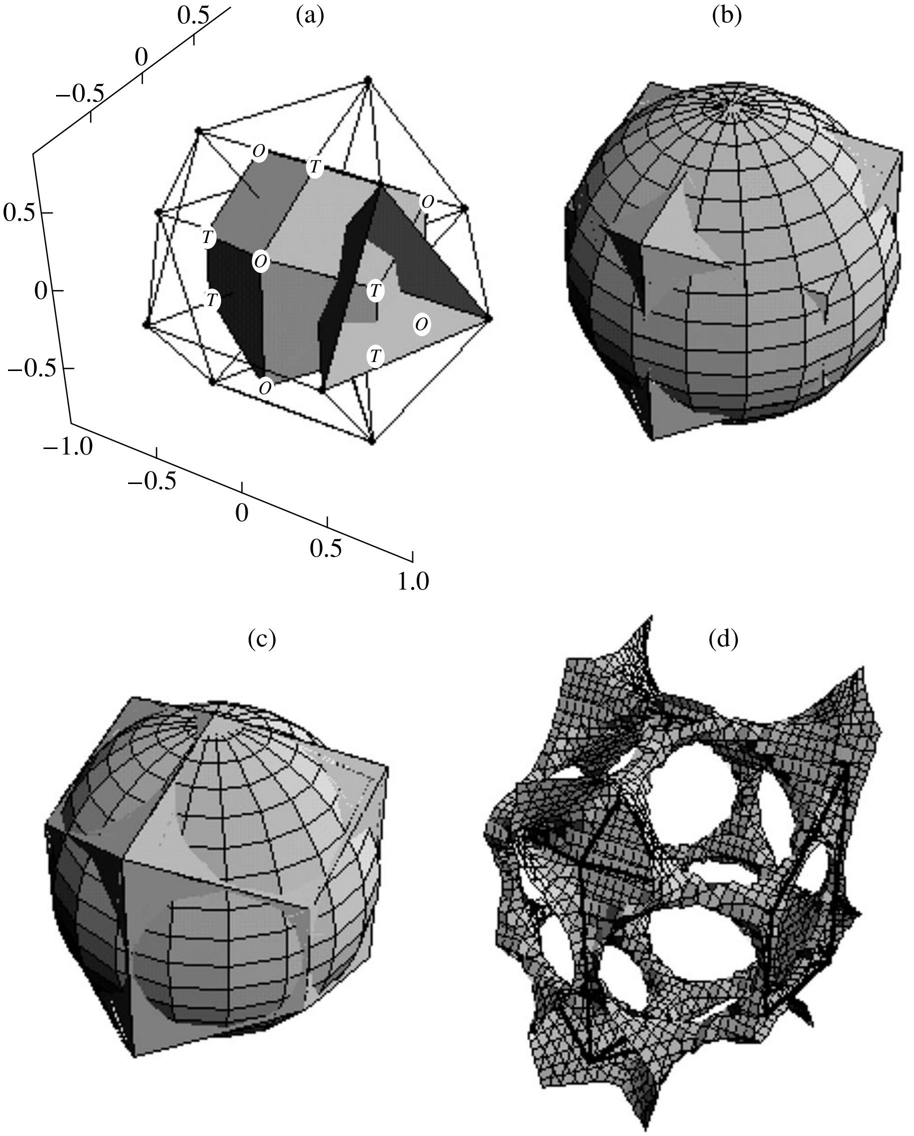

Fig. 2. Conduction channels in hcp solid electrolytes with immobile ions. (a) The coordination polyhedron (a hexagonal analog of a cuboctahedron) and a Voronoi–Dirichlet polyhedron with the vertices located in the centers of tetrahedral *T* and octahedral *O* cavities of the close packing of immobile ions. For more clear representation, the intersection of a symplectic tetrahedron with the Voronoi–Dirichlet polyhedron is shown. (b) Isolated domains of the allowed volume for β-AgI at 20°C ($r_{exc} \geq r_{face}$). (c) Junction of the allowed volumes with the formation of a net of conduction channels in the wurtzite structure at $r_{exc} = r_{face}$. (d) The allowance for nonrigidity of ion–ion interactions results in wrapping of the edges of Voronoi–Dirichlet polyhedra with conduction centers.

saddle points) on the ion path on the potential-energy surface and the Voronoi division of the immobile sublattice. The mobile-ion positions with the maximum stability are located in the vicinity of the vertices of the Voronoi–Dirichlet polyhedron. For the β-AgI electrolyte with the wurtzite structure possessing a conventional ionic conductivity, these positions are located in the centers of the tetrahedral and octahedral voids of the hexagonal close packing of anions (Fig. 2a). For silver-containing bcc electrolytes AgI, Ag_3SI, Ag_2S, and Ag_2Se, the Voronoi–Dirichlet polyhedron is a Fedorov cuboctahedron with the equilibrium Ag^+-positions at its vertices (Figs. 1a, 3a). For fcc conductors having the α-CuI electrolyte with cationic conductivity and fluorides with the fluorite MF_2 structure and anionic conductivity (M = Ca, Sr, Ba, and Pb), the Voronoi–Dirichlet polyhedron is a rhombododecahedron (Fig. 4a). However, the most stable mobile-ion positions are located at the rhombododecahedron vertices occupying the centers of tetrahedral voids of the immobile sublattice. In bcc-conductors, the saddle points on the potential-energy surfaces do not coincide with the *h*-positions (they are located close to the middle points of the edges), whereas in fcc-conductors, as will be seen from the further analysis, such saddle points located at the octahedral voids of the cubic close packing.

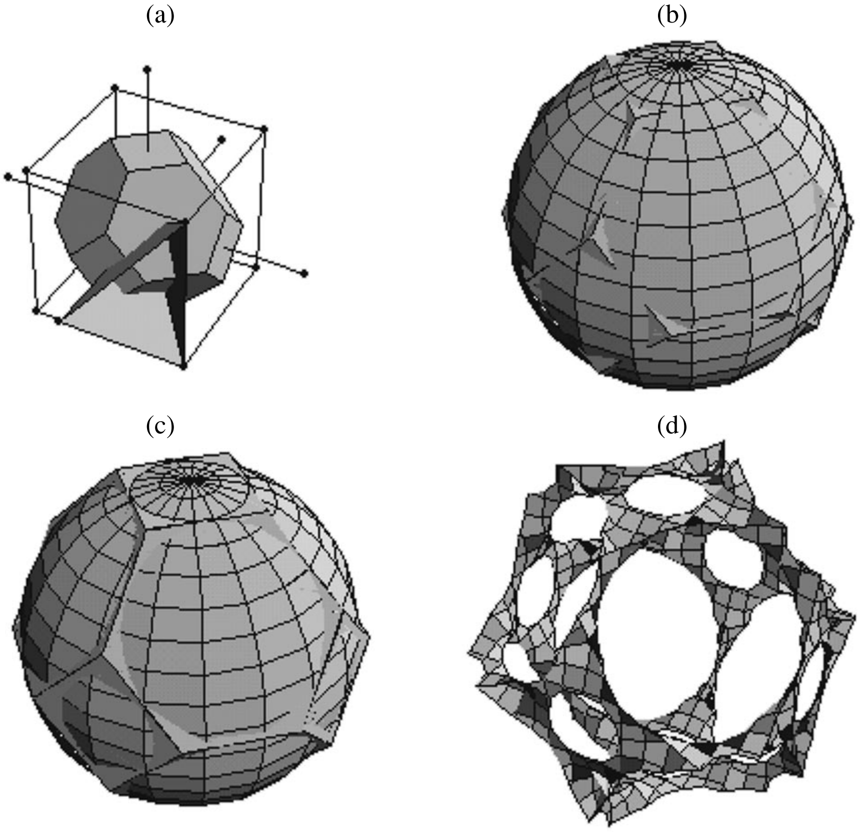

Fig. 3. Conduction channels in superionics with the body-centered cubic packing of immobile ions. (a) Fourteen nearest ions (8 + 6) of a chosen ion determine the Fedorov cuboctahedron. For a clearer presentation, the intersection of a symplectic tetrahedron with a Voronoi–Dirichlet polyhedron is shown. (b) Isolated domains of the allowed volume of a bcc lattice are shown at $r_{exc} > r_{face}$. (c) Junction of allowed volume into a net of conduction channels for α-AgI at 198°C ($r_{exc} \le r_{face}$). (d) Wrapping of the edges of Fedorov cuboctahedra with conduction channels caused by allowance for nonrigidity of ion–ion interactions.

The next step in the model construction is the determination of the intersecting circular orbits that describe the Voronoi–Dirichlet polyhedron and include the extremum points on the allowed migration path of ions. In α-AgI (Fig. 1b), each iodine ion is a center of three circular orbits located in mutually perpendicular faces of the unit cell statistically occupied by one silver ion. The orbits whose centers are located at neighboring iodine ions intersect over the whole electrolyte volume. This fact provides the electric current in the conduction channels in an applied external field—moving along the circular orbits, silver ions can move to the free orbits of the neighboring centers and continue the rotation along these new orbits, etc. The retarded rotation is explained by the necessity of overcoming a potential barrier in the change of one tetrahedral position to another. The numerical value of this barrier on the path of silver ion is equal to its activation energy.

The invocation of the second-order Jahn–Teller effect provides the unambiguous choice of the circular orbits. Using the symmetry rule relating the symmetry of the motion along the allowed path and the symmetry of molecular orbitals of the highest filled and the lowest empty energy levels of a local cluster consisting of a "mobile ion in the stable position" (or a "mobile ion in the saddle point") and "nearest counterions of the immobile sublattice."

The model of an excluded volume and the model of retarded rotational diffusion present two limiting cases of mobile-ion motion. The first model overestimates the role of the stochastic component of the motion, whereas the second one overestimates the regular component of the motion.

In the model of excluded volume, the ions move in the allowed volume of the anionic bcc-sublattice over the tetrahedral voids of α-AgI like a gas. The mobile Ag^+ ions are multiply scattered from the rigid spheres-anions until the moment when an Ag^+ cation attains a certain vicinity of a trigonal position located in the center of the face of a tetrahedron. Thus, the cation penetrates a neighboring tetrahedron, etc.

According to our model of retarded rotational diffusion, the bottleneck in the vicinity of the trigonal position in a conduction channel can be passed by silver easier if the ions move along the channel walls close to the edges of the Voronoi–Dirichlet polyhedron and are

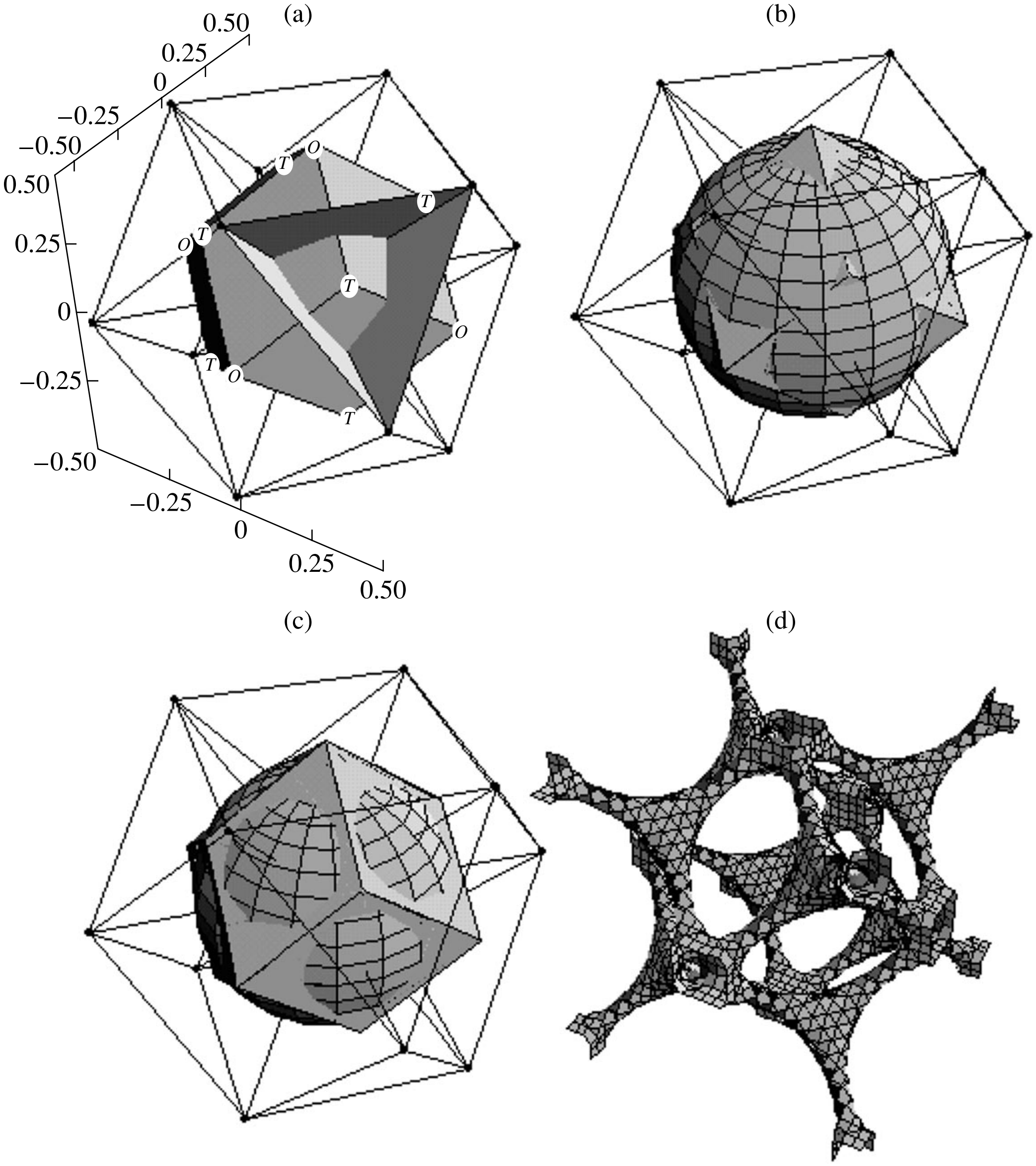

Fig. 4. Conduction channels in solid electrolytes with a fcc packing of immobile ions. (a) The edges of a coordination polyhedron (cuboctahedron) are divided into halves and are perpendicular to the faces of a Voronoi–Dirichlet polyhedron (rhombododecahedron) with the vertices lying at the centers of the tetrahedral *T* and octahedral *O* cavities for the fcc lattice. For clearer representation, the intersection of a symplectic tetrahedron with the Voronoi–Dirichlet polyhedron is shown. (b) Isolated domains of the allowed volume of an immobile fcc lattice are shown at $r_{exc} > r_{face}$. (c) Merging of allowed volumes into a net of conduction channels for α-CuI at 470°C ($r_{exc} \le r_{face}$). (d) Wrapping of the edges of rhombododecahedra with conduction channels caused by the allowance for nonrigidity of ion–ion interactions.

not multiply scattered from the walls in the motion within the whole bulk of the allowed region.

This conclusion on mobile-ion motion is based on the relation between the conduction channels and the Voronoi–Dirichlet polyhedra and, within the framework of the model of retarded rotational diffusion [5], is proved by the calculated structural and dynamical characteristics of superionic bcc-conductors AgI, Ag_3SI, Ag_2S, and Ag_2Se. The temperature dependencies of both mean-square distances between mobile ions and the ions of the immobile sublattice and diffusion coefficients are quantitatively consistent with the experimental data. Moreover, we also managed to explain the experimental fact that the motion of multivalent Cd^{2+} and In^{3+} impurities in bcc-modifications of Ag_2S, Ag_2Se, and Ag_3SI is similar, in many respects, to the motion of a monovalent Ag^+-ion [5].

METHOD OF CONSTRUCTION OF CONDUCTION CHANNELS

The walls of conduction channels are formed by the boundary surface between the allowed and forbidden volumes. An example of such a surface for the unit cell of α-AgI was obtained by the removal of the spheres of radii r_{exc} with the centers at the points of the bcc-sublattice of iodine ions (Fig. 1d).

We suggest here a simpler method for modeling allowed domains. Modeling the intersection of a Voronoi–Dirichlet polyhedron and a rigid sphere of the radius r_{exc} around this polyhedron provides the visualization of conduction channels (Figs. 2b, 2c, 3b, 3c, 4b, and 4c). Of course, this polyhedron can also be intersected by other rigid spheres with the centers located at neighboring points. The first sphere goes outside the polyhedron to the same extent as the neighboring spheres go inside this polyhedron. In other words, this method provides the visualization of the whole allowed volume per a Voronoi–Dirichlet polyhedron not intersected by a rigid sphere of the radius r_{exc}. The lower the value of r_{exc}, the more favorable the conditions for mobile-ion conduction. At a certain threshold value of the rigid-sphere radius r_{face}, no net of conduction channels can be formed in the electrolyte volume and, thus, no superionic conductivity is observed.

The temperature-dependent parameters r_{exc} and r_{face} determining the type of conduction channels in a superionic conductor are determined by optimizing the EXAFS data with the use of the model of excluded volume [1].

In such optimization, the Fourier transformed φ_{M-X} signal in the EXAFS method, where $\varphi_{M-X}(r) = \int_0^\infty d r_1/r_1^2 \rho_{M-X}(r_1)\xi_{M-X}(r-r_1)$, contains the function ξ (with a maximum, which is independent of crystal structure and temperature) and the pair-correlation function $\rho_{M-X}(r)$. Thus, all the variations of the function φ_{M-X} are due to the structure-dependent function ρ. This pair-potential function is approximated by the interaction of rigid spheres of the characteristic radius r_{exc}. It is then modified to allow for the weak flexibility of skeleton–skeleton interaction of spheres and the root-mean-square deviations of the ions in the rigid sublattice. In the final form, the contribution from the density function "mobile ion–immobile ion" has the form of a narrow Gaussian. Thus, fitting EXAFS-data in the model of an excluded volume, one obtains the optimized values of r_{exc} and r_{face} and some other parameters not discussed here. This provides the determination of the difference R between the experimental function $\varphi(r)$ and the model function $\varphi_m(r)$. Within the temperature range of existence of the superionic phase, this difference ranges from 0.6 to 2%.

Our method and the optimized values of r_{exc} and r_{face} allow us to determine the shape of conduction channels in superionics. Thus, r_{face} is the distance from the center of the face of symplectic tetrahedron of immobile ions (Figs. 2a, 3a, and 4a) to the vertices of this face, and if $r_{exc} \le r_{face}$, the allowed volume is, in fact, a simply connected domain. At the optimized values r_{exc} = 2.723 Å and r_{face} = 2.676 Å, the allowed volume in β-AgI at the temperature of 20°C [1] consists of isolated domains (Fig. 2b) and we observed the conventional ionic conductivity (if the condition $r_{exc} = r_{face}$ was fulfilled, the conduction channels would have had the shape shown in Fig. 2c). In α-AgI at 198°C, we have r_{exc} = 2.682 Å and r_{face} = 2.736 Å and the relation between r_{exc} and r_{face} is opposite to that for β-AgI. In this case, the conduction channels penetrate the whole electrolyte volume (Fig. 3c) and superionic conduction takes place. If $r_{exc} = r_{face}$, the allowed volume consists of isolated domains shown in Fig. 3b.

Our method allows the interpretation of the ionic conduction in the low-temperature phase γ-AgI with the sphalerite structure. The conductivity is close to conductivity in β-AgI. In all the three phases, the silver ion has tetrahedral environment and the Ag–I distances differ by less than 0.02 Å. Assuming that the r_{exc} values for the γ and the β phases, stable at lower temperatures, are equal, we arrive at isolated domains (see Figs. 2b, 4b). In the α-CuI superionic with the same fcc anionic sublattice, the optimized values r_{exc} = 2.44 Å and r_{face} = 2.53 Å at the temperature of 470°C lead to a net of conduction channels (see Fig. 4c) [10].

In Figs. 2b, 2c, 3b, 3c, 4b, and 4c we used the optimized values of r_{exc} and r_{face} and the rigid spheres. The next natural step is to admit that the spheres are not quite rigid and the root-mean-square deviations. These two factors affect the shape of the conduction channels.

The density of mobile ions is usually represented as the approximation of a step function by the error function [10].

If an ion of the rigid sublattice is located at the origin, the one-center ion density is related to the potential by the Boltzmann relationship $\rho(\mathbf{r}) = \rho_0\exp[-V(\mathbf{r})/k_B T]$. In the improved model [10], the one-center ion density is given by

$$\rho(\mathbf{r})/\rho_0 = \begin{cases} 1-\operatorname{erfc}(x)/2, & r > r_{exc} \\ \operatorname{erfc}(x)/2, & r \le r_{exc}, \end{cases}$$

where $x^2 = (r - r_{exc})^2/(2\varepsilon^2)$ and r_{exc} and ε are the model parameters. The multicenter density is obtained if one takes into account the effect of the nearest ions from the rigid sublattice [10]. The calculation of the function ρ shows that, first, the densities of mobile ions are localized at the potential minima in the vicinity of the vertices of the Voronoi–Dirichlet polyhedron and later merge into a net of conduction channels around the Voronoi–Dirichlet polyhedron (wraps it). Figures 2d, 3d, and 4d show the surfaces of the density of mobile ions corresponding to minimum of this function, which provides the connectedness over the whole electrolyte volume, i.e., the formation of the walls of the conduction channels.

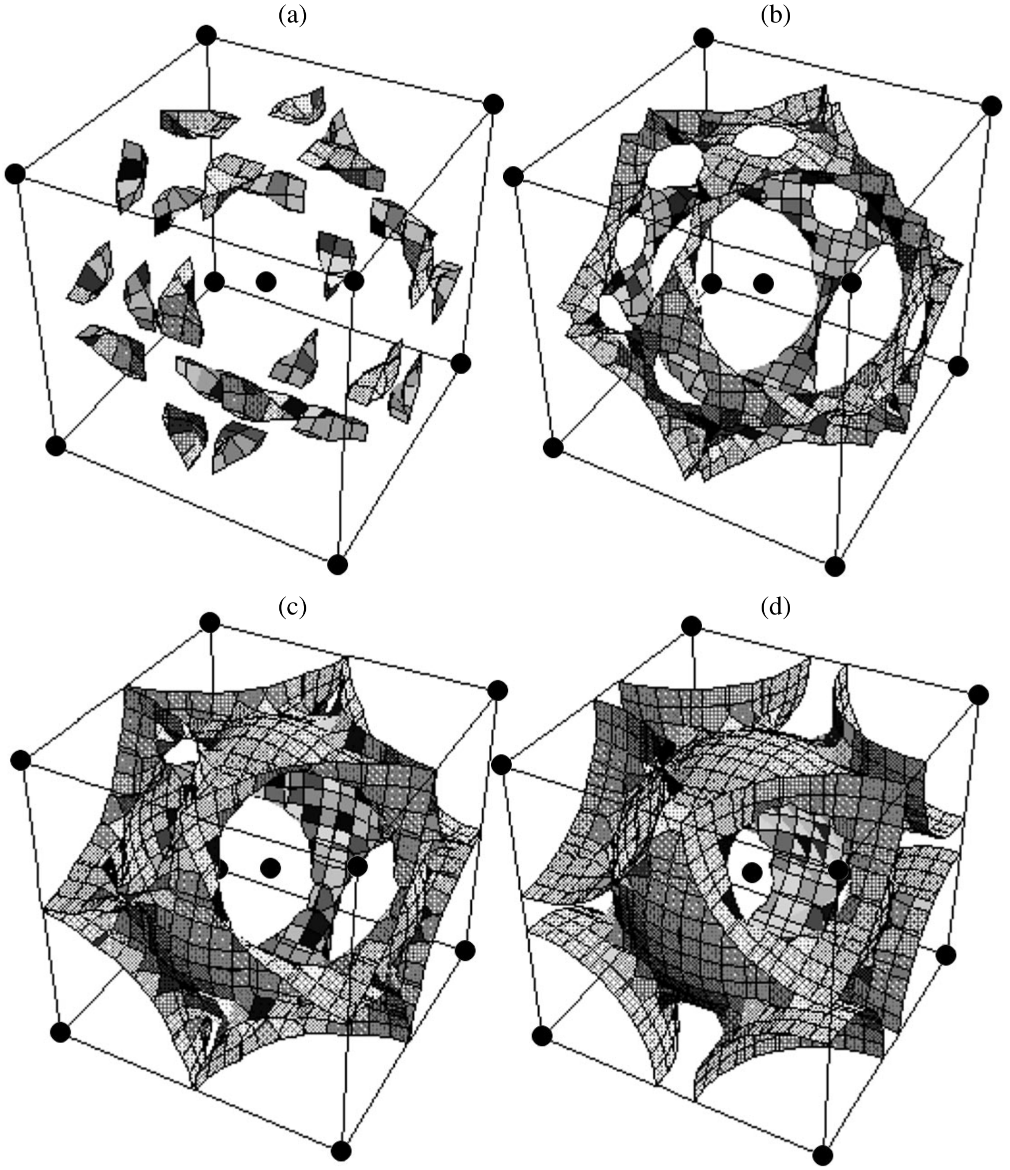

Fig. 5. Equipotential surfaces of Ag^+ motion in AgI. (a) Localization of the averaged Ag^+ density in the vicinity of tetrahedral positions at the potential energy lower than E_a. (b) Merging of the averaged density into a net of conduction channels with an increase of the potential energy to values higher than E_a. (c, d) Enlarging of the domains of motion for mobile ions with a further increase of the potential energy.

If one assumes that Figs. 3d and 4d really represent the regions of migration of mobile ions along the conduction-channel walls in α-AgI or α-CuI, then the discrepancies between the structural models become more understandable. In α-AgI, the regions of ion migration closely wrap the tetrahedral positions, but do not intersect them. These regions are extended in accordance with the model of displaced equilibrium positions [7]. In α-CuI, the conduction-channel walls wrap the tetrahedral positions and are located in the vicinity of the equilibrium positions displaced along ⟨111⟩, as was predicted by Bührer and Hälg [11].

CONDUCTION-CHANNEL WALLS AS REGIONS OF ION MOTION

The fact that conduction-channel walls play the role of regions of ion migration is confirmed by the calculations of the dynamical characteristics of AgI [5] and the interionic potential in α-AgI [12]. Figure 5 shows the surfaces of the interionic potential in AgI providing the motion of silver ion. The interionic potential is modeled as a parametric superposition of a lattice sum of the Lennard–Jones iodine–silver interaction potentials and the potential of a uniform charge distribution of silver ions acting inside a unit cell. The parameters of the

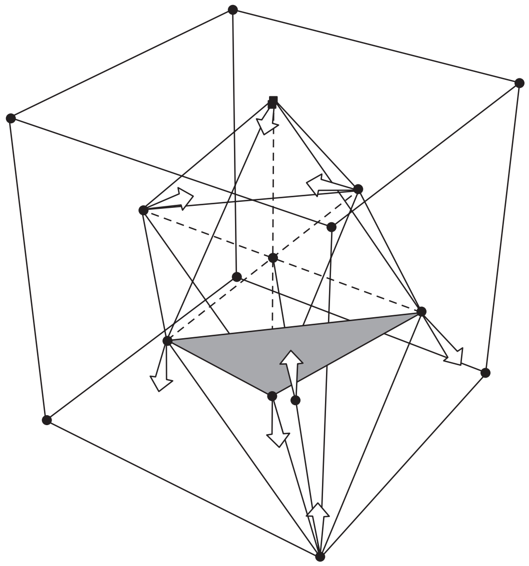

Fig. 6. Symmetry rules for the allowed trajectories of a mobile Cu^+-ion in α-CuI.

three-dimensional interionic potential are sought by optimization by the least squares method performed in a way to approach the one-dimensional effective iodine–silver potential in the modified EXAFS-method [13] independent of any restrictions imposed by structural models, in particular, the model of excluded volume. Calculation of the interionic potential is considered in detail elsewhere [14].

For energies lower than the activation energy E_a = 0.1 eV [1], the regions of Ag^+ migration are anisotropic and localized.

For energies close to E_a, the narrowest sites (Fig. 5b) coincide with the *h*-positions; the *b*-positions are first avoided but, at higher energies, are then filled with ions (Fig. 5c). At high energy values, there are no special positions for ion migration: the surface in Fig. 5d consists of external sections of intersecting spheres in the body-centered cubic lattice. Since the density of mobile ions is related to the potential by the Boltzmann relationship ($\rho(\mathbf{r}) = \rho_0 \exp[-V(\mathbf{r})/k_B T]$), the surfaces shown in Figs. 5a–5d correspond to the surfaces arranged in the order of decreasing density. For energies close to E_a, the motion regions first become larger (Fig. 5a) and, with the further energy increase, they merge and form a net of conduction channels (Fig. 5b).

In terms of the theory of absolute reaction rates [15], the set of equipotential surfaces (Fig. 5) specifies the transition to the superionic state characterized by minimum energy. The crystallochemical "wrapping" shape (Fig. 5b) corresponds to the saddle point on a multidimensional potential surface.

The minimum-energy path is a path in a bcc unit cell along which a silver ion moves without friction from one tetrahedral equilibrium position to another via a saddle point in the vicinity of a trigonal position. In other words, this path provides the transition of the system into the superionic state with the minimum energy loss. It is worth noting that the surfaces in Figs. 1d, 3d, and 5b obtained by different reasonings lead to the same picture of mobile-ion motion and show an important role of conduction-channel walls, which are, in fact, the motion regions related to the Voronoi–Dirichlet polyhedra.

SYMMETRY RULES AND MOTION REGIONS FOR MOBILE IONS IN α-CUI

Structural studies of the superionics with the rigid fcc sublattice with anionic and cationic conductivity show that the octahedral position is not occupied. Mobile ions only migrate in the vicinity of this position [16], but do not enter it (Fig. 4d). Within the framework of the model of excluded volume, this conclusion seems to be quite surprising because, from the crystallographic standpoint, the octahedral position is the most favorable.

We consider this situation on an example of α-CuI with the invocation of the second-order Jahn–Teller effect [17], successfully used earlier on α-AgI [5].

Let us single out a tetrahedral and an octahedral fragments sharing the face (Fig. 6). Being alternately located at the centers of the faces of these polyhedra, a mobile Cu^+ ion forms the $[CuI_4]^{3-}$ and $[CuI_6]^{5-}$ local clusters. It is known from the theory of ligand fields that tetrahedral and octahedral complexes with π-ligands have higher filled and lower empty energy levels with the symmetries $\Gamma_{\mathrm{HFMO}} = t_2$ and $\Gamma_{\mathrm{LEMO}} = a_1$ for $[CuI_4]^{3-}$ and $\Gamma_{\mathrm{HFMO}} = e_g$ and $\Gamma_{\mathrm{LEMO}} = t_{1u}$ for $[CuI_6]^{5-}$. The symmetry rules $\Gamma_{\mathrm{HFMO}} \otimes \Gamma_{\mathrm{LEMO}} \supset \Gamma_{\mathrm{Q}}$ [17] define the possible types of the symmetry Γ_{Q} for the oscillatory coordinate, along which the tetrahedron (with $t_2 \otimes a_1 = \mathrm{T}_2$) and octahedron (with $e_g \otimes t_{1u} \supset \mathrm{T}_{1u}$) are distorted as a result of the spontaneous process. Possible distortions of the tetrahedron and octahedron in the oscillatory coordinates for the T_2 and T_{1u} symmetries are shown in Fig. 6. It is seen that the displacements of copper and iodine ions are correlated and that their point group C_{3V} is preserved irrespectively of distortion of local clusters.

If one assumes that the transient state is implemented at the center of the octahedral void, the following contradiction arises. A degenerate oscillation mode T_{1u} corresponds to several allowed paths from the initial tetrahedral position to the free ones; this is seen from Fig. 4d. However, to each transient state there corresponds only one path: "a saddle can only connect two valleys" [17]. Hence, the transient state corresponds to lowering of the octahedral symmetry to the C_{3V}. The same symmetry is possessed by the local ionic configuration at conventional (not extremum) points on the ion paths (Fig. 6). According to the symmetry rules [17], this oscillation mode is completely symmetric. It follows from the table for irreducible representations of the C_{3V} group that the T_{1u} representation becomes fully symmetric. This exhausts the consideration of allowed ion paths.

REFERENCES

1. J. B. Boys and T. M. Hayes, in *Physics of Superionic Conductors*, Ed. by M. B. Salamon (Springer-Verlag, Berlin, 1979; Zinatne, Riga, 1982).
2. S. M. Shapiro and F. Reidinger, in *Physics of Superionic Conductors*, Ed. by M. B. Salamon (Springer-Verlag, Berlin, 1979; Zinatne, Riga, 1982).
3. H. U. Beyeler, P. Brüesch, L. Pietronero, *et al.*, in *Physics of Superionic Conductors*, Ed. by M. B. Salamon (Springer-Verlag, Berlin, 1979; Zinatne, Riga, 1982).
4. T. Geisel, in *Physics of Superionic Conductors*, Ed. by M. B. Salamon (Springer-Verlag, Berlin, 1979; Zinatne, Riga, 1982).
5. V. I. Polyakov, Zh. Fiz. Khim. **71** (7), 1248 (1997); **72** (11), 2002 (1998); **72** (12), 2247 (1998).
6. L. W. Strock, Z. Phys. Chem., Abt. B **25**, 441 (1934); **31**, 132 (1936).
7. W. Bührer and W. Hälg, Helv. Phys. Acta **47**, 27 (1974).
8. R. J. Cava, F. Reidinger, and B. J. Wuensch, Solid State Commun. **24**, 411 (1977).
9. H. G. Schnering and R. Nesper, Angew. Chem. Int. Ed. Engl. **26**, 1059 (1987).
10. J. B. Boyce, T. M. Hayes, J. C. Mikkelsen, *et al.*, Solid State Commun. **33**, 183 (1980).
11. W. Bührer and W. Hälg, Electrochim. Acta **22**, 701 (1977).
12. Y. Kaneko, A. Ueda, and Y. Hiwatari, J. Phys. Soc. Jpn. **55** (4), 1244 (1986).
13. G. Dalba, P. Fornasini, R. Gotter, *et al.*, Philos. Mag. B **71** (4), 751 (1995).
14. V. I. Polyakov, Zh. Fiz. Khim. **73** (9), 1601 (1999).
15. S. Glasstone, K. J. Laidler, and H. Eyring, *Theory of Rate Processes* (McGraw-Hill, New York, 1941; Inostrannaya Literatura, Moscow, 1948).
16. R. Bachmann and H. Schulz, Solid State Ionics **9/10**, 521 (1983).
17. R. Pearson, *Symmetry Rules for Chemical Reactions* (Academic, New York, 1976; Mir, Moscow, 1979).

Translated by V. Chechin

Crystallography Reports, Vol. 46, No. 3, 2001, pp. 444–449. Translated from Kristallografiya, Vol. 46, No. 3, 2001, pp. 494–499.
Original Russian Text Copyright © 2001 by Bashirov.

LATTICE DYNAMICS

Spontaneous Break of Symmetry in Molecular Crystals

F. I. Bashirov
Physics Department, Kazan State University, Kremlevskaya ul. 18, Kazan, 420008 Tatarstan, Russia
e-mail: fbashir@ksu.ru

Received February 17, 1999

Abstract—The structural dissymmetry of crystals with coordinated groups of atoms performing some motion in the crystal is described in terms of the theory of hindered molecular motion based on the dynamic principles of invariance for the extended angular jump model. The spontaneous break of the symmetry in the ordered ammonium chloride phase is discussed with the invocation of the proton-relaxation data. *© 2001 MAIK "Nauka/Interperiodica".*

INTRODUCTION

Electromagnetic and neutron diffraction spectroscopies are widely used for experimental studying hindered molecular motion in condensed media. Usually, the results obtained are interpreted in terms of the geometric principles of the invariance of the autocorrelation-function of lattice variables [1–7]. A considerable progress in the theories of decelerated molecular motion for crystals was attained due to the description of the motion symmetry with the aid of the finite groups of rotation [4–7]. The theory [8], which takes into account for the effect of the crystalline environment on the hindered molecular motion was developed with the use of the dynamic principles of invariance. The present study was undertaken with the aim to apply the theory [8] to the quantitative description of the spontaneous symmetry break in molecular and ionic–molecular crystals.

THE DYNAMIC SYMMETRY OF THE HINDERED MOLECULAR MOTION

In liquids and solids isolated from the effect of any external factors, most of the molecules, their ions, and fragments are mainly in the ground electronic, vibration, and rotational states. For a molecule with several configurational equilibrium states separated by infinitely high energy barriers, the classical probability to escape from the potential well is zero and the ground state of this molecule is degenerate. The degeneracy multiplicity equals the number of equilibrium molecular configurations, which is equal to the order σ of the abstract (geometric) point symmetry group G, which describes the molecule motion [9–12]. If some of the molecule configurations are equivalent, the degeneracy is partly lifted. For nonequivalent molecular configurations, the degeneracy is completely lifted. The splitting value depends on the potential-well depth and the inertia of the molecule.

Within the framework of the theory of representations, the symmetry groups, each irreducible representation Γ_α of the group G of molecular motion can be brought in correspondence to a "hindered state" of the molecule. Since the classical motion is described by scalar perturbation operators not leading to the mixing of molecular states of different symmetries at mechanical interchange of the nuclei, these states are the motion invariants. Then, the statistical weight (probability) of the hindered state is equal to a fraction of the molecular quantity transforming according to the given irreducible representation. Neglecting the effect of nuclear spin isomerism at temperatures not too low ($T > 40$ K), we also neglect the symmetry of the nuclear spin states (i.e., the statistical nuclear weight) [11]; thus, the weight of a certain state $\langle\alpha|$ equals the dimension μ_α of the irreducible representation corresponding to this state [12]. Then the total weight of all the states equals the weight of the reducible (at the point group) representation $D^{(\nu)}$ of the rank ν of the continuous symmetry group O^{3+} of the three-dimensional rotation

$$\sum_\alpha \mu_\alpha = 2\nu + 1, \tag{1}$$

whereas the weight $q_\alpha^{(\nu)}$ of the state $\langle\alpha, \nu|$ normalized to unity equals

$$q_\alpha^{(\nu)} = \mu_\alpha/(2\nu + 1) \equiv \chi_{\alpha E}/(2\nu + 1), \tag{2}$$

$$\sum_\alpha q_\alpha^{(\nu)} = 1, \tag{3}$$

where $\chi_{\alpha E}$ is the character of the identity element.

Evidently, the above reasoning holds only if the order of the symmetry group of the molecule position is not lower than the order of the symmetry group of the molecule motion. Usually, such a situation takes place for liquids and the plastic phases of molecular crystals. In the ordered phase of molecular crystals, the symmetry of the molecule position can be lower than the symmetry of hindered molecular motion. As a result, the symmetry of the motion is distorted. In accordance with the Neumann principle [13], this phenomenon is called the symmetry break or dissymmetrization. In terms of the group theory, the break of the motion symmetry by the "position symmetry" can be identified with the deformation of the space of representations. The distortion of the abstract point symmetry group can be taken into account by attributing to the weights $q_\alpha^{(\nu)}$ the values of the current parameters, which, in general, can vary within the range $0 \le q_\alpha^{(\nu)} \le 1$. At the same time, the individual events of molecular motion are brought into correspondence with the symmetry elements and the characters of the representations of the initial (undistorted) group G. As a result, the magnitude and the sign of the deviations of the weights $q_\alpha^{(\nu)}$ from their values calculated by Eq. (2) provide the allowance for the effect of the symmetry of position on the transformation properties of the basis functions of the group of motion and, thus, also on the transformation properties of molecular quantities usually represented in the form of expansions in their basis functions.

According to Wigner [14], the above properties of the symmetry of hindered molecular motion can be interpreted as the manifestation of a natural law of invariance of the molecular motion related to the symmetry of the molecule interaction with its environment. Thus, the symmetry group of molecular motion in the deformed configurational space can be called the dynamic point symmetry group and the normalized weights $q_\alpha^{(\nu)}$ of the irreducible representations, the dynamic weights of the hindered states. In the limiting case of the undistorted geometry, the dynamic weights $q_\alpha^{(\nu)}$ are specified by Eqs. (2) (i.e., they are equal to the weights of irreducible representations of the abstract point symmetry group). In other words, they acquire the physical sense of the statistical weights of hindered states.

ORIENTATIONAL AUTOCORRELATION FUNCTIONS

In molecular spectroscopy, the theoretical interpretation of the experimental data is made in terms of the calculated autocorrelation functions of the unit spherical tensors, whose explicit form is specified by the model of the random local molecular motion. It was found that for liquids, a sufficiently adequate model is that of rotational diffusion [2, 3, 15]. In solids, molecular motion is usually represented in the form of angular jumps of rigid molecules over the fixed orientational equilibrium states (the so-called model of fixed angular jumps) [5, 6, 16]. Taking into account that many physical characteristics of molecular liquids are similar to those of molecular solids, one could expect that in the limiting case of transition from solids to liquids the theories of hindered molecular motion would have given identical results. However, all the alternative models proved to be mutually exclusive.

This situation gave an impetus to development of a certain intermediate model of the local molecular motion [4]. Because of the ordered local environment of molecules in condensed media, the stable orientations of molecules (and, hence, of the molecular vectors) are fixed. The thermal perturbations with the energy insufficient for overcoming the free rotation barrier "spread" the vector orientations within the potential wells produced by the crystalline field of the environment. An event of molecular motion is considered as having taken place if at least one of the vectors had passed from one potential well to another. If the vector reorientation brought a molecule into coincidence with itself, the transformation is called the identical transformation. Since the model combines the discreteness of the rotation angles and the continuity of the admitted angular equilibrium states, it is given the name of the extended angular-jump model [8]. The model of the rotational diffusion in the potential field of the environment in the crystal seems to be a modified version of the above model [7].

The solution of the statistical problem of hindered molecular motion within the framework of the extended angular jump model is given in [8]. For single crystals, the autocorrelation function of the spherical unit tensors is expressed in the analytical form as a linear combination of the exponents $\exp\left(-\frac{t}{\tau_\alpha}\right)$ with the coefficient dependent on the polar, θ, and the azimuthal, ε, angles of the orientation of the principal symmetry axis of the molecule in the axially symmetric laboratory system of coordinates:

$$K_m^{(\nu)}(q_\alpha^{(\nu)}, \tau_\alpha, \varepsilon, \theta, t) = \frac{2\nu+1}{4\pi}\sum_{\alpha=1}^{3}\sum_{l=0}^{\nu} q_\alpha^{(\nu)} a_{\alpha l m}^{(\nu)}(\varepsilon)\cos^{2l}\theta\exp\left(-\frac{t}{\tau_\alpha}\right), \tag{4}$$

where τ_α are the symmetrized correlation times. The superscript ν and subscript m indicate the rank and the ordinal number of the autocorrelation-function component sought; the subscripts α and l indicate the ordinal numbers of the irreducible representation Γ_α of the point group G and of spherical-harmonic component $Y_l^{(\nu)}(g)$, in which the basic functions $\Psi_{\alpha\beta}^{(\nu)}(g)$ are expanded [17]. The values of the coefficients $a_{\alpha l m}^{(\nu)}(\varepsilon)$ calculated for some groups of cubic and hexagonal–trigonal systems, where $\nu = 2$, are given in Table 1. For polycrystals, Eq. (4) is reduced to the form

$$K_m^{(\nu)}(q_\alpha^{(\nu)}, \tau_\alpha, t) = \frac{\delta_{mm}}{4\pi}\sum_{\alpha=1}^{3} q_\alpha^{(\nu)}\exp\left(-\frac{t}{\tau_\alpha}\right). \tag{5}$$

Table 1. Coefficients $a_{\alpha l m}^{(2)}(\varepsilon)$ specifying the explicit form of the second-rank autocorrelation functions for the cubic and the hexagonal–trigonal systems

Crystallographic system	ε	l	0	1	2
		m	$\alpha = 1$		
Cubic	ε	0	$(1/8)(1 + 3\cos^2 2\varepsilon)$	$-(3/4)(1 + \cos^2 2\varepsilon)$	$(3/8)(3 + \cos^2 2\varepsilon)$
		1	$(1/4)(1 - \cos^2 2\varepsilon)$	$(1/2)(1 + \cos^2 2\varepsilon)$	$-(1/4)(3 + \cos^2 2\varepsilon)$
		2	$(1/16)(3 + \cos^2 2\varepsilon)$	$-(1/8)(1 + \cos^2 2\varepsilon)$	$(1/16)(3 + \cos^2 2\varepsilon)$
	0 or π/2	0	1/2	–3/2	3/2
		1	0	1	–1
		2	1/4	–1/4	1/4
	π/4	0	1/8	–3/4	9/8
		1	1/4	1/2	–3/4
		2	3/16	–1/8	3/16
Hexagonal–trigonal	ε	0	3/8	–3/4	3/8
		1	1/4	0	–1/4
		2	1/16	3/8	1/16
Crystallographic system	ε	l	0	1	2
		m	$\alpha = 2$		
Cubic	ε	0	$(1/4)(1 - \cos^2 2\varepsilon)$	$(1/2)(1 + \cos^2 2\varepsilon)$	$-(1/4)(3 + \cos^2 2\varepsilon)$
		1	$(1/6)(1 - \cos^2 2\varepsilon)$	$-(1/3)(1 + \cos^2 2\varepsilon)$	$(1/6)(3 + \cos^2 2\varepsilon)$
		2	$(1/24)(5 - \cos^2 2\varepsilon)$	$(1/12)(1 + \cos^2 2\varepsilon)$	$-(1/24)(3 + \cos^2 2\varepsilon)$
	0 or π/2	0	0	1	–1
		1	0	–2/3	2/3
		2	1/6	1/6	–1/6
	π/4	0	1/4	1/2	–3/4
		1	1/6	–1/3	1/2
		2	5/24	1/12	–1/8
Hexagonal–trigonal	ε	0	0	3/2	–3/2
		1	1/4	–3/4	1
		2	1/4	0	–1/4

The times τ_α are written as

$$\tau_\alpha = \left(1 - \chi_{\alpha E}^{-1}\sum_i p_i \chi_{\alpha i}\right)^{-1}\tau, \qquad (6)$$

where τ is the average time between two subsequent events of motion, p_i are the probabilities of the occurrence of individual events, and $\chi_{\alpha i}$ and $\chi_{\alpha E}$ are the characters of the ith and the identity classes. The time τ obeys the Arrhenius relationship [16]:

$$\tau = \tau_0 \exp(E_a/RT), \qquad (7)$$

where E_a is the height of the energy barrier of activation of hindered molecular motion averaged over the group of motion and τ_0 is the average time between two successive attempts of overcoming the barrier.

Contrary to the autocorrelation functions derived earlier [1–7], those given by Eqs. (4) and (5) contain new dynamic parameters $q_\alpha^{(\nu)}$—the dynamic weights of the hindered states of a molecule. These parameters take into account the effect of the environment (the position symmetry) upon the transformational properties of the molecular variable. In turn, the dynamic weights $q_\alpha^{(\nu)}$ in the autocorrelation functions allows one to establish the position symmetry of the molecule from the experimental values of these functions.

Figure 1 shows the amplitudes of the second-rank autocorrelation functions $K_0^{(2)}(q_1, \theta, t = 0)$ as a function of one of the dynamic weights $q_1 = q_1^{(2)}$ and the polar angle θ for molecules whose motion is described by the point symmetry, which is described either by the

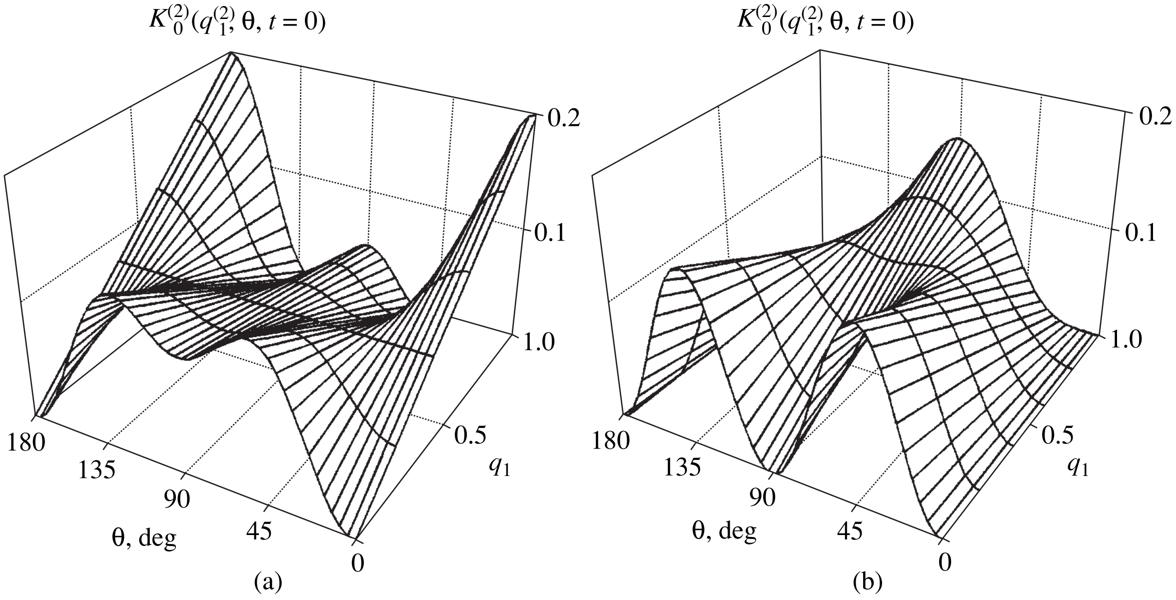

(a) (b)

Fig. 1. The dependence of the amplitudes of the second-rank autocorrelation functions $K_0^{(2)}(q_1, \theta, t = 0)$ on the orientation angle θ of the principal symmetry axis of the molecule in the axially symmetric laboratory coordinate system and the dynamic weight q_1 of the two-dimensional irreducible representation for the symmetry group of the hindered molecular motion in (a) the cubic ($\varepsilon = \pi/4$) and (b) the hexagonal–trigonal (arbitrary ε) systems.

groups of the cubic (Fig. 1a, $\varepsilon = 45°$) or the hexagonal–trigonal (Fig. 1b) systems. The variable q_1 corresponds to the dynamic weight of the two-dimensional irreducible representation for the cubic groups or to one of the two two-dimensional representations of the trigonal or the hexagonal groups. The straight line parallel to θ-axis in Fig. 1a corresponds to the isotropic amplitude of the autocorrelation function for the dynamic weight equal to the statistical weight $q_1 = 0.4$. If the position symmetry deviates from the cubic symmetry ($q_1 \neq 0.4$), the autocorrelation function becomes the anisotropic second-rank function in full accordance with the Neumann principle [13]. The tetragonal and the trigonal distortions of the position symmetry correspond to the q_1-values ranging within $0 < q_1 < 0.4$ and $0.4 < q_1 < 1$, respectively. This conclusion follows from the comparison between the characters of two second-rank irreversible representations of the cubic groups [10].

For the remaining symmetry groups describing the motion of molecules, the amplitudes of the second-rank autocorrelation functions are always anisotropic, but the anisotropy of the amplitudes is independent of the azimuthal angle ε. The form of the anisotropy for the hexagonal and the trigonal groups is illustrated by Fig. 1b. For the sake of definiteness, the weight of the identity representation is taken to be $q_0 = 0$.

STRUCTURAL DISSYMMETRY IN AMMONIUM CHLORIDE

Ammonium chloride has the CsCl-type body-centered cubic structure. Below 242.9 K, the crystal is in the ordered phase. In this phase, the "hard" ammonium ions perform a local motion in the form of random rotations, which, however, does not change the ordered structure of the whole crystal; in other words, this ion motion is described by the symmetry group of a tetrahedron, *T*. This motion modulates the magnetic interaction between protons and, thus, provides the efficient channel for nuclear magnetic relaxation. As the distance between the centers of the closest ions exceeds the interprotonic distance inside the ions by a factor of 2.25, the intermolecular contribution to the relaxation is small. Therefore, one can assume that the relaxation occurs by the intramolecular mechanism. The protonic magnetic relaxation in a NH_4Cl crystal in terms of the theory of hindered molecular motion (used as the basic one for the theory developed in our study) was discussed in [4].

In the case of the cubic symmetry of motion, it is convenient to use the simplified expression for the relaxation rate corresponding to the azimuthal angle $\varepsilon = 45°$ of the crystal orientation in the external axial magnetic field to extract the data on the dynamics of the hindered molecular motion. Within the Redfield theory of nuclear magnetic relaxation [1], the calculated formula for the relaxation rate of the protons in NH_4Cl in the rotating coordinate system has the form

$$T_{1\rho}^{-1} = \frac{27}{32}\gamma^4\hbar^2 b^{-6}\left[q_1\tau_1\frac{(1-3\cos^2\theta)^2}{1+(2\omega_1\tau_1)^2} + 2q_2\tau_2\frac{1+2\cos^2\theta-3\cos^4\theta}{1+(2\omega_1\tau_2)^2}\right]. \quad (8)$$

Table 2. Experimental and theoretical proton spin-lattice relaxation times $T_1^{(\min)}$ and $T_{1\rho}^{(\min)}$ determined at the minimum of their temperature dependences for crystalline ammonium chloride

θ, deg	ν_0, MHz	$T_1^{(\min)}$, μs		B_1, mT	$T_{1\rho}^{(\min)}$, μs		Dynamic weights
		experiment ±5%	theory		experiment ±10%	theory	
0	14	2.78	2.76	3.26	170		$g_1 = 0.25$
54	14	2.88	2.93	3.26	89		$g_2 = 0.73$
90	14	2.85	2.88	3.26	100	101	
Polycrystals	14	2.79	2.85	3.26	100	108	
Polycrystals	14			1.61	53.6	53.3	

Note: The angles θ = 0°, 54°, and 90° correspond to three main orientations, [1, 0, 0], [1, 1, 1], and [1, 1, 0], of an NH_4Cl single crystal in a constant magnetic field.

This formula is obtained under the condition of slow motion of NH_4^+ ions in the laboratory coordinate system using Eq. (4) and the coefficients $a_{\alpha lm}^{(2)}(\varepsilon)$ for cubic groups given in Table 1 for $\varepsilon = \pi/4$.

We used the following standard rotation: $\omega_1 = \varphi B_1$ is the resonance frequency in the rotating coordinate system, γ is the nuclear gyromagnetic ratio, $\hbar$ is Planck constant, b is the interprotonic distance, and θ is the polar angle between the principal symmetry axis of the NH_4Cl cube and the induction vector of an external magnetic field. We also introduced the variables τ_1, τ_2, q_1, and q_2 ($q_2 = 1 - q_1$) to denote the correlation times and the dynamic weights symmetrized according to the two-dimensional E (for τ_1 and q_1) and the three-dimensional F (for τ_2 and q_2) irreducible representations of the group T. The times τ_α ($\alpha = 1, 2$) are related to the average time τ between two successive reorientations of NH_4^+-ions by Eq. (6), where the subscript i corresponds to the E, C_2, and C_3 classes of the point symmetry group of a tetrahedron [10].

Table 2 lists the values of the relaxation times and dynamic weights, calculated by Eq. (8) along with the experimental data given in [4] for the temperature minima T_1 and T_ρ in an NH_4Cl single crystal calculated under the assumption that the symmetrized correlation times are approximately equal, i.e., that $\tau_1 = \tau_2 = \tau$. The calculations were performed by the following scheme: first, the theoretical dynamic weights were calculated from the experimental $T_{1\rho}^{(\min)}$ values for two different orientations of the single crystal (Table 2). These values are $q_1 = 0.25$ and $q_2 = 0.73$. Then these values were used to calculate all the other $T_{1\rho}^{(\min)}$ and $T_1^{(\min)}$ values for a single crystal and a polycrystal. Comparing the values $q_1 = 0.25 < 0.4$ and $q_2 = 0.73 > 0.6$ with the results of the theory of hindered molecular motion with due regard for the symmetry of the local motion of the coordinated groups, we made a conclusion on the tetragonal distortion in the position symmetry of the NH_4^+ ions in the ordered phase of the NH_4Cl crystal.

Moreover, using Eqs. (6) and (7), the tabulated values of the characters of the group of a tetrahedron [10], and the minimum values of the relaxation times for a single crystal, it is possible to determine the probabilities of the individual (for various classes) rotations. These are $p(E) = 0.083$ (0.083), $p(C_3) = 0.697$ (0.667), and $p(C_2) = 0.22$ (0.25) the probable classes for an ideal tetrahedral symmetry of motion are given in parentheses). Using Eq. (6), we can establish the quantitative relation between the symmetrized correlation times τ_α and the average time τ between two successive reorientations of the NH_4^+- ion in the ordered NH_4Cl phase. We have $\tau_1 = 0.96\tau$, and $\tau_2 = 1.01\tau$. The latter result justifies the above assumption on approximate equality of symmetrized correlation times τ_1 and τ_2.

CONCLUSIONS

In the course of editing this paper, publications on the use of the theory of hindered molecular motion in the description of the dielectric spectra [18] and experimental line broadening in the Raman, the Rayleigh scattering, and the IR [19, 20] spectra of molecular crystals and liquids had appeared. Of course, these are only some of the possible useful applications of the theory, which takes into account the dynamic properties of the symmetry and hindered molecular motion. The method of determination of the dynamic group and the group proper can be used in numerous cases. The introduction of hindered states classified by irreducible representations for the classical molecular motion provides an exhaustive description of the effect of hindered molecular motion on the molecular variables, which, in turn, opens new information possibilities of the spectroscopic techniques. The use of the dynamic principles of invariance instead of the geometric ones in the condensed matter physics can also be useful for developing a unified theoretical approach for studying not only hindered molecular motion but also tunnel transitions and proton exchange in such transitions.

REFERENCES

1. A. Abragam, *The Principles of Nuclear Magnetism* (Clarendon Press, Oxford, 1961; Inostrannaya Literatura, Moscow, 1963).
2. K. A. Valiev and L. D. Éskin, Opt. Spektrosk. **12**, 758 (1962).
3. E. N. Ivanov, Zh. Éksp. Teor. Fiz. **45**, 1509 (1963) [Sov. Phys. JETP **18**, 1041 (1963)].
4. F. I. Bashirov, Yu. L. Popov, K. S. Saĭkin, and R. A. Dautov, Zh. Éksp. Teor. Fiz. **62** (5), 1803 (1972) [Sov. Phys. JETP **35**, 937 (1972)].
5. P. Rigny, Physica (Amsterdam) **59**, 707 (1972).
6. E. N. Ivanov, J. Stat. Phys. **8** (2), 177 (1973).
7. M. Bée, Mol. Phys. **47**, 83 (1982).
8. F. I. Bashirov, *Proceedings of the XXVII Ampére Congress on Magnetic Resonance and Related Phenomena, Kazan, 1994*, Vol. 1, p. 282.
9. K. Tomita, Phys. Rev. **89** (2), 429 (1953).
10. L. D. Landau and E. M. Lifshitz, *Course of Theoretical Physics,* Vol. 3: *Quantum Mechanics: Non-Relativistic Theory* (Fizmatgiz, Moscow, 1963; Pergamon, New York, 1977).
11. *Introductory Essays Presented as Lectures at the 4th Waterloo International Summer School on Nuclear Magnetic Resonance, Univ. of Waterloo, 1975*, Ed. by M. M. Pintar (Springer-Verlag, Berlin, 1976), MNR **13**, 125 (1976).
12. R. S. Knox and A. Gold, *Symmetry in the Solid State* (Benjamin, New York, 1964; Nauka, Moscow, 1970).
13. J. F. Nye, *Physical Properties of Crystals: Their Representation by Tensors and Matrices* (Clarendon Press, Oxford, 1964; Mir, Moscow, 1967).
14. E. P. Wigner, Phys. Today **17**, 34 (1964) [Usp. Fiz. Nauk **83**, 729 (1964)].
15. P. Debye, *Polar Molecules* (Chemical Catalog Co., New York, 1929; Gostekhizdat, Moscow, 1934).
16. Ya. I. Frenkel, *Kinetic Theory of Liquids* (Akad. Nauk SSSR, Moscow, 1959), Vol. 3.
17. A. M. Leushin, *Tables of Functions Transformed by Irreducible Representations of Crystallographic Point Groups* (Nauka, Moscow, 1968).
18. F. I. Bashirov, Eur. Phys. J.: Appl. Phys. **8**, 99 (1999).
19. F. I. Bashirov, Mol. Phys. **91**, 281 (1997).
20. F. I. Bashirov and N. K. Gaisin, J. Raman Spectrosc. **29**, 131 (1998).

Translated by A. Zolot’ko

Crystallography Reports, Vol. 46, No. 3, 2001, pp. 450–455. Translated from Kristallografiya, Vol. 46, No. 3, 2001, pp. 500–505.
Original Russian Text Copyright © 2001 by Bogdanov, Zubrinov, Pestryakov, Petrov, Semenov, Alimpiev.

LATTICE DYNAMICS

Elastic Properties of Beryllium–Lantanum Hexaaluminate Crystal, $BeLaAl_{11}O_{19}$

S. V. Bogdanov*, I. I. Zubrinov*, E. V. Pestryakov, V. V. Petrov**,**
V. I. Semenov*, and A. I. Alimpiev******

** Institute of Laser Physics, Siberian Division, Russian Academy of Sciences,*
pr. Lavrent’eva 13/3, Novosibirsk, 630090 Russia
*** Institute of Semiconductor Physics, Siberian Division, Russian Academy of Sciences,*
pr. Akademika Lavrent’eva 13, Novosibirsk, 630090 Russia
**** Novosibirsk State University, ul. Pirogova 2, Novosibirsk, 630090 Russia*
***** Design and Technological Institute for Single Crystals, Siberian Division, Russian Academy of Sciences,*
Novosibirsk, 630058 Russia
e-mail: perfic@laser.nsc.ru

Received May 17, 2000

Abstract—The elastic properties of beryllium–lantanum hexaaluminate, $BeLaAl_{11}O_{19}$ (sp. gr. $P6_3/mmc$), a new crystal from the family of hexagonal aluminates, have been studied. The velocities of elastic-wave propagation in the crystals are measured by a new acoustooptic interference method. The values of all the independent components of elastic-constant tensor are determined and used to calculate a number of dynamic parameters of the crystal such as the Young’s and shear moduli, the modulus of volume elasticity, Poisson’s ratio as well as the Debye temperature and specific heat. The data obtained are compared with the same parameters for the well-known magnesium–lantanum hexaaluminate $MgLaAl_{11}O_{19}$ laser crystals. It is shown that the dynamic properties of the $BeLaAl_{11}O_{19}$ crystal are close to those of $MgLaAl_{11}O_{19}$ and are a promising matrix for designing new laser media.© *2001 MAIK “Nauka/Interperiodica”.*

INTRODUCTION

A crystal of beryllium–lantanum hexaaluminate of the composition $BeLaAl_{11}O_{19}$ belongs to multicomponent oxide systems with complex crystal structures. Several types of aluminates, which crystallize in the hexagonal system, are known. Their structural motif consists of spinel-like blocks formed by oxygen ions and aluminium, magnesium and some other cations. The sizes of such blocks are different in different hexaaluminates. The nature and properties of the layers located between these blocks are also different [1].

Hexagonal aluminates were first used as crystalline matrices for luminophors. Such luminophors were characterized by a high efficiency and thermal and radiative stability. In recent years, interest in these compounds have increased again in connection with their possible use as active media for multifunctional solid-state laser-radiation sources [1–5]. The hexaaluminate lattice allows the activation of crystals by substituting lantanum by ions with the *f*-shell configuration (Nd, Er, Ho, etc.) and aluminium by ions with *d*-shell configuration (Cr, Ti, Ni, *et al.*). Thus, it is possible to design laser media that can be used in different spectral ranges. Today, the most interesting laser characteristics are obtained in crystals with trivalent neodymium ions introduced into the crystal lattice of $MgLaAl_{11}O_{19}$ and $SrLaAl_{11}O_{19}$ [5]. A number of laser parameters of these media make them comparable with the well-known laser crystals such as yttrium aluminium garnet $Y_3Al_5O_{12}$: Nd and yttrium aluminate $YAlO_3$: Nd.

Beryllium–lantanum hexaaluminate, $BeLaAl_{11}O_{19}$, is isostructural to the well-known magnesium–lantanum hexaaluminate laser crystal $MgLaAl_{11}O_{19}$ from the hexagonal–aluminate family. The crystal lattice of $BeLaAl_{11}O_{19}$ provides the activation with all the transition-metal ions [6]. A detailed study of the beryllium–lantanum hexaaluminate would provide more detailed information on its physical properties necessary for its use as an active medium for solid-state lasers.

Below, we describe the study of elastic properties of $BeLaAl_{11}O_{19}$ crystals and compare them with the analogous properties of $MgLaAl_{11}O_{19}$. The values of all the five independent components c_{mn} of the elastic-constant tensor are determined and used to calculate a number of dynamic and thermal parameters of the crystal such as the shear modulus, the Debye temperature, and the specific heat. The studies of the elastic and thermal parameters of a $BeLaAl_{11}O_{19}$ crystal show that this crystal can be a promising matrix for designing multifunctional laser media.

1063-7745/01/4603-0450$21.00 © 2001 MAIK “Nauka/Interperiodica”

CRYSTAL SYNTHESIS AND GROWTH

Czochralski-grown beryllium–lantanum hexaaluminate crystals were obtained in iridium crucibles on a crystal growth apparatus with induction heating. Both $BeLaAl_{11}O_{19}$ and $MgLaAl_{11}O_{19}$ compounds are crystallized in the magnetoplumbite $PbFe_{12}O_{19}$ structure type of the hexagonal system (sp. gr. $P6_3/mmc$, $Z = 2$). The unit-cell parameters of both crystals are close: $a = 5.54$ Å, $c = 21.95$ Å for $BeLaAl_{11}O_{19}$ and $a = 5.58$ Å, $c = 21.99$ Å for $MgLaAl_{11}O_{19}$.

The highest growth rate is observed along the [100] direction. The best crystals $BeLaAl_{11}O_{19}$ with a high optical quality were obtained at a rate of 0.5 mm/h in an argon atmosphere. However, the crystals had a perfect cleavage in the (001) plane. According to the differential thermal analysis (DTA) data, the $BeLaAl_{11}O_{19}$ crystals melt incongruently at a temperature of 1850°C [6].

The crystal density was measured by the method of hydrostatic weighting. The density determined at room temperature was 4.17 g/cm^3; i.e., it was slightly lower than for $MgLaAl_{11}O_{19}$ (4.26 g/cm^3).

ELASTIC CONSTANTS OF HEXAGONAL ALUMINATES

The most important crystal parameters are elastic constants, which can be measured both under isothermal or adiabatic conditions [7]. As is well known, the adiabatic conditions are fulfilled for dynamic methods of measurements, which seem to be attractive since they provide the excitation of sonic vibrations in crystals. The record of these vibrations can be best demonstrated with the aid of a light diffraction from vibrations. We should like to emphasize that the elastic constants can be measured either in a constant electric field or at constant electric induction, which is of great importance for piezoelectric crystals. Since a $BeLaAl_{11}O_{19}$ crystal is centrosymmetric and, thus, has no piezoelectric effect, its elastic constants c_{ijkl} are measured in a constant electric field.

Elastic constants of a crystal measured by a dynamic method are determined from the condition of propagation in this crystal of plane elastic waves with the wave vector **k** and the angular frequency Ω [7, 8]. The equation of propagation of these waves in an anisotropic medium of the density ρ is described by the Christoffel equation

$$(\Gamma_{ik} - \rho v^2_{[i,j,k]}\delta_{ik})u_k = 0, \tag{1}$$

where $\Gamma_{ik} = c_{ijkl}n_i n_l$ is the Christoffel tensor, c_{ijkl} are the components of the elastic-constant tensor, n_i are the components of the unit vector of the wave normal, $v_{[i,j,k]}$ is the phase velocity for the elastic wave with the wave normal $\mathbf{n} = [i, j, k]$, δ_{ik} is Kronecker tensor, and u_k are the components of the displacement vector.

According to the Neumann principle, there are only five independent nonzero components of the elastic-constant tensor $c_{ij,kl} = c_{mn}$ of hexagonal crystals [8]:

$$c_{11} = c_{22}; \quad c_{33}; \quad c_{44} = c_{55}; \quad c_{12} = c_{21};$$
$$c_{13} = c_{23} = c_{31} = c_{32}$$

and $2c_{66} = c_{11} - c_{12}$.

Therefore, the components of the Christoffel tensor are transformed as

$$\Gamma_{11} = c_{11}n_1^2 + c_{66}n_2^2 + c_{55}n_3^2, \quad \Gamma_{13} = (c_{13} + c_{55})n_1n_3,$$
$$\Gamma_{22} = c_{66}n_1^2 + c_{22}n_2^2 + c_{44}n_3^2, \quad \Gamma_{23} = (c_{23} + c_{44})n_2n_3, \tag{2}$$
$$\Gamma_{33} = c_{55}n_1^2 + c_{44}n_2^2 + c_{33}n_3^2, \quad \Gamma_{12} = (c_{12} + c_{66})n_1n_2.$$

In the Cartesian coordinate system of a hexagonal crystal, we have $n_1 = \sin\theta\cos\varphi$; $n_2 = \sin\theta\sin\varphi$; $n_3 = \cos\theta$, and θ and φ angles are measured from the z- and x-axes, respectively.

In accordance with Eqs. (1) and (2), measuring the velocities of the longitudinal and transverse elastic waves propagating along the crystallographic [100] and [001] axes, one can determine the tensor components c_{66}, c_{55}, c_{33}, c_{12}, and c_{11}. Measuring the velocity of the [010]-polarized shear wave propagating along the [101]-direction, one can determine the c_{13}-component

$$\begin{aligned} c_{13} = {} & 1/2\{[4\lambda_s - (c_{11} + c_{33} + 2c_{44})]^2 \\ & - (c_{11} - c_{33})^2\}^{1/2} - c_{44}, \end{aligned} \tag{3}$$

where $\lambda_s = \rho v^2_{[101]}$ and $v_{[101]}$ is the velocity of a shear wave.

MEASUREMENTS OF ELASTIC-WAVE VELOCITIES

Velocities of elastic waves propagating in crystals were measured by specially developed acoustooptical interference method [9] based on the “long pulse method” [7]. The method provides the measurement of a sound velocity with an accuracy of 1 m/s. The essence of the method reduces to the observation of two superimposing sound pulses—a pulse reflected from the front face of the specimen and the pulse reflected from the back face (i.e., passed an additional distance equal to double length of a specimen, $2L$). If these two pulses are in phase, the interference maximum is formed. This means that there are integral number of acoustic waves within the specimen length L. With the change of the sound frequency, this situation is periodically repeated. Thus, knowing the number N of maxima within the frequency range Δf from the first maximum at the frequency f_1 to Nth maximum at the frequency f_N ($\Delta f = f_N - f_1$), one can readily find the sound velocity v in a

Table 1. The velocity of propagation of elastic waves in $BeLaAl_{11}O_{19}$ and $MgLaAl_{11}O_{19}$ crystals at 300 K

Crystal	Direction of wave propagation/polarization of transverse wave, [*abc*]/[*abc*]	Velocity of elastic waves, 10^3 m/s		Error, %
		type of wave		
		longitudinal	transverse	
$BeLaAl_{11}O_{19}$	[100]/[001]	10.073	5.206	0.1
	[010]/[100]	10.086	5.679	0.1
	[001]/[010]	8.859	5.209	0.1
$MgLaAl_{11}O_{19}$	[100]/[001]	9.924	5.161	0.1
	[010]/[100]	9.924	5.468	0.1
	[001]/[010]	8.753	5.160	0.1

medium:

$$v = 2L\Delta f/N. \quad (4)$$

In the above method, the sound vibrations are excited in a buffer consisting of a specimen made of a transparent material, which is in an acoustic contact with the crystal under study. It is in this buffer that the superposition and interference of two reflected pulses take place. The interference is recorded by the optical method: a narrow laser beam is transmitted through the buffer and the beam diffracted from ultrasound is observed. The maxima of the light diffraction correspond to the interference acoustic maxima. To provide a high quality of the recorded diffraction maxima, the buffer specimen was prepared from a material of high acoustooptical quality, which allows the efficient observance of light diffraction from elastic vibrations. Thus, the basic concept of the method consist in the following. Considering the light diffraction from the overlapping pulses in the buffer, one establish the condition of their interference and determines the frequencies at which this phenomenon takes place. The sound velocity is measured by this method with a rather high accuracy and, under a certain condition, reaches a value of $\Delta v/v \sim 10^{-4}$–10^{-5}.

In the experiment, the buffer length and the position of the light beam should be chosen in such a way that the interfering pulses are located within the spacing between the spurious reflections in the buffer. To meet this condition, the buffer length should exceed the crystal length. In our case, the measurements were made on 10-mm-long crystals, with the buffer being 30-mm-long fused-quartz specimens. The measuring circuit was similar to that considered in [9]. The velocities of elastic-wave propagation at the frequencies of 30–150 MHz were measured with an accuracy not worse than 0.1%.

The measured values of the velocities of elastic-wave propagation along various directions in a $BeLaAl_{11}O_{19}$ crystal are shown in Table 1. For comparison, Table 1 also shows the velocities measured by the same method in $MgLaAl_{11}O_{19}$.

The experimental data in Table 1 confirm the Neumann principle [8], according to which the elastic properties should be equivalent in all the planes normal to the sixfold axes. Thus, the wave velocities are independent of the propagation direction in the plane normal to the sixfold axis. Indeed, it is easy to see that the velocities of elastic waves in the [100] and [010] direction differ by less than 10% both in $BeLaAl_{11}O_{19}$ and $MgLaAl_{11}O_{19}$ crystals.

ELASTIC CONSTANTS OF $BeLaAl_{11}O_{19}$ CRYSTALS AND CAUCHY RELATIONS

The components of the elastic-constant tensor c_{mn} for $BeLaAl_{11}O_{19}$ and $MgLaAl_{11}O_{19}$ crystals, calculated by experimental velocities of elastic vibrations and Eqs. (2) and (3), are given in Table 2. The components of the elastic-compliance tensor s_{nm} for these crystals are determined using the well-known formula relating the tensors $c_{mn}s_{np} = \delta_{mp}$ [8] (Table 3).

According to the dynamical theory of crystal lattices [10, 11], the elastic constant tensor $c_{ij,\,kl} = c_{mn}$ is symmetric with respect to all the indices if the atomic interactions for centrosymmetrical crystals are described in terms of the central forces (i.e., the forces acting along straight line between the neighboring atoms), whereas the elastic stresses give no rise to any internal strains. This leads to the additional relationships between the components, the so-called Cauchy relations [10]:

$$c_{12} = c_{66};\quad c_{13} = c_{55};\quad c_{23} = c_{44};\quad c_{14} = c_{56}; \\ c_{25} = c_{46};\ c_{36} = c_{45}. \quad (5)$$

The Cauchy relations actually reflect the noncentral character of the atomic interactions in crystals.

For hexagonal crystals, the Cauchy relations yield $c_{13} = c_{44}$ and $c_{12} = c_{66}$. However, since in hexagonal crystals $c_{11} - c_{12} = 2c_{66}$, the latter relation is transformed to the form $c_{11} = 3c_{12}$. Thus, in hexagonal crystals similar to $BeLaAl_{11}O_{19}$ and $MgLaAl_{11}O_{19}$, the fulfillment of Eq. (5) signified that only two components of the elastic-constant tensor remain independent. Then the Cauchy relations take the form

$$c_{11} = 3c_{12} \text{ and } c_{13} = c_{44}. \tag{6}$$

Table 2 shows that the components c_{13}, c_{44} and $3c_{12}$, c_{11} in a $BeLaAl_{11}O_{19}$ crystal differ by less than 10%. For a $MgLaAl_{11}O_{19}$ crystal, c_{13} and c_{44} differ by about 10%, and $3c_{12}$ and c_{11}, by about 20%. These data lead to a conclusion that the Cauchy relations for $MgLaAl_{11}O_{19}$ crystals are fulfilled slightly worse than for $BeLaAl_{11}O_{19}$. Taking into account that both crystals have a center of inversion, one can state that the atomic interactions are of a more pronounced central character for $BeLaAl_{11}O_{19}$ than for $MgLaAl_{11}O_{19}$.

It should be emphasized that to provide the stability of crystal lattice the deformation energy should be positive [11]. This condition imposes some additional restrictions on the relations between the elastic-constant components. Thus, for hexagonal $BeLaAl_{11}O_{19}$ and $MgLaAl_{11}O_{19}$ aluminates, we obtain the additional inequalities

$$c_{11} > c_{12}; \quad c_{44} > 0, \quad (c_{12} + c_{11})c_{33} > 2c_{13}^2.$$

It is easy to see that these inequalities are fulfilled rather well. This means that in terms of lattice dynamics both crystals are stable.

FACTOR OF ELASTIC ANISOTROPY

The factor of elastic anisotropy A_{mn} is another essential characteristic of elastic properties of a crystalline media [11, 12]. This parameter is very important for studying phonon focusing in anisotropic media. Because of the specific role of the [001] direction in hexagonal crystals, there are two anisotropy factors—A_{zx} in the plane of the sixfold axis and A_{xy} in the plane normal to sixfold axis [12].

$$A_{zx} = 2c_{44}/(c_{33} - c_{13}), \quad A_{xy} = 2c_{44}/(c_{11} - c_{12}). \tag{7}$$

Using the components of the elastic constant tensor from Table 2, we obtain the following elastic anisotropy factors:

$A_{zx} = 1.035$ and $A_{xy} = 0.84$ for $BeLaAl_{11}O_{19}$,

$A_{zx} = 1.02$ and $A_{xy} = 0.89$ for $MgLaAl_{11}O_{19}$.

One can see that the anisotropy factors are close to unit in both crystals. Thus, we can state that the elastic properties of $BeLaAl_{11}O_{19}$ and $MgLaAl_{11}O_{19}$ allow us to consider these crystals as elastoisotropic media.

DEBYE TEMPERATURE, ELASTICITY MODULUS AND SPECIFIC HEAT

The components of the elastic-constant tensor listed in Table 2 make it possible to calculate the Debye temperature T_D [10, 11, 13] for $BeLaAl_{11}O_{19}$ and $MgLaAl_{11}O_{19}$ crystals, which is very important because it allows the determination of the maximum frequency ν_m of vibration spectrum of the crystal and specific heat of its lattice, c_v.

Table 2. Components of elastic-constant tensor c_{mn} for $BeLaAl_{11}O_{19}$ and $MgLaAl_{11}O_{19}$ crystals at 300 K

Crystal	Components of elastic-constant tensor, c_{mn}, 10^{11} N/m^2					
	c_{11}	c_{33}	c_{44}	c_{66}	c_{12}	c_{13}
$BeLaAl_{11}O_{19}$	4.235	3.27	1.13	1.345	1.54	1.088
$MgLaAl_{11}O_{19}$	4.196	3.26	1.135	1.275	1.647	1.025

Table 3. Components of elastic-compliance tensor s_{mn} for $BeLaAl_{11}O_{19}$ and $MgLaAl_{11}O_{19}$ crystals at 300 K

Crystal	Components of elastic-compliance tensor, S_{mn}, 10^{11} m^2/N					
	s_{11}	s_{33}	s_{44}	s_{66}	s_{12}	s_{13}
$BeLaAl_{11}O_{19}$	0.389	0.35	0.885	0.746	–0.087	–0.066
$MgLaAl_{11}O_{19}$	0.215	0.345	0.88	0.746	–0.099	–0.097

According to the dynamical theory [10, 11], the vibration spectrum of a crystal is determined by the sum of the contributions of all the types of elastic waves whose velocities depend on the directions of their propagation. Therefore, to determine the total number of vibrations, one has to sum them over all the directions of wave propagation. This is reflected in the following expression for the characteristic Debye temperature T_D [11]:

$$T_D = (h/k_B)\nu_m = h/k_B(9N/4\pi V)^{1/3} \times \left\{ \int [(1/v_L)^3 + 2(1/v_t)^3] d\Omega/4\pi \right\}^{-1/3}, \tag{8}$$

where h and k_B are Planck and Boltzmann constants, respectively; ν_m is the phonon frequency; N is the number of atoms; V is the crystal volume; $d\Omega$ is an element of the solid angle; and v_L and v_t are the longitudinal and transverse velocities of the elastic wave, respectively.

Substituting the elastic-wave velocities in Eq. (8) with the corresponding elastic constants according to Christoffel Eq. (2), one can determine T_D by direct numerical integration. There are several simple methods for calculating the Debye temperature, of which the most efficient is the simplification of Eq. (8) by eliminating integration. For any anisotropic crystal, the dependence of T_D on the velocity spectrum may be modified by introducing the average isotropic velocity v_m [14]:

$$v_m^3 = \frac{1}{3}[(1/v_{mL})^3 + 2(1/v_{mt})^3]^{-1}, \tag{9}$$

Table 4. Dynamic parameters of $BeLaAl_{11}O_{19}$ and $MgLaAl_{11}O_{19}$ crystals at 300 K

Crystal	Average elastic-wave velocity, 10^3 m/s			Volume elasticity modulus	Shear modulus	Young's modulus	Poisson's ratio
	v_{mL}	v_{mt}	v_m	K, 10^{11} N/m^2	G, 10^{11} N/m^2	E, 10^{11} N/m^2	μ
$BeLaAl_{11}O_{19}$	9.12	5.48	6.06	2.08	1.25	3.05	0.22
$MgLaAl_{11}O_{19}$	9.00	5.40	5.97	2.08	1.24	3.03	0.22

where v_{mL} and v_{mt} are the isotropic velocities of longitudinal and transverse elastic waves, respectively. This transformation can be made rigorously for crystals in which the elastic wave velocity either slightly depends on the propagation direction or is independent of it, i.e., for elastoisotropic media. In this approximation, the expression for the Debye temperature is written in the form

$$T_D = h/k_B(3pN\rho/4\pi M)^{1/3}v_m, \qquad (10)$$

where p is the number of atoms per material molecule, N is Avogadro's number, and M is the molecular weight in grams.

The values of the isotropic velocities in an anisotropic medium are readily determined from elastic constants c_{mn} averaged over all the possible crystal orientations and elastic compliances s_{nm} by the Hill method [13]. Thus, an anisotropic crystal is considered as an elastoisotropic material, and the averaged c_{mn} and s_{nm} values are used to determine its elastic parameters, i.e., the shear modulus G, the modulus of volume elasticity K, Young's modulus E, and Poisson's ratio μ [13–15]. This method of T_D determination for $BeLaAl_{11}O_{19}$ and $MgLaAl_{11}O_{19}$ crystals is quite reliable, since the elastic anisotropy parameters of these crystals are close to unity.

The averaged values of the elastic moduli (the shear modulus, the modulus of volume elasticity, Young's modulus, and Poisson's ratio), isotropic velocities, and the Debye temperatures for $BeLaAl_{11}O_{19}$ and $MgLaAl_{11}O_{19}$ crystals calculated by this method are listed in Tables 4 and 5. The Debye temperatures for both crystals (Table 5) show that the maximum frequency of the phonon spectrum for the $BeLaAl_{11}O_{19}$ $\nu_m = 665$ cm^{-1} is slightly higher than for $MgLaAl_{11}O_{19}$ ($\nu_m = 595$ cm^{-1}).

Table 5. Thermodynamic parameters of $BeLaAl_{11}O_{19}$ and $MgLaAl_{11}O_{19}$ crystals at 300 K

Crystal	Density, ρ, g/cm^3	Heat conductivity, λ, W/(m deg)	Debye temperature, T_D, K	Specific heat, c_p, J/(g deg)
$BeLaAl_{11}O_{19}$	4.17	–	860	0.5
$MgLaAl_{11}O_{19}$	4.26	14	845	0.67

The dynamical theory of the crystal lattice also reliably describes the specific heat for simple compounds [11, 14]. In the low temperature region $T \le T_D/10$, it provides the determination of the specific heat by the equation

$$c_V(T) = (3/5)4\pi^4 k_B N(T/T_D)^3. \qquad (11)$$

Comparison with the experiment shows that the approximation (11) not only describes the temperature dependence of specific heat qualitatively well but also provides the proper quantitative estimation of the specific heat for many dielectric crystals [14, 15]. The c_V-values for $BeLaAl_{11}O_{19}$ and $MgLaAl_{11}O_{19}$ crystals calculated by Eq. (12) are listed in Table 5.

CONCLUSION

The velocities of elastic-wave propagation in hexagonal $BeLaAl_{11}O_{19}$ crystals have been measured with high precision by acousto-optical interference method. For comparison, the analogous data were also obtained for the well-known $MgLaAl_{11}O_{19}$ crystal. Using these data, we calculated all five independent components c_{mn} of the elastic constant tensor. Within the framework of the dynamical theory of crystal lattices, a number of important dynamic parameters, the Debye temperature, and the specific heat have been determined for both crystals.

The data obtained allow us to state that most of the dynamic properties of $BeLaAl_{11}O_{19}$ are close to those of an isostructural $MgLaAl_{11}O_{19}$ crystal. The comparison of the dynamic characteristics of $BeLaAl_{11}O_{19}$ with analogous parameters for other beryllium-containing oxides, e.g., $BeAl_2O_4$, $BeAl_6O_{10}$, and $Be_3Al_2Si_6O_{18}$ [16, 17], shows that the dynamic properties of $BeLaAl_{11}O_{19}$ are not worse (sometimes even better) than those of other crystals. The set of elastic properties of the beryllium–lantanum hexaaluminate shows that this crystal is a promising active medium for solid-state lasers.

ACKNOWLEDGMENTS

The authors are grateful to V.I. Alimpiev, V.I. Trunov, A.V. Kirpichnikov, and E.V. Ivanov for their help and useful discussions. This study was supported by the Russian Foundation for Basic Research, projects nos. 97-02-18555 and 98-02-17787.

REFERENCES

1. P. I. Bykovskiĭ, V. A. Lebedev, V. F. Pisarenko, and V. V. Petrov, Zh. Prikl. Spektrosk. **44** (5), 711 (1986).
2. L. D. Garmash, A. A. Kaminskii, A. I. Polyakov, *et al.*, Phys. Status Solidi A **75** (2), K111 (1983).
3. Kh. S. Bagdasarov, L. M. Dorozhkin, L. A. Ermakova, *et al.*, Sov. J. Quantum Electron. **13** (8), 1082 (1983).
4. L. D. Schearer, M. Leduc, D. Vivien, *et al.*, IEEE J. Quantum Electron. **22** (5), 713 (1986).
5. N. Memilliod, R. Romero, I. Chartier, *et al.*, IEEE J. Quantum Electron. **28** (4), 1179 (1992).
6. A. I. Alimpiev, V. S. Gulev, and P. V. Mokrushnikov, Cryst. Res. Technol. **30** (3), 295 (1995).
7. R. Truell, Ch. Elbaum, and B. Chick, *Ultrasonic Methods in Solid State Physics* (Academic, New York, 1969; Mir, Moscow, 1972).
8. J. F. Nye, *Physical Properties of Crystals: Their Representation by Tensors and Matrices* (Clarendon Press, Oxford, 1957; Mir, Moscow, 1960).
9. S. V. Bogdanov, I. I. Zubrinov, V. K. Sapozhnikov, and E. V. Pestryakov, Akust. Zh. **46**, 35 (2000) [Acoust. Phys. **46**, 27 (2000)].
10. G. Leibfried, in *Handbuch der Physik*, Ed. by S. Flugge (Springer-Verlag, Berlin, 1955; Fizmatgiz, Moscow, 1963), Vol. 7, Part 1, p. 104.
11. M. Born and K. Huang, *Dynamical Theory of Crystal Lattices* (Clarendon Press, Oxford, 1954; Inostrannaya Literatura, Moscow, 1958).
12. K. Lau and A. McCurdy, Phys. Rev. B **58** (14), 8980 (1998).
13. *Physical Acoustics: Principles and Methods*, Ed. by W. P. Mason (Academic, New York, 1965; Mir, Moscow, 1968), Vol. IIIB, p. 162.
14. J. A. Reissland, *The Physics of Phonons* (Wiley, New York, 1973; Mir, Moscow, 1975).
15. V. Plekhanov, Opt. Spektrosk. **82** (1), 105 (1997) [Opt. Spectrosc. **82**, 95 (1997)].
16. C. F. Cline, R. C. Morris, M. Dutton, and P. Harget, J. Mater. Sci. **14**, 941 (1979).
17. I. I. Zubrinov, V. I. Semenov, E. V. Pestryakov, *et al.*, Kristallografiya **43** (4), 701 (1998) [Crystallogr. Rep. **43**, 657 (1998)].

Translated by T. Dmitrieva

Crystallography Reports, Vol. 46, No. 3, 2001, pp. 456–460. Translated from Kristallografiya, Vol. 46, No. 3, 2001, pp. 506–510.
Original Russian Text Copyright © 2001 by Kaminskii.

PHYSICAL PROPERTIES OF CRYSTALS

Nonlinear-Laser ($\chi^{(2)} + \chi^{(3)}$) Effects in Acentric Cubic $Bi_4Ge_3O_{12}$ and $NaClO_3$ Crystals

A. A. Kaminskii

Institute of Crystallography, Russian Academy of Sciences, Leninskiĭ pr. 59, Moscow, 117333 Russia

Received January 15, 2001

Abstract—The effects of the self-frequency summing of IR-pumping and Stokes and anti-Stokes generation have been revealed in stimulated Raman scattering in ($\chi^{(2)} + \chi^{(3)}$)-nonlinear $Bi_4Ge_3O_{12}$ and $NaClO_3$ crystals. The recorded components of Raman-induced parametric generation have been identified. *© 2001 MAIK "Nauka/Interperiodica".*

INTRODUCTION

Whenever a new nonlinear-laser crystal, which manifested its $\chi^{(2)}$- and $\chi^{(3)}$-properties in efficient second-harmonic generation (SHG) or stimulated Raman scattering (SRS) was discovered, it was inevitably followed by the attempts of using it in SRS-lasers or in lasers with self-frequency doubling [1]. Recently, new phenomena of Raman-induced parametric generation have been discovered in the experiments on ($\chi^{(2)} + \chi^{(3)}$)-active acentric crystals in which the multicomponent Stokes and anti-Stokes generation takes place in the range of pumping frequency and the second-harmonic generation, thus covering almost the whole range of the optical transparency [2, 3]. It should be emphasized that to date, the nonlinear-laser ($\chi^{(2)} + \chi^{(3)}$)-interactions have been observed only in anisotropic crystals. Below, these effects are reported for the first time for acentric isotropic $Bi_4Ge_3O_{12}$ (sp. gr. T_d^6–$I\bar{4}3d$) and $NaClO_3$ (sp. gr. T^4–$P2_13$) crystals. In the experiments on simulated Raman scattering in which the excitation was attained with the aid of 1-μm picosecond pulses of an

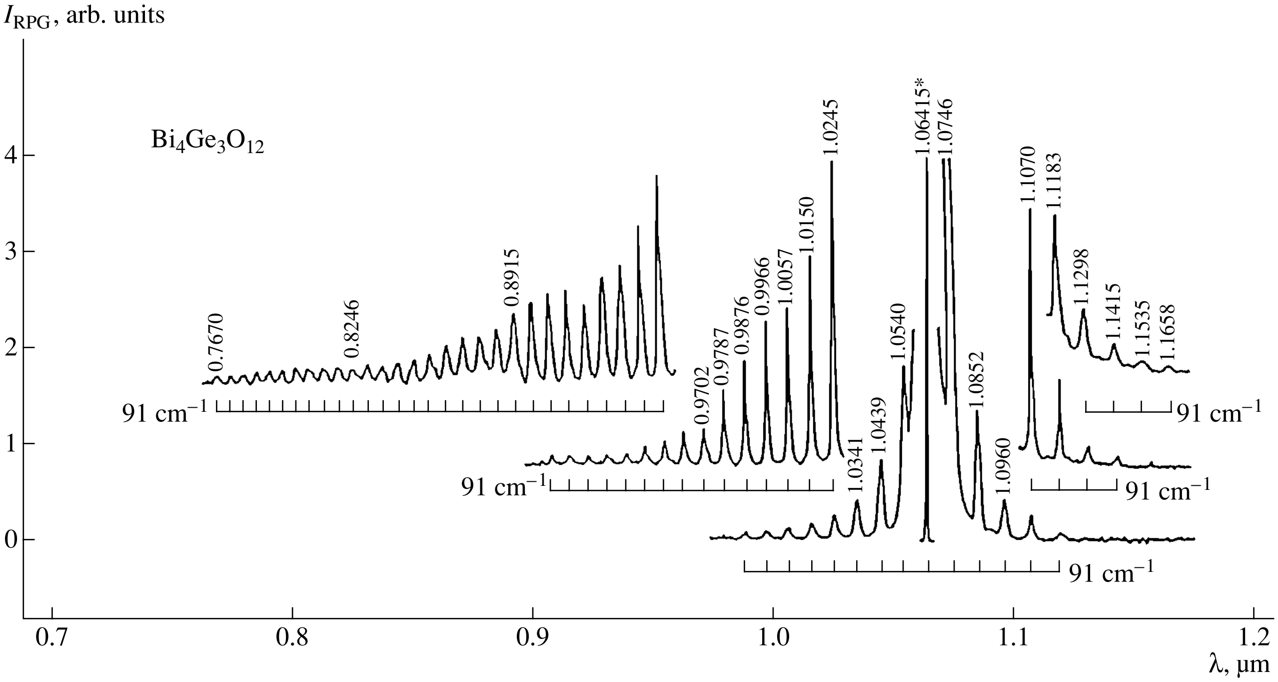

Fig. 1. Raman-induced parametric generation spectrum of $Bi_4Ge_3O_{12}$ crystal in the infrared range obtained at picosecond pumping with λ_{p1} = 1.06415 μm (marked by an asterisk) at 300 K. The wavelengths are indicated in micrometers (for the anti-Stokes wing, the wavelengths of only a few lines are indicated). The line intensities were not corrected for the spectral sensitivity of the recording system based on the Si-CCD matrix. The relation of the $\chi^{(3)}$-generation components and the SRS-active vibration mode ω_{SRS} = 91 cm^{-1} of the crystal is indicated by brackets.

1063-7745/01/4603-0456$21.00 © 2001 MAIK "Nauka/Interperiodica"

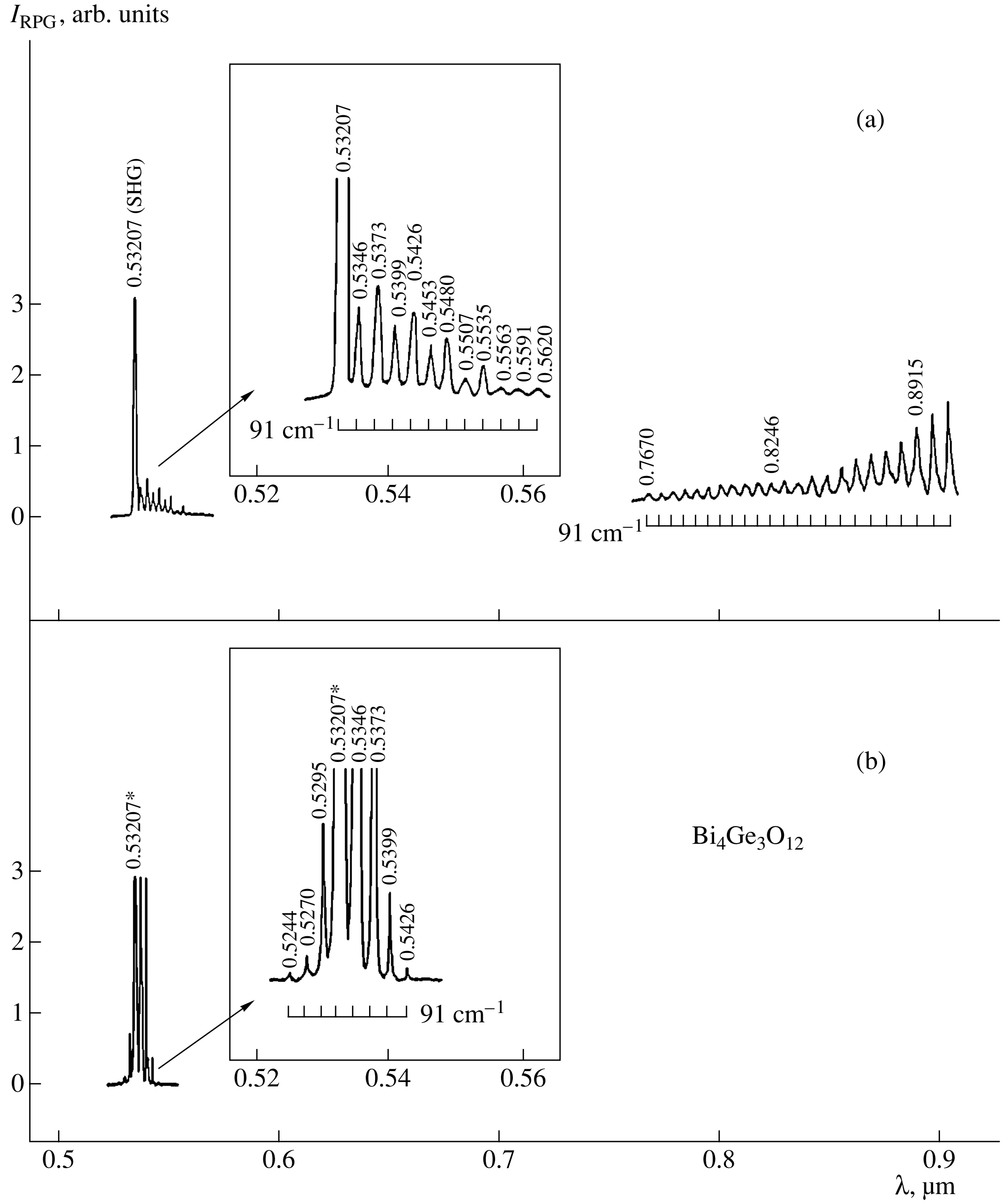

Fig. 2. Raman-induced parametric generation spectra of $Bi_4Ge_3O_{12}$ crystal at 300 K: (a) the short wavelength part of the spectrum shown in Fig. 1 and (b) the spectrum obtained at pumping with λ_{p2} = 0.53207 μm. For notation see Fig. 1.

$Nd^{3+} : Y_3Al_5O_{12}$ laser, the multiwave generation in the visible provided by self-frequency summing of the Raman-induced parametric generation, pumping, and its IR SRS lines in the 1-μm range was observed along with efficient second-harmonic generation. In these experiments, we also managed to excite for the first time a pronounced higher order stimulated Raman scattering (up to the 40th anti-Stokes component with $\lambda_{ASt_{40}}$ = 0.7670 μm) with a low-frequency translational vibration mode (ω_{SRS} = 91 cm^{-1}) in a $Bi_4Ge_3O_{12}$ crystal. The effects of self-frequency summing of laser emission are important not only for science but also for practical applications. For example, it is easier to design nonlinear elements for optoelectronics (such as crystalline fibers and nanocrystalline ceramic films) on the basis of cubic crystals.

In our experiment, we used 30- to 40-mm-long $Bi_4Ge_3O_{12}$ and $NaClO_3$ samples cut along ~⟨111⟩ directions with a 8 × 8 mm^2 cross section. The plane-parallel end faces had no antireflection coating. Raman-induced parametric generation in these samples was excited by the pulses emitted by a $Nd^{3+} : Y_3Al_5O_{12}$ laser at λ_{p1} = 1.06415 μm with $\tau_{p1} \approx 110$ ps and at λ = 0.53207 (the second harmonic) with $\tau_{p2} \approx 80$ ps in the single-pass geometry. The samples were placed into the "focal volume" of the pumping beam with the Gaussian intensity

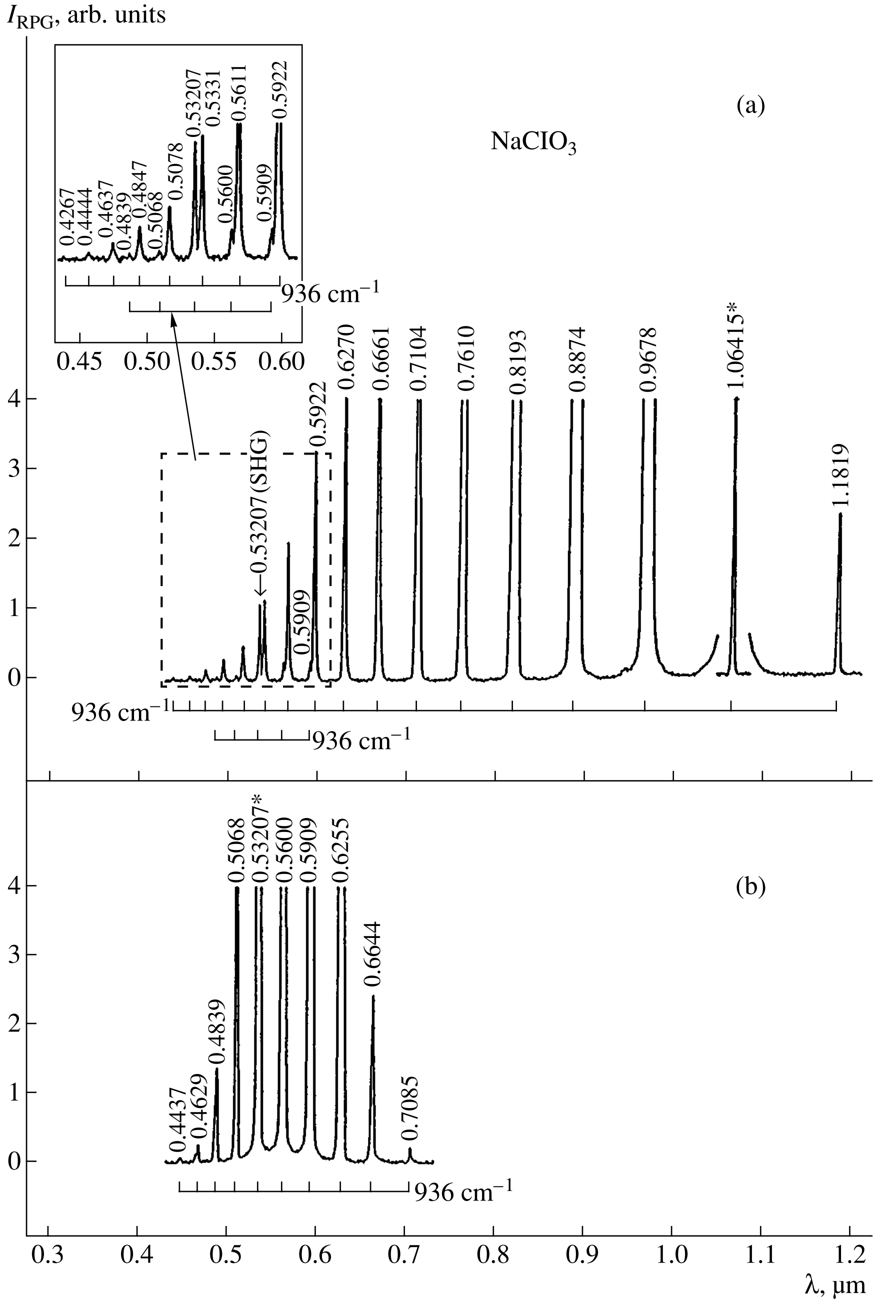

Fig. 3. Raman-induced parametric generation spectra of a $NaClO_3$ crystal obtained at picosecond pumping at 300 K with (a) λ_{p1} = 1.06415 μm and (b) λ_{p2} = 0.53207 μm. The relation of the $\chi^{(3)}$-generation components and the SRS-active vibration mode ω_{SRS} = 936 cm^{-1} of the crystal is indicated by brackets. For notation see Fig. 1.

profile was focused by a lens with a focal distance of $f \approx 15$ cm and the waist diameter was ~ 25 μm. The spectral composition of the Raman-induced parametric generation was measured with the aid of a CSMF multichannel spectrometric analyzer with a Si-CCD matrix detector [4]. The measured data and the results of the spectral identification are shown in Figs. 1–3 and indicated in the table. The data obtained at a 1-μm pumping are presented in the table in more detail. It is worth noting here that the SRS-active vibration mode (ω_{SRS} = 936 cm^{-1}) of $NaClO_3$ crystal is associated with the totally symmetric *A*-phonons of ClO_3^- ions [4]. For the steady-state SRS, the Raman gain coefficient in the near IR region in $NaClO_3$ equals g_{ssR} = 3.1 ± 0.8 cm/GW. For $Bi_4Ge_3O_{12}$; this parameter was estimated as $g_{ssR} \approx 0.8$ cm/GW. It should also be noted that the higher order components were not observed for the

Spectral composition of the Raman-induced parametric generation at picosecond $Nd^{3+} : Y_3Al_5O_{12}$-laser excitation at λ_{p1} = 1.06415 μm in the acentric cubic $Bi_4Ge_3O_{12}$ and $NaClO_3$ crystals at 300 K

Characteristics of Raman-induced parametric generation					
λ*, μm	line	line identification	λ*, μm	line	line identification
$Bi_4Ge_3O_{12}$ (ω_{SRS} = 91 cm^{-1})			$NaClO_3$ (ω_{SRS} = 936 cm^{-1})		
1.1658	St_9	$\omega_{p1} - 9\omega_{SRS}$	1.1819	St_1	$\omega_{p1} - \omega_{SRS}$
1.1535	St_8	$\omega_{p1} - 8\omega_{SRS}$	1.06415	λ_{p1}	ω_{p1}
1.1415	St_7	$\omega_{p1} - 7\omega_{SRS}$	0.9678	ASt_1	$\omega_{p1} + \omega_{SRS}$
1.1298	St_6	$\omega_{p1} - 6\omega_{SRS}$	0.8874	ASt_2	$\omega_{p1} + 2\omega_{SRS}$
1.1183	St_5	$\omega_{p1} - 5\omega_{SRS}$	0.8193	ASt_3	$\omega_{p1} + 3\omega_{SRS}$
1.1070	St_4	$\omega_{p1} - 4\omega_{SRS}$	0.7610	ASt_4	$\omega_{p1} + 4\omega_{SRS}$
1.0960	St_3	$\omega_{p1} - 3\omega_{SRS}$	0.7104	ASt_5	$\omega_{p1} + 5\omega_{SRS}$
1.0852	St_2	$\omega_{p1} - 2\omega_{SRS}$	0.6661	ASt_6	$\omega_{p1} + 6\omega_{SRS}$
1.0746	St_1	$\omega_{p1} - \omega_{SRS}$	0.6270	ASt_7	$\omega_{p1} + 7\omega_{SRS}$
1.06415	λ_{p1}	ω_{p1}	0.5922	ASt_8	$\omega_{p1} + 8\omega_{SRS}$
1.0540	ASt_1	$\omega_{p1} + \omega_{SRS}$	0.5909	$\Sigma\omega_{p1}$, St_2***	$\omega_{p1} + (\omega_{p1} - 2\omega_{SRS})$
0.9702	ASt_{10}	$\omega_{p1} + 10\omega_{SRS}$	0.5611	ASt_9	$\omega_{p1} + 9\omega_{SRS}$
0.8915	ASt_{20}	$\omega_{p1} + 20\omega_{SRS}$	0.5600	$\Sigma\omega_{p1}$, St_1***	$\omega_{p1} + (\omega_{p1} - \omega_{SRS})$
0.8246	ASt_{30}	$\omega_{p1} + 30\omega_{SRS}$	0.5331	ASt_{10}	$\omega_{p1} + 10\omega_{SRS}$
0.7670	ASt_{40}	$\omega_{p1} + 40\omega_{SRS}$	0.53207	SHG	$2\omega_{p1}$
0.5620	$\Sigma\omega_{p1}$, St_{11}***	$\omega_{p1} + (\omega_{p1} - 11\omega_{SRS})$	0.5078	ASt_{11}	$\omega_{p1} + 11\omega_{SRS}$
0.5591**	$\Sigma\omega_{p1}$, St_{10}***	$\omega_{p1} + (\omega_{p1} - 10\omega_{SRS})$	0.5068	$\Sigma\omega_{p1}$, ASt_1***	$\omega_{p1} + (\omega_{p1} + \omega_{SRS})$
0.5563	$\Sigma\omega_{p1}$, St_9***	$\omega_{p1} + (\omega_{p1} - 9\omega_{SRS})$	0.4847	ASt_{12}	$\omega_{p1} + 12\omega_{SRS}$
0.5535**	$\Sigma\omega_{p1}$, St_8***	$\omega_{p1} + (\omega_{p1} - 8\omega_{SRS})$	0.4839	$\Sigma\omega_{p1}$, ASt_2***	$\omega_{p1} + (\omega_{p1} + 2\omega_{SRS})$
0.5507	$\Sigma\omega_{p1}$, St_7***	$\omega_{p1} + (\omega_{p1} - 7\omega_{SRS})$	0.4637	ASt_{13}	$\omega_{p1} + 13\omega_{SRS}$
0.5480**	$\Sigma\omega_{p1}$, St_6***	$\omega_{p1} + (\omega_{p1} - 6\omega_{SRS})$	0.4444	ASt_{14}	$\omega_{p1} + 14\omega_{SRS}$
0.5453	$\Sigma\omega_{p1}$, St_5***	$\omega_{p1} + (\omega_{p1} - 5\omega_{SRS})$	0.4267	ASt_{15}	$\omega_{p1} + 15\omega_{SRS}$
0.5426**	$\Sigma\omega_{p1}$, St_4***	$\omega_{p1} + (\omega_{p1} - 4\omega_{SRS})$			
0.5399	$\Sigma\omega_{p1}$, St_3***	$\omega_{p1} + (\omega_{p1} - 3\omega_{SRS})$			
0.5373**	$\Sigma\omega_{p1}$, St_2***	$\omega_{p1} + (\omega_{p1} - 2\omega_{SRS})$			
0.5346	$\Sigma\omega_{p1}$, St_1***	$\omega_{p1} + (\omega_{p1} - \omega_{SRS})$			
0.53207	SHG	$2\omega_{p1}$			

* Measurement accuracy is ±0.0003 μm.

** The wavelength coinciding with the second-harmonic wavelength of one of the IR Raman-induced parametric generation lines.

*** The symbol Σ indicates the process the self-summation of the frequencies of the corresponding lines of the Raman-induced parametric generation.

Stokes wings of the SRS spectra of the crystals studied because of the almost “zero” sensitivity of the Si-CCD matrix (Hamamatsu S3923-1024Q) in the IR spectral range at $\lambda > 1.15$ μm (Figs. 1, 3a). At the same time, these components are clearly seen in Raman-induced parametric generation spectra with self-summation of frequencies in the visible range of the RPG spectra (see table and Figs. 2a, 3a).

Thus, the effects of the self-frequencies of the components of Raman-induced parametric and second-harmonic generation and the multiwave Stokes and anti-Stokes generation have been established in $Bi_4Ge_3O_{12}$

and $NaClO_3$ crystals, which indicates the high efficiency of the ($\chi^{(2)} + \chi^{(3)}$)-interactions in the acentric cubic crystals.

ACKNOWLEDGMENTS

This study was supported by the Russian Foundation for Basic Research, project no. 00-02-16071, and the Federal Programs *Fundamental Metrology* and *Fundamental Spectroscopy.* The author is grateful to S.N. Bagaev, F.A. Kuznetsov, H.J. Eichler, and J. Hulliger (the Joint Open Laboratory *Laser Crystals and Precise Laser Systems*) without whose assistance this study could hardly be possible.

REFERENCES

1. A. A. Kaminskii, *Crystalline Lasers: Physical Processes and Operating Schemes* (CRC Press, Boca Raton, 1996).
2. A. A. Kaminskii, A. V. Butashin, H. J. Eichler, *et al.*, J. Raman Spectrosc. **29** (7), 645 (1998).
3. A. A. Kaminskii, S. N. Bagaev, A. M. Yurkin, *et al.*, Dokl. Akad. Nauk **367** (4), 468 (1999) [Dokl. Phys. **44**, 495 (1999)].
4. A. A. Kaminskii, S. N. Bagayev, J. Hulliger, *et al.*, Appl. Phys. B: Lasers Opt. **B67** (1), 157 (1998).

Translated by A. Zolot’ko

Crystallography Reports, Vol. 46, No. 3, 2001, pp. 461–467. Translated from Kristallografiya, Vol. 46, No. 3, 2001, pp. 511–518.
Original Russian Text Copyright © 2001 by Egorysheva, Burkov, Gorelik, Kargin, Chervyakov.

PHYSICAL PROPERTIES OF CRYSTALS

Raman Scattering in Sillenite-Type Crystals

A. V. Egorysheva, V. I. Burkov**, V. S. Gorelik***,**
Yu. F. Kargin*, and A. V. Chervyakov***

** Kurnakov Institute of General and Inorganic Chemistry, Russian Academy of Sciences,*
Leninskiĭ pr. 31, Moscow, 117907 Russia
*** Moscow Physicotechnical Institute, Institutskiĭ proezd 9,*
Dolgoprudnyĭ, Moscow oblast, 141700 Russia
**** Lebedev Physical Institute, Russian Academy of Sciences,*
Leninskiĭ pr. 53, Moscow, 117924 Russia

Received May 15, 2000

Abstract—The Raman spectra of $Bi_{24}AlPO_{40}$ and $Bi_{38}ZnO_{58}$ crystals have been studied for the first time. The polarization Raman spectra of $Bi_{12}GeO_{20}$, $Bi_{12}TiO_{20}$, $Bi_{24}AlPO_{40}$, and $Bi_{38}ZnO_{58}$ crystals are also studied. The lines in the Raman spectra of $Bi_{12}TiO_{20}$, $Bi_{24}AlPO_{40}$, and $Bi_{38}ZnO_{58}$ are identified and compared with the lines of the $Bi_{12}GeO_{20}$ spectra studied earlier. It is shown that the differences in the Raman spectra of the crystals studied are associated with the specific features of their atomic structures.© *2001 MAIK “Nauka/Interperiodica”.*

INTRODUCTION

Cubic crystals with the sillenite-type structure described by the general formula $Bi_{12}M^{+n}O_{20 \pm \delta}$, where M is an element of groups II–V of the Periodic Table, belong to the sp. gr. *I*23. The considerable interest in the studies of sillenite-type single crystals is caused by the unique set of valuable properties possessed by these compounds—a high selective photosensitivity, a linear electrooptical effect, gyration, and also good piezo- and acoustooptic characteristics [1, 2]. The spectroscopic properties of these compounds are essentially dependent on their structural characteristics [3], which, in turn, are determined by the oxidation degree of *M*-cations in the sillenite crystal lattice [4].

The Raman spectra of the $Bi_{12}GeO_{20}$, $Bi_{12}SiO_{20}$, and $Bi_{12}TiO_{20}$ crystals were studied in [5–7]; the *M*-cations in these compounds are characterized by the oxidation degree 4+, which determines the existence of only insignificant differences between crystal lattices that are associated, first of all, with the occupancy of the *M*-positions. However, these compounds do not exhaust the broad spectrum of synthesized single crystals with the sillenite structure.

The present study was aimed at the detection and study of the specific features of the atomic structures of various sillenites which manifest themselves in the Raman spectra. Along with the spectra of the compounds studied earlier, such as $Bi_{12}GeO_{20}$ (BGO) and $Bi_{12}TiO_{20}$ (BTO), we also studied for the fist time the Raman spectra of $Bi_{24}AlPO_{40}$ (BAlPO) and $Bi_{38}ZnO_{58}$ (BZnO).

EXPERIMENTAL

Czochralski- and TSSG-grown [8] BGO, BTO, BAlPO, and BZnO single crystals were studied by the method of X-ray phase analysis on an Geigerflex X-ray diffractometer. It was shown that all the crystals have the sillenite structure. The specimens had the shape of parallelepipeds with the faces corresponding to the crystallographic {100} planes.

The vibrational spectra of sillenite were studied on an automated Raman spectrometer consisting of a DFS-12 double monochromator, a system for counting phonons, an interface, and a controlling computer. The spectral slit width was 2 cm^{-1}. Raman spectra were excited by an ILA-120 Ar-laser (the excitation wavelength $\lambda = 488.0$ nm, the generation power 100 mW). The crystals were studied with the use of the scattering scheme close to the 180°-scheme. One of the specimen faces was set at a Brewster angle to make the polarization measurements.

RESULTS AND DISCUSSION

As is seen from Figs. 1–4, the main characteristics of the Raman spectra of the BGO, BAlPO, BTO, and BZnO crystals are similar, which indicates the key role of the Bi–O sublattice in the formation of the vibrational spectra in the frequency range studied. The Raman spectra were most similar in the frequency range up to 150 cm^{-1} (Figs. 1–4), corresponding to the most intense, narrowest lines of the spectra. The most pronounced differences in the spectra are observed in the frequency range 200–400 cm^{-1}, corresponding to broad overlapping lines. The spectra consist of 16 to 20 bands (Tables 1–4), with some of them being char-

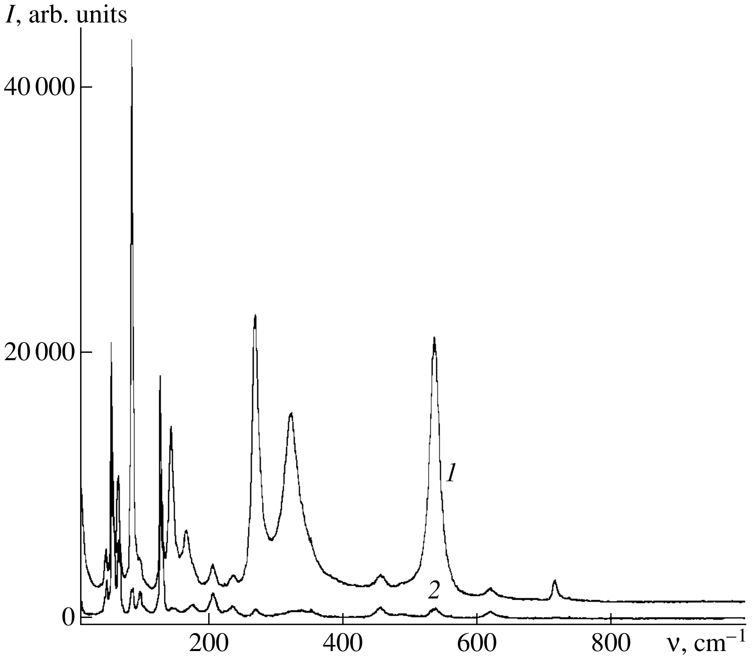

Fig. 1. Raman spectra from BGO crystals, (*1*) $x(zz)\bar{x}$, (*2*) $x(zy)\bar{x}$.

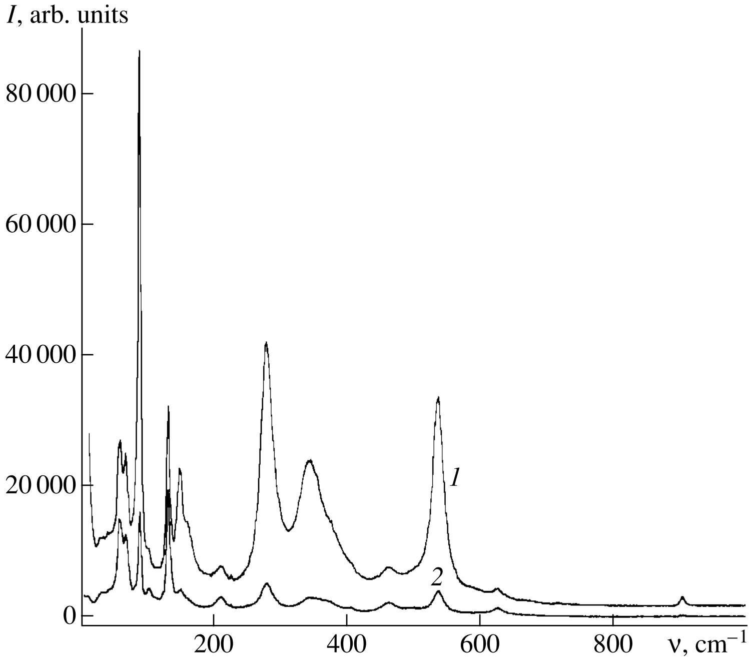

Fig. 2. Raman spectra from BAlPO crystals, (*1*) $x(zz)\bar{x}$, (*2*) $x(zy)\bar{x}$.

acterized by a rather complicated structure. The band positions in the Raman spectra of BGO and BTO crystals, as well as in the BZnO spectrum obtained earlier on a polycrystal powderlike specimen in [6], and their intensities are consistent with the published data [5, 7].

The experimental geometry (mutual arrangement of polarizers) influences the form of the Raman spectra. For all the crystals studied, the number of lines and their intensities in the $x(zz)\bar{x}$ spectra were higher than the analogous values for the $x(zy)\bar{x}$ spectra (Figs. 1–4).

Table 1. Position (cm^{-1}), intensity (Hz*), and width (cm^{-1}) of the bands in the Raman spectra of BGO crystals

Position	Intensity	Width	Position	Intensity	Width	Symmetry typ
$x(zz)\bar{x}$			$x(zy)\bar{x}$			
46.0	2814	2.4	47.0	2464	3.0	F
56.0	19476	3.3	56.5	19862	2.6	F
65.8	8670	3.6	66.1	5694	3.8	E
86.9	46025	3.2	86.1	2051	3.9	A, E
98.0	1563	4.4	97.7	1590	6.0	F
128.5	16491	3.3	129.1	10852	3.7	E, F
144.5	12205	8.0	148.4	383	9.3	A
167.1	4052	15.2	174.8	718	14.9	A, F
205.1	1692	7.6	205.8	1649	10.1	F
236.3	735	10.0	234.8	676	11.0	E
269.5	20564	11.5	269.9	507	7.7	A
323.3	12711	34.4	324.7	410	53.7	A, E, F
–	–	–	344.6	249	31.2	F
454.8	779	9.1	454.5	720	16.8	E
–	–	–	487.6	223	25.5	F
535.9	19909	16.2	536.4	684	16.1	A
619.6	649	10.0	618.9	468	17.8	E
715.6	1525	10.2	716.5	64	7.1	A

* Photons/s.

Unfortunately, the high optical activity of sillenite crystals (~45deg/mm at λ = 488 nm for BGO crystals) and the strong photochromic effect resulting in the appearance of the spatial charge and, as a consequence, the induced birefringence did not allow us to calculate the matrix elements of the polarization tensors A, E, and F of the phonons under the experimental conditions. However, using the results obtained for the BGO crystals [5], one can determined the symmetry of vibrations which make the contribution to the Raman spectra (Table 1). Among the lines of the BGO Raman spectra, there exist both isolated and superimposed lines caused by vibrations of different symmetries. Therefore, Table 1 indicates the symmetry types of all the vibrations corresponding to the given line of the Raman spectra. The first letter indicates the symmetry of the most intense component. Because of the close frequencies of TO + TO, and LO symmetries of vibrations and the inability to resolve the corresponding bands in the spectra at room temperature, they are referred to as F vibrations in Table 1.

Analyzing Table 1, one can single out some tendencies in the line behavior. The most intense lines in the $x(zz)\bar{x}$ spectrum are caused by totally symmetric vibrations. In the transition to the $x(zy)\bar{x}$ spectrum, the intensities of these lines decrease by 20–40 times. In the transition from the $x(zz)\bar{x}$ to $x(zy)\bar{x}$ spectra, the intensities of the lines provided by E-type vibrations decrease only insignificantly (by a factor of 1.5–2.0). The intensity of the lines, which are the superpositions of triply degenerate normal F vibrations, are almost constant. The lines associated with the vibrations of only TO and LO symmetry (344.6 and 487.6 cm^{-1}) are seen only in the $x(zy)\bar{x}$ spectrum. Using these characteristics, one can determine the probable vibration symmetry which determines, to a larger extent, the line intensities in the Raman spectra of the BAlPO, BTO, and BZnO crystals (Tables 2–4).

Now, using the symmetry data obtained, compare the Raman spectra of the BGO, BAlPO, BTO, and BZnO crystals. Table 5 lists the line frequencies in the spectra of the crystals grouped in accordance with their positions, intensities, and probable vibration symmetries. Some lines have no analogues in the spectra of other compounds (e.g., the lines at 236.3 and 344.6 cm^{-1} in the BGO spectra, the lines at 224.0 and 372.3 cm^{-1} in the BTO spectra, and the line at 560.7 cm^{-1} in the BZnO spectra). Therefore, these lines are not indicated in Table 5. It is also seen from Table 5 that the frequencies of most lines decrease in the order BGO, BAlPO, BTO, and BZnO. This result is not surprising, because the lattice parameters of the crystals and, as a result, the interatomic distances increase in the same order (10.145 in BGO, 10.146 in BAlPO, 10.174 in BTO, and 10.207 Å

Table 2. Position (cm^{-1}), intensity (Hz), and width (cm^{-1}) of the bands in the Raman spectra of BAlPO crystals

Position	Intensity	Width	Position	Intensity	Width	Symmetry type
$x(zz)\bar{x}$			$x(zy)\bar{x}$			
–	–	–	30.1	903	6.9	
–	–	–	40.9	754	10.1	
58.5	15365	8.2	58.5	11778	9.5	F
67.8	12308	7.9	67.5	7690	6.4	E
87.3	50256	4.7	87.9	13272	4.4	A, E
89.0	46278	3.0	–	–	–	A
101.9	1356	2.3	102.3	1457	5.4	F
131.0	25897	5.5	130.8	17854	5.5	E, F
148.4	14894	9.4	149.8	2043	17.7	A
161.1	6363	15.1	–	–	–	A
209.4	2084	15.5	208.8	1673	12.1	F
278.9	37152	21.8	278.3	3945	22.4	A
342.4	17885	44.1	343.5	2060	50.5	A
377.7	4775	56.0	372.0	700	24.4	A, E
–	–	–	405.5	296	7.2	F
460.1	1563	19.3	464.8	1357	33.1	E
535.3	29855	18.9	534.9	3232	20.2	A
619.7	918	45.9	624.3	898	20.2	E
717.7	168	7.6	–	–	–	A
902.7	1417	7.8	902.6	173	6.7	A

in BZnO). However, such a tendency is observed only for some lines of the Raman spectra. The spectra are most similar for BGO and BTO crystals, but not for BGO and BAlPO, which have practically equivalent lattice parameters. The most pronounced differences are observed between the BGO and the BZnO Raman spectra. These differences are caused by the specific features of the crystal lattices of each of these crystals.

As is well known [4], the framework of the sillenite-type structure is formed by sharing—edges [BiO_5E]-polyhedra (where E is a lone pair of $6s^2$-electrons) forming dimers. The coordination sphere of Bi atoms consists of five oxygen atoms—O(1*a*), O(1*b*), O(2), O(1*c*), and O(3). The *M*-atoms located at the vertices and in the center of the cubic lattice (in the 2*a* positions) are coordinated with O(3) atoms and form regular tetrahedral [$M\mathrm{O}_4$]-groups. According to the neutron diffraction data, the ideal sillenite lattice is possessed by BGO crystals. Because of a larger size of a Ti-atom (in comparison with a Ge-atom), whose degree of oxidation, similar to Ge, equals +4, 10% of the 2*a* positions in BTO crystals are empty. The formation of *M* vacancies is accompanied by the formation of two O(3) vacancies. In this case, Bi-polyhedra, which have lost one of the O(3) vertices, are transformed into trigonal [BiO_4E]-bipyramids, and the structure framework is formed by the [BiO_4E]- and [BiO_5E]-polyhedra. The specific feature of $\mathrm{Bi}_{12}M^{+n}\mathrm{O}_{20\pm\delta}$ having M^{+n} cations and being characterized by the oxidation degree less than +4 is the occupancy with M^{+3}-cations of only some of the 2*a* positions (one-half of the total number of positions in the case of M^{+3} and one-third of the positions, in the case of M^{+2}). The remaining tetrahedral positions in the lattice are occupied by Bi^{3+} coordinated with three O(3) atoms. Thus, the crystal lattice of sillenite-type crystals with the oxidation degree of M^{+n}-cations less than +4 contains [BiO_3E]-, [BiO_4E]-, and [BiO_5E]-polyhedra at the comparable concentrations. In the complicated compounds formed by cations of different valences, $M = (\mathrm{A}^{3+}_{1/2}\mathrm{B}^{5+}_{1/2})$, $[\mathrm{A}^{3+}\mathrm{O}_4]$, and $[\mathrm{B}^{5+}\mathrm{O}_4]$, the tetrahedral groups are distributed statistically, and the fractions of [BiO_3E]- and [BiO_4E]-polyhedra are small in comparison with the fraction of [BiO_5E]-polyhedra.

It should be emphasized that the Bi–O bond lengths in [BiO_3E]-, [BiO_4E]-, and [BiO_5E]-polyhedra are very close and lie within the narrow range from 2.02 to 2.76 Å, which considerably hinders the interpretation of the lines corresponding to the atomic vibrations in these complexes. The formation of [BiO_3E]- and [BiO_4E]-polyhedra and the [BiO_5E]-groups should

Table 3. Position (cm^{-1}), intensity (Hz), and width (cm^{-1}) of bands in the Raman spectra of BTO crystals

Position	Intensity	Width	Position	Intensity	Width	Symmetry type
$x(zz)\bar{x}$			$x(zy)\bar{x}$			
–	–	–	46.8	136	2.7	F
56.6	270	5.6	56.6	1694	4.3	F
66.4	677	5.5	67.5	47	4.8	E
85.8	3530	3.6	84.7	95	4.4	A, E
–	–	–	96.7	244	9.4	F
–	–	–	111.2	56	24.2	F
128.5	100	4.8	129.1	299	6.9	E, F
144.9	518	9.1	–	–	–	A
165.7	276	17.6	162.6	84	23.6	A, E
–	–	–	207.8	150	17.3	F
224.0	85	13.6	–	–	–	
261.7	663	17.6	–	–	–	A
319.2	640	52.5	–	–	–	A
–	–	–	372.3	17	28.2	F
450.4	59	20.8	–	–	–	
–	–	–	485.9	19	18.2	F
535.3	1062	20.1	549.1	14	18.4	A
620.5	44	16.2	–	–	–	E
720.4	83	28.2	–	–	–	A

result in the formation of additional lines in the Raman spectra of these compounds, which cannot be spectrally resolved at room temperature. These additional lines are responsible for band broadening and the change in their intensities in the Raman spectra. Indeed, as is seen from Fig. 1, the nearest, most intense lines are obtained in the BGO Raman spectra with an ideal lattice. The most diffuse spectrum is obtained for the BZnO crystals whose crystal lattice mostly deviates from the ideal one (Fig. 4).

It is seen from Table 5 that the position, intensity, and the behavior of the intense line at 86.9 cm^{-1} in the BGO spectrum can be brought into correspondence with the corresponding characteristics of two lines at 89.0 and 87.3 cm^{-1} in the BAlPO spectra, two lines at 83.0 and 93.2 cm^{-1} in the BZnO spectra, and only one line at 85.9 cm^{-1} in the BTO spectrum. Although the line at 86.9 cm^{-1} in the BGO spectrum is not isolated, it is formed by the superposition of several vibrations. The main contribution to its intensity comes from the totally symmetric vibration [5] interpreted as the vibration of the Bi–O(3) bond [9]. Such an interpretation is well consistent with our results and the structural features of the crystals studied [4]. The existence of two types of [BiO$_5$E]-polyhedra sharing the O(3) vertex with other groups [AlO$_4$]- and [PO$_4$]-tetrahedra in BAlPO and [ZnO$_4$]- and [BiO$_3$E]-groups in BZnO) results in the formation of two totally symmetric vibrations provided by various Bi–O(3) bonds (unlike the Raman spectra of BTO crystals) for the structure having only one characteristic type of [BiO$_5$E]-polyhedra.

Comparing the Raman spectra of BGO and BZnO crystals, we see that in the range 250–400 cm^{-1}, to two intense lines at 269.5 and 323.3 cm^{-1} in the BGO spectrum there correspond three broad bands with the maxima at 256.8, 310.7, and 376.5 cm^{-1} in the BZnO spectra. In the BGO spectrum, the line at 269.5 cm^{-1} is isolated [5]. In accordance with Table 5, to this line there corresponds the maximum at 256 cm^{-1}. The symmetry of the main vibration determining the position and the intensity of this maximum is of the A type. The position of this band in the BZnO spectrum, as well as the positions of the corresponding bands in the BGO, BAlPO, and BTO spectra, correlates well with the change in the Bi–O(1*c*) distance [4]. The totally symmetric vibration of this bond is attributed to the line at 269.5 cm^{-1} in the BGO spectrum [9].

The line at 323.3 cm^{-1} in the BGO Raman spectra is not isolated, but the intensity of the main component of this line considerably exceeds the intensity of the neighboring lines [5]; therefore, it can be considered as a quasi-isolated line. In the BGO spectra, this line is attributed to totally symmetric vibrations of the Bi–O(1*b*) bond [9]. The shift of this line observed in the

Table 4. Position (cm^{-1}), intensity (Hz), and width (cm^{-1}) of bands in the Raman spectra of BZnO crystals

Position	Intensity	Width	Position	Intensity	Width	Symmetry type
$x(zz)\bar{x}$			$x(zy)\bar{x}$			
36.1	4492	12.7	37.5	536	8.3	
56.4	11290	27.0	55.4	4993	16.0	F
83.0	61119	6.9	83.3	3618	7.5	A
93.2	5952	7.2	–	–	–	A
126.7	16428	6.3	127.7	3596	7.2	E, F
141.3	9182	13.9	141.5	273	2.9	A
166.0	4886	23.9	166.1	926	80.4	A, F
–	–	–	209.2	369	32.6	F
256.8	14167	20.1	254.0	727	13.2	A
–	–	–	267.3	342	21.1	F
310.7	13747	81.2	308.9	825	74.1	A
376.5	6642	40.2	379.9	479	46.1	A, E
434.2	3513	83.4	441.5	361	114.9	E
526.1	20796	40.7	526.5	1416	40.4	A
560.7	4237	56.3	563.2	318	56.6	A
621.5	1982	37.2	621.3	219	37.6	E

Table 5. Comparison of the line frequencies (cm^{-1}) in the Raman spectra of BGO, BAlPO, BTO, and BZnO crystals. The rows indicate the frequencies of the identical lines

No.	BGO	BAlPO	BTO	BZnO	Vibration
1	56.0	58.5	56.6	56.4	
2	65.8	67.8	66.4	–	E, Bi–O(2)
3	86.9	87.3, 89.0	85.8	83.0, 93.2	A, Bi–O(3)
4	98.0	101.9	96.7	93.2	
5	128.5	131.0	128.5	126.7	
6	144.5	148.4	144.9	141.3	
7	167.1	161.1	165.7	166.0	
8	205.1	209.4	204.5	209.2	
9	269.5	278.9	261.7	256.8	A, Bi–O(1*c*)
10	323.3	342.4	319.2	310.7	A, Bi–O(1*b*)
11	–	377.7	–	376.5	
12	454.8	460.1	450.4	434.2	
13	487.6	–	485.9	–	
14	535.9	535.3	535.3	526.1	A, Bi–O(1*a*)
15	619.6	619.7	620.5	621.5	E, Bi–O(2)
16	715.6	717.7, 902.7	720.4	–	A, M–O(3)

row BGO, BAlPO, BTO, and BZnO, as well as the shift of the isolated line at 535.9 cm^{-1} in the BGO spectrum, correlates well with the structural data [4] and is attributed to the totally symmetric vibration of the Bi–O(1*a*) bond [9].

Analyzing the spectra of the compounds having the specific features in comparison with an ideal BGO crystal, the bands at 65.8 and 619.6 cm^{-1} [10] can be attributed to twice the degenerate normal vibration of the O(2)Bi$_3$-complex. As is seen from Table 5, despite the differences in the lattice parameters and the degree of imperfection of the crystals studied, the positions of these bands (nos. 2 and 5) remain practically the same. The O(2) atom lies on a threefold axis of the bcc unit cell and, therefore, the distances and the angles in the O(2)Bi_3–complex practically remain unchanged during disordering of the sillenite structure associated with the isomorphous substitution of M-cations with different degrees of oxidation. The attempt to attribute band no. 12 [9] with a varying position to the same vibration seems to be less grounded.

The intensities of the lines corresponding to the vibrations of the bonds in [GeO_4]-, [AlO_4]-, [PO_4]-, [TiO_4]-, and [ZnO_4]-tetrahedra are lower than the intensities of the lines due to Bi–O vibrations and the difference in concentrations in Bi-polyhedra and [MO_4]-groups. Therefore, it seems impossible to single out these vibrations in the range of intense Bi–O vibrations ($\nu < 600$ cm^{-1}). However, in the high-frequency range of the BGO, BAlPO, and BTO spectra, there are bands at 715.6, 717.7, 902.7, and 720.4 cm^{-1}, which can be attributed to the totally symmetric vibrations of [GeO_4], [AlO_4], [PO_4]-, and [TiO_4]-tetrahedra, respectively. The vibration frequencies corresponding to [ZnO_4]-groups are lower and observed in the range of Bi–O vibrations.

We should like to emphasize that all the above lines are isolated or quasi-isolated in the BGO spectrum [5]. The interpretation of the remaining lines of the spectra is not possible within the framework of the present study because of their complicated structure at room temperature.

CONCLUSIONS

The Raman spectra of the $Bi_{24}AlPO_{40}$ and $Bi_{38}ZnO_{58}$ crystals have been studied for the first time. It is shown that the differences observed in the Raman spectra of $Bi_{12}GeO_{20}$, $Bi_{24}AlPO_{40}$, $Bi_{12}TiO_{20}$, and $Bi_{38}ZnO_{58}$ are associated with the structural characteristics of sillenite crystals $Bi_{12}M_xO_{20 \pm \delta}$ caused by isomorphous substitutions of *M*-atoms. It is also established that the band broadening in the $Bi_{24}AlPO_{40}$ and $Bi_{38}ZnO_{58}$ spectra (in comparison with the bands in the $Bi_{12}GeO_{20}$ spectrum) is caused by disordering of the structures of these compounds.

REFERENCES

1. S. I. Stepanov, Rep. Prog. Phys. **57** (1), 39 (1994).
2. Yu. V. Gulyaev, V. V. Proklov, and G. N. Shkerdin, Usp. Fiz. Nauk **124** (1), 61 (1978) [Sov. Phys. Usp. **21**, 29 (1978)].
3. V. V. Volkov, A. V. Egorysheva, and V. M. Skorikov, Neorg. Mater. **29** (5), 652 (1993).
4. S. F. Radaev and V. I. Simonov, Kristallografiya **37** (4), 914 (1992) [Sov. Phys. Crystallogr. **37**, 484 (1992)].
5. S. Venugopolan and A. K. Ramdas, Phys. Rev. B **5** (10), 4065 (1972).
6. R. J. Betsh and W. B. White, Spectrochim. Acta A **34**, 505 (1978).
7. Yu. G. Zaretskiĭ, G. A. Kurbatov, V. V. Prokof’ev, *et al.*, Opt. Spektrosk. **54** (3), 569 (1983) [Opt. Spectrosc. **54**, 338 (1983)].
8. V. V. Volkov, Yu. F. Kargin, N. I. Nelyapina, and V. M. Skorikov, Zh. Neorg. Khim. **34** (12), 3131 (1989).
9. Yu. G. Zaretskiĭ, Yu. I. Ukhanov, and Yu. V. Shmartsev, Fiz. Tverd. Tela (Leningrad) **33** (4), 1202 (1991) [Sov. Phys. Solid State **33**, 681 (1991)].
10. G. A. Babonas, E. A. Zhogova, Yu. G. Zaretskiĭ, *et al.*, Fiz. Tverd. Tela (Leningrad) **24** (6), 1612 (1982) [Sov. Phys. Solid State **24**, 921 (1982)].

Translated by L. Man

Crystallography Reports, Vol. 46, No. 3, 2001, pp. 468–473. Translated from Kristallografiya, Vol. 46, No. 3, 2001, pp. 519–524.
Original Russian Text Copyright © 2001 by Alshits, Lyubimov, Radowicz, Shuvalov.

Specific Characteristics of the Configurations of Optical Axes in Absorptive Crystals

V. I. Alshits*, V. N. Lyubimov*, A. Radowicz, and L. A. Shuvalov***

** Shubnikov Institute of Crystallography, Russian Academy of Sciences,*
Leninskiĭ pr. 59, Moscow, 117333 Russia

*** University of Technology, al. Tysiacelecia Panstwa Polskiego 7, Kielce, 25-314 Poland*

Received October 20, 1999

Abstract—The spherical coordinates of four optical axes in absorptive orthorhombic crystals have been determined in terms of the components of the tensor of inverse permittivity constant $\hat{B} = \hat{\varepsilon}^{-1}$. The evolution of the configurations of these four vectors has been studied as a function of the complex tensor $\hat{B}$. It was shown that anomalous changes in the angles formed by the optical axes and the orientations of the planes in which these vectors are located occur if the parameters of dielectric anisotropy of the crystal are comparable with the absorption level. In particular, these dramatic changes can be seen in the description of the optical-axis splitting in absorptive uniaxial crystals caused by “inclusion” into consideration of feeble orthorhombic anisotropy. In these cases, the slight absorption anisotropy considerably influences the configurations that cannot be reduced to small corrections. *© 2001 MAIK “Nauka/Interperiodica”.*

INTRODUCTION

Two independent electromagnetic eigenwaves belonging to two different sheets of the wave surface of refractive indices can propagate along an arbitrary direction in an anisotropic medium. These waves propagate with different velocities and are differently absorbed by the medium. However, in an arbitrary absorptive medium, one can always find such particular directions along which this pair of eigenwaves would propagate with the same phase velocities and the same absorption coefficients. These directions are called the optical axes [1–6].

The orientation of the optical axes in crystals is fully determined by the setting of the permittivity tensor $\hat{\varepsilon}$, which is a complex quantity in absorptive crystals. The components of this tensor considerably change in the phase transitions; therefore, their magnitude can be controlled by varying the frequency, the temperature, and the applied external electric and magnetic fields or mechanical loads.

In the general case, the transparent nonabsorptive crystals can only have two optical axes [1–4]. Absorption drastically changes the situation and, in the general case, instead of two optical axes, four optical axes can exist [5, 6]. Of special importance are the cases where the role of absorption cannot be reduced to the introduction of small corrections. It is important to consider the situations, where small changes in the material characteristics of the crystal (the components of $\hat{\varepsilon}$) would result in considerable changes in the configurations of the optical axes. Below, this problem is considered for the general case of absorptive orthorhombic crystals admitting simple analytical solutions.

INITIAL RELATIONSHIPS

The directions of the optical axes in anisotropic media can be conveniently set with the aid of the inverse permittivity tensor $\hat{B} = \hat{\varepsilon}^{-1}$. In the case of absorptive orthorhombic crystals, this tensor is complex and its real and imaginary parts have the common system of the principal axes and can simultaneously be reduced to the diagonal form [6]. This tensor is also diagonal in the standard crystallographic coordinate system [1] and has the form

$$\hat{B} \equiv \begin{bmatrix} B_1 & 0 & 0 \\ 0 & B_2 & 0 \\ 0 & 0 & B_3 \end{bmatrix} = \begin{bmatrix} \beta_1 - i\beta'_1 & 0 & 0 \\ 0 & \beta_2 - i\beta'_2 & 0 \\ 0 & 0 & \beta_3 - i\beta'_3 \end{bmatrix}, \quad (1)$$

where

$$\beta_j > 0, \quad \beta'_j \geq 0.$$

Using the Fedorov formalism [5], tensor (1) can be represented in the axial form

$$\hat{B} = B_2 + \frac{B_3 - B_1}{2}(\mathbf{c}_1 \otimes \mathbf{c}_2 + \mathbf{c}_2 \otimes \mathbf{c}_1), \quad (2)$$

where the symbol ⊗ denotes the diadic product of the vectors $\mathbf{c}_1$ and $\mathbf{c}_2$, which are the axes of the tensor $\hat{B}$.

These two vectors can be written as

$$\mathbf{c}_{1,2} = (\pm R_1, 0, R_3), \qquad (3)$$

where

$$R_1 = \sqrt{\frac{B_2 - B_1}{B_3 - B_1}}, \quad R_3 = \sqrt{\frac{B_3 - B_2}{B_3 - B_1}}.$$

The knowledge of the complex vectors $\mathbf{c}_1$ and $\mathbf{c}_2$ Eq. (3) allows the direct determination of the directions of all the four optical axes $\mathbf{m}_j^{\pm}$ in the absorptive crystals under consideration [5],

$$\mathbf{m}_j^{\pm} = (\mathbf{c}_j + \mathbf{c}_j^* \pm i[\mathbf{c}_j\mathbf{c}_j^*])/(1 + |\mathbf{c}_j|^2), \qquad (4)$$

where

$$j = 1; 2, \quad (\mathbf{m}_j^{\pm})^2 = 1.$$

ORIENTATIONS OF THE OPTICAL AXES AS FUNCTIONS OF THE COMPONENTS OF TENSOR $\hat{B}$

The orientation of any of the four optical axes can be conveniently described in the standard spherical coordinate system in which the angle ϑ is measured from the x_3-axis and the angle φ, from the x_1-axis in the plane x_1x_2. Then, the orientation of all the four optical axes of an absorptive orthorhombic crystal is set by the angles

$$(\vartheta, \pm\varphi), \quad (\vartheta, \pm\varphi + \pi). \qquad (5)$$

Omitting the intermediate calculations based on Eqs. (3) and (4), we give only the final relationships showing the dependence of the angles ϑ and φ on the components of the tensor $\hat{B}$ Eq. (1)

$$\vartheta = \arccos\sqrt{\frac{\rho[\rho(1-\tilde{\eta}) + 1]}{(\rho + 1)(r + 1) + \rho^2\tilde{\eta}}},$$
$$\varphi = \arcsin\sqrt{\frac{\rho(\rho\tilde{\eta} + r)}{r(\rho + r + 1)}}, \quad r = \sqrt{\rho^2(2\tilde{\eta} - 1) + 1}, \qquad (6)$$

where

$$\tilde{\eta} \equiv \tilde{\eta}(\eta, \kappa) = \eta - \kappa\frac{d'_3}{d_3} = \frac{d_1 d_3 + d'_1 d'_3}{d_3^2 + (d'_3)^2}, \qquad (7)$$

$$\rho \equiv \rho(\eta, \kappa) = \frac{1}{\sqrt{(\tilde{\eta} - 1)^2 + \kappa^2}}. \qquad (8)$$

In the above equations, we have

$$\eta = \frac{d_1}{d_3}, \quad \kappa = \frac{-d'_1 d_3 + d'_3 d_1}{d_3^2 + (d'_3)^2},$$
$$d_k = \beta_k - \beta_2, \quad d'_k = \beta'_k - \beta'_2 \ (k = 1, 3). \qquad (9)$$

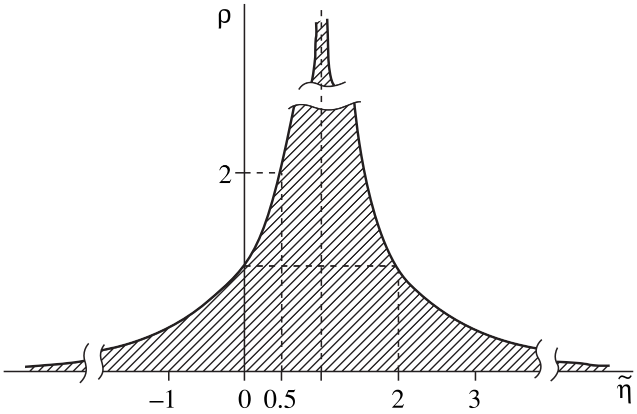

Fig. 1. The range of permittivity variations for absorptive orthorhombic crystals $0 \le \rho(\tilde{\eta}) \le \rho_{\max}(\tilde{\eta})$.

Thus, we see that all the configurations of the optical axes determined by Eqs. (5)–(9) are dependent only on the parameters d_k and d'_k characterizing the crystal anisotropy. The angles ϑ and φ can be considered, in full accordance with Eqs. (7)–(9), as functions of η and κ, which allows the direct separation of the absorption anisotropy characterized by the parameter κ.

EVOLUTION OF CONFIGURATION OF OPTICAL AXES WITH THE CHANGE OF THE COMPONENTS OF THE TENSOR $\hat{B}$

Using formulas (5)–(9), consider the evolution of the configurations of four optical axes $\mathbf{m}_k$ (where $k = 1, 2, 3, 4$) with the change of the material characteristics of the crystal.

As is seen from Eq. (8), at any fixed value of $\tilde{\eta}$ $(-\infty \le \tilde{\eta} \le +\infty)$, the parameter ρ changes from zero (at $\kappa^2 = \infty$) to $\rho_{\max}(\tilde{\eta}) = 1/|\tilde{\eta} - 1|$ (at $\kappa = 0$). The range of possible values of the parameters $\tilde{\eta}$ and ρ is shown in Fig. 1. In particular, the upper boundary of this range, $\rho = \rho_{\max}(\tilde{\eta})$ ($\kappa = 0$), corresponds either to zero absorption (i.e., to transparent crystals) and or to absorptive crystals if at least one of the following two requirements is met:

$$d'_k = 0 \qquad (10)$$

or

$$\frac{d'_1}{d'_3} = \frac{d_1}{d_3}.$$

In the two latter cases, the angles ϑ and φ are the functions of only one parameter η Eq. (9) and the directions of the optical axes are exactly the same as in the transparent crystals (we mean here an accidental degeneracy). The lower boundary of the existence range of the

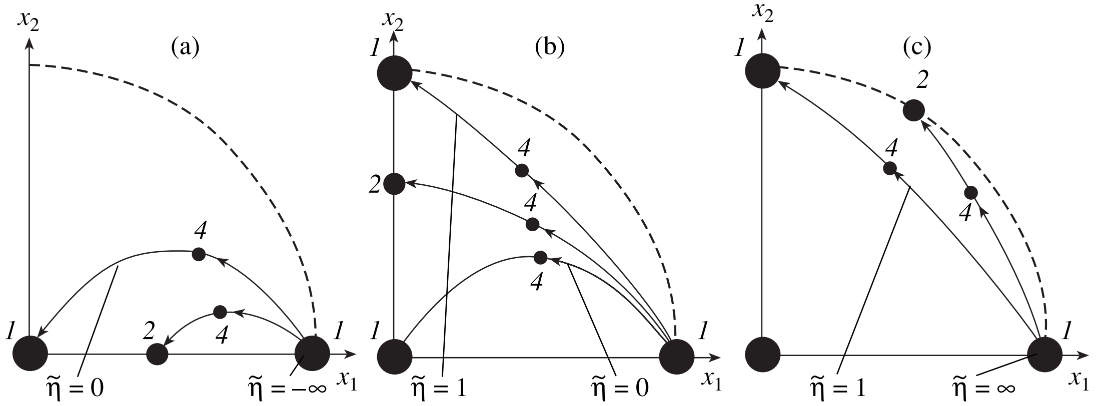

Fig. 2. Evolution of the optical-axis configurations on the lines $\tilde{\eta}(\rho) = \text{const}$ with an increase of the parameter ρ from 0 to $\rho_{\max}(\tilde{\eta})$; (a) $-\infty < \tilde{\eta} = \text{const} < 0$, (b) $0 < \tilde{\eta} = \text{const} < 1$, and (c) $1 < \tilde{\eta} = \text{const} < \infty$. The numbers at the circles indicate the multiplicity of the corresponding parameter in the crystal (the number of optical axes). Only independent fragments of the projections are shown.

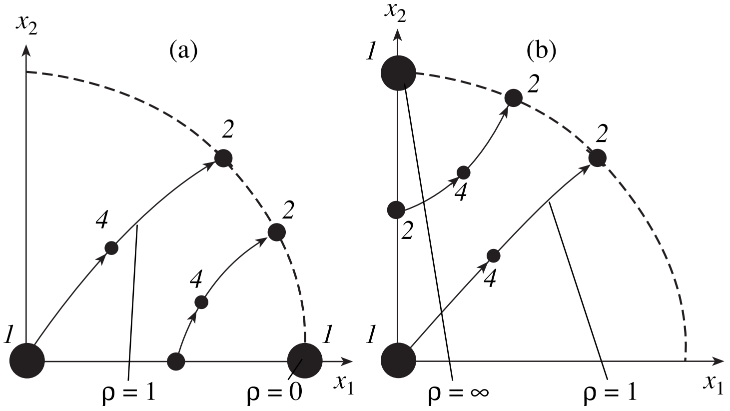

Fig. 3. Evolution of the optical-axis configurations on the lines $\rho(\tilde{\eta}) = \text{const}$ with an increase of the parameter $\tilde{\eta}$ from $\tilde{\eta}_{\min}(\rho)$ to $\tilde{\eta}_{\max}(\rho)$; (a) $0 < \rho = \text{const} < 1$ and (b) $1 < \rho = \text{const} < \infty$.

optical axes $\rho = 0$ ($\kappa^2 = \infty$) corresponds to the case of optically uniaxial media $\mathbf{m}_k = \mathbf{m}_0 \parallel x_1$.

To each point in the two-dimensional region $(\tilde{\eta}, \rho)$ shown in Fig. 1 there corresponds its own configuration of the optical axes. Figure 2 shows three topologically different types of stereographic projections, which show the change in the optical-axis orientation with the variation of the parameters at $\tilde{\eta}(\rho) = \text{const}$ in the hatched region in Fig. 1 (this condition corresponds to the motion along the vertical lines in Fig. 1). To each topological type there corresponds its own range of $\tilde{\eta}$ variation. The lines on all the three projections have the same origin but end in different coordinate planes. The jumpwise change of the planes takes place at the critical values of the parameter $\tilde{\eta}$, namely, at $\tilde{\eta} = 0$ and 1, i.e., in the situations where a crystal “passes through” an optically uniaxial medium (a catastrophe-like transition).

Figure 3 shows two topologically different types of stereographic projections showing the changes in the configurations of the optical axes at $\rho(\tilde{\eta}) = \text{const}$ (this condition corresponds to the motion along the horizontal lines in the hatched region in Fig. 1). Each topological type is characterized by its own range of variation of the parameter ρ. All the lines on these two projections end in the same coordinate plane, but their origins are located in different coordinate planes. Thus, two types of projections differ by the location of the line origins and ends. The jumpwise change of the planes occurs at the critical value $\rho = 1$. The coordinate planes in Figs. 2 and 3 correspond to the condition $\kappa = 0$, which is also valid for transparent crystals.

As an example, consider the line $\tilde{\eta}(\rho) = 0.5$. In this case, Eqs. (6) are considerably simplified:

$$\vartheta = \arccos\sqrt{\rho/(\rho+2)}, \quad \varphi = \arcsin\sqrt{\rho/2} \qquad (11)$$

and

$$0 \le \rho \le 2 \text{ and } \kappa^2 = \frac{1}{\rho^2} - \frac{1}{4}. \qquad (12)$$

The evolution of the optical-axis configurations described by formulas (11) and (12) is represented by the curves in Fig. 4. If $\rho = 2$, then $\kappa = 0$, as in transparent crystals. In this case, there are only two optical axes and their angular coordinates are set by the relationships

$$(\vartheta = \pi/4, \varphi = \pm\pi/2). \qquad (13)$$

In "switching on" the absorption anisotropy, $\kappa^2 \ll 1$ $(2 - \rho \ll 1)$, the splitting of these optical axes occurs linearly with respect to the parameter κ,

$$\Delta\varphi = \pm\sqrt{2}|\kappa|. \qquad (14)$$

SPLITTING OF AN OPTICAL AXIS OF AN ABSORPTIVE UNIAXIAL CRYSTAL

Consider splitting of the optical axis $\mathbf{m}_0 \parallel x_3$ of an absorptive uniaxial crystal under the effect of an anisotropic perturbation.

In the zeroth approximation, we have

$$\vartheta = 0, \quad \tilde{\eta} = \eta = 0, \quad \rho = 1, \quad \kappa = 0. \qquad (15)$$

In the case of perturbation (η^2, $\kappa^2 \ll 1$, $d_3'/d_3 \sim \kappa$), the characteristics of optical axes Eqs. (6) we are interested in have the form

$$\vartheta = \sqrt[4]{\eta^2 + \kappa^2}, \quad \varphi = \arcsin\sqrt{\frac{1}{2}\left[1 + \frac{\operatorname{sgn}\eta}{\sqrt{(\kappa/\eta)^2 + 1}}\right]}. \qquad (16)$$

If, e.g., the absorption-anisotropy parameter κ is zero, then, in correspondence with Eq. (16), the optical axis $\mathbf{m}_0$ is split into two optical axes, as in the transparent crystals. These axes lie either in the coordinate plane x_2x_3 $(\varphi = \pi/2)$ at $\eta > 0$ (Fig. 5) or in the coordinate plane x_1x_3 $(\varphi = 0)$ at $\eta < 0$. Switching on the absorption anisotropy, $\kappa \neq 0$, drastically change the optical-axis configurations: four optical axes arise and, generally speaking, the planes in which these axes lie deviate from the coordinate planes by rather large angles. Thus, the angle φ in Eq. (16) is determined by the ratio of the small parameters κ and η, which can change within rather wide ranges (Figs. 5, 6).

In correspondence with Eqs. (16), the reversal of the sign of the parameter η $(\eta \longrightarrow -\eta)$ results in the substitution $\varphi \longrightarrow \pi/2 - \varphi$, i.e., the coordinate axes x_1 and x_2 are interchanged.

As is seen from Eqs. (16), the angle between the optical axes $\alpha = 2\vartheta$ depends anomalously strongly on the perturbation value

$$\alpha \ge 2\sqrt{|\eta|} \gg |\eta|. \qquad (17)$$

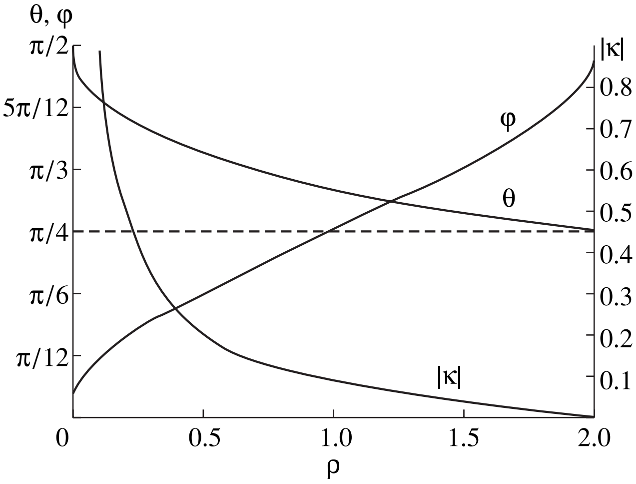

Fig. 4. Characteristics of the optical-axis configurations on the line $\tilde{\eta}(\rho) = 0.5$.

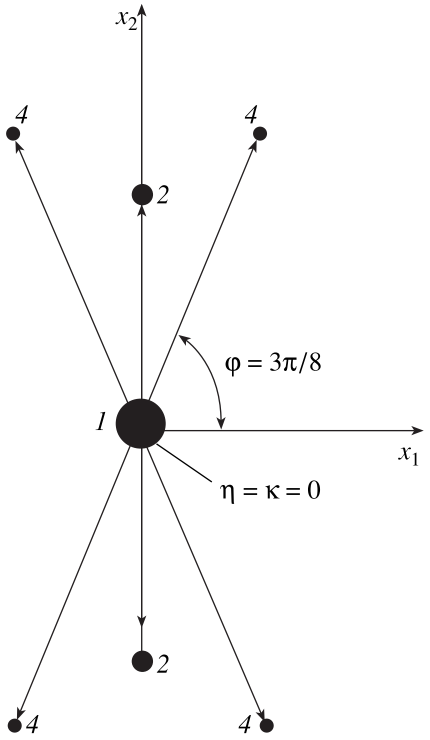

Fig. 5. Splitting of the optical axis in an absorptive $(0 < \eta, \kappa \ll 1, \theta = \sqrt{2\eta}, \varphi = 3\pi/8)$ and transparent $(\kappa = 0, \theta = \sqrt{|\eta|}, \varphi = \pi/2)$ uniaxial crystals.

In order to estimate the splitting angle of the optical axes with the change of the material parameters of an optically uniaxial medium, we assume, e.g., that $|\eta| = |\kappa| = 0.01$. Thus, we arrive at the following estimate $\alpha = 2\sqrt[4]{2}\sqrt{|\eta|} \approx 0.24$ $(\sim 14^0)$. Despite the perturbation smallness, the angle α is rather large.

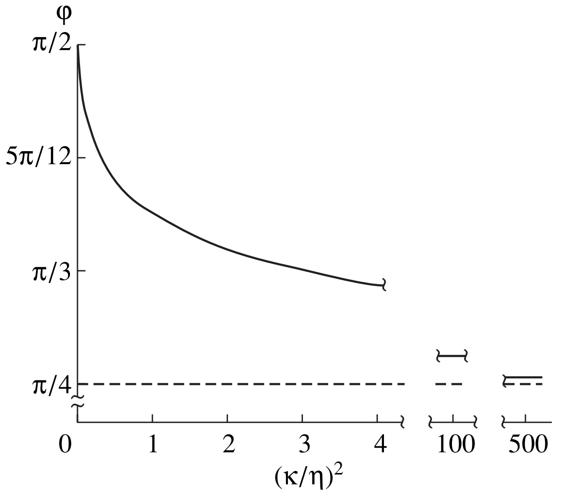

Fig. 6. The orientation set by the angle φ in the plane of the optical axes formed due to splitting of the optical axis in an absorptive uniaxial crystal (φ as a function of the perturbation parameters at η > 0).

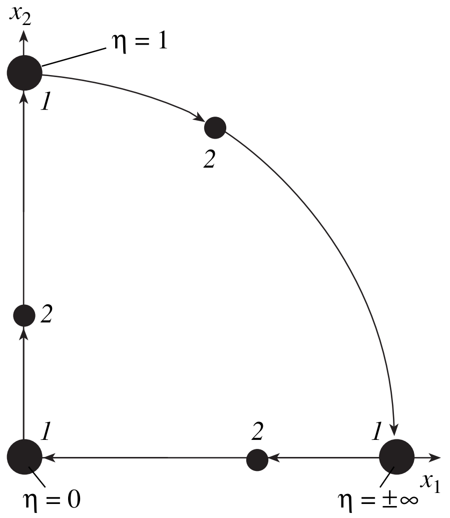

Fig. 7. Stereographic projection showing the "motion" of optical axes of a transparent triclinic crystal with an increase of the parameter η from –∞ to +∞.

The perturbation used transforms the optically uniaxial medium into the orthorhombic one. In the case under consideration, we can also introduce a general form of perturbation resulting in the triclinic distortion of the medium. In this case, splitting of the optical axes (Fig. 5) is less symmetric but no qualitatively new features of the phenomenon are observed. Similar transformations can also take place in the structural phase transitions.

ANOMALIES IN SENSITIVITY OF OPTICAL-AXIS CONFIGURATIONS

An important characteristic of the configurations considered here is their sensitivity to the changes in the material parameters of the crystal. This sensitivity can be characterized, e.g., by the derivatives

$$\partial\vartheta/\partial\xi \text{ and } \partial\varphi/\partial\xi, \tag{18}$$

where

$$\xi = \tilde{\eta}, \rho.$$

Invoking Eqs. (16), which describe the splitting of the optical axis in a uniaxial crystal, we can describe the sensitivity by the following derivatives:

$$\partial\vartheta/\partial(\eta^2) = \partial\vartheta/\partial(\kappa^2) = 1/4\vartheta^3, \tag{19}$$

$$\frac{d\varphi}{d(\kappa^2/\eta^2)} = \frac{-\operatorname{sgn}\eta}{4(\sin 2\varphi)(\kappa^2/\eta^2+1)^{3/2}}. \tag{20}$$

It is seen that if the perturbation parameters tend to zero (at $\vartheta \longrightarrow 0$), derivative (19) has a singularity (i.e., it goes to infinity), whereas derivative (20) goes into infinity at $\varphi = \pi/2$ if $\eta > 0$ (Fig. 6) and at $\varphi = 0$ if $\eta < 0$.

CONFIGURATIONS OF OPTICAL AXES IN TRANSPARENT CRYSTALS

At $\kappa = 0$, all the optical-axis configurations are the functions of only one parameter, η (14), whereas the general Eqs. (6) yield the following relationships, also valid for absolutely transparent crystals:

$$\begin{aligned}
&\vartheta = \arctan\sqrt{-\eta}, \quad \varphi = 0, \pi; \quad -\infty \le \eta \le 0,\\
&\vartheta = \arctan\sqrt{\frac{\eta}{1-\eta}}, \quad \varphi = \pm\frac{\pi}{2}; \quad 0 \le \eta \le 1,\\
&\vartheta = \frac{\pi}{2}, \quad \varphi = \pm\arctan\frac{1}{\sqrt{\eta-1}}; \quad 1 \le \eta \le \infty.
\end{aligned} \tag{21}$$

The above equations are valid in the most general case of a transparent triclinic crystal. The optical axes $\mathbf{m}_1$ and $\mathbf{m}_2$ can lie only in the coordinate planes. With the change of the parameter η in the range of its possible values $-\infty \le \eta \le \infty$, these axes successively "scan" all three coordinate planes (Fig. 7). To each coordinate plane in which the optical axes lie there corresponds its own range of the η variation in Eqs. (21).

CONCLUSION

The specific features of the optical-axis configurations in absorptive crystals considered above are provided by the medium anisotropy. At the same time, the most pronounced effects arise at small parameters of the dielectric anisotropy comparable with the absorption level. Indeed, at small anisotropy of dielectric properties, the complex refractive indices of two independent eigenwaves are close to each other irrespectively of the direction of their propagation, so that even small changes in the anisotropy parameters drastically change the coordinates of the contact points of the wave-surface sheets, i.e., the orientations of the optical axes. It is seen from Eqs. (7) and (9) that with the anisotropy parameters d_k and d'_k tending to zero, the coefficients $\tilde{\eta}$, η, and κ (directly determining the directions of the optical axes) in the limit become the 0/0-type uncertainties and can vary over a large range of values even at small variations in d_k and d'_k. It is natural that the configurations of the optical axes in this case also dramatically change.

It should be emphasized that, in a conventional transparent biaxial crystal, splitting of its two optical axes with switching on the absorption occurs without any anomalies—the splitting angle is proportional to the absorption anisotropy. For orthorhombic crystals, this angle is proportional to d'_k (see Eqs. (13) and (14) and [6]). However, the situation dramatically changes if the initial angle formed by the axes of a biaxial crystal is small. This occurs in the vicinity of the critical values of the parameter $\eta = \pm\infty; 0; 1$ [see Eq. (21)], when the crystal becomes similar to optically uniaxial one. In this case, small variations in absorption and in η can result in dramatic rearrangements of the optical-axis configurations.

Similar rearrangements also take placed in practice either because of the change in the crystal symmetry in the phase transition or as a result of the dependence of the components of the tensor $\hat{B}$ on the temperature, pressure, wavelength, and other physical parameters. In particular, in some instances, one manages to find such a combination of the physical conditions that the quantity η passes through the above critical values, whereas the crystal, through the state of a uniaxial medium. These processes should be accompanied by a jumpwise change of the planes in which the optical axes are located, which was observed in brookite crystals (the orthorhombic modification of TiO_2) with the change in the wavelength of the light wave [1]. A similar phenomenon was also observed in orthorhombic ammonium trihydroselenite crystals, $NH_4H_3(SeO_3)_2$ [7], where the varied parameters were the wavelength and the temperature.

ACKNOWLEDGMENTS

The authors are grateful to A.F. Konstantinova for useful advice and the University of Technology, Kielce, Poland, for financial support. The study was also supported by the Russian Foundation for Basic Research, project no. 98-02-16069.

REFERENCES

1. Yu. I. Sirotin and A. M. Shaskolskaya, *Fundamentals of Crystal Physics* (Nauka, Moscow, 1979; Mir, Moscow, 1982).
2. B. N. Grechushnikov, L. A. Shuvalov, *et al.*, in *Modern Crystallography*, Vol. 4: *Physical Properties of Crystals*, Ed. by B. K. Vainshtein, A. A. Chernov, and L. A. Shuvalov (Nauka, Moscow, 1981; Springer-Verlag, Berlin, 1988).
3. A. F. Konstantinova, B. N. Grechushnikov, B. V. Bokut', and E. G. Valyashko, *Optical Properties of Crystals* (Nauka i Tekhnika, Minsk, 1995).
4. F. I. Fedorov and V. V. Filippov, *Reflection and Refraction of Light by Transparent Crystals* (Nauka i Tekhnika, Minsk, 1976).
5. F. I. Fedorov, *Theory of Gyrotropy* (Nauka i Tekhnika, Minsk, 1976).
6. V. I. Alshits and V. N. Lyubimov, Kristallografiya **45** (4), 731 (2000) [Crystallogr. Rep. **45**, 670 (2000)].
7. N. R. Ivanov and A. F. Konstantinova, Kristallografiya **15** (3), 490 (1970) [Sov. Phys. Crystallogr. **15**, 416 (1970)].

Translated by L. Man

Crystallography Reports, Vol. 46, No. 3, 2001, pp. 474–479. Translated from Kristallografiya, Vol. 46, No. 3, 2001, pp. 525–530.
Original Russian Text Copyright © 2001 by Petukhov.

The Dependence of Anomalous Temperature Peak of a Deforming Stress on Microstructural Parameters

B. V. Petukhov

Shubnikov Institute of Crystallography, Russian Academy of Sciences, Leninskiĭ pr. 59, Moscow, 117333 Russia
e-mail: petukhov@ns.crys.ras.ru

Received October 10, 2000

Abstract—The temperature dependence of a deforming stress (including both low-temperature decreasing branch and an anomalous high-temperature peak) has been calculated on the basis of one mechanism. The theory developed takes into account spontaneous thermally activated processes of dislocation locking and unlocking and describes the transition from conventional dislocation gliding to the jumpwise motion of dislocations with the change of the temperature (in full accordance with the *in situ* electron microscopy observations). The dependences of the plasticity characteristics (flow stress, strain-rate sensitivity, etc.) on the microstructural parameters such as free dislocation path and the energy barriers that should be overcome by dislocations for transformation of their cores from the “gliding” to the “sessile states” and back have also been determined. *© 2001 MAIK “Nauka/Interperiodica”.*

INTRODUCTION

The crystalline structure of materials gives rise to a number of specific practically important characteristics of the dynamic behavior of dislocations and plasticity that are different from the behavior predicted by the continuum approach. In addition to obvious anisotropy in plastic flow dictated by the crystallographic set of gliding systems, of great importance are also the effects caused by the fine structure of a dislocation core that can be rearranged between different energy states in accordance with the crystal symmetry [1, 2]. It is assumed that in some materials, these effects can result in an anomalous increase of the yield stress at high temperatures, which opens new possibilities for various high-temperature applications of these materials and, thus, is also of great practical interest (see reviews [3–7]).

Of special importance is the possibility to vary the temperature range of the manifestation of this effect, i.e., the temperature of the anomalous maximum T_M and the stress amplitude $\sigma_M = \sigma(T_M)$. This can be achieved, e.g., with the aid of alloying, because, as was shown experimentally, both T_M and σ_M are rather sensitive to the impurity concentration [8]. It was shown that alloying somewhat modifies the microstructural parameters controlling the mechanisms of dislocation motion and, thus, also the material plasticity. The possibility of purposeful change of the microstructural parameters requires the knowledge of the dependence of the plasticity characteristics on those parameters, whose modification can be the most efficient. Unfortunately, at present, there are only some qualitative data to the effect, but no consistent and complete description of the dependence of the anomalous temperature peak of the deforming stress on the microstructural parameters within one, even considerably simplified model has been made as yet. The present study is aimed at developing a simplified unified model of the effect to attain the first approximation to the real situation. Such an approximation can be the first semiqualitative landmark in clarifying the degree of influence of one or another microstructural parameter on the anomalous plasticity of materials.

The anomalous behavior of intermetallic alloys with the Ll_2 structure type (as the Ni_3Al alloy) is usually interpreted as the transition of a split dislocation from the mobile configuration in the glide plane to the sessile configuration (the so-called Kear–Wilsdorf localization [3, 6]). Another interesting example is the jumpwise motion of dislocations on the prismatic planes in Be and Ti crystals: in accordance with the *in situ* electron-microscopy study [1], a dislocation which has passed several lattice periods stops for some time; then the process is repeated many times. This phenomenon is usually interpreted under the assumption that a dislocation core can have several states—mobile and immobile—and that it can be transformed from one state to another and back. In turn, this is usually considered in terms of dislocation resplitting in various crystallographic planes [1, 2]. Consider also the behavior of plasticity in γ-TiAl: it is interpreted as a dislocation motion in a multi-valley Peierls–Nabarro relief with the regular dislocation “sticking” to deep relief minima. Upon a rather long process of thermally activated liberation of these dislocations from the deep minima, they start moving rather fast over a shallower relief [7]. In the present study, we did not consider any concrete microscopic mechanism of dislocation locking; instead, we use a generalized phenomenological description based on the general concepts of the thermally activated kinetics. As a result, we managed to describe some characteristic features of macroscopic plastic deformation of materials in a rather simple and general way.

As an alternative to this model with the spontaneous thermally activated fluctuation-like liberation of dislocations developed in our study, it is also possible to describe the process within alternative models with the local mechanically forced unpinning of dislocations which, in turn, initiates the process of the so-called dislocation unzipping [9, 10]. There also exist some statistical models of dislocation immobilization [11] and other approaches (see reviews [3–7] and [12–15]).

KINETICS OF DISLOCATION MOTION

Generalize the conventional mechanism of dislocation gliding by including into consideration spontaneous processes of dislocation-core rearrangement between the mobile and immobile configurations. It is assumed that, in addition to the conventional gliding states (g), there also exist the sessile states (s) and that dislocations can perform mutual transitions from the gliding to the sessile states with a frequency J_- and back from the sessile to the gliding states with a frequency J_+. Unlike the transitions between various gliding states, which should necessarily be taken into account, the transitions between various sessile states can be ignored.

Denote the probabilities that by the moment t a dislocation is in the gliding state by $N_g(t)$ and, in the sessile state, by $N_s(t)$, so that $N_g(t) + N_s(t) = 1$. Then, the kinetics of the change in the fraction of gliding states can be described by the equation

$$dN_g/dt = J_+N_s - J_-N_g, \tag{1}$$

which can readily be solved by excluding the quantity N_s from it using the Eq. $N_g + N_s = 1$ and the initial conditions $N_g(0) = 1$ and $N_s(0) = 0$. Thus, we obtain

$$N_g(t) = \frac{J_+}{J_+ + J_-} + \frac{J_-}{J_+ + J_-}\exp[-(J_+ + J_-)t]. \tag{2}$$

A dislocation moves over the gliding states with a certain velocity v, and the sessile states give no contributions to its spatial displacement. Thus, a dislocation moves in a jumplike manner via stochastic hoppings through the glide states between the events of its successive locking. The average dislocation position, $\langle x(t)\rangle$, varies with time according to the Eq. $\langle dx(t)/dt\rangle = vN_g(t)$. Integrating the latter equation, we obtain

$$\langle x(t)\rangle = vt\frac{J_+}{J_+ + J_-} + v\frac{J_-}{(J_+ + J_-)^2}\{1 - \exp[-(J_+ + J_-)t]\}. \tag{3}$$

One can readily see that, in this case, the averaged motion of dislocations is time-inhomogeneous. As follows from Eq. (3), at short $t \ll 1/(J_- + J_+)$, the above relationship describes conventional dislocation gliding $\langle x(t)\rangle \approx vt$. Within a rather long time, $t \gg 1/(J_- + J_+)$, the dislocation has the time to perform quite a large number of hoppings and its path is determined mainly by the renormalized averaged motion velocity

$$\langle x(t)\rangle \approx vtJ_+/(J_- + J_+). \tag{4}$$

If the probabilities of the dislocation sticking in the sessile states and their liberation from these states are considerably different, $J_+ \ll J_-$, the reduction of the dislocation velocity can be essential. Equation (3) also provides the description of a transient behavior of dislocations, where the change in the parameters, e.g., the temperature, results in the change of the controlling mechanism from simple dislocation gliding to the jumplike motion. The transient-type of dislocation behavior becomes essential if the total dislocation path l_p is limited, l_p, i.e., if the lifetime of a mobile dislocation becomes comparable with the average time necessary for a single hopping. The change in the mobilities of individual dislocations also modifies the characteristic features of the macroscopic plastic flow of the material.

MACROSCOPIC PLASTICITY

Now let us use the above results to describe the macroscopic plastic deformation. For the average velocity v of the motion of dislocations having the density ρ, the rate $\dot{\varepsilon}$ of the plastic flow is given by the Orovan equation $\dot{\varepsilon} = \rho b v(\sigma, T)$, where b is the Burgers-vector length. In deformation occurring at a constant rate and the known dependence of the motion velocity on stress σ and temperature T, the latter relationship can also be used to determine the temperature dependence of the deforming stress, $\sigma(T)$.

For a thermally activated motion, dependent only on the elementary process of overcoming similar obstacles, the dependences of v on σ and T are determined mainly by the Arrhenius factor $v = v_0\exp(-E(\sigma)/kT)$, where $E(\sigma)$ is the corresponding activation energy and v_0 is an unessential preexponential factor. As a result, we arrive at a simple law of plastic flow in the form $\dot{\varepsilon} = \dot{\varepsilon}_0 \exp(-E(\sigma)/kT)$ or

$$E(\sigma) = kT\ln(\dot{\varepsilon}_0/\dot{\varepsilon}), \tag{5}$$

where $\dot{\varepsilon}_0 = \rho b v_0$. Assuming that the dislocation density ρ and the factor v_0 only weakly depend on the temperature and the stress in comparison with the Arrhenius factor, we can take in what follows that $\dot{\varepsilon}_0$ is a certain constant. At $\dot{\varepsilon} = \text{const}$, the deforming stress determined from Eq. (5) monotonically decreases with the temperature (the so-called "normal behavior").

In the case we are interested in, the dislocation motion is accompanied by spontaneous transitions

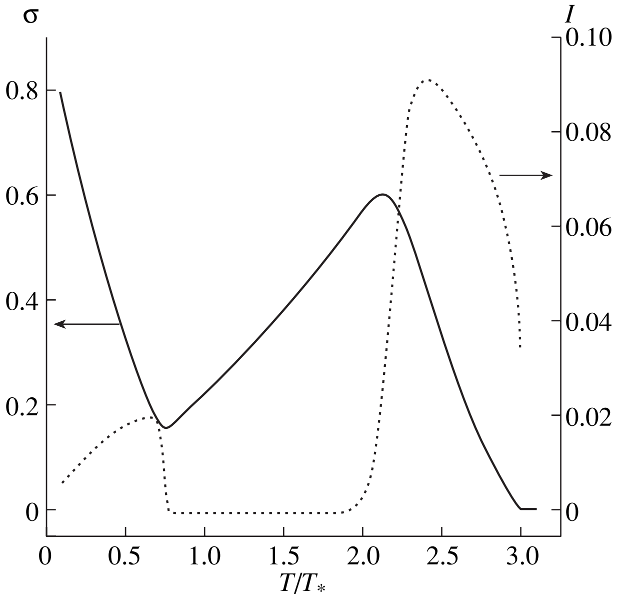

Fig. 1. Temperature curves of deforming stress [($\sigma(T)$), solid line] and its rate sensitivity [$I(T)$, dashed line] calculated by Eq. (6) at the parameter values $E_+ = 3E_0$, $E_- = E_0$, $\ln(\dot\varepsilon_0/\dot\varepsilon) = 25$, $p = 1.3$, $q = 0.8$, and $T_* = E_0/(k\ln(\dot\varepsilon_0/\dot\varepsilon))$.

from the gliding to the sessile states and back, and Eq. (5) should be somewhat modified. Taking into account the time inhomogeneity of the process, we can substitute the motion velocity v by its effective value $v_{\text{eff}} = l_p/t_p$, where l_p is the total average free path of the dislocation until the moment of its "getting out of the game" (emergence to the surface, annihilation with other dislocations, etc.) and t_p is the corresponding travel time. At the given path l_p, the travel time can be determined from the equation $\langle x(t_p)\rangle = l_p$ with the aid of the kinetic law Eq. (3). This provides the determination of the modified temperature dependence of the deforming stress. We assume the thermally activated nature of the transitions between the gliding and the sessile states $J_{+,-} = J_{0+,-}\exp(-E_{+,-}/kT)$ with the activation energies E_+ and E_- and limit our consideration to the case where $J_+/J_- \ll 1$. Determining the travel time $t_p = \rho b l_p/\dot\varepsilon$ from the Orovan equation and substituting it into Eq. (3), we arrive at the modified equation for the temperature- and velocity-dependent deforming stress

$$E(\sigma) = E_- + kT\ln\{[1 + z_+ - \exp(-(z_+ + z_-))]/l\}, \quad (6)$$

where $l = l_pJ_{0-}/v_0$, $z_{+,-} = (\dot\varepsilon_0/\dot\varepsilon)(l_pJ_{0+,-}/v_0)\exp(-E_{+,-}/kT)$.

At a high locking barrier E_-, this equation is reduced to conventional Eq. (5) for $\sigma(T)$ for usual gliding. If the barrier is not too high and the thermal activation of the locking process occurs at a noticeable frequency, the value of the deforming stress is changed. In the general case, the effect of dislocation sticking in the sessile states results in an increase of the deforming stress. At a relatively low barrier of the dislocation liberation and the transition to the mobile state (with the energy E_+), the resulting temperature dependence of the deforming stress on temperature is weakened (flattened out) as in Ti [1, 2] and a number of other materials (for details see [16]). At a sufficiently high unlocking energy E_+, the curve $\sigma(T)$ forms the maximum and the deforming stress shows an anomalous positive temperature sensitivity in a certain temperature range. Figure 1 shows the modified temperature dependence $\sigma(T)$ obtained from the above equations for the following set of the parameters: $E_+ = 3E_0$, $E_- = E_0$, $J_{0+} = J_{0-}$, $l = 10^4$, and $\ln(\dot\varepsilon_0/\dot\varepsilon) = 25$. To illustrate the calculation performed, we used the model dependence of the activation energy on stress from [17]:

$$E(\sigma) = E_0[1 - (\sigma/\sigma^*)^q]^p. \quad (7)$$

Thus, for the dislocation motion in a harmonic Peierls–Nabarro relief, the dependence of the activation energy on stress is given by Eq. (7) with $p = 1.3$ and $q = 0.8$ [18]. As is seen from Fig. 1, the temperature dependence $\sigma(T)$ consists of a decreasing low-temperature (normal) branch and a high-temperature (anomalous) peak described by the generalized Eq. (6).

This basic relationship also allows the calculation of other characteristics of material plasticity, e.g., the strain-rate sensitivity $I(T) = d\sigma/d\ln\dot\varepsilon$. In the case under study, the dependence $I(T)$ does not determine the microscopic characteristic of overcoming the barrier by a dislocation—its activation volume (as is the case in simple gliding). Nevertheless, this quantity, being a parameter that can be measured experimentally, is of a considerable interest.

Equation (6) is valid and can be solved irrespectively of the dependence of the locking E_- and unlocking E_+ energies on stress. However, we illustrate the stated above on a simpler particular case, where the energies E_+ and E_- are constant. Performing the differentiation, we obtain from Eq. (6) that

$$\frac{d\sigma}{d\ln(\dot\varepsilon)} = \frac{kT}{V_0[1 + z_+ - \exp(-(z_+ + z_-))]} \times [z_+ + (z_+ + z_-)\exp(-(z_+ + z_-))]. \quad (8)$$

Here, $V_0 = -dE(\sigma)/d\sigma$.

Figure 1 also illustrates the temperature dependence of the strain-rate sensitivity $I(T) = d\sigma/d\ln\dot\varepsilon$. It is seen from Fig. 1 that locking processes result in the considerable anomaly in the strain-rate sensitivity, which gives rise to its dramatic decrease in a certain temperature range. The cause of this phenomenon is considered in detail in the next section.

In addition to the deforming stress and its strain-rate sensitivity $d\sigma/d\ln\dot\varepsilon$, one also measures in mechanical tests the rate of stress relaxation at the fixed total (elastic + plastic) deformation. In this case, one determines simultaneously both $d\sigma/dt \sim -\dot\varepsilon$ and σ as functions of time. These two functions parametrically determine (with the time t as a parameter) the dependence of the plastic flow rate on stress. The construction of the dependence $\ln(-d\sigma/dt)$ as a function of σ (the so-called relaxation curves [19]) in the case where the plastic flow is determined only by one elementary process of thermally activated overcoming an obstacle provides the determination of the activation energy of this process, because in this case, we have $\ln(-d\sigma/dt) \sim \ln(\dot{\varepsilon}) \sim -E(\sigma)/kT$ (within the accuracy of the additive constants of the type of elastic module and $\ln(\dot{\varepsilon}_0)$).

Let us consider the qualitative change of the relaxation curves for the dislocation-motion mechanism under consideration, which includes the locking–unlocking processes. This can be done with the aid of basic Eq. (6). Figure 2 shows the $\ln\dot{\varepsilon}$ as a function of σ obtained by the numerical solution of Eq. (6) at the parameters $E_+ = 1.5E_0$, $E_- = E_0$, and $l = 10^4$ at two different temperatures $T = 2E_0/(25k)$ (curve *1*) and $T = 2.5E_0/(25k)$ (curve *2*). The form of the relaxation curves clearly shows the transition between two different activation energies $E(\sigma)$ and $E(\sigma) + E_+ - E_-$. The relaxation curves corresponding to these activation energies in simple gliding are indicated by dashed lines.

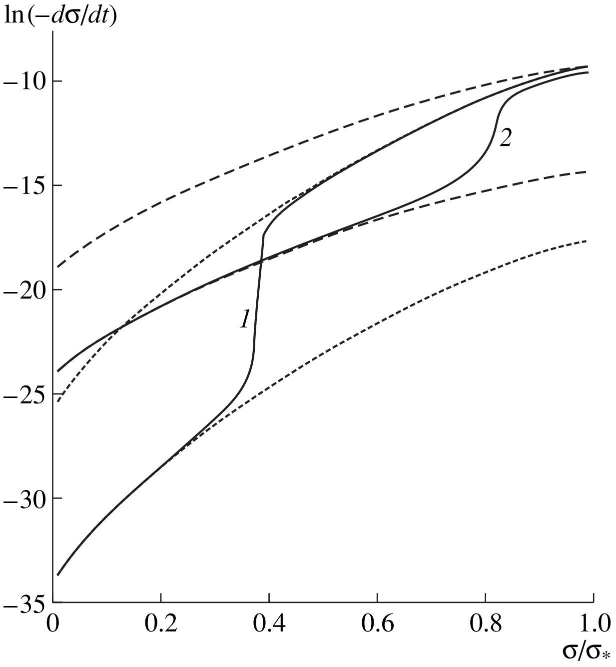

Fig. 2. Relaxation curves $\ln(-d\sigma/dt) = f(\sigma)$ calculated by Eq. (6) at the parameter values (*1, 2*) $E_+ = 1.5E_0$, $E_- = E_0$, $\ln(\dot{\varepsilon}_0/\dot{\varepsilon}) = 25$, $p = 1.3$, $q = 0.8$; $T =$ (*1*) $2E_0/25k$ and (*2*) $2.5E_0/25k$.

It should be emphasized that an attempt to describe the plastic flow of this type as being controlled by one thermally activated process can lead to erroneous conclusions. Thus, a stress relaxation slower than that dictated by the occurrence of one elementary process can be interpreted as the manifestation of collective effects (such as exhaustion of mobile dislocations); however, in the actual fact, it is caused by quite another cause. The calculations performed in our present study show that even without the allowance for the collective effects, the dynamic behavior of individual dislocations can be explained by spontaneous pinning of a dislocation at the sessile state observed every now and then.

It is expedient to study the temperature range of the anomaly in plasticity and the characteristics of the anomalous peak of the deforming stress in more detail.

ANOMALOUS PEAK

In the high-temperature range corresponding to the anomaly, the exponential term in Eq. (6) is rather small and, thus, can be omitted. Then, the peak shape is described by the relationship

$$\begin{aligned} E(\sigma) &\approx E_- + kT\ln[(1+z_+)/l] \\ &= E_- + kT\ln[1/l + (\dot{\varepsilon}_0/\dot{\varepsilon})\exp(-E_+/kT)] \end{aligned} \tag{9}$$

(for the sake of simplicity, we assumed that $J_{0+} = J_{0-}$).

Because of the exponential character of the temperature dependence of the quantity z_+, equation (9) determines two alternating branches of the dependence $\sigma(T)$ corresponding to the conditions $z_+ \ll 1$ (a lower temperature) and $z_+ \gg 1$ (a higher temperature). As was indicated in the previous section, the high-temperature branch corresponds to gliding with the activation energy $E(\sigma) + E_+ - E_-$ and a decrease in $\sigma(T)$ with the temperature, which is "normal" for the thermally activated motion. A low-temperature branch in the range $z_+ \ll 1$ is approximately described by the relationship

$$E(\sigma) \approx E_- - kT\ln l. \tag{10}$$

One can see that, in accordance with Eq. (10), an increase of the temperature corresponds to a decrease of $E(\sigma)$. Then, since $E(\sigma)$ is a decreasing function of σ, the deforming stress increases. Thus, the anomalous rising branch of $\sigma(T)$ can approximately be described by the simple relationship (10)—the dependence of $\sigma(T)$ on the locking-barrier energy E_- and the dislocation path and also the absence of any dependence on E_+ and the deformation rate $\dot{\varepsilon}$. The latter fact explains the anomalous minimum in the strain-rate sensitivity.

The temperature sensitivity of the deforming stress $d\sigma/dT$ obtained by differentiation of Eq. (6) at constant E_+ and E_- is

$$\frac{d\sigma}{dT} = \frac{1}{V_0}\left[\ln\left(\frac{1+z_+}{l}\right) + \frac{z_+}{1+z_+}\ln\left(\frac{\dot{\varepsilon}_0 l}{\dot{\varepsilon}_0 z_+}\right)\right]. \tag{11}$$

The point of the maximum in T_M is determined from the conditions $d\sigma/dT = 0$ approximately corresponding

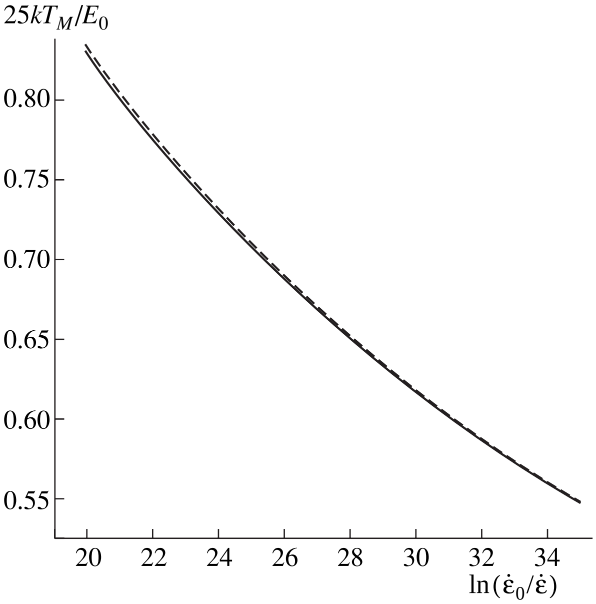

Fig. 3. The dependence of the temperature of the maximum deforming stress, T_M, on deformation rate $\dot\varepsilon$ at $l = 10^4$. Dashed line indicates the approximate analytical curve described by relationship (12).

to $z_+ \approx \dfrac{\ln(l)}{\ln(\dot\varepsilon_0/\dot\varepsilon)}$ and

$$T_M \approx \frac{E_+}{k\ln\left\{\dfrac{\dot\varepsilon_0}{\dot\varepsilon}l\ln\left[\dfrac{\ln(\dot\varepsilon_0/\dot\varepsilon)}{\ln(l)}\right]\right\}}. \tag{12}$$

Thus, the temperature position of the peak in the above approximation is independent of E_- and is determined mainly by the quantity E_+. The dependence of T_M on the deformation rate $\dot\varepsilon$ is illustrated by Fig. 3. The comparison of the T_M value numerically calculated from the rigorous equation $d\sigma/dT = 0$ with the analytical approximation (12) shows the high efficiency of the latter.

The peak stress σ_M is determined by substituting the T_M value obtained into Eq. (9):

$$E(\sigma_M) \approx E_- - \frac{E_+}{\ln\left\{\dfrac{\dot\varepsilon_0}{\dot\varepsilon}l\ln\left[\dfrac{\ln(\dot\varepsilon_0/\dot\varepsilon)}{\ln(l)}\right]\right\}}\ln\left(\frac{l}{1+\dfrac{\ln(l)}{\ln(\dot\varepsilon_0/\dot\varepsilon)}}\right). \tag{13}$$

Since the coefficient before E_+ in Eq. (13) at the typical parameter values is less than unity, the peak stress depends on the value of E_- to a larger degree. At the fixed E_+/E_- ratio, the dependence of σ_M on E_- is illustrated for $\ln(\dot\varepsilon_0/\dot\varepsilon) = 25$ and $l = 10^4$ by Fig. 4. It is seen that with a proportional decrease of the energy barriers E_+ and E_-, the temperature position of the peak is shifted toward lower temperatures, whereas its amplitude σ_M increases. A similar behavior was observed in doping of Ni_3Al with Hf (Fig. 5 in [8]) ($E_+ = 2.574E_0$, and $E_- = 1.31E_0$ for curve *1*, whereas E_+ and E_- for curve *2* are less by a factor of 1.4).

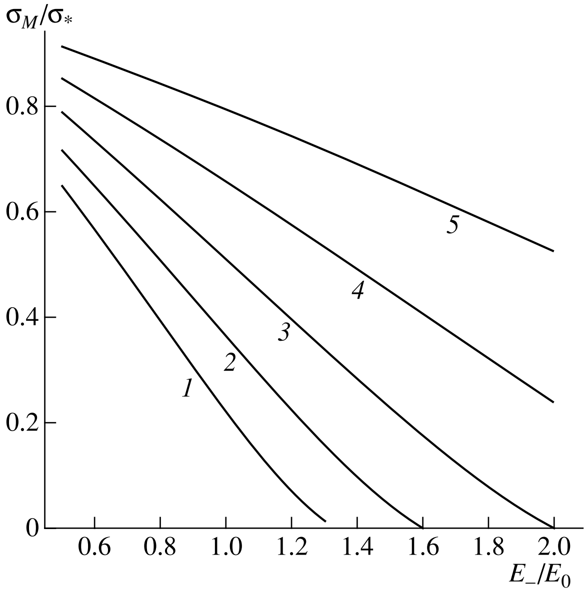

Fig. 4. Dependence of the peak stress $\sigma_M = \sigma(T_M)$ on the locking-barrier height: E_- at $\ln(\dot\varepsilon_0/\dot\varepsilon) = 25$ and $l = 10^4$ at different values of the E_+/E_- ratio: (*1*) 1.0, (*2*) 1.5, (*3*) 2.0, (*4*) 2.5, and (*5*) 3.0.

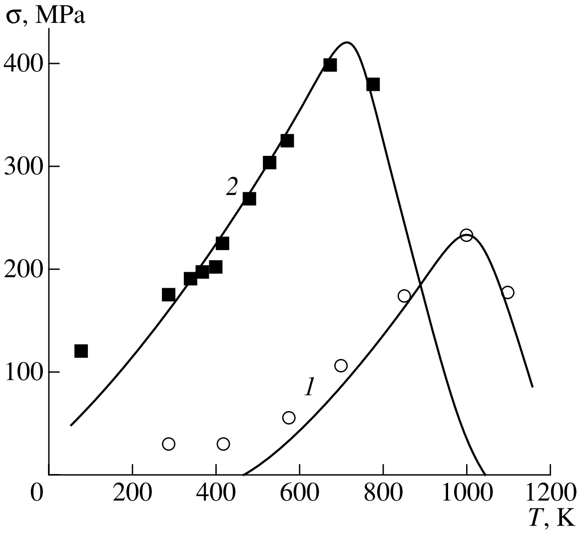

Fig. 5. Temperature dependence of the deforming stress at the proportional variation of the barrier heights (*1*) $E_+ = 2.574E_0$, $E_- = 1.31E_0$, (*2*) $E_+ = 1.839E_0$, $E_- = 0.9357E_0$ ($\ln(\dot\varepsilon_0/\dot\varepsilon) = 25$ and $l = 10^4$, $p = 1.3$, and $q = 0.8$). Circles indicate the experimental data [8] for deformation in $Ni_{76.6}Al_{23.4}$, squares indicate the experimental data for $Ni_{74.8}Al_{21.9}Hf_{3.3}$.

CONCLUSION

The existence of a positive anomalous temperature dependence of deforming stresses indicates that the plastic flow of the material is not controlled by just one thermally activated elementary process.

This requires the modification of the conventional scheme for the thermally activated analysis in treatment of the corresponding experimental data. In the present study, we extended the elementary model of the thermally activated gliding dislocation to the case of thermally activated spontaneous rearrangement of dislocation cores between the gliding and the sessile states. We also obtained the analytical relationships describing the averaged laws of jumpwise dislocation motion and determined the dependence of the characteristics of the plastic flow of the materials on the temperature; the applied stress; and the internal parameters such as the density of mobile dislocations, the complete lengths of their free paths, and the energy barriers for the rearrangements of dislocation cores between different states. In addition to the qualitative interpretation of the characteristic temperature dependences of the deforming stress $\sigma(T)$ and its sensitivity to rate $d\sigma/d\ln\dot{\varepsilon}$, the results obtained also describe the tendencies in the modification in anomalous-peak characteristics, its temperature position, and the amplitude with the change of the microstructural parameters. This can be of great help in the search for the methods for controlling the mechanical properties of various materials.

REFERENCES

1. S. Farenc, D. Caillard, and A. Couret, Solid State Phenom. **35–36**, 429 (1994).
2. S. Naka, A. Lasalmonie, P. Costa, and L. P. Kubin, Philos. Mag. A **57**, 717 (1988).
3. P. Veyssiere and G. Saada, in *Dislocations in Solids*, Ed. by F. R. N. Nabarro and M. J. Duesbery (Elsevier, Amsterdam, 1996), Vol. 10, p. 253.
4. M. Yamaguchi and H. Inui, in *Proceedings of the 1st International Symposium on Structural Intermetallics*, Ed. by R. Dariolia *et al.* (The Minerals, Metals and Materials Society, Warrendale, 1993), p. 127.
5. M. J. Mills, in *Multiscale Phenomena in Plasticity: From Experiments to Phenomenology, Modelling and Materials Engineering*, Ed. by J. Lepinoux *et al.* (Kluwer, Dordrecht, 2000), Vol. 367, p. 469.
6. V. Vitek, D. P. Pope, and J. L. Bassani, in *Dislocations in Solids*, Ed. by F. R. N. Nabarro and M. J. Duesbery (Elsevier, Amsterdam, 1996), Vol. 10, p. 135.
7. B. A. Grinberg and M. A. Ivanov, Fiz. Met. Metalloved. **78**, 3 (1994).
8. J. L. Martin and J. Bonneville, in *Proceedings of the 19th Riso International Symposium on Materials Science: Modelling of Structure and Mechanics of Materials from Microscale to Product*, Ed. by J. V. Carstensen *et al.* (Riso National Laboratory, Roskilde, 1998), p. 367.
9. F. Louchet and B. Viguier, Philos. Mag. A **71**, 1313 (1995).
10. B. V. Petukhov, Kristallografiya **43** (6), 1118 (1998) [Crystallogr. Rep. **43**, 1058 (1998)].
11. D. C. Chrzan and M. S. Daw, Phys. Rev. B **55**, 798 (1997).
12. P. B. Hirsch, Philos. Mag. A **65**, 569 (1992).
13. M. J. Mills and D. C. Chrzan, Acta Metall. Mater. **40**, 3051 (1992).
14. V. Paidar, Mater. Sci. Eng. A **234–236**, 15 (1997).
15. M. A. Ivanov, B. A. Grinberg, and N. A. Kruglikov, Fiz. Met. Metalloved. **89**, 5 (2000).
16. B. V. Petukhov, Fiz. Tverd. Tela (St. Petersburg) **43** (5), 813 (2001) [Phys. Solid State **43**, 845 (2001)].
17. U. F. Kocks, A. S. Argon, and M. F. Ashby, Prog. Mater. Sci. **19**, 291 (1975).
18. B. V. Petukhov, Kristallografiya **44** (4), 667 (1999) [Crystallogr. Rep. **44**, 620 (1999)].
19. U. Messerschmidt, D. Baither, B. Baufeld, and M. Bartsch, Mater. Sci. Eng. A **233**, 61 (1997).

Translated by L. Man

Crystallography Reports, Vol. 46, No. 3, 2001, pp. 480–482. Translated from Kristallografiya, Vol. 46, No. 3, 2001, pp. 531–533.
Original Russian Text Copyright © 2001 by Chudakov.

PHYSICAL PROPERTIES OF CRYSTALS

Measurements of Photoelastic Constants on Crystal Disks

V. S. Chudakov

Shubnikov Institute of Crystallography, Russian Academy of Sciences,
Leninskiĭ pr. 59, Moscow, 117333 Russia

Received November 3, 1999

Abstract—Determination of the photoelastic constant on crystal disks subjected to compression along the diameter have been considered. The possibility of measuring the photoelastic constant on disk-shaped plates with pronounced inhomogeneously distributed birefringence is analyzed by example of a KRS-5 single crystal. *© 2001 MAIK “Nauka/Interperiodica”.*

The method of determining the piezooptical coefficients of cubic crystals on disk-shaped (100)-oriented plates with subjected to a compression along the diameter was described in [1]. Earlier, similar measurements were made on special precisely cut prisms. This method essentially facilitates the extraction of a valuable information on crystals and possible changes in its properties.

In practice, one usually deals with stressed isotropic disks, in particular with the (111)-oriented disks, with their photoelastic constant and its dispersion being unknown. The distribution of the initial stresses and their values in crystals can range within large intervals of values. For example, in high-quality Czochralski-grown crystals, the stress distribution is characterized by the axial symmetry [2], which results in the absence of induced birefringence in the center of the plate cut out normally to the growth direction. The measurement of the photoelastic constant in such plates is essentially simplified. In crystals grown by less developed technologies, the distribution of internal stresses caused by local stress sources or a thermal shock is more complicated. The random choice of the point of measuring the photoelastic constant in such crystals may result in a considerable error in the measured value.

Below, we describe the method providing the determination of the photoelastic constant with minimum errors even in strongly stressed crystals. The measurement procedure is reduced to the following. First, the initial stressed state of a the crystalline disk is studied by scanning it across one of its diameters. The result is represented as a curve reflecting the variations in interference of the polarized radiation used for the analysis. These variations are caused by the distribution of internal-stress-induced birefringence. Then, depending on the data obtained, one chooses the strategy of further studies. This choice depends on the presence of the point with the zero-birefringence in the vicinity of the disk center and the point at which the interference maximum is observed. The latter can readily be used for a simplified calibration of the instrument.

If both characteristic points are present, the determination of the photoelastic constant requires the determination of the change in the ordinate of the initial curve at the point of zero birefringence under the external loading along the diameter normal to the scanning direction. The loading should be chosen in such a way that the signal recorded at point with the zero birefringence would multiply exceed the noise level of the electronic system of the instrument. If this condition is met, the measurement error is considerably reduced even at the minimum mechanical loading.

The stressed state of the disk is studied by the modulation method for determining birefringence [3] with the use of a rotating analyzer. The interference maxima H_M are observed at the points where the path difference equals $(2n-1)\lambda/4$ (here n is an integer number and λ is the radiation wavelength). At moderate stresses and not too thick objects, $n = 1$. The linear dimensions of the ordinates H on the curves depend on both instrument and crystal parameters as

$$H = H_M \sin(2\pi C\Delta\sigma d/\lambda), \qquad (1)$$

where C is the photoelastic constant, $\Delta\sigma$ is the difference between the principal stresses, and d is the disk thickness. If the point of zero-birefringence is located in the disk center, the external loading P induces at this point the stress difference

$$\Delta\sigma = 4P/\pi Rd, \qquad (2)$$

where R is the disk radius. The induced difference $\Delta\sigma$ gradually decreases with the distance from the measurement point from the disk center. If the measurement points are located along the diameter orthogonal

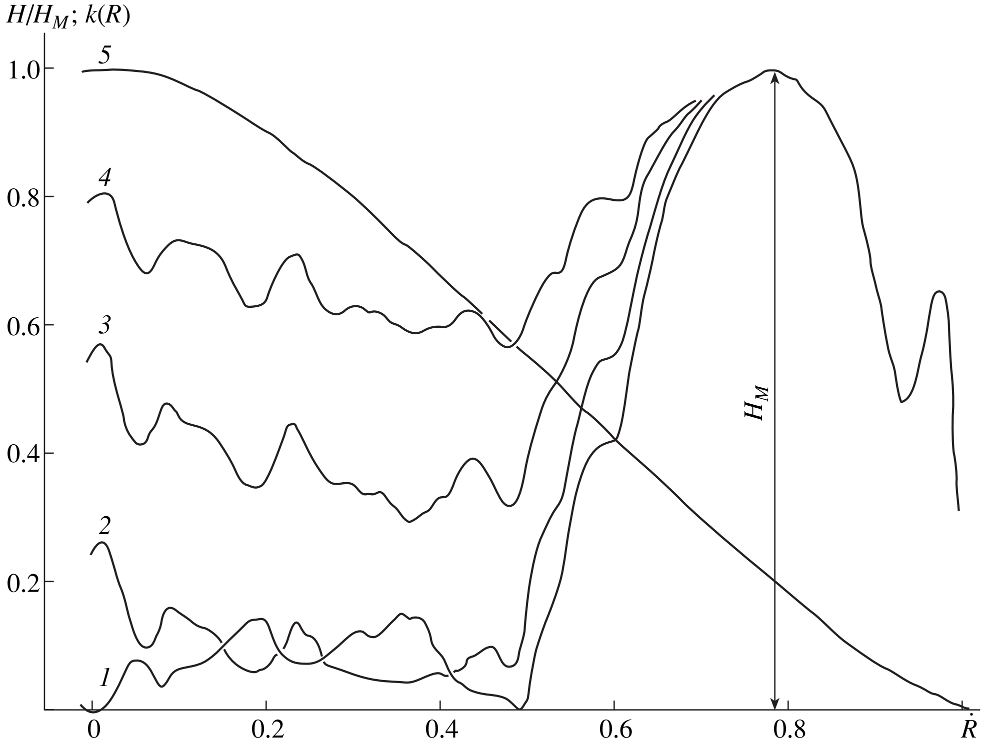

Variations in interference of polarized IR radiation scanning of a stressed disk cut out from a KRS-5 single crystal. (*1*) Corresponds to the initial state; (*2*, *3*, *4*) are obtained under loading of 0.97, 2.07, and 3.21 kgf, respectively; (*5*) shows a relative loading-induced decrease of $k(R)$ at the points lying on the diameter normal to the loading direction far from the center. Here, R is the disk radius, O is its center, H is the ordinate, H_M is the height of interference maximum.

to the loaded diameter, the relative decrease in $\Delta\sigma(R)$ from unity in the disk center to zero at its edge can be represented as curve *5* in figure. The ordinates of this curves are proportional to the decay coefficient $k(R)$ used in the calculation of the photoelastic constant. The $k(R)$ values and the data obtained from Eqs. (1) and (2) provide the determination of the photoelastic constant as

$$C = \lambda R \arcsin(H/H_M)/8Pk. \tag{3}$$

If the point with zero birefringence does not lie on the "orthogonal diameter," then Eq. (2) and $k(R)$ cannot be used. In this case, C should be determined from the formulas given in [4].

If the initial curve has no interference maximum, the photoelastic constant is determined in different way. In order to determine the value of nonexisting maximum H_M, one has to measure again the ordinate of the initial curve at the point with zero birefringence point under a more pronounced loading. To increase the accuracy, the second measurement should be made under a loading two or three times heavier.

The H_M value is determined by Eq. (1) represented in the form

$$H = H_M \sin(aP). \tag{4}$$

In practice, the argument aP does not exceed 30°–40°. Therefore, one can write within the sufficient accuracy that

$$H = H_M aP(1 - a^2P^2/\sigma). \tag{5}$$

The coefficient a can be obtained from the H_2/H_1 ratio:

$$a = [\sigma(P' - H')/(P'P_2^2 - H'P_1^2)]^{1/2}, \tag{6}$$

where $P' = P_2/P_1$; $H' = H_2/H_1$; and the subscripts 1 and 2 indicate the first and second runs of measurements, respectively. The use of Eqs. (4) and (6) yields $H_M = H_2/\sin(aP_2)$. The H_M-values obtained are substituted into Eq. (3) to determine the photoelastic constant.

We used a KRS-5 crystal with high photoelasticity value [5] to illustrate the use of the first variant for determining the photoelastic constant. The disk-shaped (111)-oriented plate with a thickness of 10 and a diameter of 50 mm was cut out. The chosen dimensions provided the formation of the interference maximum. The measurements were made on an FPD-1 photoelectric polariscope–flaw detector designed at the Institute of Crystallography of the Russian Academy of Sciences. IR radiation in the 2-μm range was used. The disk was compressed with the aid of a special lever-based device. The effective loading was equal to 0.97, 2.07, and 3.21 kgf. The response of a loaded crystal is shown by the curves *2*, *3*, and *4* in the figure. It is found that the variations in H at the point with the initial zero birefringence agree quite well with the loads applied. The calculated photoelastic constant was found to be 1.8×10^{-5} cm^2/kgf.

REFERENCES

1. V. S. Chudakov, Kristallografiya **39** (6), 1073 (1994) [Crystallogr. Rep. **39**, 986 (1994)].
2. *Stresses and Dislocations in Semiconductors. Collection of Articles*, Ed. by M. V. Klassen-Neklyudova (VINITI, Moscow, 1962), p. 19.
3. V. S. Chudakov, B. N. Grechushnikov, and G. G. Prave, Kristallografiya **16** (5), 939 (1971) [Sov. Phys. Crystallogr. **16**, 813 (1971)].
4. M. M. Frocht, *Photoelasticity* (Wiley, New York, 1941; GITTL, Moscow, 1950), Vol. 2, p. 130.
5. *Optical Materials for Infrared Technology. Reference Book*, Ed. by A. A. Askochenskiĭ (Nauka, Moscow, 1965).

Translated by A. Zalesskiĭ

Crystallography Reports, Vol. 46, No. 3, 2001, pp. 483–487. Translated from Kristallografiya, Vol. 46, No. 3, 2001, pp. 534–539.
Original Russian Text Copyright © 2001 by Bohigas, Lluma, Tejada, Krivandina, Sobolev.

PHYSICAL PROPERTIES OF CRYSTALS

Magnetic Susceptibility of Sodium Rare-Earth Fluorites $Na_{0.5-x}R_{0.5+x}F_{2+2x}$ (R = Dy, Ho, Er, Tm, Yb) and Some Ordered Phases

X. Bohigas*, J. Lluma, J. Tejada**, E. A. Krivandina***, and B. P. Sobolev*****
** Departament de Fisica i Engineyeria Nuclear, Universitat Politecnica de Catalunya, Barcelona, Catalonia, Spain*
*** Departament de Fisica Fondamental, Universitat de Barcelona, Catalonia, Spain*
**** Shubnikov Institute of Crystallography, Russian Academy of Sciences, Leninskiĭ pr. 59, Moscow, 117333 Russia*
e-mail: sobolev@crossovers.com

Received August 17, 2000

Abstract—Magnetic properties of the nonstoichiometric phases with the fluorite-type “defect” structure $Na_{0.4}R_{0.6}F_{2.2}$ (R = Ho, Er, Tm, Yb) and $Na_{0.35}Dy_{0.65}F_{2.3}$ have been studied as well as some ordered phases with different distortions of the initial fluorite lattice ($NaHo_2F_7$, $Na_7Tm_{13}F_{46}$, $NaYb_2F_7$, and $Na_7Yb_{13}F_{46}$) and $Na_{1.5}Dy_{1.5}F_6$ with the gagarinite-type structure ($NaCaYF_6$). Magnetic susceptibility χ was measured with the aid of the Faraday balance in the temperature range from 20 to 300 K. The crystals with R = Dy, Ho, Er, Tm are paramagnetic; their temperature dependence χ is described by the Curie–Weiss law. It is shown that in the temperature range studied, magnetic susceptibility does not depend on the degree of order of Dy, Ho, Er, and Tm ions in the structure. Below 80 K, the temperature dependence of magnetic susceptibility of the the Yb^{3+}- containing phases differs from the analogous dependence χ of an ideal paramagnetic crystal, which is assumed to be caused by the interaction of the crystalline field with Yb^{3+} ions. © *2001 MAIK “Nauka/Interperiodica”.*

INTRODUCTION

The formation of crystals with the “defect” CaF_2-type structure and gross nonstoichiometry is characteristic of MF_2–RF_3 -type (M = Ca, Sr, Ba, Cd, and Pb; R-rare-earth element) and MF–RF_3-type (M = Na, K; R-rare-earth element) binary systems. Single crystals of these phases are promising materials for practical use because one can modify their defect structure and properties [1].

The fluorite nonstoichiometric phases with the general formula $M_{1-x}R_xF_{m(1-x)+nx}$ are heterovalent solid solutions. The isomorphous substitution of M^{2+}- and M^{1+}- ions by R^{3+}- rare-earth ions results in the formation of structural defects in both anionic and cationic sublattices of the unperturbed CaF_2-type lattice. In the $M_{1-x}R_xF_{2+x}$ fluorite phases, the defects in the anionic sublattice (i.e., the fluoride ions in interstitial positions and the fluoride vacancies in the main position) are studied by the methods of X-ray diffraction analysis, neutron diffraction analysis, diffuse neutron scattering and many other techniques. For $Na_{0.5-x}R_{0.5+x}F_{2+2x}$ phases, the defect structure has been studied for only one composition (R = Y; x = 0.1).

By analogy with the data on the $Na_{0.5-x}R_{0.5+x}F_{2+2x}$ fluorite-phase structure and the proposed cluster model of the $NaYb_2F_7$ ordered phase, one can assume that all the nonstoichiometric and ordered phases contain the complexes (clusters) of the rare-earth ions in octahedral coordination. A group of nonstoichiometric phases is characterized by statistic distribution of centers of gravity of these clusters and incomplete occupancy of octahedron vertices by rare-earth ions. In the ordered phases, clusters formed by defects become the structural units. Their centers of gravity form an individual sublattice, whereas the cation component of the former cluster complexes tend to occupy all the octahedron vertices. In the $Na_{1.5}Dy_{1.5}F_6$ crystals with the gagarinite-type structure ($NaCaYF_6$), the ions with different valences occupy different crystallographic positions, whereas rare-earth ions do not form any clusters.

With a decrease of the temperature, the nonstoichiometric fluorite phases crystallized from melt in many systems start ordering. Defect clusters become the structural units in which the cation positions and the chemical composition can be unambiguously determined. However, the difficulties encountered in growth of single crystals of the ordered phases resulted in the fact that, at present, only two structures of these phases have been studied. The analysis of the relevant data shows that the cation–cation distances in these structural units differ from the statistically averaged distances in the initial disordered phase.

Thus, it was expedient to establish whether the degree of disorder and small variations in the relative positions of the rare-earth ions in the nonstoichiometric and the ordered phases influence on the properties of these phases. Since most of the rare earth elements are characterized by pronounced magnetic moments, these

1063-7745/01/4603-0483$21.00 © 2001 MAIK “Nauka/Interperiodica”

phases seem to be favorable objects for studying their magnetic susceptibility.

No such studies of the phases formed in the NaF–RF$_3$ systems have been performed as yet. In particular, $Na_{0.5-x}R_{0.5+x}F_{2+2x}$ crystals differ from analogous nonstoichiometric $M_{1-x}R_xF_{2+x}$ fluorite phases by much higher rare-earth ions concentrations. In $M_{1-x}R_xF_{2+x}$, the maximum content of RF_3 is 50 mol % (at normal pressure), whereas in $Na_{0.5-x}R_{0.5+x}F_{2+2x}$, it reaches 70 mol % RF_3. Moreover, the conditions of growing $M_{1-x}RF_{2+x}$ single crystals with the maximum rare-earth ion concentration are extremely unfavorable, whereas $Na_{0.5-x}R_{0.5+x}F_{2+2x}$ the compositions of phases with the maximum rare-earth ion concentrations are close to the compositions of congruently melting phases. This allows one to grow high-quality $Na_{0.5-x}R_{0.5+x}F_{2+2x}$ single crystals [2].

Below, we describe the magnetic susceptibility for nonstoichiometric $Na_{0.5-x}R_{0.5+x}F_{2+2x}$ fluorite phases and compare the results of measurements with similar data for several types of ordered phases with the fluorite-derived structure and with the gagarinite-type structure of $Na_{1.5}Yb_{1.5}F_6$.

EXPERIMENTAL

We studied the phases with different types of the rare-earth ion distributions over the crystal structures—highly disordered phases in nonstoichiometric fluorites, partly ordered phases with the fluorite-derived structure, and the ordered phase in the gagarinite-type structure.

We obtained two groups of specimens, depending on the method of their growth. The first group is formed Bridgman-grown (from melt) $Na_{0.5-x}R_{0.5+x}F_{2+2x}$ single crystals (the growth conditions are described elsewhere [2]). The chemical composition of these crystals was refined using the concentration curves of the unit-cell parameters obtained by the X-ray powder analysis.

The second group is formed by the ordered phases with the fluorite-derived structure and a $Na_{1.5}Dy_{1.5}F_6$ gagarinite-type phase. In most cases, these phases are formed at lowering the temperature of nonstoichiometric phases of the same composition. However, their composition can lie outside the homogeneity range of the fluorite phase. In both cases, the ordered phases were obtained by prolong annealing of the mixture of components in nickel ampules, placed into a nickel container with the fluorinating atmosphere provided by the products of teflon pyrolysis. The equilibrium ordered phases thus obtained were quenched. The types of fluorite-lattice distortions and the stability ranges of these phases in the NaF–RF_3 systems have been studied earlier [3]. Some of the corresponding phase diagrams can be found in [4–7]. The details of the solid-phase synthesis are given in [8].

The magnetic susceptibility χ was measured using a Faraday balance. The specimen was placed into a plastic capsule suspended on a 1-m-long quartz fiber to the arm of a precision balance. The magnetic moment of the specimen interacted with an electromagnet-induced nonuniform magnetic field, and the balance recorded the change in the effective mass of the specimen. A preliminary calibration of the device was made on standard $HgCo(NCS)_4$ [9] specimens and allowed one to determine magnetic susceptibility per unit mass of the specimen. The molar magnetic susceptibility was obtained by multiplying the magnetic susceptibility thus measured by the molar mass of the compound studied. The diamagnetic correction was taken into account by the Pascal method using data [10]. The specimens were placed into a helium cryostat providing the measurements in the temperature range from 20 to 300 K.

The Yb^{3+}-containing $Na_{0.4}Yb_{0.6}F_{2.2}$, $NaYb_2F_7$, and $Na_7Yb_{13}F_{46}$ crystals were studied on a standard SQUID magnetometer in the temperature range from 5 to 300 K.

Below, we present the results of the measurements performed on ten specimens of different compositions. The data obtained can be divided into three groups depending on their structural characteristics dependent on the arrangement of rare-earth ions.

(1) Crystals with disordered distribution of rare-earth ions presumably having a tendency to formation of complexes (clusters). These are the nonstoichiometric $Na_{0.5-x}R_{0.5+x}F_{2+2x}$ phases with the defect fluorite structure and the composition $Na_{0.4}R_{0.6}F_{2.2}$ with R = Ho, Er, Tm, and Yb. The $Na_{0.35}Dy_{0.65}F_{2.3}$ phase also has the disordered fluorite structure.

(2) Specimens with the of fluorite-derived structures formed during lowering of the temperature (ordered phases). They showed a long-range order in the arrangement of the structural defects. The clusters of defects statistically distributed in the nonstoichiometric crystals become the structural units in the ordered phases whose centers of gravity form an individual sublattice. The rare-earth ions also become ordered, whereas, depending on the type of the rare-earth ion, the phases can have different distortions of the fluorite lattices. The $NaHo_2F_7$ phase is characterized by the trigonal distortion and is stable in a narrow temperature range; the $NaYb_2F_7$ phase has the monoclinic (pseudo-orthorhombic) distortion; the $Na_7Tm_{13}F_{46}$ shows tetragonal distortions; and, finally, the a $Na_7Yb_{13}F_{46}$ phase has the orthorhombic distortion of the fluorite lattice [3].

(3) The $Na_{1.5}Dy_{1.5}F_6$ composition has the gagarinite-type structure ($NaCaYF_6$) and is characterized by an ordered arrangement of rare-earth ions not forming any clusters similar to the octahedral clusters in the nonstoichiometric fluorite $Na_{0.5-x}R_{0.5+x}F_{2+2x}$ phases.

RESULTS AND DISCUSSION

The temperature curves of magnetic susceptibility for most specimens point to their paramagnetic state in the temperature range from 20 to 300 K. They are well described by the Curie–Weiss law,

$$\chi_{\text{mol}} = C/(T - \theta), \qquad (1)$$

where χ_{mol} is the molar magnetic susceptibility, T is the measurement temperature, C is the Curie constant, and θ is the Curie temperature (hereafter, we shall use χ instead of χ_{mol}).

Figure 1 shows the temperature dependence of the reciprocal χ the $Na_{0.4}Ho_{0.6}F_{2.2}$ specimen. As is seen, the dependence measured is described, within the accuracy of an experimental error, by the Curie–Weiss law. In the table, the χ values for are given at two temperatures—20 and 300 K. The specimens are divided into five groups. Each of them (with the exception of $Na_{0.4}Er_{0.6}F_{2.2}$) consists of phases having disordered fluorite structures and the ordered phase from the same NaF–RF_3 system. For the first four groups, the Curie–Weiss law is valid at temperatures above 20 K.

More complex temperature dependences $\chi(T)$ were obtained for three Yb^{3+}-containing phases of the fifth group. A typical $\chi(T)$ dependence for the $Na_{0.4}Yb_{0.6}F_{2.2}$ specimen is shown in Fig. 1. At $T > 80$ K, the dependence $\chi(T)$ is described by the Curie–Weiss law (1). At $T < 80$ K, the curve *2* considerably deviates from the curve characteristic for temperature range, of paramagnetic of this deviation for all three phases. The is indicated in table.

The electron configuration of the outer electron shells of rare-earth ions, $4f^{0-14}5s^25p^6$ (additional to the electron shell of xenon), consists of unfilled $4f$-shell and filled outer $5s^2$ and $5p^6$ shells. The $4f$-electrons are responsible for the magnetism of rare-earth ions, and the filled outer shells shield $4f$-electrons from the crystalline field (which is rather weak if at all).

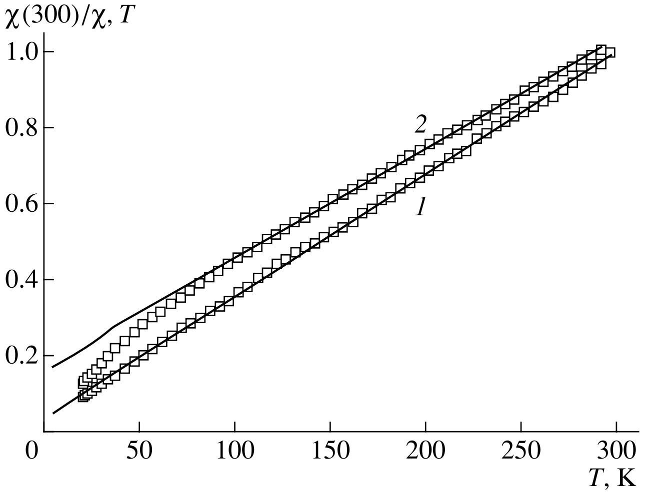

Fig. 1. Temperature dependence of reciprocal magnetic susceptibility for (*1*) $Na_{0.4}Ho_{0.6}F_{2.2}$ and (*2*) $Na_{0.4}Yb_{0.6}F_{2.2}$. Squares indicate experimental points; solid lines show the values calculated by the Curie–Weiss formula with the use of the parameters indicated in table.

The present study was undertaking to establish the presence (or the absence) of fine variations in the crystal structure caused by relative arrangement of rare-earth ions on the χ-value.

The Curie constant in Eq. (1) is determined by the concentration of rare-earth ions and their effective magnetic moment μ_{eff} (hereafter is μ) [11, 12],

$$C = \frac{\mu^2 N_A}{3k_B}x, \qquad (2)$$

where N_A is the Avogadro number, x is the molar part of R^{+3}-ions, k_B is the Boltzmann constant, and μ is the

Magnetic properties of nonstoihiometric fluorite $Na_{0.4}R_{0.6}F_{2.2}$ phases (R = Dy, Ho, Er, Tm, and Yb) and ordered phases in some NaF–RF_3 systems

Group	Specimen	Specimen composition	Type of structure	Magnetic susceptibility χ, emu/mol		Deviation from the Curie–Weiss law, K	Magnetic moment, Bohr magneton, μ_B		θ, K
				20 K	300 K		μ_{exp}	μ_{theor}	
I	1	$Na_{0.35}Dy_{0.65}F_{2.3}$	CaF_2	$6.14e^{-1}$	$4.82e^{-2}$		10.76 ± 0.04	10.63	5.9
	2	$Na_{1.5}Dy_{1.5}F_6$	$NaCaYF_6$	$6.12e^{-1}$	$4.87e^{-2}$		10.86 ± 0.03	10.63	6.0
II	3	$Na_{0.4}Ho_{0.6}F_{2.2}$	CaF_2	$5.15e^{-1}$	$4.57e^{-2}$		10.74 ± 0.03	10.60	11
	4	$NaHo_2F_7$	Ordered	$5.00e^{-1}$	$4.67e^{-2}$		10.80 ± 0.02	10.60	11
III	5	$Na_{0.4}Er_{0.6}F_{2.2}$	CaF_2	$3.94e^{-1}$	$3.91e^{-2}$		9.88 ± 0.03	9.59	14
IV	6	$Na_{0.4}Tm_{0.6}F_{2.2}$	CaF_2	$2.02e^{-1}$	$2.33e^{-1}$		7.74 ± 0.02	7.57	21
	7	$Na_7Tm_{13}F_{46}$	Ordered	$2.33e^{-1}$	$2.22e^{-2}$		7.63 ± 0.04	7.57	16
V	8	$Na_{0.4}Yb_{0.6}F_{2.2}$	CaF_2	$7.02e^{-2}$	$7.84e^{-2}$	20–80	4.60 ± 0.02	4.54	56
	9	$Na_7Yb_{13}F_{46}$	Ordered	$7.52e^{-2}$	$1.03e^{-2}$	20–80	4.93 ± 0.03	4.54	80
	10	$NaYb_2F_7$	Ordered	$8.15e^{-2}$	$9.66e^{-3}$	20–80	5.31 ± 0.04	4.54	79

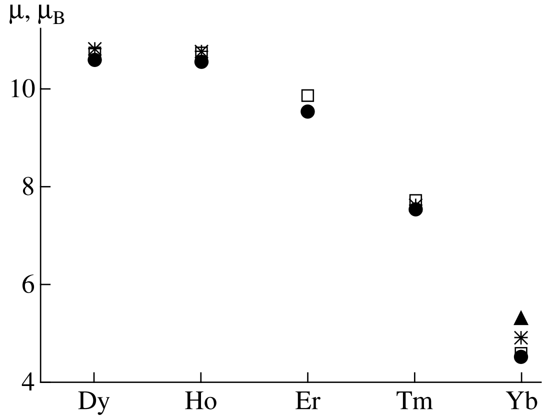

Fig. 2. Effective magnetic moments (in Bohr magnetons, μ_B) of the rare-earth ions in some phases in the NaF–RF_3 system (R = Dy, Ho, Er, Tm, Yb). Squares indicate the experimental points for nonstoichiometric fluorite phases; asterisks and triangles indicate the experimental points for ordered phases; and filled circles the theoretical values calculated by formula (3).

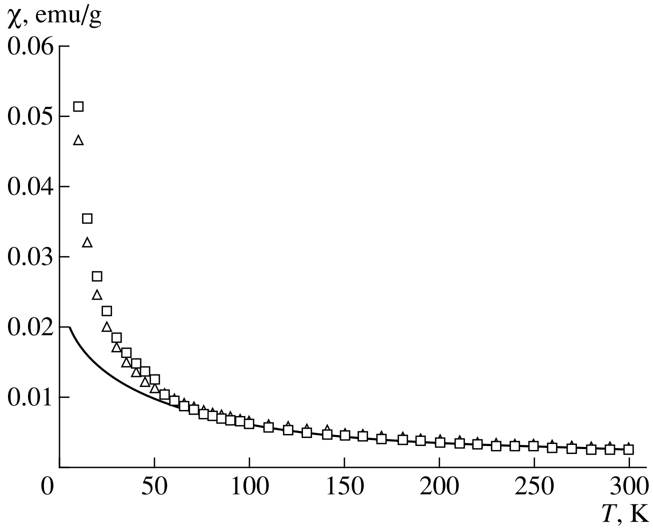

Fig. 3. The temperature dependence of magnetic susceptibility for $NaYb_2F_7$. The experimental values for the specimens cooled in a 100-Oe magnetic field are shown by squares; those for the specimens cooled without magnetic field, by triangles; the theoretical curve, calculated by the Curie–Weiss law and the parameters indicated in table are shown by the solid line.

effective magnetic moment, determined by the expression

$$\mu = \left[\frac{3}{2} + \frac{1}{2}\frac{S(S+1) - L(L+1)}{J(J+1)}\right] \times [J(J+1)]^{\frac{1}{2}}\mu_B + \alpha_V, \quad (3)$$

where μ_B is the Bohr magneton; S, L, and J are the quantum numbers of a rare-earth ion in the ground state; and α_V is the Van Vleck term that can be neglected in this case.

Using the high temperature part of the experimental dependence of χ and Eqs. (1) and (2), we can determine the experimental value of the effective magnetic moment μ_{exp} of the rare-earth ion. The μ_{exp}- and μ_{theor}-values calculated by Eq. (3) are listed in the table.

As is seen from the table and Fig. 2, the experimental and the theoretical values of the effective magnetic moment are equal with in an accuracy of about 2% for the nonstoichiometric and the ordered phases with the compositions from 1 to 7 (see table). The simultaneously measured effective magnetic moments are close to (on average, they are slightly higher than) the theoretical values for rare-earth ions.

Earlier, such a good agreement between μ_{exp} and μ_{theor} was also observed for crystals of the $M_{1-x}R_xF_{2+x}$-type solid solutions with the fluorite defect structure but at much lower rare-earth-ion concentrations [13–16]. The analysis of the μ_{exp}-values obtained (see table) shows that the magnetic moments of all the rare-earth ions studied are independent (within the accuracy of experimental error) of the state of rare-earth ions in the crystalline matrices characterized by various degrees of order.

At rather high temperatures, the magnetic susceptibility of all the phases follows the Curie–Weiss law with the negative value of the Curie temperature θ. This means that the interaction between magnetic rare-earth ions is of the antiferromagnetic nature.

To establish possible ferromagnetic order in $Na_7Yb_{13}F_{46}$ and $NaYb_2F_7$, deviating from the Curie–Weiss law below 80 K, we made measurements in two modes. In the first mode, the specimens were cooled from room temperature to 5 K in an applied 100-Oe field. Then, the field was switched off, and the measurements were made during specimens heating. In the second mode, the specimen temperature was reduced without the field application.

Figure 3 shows the temperature dependence of magnetic susceptibility for $NaYb_2F_7$ measured with the aid of a standard SQUID magnetometer in the temperature range from 5 to 300 K. Triangles show the data measured during heating of the specimen preliminarily cooled in the absence of a magnetic field (the second mode). Squares show the susceptibility data obtained from the same specimen but preliminarily cooled to 5 K in a 100-Oe static magnetic field.

The absence of a pronounced hysteresis for the data obtained in two different modes can be indicative to the absence of magnetic ordering in the specimen in the vicinity of 5 K. The deviations of the magnetic susceptibility at low temperatures may be interpreted as caused by the interaction of the crystalline field with Yb^{3+}-ions. A similar result was also obtained for the ordered $Na_7Yb_{13}F_{46}$ phase.

Similar to all the other specimens (see table, the compositions 1–7), the nonstoichiometric $Na_{0.4}Yb_{0.6}F_{2.2}$ fluorite phase possesses the effective magnetic moment close to its theoretical value. The magnetic moment of the ordered $Na_7Yb_{13}F_{46}$ phase is 9% higher, and the moment of the $NaYb_2F_7$ phase with almost the same a Yb^{3+} concentration is 17% higher than the theoretical value. Unfortunately, this difference in the magnetic moments of the nonstoihiometric and the ordered phases has not been interpreted as yet. This difference exceeds the possible experimental errors and possible error in the determination of the chemical composition.

Modeling of a possible defect structure of the $NaYb_2F_7$ phase [16] led to the conclusion on the formation of a certain defect configuration in the $\{Na_8Yb_6F_{68}\}$ structure. This configuration involves only a part of the Yb^{3+} ions occupying the positions outside of the cluster. As a result, the crystallochemical formula of the $NaYb_2F_7$ phase should be written as $Na_4Yb_6Yb_2F_{28}$, which reflects different positions of the Yb^{3+}-ions in the structure of the ordered phase. Up to now, it has been difficult to say whether the anomalies in magnetic behavior of the phases in forming the fifth group (table, compositions 8–10) are explained by different positions of the Yb^{3+}-ions in the structure. To establish the nature of these anomalies, some additional studies are required.

The measurements of all the specimens, except of those containing Yb-ions, were performed at temperatures much higher than θ, which might explain the fact that, no deviations from the Curie–Weiss law for these specimens were observed.

Magnetic susceptibility of the Yb^{3+}-containing phases was measured at the temperatures much lower than θ. The corresponding temperature dependence considerably deviates from the Curie–Weiss law (Fig. 1). We cannot exclude that similar deviations would also be observed at lower temperatures for specimens containing other rare-earth ions.

CONCLUSIONS

The temperature dependence of the magnetic susceptibility in the phases formed in the NaF–RF_3 systems (R = Dy, Ho, Er, Tm) obeys the Curie–Weiss law in the temperature range from 20 to 300 K. The magnetic moments of the rare-earth ions obtained from the paramagnetic range of the temperature dependence of magnetic susceptibility agree quite well with the theoretical data. The analysis of the μ_{exp} values obtained shows that, within the experimental error, the magnetic moments of all the rare-earth ions are independent of whether or not the rare-earth ions are ordered or disordered in the crystal structure.

The phases in the NaF–YbF_3 system studied in the temperature range from 5 to 300 K show some deviations from the Curie–Weiss law. The nonstoichiometric fluorite $Na_{0.4}Yb_{0.6}F_{2.2}$ phase, as well as all the other phases, has μ_{exp} close to its theoretical value. For the ordered $Na_7Yb_{13}F_{46}$ and $NaYb_2F_7$ phases, the μ_{exp} values exceed the theoretical ones by 9 and 17%, respectively. As shown by the experiments, the deviation of the temperature dependence χ of magnetic susceptibility from the paramagnetic behavior at $T< 80$ K for Yb-containing specimens cannot be explained by magnetic ordering. A possible effect of the crystal field on Yb^{3+}-ions resulting in the deviations from the Curie–Weiss law at low temperatures requires a more detailed study.

ACKNOWLEDGMENTS

The authors are grateful to A.A. Bystrova and L.L. Vistin for their help in specimen preparation and L.E. Svistov for useful discussions. This study was supported by the Russian Foundation for Basic Research, project no. 99-02-18067 and INTAS (International Association for the Promotion of Cooperation with Scientists from the New Independent States of the Former Soviet Union), project no. 97-32045.

REFERENCES

1. B. P. Sobolev, Bull. Soc. Cat. Cien. **12** (2), 275 (1991).
2. E. A. Krivandina, A. A. Bystrova, B. P. Sobolev, *et al.*, Kristallografiya **37** (6), 1523 (1992) [Sov. Phys. Crystallogr. **37**, 825 (1992)].
3. P. P. Fedorov, L. N. Pavlova, O. S. Bondareva, *et al.*, Preprint No. 11 (Shubnikov Institute of Crystallography, Russian Academy of Sciences, Moscow, 1990).
4. P. P. Fedorov, I. I. Buchinskaya, A. A. Bystrova, *et al.*, Zh. Neorg. Khim. **41** (10), 1715 (1996).
5. P. P. Fedorov, I. I. Buchinskaya, O. S. Bondareva, *et al.*, Zh. Neorg. Khim. **41** (11), 1923 (1996).
6. P. P. Fedorov, L. N. Pavlova, L. A. Ol’khovaya, *et al.*, Zh. Neorg. Khim. **35** (11), 2948 (1990).
7. L. N. Pavlova, P. P. Fedorov, L. A. Ol’khovaya, *et al.*, Zh. Neorg. Khim. **34** (8), 2168 (1989).
8. L. L. Vistin’, O. S. Bondareva, P. P. Fedorov, *et al.*, Bull. Soc. Cat. Cien. Fis., Quim. Mat. **13** (1), 285 (1992).
9. D. B. Brown, V. H. Crawford, J. W. Hall, and W. E. Hatfield, J. Phys. Chem. **81**, 1303 (1977).
10. R. R. Gupta, *Landolt–Bornstein: Numerical Data and Fundamental Relationships in Science and Technology, New Series* (Springer-Verlag, Berlin, 1986), Vol. 2/16, p. 235.
11. A. Frank, Phys. Rev. **39**, 119 (1932).
12. R. L. Carlin, *Magnetochemistry* (Springer-Verlag, Berlin, 1986), p. 69.
13. N. I. Sorokin, X. Bohigas, A. Folch, *et al.*, Kristallografiya **37** (4), 960 (1992) [Sov. Phys. Crystallogr. **37**, 510 (1992)].
14. X. Bohigas, A. Folch, J. Tejada, *et al.*, J. Solid State Chem. **102** (1), 198 (1993).
15. X. Bohigas, J. Lluma, J. Tejada, *et al.*, Bull. Soc. Cat. Cien. Fis., Quim. Mat. **13** (1), 273 (1992).
16. A. M. Golubev, P. P. Fedorov, O. S. Bondareva, *et al.*, Kristallografiya **36** (3), 651 (1991) [Sov. Phys. Crystallogr. **36**, 363 (1991)].

Translated by T. Dmitrieva

Crystallography Reports, Vol. 46, No. 3, 2001, pp. 488–495. Translated from Kristallografiya, Vol. 46, No. 3, 2001, pp. 540–548.
Original Russian Text Copyright © 2001 by Nasibullaev, Krekhov.

Behavior of a Nematic Liquid Crystal in Oscillatory Flow at Weak Surface Anchoring

I. Sh. Nasibullaev and A. P. Krekhov

Institute of Physics of Molecules and Crystals, Ufa Scientific Center, Russian Academy of Sciences,
pr. Oktyabrya 147, Ufa, 450075 Bashkortostan, Russia
e-mail: Nasibullayev IS@ic.bashedu.ru

Received March 28, 2000

Abstract—The effect of the surface viscosity on the orientational dynamics of a nematic liquid crystal in an oscillatory flow has been studied. For the shear and the Poiseuille flows, the approximate analytical solutions of the nematodynamic equations are obtained at small flow amplitudes. The frequency range of the oscillatory flow is determined, in which the surface viscosity strongly affects the optical response of a nematic layer. The results obtained are compared with the data of direct numerical simulation of the nematodynamic equations and the method for the experimental determination of surface viscosity is proposed. *© 2001 MAIK "Nauka/Interperiodica".*

INTRODUCTION

The anisotropy of viscoelastic properties and interaction between the velocity field **v** and the averaged molecular orientation specified by the director $\hat{\mathbf{n}}$ lead to a specific behavior of a nematic liquid crystal (NLC) in a flow. Up to now, the orientational dynamics of a NLC in a flow has been studied mainly for the so-called strong anchoring (at the fixed director orientation on the surfaces limiting the NLC layer). Depending on the treatment mode of the limiting surfaces and the character of the interaction between the NLC molecules and the substrate, the NLC orientation at the boundary is governed by the competing surface forces and the bulk torques acting on the director. In the steady-state case, the director orientation at the substrate is specified by the surface anchoring energy [1], whereas the description of the dynamics of NLC reorientation requires using the surface viscosity providing the dissipation in the boundary layer [2, 3]. The hydrodynamic model of the surface viscosity in a NLC was further developed in [4], where one of the possible mechanisms of the dissipation had been analyzed for weak anchoring.

The investigation of the director reorientation in an oscillatory Poiseuille flow [5] in an external electric field [6–8] and the experiments on the dynamical scattering of light by a NLC in a porous matrix [9, 10] indicate the necessity of taking into account the effect of surface viscosity on the orientational dynamics of a NLC. The weak surface anchoring of a NLC results in the transition from the planar to oblique orientation induced by an oscillating shear flow, which allow one to estimate the surface viscosity [11]. Despite the evergrowing interest in the effect of weak anchoring on the orientational dynamics in a NLC, a number of problems have not been solved, e.g., the relationship between anchoring strength and the surface viscosity and the possibility of measuring surface viscosity.

In the present paper, we theoretically study the behavior of an NLC in an oscillatory flow at weak anchoring and analyze the effect of the surface viscosity on the director dynamics in the bulk and at the limiting substrates. A nematic layer between two identical substrates providing weak planar or homeotropic anchoring is considered. We also discuss the oscillatory shear flow induced by the time-periodical in-plane motion of one of the limiting substrates and the oscillatory Poiseuille flow induced by oscillations of the pressure gradient applied along the layer.

THEORETICAL ANALYSIS

Consider a nematic layer of thickness d between two infinite parallel plates providing weak anchoring. The origin of the Cartesian coordinate system is chosen in the layer center with the z-axis being perpendicular to the layer. In the case of a shear flow, the upper substrate oscillates along the x-axis its plane as $A_x\sin(\omega t)$ (A_x is the oscillation amplitude, ω is the circular frequency). The oscillatory Poiseuille flow is formed under the effect of a periodically varying pressure gradient $(\Delta P/\Delta x)\cos(\omega t)$ applied along the x-axis. In the absence of the flow, the director is oriented along the z-axis at weak homeotropic anchoring and along the x-axis for weak planar anchoring.

The solution of the nematodynamic equations is sought for the director $\hat{\mathbf{n}}$ and the velocity **v** lying in the plane x–z, which are the functions of the distance to the plates (z) and time (t):

$$\begin{aligned} n_x &= \cos\theta(z,t), \quad n_y = 0, \quad n_z = \sin\theta(z,t), \\ v_x &= v_x(z,t), \quad v_y = 0, \quad v_z = 0, \end{aligned} \tag{1}$$

where θ is the angle formed by the orientations of the director and the x-axis. Such a choice of the dynamical variables is justified if the amplitudes of the velocity oscillations do not exceed the corresponding critical values of uniform [12, 13] and the space–periodical instabilities [14]. The dimensionless equations are obtained if one chooses the layer thickness d to be the characteristic length and the characteristic time as $1/\omega$, so that the dimensionless variables are $\tilde{z} = z/d$, $\tilde{t} = t\omega$, and $\tilde{v}_x = v_x/(d\omega)$, and the nematodynamic equations are written as [13, 15, 16]

$$\theta_{,t} - K(\theta)v_{x,z} = \varepsilon\left[P(\theta)\theta_{,zz} + \frac{1}{2}P'(\theta)\theta_{,z}^2\right], \tag{2}$$

$$\begin{aligned} \delta v_{x,t} &= -a_p\cos(t) \\ &+ \partial_z\{-(1-\lambda)K(\theta)\theta_{,t} + Q(\theta)v_{x,z}\}. \end{aligned} \tag{3}$$

In the above equations, the tildes are omitted and

$$\begin{gathered} K(\theta) = \frac{\lambda\cos^2\theta - \sin^2\theta}{1-\lambda}, \quad \lambda = \alpha_3/\alpha_2, \\ P(\theta) = \cos^2\theta + K\sin^2\theta, \quad K = K_{33}/K_{11}, \\ Q(\theta) = \frac{1}{2(-\alpha_2)} \\ \times[\alpha_4 + (\alpha_5 - \alpha_2)\sin^2\theta + (\alpha_3 + \alpha_6 + 2\alpha_1\sin^2\theta)\cos^2\theta], \\ \varepsilon = 1/(\tau_d\omega), \quad \tau_d = \gamma_1 d^2/K_{11}, \\ \gamma_1 = \alpha_3 - \alpha_2, \quad \delta = \tau_v\omega, \quad \tau_v = \rho d^2/(-\alpha_2). \end{gathered} \tag{4}$$

Here, α_i are the viscosity coefficients, $f_{,j} = \partial f/\partial j$, K_{11} and K_{33} are the elastic (Frank) constants, and ρ is the mass density of a NLC. For an oscillatory shear flow, the dimensionless amplitude of the pressure gradient is $a_p = 0$; for a Poiseuille flow, it equals

$$a_p = \frac{\Delta P}{\Delta x}\frac{d}{(-\alpha_2)\omega}. \tag{5}$$

The τ_d and τ_v values have the meaning of the characteristic times of the director relaxation and velocity, respectively.

Equations (2) and (3) are written for the incompressible fluid ($\nabla \cdot \mathbf{v} = 0$). In order to obtain the oscillatory Poiseuille flow in the experiments for the geometry where the pressure is applied only to one end of the cell, whereas (the other end is open) [5], the length of the LC cell should be less than the distance at which the velocity obviously decays due to the finite compressibility. Here, the velocity reduction by the factor of e is observed at a distance of $l_e = d\sqrt{2\rho c^2/(\pi^2\omega\eta)}$ [5, 17], where c is the sound velocity in a NLC and η is the effective nematic viscosity. For the material parameters of a MBBA nematic ($\rho \approx 10^3$ kg/m^3, $c \approx 1.5 \times 10^3$ m/s, and $\eta \approx 10^{-1}$ N s/m^2) with the layer thickness $d = 20$ μm and the frequency $f = 10$ kHz, we have $l_e \approx 0.5$ cm. One of the possible methods of considerable reduction of the compressibility effect is to apply pressure to both sides of the LC-cell in such a way that pressure would change in the counterphase.

The boundary conditions for the velocity in the case of the oscillatory shear ($a_p = 0$) are

$$v_x(z = -1/2) = 0, \quad v_x(z = +1/2) = a\cos(t), \tag{6}$$

where $a = A_x/d$; for the Poiseuille flow ($a_p \neq 0$), we have

$$v_x(z = \pm 1/2) = 0. \tag{7}$$

These conditions are specified by the "sticking condition" (on the substrate, an NLC moves with the velocity of the substrate). Using the Reynolds number [17] and the effective viscosity of MBBA, one can estimate the critical flow velocity which changes this condition, $v_c \sim$ 300 m/s. For the small amplitudes ($a \leq 1$, $a_p \leq 1$) and low frequencies ($f \leq 10$ kHz) of the oscillatory flow considered here, the velocity is not higher than ~ 1 m/s and, thus, boundary conditions (6) and (7) are fulfilled.

The weak NLC anchoring at the bounding substrates is mathematically described in terms of the specific surface energy per unit area

$$F_s = \frac{1}{2}Wf_s(\theta - \theta_0), \tag{8}$$

where W is the strength of anchoring and the function f_s is minimal at $\theta = \theta_0$. A simple phenomenological expression for the surface energy is given by the Rapini potential $f_s(\theta_0 - \theta) = \sin^2(\theta - \theta_0)$ [1]. The boundary conditions for the director orientation can be obtained from the balance of the torques acting on the NLC director [4, 8, 15]

$$\mp P(\theta)\theta_{,z} + \frac{1}{2}\frac{Wd}{K_{11}}\frac{\partial f_s}{\partial\theta} + \frac{\omega d}{K_{11}}\eta_s\frac{\partial\theta}{\partial t} = 0. \tag{9}$$

Here, the signs "–" and "+" before P correspond to $z =$ –1/2 and +1/2, respectively; $\eta_s = \gamma_1 l_{\gamma_1}$ is the surface viscosity; γ_1 is the bulk rotational viscosity; and l_{γ_1} characterizes the thickness of the subsurface layer in which the energy dissipation plays the most important role in director reorientation at the substrate [2, 3, 4].

Nematodynamic equations (2) and (3) are nonlinear and, therefore, in order to obtain an approximate analytical solution, we have to use the expansion in the small amplitude. Here, the small parameter a or a_p is the ratio of the amplitude of the oscillatory flow to the nematic layer thickness:

$$\begin{aligned} \theta &= \theta_0 + \tilde{\theta}, \quad |\tilde{\theta}| \ll 1, \\ v_x &= v_{x0} + U, \quad |U| \ll 1, \end{aligned} \tag{10}$$

where θ_0 = const and $v_{x0} = 0$ is the solution of Eqs. (2) and (3) in the absence of the flow ($a = 0$, $a_p = 0$), while the value of θ_0 is determined from the condition of the minimum surface energy. At small amplitudes of the flow-velocity oscillations, the director deviations from θ_0 are also small. Thus, for the angular dependence of the surface energy Eq. (8) we can write $f_s = \tilde{\theta}^2$.

Consider the case of low frequencies of the oscillatory flow $f = \omega/2\pi$, where $\omega \ll \tau_v^{-1}$ (the length of the viscous wave $l \sim \sqrt{\eta/(\rho\omega)}$ considerably exceeds d), i.e., $\delta \ll 1$. For the typical values of the nematic material parameters, $\rho \approx 10^3$ kg/m^3, $\eta \approx 10^{-1}$ N s/m^2 and d = 20 μm, we have $\delta \ll 1$ at $f \ll 40$ kHz. Here, one can ignore the adiabatic variation of the velocity in the left-hand side of Eq. (3) (the term $\delta v_{x,t}$). Within the frequency range in which the condition $\omega \ll \tau_v^{-1}$ is satisfied, there are two oscillation modes (depending on the flow frequency): (1) the oscillations of the director, which are in phase with the velocity oscillations (for $\omega \ll \tau_d^{-1}$), and (2) the oscillations of the director in counterphase with the velocity oscillations (for $\omega \gg \tau_d^{-1}$).

1. In the first order of smallness of $\tilde{\theta}$ and U, Eqs. (2) and (3) for the oscillating shear have the form

$$\begin{aligned} \tilde{\theta}_{,t} - K_0 U_{,z} &= \varepsilon P_0 \tilde{\theta}_{,zz}, \\ (1-\lambda)K_0\tilde{\theta}_{,tz} &= Q_0 U_{,zz} = 0, \end{aligned} \tag{11}$$

where $K_0 = K(\theta_0)$, $P_0 = P(\theta_0)$, and $Q_0 = Q(\theta_0)$ with the following boundary conditions:

$$\begin{gathered} U(z = -1/2) = 0, \quad U(z = 1/2) = a\cos(t), \\ \tilde{\theta}_{,z} - E\tilde{\theta} - G\tilde{\theta}_{,t} = 0|_{z=-1/2}, \\ \tilde{\theta}_{,z} - E\tilde{\theta} - G\tilde{\theta}_{,t} = 0|_{z=1/2}. \end{gathered} \tag{12}$$

Here, $E = Wd/(P_0K_{11})$ and $G = \eta_s\omega d/(P_0K_{11})$. Since Eq. (11) and boundary conditions (12) are linear and the external action is of the periodic nature, the solution has the form

$$\tilde{\theta}(z, t) = T_1(z)\cos(t) + T_2(z)\sin(t), \tag{13}$$

$$U(z, t) = U_1(z)\cos(t) + U_2(z)\sin(t). \tag{14}$$

Substituting Eqs. (13) and (14) into Eq. (11) and solving the resulting system of ordinary differential equations with due regard for boundary conditions (12), we obtain for the angle of the director deviation $\tilde{\theta}$

$$\begin{aligned} T_1(z) &= aK_0\frac{C_1F_1(z) - C_2F_2(z)}{C_1^2 + C_2^2}, \\ T_2(z) &= -aK_0\frac{C_1F_2(z) + C_2F_1(z)}{C_1^2 + C_2^2} \end{aligned} \tag{15}$$

and the equations for velocity U

$$\begin{aligned} U_1(z) &= a\left(\frac{1}{2} + z\right) + a\frac{(1-\lambda)K_0^2}{2Q_0k}\frac{C_1F_3(z) - C_2F_4(z)}{C_1^2 + C_2^2}, \\ U_2(z) &= -a\frac{(1-\lambda)K_0^2}{2Q_0k}\frac{C_1F_4(z) + C_2F_3(z)}{C_1^2 + C_2^2}. \end{aligned} \tag{16}$$

Expressions for the functions $F_i(z)$ and coefficients C_i are given in Appendix A.

2. For small amplitudes of the director oscillations and the velocity in the oscillatory Poiseuille flow, we have

$$\begin{aligned} \tilde{\theta}_{,t} - K_0 U_{,z} &= \varepsilon P_0 \tilde{\theta}_{,zz}, \\ -(1-\lambda)K_0\tilde{\theta}_{,tz} + Q_0 U_{,zz} &= a_p\cos(t) \end{aligned} \tag{17}$$

with the boundary conditions

$$\begin{gathered} U(z = \pm 1/2) = 0, \\ \tilde{\theta}_{,z} - E\tilde{\theta} - G\tilde{\theta}_{,t} = 0|_{z=-1/2}, \\ \tilde{\theta}_{,z} + E\tilde{\theta} - G\tilde{\theta}_{,t} = 0|_{z=1/2}. \end{gathered} \tag{18}$$

In a way similar to that used for the shear flow, we seek the solution of Eqs. (17) in the form of Eqs. (13) and (14). Then, we obtain for the angle of the director deviation $\tilde{\theta}$

$$\begin{aligned} T_1(z) &= -a_pK_0M_0\frac{c_1f_1(z) - c_2f_2(z)}{c_1^2 + c_2^2}, \\ T_2(z) &= -a_pK_0M_0\left[\frac{c_2f_1(z) + c_1f_2(z)}{c_1^2 + c_2^2} - 2z\right] \end{aligned} \tag{19}$$

and for the velocity U

$$\begin{aligned} U_1(z) &= -a_pM_0\left[\left(\frac{1}{4} - z^2\right) + \frac{(1-\lambda)K_0^2}{2Q_0k}\frac{c_1f_3(z) - c_2f_4(z)}{c_1^2 + c_2^2}\right], \\ U_2(z) &= -a_pM_0\frac{(1-\lambda)K_0^2}{2Q_0k}\frac{c_2f_3(z) + c_1f_4(z)}{c_1^2 + c_2^2}. \end{aligned} \tag{20}$$

The functions $f_i(z)$ and the coefficients c_i given in Appendix A.

In both shear flow and Poiseuille flow, the director oscillates about the initial orientation θ_0 with the phase

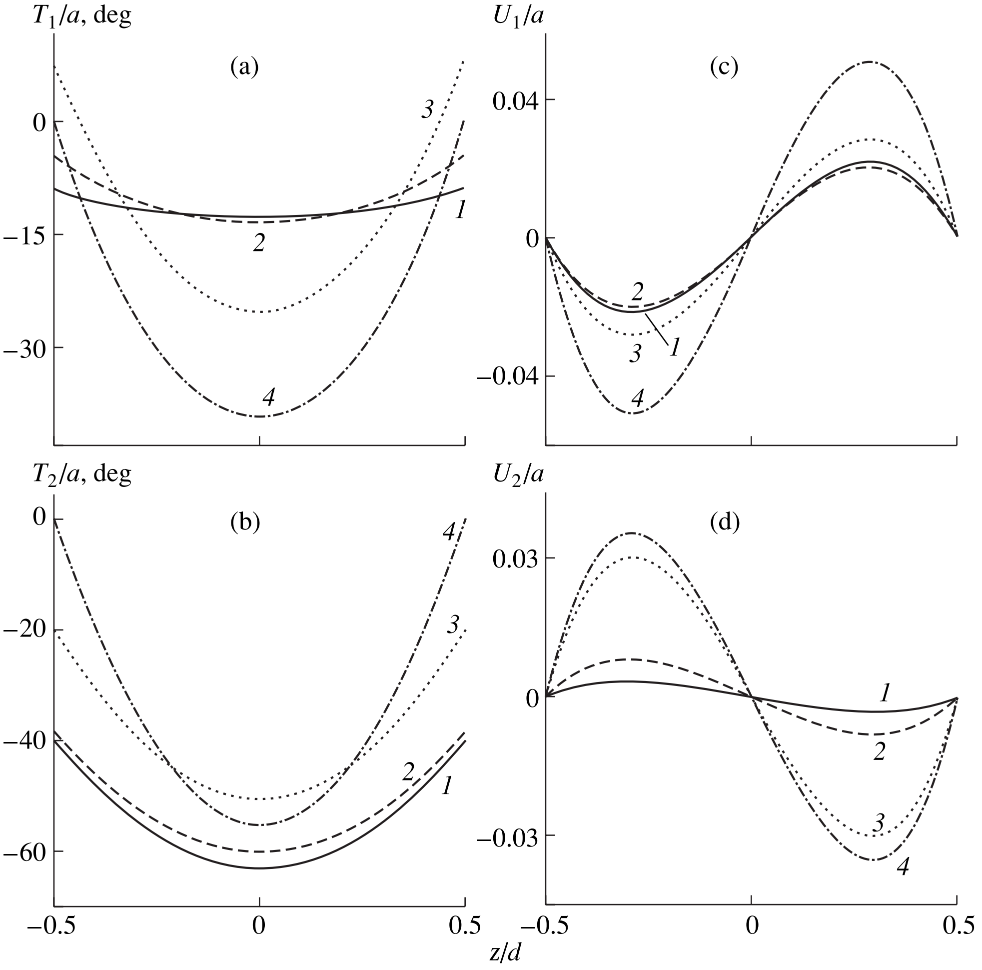

Fig. 1. The profiles of (a, b) the NLC director and (c, d) the velocity of the oscillatory shear flow at $a = 0.2$; $f = 0.5$ Hz; $d = 20$ μm; and $W = 10^{-6}$ J/m^2 for l_{γ_1} equal to (*1*) 0, (*2*) 10^{-6}, and (*3*) 10^{-5} m and (*4*) for strong anchoring everywhere (Figs. 2–4).

shift with respect to the velocity oscillations, which depends on the anchoring strength W and the surface viscosity η_s. At the surfaces limiting the NLC layer, we have $\tilde{\theta}_s = 0$ for rigid anchoring and $\tilde{\theta}_s = \tilde{\theta}_s(t; W, \eta_s)$ for nonrigid anchoring. Analyzing expressions for $T_1(z)$ and $T_2(z)$, we see that $\tilde{\theta}_s(t; W, \eta_s) \longrightarrow 0$ at $W \longrightarrow \infty$ or $\eta_s \longrightarrow \infty$. Moreover, since the surface viscosity is characterized by the dimensionless parameter $G \sim \eta_s\omega$, an increase of the flow oscillations yields $\tilde{\theta}_s(t; W, \eta_s) \longrightarrow 0$.

DISCUSSION AND CONCLUSIONS

Analysis of solution (15) for a shear flow shows that the amplitude of the director oscillations is proportional to $K(\theta_0)$ and is much more pronounced for the homeotropic orientation ($\theta_0 = \pi/2$) than for the planar one ($\theta_0 = 0$) (for the material parameters of the MBBA nematic, $K(\pi/2)/K(0) \approx 10^2$). Similarly, for the Poiseuille flow [see Eqs. (19)], the amplitude of the director oscillations is proportional to $K(\theta_0)M(\theta_0)$, with the ratio between the amplitudes for the planar and the homeotropic MBBA layers being ~70.

The profiles of the components of the director deviation from the initial homeotropic orientation ($\theta_0 = \pi/2$), calculated with the use of the MBBA parameters, are shown in Figs. 1a and 1b and in Figs. 2a and 2b for the oscillatory shear and Poiseuille flows, respectively. The $T_1(z)$ and $T_2(z)$ curves for the fixed value $W = 10^{-6}$ J/m^2 typical of weak homeotropic anchoring [18] are given in Fig 1 and 2 for different values of the surface viscosity and $\eta_s = \gamma_1 l_{\gamma_1}$ within the experimental estimations of $l_{\gamma_1} = 10^{-7}$–10^{-5} m [6, 7, 9–11].

Figures 1c, 1d and 2c, 2d also show the related profiles of the velocity components $U_1(z)$ and $U_2(z)$ (in Fig. 1c, the component $U_1(z)$ in the oscillatory shear flow is shown in terms of its deviation from the linear profile $\Delta U_1 = U_1(z) - a(1/2 - z)$. It is seen that, depending on the surface viscosity, the orientational nematodynamics is changed both in the boundary layer and in the NLC bulk. For the chosen anchoring strength, nem-

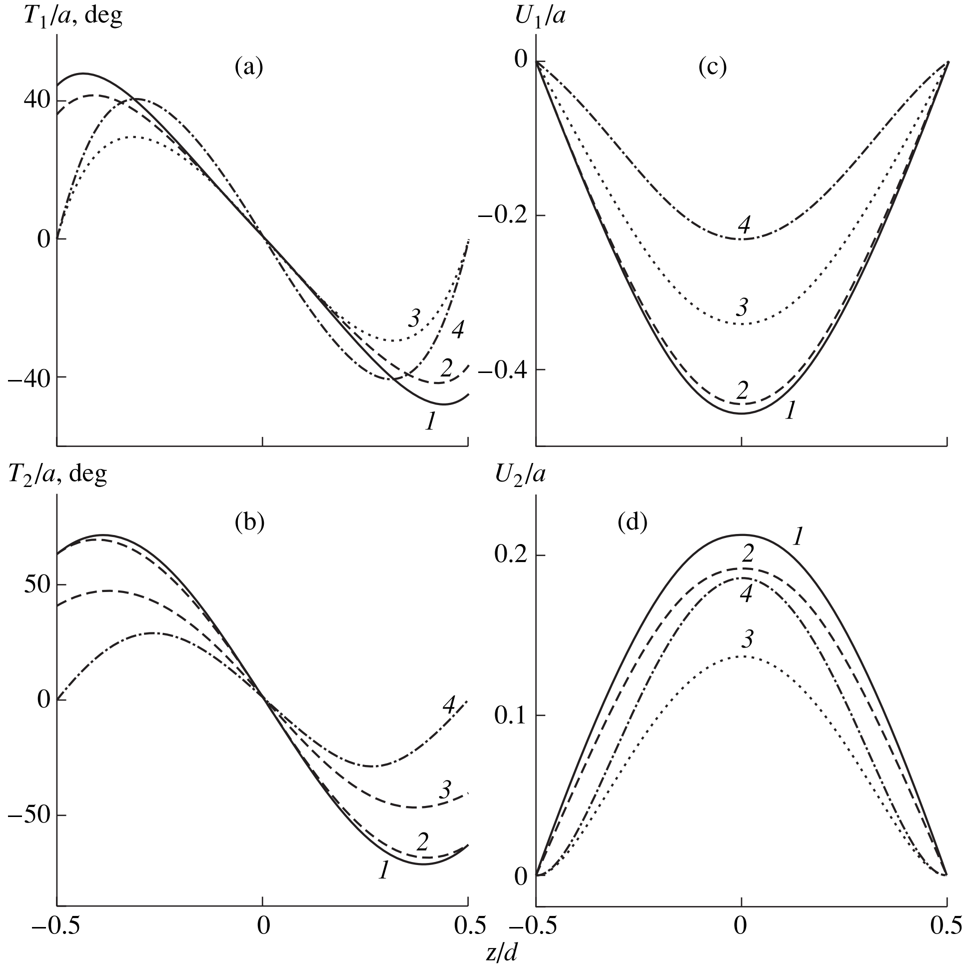

Fig. 2. The profiles of (a, b) the NLC director and (c, d) the velocity for the Poiseuille flow at $a_p = 0.2$; $f = 5$ Hz; $d = 20$ μm; and $W = 10^{-6}$ J/m^2 for l_{γ_1} equal to (*1*) 0, (*2*) 10^{-7}, and (*3*) 10^{-6} m and (*4*) for strong anchoring.

atic-layer thickness, and the frequency of the flow oscillations, the variation of profiles in comparison with the case of rigid anchoring is more pronounced in the range $l_{\gamma_1} = 10^{-6}$–10^{-5} m for the shear flow and in the range $l_{\gamma_1} = 10^{-7}$–10^{-6} m for the Poiseuille flow.

Initial equations (2) and (3) with boundary conditions (6), (7), and (9) and the corresponding solutions ($\tilde{\theta}$, U) are invariant with respect to the scale transformation

$$\begin{gathered} W \longrightarrow \alpha^{-1}W, \quad \eta_s \longrightarrow \alpha\eta_s, \\ d \longrightarrow \alpha d, \quad \omega \longrightarrow \alpha^{-2}\omega, \quad a_p \longrightarrow \alpha^3 a_p. \end{gathered} \tag{21}$$

Thus, the dependences in Figs. 1 and 2 are sufficiently universal and, with due regard for Eq. (21), provide the determination of the director and velocity distributions at other W values.

The simplest and the most widespread method of experimental study of the director dynamics is the measurement of the polarized-light intensity (the optical response). In crossed polarizers oriented at an angle of 45° to the x-axis, the intensity of the transmitted light is given by

$$I = I_0 \sin^2\frac{\Psi}{2} \tag{22}$$

with the phase delay

$$\Psi = \frac{2\pi d}{\Lambda}\int_{-1/2}^{1/2}\left[n_o\left(1 - \frac{n_e^2 - n_o^2}{n_e^2}\cos^2\theta\right)^{-1/2} - n_o\right]dz, \tag{23}$$

where n_o and n_e are the refractive indices for the ordinary and the extraordinary rays, respectively, and Λ is the wavelength of the monochromatic light.

Figures 3a and 4a show the temporal dependences of the intensity of the light transmitted by a nematic layer for an oscillation period at the frequencies 0.5 Hz (shear flow) and 5 Hz (Poiseuille flow) calculated with the use of "small-amplitude" solutions. The surface viscosity affects both the maximum intensity and the phase shift of the optical response with respect to the

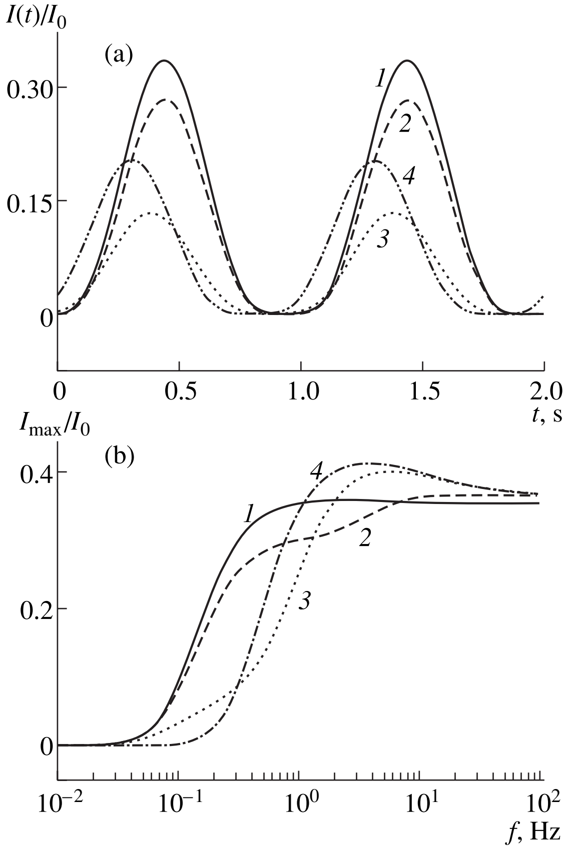

Fig. 3. (a) The temporal dependence of the optical response and (b) the frequency dependence of the intensity maximum for the oscillatory shear flow, the parameters *a, f, d, W,* and l_{γ_1} being the same as in Fig. 1.

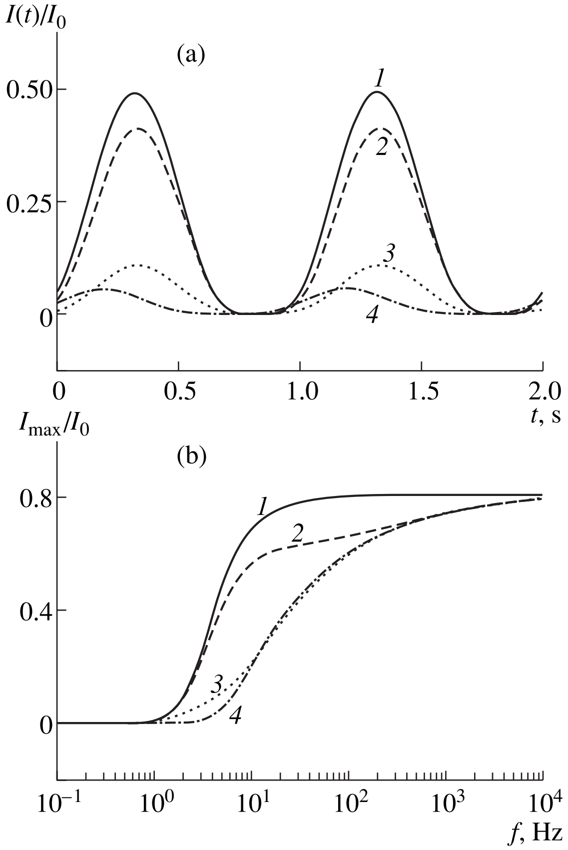

Fig. 4. (a) The temporal dependence of the optical response and (b) the frequency dependence of the intensity maximum for the Poiseuille flow, the parameters a_p, *f, d, W,* and l_{γ_1} being the same as in Fig. 2.

flow oscillations. The dependences of the maxima of relative intensity on the frequency of the flow oscillations are shown in Figs. 3b and 4b for different values of the surface viscosity $\eta_s = \gamma_1 l_{\gamma_1}$. At low oscillation frequencies, the intensities are also low, because the director orientation is changed significantly, and the determination of the effect of surface viscosity on the orientational nematodynamics of an NLC is practically impossible. At high frequencies, the thickness of the boundary layer [13] decreases, the surface viscosity increases ($G \sim \eta_s\omega$), and the orientational behavior of an NLC approaches the situation corresponding to the rigid anchoring. Now, there is the narrow frequency range (0.05–5 Hz for the shear flow and 1–100 Hz for the Poiseuille flow at the chosen anchoring strength and the nematic layer thickness) where the effect of the surface viscosity is still very pronounced.

Variation in the anchoring force does not affect the type of the frequency dependence of the maximum intensity of the light transmitted by the nematic layer. Thus, for a fixed *W* value, one can always determine the optimum nematic-layer thickness and the frequency range of the flow oscillations such that the effect of the surface viscosity is important. This makes it possible, using η_s as fitting parameter, to find the value of the surface viscosity from the comparison of the optical responses—experimentally recorded and theoretically calculated.

To determine the applicability range of the flow amplitudes (a, a_p) where the approximate solutions, we numerically simulated basic equations (2) and (3) with boundary conditions (6), (7), and (9) by the Krank–Nicholson method [19]. Figures 5 shows compares the amplitude dependences of the optical response obtained with the use of the approximate analytical and numerical solutions. At the amplitudes $a \leq 0.2$ and $a_p \leq 0.2$, the corresponding difference does not exceed 5% for the oscillatory shear flow and 15% for the Poiseuille flow.

Thus, we have analyzed the effect of the weak anchoring and the surface viscosity on the orientational nematodynamics in the oscillating shear and Poiseuille flows. The approximate analytical solutions of the nematodynamic equations are derived with due regard for the weak surface anchoring at the limiting surfaces, which are also valid at small amplitudes of the flow

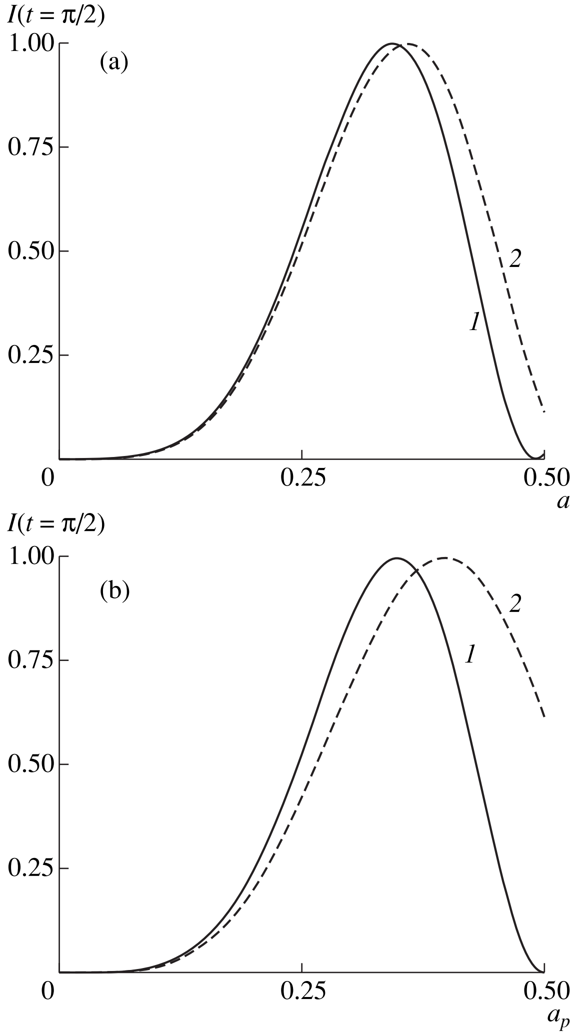

Fig. 5. The dependence of the optical response on the amplitude of the oscillatory (a) shear ($f = 0.5$ Hz, $l_{\gamma_1} = 10^{-6}$ m) and (b) Poiseiuille ($f = 5$ Hz, $l_{\gamma_1} = 10^{-7}$ m) flows at $d = 20$ μm and $W = 10^{-6}$ J/m^2: (*1*) analytical and (*2*) numerical solutions.

oscillations. A certain frequency range of the oscillatory flow, in which the NLC optical response is essentially affected by the surface viscosity, has also been determined. This effect can be used to determine experimentally the surface viscosity and study the orientational nematodynamics at weak anchoring.

APPENDIX A

Functions and Coefficients

$$k = \sqrt{\frac{Q_0 - (1-\lambda)K_0^2}{2\varepsilon Q_0 P_0}}, \quad M_0 = \frac{1}{2(Q_0 - (1-\lambda)K_0^2)},$$

$$F_1(z) = \cosh(kz)\cos(kz) - \cosh(k/2)\cos(k/2)$$

$$+ \frac{kE}{E^2+G^2}\{\cosh(k/2)\sin(k/2) - \sinh(k/2)\cos(k/2)\}$$

$$- \frac{kG}{E^2+G^2}\{\cosh(k/2)\sin(k/2) + \sinh(k/2)\cos(k/2)\},$$

$$F_2(z) = \sinh(kz)\sin(kz) - \sinh(k/2)\sin(k/2)$$

$$- \frac{kE}{E^2+G^2}\{\cosh(k/2)\sin(k/2) + \sinh(k/2)\cos(k/2)\}$$

$$- \frac{kG}{E^2+G^2}\{\cosh(k/2)\sin(k/2) - \sinh(k/2)\cos(k/2)\},$$

$$F_3(z) = \sinh(kz)\cos(kz) - \cosh(kz)\sin(kz)$$

$$- 2z(\sinh(k/2)\cos(k/2) - \cosh(k/2)\sin(k/2)),$$

$$F_4(z) = \sinh(kz)\cos(kz) + \cosh(kz)\sin(kz)$$

$$- 2z(\sinh(k/2)\cos(k/2) + \cosh(k/2)\sin(k/2)),$$

$$f_1(z) = \cosh(kz)\sin(kz) + \frac{2E}{E^2+G^2}\cosh(kz)\sin(kz)$$

$$- \frac{2G}{E^2+G^2}\sinh(kz)\cos(kz),$$

$$f_2(z) = \sinh(kz)\cos(kz) + \frac{2E}{E^2+G^2}\sinh(kz)\cos(kz)$$

$$+ \frac{2G}{E^2+G^2}\cosh(kz)\sin(kz),$$

$$f_3(z) = A_1(z)\left\{1 + 2\frac{E-G}{E^2+G^2}\right\} + A_2(z)\left\{1 + 2\frac{E+G}{E^2+G^2}\right\},$$

$$f_4(z) = A_1(z)\left\{1 + 2\frac{E+G}{E^2+G^2}\right\} - A_2(z)\left\{1 + 2\frac{E-G}{E^2+G^2}\right\},$$

$$A_1(z) = \cosh(kz)\cos(kz) - \cosh(k/2)\cos(k/2),$$

$$A_2(z) = \sinh(kz)\sin(kz) - \sinh(k/2)\sin(k/2),$$

$$C_1 = \sinh(k/2)\sin(k/2)$$

$$- \frac{(1-\lambda)K_0^2}{Q_0 k}[\cosh(k/2)\sin(k/2) - \sinh(k/2)\cos(k/2)]$$

$$+ \frac{kE}{E^2+G^2}\{\cosh(k/2)\sin(k/2) + \sinh(k/2)\cos(k/2)\}$$

$$+ \frac{kG}{E^2+G^2}\{\cosh(k/2)\sin(k/2) - \sinh(k/2)\cos(k/2)\},$$

$$C_2 = \cosh(k/2)\cos(k/2)$$

$$-\frac{(1-\lambda)K_0^2}{Q_0 k}[\cosh(k/2)\sin(k/2) + \sinh(k/2)\cos(k/2)]$$

$$-\frac{kE}{E^2+G^2}\{\cosh(k/2)\sin(k/2) - \sinh(k/2)\cos(k/2)\}$$

$$+\frac{kG}{E^2+G^2}\{\cosh(k/2)\sin(k/2) + \sinh(k/2)\cos(k/2)\},$$

$$c_1 = \sinh(k/2)\cos(k/2)$$

$$+\frac{kE}{E^2+G^2}(\cosh(k/2)\cos(k/2) - \sinh(k/2)\sin(k/2))$$

$$+\frac{kG}{E^2+G^2}(\cosh(k/2)\cos(k/2) + \sinh(k/2)\sin(k/2)),$$

$$c_2 = \cosh(k/2)\sin(k/2)$$

$$+\frac{kE}{E^2+G^2}(\cosh(k/2)\cos(k/2) + \sinh(k/2)\sin(k/2))$$

$$-\frac{kG}{E^2+G^2}(\cosh(k/2)\cos(k/2) - \sinh(k/2)\sin(k/2)).$$

APPENDIX B

Material Parameters

The numerical calculations were based on the following parameters of a MBBA nematic liquid crystal at 25°C [20, 21]. The viscosity coefficients, 10^{-3} N s/m^2: $\alpha_1 = -18.1$, $\alpha_2 = -110.4$, $\alpha_3 = -1.1$, $\alpha_4 = 82.6$, $\alpha_5 = 77.9$, and $\alpha_6 = -33.6$. The elasticity coefficients, 10^{-12} N: $K_{11} = 6.66$, $K_{22} = 4.2$, and $K_{33} = 8.61$. The density $\rho = 10^3$ kg/m^3. The refractive indices at the monochromatic wavelength of the light $\Lambda = 670$ nm [22]: $n_o = 1.542$ and $n_e = 1.7435$.

ACKNOWLEDGMENTS

We are grateful to Yu.A. Lebedev and M.V. Khazimullina for fruitful discussion and criticism of the manuscript. This study was supported by the INTAS, project no. 96-498, and the Federal Program "Integration," project no. A0002.

REFERENCES

1. A. Rapini and M. Papoular, J. Phys. (Paris), Colloq. **30**, C4 (1969).
2. A. Rapini, Can. J. Phys. **53**, 968 (1975).
3. S. Pikin, G. Ryschenkow, and W. Urbach, J. Phys. (Paris) **37**, 241 (1976).
4. G. E. Durand and E. G. Virga, Phys. Rev. E **59**, 4137 (1999).
5. L. M. Blinov, S. A. Davidyan, V. N. Reshetov, *et al.*, Zh. Éksp. Teor. Fiz. **97**, 1597 (1990) [Sov. Phys. JETP **70**, 902 (1990)].
6. A. Gharbi, F. R. Fekin, and G. Durand, Liq. Cryst. **12**, 515 (1992).
7. V. P. Vorflusev, H.-S. Kitzerow, and V. G. Chigrinov, Appl. Phys. Lett. **70**, 3359 (1997).
8. P. J. Kedney and F. M. Leslie, Liq. Cryst. **24**, 613 (1998).
9. A. Mertelj, L. Spindler, and M. Čopič, Phys. Rev. E **56**, 549 (1997).
10. A. Mertelj and M. Čopič, Phys. Rev. Lett. **81**, 5844 (1998).
11. M. V. Khazimullin, T. Börzsönyi, A. P. Krekhov, and Yu. A. Lebedev, Mol. Cryst. Liq. Cryst. **329**, 247 (1999).
12. A. P. Krekhov and L. Kramer, J. Phys. II **4**, 677 (1994).
13. A. P. Krekhov and L. Kramer, Phys. Rev. E **53**, 4925 (1996).
14. T. Börzsönyi, A. Buka, A. P. Krekhov, and L. Kramer, Phys. Rev. E **58**, 7419 (1998).
15. S. A. Pikin, *Structural Transformations in Liquid Crystals* (Nauka, Moscow, 1981; Gordon and Breach, New York, 1991).
16. P. G. de Gennes and J. Prost, *The Physics of Liquid Crystals* (Clarendon Press, Oxford, 1993).
17. L. D. Landau and E. M. Lifshitz, *Course of Theoretical Physics*, Vol. 6: *Fluid Mechanics* (Nauka, Moscow, 1986; Pergamon, New York, 1987).
18. L. M. Blinov, A. Yu. Kabayenkov, and A. A. Sonin, Liq. Cryst. **5**, 645 (1989).
19. O. S. Tarasov and A. P. Krekhov, Kristallografiya **43** (3), 516 (1998) [Crystallogr. Rep. **43**, 476 (1998)].
20. W. H. de Jeu, W. A. P. Claassen, and A. M. J. Spruijt, Mol. Cryst. Liq. Cryst. **37**, 269 (1976).
21. H. Kneppe, F. Schneider, and N. K. Sharma, J. Chem. Phys. **77**, 3203 (1982).
22. M. Brunet-Germain, C. R. Seances Acad. Sci., Ser. B **271**, 1075 (1970).

Translated by A. Zolot'ko

Crystallography Reports, Vol. 46, No. 3, 2001, pp. 496–502. Translated from Kristallografiya, Vol. 46, No. 3, 2001, pp. 549–555.
Original Russian Text Copyright © 2001 by Shibkov, Golovin, Zheltov, Korolev, Vlasov.

Kinetics and Morphology of Nonequilibrium Growth of Ice in Supercooled Water

A. A. Shibkov, Yu. I. Golovin, M. A. Zheltov, A. A. Korolev, and A. A. Vlasov
Tambov State University, ul. Internatsional'naya 33, Tambov, 392622 Russia
e-mail: golovin@inbox.ru

Received July 5, 1999

Abstract—The kinetics of free growth of ice in a distilled-water film supercooled to –30°C was studied by the video recording technique in the polarized light. In the supercooling range $12 < \Delta T < 16$ K, a first-order kinetic morphological transition was observed between the structure formed by needlelike crystals of ice and the quasi-adiabatic "structure" of single grains having the shape of planar platelets with the thickness proportional to the thickness of the water film and relative supercooling. It was found that this transition is accompanied by jumplike changes in the main crystallization parameters such as the growth rate of grains, their size and number, their kinetic behavior, and the fractal dimension of the structure. *© 2001 MAIK "Nauka/Interperiodica".*

INTRODUCTION

The role of growth defects in a crystal structure and their close relation to the whole set of physical properties of crystals are well known and motivate the constant interest in the mechanisms of crystal growth. In the last two decades, new surprising aspects of this problem were revealed which are of great importance for both fundamental and applied sciences. In fact, crystal growth proceeding by the normal mechanism with characteristic atomically rough surface of the phase boundary, its morphological instability, and several possible types of morphology has numerous analogs in different fields of physics, chemistry, geophysics, and biology. Such growth is also referred to as nonequilibrium growth. Among its most well known analogs are instability phenomena accompanying the propagation of flow fronts of immiscible fluids with different viscosities [1], diffusion-induced combustion [2], the chemical reaction and impact ionization at surfaces of solids [3, 4], diffusion-driven aggregation of particles [5], fracture of amorphous films [6], rearrangement of rock fabrics [7], growth of bacterium populations [8], etc. Numerous analytical studies showed [9–15] that crystallization of a supercooled melt is a convenient model describing the formation of structures in the large class of nonlinear nonequilibrium dynamical systems. Prigogine [16], Mandelbrot [17], Feigenbaum [18], Langer [9], and many other researchers state that the evolution of such systems is of the universal character.

The *in situ* study of the structural evolution of a polycrystal growing from a melt is also of great applied importance: most structural materials, in particular, steels and alloys, are used in the polycrystalline state, in which the mechanical characteristics and the physical properties are essentially dependent on the shape, size, and orientation of constituent grains; the specific features of grain boundaries; etc. Moreover, the dendritic forms of some crystals are used in the medical diagnostics. Thus, in addition to the traditional problem of crystal physics (growth of single crystals with the specified physical properties under quasi-equilibrium thermal conditions), we face a new burning problem of detailed experimental and theoretical analysis of morphology and kinetics of nonequilibrium growth, especially at high rates of the crystallization front, which is of great importance for both fundamental and applied science.

Despite of a large number of studies in the field of theoretical analysis and computer simulation of the mechanisms underlying the morphology and genesis of dissipative systems, the problem of selection of global morphological types in nonequilibrium growth is still open mainly because of the lack of experimental data. As is well known, the selection structures in actual growth processes is implemented via kinetic morphological transitions, i.e., via gradual or jumplike changes in the morphology of the phase surface under the conditions of continuous variation of the driving force of crystallization–relative supercooling $\theta = \Delta T/(q/c_p)$, where $\Delta T = T_m - T$ is the absolute supercooling, T_m is the melting point, c_p is the specific heat of the melt, and q is the latent heat of crystallization. The morphological transitions are the manifestations of self-organization in nonequilibrium systems. The morphological transitions accompanying crystallization from melts are less studied than those in crystallization from gas phase. Thus, it is well known that the shape of ice crystals grown from the gas phase depends on the temperature and pressure of water vapor [19, 20]. Maeno [21] classified the shapes of snowflake in the temperature range from –0.1 to –30°C (altogether nine shapes).

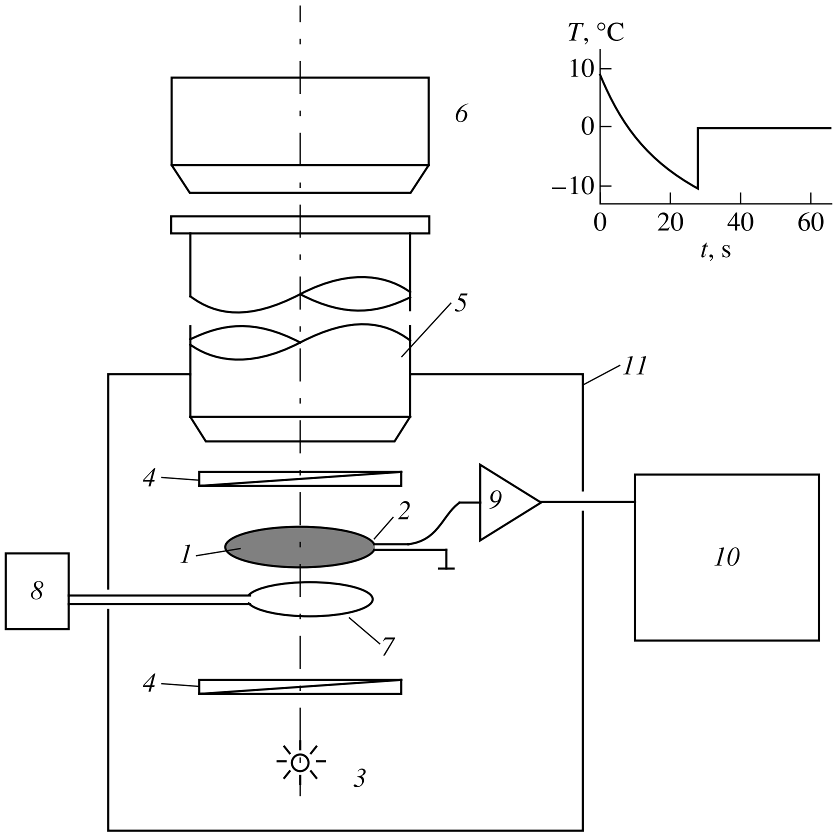

Fig. 1. Schematic of experimental setup for *in situ* studies of kinetics of spontaneous crystallization in thin water films: (*1*) water film in the form of a membrane; (*2*) wire ring (thermocouple); (*3*) light source; (*4*) polarizers; (*5*) microscope; (*6*) photoreceiver (photomultiplier or video camera); (*7*) electric heater; (*8*) power supply for the electric heater; (*9*) preamplifier; (*10*) oscillograph S8-13; (*11*) freezing chamber. The inset shows a typical thermogram of the film cooling and crystallization.

Similar data on growth of ice from supercooled water are obtained only for supercooling of the order of several degrees centigrade [22].

Therefore, we undertook the experimental study of kinetics and morphology of nonequilibrium growth of ice in a supercooled water conventionally used as a model object in range of supercooling $0.1 < \Delta T < 30$ K not considered earlier and covering almost the whole domain of heterogeneous nucleation of ice crystals in water under atmospheric pressure. We also analyzed the morphological phase transitions between nonequilibrium structures and constructed the kinetic morphological diagram in this range of supercooling.

EXPERIMENTAL TECHNIQUE

The kinetics of ice growth in a supercooled distilled-water film was studied by the optical method in the polarized light (Fig. 1). A 100-μm-thick film (*1*) had the form of a free membrane pulled onto a wire ring (*2*). The optical channel for recording the crystallization process consisted of a light source (*3*), polarizers (*4*), a microscope (*5*), and a video camera (*6*). In some cases, in order to study the crystallization kinetics at supercooling in the range $20 < \Delta T < 30$ K, a photomultiplier was used instead of the video camera. To provide thermal monitoring of phase transitions, a special wire ring was made of two conductors (copper and manganin) forming a thermocouple with the sensitivity of 20 μW/K and the speed of response determined by the thermal relaxation time $t_T \sim d^2/a < 10^{-3}$ s, where $d = 100$ μm is the wire diameter and $a \sim 10^{-4}$ m^2/s is the thermal diffusivity of the metal. The accuracy of temperature measurements was 0.05 K. A sample was placed into a measuring cell located in a small freezing chamber and was completely frozen. Then, the sample was defrozen by a local electric heater (*7*). On the thermogram, the moment of switching-off of the electric heater was taken to be the origin of the time axis. At a certain stage of cooling, first ice crystals were formed in the film.

Preliminary optical observations showed that growth of ice under these conditions starts by the freezing of a water film at the loop mouth of the wire. As a result, a cylindrical (hemispherical at the thermocouple junction) crystallization front is formed, which, because of Mullins–Sekerka morphological instability [19], generates an almost parabolic protrusion. In the course of further growth, these protrusions are transformed into grains of different shapes depending on the

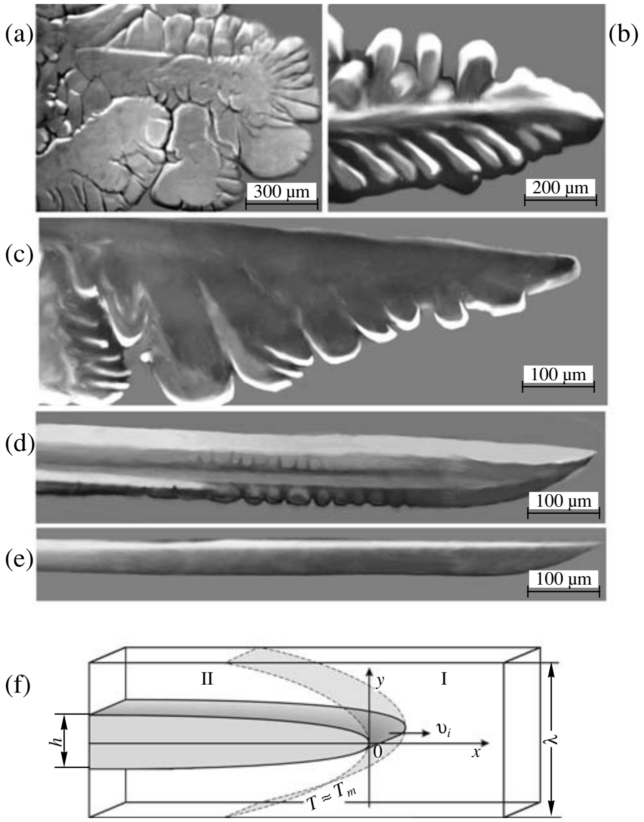

Fig. 2. Typical shapes of a grain freely growing in supercooled water at several values of ΔT: (a) 0.3; (b) 1; (c) 2; (d) 4; (e) 7; (f) 12–30 K.

initial supercooling of water. The first ice protrusions most probably arises at the thermocouple junction, which thus plays the role of a "heterogeneous concentrator" of nonequilibrium growth of ice. Therefore, the temperature jump at the thermocouple junction caused by release of the latent heat of crystallization provides the record of the initial moment of the phase transition at a resolution of about 1 ms and the measurement of the initial supercooling necessary for the construction of the morphological diagram. Thus, the proposed method allows video recording of water crystallization in the range of heterogeneous nucleation of ice at the maximum supercooling $\Delta T_{\max} \approx 30$ K at a temporal resolution of about 40 ms and a spatial resolution not lower than ~10 μm. Earlier, similar methods were limited to a supercooling of $\Delta T_{\max} = 8.5$ K [20].

EXPERIMENTAL RESULTS

In the first series of experiments, we studied the kinetics and morphology of the first grain grown from the ice protrusion on the thermocouple junction or in the close vicinity of it. The evolution of the grain shape depending on initial water supercooling is illustrated by Fig. 2 for the range of heterogeneous nucleation of ice $\Delta T < 30$ K. At $\Delta T < 0.5$ K, ice growth is characterized by split of dendrite tips [15, 22] (Fig. 2a), whereas in the range $0.5 < \Delta T < 4$ K the grain has the form of a dendrite shown in Figs. 2b–2d. With an increase in supercooling, the ratio of the growth rates of the side branches and the tip of the dendrite stem decreases. The distance from the tip where the first side branches appeared also increases and in the range $5 < \Delta T < 12$ K, the grain is transformed into a needlelike crystal (Fig. 2e). In the range $12 < \Delta T < 30$ K, a single grain spontaneously arises in the avalanchelike manner in the film in the form of a thin platelet (Fig. 2f). Within the time interval $\Delta t \approx 70$–200 ms, this platelet grows over the whole horizontal cross section of the film. The platelet thickness is proportional to the initial supercooling of water

$$h = c\Delta T, \tag{1}$$

where $c \approx 1.2$ μm/K. In the temperature range under study, the thickness is $h \approx 20$–40 μm. The initial supercooling range $12 < \Delta T < 16$ K corresponds to the range of "natural selection" between the needlelike and plateletlike shapes of the grain. In this range, the relative number of events corresponding to the spontaneous formation of a needlelike crystal in the vicinity of the thermocouple junction with an increase in ΔT decreases from one to zero, whereas for a platelet, the relative number of such events increases from zero to one.

The grains form four main structures of nonequilibrium growth in the supercooling range under study. The growth accompanied the splitting of "finger tips" results in the formation of a developed branched structure. With an increase of ΔT, this morphology is gradually transformed into the dendritic morphology. Needlelike crystals nucleated at different sites of the thermocouple loop form packets consisting of tens of parallel needles. As a result, needles form a characteristic "parquet"-type structure (Fig. 3a), which is transformed into a planar single grain with a further increase of supercooling.

The morphological transitions between the developed branched and dendrite structures are observed in the range $0.5 < \Delta T_{12} < 1.5$ K; between the dendrite and needlelike structure, in the range $4 < \Delta T_{23} < 5$ K; and between the needlelike structure and the "structure" consisting of a single planar grain, in the range $12 < \Delta T_{34} < 16$ K. In temperature ranges ΔT_{12}, ΔT_{23}, and ΔT_{34}, both structures participating in the corresponding morphological transition are observed (Fig. 3b), and the relative volume fraction of a "warmer structure" decreases with an increase of supercooling in these ranges. The optical observations and the morphological diagram (Fig. 4) show that the first two transitions are of the gradual evolutionary character, whereas in the transition between the needles and the platelet, all the main structural and kinetic parameters of the phase transition are changed in the jumplike manner—the tip velocity v_t increases by a factor of 3–4, the number of grains equal in the needlelike structure to $N \sim 10^2$ drops down to $N = 1$ in the platelet structure, and the grain size increases by two orders of magnitude (the volume of a typical needlelike crystal is $(0.5–2) \times 10^{-2}$mm^3 and the final volume of a spontaneously grown ice plate is 0.6–0.7 mm^3). It should be emphasized that the analysis of more than 200 video films of the crystallization process in the region of the needle–platelet transition did not reveal any intermediate structures that could have indicated the gradual merging of needles (or grains of another shape) into one platelet. In other words, this morphological transition is essentially of a jumplike synergetic nature. By analogy with thermodynamic phase transitions, it was proposed [15] to classify kinetic morphological transitions as those of the first- and the second-order transitions. The first-order morphological transitions are characterized by jumplike changes in the growth rate, whereas the second-order ones, by continuous changes in the growth rate (a jump is characteristic of the derivative of the growth rate). According to this classification, the transformation of needles into a platelet is a first-order kinetic transition.

In addition, this transition is also accompanied by a jump in the fractal dimension of the structure, $D = D' + 1$, where D' is the fractal dimension of the "coastline" (the line of intersection of the solid-phase surface by a horizontal plane), which can be determined from the relation between the coastline perimeter P and the area A of the surface bounded by this coastline described by the Mandelbrot formula [17, 23]

$$P \sim A^{D'/2}. \qquad (2)$$

The analysis of video films recording the formation of the needlelike structure showed that its fractal dimension is $D = 2.41 \pm 0.08$ (it was measured using a "standard" of length $\delta = 10$ μm), whereas the fractal dimension for the platelet (nonfractal form) is $D = 2$. Thus, in the observed first-order morphological transition, the fractal geometry of the interface (Fig. 3a) is changed to the Euclidean form of an almost plane-parallel platelet with the rounded edge (Fig. 2f).

Note that the morphological transitions observed in spontaneous crystallization of a water film do not follow from specially chosen model experimental conditions. In fact, they agree, both qualitatively and quantitatively, with the results of video recording of the crystallization process in the ~10^{-2}- to 10^2 m^3-large water samples. In spite of a more complicated spatial pattern of ice grains, their shapes and kinetics correspond to the morphological diagram for a membrane.

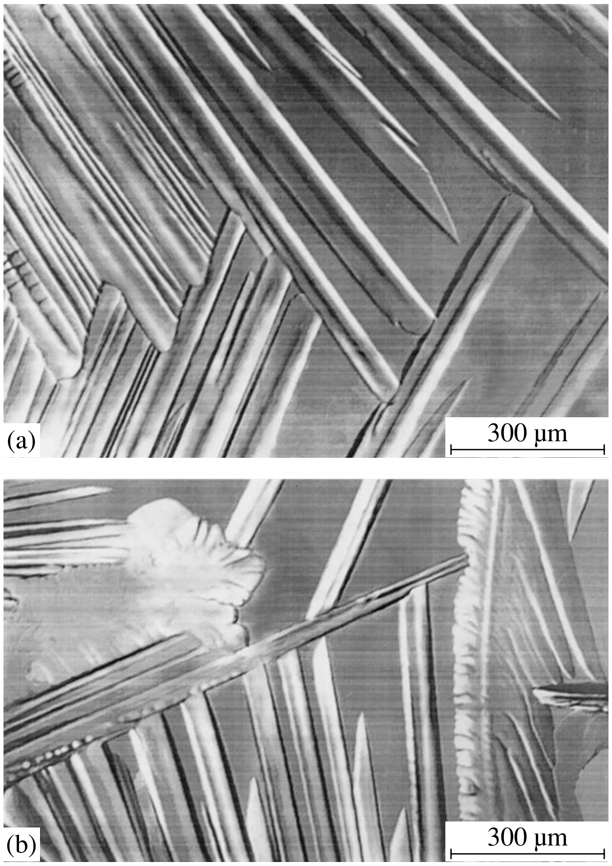

Fig. 3. Typical polycrystal structures of ice formed under the free growth conditions at various values of initial supercooling of distilled water: (a) needlelike structure, $\Delta T = 5$ K and (b) structure formed in the region between dendrites and needles, $\Delta T = 4.5$ K.

DISCUSSION

It is well known that the fundamental mechanism controlling the crystallization rate in a one-component melt is the transfer of the latent heat of phase transition from the interface into the liquid and solid phases. Under the conditions for the normal growth mechanism, the crystallization front becomes morphologically unstable and its evolution results in the formation of various polycrystal structures, in particular, dendritic ones. According to the theory of dendrite growth [9–15], the typical sequence of events at the initially unperturbed surface (planar, spherical, or cylindrical) of a crystal growing at the rate v in a supercooled melt includes the formation of protrusions oriented mainly along crystallographic directions (in water supercooled to $\Delta T \sim 1$ K, the tips of ice protrusions grow in the $\langle 11\bar{2}0\rangle$ directions [24]). Because of a higher temperature gradient in the vicinity of the protrusion tip, this tip grows faster than the unperturbed crystallization front. If the protrusion length exceeds the value of the order of a/v (where a is the thermal diffusivity of the melt), its evolution does not depend on the conditions of its formation [25] and is characterized by an almost constant growth rate of the tip v_t and its curvature radius R_t. Under the conditions of free growth, the product of these two parameters is determined by the relative supercooling θ of the melt [9, 26]. These initial ledges of the needlelike shape are unstable with respect to the formation of side branches, which, in turn, are unstable

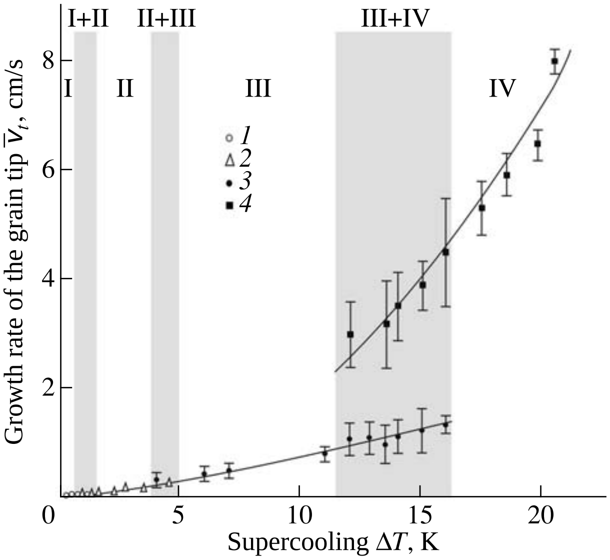

Fig. 4. Kinetic morphological diagram, that is, the dependence of average growth rate $\bar{v}_t$ of the grain tip on initial supercooling ΔT in different structures: I—developed branched structure; II—dendritic structure; III—needlelike structure; IV—“structure” consisting of a single platelet. Solid lines are the functions approximating this dependence: $\bar{v}_t = 0.05\Delta T^{1.2}$ cm/s for a needlelike crystal and $\bar{v}_t = 0.018\Delta T^2$ cm/s for a plate.

with respect to the formation of secondary branches, etc.

Video recordings of the nucleation stage in the polarized light show that the growth rate v of cylindrical (hemispherical at the thermocouple junction) crystallization front formed at the loop mouth attains about 0.3–3 mm/s by the moment of appearance of the first needlelike protrusions (in the temperature range of supercooling, $1 < \Delta T < 10$ K). The evolution of a protrusions with the size exceeding, at least, $a/v \sim 300$ μm (where $a = 1.4 \times 10^{-7}$ m^2/s is the thermal diffusivity of water at 0°C) is independent of its formation and growth conditions and is determined only by the initial water supercooling and the anisotropy in surface energy at the ice–water interface [9]. In the course of further growth, the protrusions become unstable with respect to perturbations (caused, for example, by the thermal noise [25]) and have the characteristic stability wavelength

$$\lambda_s = 2\pi\sqrt{d_0 l_T}, \tag{3}$$

where $d_0 = \gamma T_m c_p/q^2$ is the capillary length, γ is the surface energy of the ice–water interface, and $l_T = a/v$ is the characteristic length of thermal diffusion. The wavelength λ_s is characterized by the order of magnitude of the scale of instability giving rise to the formation of dendritic structure [9, 14]. A typical perturbation in the shape of the dendrite stem growing, for example, at $\Delta T = 4$ K has the form of a “wave packet” with the wavelength of 20–30 μm (Fig. 2e). Substituting $\gamma \approx 30$ mJ/m^2 [27], $T_m = 273$ K, $c_p = 4.19$ J/(kg K), and $q = 332$ kJ/ kg into Eq. (3) and taking into account the morphological diagram (Fig. 4), $v_t \approx 1$ mm/s (at $\Delta T = 4$ K) and the average growth rate of the side surface of the stem $\bar{v} \approx v_t b/L \approx 20$ μm/s (where L is the dendrite length by the moment of its distortion and b is its width at the base), we obtain the value $\lambda_s \approx 14$ μm, which agrees with the optical observations within the accuracy better than an order of magnitude. With an increase of the water temperature, the growth rate decreases and λ_s increases and, therefore, the distortion wave of the stem shape approaches to the dendrite tip. At $\Delta T < 0.5$ K, we have $\bar{v} \le 0.5$ μm/s and, according to Eq. (3), the wavelength, $\lambda_s \sim 100$ μm, becomes comparable with the curvature radius of the tip, which results in tip splitting. Thus, the evolution of the shape of first grains formed in supercooled water at $\Delta T < 5$ K is quite consistent with the predictions of the theory of dendrite growth and the experimental data obtained at relatively low values of T, $\Delta T < 1$ K, in particular, with the results of the detailed study of the evolutionary morphological transition from the developed branched to the dendritic structure under the conditions of free growth of ice in supercooled water [22]. Now, we discuss in more detail the kinetic morphological transition observed in our study at high degrees of supercooling $12 < \Delta T_{34} < 16$ K. First, consider the explosion-like formation of an ice platelet in a supercooled water film. Within the first approximation, growth of ice platelet can be assumed to be a quasi-adiabatic process with due regard for its high rate and relatively short duration ($\Delta t \sim 0.1$ s). The heat transfer between the film and the surrounding thermostat can be ignored. In fact, the ratio of the heat passed through the outer film surface due to the heat transfer obeying the Newton law during the time interval Δt and the latent heat of crystallization is described as

$$\xi = \alpha(T_s - T_0)S_2\Delta t/qm_1, \tag{4}$$

where α is the coefficient characterizing the heat transfer through a horizontal water–air interface, $m_1 = \rho_1 Sh$ is the mass of the ice platelet, $S_2 \approx 2S$ is the area of the outer surface of the film, T_s is the film temperature (close to the melting point T_m because of the released latent heat of the phase transition), and T_0 is the thermostat temperature. Taking into account that the film temperature equals $T \approx T_0$ prior to the beginning of spontaneous crystallization and substituting the typical values of the parameters: $\alpha \approx 10$ (W/m^2) K, $\rho_1 = 0.92$ g/cm^3, $S = 30$ mm^2, $\Delta t = 70$–200 μs, $h = 20$–40 μm, and $\Delta T = 12$–30 K, we obtain that $\xi \approx (3–7) \times 10^{-3}$.

Now, estimate the thickness h_a, of an ice platelet adiabatically increasing in the water film of thickness λ with the temperature $T = T_m - \Delta T$ prior to crystallization. The energy balance shows that

$$c_p \Delta T(\lambda - h_a) = q h_a \rho_1/\rho_2, \quad (5)$$

where ρ_1 and ρ_2 are the densities of ice and water, respectively. It follows from Eq. (5) that

$$h_a = \lambda\theta/(\theta + \rho_1/\rho_2). \quad (6)$$

Substituting the data of a typical experiment, $\lambda = 100\ \mu\text{m}$, $\rho_1/\rho_2 = 0.92$ into Eq. (6), we arrive at the estimate of the thickness of the adiabatic platelet, $h_a = c\Delta T$, where $c = 1.05$–$1.14\ \mu\text{m/K}$ in the range $16\ \text{K} < \Delta T < 30\ \text{K}$. This estimate agrees quite well with the empirical equation (1). In the adiabatic approximation, the cross section profile for the platelet can be estimated if one invokes the well-known problem of determination of the crystallization front propagating in a supercooled melt bounded by the heat-insulating walls. It was shown for the two-dimensional case [28] that neglecting the surface tension, one can write the equation for the crystallization front in the form of the Saffman–Taylor relationship

$$Y(X) = \frac{1-\theta}{\pi}\ln\cos\frac{\pi X}{\theta}, \quad (7)$$

where $X = 2x/\lambda$ and $Y = 2y/\lambda$ are the dimensionless coordinates (Fig. 2f). This equation provides the determination of the distribution of the normal growth rate $v_n(x, y)$ along the phase interface

$$\begin{aligned} v_n &= v_t/[1 + (Y')^2]^{1/2} \\ &= v_t/\left[1 + \left(\tan^2\frac{\pi X}{\theta}\right)(1-\theta)^2/\theta^2\right]^{1/2}. \end{aligned} \quad (8)$$

The position of the isotherm $T \approx T_m$ can be determined using the thermal diffusion length $l_T = a/v_n$. Taking into account that the velocity of the platelet tip is $v_s \sim 10$ cm/s, we can estimate the position of the zero isotherm in the vicinity of the tip for the temperature regime under study ($l_T \sim 1\ \mu\text{m}$), whereas $l_T \approx 40\ \mu\text{m}$ at the distance of 100 μm from the tip, and the front of the thermal "wave" reaches the outer surface of the film. Thus, the temperature distribution in the liquid phase is characterized by the existence of two regions: "cold" region I with temperature $T_{\text{I}} = T_m - \Delta T$ and "warm" region II with temperature $T_{\text{II}} \approx T_m$, which hinders an increase of the platelet thickness (Fig. 2f).

In the case of free dendrite growth at a negligibly low surface tension, the formula relating the velocity of the crystallization front and the relative supercooling is given by the Ivantsov function [26]

$$\theta = I\nu(p) = 2\sqrt{p}e^p \int_{\sqrt{p}}^{\infty} \exp(-X^2)dX, \quad (9)$$

where $p = v_t R_t/a$ is the thermal Péclet number equal to the ratio of tip radius of the dendrite R_t to thermal diffusion length l_T. The analysis of this function performed in [14] for different types of nonequilibrium growth at $\theta < 1$ leads to the power dependence of the velocity of the dendrite tip and the melt supercooling, $v_t = A\Delta T^n$, where $n = 1.2$ for the paraboloid of rotation, $n \approx 2$ for a planar dendrite, and A is a constant. From the morphological diagram (Fig. 4) it follows that the temperature dependence of the average velocity of the tip for the needlelike crystals in the structure under study is described quite well by the function $\bar{v}_t = 0.05\Delta T^{1.2}$ cm/s, whereas in the case of the platelet, we have $\bar{v}_t = 0.018\Delta T^2$ cm/s.

Note that the observed morphological transition from the needles and a platelet has an analog in the Saffman–Taylor problem. According to [1, 9, 23], with an increase in the pressure and velocity of a moving interface between two immiscible fluids having different viscosities in a flat channel (the Hele–Shaw cell), a pattern with several "viscous fingers" is formed. Upon the attainment of a certain critical pressure, only one finger remains, whose width is proportional to the pressure and the channel width and whose profile is given by formula (7).

Thus, on the basis of the experimental data obtained, we constructed, for the first time, the morphological diagram for nonequilibrium growth of ice in distilled water supercooled within the range $0.1\ \text{K} < \Delta T < 30\ \text{K}$ corresponding to a heterogeneous mechanism of solid-phase nucleation. It is shown that the following structures are formed with an increase in ΔT: the well-developed branched, dendrite, and needlelike structures, and also the "structure" consisting of one plane grain. It is also shown that the transition between the last two structures occurring in the range $12\ \text{K} < \Delta T < 16\ \text{K}$ is a first-order kinetic morphological transition with the jump in supercooling at the crystallization front. This transition is accompanied by jumplike changes in all the kinetic and topological parameters of the crystallization process such as the average growth rate of a grain, the exponent in the power dependence of the growth rate on supercooling, the number of grains in the structure, their average size, and the fractal dimension of the ice–water interface. It is reasonable to assume that the order parameter characterizing such a morphological transition is the deviation of the fractal dimension D of the structure from the integral value corresponding to the Euclidean form of the interface. To verify this assumption, one has to perform more detailed experimental studies of the relation between D and θ.

ACKNOWLEDGMENTS

The study was supported by the Russian Foundation for Basic Research, project no. 98-02-17054.

REFERENCES

1. P. G. Saffman and G. I. Taylor, Proc. R. Soc. London **245** (2), 312 (1958).
2. Ya. B. Zel'dovich, G. I. Barenblatt, V. B. Librovich, and G. M. Makhvaladze, *Mathematical Theory of Combustion and Explosion* (Nauka, Moscow, 1980).
3. G. Daccord, Nature, No. 325, 41 (1987).
4. J. Nittman and H. E. Stanley, Nature **321**, 663 (1986).
5. T. A. Witten and L. M. Sander, Phys. Rev. **B27**, 5686 (1983).
6. G. Caldarelli, C. Castellano, and A. Vespignani, Phys. Rev. E **49** (4), 2673 (1994).
7. G. Yu. Ivanyuk, Fiz. Zemli, No. 3, 21 (1997).
8. C. Misbah and H. Müller-Kurmbhaar, Ann. Phys. (Paris) **19**, 601 (1994).
9. J. S. Langer, Science **243** (3), 1150 (1989).
10. D. A. Kessler, J. Koplik, and A. Levine, Adv. Phys. **37** (3), 255 (1988).
11. K. Kassner, C. Misbah, H. Müller-Krumbhaar, and A. Valance, Phys. Rev. E **49** (6), 5477 (1994).
12. K. Kassner, C. Misbah, H. Müller-Krumbhaar, and A. Valance, Phys. Rev. E **49** (6), 5495 (1994).
13. J. S. Langer and H. Müller-Krumbhaar, J. Cryst. Growth **42**, 11 (1977).
14. V. Laxmanan, Acta Metall. Mater. **33** (6), 1023 (1985).
15. E. Ben-Jacob and P. Garik, Physica D (Amsterdam) **38**, 16 (1989).
16. G. Nicolis and I. Prigogine, *Self-Organization in Non-Equilibrium Systems* (Wiley, New York, 1977; Mir, Moscow, 1979).
17. B. B. Mandelbrot, *The Fractal Geometry of Nature* (Freeman, New York, 1983).
18. M. J. Feĭgenbaum, Usp. Fiz. Nauk **141** (2), 343 (1983); Los Alamos Sci. **1** (1), 4 (1980).
19. W. W. Mullins and R. F. Sekerka, J. Appl. Phys. **34** (2), 323 (1963).
20. K. Ohsaka and E. H. Trinh, J. Cryst. Growth **194**, 138 (1998).
21. N. Maeno, *The Science of Ice* (Hokkaido Univ. Press, Sapporo, 1984; Mir, Moscow, 1988).
22. K. Koo, R. Ananth, and W. N. Gill, Phys. Rev. A **44** (6), 3782 (1991).
23. J. Feder, *Fractals* (Plenum, New York, 1988; Mir, Moscow, 1991).
24. K. Nagahima and Y. Furukawa, J. Cryst. Growth **171**, 577 (1997).
25. E. Brener, H. Müller-Krumbhaar, D. Temkin, and T. Abel, Physica A (Amsterdam) **249**, 73 (1998).
26. G. P. Ivantsov, Dokl. Akad. Nauk SSSR **58** (4), 567 (1947).
27. W. B. Hillig, J. Cryst. Growth **183**, 463 (1998).
28. E. A. Brener, S. V. Iordanskiĭ, and V. I. Mel'nikov, Zh. Éksp. Teor. Fiz. **94** (12), 320 (1988) [Sov. Phys. JETP **67**, 2574 (1988)].

Translated by K. Kugel

Crystallography Reports, Vol. 46, No. 3, 2001, pp. 503–505. Translated from Kristallografiya, Vol. 46, No. 3, 2001, pp. 556–558.
Original Russian Text Copyright © 2001 by Palazhchenko, Levitskiĭ.

CRYSTAL GROWTH

Inclusions of Second Phase in Bi–Te and Bi–Se Solid Solutions

V. I. Palazhchenko and Yu. T. Levitskiĭ

Amur Institute of Integrated Research, Far East Division, Russian Academy of Sciences,
Blagoveshchensk, 675000 Russia

Received June 16, 1999; in final form, February 7, 2000

Abstract—The structures of single crystals of Bi–Te and Bi–Se solid solutions grown by zone melting have been studied by the methods of chemical and ion etching, ion bombardment, high-resolution scanning electron microscopy, and electron-probe X-ray microanalysis. It has been established that impurities enter the matrix not only in the form of individual atoms, but some enter it as inclusions of a second phase. Single crystals of the Bi–Te and Bi–Se solid solutions have two types of inclusions. *© 2001 MAIK “Nauka/Interperiodica”.*

INTRODUCTION

Doping is a common method used for modifying the properties of semimetals and semiconductors. An important problem here is the growth of uniform single crystals of doped materials without defects that can deteriorate crystal properties.

It is well known that Se and Te, elements of group VI of the Periodic System, form a limited series of solid solutions with bismuth [1]. Each Se atom in the Bi–Se alloys with the Se concentration ranging within 0.1–0.2 at. % Se increases its “electron concentration” by 0.16 electron, whereas a Te atom, by 0.6 electron under the same conditions. In other words, the doping efficiencies are $\eta_{Se} = 0.16$ and $\eta_{Te} = 0.60$, respectively [2, 3]. In both cases, lowering of the temperature increases the doping efficiencies.

The nature of the effects described above is disputable. The data obtained by various researchers are contradictory and have a low reproducibility. This is presumably caused by specific dopant distribution in the crystal bulk and probable existence of dopants in several states simultaneously.

EXPERIMENTAL

The alloys were prepared from bismuth of the trade mark Vi-000 (RTU114-59) and Te and Se of the extrapure grade. First, necessary amounts of dopants were weighed within an accuracy of ±0.01 mg on a VM-20M microanalytical balance. Then, the necessary amount of Bi calculated from the dopant weight and the desired dopant concentration (up to 0.5 at. % Te or 0.4 at. % Se) was taken. The growth containers were ampules made from molybdenum-glass washed with an acidic (hydrochloric acid with bichromate) and alkali (sodium hydroxide with potassium permanganate) solutions and then rinsed with distilled water, and dried for 30 min in a drying chamber at 650–700 K.

Then, the ampules with the charge were sealed, and placed into a rocking furnace for charge homogenization for 24 h at a temperature ranging from 700 to 750 K depending on the charge composition. The final stage of growth consisted of zone levelling performed in six–eight passages of the zone in an apparatus for horizontal zone melting. The 20- to 25-mm-thick molten zone moved with the velocity from 2 to 22 mm/h. The final cycle was performed in a ~10^{-3} Pa vacuum.

RESULTS AND DISCUSSION

As a rule, Se and Te crystals belong to the trigonal system. The atoms form helical chains parallel to the *c*-axis. Each atom has two nearest neighbors. Intrachain interactions result in the formation of the filled valence subshell with the shared electrons. Thus, there are no vacant orbitals. Both substances melt without the break of intrachain bonds, and the equilibrium melt consists of randomly oriented –Se–Se–…–Se– and –Te–Te–…–Te– chains of different lengths [4]. With a further heating of the melt, the chains of Te atoms broke into individual atoms at a temperature slightly exceeding the melting point, whereas the chains of Se atoms are preserved even at higher temperatures.

All the above leads to the conclusion that a great part of a dopant in the crystals enter the crystal not as individual atoms located at lattice points but rather as chains, clusterlike aggregates, and microscopic inclusions of a dopant or as bismuth compounds. The present study was undertaken for a direct observation of microscopic inclusions in the crystal bulk.

To visualize inclusions of the second phase, crystal cuts were polished and etched in the $HNO_3 + C_2H_5OH$ mixture in the 1 : 1 ratio. It is well known that Te inter-

1063-7745/01/4603-0503$21.00 © 2001 MAIK “Nauka/Interperiodica”

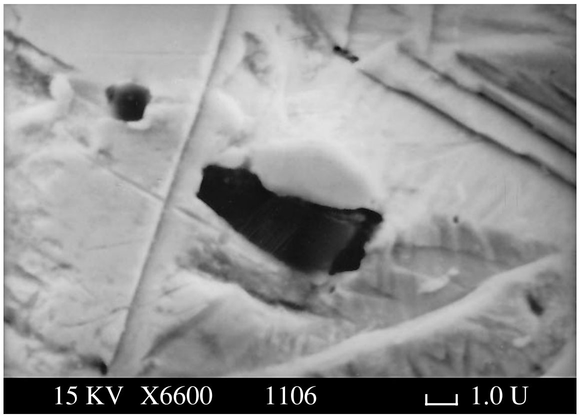

Fig. 1. An inclusion revealed in the sample of the Bi–Te system by chemical etching.

acts with nitric acid to form low-soluble TeO_2 or $Te(NO_3)_2$. Therefore, in order to remove the reaction products, the surface was additionally treated with acetone or the H_2O_2 + HCl mixture in the 1 : 1 ratio. Under the action of the above reagents, both Te and its compounds acquire black color and thus become visible (Fig. 1), which allows their primary identification.

Some preliminarily polished samples were irradiated with low-energy (100–1000 eV) Ar^+-ions in an ~1.3×10^{-3} Pa vacuum. The accelerating voltage, ion current, and exposure were selected with due regard for the sample characteristics in order to prevent its overheating and melting. Thus, we managed to reveal the structure of the inclusion boundaries in the crystal matrix (Fig. 2).

In the cleavage plane, the inclusions in Bi–Te alloys are well-pronounced hexagons (Fig. 2a); in Bi–Se alloys, inclusions have the shape of regular triangles with the ~4-μm-long sides (Fig. 2b). In both Bi–Te and Bi–Se, the microinclusion boundaries are quite clear; no mutual penetration of the matrix and inclusion was observed. A short-term chemical polishing of the sample in the Bi–Te system revealed somewhat larger (~5–6 μm in length) almost hexagonal inclusions with diffuse boundaries.

The images normal to the cleavage plane show irregular extended inclusions with diffuse boundaries (Fig. 3). Differentiation and *Y*-modulation of the signal revealed that the inclusions can penetrate the crystal bulk. The earlier observations (Fig. 2) lead to the assumption that the cross sections of inclusions (Fig. 3) are hexagons. At higher magnification, one can see that the sample was subjected to selective etching (triangular etch pits).

Most probably, the above inclusions are dopant microcrystals, because the corresponding regions on the micrographs obtained in the mode of local cathodoluminescence are enriched with the dopant. We failed to determine the elemental composition by the electron-probe microanalysis because some inclusions were too small.

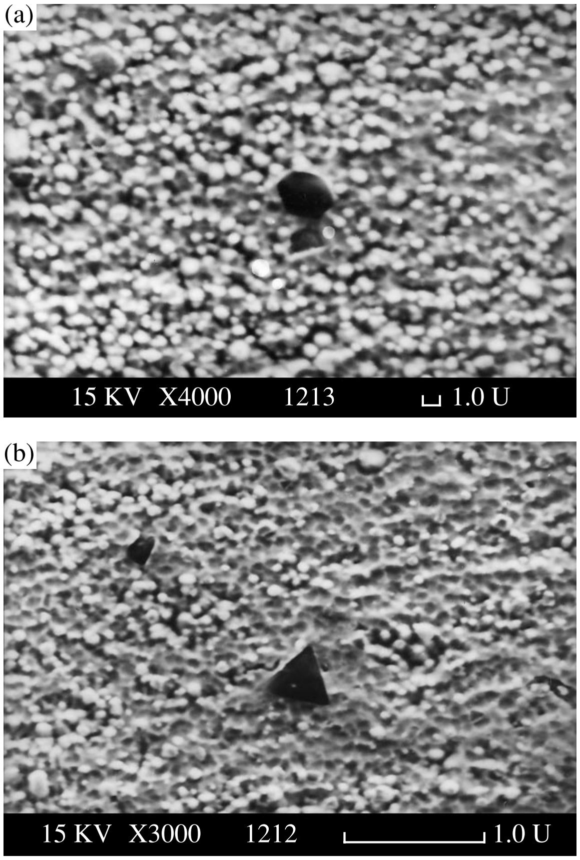

Fig. 2. Inclusions revealed in a (111)-oriented sample of (a) Bi–Te and (b) Bi–Se system by ion bombardment.

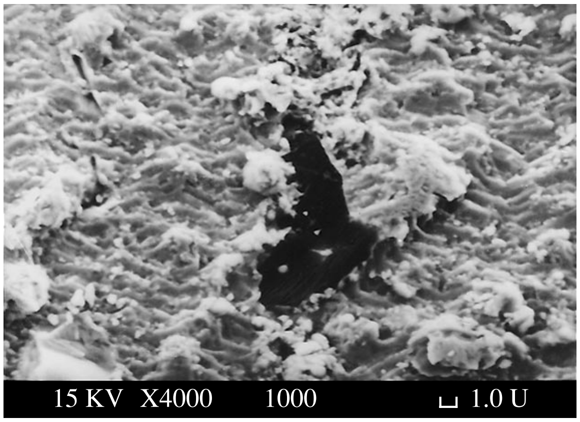

Fig. 3. An inclusion in a (110)-oriented sample of a Bi–Te alloy.

In addition to above inclusions, the Te-doped samples also had much larger second-phase inclusions. In the mode of secondary electrons, these microinclusions are almost unseen but they become visible in the mode of absorbed current sensitive to the sample composi-

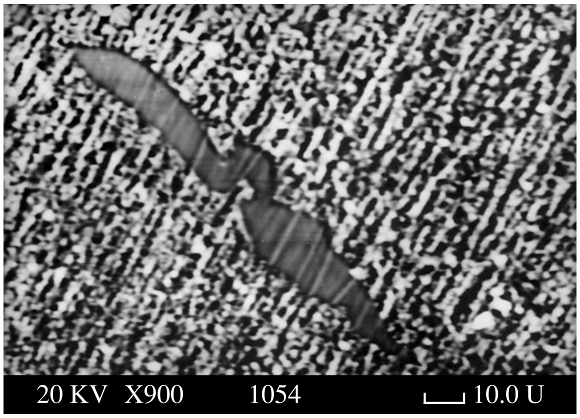

Fig. 4. An inclusion revealed in a (111)-oriented sample of a Bi–Te alloy by ion bombardment.

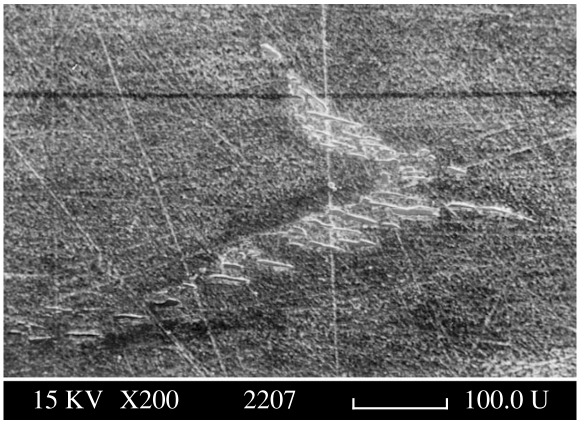

Fig. 5. A fragment of a regular pattern of microscopic inclusions in single crystals of the Bi–Te system grown at a rate of 2 mm/h.

tion. Ion etching reveals both the structure and the boundaries of the inclusions (Fig. 4). The electron-probe microanalysis showed that microinclusions are enriched with Te and have the composition close to Bi_2Te_3.

Morphology, microstructure, and the boundaries lead to the assumption that the first type of inclusions could arise even during stirring of the charge in the rocking furnace because of the separation of fractions. During the growth processes, these fractions could be trapped by the growing crystal as a mechanical impurity. Inclusions of the second type could arise as a result of the accumulation of an impurity at the growth front. It is established that the distribution of inclusions of the second type over the crystal bulk depends on the growth rate. At the growth rate 22 mm/h, the inclusions were randomly distributed over the crystal. At the growth rate 2 mm/h, the inclusions were regularly distributed over the crystal (Fig. 5). However, the volume occupied by inclusions did not depend on the growth rate: it was of the same order of magnitude in all the samples with the same dopant content.

CONCLUSION

A combination of several analytical methods (chemical etching, ion bombardment, high-resolution scanning electron microscopy, and electron-probe microanalysis) for studying of single crystals in the Bi–Te and Bi–Se systems allowed us to state that the biggest part of the dopant is incorporated into the structure not as separate atoms located in the regular lattice sites but as second-phase inclusions. Two types of inclusions have been revealed—dopant microcrystals and dopants forming a chemical compound with bismuth. The mechanism of inclusion formation is suggested.

REFERENCES

1. M. Hansen and K. Anderko, *Constitution of Binary Alloys* (McGraw-Hill, New York, 1958; Metallurgizdat, Moscow, 1962), Vols. 1, 3.
2. L. I. Mokievskiĭ and G. A. Ivanov, Zh. Tekh. Fiz. **27** (8), 1695 (1957) [Sov. Phys. Tech. Phys. **2**, 1576 (1958)].
3. N. B. Brandt, V. A. Yastrebova, and Ya. G. Ponomarev, Fiz. Tverd. Tela (Leningrad) **68** (1), 102 (1974) [Sov. Phys. Solid State **16**, 59 (1974)].
4. W. B. Pearson, *Crystal Chemistry and Physics of Metals and Alloys* (Wiley, New York, 1972; Mir, Moscow, 1977), Part 1.

Translated by A. Mel'nikova

Crystallography Reports, Vol. 46, No. 3, 2001, pp. 506–510. Translated from Kristallografiya, Vol. 46, No. 3, 2001, pp. 559–564.
Original Russian Text Copyright © 2001 by Burova, Shchedrin.

CRYSTALLOGRAPHIC SOFTWARE

On Design of Expert Systems for Processing and Interpretation of Diffraction Data

E. M. Burova and B. M. Shchedrin
Moscow State University, Vorob'evy gory, Moscow, 119899 Russia

Received April 13, 1998

Abstract—The major concepts, ideas, and methods of the theory of expert systems are shortly reviewed. The possibilities and perspective of their application to diffraction data processing are discussed. © *2001 MAIK "Nauka/Interperiodica".*

In recent decades, considerable efforts have been made to create expert and intellectual programs simulating the professional activity of a man. Expert systems can be used in those fields of man's activity or at such stages of data processing, where it is difficult to develop and use a single algorithm for solving a complex problem or where one has to use fuzzy data. The problems of processing and interpretation of the data obtained in sophisticated physical experiments can also be solved with the aid of expert systems.

Expert systems are dialogue systems using the knowledge accumulated in certain fields of knowledge for solving concrete problems. The architecture of a modern expert system is based on the clear separation of a system of facts from the inference mechanism formed by two constituent subsystems—the so-called knowledge base and inferencing machine. An important role is also played by the service components of the system—the editor of the data base and the subsystem of explanations. An essential feature of the expert system is its ability to complement the data base with new information obtained from an expert in the process of their dialogue. First, the necessity of complementing the knowledge base with new facts is analyzed; i.e., it is checked whether the fact to be introduced into the knowledge base is really new and whether it is consistent with the other facts of the base. The subsystem of explanations provides the dialogue (relation) with a user. The main goal of this subsystem is to make the performance of the program understandable to the user. All the expert systems are based on the knowledge collected in the field under study.

The main form of the knowledge representation reduces to the so-called IF–THEN relations or production rules or simply productions. Productions consist of two parts: a premise (IF) and an inference (THEN), with each of them consisting, in turn, of a combination of statements of a lower detalization level. The statements entering productions can be interpreted as elements of a certain set of events that can be treated with the aid of the mathematical apparatus of the Boolean algebra. Another possible form of knowledge representation is the use of the object–attribute–value triads, such as, e.g., mineral–color–green. This form is convenient for the knowledge fields with a large number of easily distinguishable objects sharing a multitude of attributes. The method of electronic tables was further developed in the processing of the knowledge field in the form of the so-called frames—entitled tables with slots (entitled cells, which acquire certain values in the process of operation of the inferencing machine). The knowledge can be represented by the trees of solutions. The vertices of such a graph tree are questions with enumerated possible answers. The selection of the answer determines the direction of the tree branch (graph arc) leading to the next question, which includes all the details of the problem and better approximates the problem its solution. This form is very convenient in studying objects with a hierarchic structure. Upon representing the knowledge as a graph tree, one can pass to the representation in the form of productions (Fig. 1). One more form of knowledge representation is a semantic chain, i.e., an oriented graph with the vertices corresponding to the objects (events) and the arcs describing the relationships between the vertices. However, in practice, the knowledge is represented in mixed forms: production–frame and frame–production models and frame nets. It was also assumed [1] that the possible reduction of the knowledge represented in the form of a tree of solutions to the knowledge represented in the form of productions is not accidental. Since various types of the knowledge representation deal with the objects of the same nature—knowledge—then, at a certain deep level, all the forms of the knowledge representation should become equivalent.

When designing the knowledge-based systems, the ideology of programming (Data + Algorithm = Program) is changed to the ideology Knowledge + Inference = System. Some scientists believe that such a division is quite revolutionary [1], because the knowledge is a qualitatively new form of information and is different from the data used in the traditional programming.

1063-7745/01/4603-0506$21.00 © 2001 MAIK "Nauka/Interperiodica"

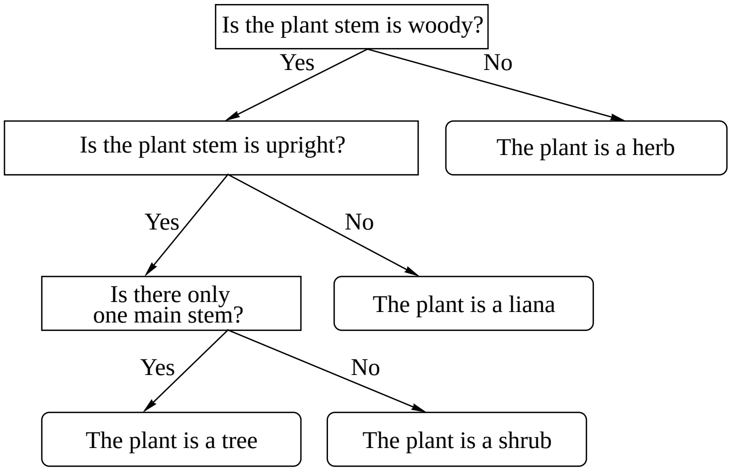

Fig. 1. A fragment of the scheme for determining the form of an object (a plant). A digital graph (solution tree) and the corresponding productions forming the knowledge base.

IF the plant stem is not woody, THEN the plant is a herb.

IF the plant stem is woody, THEN one has to indicate whether it is upright or not.

IF the stem is woody AND IS NOT upright, THEN the plant is a liana.

IF the stem is woody AND is upright AND is the only one, THEN the plant is a tree.

IF the plant stem is woody AND is upright and IS NOT the only one, THEN the plant is a shrub.

We believe that, in fact, knowledge is one of the possible types of the data and that the dialogue program for data processing, the so-called inferencing machine, is the implementation of the deductive algorithms.

An expert system should operate under the conditions of incomplete and fuzzy information. The necessity of taking into account the indeterminate character of events “forces” the theory of expert systems to invoke the probabilistic estimates. The rigorous introduction of the probabilistic measure requires the study of compatibility of events, separation of elementary events, and the study of completeness of groups of events, which, of course, encounters serious difficulties in various knowledge fields. Thus, one may ask which event is elementary for the medical notions of temperature and fever. How dependent are the two? The probabilistic estimates in the theory of expert systems are necessary not only for individual events but also to productions. The information about their values is provided by experts in the corresponding fields. These estimates can be used for ordering the calculated results.

Designing intellectual programs for processing of the data obtained in the physical experiments, one has to use the mathematical approaches to the formalization of the search and self-learning. The process of solving a problem can be interpreted as a search. In the formalization of the search, one uses such categories as rules (to handle the data) and control (to handle the rules). The transfer of the expert experience to the machine (“teaching the program”) can be technically implemented on some examples. The search is made among various conceptual models. The most sound variants are then stored in the knowledge base. In the narrow sense, the mechanism of teaching the program reduces to the storage of data together with their possible estimates. Teaching, in the broad sense of the word, is understood as improvement of the software by inductive methods with possible creation of new rules of data processing or control. The mathematical search can be described by the search space consisting of a set of states, a set of operators transforming one state into another one, and the sets of the initial and the final states. The search is based on the functions estimating the quality of the states. An important role is also played the search-space continuity.

Intellectual programs are created with the use of simulation methods. When teaching the program, one uses the methods of image recognition and classification of the algorithms with the determination of the classifying-function parameters on special sampling for teaching the program. The program is taught by adjusting the weights of “teaching rules.” If a rule successfully works on a test sampling, the degree of confidence to this rule automatically increases.

Of great interest is the adaptive algorithm suggested by Holland [2], which simulates the evolution of the data base (structures) depending on the compatibility of its components with the conditions of the program use. The algorithm operates with the strings of symbols and is used for the models of systems, where the representations in the form of the strings and substrings of symbols have sense. The structure can be interpreted as a set of the parameter values or as a condition–action rule.

The art of designing algorithms for expert systems reduces to the reasonable determination of the boundary, so that the largest part of the problem would be included into the data (knowledge base) and not into the program (the inferencing machine).

Now estimate the parameters of the expert system for diagnostics of the most widespread plants. The knowledge base was taken to be the handbook containing the information about 1500 plants in the form of 200 tables (solution trees) [3]. Using the information contained in a table, one can formulate about 20 rules (our computations). The knowledge base for diagnostics of 1500 plants consists of 4000 rules. The algorithm for the search with the use of the solution tree is independent of the inclusion of new knowledge to the knowledge base.

The design of an expert system in the structure electron diffraction structure analysis was considered in [4]. The authors managed to formulate about 40 rules and considered the corresponding examples. Thus, Rule 1 describes the form of an electron diffraction pattern from a polycrystal. Rules 14 and 23 describe the numerical relationships for squared interplanar spacings and Miller indices for base centered cubic and tetragonal structures.

It should be emphasized that a small number of the rules in the knowledge data are explained not by the fact that the development of the system is only at the initial stage but rather by the fact that the knowledge field based on the diffraction theory is well developed and is well described by a small number of the basic rules. It should also be indicated that the knowledge base is closely related to a system of questions and should answer these questions. For example, the questions of the type “what does the electron diffraction patter from a polycrystal look like,” “how can one reveal the presence of a superstructure,” and “how can one determine the lattice type” are appropriate for the data base of an electron handbook on electron diffraction. Fortunately, those who are not experts in electron diffraction are not obliged to deal with the problems of electron diffraction structure analysis. When the expert system is asked whether the specimen has a bcc lattice or not, it means that the user is interested in the direct answer just to his question and is not looking for an computer advice for checking the ratios of the squared interplanar spacings (i.e., the answer to the question whether this procedure will yield the correct sequence of integers or not).

The widespread method of studying complex objects is a system approach. In this field, the structure of an object is understood as a system of relations between the constituent parts of a complicated object. Let us analyze the structure of the problem solution on processing and interpretation of the diffraction data. The problem is solved in two main stages: the primary data processing and the interpretation of the curve obtained as a result of this processing. The solution of the problem in two stages corresponds to the use of various mathematical methods for solving each concrete problems. At the stage of primary processing, the focus is set on the statistical analysis or random errors, which is necessary for determining the systematic errors, rejection of anomalous measurements, the combination of the results measured with different accuracies, etc. At the stage of data interpretation, a parametric mathematical model of the experiments is constructed (usually a system of equations). The optimum values of the model parameters are determined with the use of the regularizing algorithms of mathematical programming for the solution, in the general case, of multidimensional problems of the global optimization.

In turn, the stage of the primary data processing in accordance with the process logic is performed in several steps: (1) statistical data processing and estimation of the measurement reliability, (2) the allowance for the background, (3) information smoothening and filtration, (4) removal of apparatus distortions, and (5) singling out the informatively important segments on the curve.

The stage of the interpretation of the curve obtained upon the primary data processing is performed in three steps: (1) estimation of the initial characteristics (curve invariants) of the models, (2) search for the best model in the class of the chosen models, and (3) verification of the interpretation of the result obtained in accordance with the initial information (comparison of the experimental data with the data obtained for the model used).

Processing and interpretation of the data obtained in a diffraction experiment has a two-tier hierarchic structure, which can be represented as a linear graph with eight vertices corresponding to the main steps of data processing. The structure is very simple in comparison with the algorithms that simulate the concrete steps.

Consider one more example—the graphical scheme of solving a problem of the phase analysis (Fig. 2). Similar to the previous example, the solution graph is also a two-tier hierarchic system. The stages of data processing are divided into seven steps of which the third one can be divided into two substeps. Some of the processing stages or steps can be implemented by several ways (with the use of various competing models, methods of estimation, computational algorithms, etc.). On the graph, to these paths there correspond arcs connecting the same pair of the vertices. In some particular cases, some of the stages or steps can be absent.

We should like to emphasize once again the simplicity of the solution scheme and the mathematical complexity of some algorithms in distinction from the complicated strongly branched solution tree with large number of arcs and a developed structure of the solution tree describing, e.g., the identification of a plant in biology or a decease in medicine at the relatively simple performance of the algorithms corresponding to the vertices of such graphs (the answers to the problems of the type: “is the trunk wooden or not” or “does the patient have a high temperature or not” which require the answer “yes” or “no.”

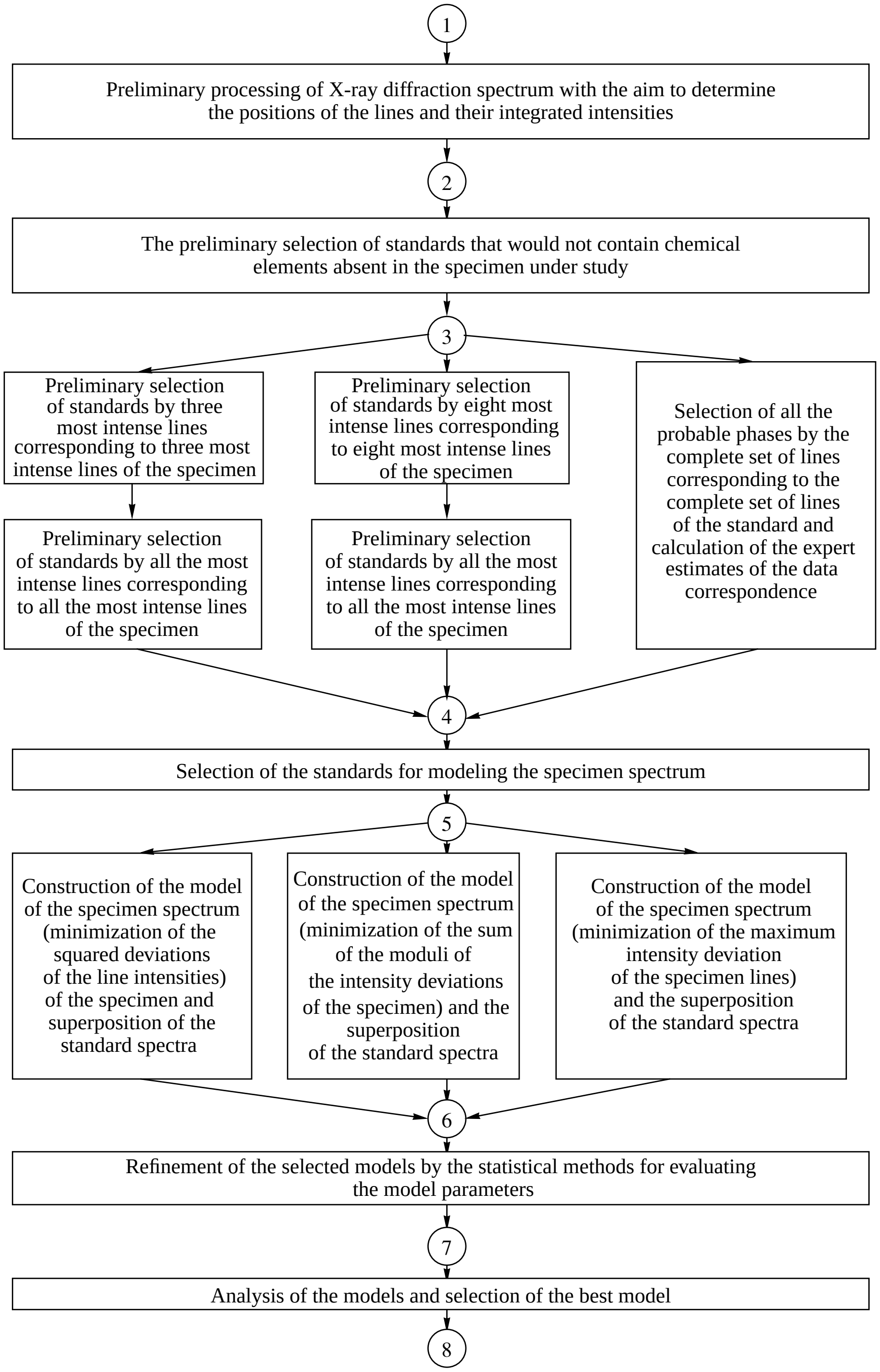

Fig. 2. Scheme of the program system for processing and interpretation of the data obtained in the X-ray phase analysis.

Upon the comparative analysis of various structures, we can state the following. In the problems with the branched solution tree, the system self-learning is attained by selecting the optimum paths along the arcs from the initial to the final conditions.

In problems characterized by solution graphs with a small number of arcs, the choice of the solution path is mathematically simple (e.g., the choice of one of the three further directions of experimental data processing, which is probably known *a priori*, because the user may be aware, e.g., of the possible texture of the specimen, so that the preliminary selection of possible phases should be made only by considering only the positions of the lines). If some processing steps are rather fast, the experimentalist can perform them all. The system should also help in comparing the results and choosing the path for the further processing. If the experimentalist can single out the classifying characteristics of the specimens studied, the system can store them together with the method of their analysis, the values of the selecting criteria, the scheme of processing, etc., and analyze the general characteristics of the series to be studied. Later, processing similar data, the user can inquire the computer and use the necessary data stored in its memory.

Usually, fuzzy data are processed and interpreted by the statistical methods still at the preliminary stage. At the stage of model-parameter estimation, they are processed by the methods of the probability theory and the mathematical statistics (including hypothesis verification). Here, there is no need to invoke the concepts and methods of the theory of expert systems at these stages, because when using fuzzy data, the theory of expert systems invokes itself the apparatus of the theory of probability and statistical methods.

Analyzing the graph of the solution structure and processing and interpreting the diffraction data, one can draw a conclusion that the characteristic feature of such problems is their separation into a comparatively small number of main stages (from two to seven in our examples) and steps which, in turn, should themselves be divided into up to five steps. Of course, processing the data of a concrete experiment, one can single out more details where the stages themselves should be divided (from one to five). Of course, when processing the data of a concrete experiment, one can give a more detailed algorithm for solution and divide the stages of processing into substages (the formation of the three-tier hierarchic level). However, the appearance of new tiers in processing a physical experiment is rather an exception than a rule. A small number of main stages, steps, etc., in a process or a phenomenon is characteristic of the science as a whole and is associated with the psychology of the human cognition. Thus, the whole time of the Earth history (4.6 billion years) is divided into only twelve main periods. Linnaeus classified all the living organisms only into two kingdoms—those of plants and animals.

The problems of processing the experimental data in natural sciences are usually solved by a small number of parallel methods (programs) consisting from one to three steps. The competing programs and methods and the principle used in practice as criteria of the uniqueness of the solution result in the “survival” of only small number of the theories, methods, and algorithms used for solving analogous problems.

The solution graph for processing and interpretating a physical experiment (Fig. 2) can readily be introduced into the program (the inferencing machine). It is hardly expedient (although possible) to include the information on several or dozens of commands indicating the sequence of the subprogram execution into a separate knowledge base.

Processing and interpreting the results of a physical experiment is not a conventional problem to be solved by an expert system. Fortunately, the development of the expert systems for processing and interpretation of the diffraction data is not the goal in itself. Usually, these problems include some subproblems solved by determined algorithms and the stages at which it is expedient to use the expert methods including the elements of self-learning and calculation of expert estimates. It is also desirable that the database would accumulate the results obtained by different methods, so that it becomes possible to compare and output the expert estimates. The analysis of a series of measurements made by one method allows one to determine the groups of specimens most appropriate for the study by this method. The analysis of the results obtained by different methods on one specimen provides the comparison of the efficiencies of these methods. This information is useful for providing recommendations on processing of analogous experimental data.

We formulated the problem of creating a self-learning system for the qualitative phase analysis of polycrystal mixtures. We have already tested some stages of the procedure and obtained quite good results. The analysis showed that similar systems can successfully operate in the structure analysis of crystals, small-angle scattering studies of globular and liquid structures, in gas electron diffraction, in the study of the structure of thin films, and in reflectometry.

REFERENCES

1. *Expert Systems. Principles and Case Studies*, R. Forsyth, Ed. (Chapman, London, 1986; Radio i Svyaz’, Moscow, 1987), p. 51.
2. J. H. Holland, *Adaptation in Natural and Artificial Systems* (Univ. of Michigan Press, Michigan, 1975), p. 217.
3. E. Lange and W. Heinrich, *Wir bestimmen Pflanzen* (Kinderbuchverlag, Berlin, 1988).
4. A. L. Tolstikhina, P. A. Artyunov, and V. V. Klechkovskaya, Kristallografiya **40** (6), 992 (1995) [Crystallogr. Rep. **40**, 918 (1995)].

Translated by L. Man

Crystallography Reports, Vol. 46, No. 3, 2001, pp. 511–519. Translated from Kristallografiya, Vol. 46, No. 3, 2001, pp. 565–574.

CRYSTALLOGRAPHIC SOFTWARE

Structure Analysis by Normalized Data.
I. Increase of Relative Accuracy of Diffraction Data

A. P. Dudka and A. A. Loshmanov

Shubnikov Institute of Crystallography, Russian Academy of Sciences,
Leninskiĭ pr. 59, Moscow, 117333 Russia

Received July 4, 2000

Abstract—A new method for obtaining physically reliable values of atomic parameters in the refinement of the structure model by the least squares method has been suggested. The method requires the use of experimental data reduced to a scale corresponding to the Bragg scattering from an ideal defect-free crystal. The reduced experimental data can be obtained by interexperimental-minimization (IEM) method—a new algorithm minimizing the difference "experiment 1–experiment 2" (between the data obtained in two experiments, 1 and 2) used in addition to the model–experiment minimization performed in the conventional least square procedure. The use of four different experimental data sets for alexandrite crystals, $Al_2BeO_4 : Cr^{3+}$, allowed us to show that the application of the IEM algorithm considerably increases the reproducibility level of the experimental data, which, in turn, increases by 30–60% the agreement between the model and the experiment. © *2001 MAIK "Nauka/Interperiodica".*

INTRODUCTION

As a rule, the parameters of a structure model in the diffraction analysis are refined by minimizing the "model–experiment difference" by the least squares (LS) method. The experimental data are usually the structure-factor modules calculated from the measured diffraction–reflection profiles. It is well known that the LS method cannot provide an unambiguous interpretation of insufficiently complete or insufficiently accurate experimental data, especially for nonlinear models [1–3]. Under these conditions, the values of the refined atomic parameters are distorted owing to mutual correlations, and the calculated standard parameter uncertainties are considerably underestimated. To reduce such distortions, one has to use the complete sets of experimental data and appropriately evaluate the measurement accuracy. The negative effect of mutual correlations between the atomic parameters can be overcome by using the correlation parameters determined prior to the main LS refinement of the structure model. This can be done using the experimental data reduced to the absolute scale corresponding to the Bragg scattering from an ideal defect-free crystal. Hereafter, the experimental data reduced to the absolute scale are called the normalized data.

In the course of conventional structure study based on the diffraction experiment, only part of the experimental information is used. The main losses in the information about various physical effects taking place during measurements are caused by recalculation of reflection profiles into the corresponding integrated intensities, which results in distortion of other parameters of the atomic model obtained in the LS refinement because of correlations between these parameters. Thus, the situation is characterized as follows:

(1) Real experimental diffraction data are distorted in comparison with the pure Bragg scattering.

(2) The model to be refined is based on the kinematical diffraction theory which fails to describe some effects or takes them into account only approximately in the form of various integrated corrections.

(3) Trying to fit the model to the experimental data using incomplete set of necessary parameters [or using mutually dependent (correlated) parameters], we obtain somewhat distorted results (the correlation effect).

(4) All the computations are performed with a weighting scheme which only approximately reflects the real accuracy of the experimental data. At the same time, each "measurements–weighting scheme" set has its own local minima of the objective function in the LS procedure [2], which results in the fact that the distortion of the refined parameters cannot be reproduced even in different runs of the experiment performed on one crystalline specimen.

As a result, it is very difficult to attain the satisfactory reproducibility of the results in the diffraction experiments. As far as we know, there are no published investigations in which the reproducibility of all the calculated parameters desirable, in terms of statistics, was attained no matter what measures were taken with this aim. The analysis of the parameter reproducibility can be made upon the statistical test of the character of the error distribution in the parameters based on the analysis of the normal-probability plot of residuals made on the "normal-probability paper" [4–6].

The loss of some experimental information, the negative effect of correlations between the parameters to be refined in the LS procedure, and the reproducibility of the results of the structure study are closely related. Obviously, one has to maximally increase the set of experimental data, on the one hand, and maximally preserve the bulk of the information obtained in the experiment, on the other hand.

One of the methods for solving this problem is suggested below. It is the so-called structure analysis by normalized data, i.e., the separation of the set of experimental data (reflection profiles) into several subsets corresponding to various characteristics of the process of radiation scattering. Thus, in order to introduce the empirical correction for the effect of thermal diffuse scattering in the isotropic approximation the average weighted velocity of sound propagation in a crystal is determined [7, 8]. This method allows one to save the information contained in the line shape (earlier, this information was lost during profile integration, which reduced the number of the parameters refined in the main LS procedure).

Another conclusion is less obvious but even more important because of the serious consequences. One has to invoke some new information to facilitate the solution of the problem associated with correlations between the parameters to be refined.

Although the correlations between the parameters to be refined in the LS procedure are of the mathematical nature, the problem also has a physical aspect. If one of the correlated parameters takes different values under different experimental conditions, then its undistorted value can be determined with a rather high accuracy. The corresponding algorithm should provide the analysis of the common and distinguishing features of the data obtained under different experimental conditions. In this case, different parameters should be refined by different experimental data.

In the structure analysis, such parameters are, first of all, the scale factor, which has different values in all the experiments, and the extinction parameters. Two sets of the data divided into scale factors can be considered as the data reduced to the absolute energy scale. Upon division into the extinction factors, the data are reduced to the common single-domain state. In a similar way, one can also pass to a twin partner in microtwinned crystals.

Thus, the additional information should be represented in the form of the second independent experimental data set. We do not mean averaging of the experimental data or the joint refinement in one procedure of the structure model using the different measurements made in [9]. Similar to the conventional LS procedure, the new algorithm varies the parameters of the theoretical model to minimize the difference between the model and the experiment and, in addition, also minimizes the difference “experiment 1–experiment 2.” In other words, a small number of parameters (most important for solving the correlation problem) are refined to minimize the difference between the data obtained in experiment 1 and experiment 2, whereas all the other parameters are refined in the basic LS procedure.

One may ask whether the gain from the use of this new algorithm is sufficient to justify obtaining the information by such a labor-consuming method. To answer this question, let us define three levels of increasing the accuracy and reliability of the results in the structural studies using the new method of structure analysis by normalized data (NDSA).

(1) To what extent does the relative accuracy of the structural results increase? The relative accuracy in the determination of the model parameters (the ratio of the sum of the parameter values to the sum of their standard uncertainties determined for the statistically significant parameters $\langle P/\sigma(P)\rangle$) can hardly be found in any publication. It is more convenient to compare the reliability factors (R) obtained in the LS procedure, because there is a one-to-one correspondence, between the reliability factor R obtained in the LS procedure and the relative accuracy of the results obtained; namely, the lower the R-factor, the higher the accuracy of the results.

(2) To what extent can the reproducibility level of the experimental data and the results obtained (the model parameters) be increased by the method structure analysis by normalized data? The corresponding estimates are obtained by using the characteristics of the normal-probability plot and the reliability factors between the experimental data and the model parameters [4, 5]. The attainment of a low R-factor in the LS procedure does not necessarily guarantee a high reproducibility of atomic parameters.

(3) To what extent are the numerical values of the calculated parameters physically reliable? We believe that the answer to this question cannot be given by the structural methods alone. Using the method of structure analysis by normalized data (NDSA), we assume that the atomic parameters are physically reliable if their values (or the values of some functions of these parameters) are well reproduced by different physical methods.

The studies were performed on lasing alexandrite crystals, $Al_2BeO_4 : Cr^{3+}$.

EXPERIMENTAL

Four experimental data sets were measured from three crystalline alexandrite specimens (Al_2). According to the growth data, alexandrite specimen I contained 0.3 at. % Cr and alexandrite specimens II and III contained 1.0 at. % Cr each. Specimens II and III had different dimensions but were cut out from the same alexandrite single crystal. The experimental conditions and the structural data were described elsewhere [10–12]. The experimental diffraction-intensity data were collected on automated diffractometers in different geometries. Orthorhombic alexandrite crystals are

Table 1. The main characteristics of experiments 1–4 for alexandrite crystals and the results obtained

Characteristic	1	2	3	4
Diffractometer	RED-4	DAR-UMB	Nonius 1	Nonius 2
Experimental geometry	Equatorial χ-ring	Equiinclined, three-circle	Equatorial, κ geometry	Equatorial, κ geometry
Specimen diameters, mm	0.37/0.31	0.21	0.43	
Cr impurity, at. %	0.3	1.0	1.0	
Absorption coefficient μ, cm^{-1}	11.29	11.48	11.48	
Unit-cell parameter, *a*, Å	9.407(4)	9.416(5)	9.4152(5)	9.4049(5)
Unit-cell parameter, *b*, Å	5.4781(5)	5.480(5)	9.4793(3)	5.4749(2)
Unit-cell parameter, *c*, Å	4.4285(3)	4.434(1)	4.4345(1)	4.4270(1)
Number of measured reflections	6256	7084	8636	12 137
$\sin\theta/\lambda_{max}$ in the refinement	1.15	1.20	1.05	1.20
Number of reflections used in refinement	1303	1137	972	1596
R-factor of averaging of, $\|F\|^2$, %	1.73	1.58	1.49	1.12

described by the sp. gr. *Pnma* with four formula units per unit cell, $z = 4$.

The intensities of X-ray diffraction reflections were measured within half-sphere of the reciprocal space, $l \geq 0$; there were four equivalent reflections, MoK_α, graphite monochromator. The experimental intensities were corrected for the Lorentz and polarization factors and for absorption by spherical specimens (the COREX complex of programs [13]). Specimen I had the shape of an ellipsoid of rotation and showed a small error in integrated intensities. Neither the program for integrated-profile analysis [8] nor our new program for averaging crystallographically equivalent reflections [13] was used. The drift in the control intensities during experiments did not exceed 1%. No corrections for thermal diffuse scattering were introduced. To check whether the new method had a negative effect on the results obtained, the primary data were processed by the standard method often used in conventional diffraction experiments.

Some characteristics of X-ray diffraction experiments and the results obtained are summarized in Table 1. Low reliability factors obtained upon averaging crystallographically equivalent reflections proved the high quality of the crystals and the experimental data obtained.

The structure model had 11 positional parameters, 28 automic-displacement parameters, two occupancy parameters for the aluminum positions, one scale factor, and one extinction parameter. For all data sets, the lower boundary was chosen to be $\sin\theta/\lambda_{min} = 0.46$ Å^{-1}, appropriate for the least square procedure in the PROMETHEUS [14] complex of programs (not using multipole models taking into account the asymmetry in the electron-density distributions).

The experimental data sets and the model structure were refined by the LS method by $|F|^2$ values, but the values of the reliability factors *R* were recalculated into $|F|$ values to provide a more reliable comparison with the previous results.

BRIEF DESCRIPTION OF THE PROGRAM ALGORITHM

The ASCALE (old version) or IEM (new version) program was considered elsewhere [3, 7, 8, 15, 16]. The main terms and expressions used to formulate the accuracy criteria for experimental data were given in [3, 16]. The IEM algorithm minimizing the "experiment 1–experiment 2" difference is based on the possibility of reducing the independent experimental data to the absolute and, first of all, to the energy scale. In other words, it is always possible to divide the structure model into the basic model and the model–perturbation.

The program requires the input of four files: two files with independent experimental data sets and the third file with the information necessary for the model refinement. The latter file also includes the command for refining all the parameters in the full-matrix variant irrespectively of the correlation level between these parameters. The fourth file contains the information necessary for the IEM program, which indicates in what way the structure model is divided into the basic model and the model–perturbation. The parameters of the model–perturbation having different values in each experiment are refined by the independent sets (e.g., those of scale factors or extinction data), whereas the remaining parameters are refined in a special way by the joint set of all the experimental data (the so-called cross set).

The programs starts with the control refinement by the independent and the averaged data sets. The main algorithm consists of four blocks which are performed in regular cycles. At the beginning of the first cycle, the independent experimental data are normalized (i.e., reduced to the absolute scale in the normalization block). In our example, normalization is reduced to the division into the corresponding scale factors and the extinction corrections.

In the statistical-test block, the normalized data are arranged in the order statistics; the intensities are averaged and attributed some weights depending on their position in the order statistics. The fraction of each independent data-set in the cross set depends on the value of the interexperimental scale factor K_w (*interfactor*) having the physical sense of the coefficient of reduction to the absolute scale. The interfactor also depends on either the characteristics of the order statistics, or, the fact how strongly the standard uncertainty of each reflection corresponds to its place in the order statistics. There is an additional possibility—one can modify all the independents data sets proceeding from the weighting scheme of the cross set.

In the third block, the basic model is refined with by the cross-set data. The parameters thus obtained are fixed and transferred to the fourth block, where they are refined in parallel by the independent data. Then, the independent data sets and the newly determined values of the parameters are transferred to the normalization block, and the second refinement cycle begins.

Thus, instead of one LS procedure of the conventional diffraction analysis, we arrive at three LS-procedures plus two blocks—the normalization block and block combining the experimental data.

NEW LEVEL OF ACCURACY IN STRUCTURAL STUDIES

The IEM procedure was designed for obtaining well-reproducible atomic-structure parameters. The *R*-factors refined in the IEM procedure are surprisingly low. The thorough consideration of the practical situation showed that the attempts to write an algorithm of searching for the minimum of the model–experiment difference, which would be more efficient than the traditional LS procedure (Newton–Gauss linearization) or the regularization methods suggested by Tikhonov [17] and Lavrent'ev and Markvardt [18, 19], could be quite successful.

Two concepts considered in this section are formulated in the following way. First, the reliability factors are considerably reduced in the course of the IEM procedure and become comparable with the those attained in other most efficient methods. Second, the cross set can be formed without any information about the theoretical model used; i.e., the cross set is not fitted to the set of the calculated structure factors.

To prove that the IEM procedure provides the attainment of a new accuracy level in the diffraction analysis, we compared various methods of increasing the accuracy in the diffraction studies. The traditional criteria for evaluating the relative accuracy of the obtained results are the reliability factor *R* upon the refinement of the structure model and the criterion *S* of the fitting quality [5].

There are two main directions for attaining better fitting of the model to the experimental data. These are the improvement of the already existing experimental methods and the creation of new models of atomic structures that more adequately describe the radiation scattering by the crystal.

Despite the design and construction of new setups based on the time-of-flight techniques in neutron scattering and the use of a powerful synchrotron radiation in X-ray scattering, the classical automated diffractometer still remains the most precise instrument for such studies and, therefore, it is hardly probable that it can be essentially improved in the nearest future. The main difficulty encountered on this path seems to be temporal limitations—it is difficult to maintain the necessary stability in the experimental conditions for more than three consecutive weeks, i.e., within the time necessary for collecting, e.g., 15 000 reflections with an accuracy providing the subsequent fitting of the model–experiment difference at a level of 1%.

A possible considerable progress in constructing an adequate model of an atomic structure is also very doubtful because of two factors: first, the general features of an atomic model applicable to many crystals have already been determined quite reliably, and, second, the description of the deviations from the ideal symmetry for each concrete crystal can improve the model–experiment agreement, but the practical use of multiparametric models in the least squares method is hindered by the difficulties associated with mutual correlations between the refined parameters.

The improvement of the methods of diffraction experiments allows one to reduce the measurement errors. On the other hand, although each new model inevitably contains a larger number of the parameters to be refined than the previous model, the reduction of the reliability factors for good models, which are consistent with the physical reality, are more serious than could have been expected because of the statistical causes only. The progress along these lines is provided by gradual improvement of the agreement between the model and the experiment.

There are several main stages in the improvement of the universal atomic model equally applicable to all the crystals. These are the allowance for (a) anomalous scattering, (b) asymmetry in the electron-density (nuclear-density) distribution, (c) possible superstructures, (d) anharmonic atomic vibrations, (e) anisotropic atomic vibrations, and (f) extinction. For alexandrite crystals, only the allowance for two latter effects and expansion of the electron density in multipoles are important. Unfortunately, the LS program used in our study did not envisage the latter procedure.

The IEM procedure processes almost a double number of the measured experimental data in comparison with the traditional methods used in diffraction analysis and, thus, provides their more adequate interpretation.

As a rule, conventional averaging of crystallographically equivalent reflections results in additional possibilities for data interpretation and reduces the reliability factors (the better agreement between the model and the experimental data). The IEM procedure is based on the use of the cross set (the experimental data set obtained upon averaging independent data sets reduced to the absolute scale). Therefore, the accuracy attained in the latter procedure is much higher than the accuracy attained by averaging a data set obtained in the same measurements. The averaged data set is only the first approximation to the cross set; the dimensions of these two sets are close, whereas the dimensions of the initial data sets are always much larger (some of the reflections in the independent data sets have no pair reflections). Therefore, it is most appropriate to compare the averaged data set with the cross-set.

The cross set perfection is evaluated by the criteria considered in [3] (interfactors K and K_w, interexperimental reliability factors R_{12} and $R_{w\,12}$, and characteristics of the normal-probability plot).

Since the cross set is the experimental data set reduced to the absolute scale, formally, the number of parameters to be refined is even less. The cross set cannot be used for refining scale factors, extinction coefficients, relative volumes of microtwin partners, and parameters responsible for distortion of the ideal crystal structure such as, the occupancies of positions by impurity atoms.

The change in the reliability factors is evaluated by rather simple formulas

$$d = 2(R_{\text{old}} - R_{\text{new}})/(R_{\text{old}} + R_{\text{new}}),$$

$$d_w = 2(R_{w\,\text{old}} - R_{w\,\text{new}})/(R_{w\,\text{old}} + R_{w\,\text{new}}).$$

The use of the statistical Hamilton tests [20] in our case would not be sufficiently justified, since they are satisfied *a priori* at the highest possible reliability level in all the variants.

Table 2 lists the reliability factors for the following four structure models: (1) isotropic atomic vibrations without the allowance for extinction, (2) an anisotropic model of atomic vibrations without the allowance for extinction, (3) isotropic atomic vibrations with the allowance for extinction, and (4) the complete model with the allowance for extinction and the anisotropy of atomic vibrations. The results of the refinement performed over the independent data sets with the use of model (4) indicate the initial level of the relative accuracy attained without the use of our algorithm. Table 3 lists the d and d_w values obtained upon the transition from simple to more sophisticated models and the calculation by the IEM procedure (the latter is averaged over the three cross-set variants). Table 4 illustrates the advantages of the IEM procedure—it compares the results of the data refinement for model (4) by the averaged data sets and the cross set.

Table 2. Reliability factors R/R_w, % obtained in the refinement of the main variants of the structure model of an alexandrite crystal calculated by independent experimental data sets

Experiment	Model			
	1	2	3	4
1	3.753/4.502	3.324/4.282	1.925/1.899	1.157/1.257
2	2.766/3.026	2.133/2.734	2.248/2.013	1.521/1.552
3	4.656/4.958	4.401/4.715	1.925/1.899	1.040/1.003
4	4.403/4.513	3.840/3.727	2.037/2.784	0.990/1.122

The crystals studied are characterized by a high degree of perfection. The specimens consist of a small number of large blocks of mosaics, which resulted in the pronounced extinction effects, so that the allowance for extinction is very important, especially for large specimen III studied in experiments 3 and 4. In other specimens, extinction plays a considerably less important role, and the transition from the isotropic to the anisotropic atomic-vibration parameters becomes more important.

The analysis of the data in Tables 2–4 leads to a conclusion that the IEM procedure increases the relative accuracy of the diffraction analysis (essentially reduces the reliability factors R by 30 to 60%) as in the transition from simple to more adequate models of the atomic structure. The reliability factors R are reduced with respect to both level obtained from the independent experiments and level obtained from the averaged data. One also has to take into account that a considerable increase in the accuracy is compared with the high accuracy level (1%) already attained. The positive changes in the results of the structural studies are associated with the successful reduction of the experimental data to the absolute scale. This is indicated by both decrease of the interexperimental R_{12}- and $R_{w\,12}$-factors and the approach of the interfactors K and K_w to their ideal values (the corresponding difference between K and K_w and the value 1.0 is as low as 0.1–0.5%).

In this paper, we repeatedly emphasized the fact that the transition to the cross set needs no information on the refined model, which follows from the program algorithm.

The most pictorial example is provided by experiments 3 and 4 made on the same specimen. Consider three operations that form an incomplete cycle of the procedure prior the use of the feedback and compare the results obtained on the averaged set and the cross-set. The first operation is the division of the integrated intensities and their standard uncertainties by a certain

Table 3. The d/d_w, % values characterizing the reduction of the R-factors in the transition from a simple model to a complicated one or the use of the IEM procedure for model 4

Experiment	1 ⟶ 2	1 ⟶ 3	1 ⟶ 4	2 ⟶ 4	3 ⟶ 4	4 ⟶ IEM
1	12/5	64/81	106/113	97/109	50/41	38/50
2	26/10	21/40	58/64	33/55	39/26	56/66
3	6/5	83/89	127/133	124/130	60/62	34/38
4	14/19	73/47	127/120	118/107	69/85	27/42

Table 4. Comparison of the reliability factors obtained in the refinement, R and R_w, and the factors of interexperimental agreement R_{12} and R_{w12}, for the averaged sets and cross sets, %

Pair	Averaged sets						Cross sets							
	N	R_{12}	R_{w12}	R	R_w	S	N	K	K_w	R_{12}	R_{w12}	R	R_w	S
1–2	1002	3.194	3.233	1.005	1.091	0.915	977	0.9968	0.9982	1.679	1.402	0.880	0.844	1.030
1–3	948	2.027	2.106	0.869	0.969	0.972	931	1.0000	1.0040	1.248	1.039	0.739	0.567	1.009
1–4	1291	2.445	2.681	0.822	0.924	0.847	1270	1.0039	1.0024	1.151	0.688	0.729	0.715	1.026
2–3	804	4.635	4.681	0.961	1.085	1.147	789	0.9994	1.0030	1.498	1.176	0.807	0.688	1.003
2–4	1118	5.194	5.193	0.974	1.078	0.969	1100	1.0003	0.9994	1.418	1.127	0.872	0.810	1.010
3–4	938	1.132	1.226	0.859	0.927	1.164	931	0.9956	1.0013	0.929	0.806	0.639	0.553	1.009

factor (number); the second operation consists in averaging the data or the creation of the cross set, and the third operation is the model refinement over the combined sets. Since the normalizing factors can be chosen arbitrarily, we can assume that they are equal to the scale factors of the independent experimental data sets.

It is seen that the main difference lies in the second operation. For the averaged data set, averaging is made with the use of the arithmetical interfactor K (the ratio of the sums of intensities). For the cross set, averaging is performed with the weighting interfactor K_w plus modification of the weighting scheme (associated with the discrepancy between the intensities of the reflections with the same Miller indices). Naturally, the fraction of each of the independent data set in the combined data set depends on the interfactor value; for the cross set, this value is calculated in the course of the verification of the statistical hypothesis; i.e., it requires the invocation of some additional information.

Table 5. Relative change in the data (cross sets) and the atomic vibrational parameters for five cycles of the IEM procedure, %

Pair	Cross sets		Parameters	
	R_{12}	R_{w12}	R_{12}	R_{w12}
1–2	0.069	0.079	1.098	1.626
1–3	0.115	0.121	1.655	2.469
1–4	0.185	0.194	0.808	1.419
2–3	0.060	0.064	0.462	0.952
2–4	0.029	0.035	0.093	0.231
3–4	0.134	0.132	0.852	1.320

Now proceed to the refinement of the structure model. As was to be expected, the above operations do not change either the model parameter or the reliability factors R in the refinement by the averaged data set: R/R_w = 0.859/0.927 and $R_{12}/R_{w\,12}$ = 1.132/1.226 (cf. with the data in Table 2). The only varying quantities are the interfactor K and the energy-scale factor of the refinement. For the cross set used in the first cycle, we have R/R_w = 0.827/0.878 and $R_{12}/R_{w\,12}$ = 1.076/0.912. The additional normalization to the extinction yields R/R_w = 0.741/0.729 and $R_{12}/R_{w\,12}$ = 0.954/0.796.

Similar results were also obtained for all the other pairs of experiments and not only for alexandrite but also for some other crystals [3, 16]. Thus, we made the following conclusions: an increase of the relative accuracy of the results is caused by new possibilities in interpreting the experimental data provided by the correct value of the interfactor (the reduction of the data to the absolute scale) and the choice of the optimum weighting scheme. All the modifications of the data are based on their mutual correspondence and the verification of the character of their error distributions.

In processing the cross set, most criteria were considerably improved even in the first cycle. The use of the positive feedback considerably improves the agreement between the experimental data; in this case as well, no data on the model were used. In the following cycles, the main changes are associated with the redistribution of reflection positions in the order statistics (the initial positions determined by the standard uncertainties of the intensities cannot be set exactly).

Earlier [3], we considered the theoretical foundation of the procedure for determining the values of the resid-

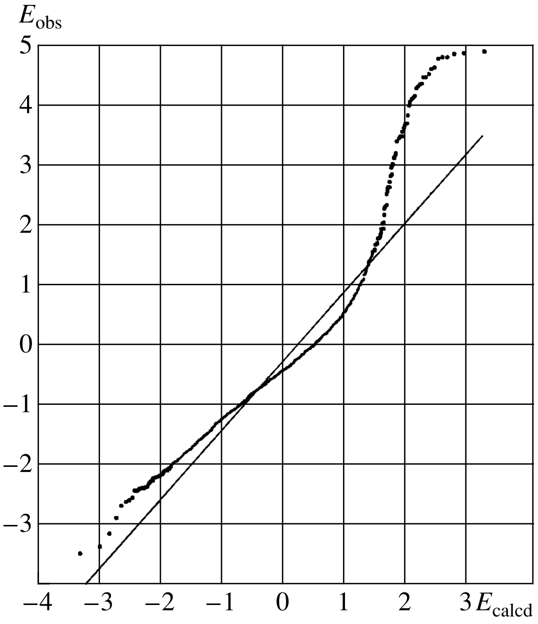

Fig. 1. Normal-probability plot for the data obtained in experiments 2 and 4 (dots) and its linear interpolation prior to the use of the IEM procedure.

ual errors in the atomic parameters and showed that these errors in the parameters of the model–perturbation are determined only by the random errors in the experimental data. When describing the algorithm of the program, we indicated that the modification of the experimental data depends only on the reflection position of in the order statistics.

Finally, the last argument in favor of the method suggested above is that it is the model that is considerably changed during the procedure and not during the experimental data. This statement can readily be verified by the reproducibility test (in this case, the difference test) for the model parameters (the so-called *P*-test) and the experimental data (the so-called *M*-test) for the first and the last cycles of the procedure. Table 5 gives the integrated characteristics of the relative changes in the data (cross sets) and the parameters of atomic vibrations for cycles 1 and 5 (the procedure converges within three to five such cycles). The changes in the positional parameters in the course of the procedure are insignificant—0.002–0.005%. The results obtained indicate that during the procedure, the model is considerably modified, whereas the experimental data are changed insignificantly.

The most obvious changes in the accuracy of the experimental data are demonstrated with the aid of the *M*-test (the dependence of the normalized experimental error $E_{obs} = I_1 - K_w I_2)/\sigma(I)$ on the normalized theoretical error in E_{calcd}). Figure 1 illustrates the comparison of experimental data sets 2 and 4. For a more compact representation, the peripheral part of the plot with large experimental errors is cut out. Specimens II and III having the same composition but considerably different dimensions (extinction absorption) were studied on diffractometers of different geometries (different shape of the scanned volumes). Therefore, it is not surprising that the plot in Fig. 1 shows considerable systematic differences between different measurements. In a similar way, the systematic discrepancies were also revealed with the aid of the *P*-test for the parameters of

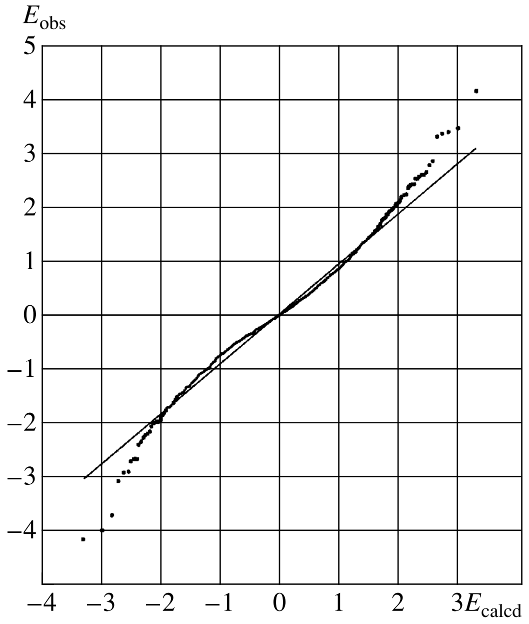

Fig. 2. Normal probability plot for the normalized data obtained in experiments 2 and 4 (dots) and its linear interpolation upon the application of the IEM procedure.

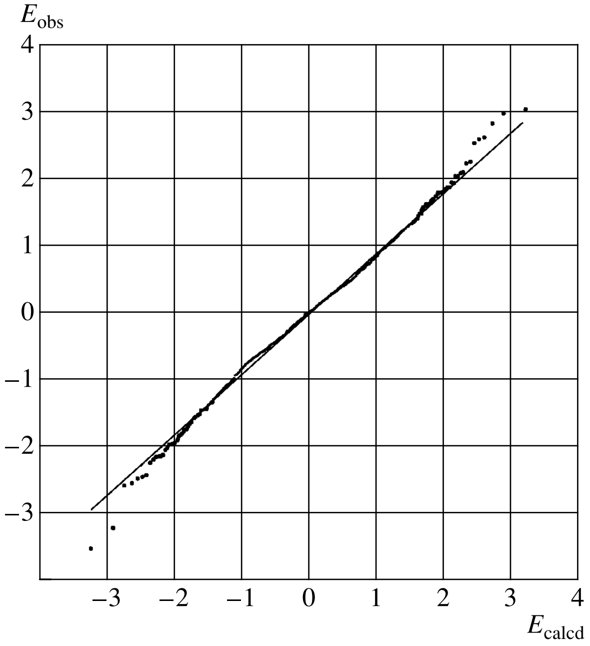

Fig. 3. Normal probability plot for cross set 24 and cross set 13 and its linear interpolation.

the model obtained independently using these experimental data sets. Upon the IEM procedure (determination of the appropriate values of the scale factors and the extinction corrections without modifying the weighting scheme for the independent experimental data), the curve in Fig. 2 becomes a straight line. The cross set 24 thus formed possesses an elevated accuracy and reproducibility in comparison with the initial data, which is seen from its comparison with cross set 13 obtained absolutely independently from the other pair of experiments 1 and 3 (Fig. 3). It is very important that the second-order cross sets are characterized by an extremely high relative accuracy: the structure refinement yields $R/R_w \sim 0.55/0.45\%$ over 750–900 reflections.

Thus, the use of the IEM procedure considerably increases the relative accuracy of the results obtained in the X-ray diffraction analysis. A better agreement between the model and the experiment is attained due to attributing higher weights to the more accurate measurements and, as a consequence, the changes of the model parameters to be refined.

CONCLUSIONS

One of the main methods of the experimental science consists in the variation of the parameters of theoretical models with the aim to attain the maximum possible agreement between the model and the experiment. The explanation of the high efficiency of the algorithm of the structure analysis by normalized data (NDSA) is the use of noncoplanar vectors and minimization of the differences between of the data obtained in experiment 1 and experiment 2.

The minimization of the interexperimental difference is attained due to reduction of the experimental data to the absolute scale. The better the agreement between different measurements, the more favorable effect they produce on the parameters to be refined and normalization of the experimental data. The independence of the measurements and the use of the laws of mathematical statistics are absolutely necessary in order to avoid or maximally decrease the systematic error potentially present in the experimental data so that they could not produce any considerable effect on the final results. The use of all the normalized independent experimental data allows one to form a set of measured data which has the accuracy higher in comparison with the accuracy of the initial experimental data. The refinement of the structure model using such a cross set necessarily results in a considerable reduction of the reliability factors.

Obviously, the algorithm suggested above is more successful in searching for the global minimum of the model–experiment difference than the LS method and determines the solution different from that obtained in the LS procedure. The IEM procedure uses the algorithm for the gradual transition to a deeper local (or global) minimum within only three to five cycles.

A small fraction of the most important parameters of the theoretical model is varied in two parallel LS refinement procedures performed with the use of the independent sets of experimental data in such a way that the measured data normalized to these parameters would best agree with one another (the so-called experiment 1–experiment 2 fitting). The remaining parameters of the model are calculated automatically and unambiguously from the experimental data set obtained by averaging the independent normalized data sets (the cross set).

In this study, we used four sets of experimental data in order to compare the results of the refinement of the structure-model parameters of alexandrite crystals ($Al_2BeO_4 : Cr^{3+}$).

(1) It has been shown that the relative accuracy of the results of the diffraction analysis (in the form of the integrated value of the model–experiment reliability factors) increases from 30 to 60% in comparison with the data obtained from the initial experimental data.

(2) The LS refinement of the structure model with 41 parameters performed by combined pairwise experimental data (cross sets) is characterized by low values of the reliability factors: R/R_w = 0.880/0.844, 0.739/0.567, 0.729/0.715, 0.807/0.688. 0.872/0.810, and 0.639/0.553% determined over 997, 931, 1270, 789, 1100, and 931 reflections, respectively. An extremely high relative accuracy is provided by the second-order cross sets: $R/R_w \sim 0.55/0.45\%$ determined over 750–900 reflections.

(3) The use of the algorithms of the structure analysis by normalized data dramatically increases the reproducibility of the experimental data: on average, the interexperimental reliability factors are reduced from $R_{12} \sim 2$–4% to $R_{12} \sim 1.0$–1.4%. The IEM procedure can be considered as a method additional to all the other well-known experimental and computational methods and can be used for attaining high relative accuracy. In other words, if there is an experiment for which one has to minimize the model–experiment difference, then, irrespectively of the quality of the equipment and the mathematical model used, the application of the IEM procedure considerably reduces the fitting criteria in comparison with the best results attained earlier by other methods. The procedure suggested here can be used not only in the diffraction analysis of crystals but also in other fields of natural sciences.

ACKNOWLEDGMENTS

The authors are grateful to V.I. Simonov, V.N. Molchanov, P.A. Verin, and B.A. Maksimov for their help in making measurements and to M.Kh. Rabodanova for the discussion of the results and useful remarks.

REFERENCES

1. L. A. Muradyan, S. F. Radaev, and V. I. Simonov, *Methods of Structure Analysis* (Nauka, Moscow, 1989), p. 5.
2. B. M. Shchedrin, I. N. Bezrukova, and E. M. Burova, in *Library of Programs for Study of Structure and Properties of Materials by Diffraction Methods* (Mosk. Gos. Univ., Moscow, 1987), p. 3.
3. A. P. Dudka, A. A. Loshmanov, and B. A. Maksimov, Kristallografiya **43** (4), 613 (1998) [Crystallogr. Rep. **43**, 565 (1998)].
4. S. C. Abrahams and E. T. Keve, Acta Crystallogr., Sect. A: Cryst. Phys., Diffr., Theor. Gen. Crystallogr. **A27**, 157 (1971).
5. *International Tables for X-ray Crystallography* (Kynoch Press, Birmingham, 1974), Vol. 4.
6. D. Schwarzenbach, S. C. Abrahams, H. D. Flack, *et al.*, Acta Crystallogr., Sect. A: Found. Crystallogr. **A45**, 63 (1989).
7. A. P. Dudka, A. A. Loshmanov, and B. A. Maksimov, in *Proceedings of the 2nd National Conference on Application of X-rays, Synchroton Radiation, Neutrons, and Electrons for Study of Materials (RSNÉ-99), Moscow, 1999*, p. 33.
8. A. P. Dudka, A. A. Loshmanov, and B. A. Maksimov, Poverkhnost’, No. 2, 2833 (2001).
9. J. K. Maichle, J. Ihringer, and W. Prandi, J. Appl. Crystallogr. **21**, 22 (1988).
10. A. P. Dudka, B. K. Sevast’yanov, and V. I. Simonov, Kristallografiya **30** (3), 480 (1985) [Sov. Phys. Crystallogr. **30**, 277 (1985)].
11. M. Kh. Rabadanov and A. P. Dudka, Neorg. Mater. **33** (1), 56 (1997).
12. M. Kh. Rabadanov and A. P. Dudka, Kristallografiya **43** (6), 1049 (1998) [Crystallogr. Rep. **43**, 991 (1998)].
13. A. P. Dudka and A. A. Loshmanov, Kristallografiya **35**, 38 (1990) [Sov. Phys. Crystallogr. **35**, 20 (1990)].
14. U. Zucker, E. Perenthaler, W. F. Kuhs, *et al.*, J. Appl. Crystallogr. **16**, 398 (1983).
15. A. P. Dudka and A. A. Loshmanov, in *Proceedings of the National Conference on Application of X-ray, Synchroton Radiation, Neutrons, and Electrons for Study of Materials (RSNÉ-97), Dubna, 1997*, p. 89.
16. A. P. Dudka, A. A. Loshmanov, and B. P. Sobolev, Kristallografiya **43** (4), 605 (1998) [Crystallogr. Rep. **43**, 557 (1998)].
17. A. N. Tikhonov and V. Ya. Arsenin, *Solutions of Ill-posed Problems* (Halsted Press, New York, 1977; Nauka, Moscow, 1979, 2nd ed.).
18. M. M. Lavrent’ev, *About Some Ill-posed Problems in Mathematical Physics* (Nauka, Novosibirsk, 1962).
19. D. W. Markvardt, J. Soc. Ind. Appl. Math. **11**, 431 (1963).
20. W. C. Hamilton, Acta Crystallogr. **18**, 502 (1965).

Translated by L. Man